ENCLOSURE 2

MFN 08-072

GEH Licensing Topical Report NEDO-32176, Revision 4,
TRACG Model Description, January 2008

Non-Proprietary Version

IMPORTANT NOTICE

This is a non-proprietary version of the document NEDE-32176P, Revision 4, from which the proprietary information has been removed. Portions of the document that have been removed are identified by white space within double square brackets, as shown here [[ ]].

HITACHI

GE Hitachi Nuclear Energy

3901 Castle Hayne Road, Wilmington, NC 28401

NEDO-32176
Revision 4
eDRF-0000-0050-3622
Class I
January 2008

Licensing Topical Report

TRACG MODEL DESCRIPTION

NON-PROPRIETARY NOTICE

This is a non-proprietary version of the document NEDE-32176P, Revision 4, from which the proprietary information has been removed. Portions of the document that have been removed are identified by white space within double square brackets, as shown here [[ ]].

IMPORTANT NOTICE REGARDING CONTENTS OF THIS REPORT

PLEASE READ CAREFULLY

The information contained in this document is furnished solely for NRC use in understanding the TRACG model in support of assessing and approving applications of the TRACG Code. The only undertakings of GEH with respect to information in this document are contained in contracts between GEH and participating utilities, and nothing contained in this document shall be construed as changing those contracts. The use of this information by anyone other than those participating entities and for any purposes other than those for which it is intended is not authorized; and with respect to any unauthorized use, GEH makes no representation or warranty, and assumes no liability as to the completeness, accuracy, or usefulness of the information contained in this document.

TABLE OF CONTENTS

TABLE OF CONTENTS

TABLE OF CONTENTS

TABLE OF CONTENTS

TABLE OF CONTENTS

TABLE OF CONTENTS

TABLE OF CONTENTS

LIST OF FIGURES

LIST OF FIGURES

LIST OF FIGURES

LIST OF FIGURES

LIST OF TABLES

LIST OF TABLES

Abstract

This document provides a description of the models in TRACG. TRACG is a computer code for the prediction of boiling water reactor transients ranging from simple operational transients to design basis loss-of-coolant accidents, stability and anticipated transients without scram. TRACG incorporates a two-fluid thermal-hydraulic model for the reactor vessel, the primary coolant system and the containment and a three-dimensional kinetics model for the reactor core. The physical models and the numerical scheme are described in this report. The basic conservation equations and their solution are detailed, and the models needed for the closure relationships are described.

Revision 1 was expanded to include detailed descriptions of the models and correlations used in the code. Thesed additional details included the technical basis and assumptions, implementation details and range of applicability for each correlation. Revision 2 limited the scope of TRACG to BWR/2-6 and ABWR. Revision 3 expands the scope of TRACG to include ESBWRs and containment modeling. Revision 4 incorporates errata and minor format changes and corrects typographical errors. Changes are marked by revision bars in the right margin. Specific changes are noted in Section 1.6: Enhancements in Revision 4.

1.0 INTRODUCTION

TRACG is a GE Hitachi Nuclear Energy (GEH) proprietary version of the Transient Reactor Analysis Code (TRAC)[1],[2]. It is a best-estimate code for analysis of boiling water reactor (BWR) transients ranging from simple anticipated operational occurrences (AOO) transients to design basis loss-of-coolant accidents (LOCAs), stability and anticipated transients without scram (ATWS).

1.1 Scope and Capabilities

TRACG is based on a multi-dimensional two-fluid model for the reactor thermal hydraulics and a three-dimensional neutron kinetics model for the reactor core.

The two-fluid model used for the thermal hydraulics in TRACG is fundamentally the same as the basic two-fluid model in TRAC-PF1[2] and TRAC-BF1[1]. The two-fluid model solves the conservation equations for mass, momentum and energy for the gas and the liquid phases. TRACG does not include any assumptions about thermal or mechanical equilibrium between the phases. The gas phase may consist of a mixture of steam and noncondensable gases, and the liquid phase may contain dissolved boron. The thermal-hydraulic model is a multi-dimensional formulation for the vessel component and a one-dimensional formulation for all other components.

The conservation equations for mass, momentum and energy are closed through an extensive set of basic models consisting of constitutive correlations for shear and heat transfer at the gas/liquid interface as well as at the wall. The constitutive correlations are flow regime dependent, and are determined based on a single flow regime map, which is used consistently throughout the code.

In addition to the basic thermal-hydraulic models, TRACG also contains a set of component models for BWR components, such as recirculation pumps, jet pumps, fuel channels, steam separators and dryers. TRACG, furthermore, contains a control system model capable of simulating the major BWR control systems such as the pressure, level and recirculation flow control systems.

The three-dimensional kinetics model is consistent with the GEH BWR core simulator PANACEA[3],[20]. It solves a modified one-group diffusion model with six delayed neutron precursor groups. Feedback is provided from the thermal-hydraulic model for moderator density, fuel temperature, boron concentration and control rod position.

The TRACG structure is based on a modular approach. The TRACG thermal-hydraulic model contains a set of basic components, such as pipe, pump, valve, tee, channel, jet pump, steam separator, heat exchanger and vessel components. System simulations are constructed using these components as building blocks. Any number of these components may be combined. The number of components, their interaction as well as the detail in each component, are specified through code input. TRACG consequently has the capability to simulate a wide range of facilities, ranging from simple separate effects tests to complete BWR plants.

TRACG has been extensively qualified against separate effects tests, component performance data, integral system effects tests and full-scale BWR plant data. Some of the

qualification for the basic models against separate effects tests and component qualification against BWR component performance data are included in this report. The purpose of this qualification is to demonstrate the applicability of the basic models in TRACG and to quantify the model uncertainty. Additional separate effects and component qualification as well as the qualification against integral system effects tests and actual plant data are reported in the TRACG qualification reports[4],[5],[6].

1.2 Background

TRAC was originally developed for pressurized water reactor (PWR) analysis by Los Alamos National Laboratory (LANL), the first PWR version of TRAC being TRAC-P1A[9]. The development of a BWR version of TRAC started in 1979 in close cooperation between GEH and Idaho National Engineering Laboratory. The objective of this cooperation was the development of a version of TRAC capable of simulating BWR LOCAs. The main tasks consisted of improving the basic models in TRAC for BWR applications and in developing models for the specific BWR components. This work culminated in the mid eighties with the development of TRACB04 at GEH (see References [11] through [17]) and TRAC-BD1/MOD1[10] at INEL, which were the first major versions of TRAC having BWR LOCA capability. Due to the joint development effort, these versions were very similar, having virtually identical basic and component models. The GEH contributions were jointly funded by GEH, the Nuclear Regulatory Commission (NRC) and Electric Power Research Institute (EPRI) under the REFILL/RE-FLOOD and FIST programs.

The development of the BWR version has continued at GEH since 1985. The objective of this development was to upgrade the capabilities of the code to include transient, stability and ATWS applications. During this phase, major developments included the implementation of the three-dimensional kinetics model and an implicit integration scheme into TRAC. The simulation of the BWR fuel bundle was also improved. TRACG was the end result of this development.

This document is intended to be a complete, stand-alone description of TRACG. Because of their common ancestry, a number of sections are similar to those for other versions of TRAC, notably TRAC-BF1. Major differences between TRACG and TRAC-BF1 are discussed in APPENDIX A.

1.3 Enhancements in Revision 1

Revision 1 of this report expanded the scope of the report to provide additional details on the models and correlations. This was done so that this report could also serve the purpose of a *Models and Correlations Report* as defined in the Compendium of ECCS Research for Realistic LOCA Analysis, NUREG-1230[18]. The expanded documentation supports the Code Scaling, Applicability and Uncertainty Methodology[19] used for the application of best-estimate computer codes. According to NUREG-1230, the objectives of the documentation on the models and correlations are to:

- Provide detailed information on (the quality of) the closure equations (i.e., on correlation models and/or criteria used in the code).
- Describe how these closure equations are coded in the program and (to) assure that what is coded is indeed, what the code uses.
- Provide a technical rationale and justification for using these closure relations in

the range of interest to nuclear power plant (NPP) safety evaluations.

These objectives are to be met by providing the following information on each model/correlation:

1. The original correlation:
    a) Source or reference
    b) Database
    c) Accuracy
    d) Applicability to NPP conditions
2. Assessment of effects if the model/correlation is applied outside its database.
3. Implementation of the model/correlation in the code.
4. Description of modifications required to overcome computational difficulties.
5. Assessment of effects of implementation and/or modification on code overall applicability and accuracy.

Table 1-1 shows where these requirements have been addressed in Sections 6.0 and 7.0. It is not practical to address the assessment of the code in detail in the Model Report. For this purpose, different versions of the *TRACG Qualification Licensing Topical Report (LTR)*[4],[5],[6] are frequently referenced. Each revision number of the *TRACG Qualification LTR* corresponds to the same revision number of this *TRACG Model LTR*. Additional qualification that is relevant to the ESBWR is contained in References [7] and [8].

In addition to the expanded documentation of the models and correlations, Revision 1 also included descriptions of new models that were required by the SBWR program that was at the time being reiviewed by the NRC staff. These new models included:

- Capability for multiple noncondensable gas species (Section 3.1). Previously only one gas could be treated in addition to steam.
- A correlation (Forster-Zuber) for pool boiling (Section 6.6.4).
- The Kuhn-Schrock-Peterson correlation for condensation in the presence of noncondensables (Section 6.6.11).
- The Uchida correlation as an option for condensation heat transfer from walls in the presence of noncondensable gases (Section 6.6.11).
- An interpolation method for the calculation of the degradation factor for heat transfer to different species of noncondensable gases (Section 6.6.11).

1.4 Enhancements in Revision 2

Revision 2 of this report was intended to support the application of TRACG to operating BWRs. Models not applicable to operating BWRs were removed.

1.5 Enhancements in Revision 3

Revision 3 of this report expands the scope of TRACG to include the ESBWR in addition to all operating BWRs. Thus, the applicability of TRACG includes BWR/2-6, ABWR and ESBWR. Revision 3 includes a number of new models and upgrades to several existing models

in order to improve the application of TRACG to LOCA and ATWS. The major additions and changes to the models are:

- Replace the 3D neutron kinetics model with a model based on PANAC11[20];
- Add the ANS decay heat models[21],[22];
- Implement a quench front model for fuel rods and channel box;
- Improve the implemenation of the hot rod model for the fuel channel component;
- Add the Shumway model[23] for the minimum stable film boiling temperature;
- Enhance the entrainment model to give better agreement with data;
- Enhance the flow regime map to give better void fraction predictions for low pressure;
- Revise the default fuel rod conductivity to be consistent with PRIME[24];
- Modify the Zircaloy oxidation rate to be consistent with the latest version of the Cathcart & Pawel correlation[25];
- Add default pump homologous curves that are more representative of large pumps;
- Improve the model for convective heat transfer at a free liquid-vapor surface;
- Improve condensation heat transfer correlations;
- Improve model for reactivity impact of soluble boron.

Of these changes, only the PANAC11 kinetics implementation has any significant impact on the previously approved applications for AOO transients; stability and ATWS overpressure events for TRACG[26],[27]. The remaining changes primarily affect and improve the application of TRACG for LOCA and ATWS with application of the standby liquid control system.

1.6 Enhancements in Revision 4

Revision 4 of this report incorporates errata previously submitted to the NRC and makes corrections to a number of equations in the models. The major corrections to the models are:

- Change the mass flux at which Biasi correlation is used from 300 kg/(m^2s) to 200 kg/(m^2s). (Section 6.6.6)
- Add a paragraph to discuss test data from PANDA pertaining to the wetwell gas space. (Section 7.11.2)
- Delete extraneous second paragraph. (Section 7.11.7.5)
- Correct definition of M_g^2 in Equation (9.1-9). (Section 9.1.1)
- Eliminate the qualifier “five” regarding number of decay heat group fractions. (Section 9.3.1)
- Change values of constants x_a and x_b from unity to x_a=2 and x_b=1 based on lattice evaluations. (Section 9.5.1)
- Correct Equation (C.1-16) representing the default correlation for thermal conductivity for unmolten UO2 when PIRT227 < 1.0 as well as the definition of its terms. (Section C.1.4)

- Clarify that stainless steel properties for the specific heat are not taken from the GE Plant Materials Handbook. (Sections C.6 and C.7)
- Correct Equations (C.6-2) and (C.7-2) used for calculating specific heat of stainless steel. (Sections C.6.2 and C.7.2)
- Update References [6] and [8]. (References Section)

Table 1-1. NUREG-1230 Requirements

Requirement	TRACG Section
1. The original correlation: a. Source or reference b. Database c. Accuracy	Technical Basis and Assumptions
d. Applicability to NPP conditions	Applicability
3. Implementation of the model/correlation in the code. 4. Description of modifications required to overcome computational difficulties.	Implementation
2. Assessment of effects if the model/correlation is applied outside its database. 5. Assessment of effects of implementation and/or modification on code overall applicability and accuracy.	Assessment

2.0 MODULAR STRUCTURE

TRACG has a modular structure and flexible geometry capability. It contains a set of basic thermal-hydraulic components, such as vessel, channel, pipe and tee components. These components are then used as building blocks to construct the system simulation. An example is shown in Figure 2-1, where a BWR/6 reactor vessel is simulated with the TRACG components. (This figure is shown for illustrative purposes. Details of the BWR nodalization and the rationale can be found in the companion *TRACG Qualification LTR*[4],[5],[6].) The components can be connected through flow paths or heat transfer paths. The components are described in detail in Section 7.0.

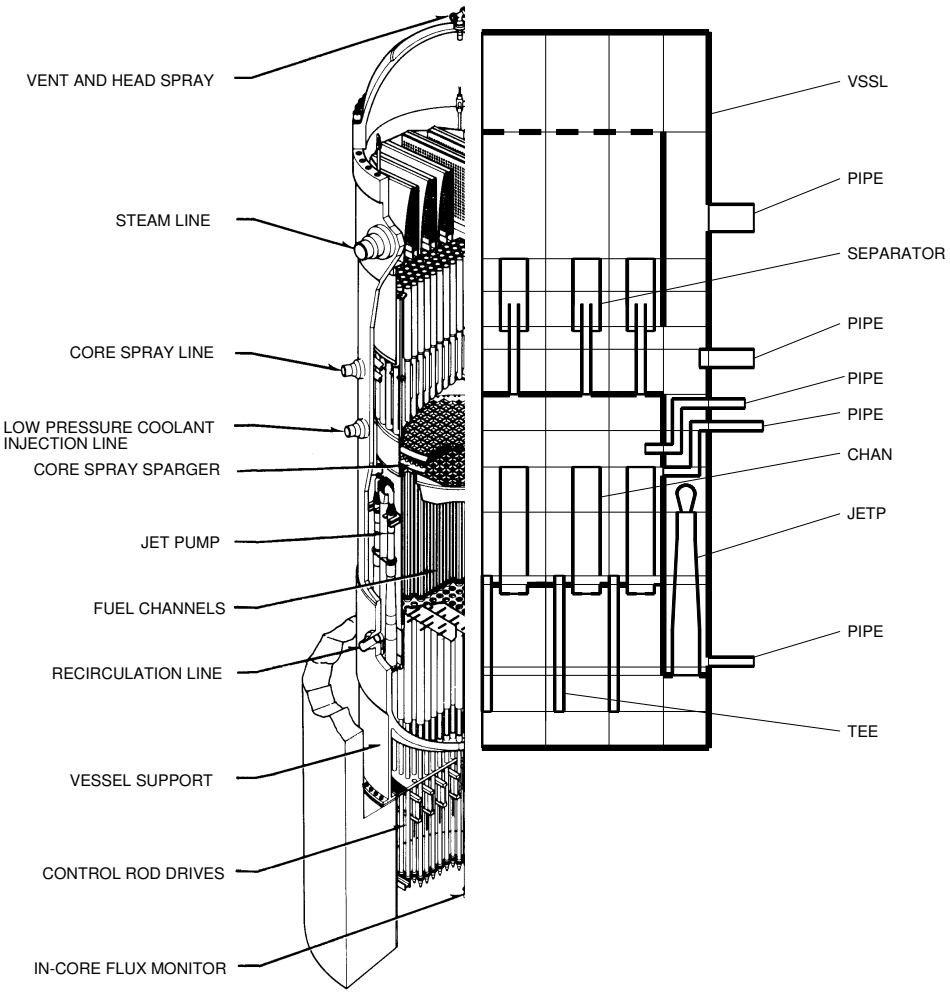

Figure 2-1. Simulation of a BWR/6

TRACG also contains a modular control system consisting of a set of control blocks. These control blocks can be connected either to each other or to thermal-hydraulic components to form complex control systems such as a BWR water level control system. The control system is described in detail in Section 10.0.

In addition to the 3-D neutron kinetics model described in Section 9.0, TRACG also contains a point kinetics model and a 1-D neutron kinetics model. The 1-D kinetics model is similar to the model used in ODYN[198]. The 1-D model has not been retested and requalified in TRACG02 and later versions of the code because it is has not been needed since the implementation of the 3-D model. The point kinetics model, on the other hand, is useful for simulating the power response prior to a scram during the early stages of a LOCA. The different options for the point kinetics model that allow the reactivity to be specified in a table versus time or simulated by reactivity coefficeints specified as functions of key parameters have also been fully retested for use in TRACG04. Other options to specify the total power or fission power via the control system or as a table versus time have also been retested. All these models have been integrated with the various decay heat models. The details for how to select and use these models are provided in the *TRACG04A,P User's Manual*[214].

2.1 Component Modules

TRACG contains the following thermal-hydraulic components:

PIPE The pipe (PIPE) component is the simplest component in TRACG. It contains a one-dimensional hydraulic model for the fluid flow in the pipe and a one-dimensional model for the radial heat conduction in the pipe wall. The number of hydraulic cells for the fluid flows and radial nodes for the wall heat transfer are specified through input.

PUMP The pump (PUMP) component is similar to the pipe component, except that a model for a pump is included at one of the cell boundaries in the component. The pump model calculates the pump speed and the hydraulic head imposed by the pump on the fluid.

VLVE The valve (VLVE) component is similar to the pipe component, except that the flow area of one of the cell boundaries can be varied to simulate the opening and closing of a valve.

TEE The tee (TEE) component consists of two pipe components that are connected together to form a TEE or a WYE.

The separator is an option to the tee component. The primary branch simulates the standpipe and the separating barrel in a BWR steam separator, and the secondary branch simulates the liquid discharge path. When the separator option is activated, special models are included to simulate the separation of the steam and liquid in the component.

JETP The jet pump (JETP) component is similar to the tee component, except that special models for the interaction and mixing of the drive and suction flows are included.

CHAN The channel (CHAN) component is based on a tee component and includes simulation of the fuel rods. The primary branch represents the active channel, and the fuel rods are included there. The secondary branch simulates the leakage flow path from the bottom of a BWR fuel channel. An optional internal branch can be specified to simulate water

rods within the channel. A one-dimensional model is included for the radial heat transfer in the fuel rods. Special models are included for the power generation and the heat transfer in the channel component.

HEAT The heat exchanger (HEAT) is a composite component. It is based on a tee component, which represents the primary side of a heat exchanger. The secondary side of the heat exchanger is simulated by a pipe component. Special models are included for the heat transfer between the primary and secondary sides of the heat exchanger. The heat exchanger component is provided to simplify input generation. A heat exchanger can be constructed using the heat transfer connection between cells of an input defined primary and secondary side simulation.

VSSL The vessel (VSSL) component is the only multi-dimensional component in TRACG. It can be nodalized in two dimensions using Cartesian coordinates and in two or three dimensions using cylindrical coordinates. A multi-dimensional version of the hydraulic model is used for the fluid flow in the vessel component. Heat slabs simulating the structures can be included at several locations in the vessel component. A lumped heat slab can be included in every vessel cell and a one-dimensional heat slab can be included at the boundary between two vessel cells either in the axial or radial direction.

All the components in TRACG utilize the same basic models. There is a common one-dimensional hydraulic model used by all the one-dimensional components. The multi-dimensional hydraulic model is used by the vessel component only, and it is identical to the one-dimensional model, when reduced to one dimension. One common heat conduction model is used by all the one-dimensional components for the wall heat transfer and by the vessel component for the radial heat slabs. The one-dimensional heat conduction model used by the vessel component for the axial heat slabs is similar except for the discretization. Finally, there is only one set of constitutive correlations for shear and heat transfer in TRACG, and it is used by all the components.

2.2 Component Interfaces

TRACG components can interface with each other either through fluid flow or through heat transfers between components.

2.2.1 Flow Connections

One-dimensional components can be connected to each other at their junctions by specifying the same junction number for two components. A typical example of this is the recirculation line for a BWR, which can be simulated by combining pipe, pump, valve and jet pump components.

One-dimensional components can be connected to any cell in the three-dimensional vessel component by specifying a corresponding junction number for the one-dimensional component and source number for the vessel component. A typical example is the channel component in Figure 2-1, which is connected to the lower and upper plena in the vessel through the channel inlet and outlet junctions, and to the bypass region of the vessel through the leakage junction. Multiple source connections can be made to a single vessel cell.

2.2.2 Heat Transfer Connections

The walls of a one-dimensional component can communicate with the fluid in any other component through heat transfer. A typical example of this feature is the channel component in Figure 2-1, where there is heat transfer from the outside of the channel wall to the fluid in the bypass region of the vessel component. Another example is a heat exchanger, where the primary and secondary sides can be modeled by tee and pipe components that are connected through heat transfer.

2.3 Control System

TRACG has a modular control system in addition to the modular components. TRACG has a large number of control blocks, which perform elementary functions such as adding two signals. A control block has up to three inputs and one output signal. The input to a control block can be an output from another control block or a parameter from one of the TRACG components. For example, the pressures calculated at different locations in the VSSL component are inputs to the water level instrumentation which in turn provides inputs to the feedwater control system simulation. The output from a control block can go to another control block or to a TRACG component. An example of the latter is the control of the flow control valve position in a BWR/6.

3.0 THERMAL-HYDRAULIC MODEL

The main purpose of the TRACG code is to solve a coupled set of field equations describing the thermal-hydraulic behavior of the fluid coolants in the BWR system, the flow of energy in the fuel and the structural components of the reactor, and the generation of the nuclear power in the reactor core.

The following sections describe the fluid field equations. The field equations for structures are described in Section 4.0 and for the neutron kinetics in Section 9.0.

3.1 Field Equations

TRACG, like TRAC-PF1/MOD1[28] and TRAC-BF1/MOD1[29], uses a two-phase two-fluid model for fluid flow in both the one-dimensional (1-D) and three-dimensional (3-D) components. Kocamustafaogullari[30], Ishii[31], and Delhaye[32] have provided detailed derivations of the equations similar to those used in TRAC, and a more concise derivation related to the TRAC equations is available in a report by Addessio[33]. The fact that this model is formally ill posed was the subject of considerable debate several years ago and is discussed by Stewart and Wendroff[34]. Experience has demonstrated that this is a moot point, since the numerical solution procedures effectively introduce minor modifications to the field equations, making them well posed. A paper by Stewart[35] confirms these observations and demonstrates clearly that, with normal models for interfacial drag and reasonable finite-difference nodalizations, the problem solved numerically is well posed.

3.1.1 Nomenclature

Before presenting the fluid field equations, we need to define certain terminology. In our nomenclature, the term *gas* implies a general mixture of steam and noncondensable gases. The subscript "v" will denote a property or parameter applying to the gas mixture; the subscript "s" indicates a quantity applying specifically to steam and the subscript "a" formerly used for air now signifies the summation of all noncondensable gases. The term *liquid* implies pure liquid water, and the subscript "ℓ" denotes a quantity applying specifically to liquid water. For convenience, we define the following terms that will be used in the subsequent equations and list them alphabetically with the Greek symbols at the end:

Nomenclature

Item	***Description***
A	flow area between mesh cells
A_i	interfacial area
B_{mix}	shear term due to turbulence
B_s	source term in momentum equation
c	concentration (boron)
e	internal energy
E_{mix}	mixing term in energy equation
E_s	source term in energy equation

Nomenclature

Item	***Description***
F_w	wall shear
f	interfacial shear
g	acceleration of gravity
$\vec{g}$	gravity vector
h	heat transfer coefficient
h	specific enthalpy, $h = e + P/\rho$
h_{fg}	latent heat of evaporation, $h_{fg} = h_g - h_f$
j	volumetric flux
K	Kutateladze constant in CCFL correlation
k	constant in virtual mass term in momentum equation
m	constant in CCFL correlation
M_{mix}	mixing term in continuity equation
M_s	source term in mass equation
P	pressure
q	heat transfer rate
R	gas constant
R	radial dimension for 3-D components
T	temperature
t	time
$\vec{u}$	unit vector oriented in positive flow direction
V	cell volume
v	velocity
x	dimension for 1-D component
z	axial dimension for 3-D components
Greek Symbols	
α	gas volume fraction
Γ_g	interfacial mass transfer rate ($\Gamma_g = \Gamma_{vi}$)
ρ	microscopic density
σ	surface tension
τ	shear tensor
θ	azimuthal dimension for 3-D components

Subscript

Nomenclature

Item	*Description*
a	all noncondensable gases
b	boron
c	continuous phase
crit	critical velocity
d	dispersed phase
f	saturated liquid
g	saturated steam
i	interface
ℓ	liquid phase
n	noncondensable gas
r	relative (vapor-liquid)
s	Steam
sat	Saturation
v	gas phase (mixture)
w	Wall
Superscript	
d	donor celled
n	time step number

In the discussion of the finite-difference equations, all quantities except for the velocities are centered in the hydrodynamic cell (cell-centered), and the velocities are cell-edge quantities.

3.1.2 Model Formulation and Assumptions

The basic two-phase, two-fluid model consists of the volume and time averaged conservation equations for mass, momentum and energy for each phase as given by Stuhmiller[36]:

Gas Mass:

$$\frac{\partial}{\partial t}\left(\alpha\rho_v\right) = -\nabla\bullet\left(\alpha\rho_v\vec{v}_v\right)+\Gamma_{vi} \tag{3.1-1}$$

Liquid Mass:

$$\frac{\partial}{\partial t}\left((1-\alpha)\rho_\ell\right)=-\nabla\bullet\left((1-\alpha)\rho_\ell\vec{v}_\ell\right)+\Gamma_{\ell i} \tag{3.1-2}$$

Conservation of mass at the interface require:

$$\Gamma_{vi} + \Gamma_{\ell i} = 0 \tag{3.1-3}$$

Gas Momentum:

$$\frac{\partial}{\partial t}\left(\alpha\rho_v\vec{v}_v\right)+\nabla\bullet\left(\alpha\rho_v\vec{v}_v\vec{v}_v\right)=-\nabla\left(\alpha P_v\right)+\nabla\bullet\left(\alpha\overline{\overline{\tau}}_v\right)+\alpha\rho_v\vec{g}+\vec{M}_v \tag{3.1-4}$$

where the interphase momentum transfer term is given by:

$$\vec{M}_v = \Gamma_{vi}\vec{v}_{vi} + P_{vi}\nabla\alpha - \nabla\alpha\bullet\overline{\overline{\tau}}_{vi} \tag{3.1-5}$$

Liquid Momentum:

$$\frac{\partial}{\partial t}\left((1-\alpha)\rho_\ell\vec{v}_\ell\right)+\nabla\bullet\left((1-\alpha)\rho_\ell\vec{v}_\ell\vec{v}_\ell\right)=-\nabla\left((1-\alpha)P_\ell\right)+\nabla\bullet\left((1-\alpha)\overline{\overline{\tau}}_\ell\right)$$

$$+(1-\alpha)\rho_\ell\,\vec{g}+\vec{M}_\ell \tag{3.1-6}$$

where:

$$\vec{M}_\ell = \Gamma_{\ell i}\vec{v}_{\ell i} + P_{\ell i}\nabla(1-\alpha) - \nabla(1-\alpha)\bullet\overline{\overline{\tau}}_{\ell i} \tag{3.1-7}$$

Conservation of momentum at the interface requires:

$$\sum_k\left(\left(P_{ki}+\frac{\Gamma_{ki}^2}{\rho_{ki}}\right)\nabla\alpha_k - \nabla\alpha_k\bullet\overline{\overline{\tau}}_{ki}\right) = f_\sigma \tag{3.1-8}$$

where k represents the liquid and gas phases and f_σ is the pressure drop caused by the curvature of the interface.

In TRACG a number of simplifying assumptions have been made for the momentum equations:

- The mass transfer terms have been neglected. This is justifiable as these terms are small compared to the other interfacial forces like the interfacial drag. (For nucleate boiling in a BWR at a power density of 50 kW/ℓ the interfacial force due to mass transfer is $\Gamma_g\, v_r = \frac{5\bullet10^7}{h_{fg}}\, v_r \approx 10$ kg/m^2-sec^2 using $h_{fg} = 1.5\bullet10^6$J/kg and $v_r = 0.3$ m/sec, whereas the interfacial drag balancing the buoyancy is given by $\alpha(1-\alpha)\,\Delta\rho\, g \approx 1.6 \bullet 10^3$ kg/m^2-sec^2, using $\alpha = 0.4$ and P = 7 MPa).
- Uniform pressure has been assumed, i.e., $P_v = P_{vi} = P_{\ell i} = P_\ell = P$. This

assumption simplifies the equations in the sense that only one pressure needs to be calculated. The effect of local pressure variations at the interface, however, is lost and must be accounted for in some other way. For dispersed flow, e.g., droplet flow, the pressure variation around a droplet is directly related to the relative velocity of the droplet[37]. The interfacial force due to the local pressure variations around the droplet can thus be correlated with the relative velocity.

In TRACG two terms have been included; a term that is a function of the relative velocity:

$$\vec{f}_{\ell v} = \vec{f}_{\ell v}\left(\vec{v}_r\right) \tag{3.1-9}$$

which is the drag term; and a term that is a function of the derivative of the relative velocity:

$$\vec{f}_{VM} = \vec{f}_{VM}\left(\frac{d\,\vec{v}_r}{dt}\right) \tag{3.1-10}$$

which is the virtual mass term.

- The shear tensor is neglected except for shear at the boundaries against solid structures and shear at the interface for separated flow. The shear against the solid boundaries can be accounted for through wall friction terms F_{wv} and $F_{w\ell}$, which can be correlated against the fluid velocity and properties. The shear at the interface for separated flow $f_{\ell v}$ can be correlated against the fluid properties and the relative velocity.
- The pressure difference between the phases due to interphase curvature is neglected. This term has little impact on the fluid properties and does not impact the relative motion of the phases. (For particles with a radius of 10^{-4}m the pressure change across the interface is less than 10^{3}Pa for typical BWR conditions.)

With these simplifications, the momentum equations reduce to:

Gas Momentum:

$$\frac{\partial}{\partial t}\left(\alpha\rho_v\vec{v}_v\right) + \nabla\bullet\left(\alpha\rho_v\vec{v}_v\vec{v}_v\right) = -\alpha\nabla P - \vec{F}_{wv} + \alpha\rho_v\vec{g} - \vec{f}_{\ell v} - \vec{f}_{VM} \tag{3.1-11}$$

This equation can be further simplified by subtracting the gas continuity Equation (3.1-1) multiplied by $\vec{v}_v$. This gives:

$$\alpha\rho_v\frac{\partial\vec{v}_v}{\partial t} + \alpha\rho_v\,\vec{v}_v\bullet\nabla\vec{v}_v = -\alpha\nabla P - \vec{F}_{wv} + \alpha\rho_v\vec{g} - f_{\ell v} - f_{VM} \tag{3.1-12}$$

Similarly, the liquid momentum equation can be simplified.

Liquid Momentum:

$$(1-\alpha)\rho_\ell \frac{\partial \vec{v}_\ell}{\partial t} + (1-\alpha)\rho_\ell \vec{v}_\ell \bullet \nabla \vec{v}_\ell = -(1-\alpha)\nabla P - F_{w\ell} + (1-\alpha)\rho_\ell \vec{g} + f_{\ell v} + f_{VM} \tag{3.1-13}$$

Gas Energy:

$$\frac{\partial}{\partial t}\left(\alpha\rho_v(e_v + \frac{v_v^2}{2})\right) + P\frac{\partial \alpha}{\partial t} = -\nabla\bullet\left(\alpha\rho_v \vec{v}_v(e_v + \frac{v_v^2}{2})\right) - \nabla\bullet(P\alpha\vec{v}_v) + q'''_{wv} + q'''_{iv} + \Gamma_g h_g \tag{3.1-14}$$

Liquid Energy:

$$\frac{\partial}{\partial t}\left((1-\alpha)\rho_\ell(e_\ell + \frac{v_\ell^2}{2})\right) - P\frac{\partial \alpha}{\partial t} = -\nabla\bullet\left((1-\alpha)\rho_\ell \vec{v}_\ell(e_\ell + \frac{v_\ell^2}{2})\right) - \nabla\bullet(P(1-\alpha)\vec{v}_\ell) + q'''_{w\ell} + q'''_{i\ell} - \Gamma_g h_f \tag{3.1-15}$$

In the energy equations similar assumptions have been made

- Uniform pressure has been assumed i.e., $P_v = P_{vi} = P_{\ell i} = P_\ell = P$.
- The terms associated with the shear tensor have been neglected.
- Conductive heat transfer in the fluid has been neglected except for heat transfer to solid structures, which is included as the wall heat transfer terms q_{wv} and $q_{w\ell}$, and heat transfer at the interface q_{iv} and $q_{i\ell}$. Neglecting conductive energy transfer within the fluid is justified as it is much smaller than the convective heat transfer for steam water mixtures.
- Potential energy has been neglected, as it is much smaller than the internal and mechanical energies.
- The mechanical energy or kinetic energy has been kept in the equations except for the terms associated with the interfacial mass and energy transfer. The omission of the kinetic energy for the latter term is justified, as the relative velocity is much smaller than the fluid velocity for conditions where the kinetic energy is important (Note that except for critical flow, the kinetic energy is insignificant).
- The fluctuating energy term arising from the averaging of the fluctuating velocity has been neglected. Similar to the kinetic energy, this term is small.

An alternative to solving both the phasic mass equations is to solve one phasic mass equation and the total mass equation. The total mass equation is obtained by adding Equation (3.1-1) and Equation (3.1-2):

Total Mass:

$$\frac{\partial}{\partial t}\left[(1-\alpha)\rho_\ell + \alpha\rho_v\right] = -\nabla\bullet[(1-\alpha)\rho_\ell\vec{v}_\ell + \alpha\rho_v\vec{v}_v] \tag{3.1-16}$$

Solving either Equation (3.1-1) or (3.1-2) together with Equation (3.1-16) is completely equivalent to solving both Equations (3.1-1) and (3.1-2).

Similarly, the total energy equation is obtained by adding Equations (3.1-14) and (3.1-15) to get:

$$\begin{aligned}\frac{\partial}{\partial t}\left(\alpha\rho_v(e_v+\frac{v_v^{\,2}}{2}) + (1-\alpha)\rho_\ell(e_\ell+\frac{v_\ell^{\,2}}{2})\right) = \\ -\nabla\bullet\left(\alpha\rho_v\vec{v}_v(e_v+\frac{v_v^{\,2}}{2}) + (1-\alpha)\rho_\ell\vec{v}_\ell(e_\ell+\frac{v_\ell^{\,2}}{2})\right) \\ -\nabla\bullet\left(P\left(\alpha\vec{v}_v + (1-\alpha)\vec{v}_\ell\right)\right) + q'''_{w\ell} + q'''_{wv}\end{aligned} \tag{3.1-17}$$

Solving either Equation (3.1-14) or (3.1-15) together with Equation (3.1-17) is completely equivalent to solving both Equations (3.1-14) and (3.1-15).

Closure is obtained for these equations with normal thermodynamic relations, which for water are described in APPENDIX B, and specifications for the interfacial-drag, the interfacial heat transfer $\left(q'''_{iv}\text{ and }q'''_{i\ell}\right)$, the phase-change rate (Γ_g), the wall shear $\left(F_{wv}\text{ and }F_{w\ell}\right)$ and the wall heat flows $\left(q'''_{wv}\text{ and }q'''_{w\ell}\right)$. These equations do not require directly the quasi-steady assumption as long as the correct closure relations for the given transient exist. A real difficulty arises because, depending on how the closure relations were developed, a different set of closure relations may be required for each transient, and each set must comply with the assumptions associated with the definition of the time and volume averaging used in the field equations. However, if a steady- or quasi-steady-state database or a relationship derived from such a database is used to represent a closure relation, the code necessarily applies the quasi-steady assumption. This latter case applies for the closure relations within TRACG. Assessment shows that this is not a major limitation for BWR applications.

The phase-change rate required by the equation set is evaluated from a simple thermal-energy jump relation:

$$\Gamma_g = -\frac{q'''_{iv}+q'''_{i\ell}}{h_{fg}} \tag{3.1-18}$$

where

$$q'''_{iv} = \frac{A_i\ h_{iv}\ (T_{sat}-T_v)}{V} \tag{3.1-19}$$

and

$$q'''_{i\ell} = \frac{A_i \; h_{i\ell} \; (T_{sat} - T_\ell)}{V} \tag{3.1-20}$$

Here, A_i and the h_i terms are the interfacial area and heat transfer coefficients and T_{sat} is the saturation temperature corresponding to the partial steam pressure. Section 6.0 discusses the closure relationships used to define A_i and h_i.

The wall heat flux is given by Newton's law:

$$q'''_{wv} = \frac{A_w \; h_{wv} \; (T_w - T_v)}{V} \tag{3.1-21}$$

and

$$q'''_{w\ell} = \frac{A_w \; h_{w\ell} \; (T_w - T_\ell)}{V} \tag{3.1-22}$$

where A_w is the actual heated surface area.

The h_{wv} and $h_{w\ell}$ of the cell include the information regarding the portion of the wall having gas and liquid contact. Section 6.6 discusses the closure relationships used to define h_{wv} and $h_{w\ell}$.

The mass and energy equations are written in fully conserving form to permit the construction of a numerical scheme that rigorously conserves some measure of the system fluid mass and energy. In previous TRAC versions, the kinetic energy was eliminated using the momentum equation. This simplified the energy equation; however, at the same time, the flow work was reduced to a non-conserving form. Consequently, energy was not perfectly conserved and energy balance errors would occur, particularly for high velocity flow as in critical gas flow. In TRACG, this simplification is not made, and the kinetic energy is implemented into the energy equations in a conserving form.

The non-conserving form of the momentum equations permits simpler numerical solution strategies and can generally be justified because the pressure and shear terms preclude a fully conserving form of the momentum equation. The shear tensor was neglected in the momentum and energy equations and shear is only accounted for through the wall and interfacial shear terms in the momentum equations. This is reasonable for most BWR applications as the wall shear is the dominant term due to the large wall surface area and corresponding small hydraulic diameter. The solution to the momentum equations will approximate a porous medium solution for these regions. Large nodes, where not all cells are in contact with the wall can only exist in the upper plenum and the containment volumes. In these regions, viscous shear is insignificant, but turbulent shear will affect the bulk motion and mixing of the fluid. In the TRACG nodalization, an average velocity is used for each node boundary. Variations in the velocity and fluid properties, however, will exist across the node boundary due to either velocity profile or turbulent fluctuations. When fluid properties are averaged over the node boundary e.g., the $\alpha\rho vv$ term in the momentum equation, two terms result: $\bar{\alpha}\bar{\rho}\bar{v}\bar{v}$ where $\bar{v}$ is the average velocity and

$\overline{\alpha \rho v' v'}$ where v' represents the velocity fluctuations. For one-dimensional flow, this latter term is usually accounted for through the wall friction. For multi-dimensional flow, the term can be included as a simple mixing term.

Such mixing terms, which are based on Prandtl's mixing length model, have been very successful in modeling the flow and phase distribution with sub-channel codes using relatively large computational cells[38]. In TRACG a mixing term has been included in the finite difference equations (Section 3.2.2). The technical basis for the mixing term is described in Section 6.7.

3.1.3 Noncondensable Gas

Multiple noncondensable gases may be included. All noncondensable gases are assumed to be in thermal equilibrium with any steam that is present and to move with the same velocity as the steam (mechanical equilibrium). Hence, only a single field equation is needed to track the noncondensable gas. The noncondensable gas mass equations are solved individually for each gas; however, it is convenient to sum the individual equations to define a single equation that represents the total for all noncondensable gases.

Total Noncondensable Gas Mass:

$$\frac{\partial}{\partial t}\left(\alpha \rho_a\right) = -\nabla \bullet \left(\alpha \rho_a \vec{v}_v\right) \tag{3.1-23}$$

With this field present, the total gas density and energy are sums of the steam and the noncondensable components.

$$\rho_v = \rho_s + \rho_a = \rho_s + \sum \rho_n \tag{3.1-24}$$

and

$$\rho_v \, e_v = \rho_s \, e_s + \rho_a \, e_a = \rho_s \, e_s + \sum \rho_n \, e_n \tag{3.1-25}$$

We assume Dalton's law applies; therefore,

$$P_v = P_s + P_a = P_s + \sum P_n \tag{3.1-26}$$

We assume that the noncondensable gases are ideal gases, so that locally the gas constant for all noncondensables is given by:

$$R_a = \frac{1}{\rho_a} \sum \rho_n R_n \tag{3.1-27}$$

The subscripts "s" and "a" indicate, respectively, the steam and total noncondensable properties. By default, the code applies the thermodynamic properties for air to a single noncondensable gas. However, the code user may select any single noncondensable gas or a combination of multiple noncondensable gases as an alternative.

3.1.4 Liquid Solute

TRACG includes a mass-continuity equation for a solute moving with the liquid field.

Liquid Solute Mass:

$$\frac{\partial}{\partial t}\left(c_b\right) = -\nabla \bullet \left(c_b \vec{v}_\ell\right) \tag{3.1-28}$$

where c_b is the solute concentration (mass of solute/unit volume) in the liquid phase.

The solute does not affect the hydrodynamics directly. If we assume that the solute represents boron, the amount of the dissolved and the plated-out boron in the core may affect the hydrodynamics indirectly through reactivity feedback. If the solute concentration exceeds the solubility at the liquid temperature in a specific hydrodynamic cell, we assume that the excess solute in that cell plates out. Plating can occur if the cell fluid flashes or boils and increases the concentration beyond the solubility limit. (The model for the boron solubility limit is described in Section B.3.4 of APPENDIX B.) The model assumes that any plated-out solute instantaneously re-dissolves to the maximum allowable concentration if more liquid enters the cell. Because the solute does not affect the hydrodynamics directly, the solute variable may be used as a tag to track the movement of fluid from a specific source through the system.

3.1.5 One-Dimensional Field Equations

In one dimension, the conservation equations reduce to:

Gas Mass:

$$\frac{\partial}{\partial t}\left(\alpha\rho_v\right) = -\frac{\partial}{\partial x}\left(\alpha\rho_v v_v\right) + \Gamma_g \tag{3.1-29}$$

Liquid Mass:

$$\frac{\partial}{\partial t}\left[\left(1-\alpha\right)\rho_\ell\right] = -\frac{\partial}{\partial x}\left[\left(1-\alpha\right)\rho_\ell v_\ell\right] - \Gamma_g \tag{3.1-30}$$

Total Noncondensable Gas Mass:

$$\frac{\partial}{\partial t}\left(\alpha\rho_a\right) = -\frac{\partial}{\partial x}\left(\alpha\rho_a v_v\right) \tag{3.1-31}$$

Liquid Solute Mass:

$$\frac{\partial}{\partial t}\left(c_b\right) = -\frac{\partial}{\partial x}\left(c_b v_\ell\right) \tag{3.1-32}$$

Gas Momentum:

$$\frac{\partial}{\partial t} v_v = -v_v \frac{\partial v_v}{\partial x} - \frac{1}{\rho_v}\frac{\partial P}{\partial x} - \frac{F_{wv}}{\alpha\rho_v} - \frac{f_{\ell v}}{\alpha\rho_v} + g - \frac{f_{VM}}{\alpha\rho_v} \tag{3.1-33}$$

Liquid Momentum:

$$\frac{\partial}{\partial t} v_\ell = -v_\ell \frac{\partial v_\ell}{\partial x} - \frac{1}{\rho_\ell}\frac{\partial P}{\partial x} - \frac{F_{w\ell}}{(1-\alpha)\rho_\ell} + \frac{f_{\ell v}}{(1-\alpha)\rho_\ell} + g + \frac{f_{vM}}{(1-\alpha)\rho_\ell} \tag{3.1-34}$$

Gas Energy:

$$\frac{\partial}{\partial t}\left(\alpha\rho_v\left(e_v + \frac{v_v^2}{2}\right)\right) + P\frac{\partial \alpha}{\partial t} = -\frac{\partial}{\partial x}\left(\alpha\rho_v v_v\left(e_v + \frac{v_v^2}{2}\right)\right) - \frac{\partial}{\partial x}(\alpha P v_v) + q'''_{wv} + q'''_{iv} + \Gamma_g h_g \tag{3.1-35}$$

Liquid Energy:

$$\frac{\partial}{\partial t}\left((1-\alpha)\rho_\ell\left(e_\ell + \frac{v_\ell^2}{2}\right)\right) - P\frac{\partial \alpha}{\partial t} = -\frac{\partial}{\partial x}\left((1-\alpha)\rho_\ell v_\ell\left(e_\ell + \frac{v_\ell^2}{2}\right)\right) - \frac{\partial}{\partial x}\left((1-\alpha)P\, v_\ell\right) + q'''_{w\ell} + q'''_{i\ell} - \Gamma_g h_f \tag{3.1-36}$$

In the momentum equations, Equations (3.1-33) and (3.1-34), the gravity term is given by $g = \vec{g}\bullet\vec{u}$ where $\vec{g}$ is the gravity vector and $\vec{u}$ is a unit vector oriented in the direction of positive flow, i.e., in the same direction that the cell numbers are increasing. Thus for a vertical pipe oriented upwards the value of "g" is minus the acceleration of gravity.

3.2 Finite Difference Formulation

3.2.1 One-Dimensional Finite Difference Formulation

For the 1-D components, the code solves Equations (3.1-29) through (3.1-36) to provide a complete description of the fluid field, although Equation (3.1-31) and/or (3.1-32) can be turned off through input. The spatial mesh used for the difference equations is staggered (Figure 3-1) with thermodynamic properties evaluated at the cell centers and velocities evaluated at the cell edges.

Donor cell differencing is used everywhere, and the flux across an interface between two cells is given by:

$$(v\phi)^d_{i+1/2} = v_{i+1/2}\begin{cases}\phi_i & \text{if } v_{i+1/2} > 0 \\ \phi_{i+1} & \text{if } v_{i+1/2} < 0\end{cases} \tag{3.2-1}$$

where ϕ can be any cell-center state variable or a combination of such variables, and v is either the liquid or vapor velocity, as appropriate. The subscript i+1/2 points to a cell interface, and the subscripts i and i+l indicate the hydrodynamic cells on each side of the cell interface.

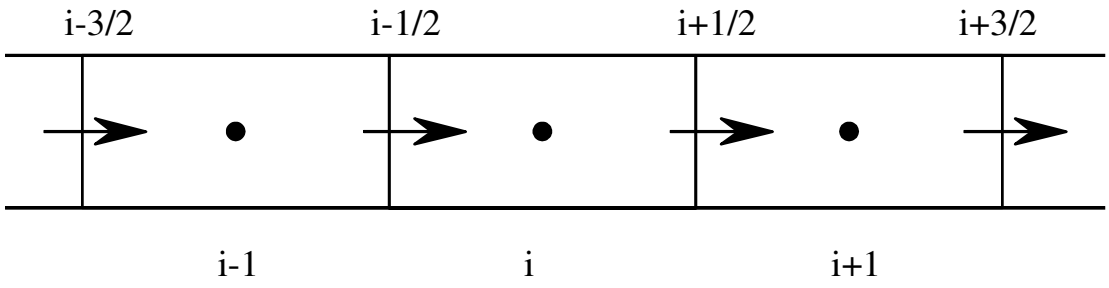

Figure 3-1. Staggered Grid Variables

For the momentum equation, the donor-cell form of $v\,\frac{\partial v}{\partial x}$ at the interface between two cells is given by:

$$v_{i+1/2}\left(\frac{\partial v}{\partial x}\right)^{d}_{i+1/2} = Dv_{i+1/2}\begin{cases}\dfrac{Ev_{i+1/2}-Fv_{i-1/2}}{\Delta x_{i+1/2}} & \text{if } v_{i+1/2}>0\\[2ex] \dfrac{Ev_{i+3/2}-Fv_{i+1/2}}{\Delta x_{i+1/2}} & \text{if } v_{i+1/2}<0\end{cases} \tag{3.2-2}$$

where $\Delta x_{i+1/2}$ is the average of Δx_i and Δx_{i+1}, respectively, the cell lengths of cells i and i+l,

$$\Delta x_{i+1/2} = \frac{\Delta x_i + \Delta x_{i+1}}{2} \text{ and } \phi_{i+1/2} = \frac{\Delta x_i \phi_i + \Delta x_{i+1}\phi_{i+1}}{\Delta x_i + \Delta x_{i+1}} \tag{3.2-3}$$

The factors D, E and F are used to obtain the correct Bernoulli (or reversible) pressure loss (gain) through area reductions (expansions). The formulations for D, E and F yield exact results for single-phase flow and approximately correct results if the change in the void fraction through the area change is small:

$$D = \frac{1}{2}\left(\frac{A_{i+1/2}}{A_i} + \frac{A_{i+1/2}}{A_{i+1}}\right) \tag{3.2-4}$$

where A_i is the average flow area in the cell:

$$A_i = \frac{V_i}{\Delta x_i} \tag{3.2-5}$$

and

$$E = \begin{cases} \dfrac{A_{i+1/2}}{A_{i+1}} & \text{for } v_{i+1/2} \geq 0 \\ \dfrac{A_{i+3/2}}{A_{i+1}} & \text{for } v_{i+1/2} < 0 \end{cases} \tag{3.2-6}$$

$$F = \begin{cases} \dfrac{A_{i-1/2}}{A_{i}} & \text{for } v_{i+1/2} \geq 0 \\ \dfrac{A_{i+1/2}}{A_{i}} & \text{for } v_{i+1/2} < 0 \end{cases} \tag{3.2-7}$$

3.2.1.1 Momentum Equations

The finite difference forms of the 1-D momentum equations are given by:

Gas Momentum:

$$\begin{aligned} &\frac{v_v^{n+1} - v_v^n}{\Delta t} + k\frac{\rho_{c,i+1/2}^n}{\left(\alpha\rho_v\right)_{i+1/2}^n}\frac{v_v^{n+1} - v_l^{n+1} - v_v^n + v_l^n}{\Delta t} = \\ &- Dv_{v,i+1/2}^n \begin{cases} \dfrac{Ev_{v,i+1/2}^{n+1} - Fv_{v,i-1/2}^n}{\Delta x_{i+1/2}} & \text{for } v_{v,i+1/2} \geq 0 \\ \dfrac{Ev_{v,i+3/2}^n - Fv_{v,i+1/2}^{n+1}}{\Delta x_{i+1/2}} & \text{for } v_{v,i+1/2} < 0 \end{cases} \\ &- k\frac{\rho_{c,i+1/2}^n}{\left(\alpha\rho_v\right)_{i+1/2}^n} v_{d,i+1/2}^n \begin{cases} \dfrac{v_{r,i+1/2}^{n+1} - v_{r,i-1/2}^n}{\Delta x_{i+1/2}} & \text{for } v_{d,i+1/2} \geq 0 \\ \dfrac{v_{r,i+3/2}^n - v_{r,i+1/2}^{n+1}}{\Delta x_{i+1/2}} & \text{for } v_{d,i+1/2} < 0 \end{cases} \\ &- \frac{1}{\rho_{v,i+1/2}^n}\frac{P_{i+1}^{n+1} - P_i^{n+1}}{\Delta x_{i+1/2}} + g_{i+1/2} + B_{sv,i+1/2} \\ &- \frac{1}{\left(\alpha\rho_v\right)_{i+1/2}^n}\left(F_{wv}^n + \frac{\partial F_{wv}^n}{\partial v_v}\left(v_v^{n+1} - v_v^n\right) + \frac{\partial F_{wv}^n}{\partial v_\ell}\left(v_\ell^{n+1} - v_\ell^n\right)\right)_{i+1/2} \\ &- \frac{1}{\left(\alpha\rho_v\right)_{i+1/2}^n}\left(f_{\ell v}^n + \frac{\partial f_{\ell v}^n}{\partial v_v}\left(v_v^{n+1} - v_v^n\right) + \frac{\partial f_{\ell v}^n}{\partial v_\ell}\left(v_\ell^{n+1} - v_\ell^n\right)\right)_{i+1/2} \end{aligned} \tag{3.2-8}$$

Here for convenience the virtual mass term has been introduced as

$$f_{VM} = f_{VM}\left(\frac{dv_r}{dt}\right) = k\rho_c\left\{\frac{\partial v_r}{\partial t} + v_d\frac{\partial v_r}{\partial x}\right\} \tag{3.2-9}$$

and a source term has been introduced to account for connections to other components.

Liquid Momentum:

$$\begin{aligned}
&\frac{v_\ell^{n+1}-v_\ell^n}{\Delta t} - k\frac{\rho^n_{c,i+1/2}}{\left((1-\alpha)\rho_\ell\right)^n_{i+1/2}}\frac{v_v^{n+1}-v_\ell^{n+1}-v_v^n+v_\ell^n}{\Delta t} = \\
&\qquad - Dv^n_{\ell,i+1/2}\begin{cases}\dfrac{Ev^{n+1}_{\ell,i+1/2} - Fv^n_{\ell,i-1/2}}{\Delta x_{i+1/2}} & \text{for } v_{\ell,i+1/2} \geq 0 \\ \dfrac{Ev^n_{\ell,i+3/2} - Fv^{n+1}_{\ell,i+1/2}}{\Delta x_{i+1/2}} & \text{for } v_{\ell,i+1/2} < 0\end{cases} \\
&\qquad + k\frac{\rho^n_{c,i+1/2}}{\left((1-\alpha)\rho_\ell\right)^n_{i+1/2}}v^n_{d,i+1/2}\begin{cases}\dfrac{v^{n+1}_{r,i+1/2}-v^n_{r,i-1/2}}{\Delta x_{i+1/2}} & \text{for } v_{d,i+1/2} \geq 0 \\ \dfrac{v^n_{r,i+3/2}-v^{n+1}_{r,i+1/2}}{\Delta x_{i+1/2}} & \text{for } v_{d,i+1/2} < 0\end{cases} \\
&\qquad - \frac{1}{\rho^n_{\ell,i+1/2}}\frac{P^{n+1}_{i+1} - P^{n+1}_i}{\Delta x_{i+1/2}} + g_{i+1/2} + B_{s\ell,i+1/2} \\
&\qquad - \frac{1}{\left((1-\alpha)\rho_\ell\right)^n_{i+1/2}}\left(F^n_{w\ell} + \frac{\partial F^n_{w\ell}}{\partial v_v}\left(v_v^{n+1} - v_v^n\right) + \frac{\partial F^n_{w\ell}}{\partial v_\ell}\left(v_\ell^{n+1} - v_\ell^n\right)\right)_{i+1/2} \\
&\qquad + \frac{1}{\left((1-\alpha)\rho_\ell\right)^n_{i+1/2}}\left(f^n_{\ell v} + \frac{\partial f^n_{\ell v}}{\partial v_v}\left(v_v^{n+1} - v_v^n\right) + \frac{\partial f^n_{\ell v}}{\partial v_\ell}\left(v_\ell^{n+1} - v_\ell^n\right)\right)_{i+1/2}
\end{aligned} \tag{3.2-10}$$

3.2.1.2 Mass and Energy Equations

The 1-D mass and energy equations are integrated over the cell volume. The conserving finite difference formulation is given by:

Gas Mass:

$$
\begin{aligned}
&V_i\left(\alpha_i^{n+1}\rho_{v,i}^{n+1} - \alpha_i^{n}\rho_{v,i}^{n}\right) = \\
&\quad + \Delta t A_{i-1/2} v_{v,i-1/2}^{n+1} \begin{cases} (\alpha\rho_v)_{i-1}^{n+1} & \text{for } v_{v,i-1/2}^{n+1} \geq 0 \\ (\alpha\rho_v)_{i}^{n+1} & \text{for } v_{v,i-1/2}^{n+1} < 0 \end{cases} \\
&\quad - \Delta t A_{i+1/2} v_{v,i+1/2}^{n+1} \begin{cases} (\alpha\rho_v)_{i}^{n+1} & \text{for } v_{v,i+1/2}^{n+1} \geq 0 \\ (\alpha\rho_v)_{i+1}^{n+1} & \text{for } v_{v,i+1/2}^{n+1} < 0 \end{cases} \\
&\quad + \Delta t V_i \Gamma_{g,i}^{n+1} + \Delta t V_i M_{sv,i}
\end{aligned}
\tag{3.2-11}
$$

Mixture Mass:

$$
\begin{aligned}
&V_i\left(\alpha_i^{n+1}\rho_{v,i}^{n+1} + (1-\alpha_i^{n+1})\rho_{\ell,i}^{n+1} - \alpha_i^{n}\rho_{v,i}^{n} - (1-\alpha_i^{n})\rho_{\ell,i}^{n}\right) = \\
&\quad + \Delta t A_{i-1/2} v_{v,i-1/2}^{n+1} \begin{cases} (\alpha\rho_v)_{i-1}^{n+1} & \text{for } v_{v,i-1/2}^{n+1} \geq 0 \\ (\alpha\rho_v)_{i}^{n+1} & \text{for } v_{v,i-1/2}^{n+1} < 0 \end{cases} \\
&\quad + \Delta t A_{i-1/2} v_{\ell,i-1/2}^{n+1} \begin{cases} ((1-\alpha)\rho_\ell)_{i-1}^{n+1} & \text{for } v_{\ell,i-1/2}^{n+1} \geq 0 \\ ((1-\alpha)\rho_\ell)_{i}^{n+1} & \text{for } v_{\ell,i-1/2}^{n+1} < 0 \end{cases} \\
&\quad - \Delta t A_{i+1/2} v_{v,i+1/2}^{n+1} \begin{cases} (\alpha\rho_v)_{i}^{n+1} & \text{for } v_{v,i+1/2}^{n+1} \geq 0 \\ (\alpha\rho_v)_{i+1}^{n+1} & \text{for } v_{v,i+1/2}^{n+1} < 0 \end{cases} \\
&\quad - \Delta t A_{i+1/2} v_{\ell,i+1/2}^{n+1} \begin{cases} ((1-\alpha)\rho_\ell)_{i}^{n+1} & \text{for } v_{\ell,i+1/2}^{n+1} \geq 0 \\ ((1-\alpha)\rho_\ell)_{i+1}^{n+1} & \text{for } v_{\ell,i+1/2}^{n+1} < 0 \end{cases} \\
&\quad + \Delta t V_i\left(M_{sv,i} + M_{s\ell,i}\right)
\end{aligned}
\tag{3.2-12}
$$

Total Noncondensable Gas Mass:

$$
\begin{aligned}
V_i \left(\alpha_i^{n+1} \rho_{a,i}^{n+1} - \alpha_i^n \rho_{a,i}^n \right) = & \\
& + \Delta t A_{i-1/2} v_{v,i-1/2}^{n+1} \begin{cases} (\alpha\rho_a)_{i-1}^{n+1} & \text{for } v_{v,i-1/2}^{n+1} \geq 0 \\ (\alpha\rho_a)_i^{n+1} & \text{for } v_{v,i-1/2}^{n+1} < 0 \end{cases} \\
& - \Delta t A_{i+1/2} v_{v,i+1/2}^{n+1} \begin{cases} (\alpha\rho_a)_i^{n+1} & \text{for } v_{v,i+1/2}^{n+1} \geq 0 \\ (\alpha\rho_a)_{i+1}^{n+1} & \text{for } v_{v,i+1/2}^{n+1} < 0 \end{cases} \\
& + \Delta t V_i M_{sa,i}
\end{aligned}
\tag{3.2-13}
$$

For a particular noncondensable gas n, the subscript a in Equation (3.2-13) is replaced by the subscript n.

Liquid Solute Mass:

$$
\begin{aligned}
V_i \left(c_{b,i}^{n+1} - c_{b,i}^n \right) = & \\
& + \Delta t A_{i-1/2} v_{\ell,i-1/2}^{n+1} \begin{cases} c_{b,i-1}^{n+1} & \text{for } v_{\ell,i-1/2}^{n+1} \geq 0 \\ c_{b,i}^{n+1} & \text{for } v_{\ell,i-1/2}^{n+1} < 0 \end{cases} \\
& - \Delta t A_{i+1/2} v_{\ell,i+1/2}^{n+1} \begin{cases} c_{b,i}^{n+1} & \text{for } v_{\ell,i+1/2}^{n+1} \geq 0 \\ c_{b,i+1}^{n+1} & \text{for } v_{\ell,i+1/2}^{n+1} < 0 \end{cases} \\
& + \Delta t V_i M_{sb,i}
\end{aligned}
\tag{3.2-14}
$$

Gas Energy:

$$V_i\left((\alpha\rho_v(e_v+\frac{v_v^{\,2}}{2}))_i^{n+1}-(\alpha\rho_v(e_v+\frac{v_v^{\,2}}{2}))_i^{n}+P_i^n(\alpha_i^{n+1}-\alpha_i^n)\right)=$$

$$+\Delta t A_{i-1/2}v_{v,i-1/2}^{n+1}\begin{cases}(\alpha\rho_v(h_v+\frac{v_v^2}{2}))_{i-1}^{n+1} & \text{for } v_{v,i-1/2}^{n+1}\ge 0\\ (\alpha\rho_v(h_v+\frac{v_v^2}{2}))_{i}^{n+1} & \text{for } v_{v,i-1/2}^{n+1}< 0\end{cases}$$

$$-\Delta t A_{i+1/2}v_{v,i+1/2}^{n+1}\begin{cases}(\alpha\rho_v(h_v+\frac{v_v^2}{2}))_{i}^{n+1} & \text{for } v_{v,i+1/2}^{n+1}\ge 0\\ (\alpha\rho_v(h_v+\frac{v_v^2}{2}))_{i+1}^{n+1} & \text{for } v_{v,i+1/2}^{n+1}< 0\end{cases}$$

$$+\Delta t\,(V_i\,\Gamma_{g,i}^{n+1}h_{g,i}^{n+1}+V_i\,q'''^{\,n+1}_{wv,i}+V_i\,q'''^{\,n+1}_{iv,i}+V_i\,E_{sv,i}) \qquad (3.2\text{-}15)$$

Liquid Energy:

$$V_i\left(((1-\alpha)\rho_\ell(e_\ell+\frac{v_\ell^2}{2}))_i^{n+1}-((1-\alpha)\rho_\ell(e_\ell+\frac{v_\ell^2}{2}))_i^{n}\right)-V_i\,P_i^n(\alpha_i^{n+1}-\alpha_i^n)=$$

$$+\Delta t A_{i-1/2}v_{\ell,i-1/2}^{n+1}\begin{cases}((1-\alpha)\rho_\ell(h_\ell+\frac{v_\ell^2}{2}))_{i-1}^{n+1} & \text{for } v_{\ell,i-1/2}^{n+1}\ge 0\\ ((1-\alpha)\rho_\ell(h_\ell+\frac{v_\ell^2}{2}))_{i}^{n+1} & \text{for } v_{\ell,i-1/2}^{n+1}< 0\end{cases}$$

$$-\Delta t A_{i+1/2}v_{\ell,i+1/2}^{n+1}\begin{cases}((1-\alpha)\rho_\ell(h_\ell+\frac{v_\ell^2}{2}))_{i}^{n+1} & \text{for } v_{\ell,i+1/2}^{n+1}\ge 0\\ ((1-\alpha)\rho_\ell(h_\ell+\frac{v_\ell^2}{2}))_{i+1}^{n+1} & \text{for } v_{\ell,i+1/2}^{n+1}< 0\end{cases}$$

$$+\Delta t(-V_i\,\Gamma_{g,i}^{n+1}\,h_{f,i}^{n+1}+V_i\,q'''^{n+1}_{w\ell,i}+V_i\,q'''^{n+1}_{i\ell,i}+V_i\,E_{s\ell,i}) \qquad (3.2\text{-}16)$$

As in the momentum equations, a source term has been introduced in these equations to account for connections to other components.

In these equations the heat flux terms are linearized with respect to void fraction and temperature as:

$$q'''^{n+1}_{iv} = \frac{A_i}{V_i}\left(h^n_{iv}\left(T^{n+1}_{sat} - T^{n+1}_v\right) + \frac{\partial h^n_{iv}}{\partial \alpha}\left(\alpha^{n+1} - \alpha^n\right)\left(T^n_{sat} - T^n_v\right)\right) \tag{3.2-17}$$

$$q'''^{n+1}_{i\ell} = \frac{A_i}{V_i}\left(h^n_{i\ell}\left(T^{n+1}_{sat} - T^{n+1}_\ell\right) + \frac{\partial h^n_{i\ell}}{\partial \alpha}\left(\alpha^{n+1} - \alpha^n\right)\left(T^n_{sat} - T^n_\ell\right)\right) \tag{3.2-18}$$

$$q'''^{n+1}_{wv} = \frac{A_w}{V_i}\, h^n_{wv}\, (T^{n+1}_w - T^{n+1}_v) \tag{3.2-19}$$

and

$$q'''^{n+1}_{i\ell} = \frac{A_w}{V_i}\, h^n_{w\ell}\, (T^{n+1}_w - T^{n+1}_\ell) \tag{3.2-20}$$

The interfacial heat transfer terms are linearized with respect to temperature and void fraction in order to assure numerical stability and to assure that the heat flux terms approach zero in case of thermal equilibrium and in the limit of α approaching 0 or 1. The wall heat transfer is linearized with respect to temperature to assure numerical stability and energy conservation in connection with the solution of the conduction equation for the wall.

3.2.2 Three-Dimensional Finite Difference Formulation

The 3-D vessel component in TRACG uses a cylindrical coordinate system, as shown in Figure 3-2.

The grid is staggered with the velocities specified at the boundary of each cell and the remaining properties such as α, P, ρ, e specified at the cell center.

Donor cell differencing is used everywhere (Section 3.2.1).

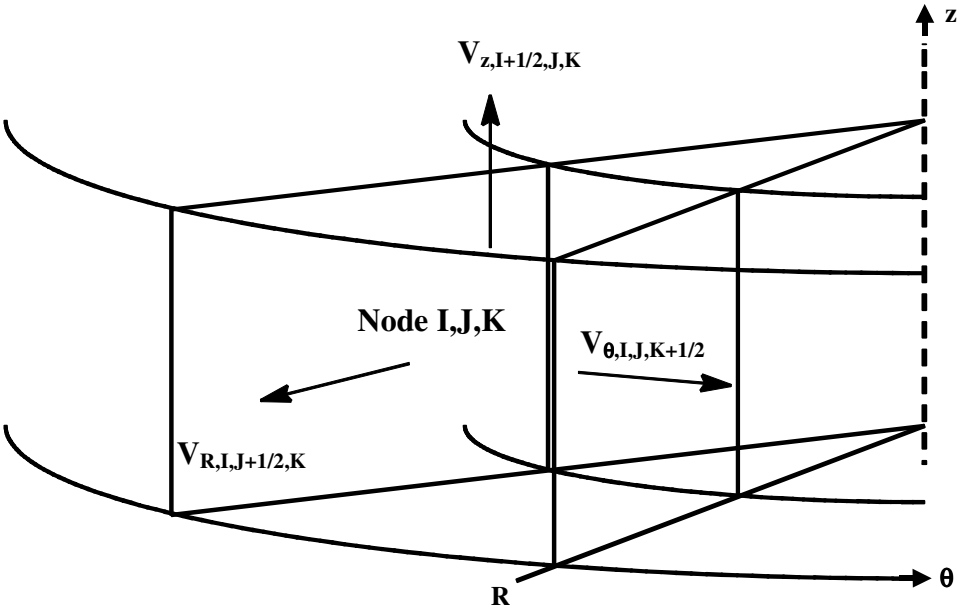

Figure 3-2. Cylindrical Coordinate System with Staggered Grid

3.2.2.1 Momentum Equations

In the 3-D formulation, when the shear tensor and the interfacial shear are integrated over the node and when the effect of local pressure variations is accounted for, terms for interaction with the walls $\vec{F}_{w\ell}$ and $\vec{F}_{wg}$ and terms for interaction between the phases will arise. As in the 1-D formulation, the interfacial drag and the virtual mass are accounted for separately. In a 3-D formulation, there will be other forces like the Bassett force and forces associated with the spatial distribution of phase, velocity and turbulent kinetic energy. TRACG, however, like the other versions of TRAC or RELAP5, uses relatively large nodes and a simulation of these terms is not meaningful. Consequently, these terms have been neglected in the 3-D finite difference formulation.

However, when the flow terms are integrated over the boundary for the node, a term will arise from the fluctuating component of the velocity. Again, with the relatively large nodes typically used in TRACG, standard turbulence models will not accurately model this term. Instead, using an equivalence to Prandtl's mixing length theory, a simple mixing term has been incorporated in the momentum equations. This way the effect of turbulent shear and mixing is included and sensitivity studies can be performed on the importance of the mixing.

The momentum equations are discretized directly for each face of the cell. In the axial momentum equations (Equations (3.2-21) and (3.2-26)) the positive direction is taken to be upward so that gravity has been introduced as "-g" where "g" is the absolute value for the acceleration due to gravity. The gravity term does not appear in the radial and azimuthal components of the momentum equation since these directions are orthogonal to gravity because the 3-D VSSL component is assumed to be oriented so that the axial direction is vertical. Neglecting the off-diagonal terms in the virtual mass, the spatially discretized equations become:

Axial Gas Momentum:

$$\frac{\partial v_{vz,I+1/2,J,K}}{\partial t}+\left[v_{vz}\left(\frac{\partial v_{vz}}{\partial z}\right)^{d}+v_{vR}\left(\frac{\partial v_{vz}}{\partial R}\right)^{d}+\frac{v_{v\theta}}{R}\left(\frac{\partial v_{vz}}{\partial \theta}\right)^{d}\right]_{I+1/2,J,K}$$

$$+\left(\frac{k\rho_c}{\alpha\rho_v}\right)_{I+1/2,J,K}\left[\frac{\partial v_{rz}}{\partial t}+v_{dz}\left(\frac{\partial v_{rz}}{\partial z}\right)^{d}\right]_{I+1/2,J,K}=$$

$$-\frac{1}{\rho_{v,I+1/2,J,K}}\frac{P_{I+1,J,K}-P_{I,J,K}}{\Delta z_{I+1/2}}-\left[g+\frac{1}{\alpha\rho_v}f_{\ell v}+\frac{1}{\alpha\rho_v}F_{wv}\right]_{z,I+1/2,J,K} \tag{3.2-21}$$

$$+B_{svz,I+1/2,J,K}+B_{mixvz,I+1/2,J,K}$$

Here, if a property is not defined at the face, linear averaging is used; e.g.:

$$\alpha_{I+1/2,J,K}=\frac{\Delta z_I\alpha_{I,J,K}+\Delta z_{I+1}\alpha_{I+1,J,K}}{\Delta z_I+\Delta z_{I+1}} \tag{3.2-22}$$

$$v_{v\theta,I+1/2,J,K}=\frac{\Delta z_I\left(v_{v\theta,I,J,K-1/2}+v_{v\theta,I,J,K+1/2}\right)+\Delta z_{I+1}\left(v_{v\theta,I+1,J,K-1/2}+v_{v\theta,I+1,J,K+1/2}\right)}{2\left(\Delta z_I+\Delta z_{I+1}\right)} \tag{3.2-23}$$

The discretization with respect to time is identical to the discretization of the 1-D equations described in Section 3.2.1.1. The superscript "d" on the convective term indicates that the convective term is calculated using donor cell differencing, as described in Section 3.2.1 (Equation (3.2-2)). (For the off-diagonal terms, a value of unity is used for D, E and F.)

Radial Gas Momentum:

$$\frac{\partial v_{vR,I,J+1/2,K}}{\partial t}+\left[v_{vz}\left(\frac{\partial v_{vR}}{\partial z}\right)^{d}+v_{vR}\left(\frac{\partial v_{vR}}{\partial R}\right)^{d}+\frac{v_{v\theta}}{R}\left(\frac{\partial v_{vR}}{\partial \theta}\right)^{d}-\frac{v_{v\theta}^2}{R}\right]$$

$$+\left(\frac{k\rho_c}{\alpha\rho_v}\right)_{I,J+1/2,K}\left[\frac{\partial}{\partial t}v_{rR}+v_{dR}\left(\frac{\partial v_{rR}}{\partial R}\right)^{d}\right]_{I,J+1/2,K}=$$

$$-\frac{1}{\rho_{v,I,J+1/2,K}}\frac{P_{I,J+1,K}-P_{I,J,K}}{\Delta R_{J+1/2}}-\left[\frac{1}{\alpha\rho_v}f_{\ell v}+\frac{1}{\alpha\rho_v}F_{wv}\right]_{R,I,J+1/2,K} \tag{3.2-24}$$

$$+B_{svR,I,J+1/2,K}+B_{mixvR,I,J+1/2,K}$$

Azimuthal Gas Momentum:

$$\frac{\partial v_{v\theta,I,J,K+1/2}}{\partial t} + \left[v_{vz}\left(\frac{\partial v_{v\theta}}{\partial z}\right)^{d} + v_{vR}\left(\frac{\partial v_{v\theta}}{\partial R}\right)^{d} + \frac{v_{v\theta}}{R}\left(\frac{\partial v_{v\theta}}{\partial \theta}\right)^{d} + \frac{v_{v\theta}\, v_{vR}}{R}\right]_{I,J,K+1/2}$$

$$+\left(\frac{k\rho_c}{\alpha\rho_v}\right)_{I,J,K+1/2}\left[\frac{\partial}{\partial t} v_{r\theta} + \frac{v_{d\theta}}{R}\left(\frac{\partial v_{r\theta}}{\partial \theta}\right)^{d}\right]_{I,J,K+1/2} =$$

$$-\frac{1}{\rho_{v,I,J,K+1/2}}\frac{P_{I,J,K+1} - P_{I,J,K}}{R_{J+1/2}\ \Delta\theta_{K+1/2}} - \left[\frac{1}{\alpha\rho_v} f_{\ell v} + \frac{1}{\alpha\rho_v} F_{wv}\right]_{\theta,I,J,K+1/2} \qquad (3.2\text{-}25)$$

$$+ B_{sv\theta,I,J,K+1/2} + B_{mixv\theta,I,J,K+1/2}$$

Similar expressions exist for the liquid phase.

Axial Liquid Momentum:

$$\frac{\partial v_{\ell z,I+1/2,J,K}}{\partial t} + \left[v_{\ell z}\left(\frac{\partial v_{\ell z}}{\partial z}\right)^{d} + v_{\ell R}\left(\frac{\partial v_{\ell z}}{\partial R}\right)^{d} + \frac{v_{\ell\theta}}{R}\left(\frac{\partial v_{\ell z}}{\partial \theta}\right)^{d}\right]_{I+1/2,J,K}$$

$$-\left(\frac{k\rho_c}{(1-\alpha)\rho_\ell}\right)_{I+1/2,J,K}\left[\frac{\partial v_{rz}}{\partial t} + v_{dz}\left(\frac{\partial v_{rz}}{\partial z}\right)^{d}\right]_{I+1/2,J,K} =$$

$$-\frac{1}{\rho_{\ell,I+1/2,J,K}}\frac{P_{I+1,J,K} - P_{I,J,K}}{\Delta z_{I+1/2}} - \left[g - \frac{1}{(1-\alpha)\rho_\ell} f_{\ell v} + \frac{1}{(1-\alpha)\rho_\ell} F_{w\ell}\right]_{z,I+1/2,J,K} \qquad (3.2\text{-}26)$$

$$+ B_{s\ell z,\, I+1/2,J,K} + B_{mix\ell z,I+1/2,J,K}$$

Radial Liquid Momentum:

$$\frac{\partial v_{\ell R,I,J+1/2,K}}{\partial t} + \left[v_{\ell z}\left(\frac{\partial v_{\ell R}}{\partial z}\right)^{d} + v_{\ell R}\left(\frac{\partial v_{\ell R}}{\partial R}\right)^{d} + \frac{v_{\ell\theta}}{R}\left(\frac{\partial v_{\ell R}}{\partial \theta}\right)^{d} - \frac{v_{\ell\theta}^{2}}{R}\right]$$

$$-\left(\frac{k\rho_c}{(1-\alpha)\rho_\ell}\right)_{I,J+1/2,K}\left[\frac{\partial}{\partial t}v_{rR} + v_{dR}\left(\frac{\partial v_{rR}}{\partial R}\right)^{d}\right]_{I,J+1/2,K} =$$

$$-\frac{1}{\rho_{\ell,I,J+1/2,K}}\frac{P_{I,J+1,K} - P_{I,J,K}}{\Delta R_{J+1/2}} - \left[\frac{-1}{(1-\alpha)\rho_\ell} f_{\ell v} + \frac{1}{(1-\alpha)\rho_\ell} F_{w\ell}\right]_{R,I,J+1/2,K} \tag{3.2-27}$$

$$+ B_{s\ell R,I,J+1/2,K} + B_{mix\ell R,I,J+1/2,K}$$

Azimuthal Liquid Momentum:

$$\frac{\partial v_{\ell\theta,I,J,K+1/2}}{\partial t} + \left[v_{\ell z}\left(\frac{\partial v_{v\theta}}{\partial z}\right)^{d} + v_{\ell R}\left(\frac{\partial v_{\ell\theta}}{\partial R}\right)^{d} + \frac{v_{\ell\theta}}{R}\left(\frac{\partial v_{\ell\theta}}{\partial \theta}\right)^{d} + \frac{v_{\ell\theta}\, v_{\ell R}}{R}\right]_{I,J,K+1/2}$$

$$-\left(\frac{k\rho_c}{(1-\alpha)\rho_\ell}\right)_{I,J,K+1/2}\left[\frac{\partial}{\partial t}v_{r\theta} + \frac{v_{d\theta}}{R}\left(\frac{\partial v_{r\theta}}{\partial \theta}\right)^{d}\right]_{I,J,K+1/2} = \tag{3.2-28}$$

$$-\frac{1}{\rho_{\ell,I,J,K+1/2}}\frac{P_{I,J,K+1} - P_{I,J,K}}{R_{J+1/2}\,\Delta\theta_{K+1/2}} - \left[\frac{-1}{(1-\alpha)\rho_\ell} f_{\ell v} + \frac{1}{(1-\alpha)\rho_\ell} F_{w\ell}\right]_{\theta,I,J,K+1/2}$$

$$+ B_{s\ell\theta,I,J,K+1/2} + B_{mix\ell\theta,I,J,K+1/2}$$

3.2.2.2 Mass and Energy Equations

The mass and energy equations are integrated over the volume of the cell to give the total change in mass and energy for the cell.

Gas Mass:

$$V_{IJK}\frac{\partial}{\partial t}\left(\alpha\rho_v\right)_{IJK} + \sum_{j=1}^{N_f}\left(A\alpha\rho_v v_v\right)^{d}_{j,IJK} = V_{IJK}\left(\Gamma_g + M_{sv}\right)_{IJK} + \sum_{j=1}^{N_f}\left(AM_{mixv}\right)_{j,IJK} \tag{3.2-29}$$

In these equations, the discretization with respect to time is identical to the discretization of the 1-D equations described in Section 3.2.1.2. The superscript "d" on the convective term indicates that the convective term is calculated using donor cell differencing, as described in Section 3.2.1 (Equation (3.2-1)). In these equations, the summation over "j" indicates the summation over all the faces of the cell with the convention that flows out of the cell is positive.

Mixture Mass:

$$V_{IJK}\frac{\partial}{\partial_t}\left[(1-\alpha)\rho_\ell+\alpha\rho_v\right]_{IJK}+\sum_{j=1}^{N_f}\left(A(1\text{-}\alpha)\rho_\ell v_\ell\right)^d_{j,JKL}+\sum_{j=1}^{N_f}\left(A\alpha\rho_v v_v\right)^d_{j,IJK}=$$

$$V_{IJK}\left(M_{s\ell}+M_{sv}\right)_{IJK}+\sum_{j=1}^{N_f}\left(A\left(M_{mixv}+M_{mix\ell}\right)\right)_{j,IJK} \tag{3.2-30}$$

Total Noncondensable Mass:

$$V_{IJK}\frac{\partial}{\partial t}\left(\alpha\rho_a\right)_{IJK}+\sum_{j=1}^{N_f}\left(A\alpha\rho_a v_v\right)^d_{j,IJK}=V_{IJK}\left(M_{sa}\right)_{IJK}+\sum_{j=1}^{N_f}\left(AM_{mixa}\right)_{j,IJK} \tag{3.2-31}$$

Liquid Solute Mass:

$$V_{IJK}\frac{\partial}{\partial t}\left(c_b\right)_{IJK}+\sum_{j=1}^{N_f}\left(Ac_b v_\ell\right)^d_{j,IJK}=V_{IJK}\left(M_{sb}\right)_{IJK}+\sum_{j=1}^{N_f}\left(AM_{mixb}\right)_{j,IJK} \tag{3.2-32}$$

Vapor Energy:

$$V_{IJK}\frac{\partial}{\partial t}\left[\alpha\rho_v\left(e_v+\frac{v_v^2}{2}\right)\right]_{IJK}+\sum_{j=1}^{N_f}\left[A\alpha\rho_v v_v\left(h_v+\frac{v_v^2}{2}\right)\right]^d_{j,IJK}+V_{IJK}\left(P\frac{\partial\alpha}{\partial t}\right)_{IJK}=$$

$$V_{IJK}\left(q'''_{iv}+\Gamma_g h_g+q'''_{wv}+E_{sv}\right)_{IJK}+\sum_{j=1}^{N_f}\left(AE_{mixv}\right)_{j,IJK} \tag{3.2-33}$$

Mixture Energy:

$$V_{IJK}\frac{\partial}{\partial t}\left[(1\text{-}\alpha)\rho_\ell\left(e_\ell+\frac{v_\ell^2}{2}\right)+\alpha\rho_v\left(e_v+\frac{v_v^2}{2}\right)\right]_{IJK}$$

$$+\sum_{j=1}^{N_f}\left[A(1\text{-}\alpha)\rho_\ell v_\ell\left(h_\ell+\frac{v_\ell^2}{2}\right)\right]^d_{j,IJK}+\sum_{j=1}^{N_f}\left[A\alpha\rho_v v_v\left(h_v+\frac{v_v^2}{2}\right)\right]^d_{j,IJK}= \tag{3.2-34}$$

$$V_{IJK}\left(q'''_{w\ell}+q'''_{wv}+E_{sv}+E_{s\ell}\right)_{IJK}+\sum_{j=1}^{N_f}\left(A\left(E_{mixv}+E_{mix\ell}\right)\right)_{j,IJK}$$

3.3 Modifications to Momentum Equations

There are several situations and places in the code where the regular momentum equations, as discussed in the previous sections, are modified or are not used. These situations and places are:

- Critical flow or choking
- Counter-current flow limitation (CCFL)
- Stratified flow with void fraction gradients
- Pump component at the location of the pump impeller
- Steam separator component at the separating face entering the side branch
- Jet pump at the mixing region
- TEE component joining cell

The last four cases will be discussed in Section 7.0. The first three cases will be discussed here, since these modifications to the momentum equations may occur for all components.

3.3.1 Critical Flow

In previous versions of TRAC, the criteria for choked flow were determined by a characteristic analysis of the partial differential equations governing the flow. However, it has been found empirically[39] that a simplified, approximate criterion may be used in place of the detailed characteristic analysis and still obtain good code/data comparisons. Accordingly, the following criterion is used in TRACG to determine whether the flow is choked:

$$\frac{\alpha\rho_\ell v_v + (1-\alpha)\rho_v v_\ell}{\alpha\rho_\ell + (1-\alpha)\rho_v} = v_{crit} \tag{3.3-1}$$

If the velocity as calculated by Equation (3.3-1) exceeds the acoustic propagation speed, the velocity is limited to the critical velocity.

When the velocities are limited, an additional requirement is needed to determine the individual velocities. Conservation of the slip ratio is chosen as the additional criterion. The velocity is set to the maximum allowed value by the critical flow or by the CCFL. The critical flow model is described in Section 6.3 and the CCFL is described in Section 6.1.7.2. The check is made following the explicit prediction of the velocity as calculated from the momentum Equations (8.2-3) and (8.2-4). If the maximum velocity as allowed by either the CCFL correlation or the choked flow model is exceeded, then the velocity is reset and the derivative of the velocity with respect to the pressure drop is re-evaluated such that the limiting characteristics are modeled as the pressure changes. In other words the explicit predicted velocities and the derivatives are re-evaluated based on either the CCFL or the choked flow characteristics. The remaining part of the solution, involving the pressure solution and the back substitution as described in Section 8.2.2 is unchanged. This assures that the mass and energy balances are maintained.

3.3.2 Counter-Current Flow Limitation

Counter-current flow limitation (CCFL), also called flooding, determines the amount of liquid that can penetrate flow restrictions. If limitation occurs (e.g., at the upper tie plate of a BWR fuel bundle), the amount of liquid that can penetrate into the bundle is reduced.

CCFL is a complicated hydrodynamic phenomenon and is thought to arise as a result of the interfacial friction between the liquid and the vapor phases[40]. CCFL in a BWR has been found to be described by a Kutateladze-type[41],[42] correlation of the form:

$$\sqrt{K_v} + m\sqrt{-K_\ell} = \sqrt{K} \tag{3.3-2}$$

where:

$$K_v = \frac{j_v \sqrt{\rho_v}}{(\Delta\rho g\sigma)^{1/4}} \tag{3.3-3}$$

$$K_\ell = \frac{j_\ell \sqrt{\rho_\ell}}{(\Delta\rho g\sigma)^{1/4}} \tag{3.3-4}$$

This correlation specifies the maximum downflow liquid velocity in counter-current flow through flow restrictions that can be obtained for a given upward vapor velocity. Thus, CCFL represents an upper limit to the liquid penetration in counter-current flow. That is analogous to critical flow, which determines the upper limit of the discharge flow rate in co-current flow from a source of fluid at high pressure. A detailed description of the CCFL model is given in Section 6.1.7.2. If the calculated liquid velocity exceeds that allowed by the CCFL correlating it is limited such that the CCFL correlation is satisfied (see Section 3.3.1).

3.3.3 Stratified Horizontal Flow

In a horizontal flow path at low flow rates, a horizontally stratified flow will develop with a force resulting from the difference in the hydrostatic heads in adjacent computational cells (Figure 3-3). This force term is given by:

$$\Delta P_{strat,i+1/2} = (P_i - P_{i+1})_{strat} = (\rho_\ell - \rho_v)_{i+1/2}\ g_{T,i+1/2}(\alpha_{i+1} - \alpha_i)\Delta z \tag{3.3-5}$$

where $g_{T,i+1/2}$ is the component of gravity perpendicular to the pipe orientation at the boundary between node "i" and node "i+1".

This force is added to the liquid phase momentum equation. The main effect of this term is to equalize the liquid levels between the two cells. The term added to the momentum equation represents information lost in the derivation of the 1-D momentum equations by the integration over the cross-sectional area perpendicular to the flow direction.

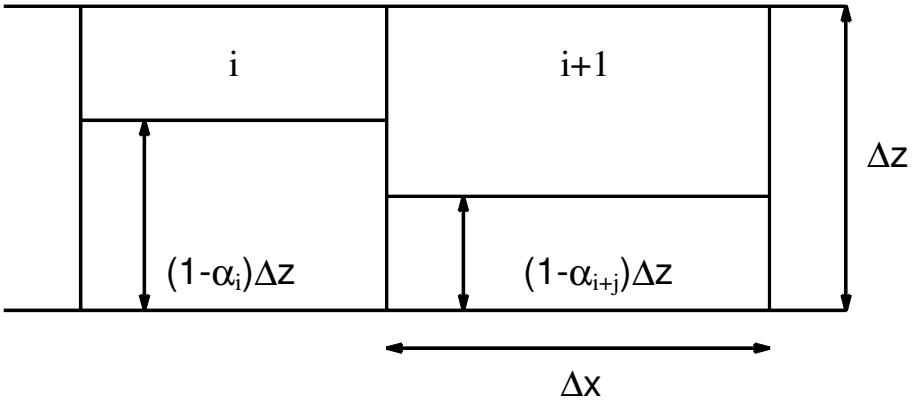

Figure 3-3. Void Gradient Gravity Head

4.0 HEAT CONDUCTION MODEL

TRACG solves the heat conduction equation for the fuel rods and other structural materials in the system. The structures include the pipe walls for the one-dimensional (1-D) components, the outer wall of the vessel component, and internal heat slabs in the vessel component. For the 1-D component walls, the inside heat transfer is to the fluid in the component. The outside heat transfer can be to the fluid in any other component. The internal heat slabs in the vessel component can be placed either completely inside a vessel cell or at the boundary between two vessel cells, either in the axial or in the radial direction.

The nomenclature used for the heat conduction equation is as follows:

Nomenclature

Item	***Description***
A	surface area
C_p	specific heat
h	heat transfer coefficient
k	conductivity
M	mass
q	heat flux
r	radial dimension
q"	heat flux
q"'	volumetric heat generation rate
t	time
T	temperature
z	axial dimension
Greek Symbols	
ρ	density
θ	indicator for implicit/explicit integration (hydraulic model)
ζ	indicator for implicit/explicit integration (heat conduction model)
	length measured in the direction normal to the surface
Subscript	
gap	fuel gas gap
v	vapor
ℓ	liquid
w	wall
i	inner surface
o	outer surface

Nomenclature

Item	*Description*
j	node number
rad	thermal radiation
N	last node number
M	last node number in fuel (next to the gap)
Superscript	
n	time step number

4.1 Governing Equation for Heat Conduction in Solid Materials

Because the heat flux in solid material is a vector quantity, the following general equation describes the heat conduction process in an arbitrary geometry:

$$\rho C_p \frac{\partial T}{\partial t} = -\nabla \bullet \vec{q} + q''' \tag{4.1-1}$$

The heat flux $\vec{q}$ can be expressed in terms of the temperature gradient by Fourier's law of conduction[43]:

$$\vec{q} = -\, k\, \nabla T \tag{4.1-2}$$

Inserting Equation (4.1-2) into Equation (4.1-1) gives:

$$\rho C_p \frac{\partial T}{\partial t} = \nabla \bullet (k \nabla T) + q''' \tag{4.1-3}$$

Equation (4.1-3) does require boundary conditions on the surface of the heat structure given by:

$$-\, k \frac{\partial T}{\partial \zeta} = q'' \tag{4.1-4}$$

where ζ is length measured in the direction normal to the surface and q'' is the transport of thermal energy away from the surface. An adiabatic boundary condition corresponds to $q'' = 0$.

TRACG solves the heat conduction equation for the heat slabs either as a lumped slab model or using a one-dimensional model.

4.1.1 Lumped Slab Formulation of the Heat Conduction Model

The lumped slab model is used for the heat slabs internal to one vessel cell, and is given by:

$$MC_p \frac{\partial T}{\partial t} = -\, A \left[h_\ell (T - T_\ell) + h_v (T - T_v) \right] \tag{4.1-5}$$

The flow regime map is described in Section 5.0 and the wall heat transfer is described in Section 6.6. If liquid is in contact with the wall as in single-phase liquid convection or nucleate boiling, $h_v = 0$. If vapor is in contact with the wall as in single phase vapor convection or film boiling, $h_\ell = 0$. In transition boiling, an interpolation is performed between h_v and h_ℓ as described in Section 6.6.8.

No heat generation is included for the lumped slabs.

4.1.2 One-Dimensional Formulation of the Heat Conduction Model

The 1-D heat conduction model is used for the 1-D component walls and the double-sided vessel slabs. For the double-sided heat slabs connecting two axial levels, the heat conduction equation is formulated as:

$$\rho C_p \frac{\partial T}{\partial t} = \frac{\partial}{\partial z}\left(k \frac{\partial T}{\partial z} \right) + q''' \tag{4.1-6}$$

For the double-sided heat slabs connecting two radial rings, for the 1-D component walls, and for the fuel rods, the heat conduction equation is formulated in cylindrical coordinates:

$$\rho C_p \frac{\partial T}{\partial t} = \frac{1}{r} \frac{\partial}{\partial r}\left(rk \frac{\partial T}{\partial r} \right) + q''' \tag{4.1-7}$$

The heat generation rate can either be specified through input, calculated from the kinetics model, or be a result of metal-water reaction.

The heat flux at the fuel rod or 1-D heat slab surfaces consists of convection heat transfer given by Newton's law of cooling and thermal radiation heat transfer (fuel channels only):

$$q'' = h_\ell \ (T - T_\ell) + h_v \ (T - T_v) + q''_{rad} \tag{4.1-8}$$

4.2 Finite Difference Formulation of Heat Conduction Equation

The heat conduction equation for the fuel rods and heat slabs is solved using either a lumped slab model or a 1-D model. The 1-D model can be formulated either in Cartesian coordinates or in cylindrical coordinates. The lumped slab model is used for heat slabs completely internal to a single cell in the vessel component. The 1-D model using Cartesian coordinates is used for heat slabs in the vessel component situated between two axial levels. The 1-D model using cylindrical coordinates is used for the fuel rods, the walls of a 1-D component, and for heat slabs in the vessel component situated between two radial rings.

4.2.1 Lumped Slab Heat Conduction

The lumped slab heat conduction model is given by:

$$M_w \; C_{pw}^n \quad \left(T_w^{n+1} - T_w^n \right) =$$

$$-A_w \; h_{w\ell} \Delta t \left[(1-\theta) \left(T_w^n - T_\ell^n \right) + \theta \left(T_w^{n+1} - T_\ell^{n+1} \right) \right] \tag{4.2-1}$$

$$-A_w \; h_{wv} \Delta t \left[(1-\theta) \left(T_w^n - T_v^n \right) + \theta \left(T_w^{n+1} - T_v^{n+1} \right) \right]$$

In this equation, $\theta = 0$ corresponds to an explicit integration of the hydraulic model, while $\theta = 1$ corresponds to an implicit integration.

4.2.2 One-Dimensional Heat Conduction in Cartesian Coordinates

The 1-D heat conduction equation in Cartesian coordinates is given by Equation (4.1-6) 4.1-6. The slab is divided into N nodes as shown in Figure 4-1.

For the first node, j = 1, the linearized heat conduction equation becomes:

$$\Delta z \rho_1 C_{pl}^n \; \Delta T_{w,1}^{n+1} = -\Delta th_{wli}^n \left[T_{w,1}^n - T_{li}^n + \theta \left(\Delta T_{w,1}^{n+1} - \Delta T_{li}^{n+1} \right) \right]$$

$$-\Delta th_{wvi}^n \left[T_{w,1}^n - T_{vi}^n + \theta \left(\Delta T_{w,1}^{n+1} - \Delta T_{vi}^{n+1} \right) \right] \tag{4.2-2}$$

$$+\Delta tk_{l+1/2}^n \frac{T_{w,2}^n - T_{w,1}^n + \zeta \left(\Delta T_{w,2}^{n+1} - \Delta T_{w,1}^{n+1} \right)}{\Delta z} + \Delta t \; q''' \Delta z$$

In this equation, $\theta = 0$ corresponds to an explicit integration of the hydraulic model, while $\theta = 1$ corresponds to an implicit integration. $\zeta = 0$ corresponds to an explicit integration of the heat conduction model, while $\zeta = 1$ corresponds to an implicit integration.

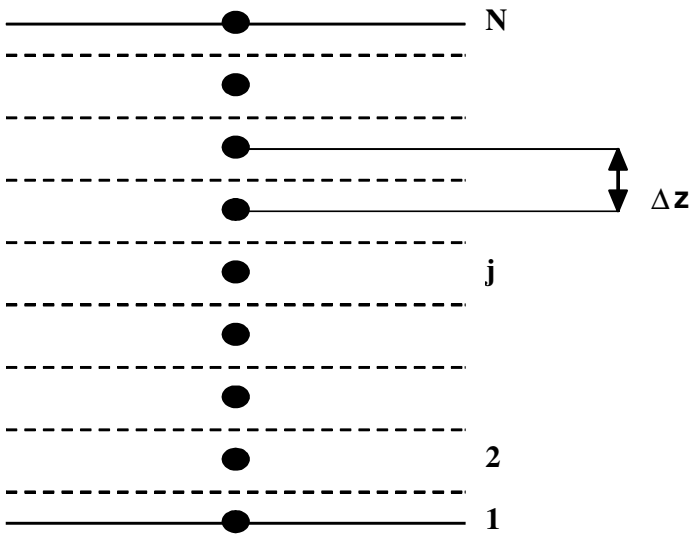

Figure 4-1. One-Dimensional Wall Geometry in Cartesian Coordinates

For the subsequent nodes, $1 < j < N$, the linearized heat conduction equation becomes:

$$\begin{aligned}\Delta z\,\rho_j C_{pj}^n \Delta T_{w,j}^{n+1} = {} & \Delta t k_{j+\frac{1}{2}}^n \frac{T_{w,j+1}^n - T_{w,j}^n + \zeta\left(\Delta T_{w,j+1}^{n+1} - \Delta T_{w,j}^{n+1}\right)}{\Delta z} \\ & + \Delta t k_{j-\frac{1}{2}}^n \frac{T_{w,j-1}^n - T_{w,j}^n + \zeta\left(\Delta T_{w,j-1}^{n+1} - \Delta T_{w,j}^{n+1}\right)}{\Delta z} \\ & + \Delta t\; q''' \Delta z\end{aligned} \tag{4.2-3}$$

For the last node, $j = N$, the linearized heat conduction equation becomes:

$$\begin{aligned}\Delta t \rho_N C_{pN}^n \Delta T_{w,N}^{n+1} = {} & -\Delta t h_{w\ell o}^n \left[T_{w,N}^n - T_{\ell o}^n + \theta\left(\Delta T_{w,N}^{n+1} - \Delta T_{\ell o}^{n+1}\right)\right] \\ & - \Delta t h_{wvo}^n \left[T_{w,N}^n - T_{vo}^n + \theta\left(\Delta T_{w,N}^{n+1} - \Delta T_{vo}^{n+1}\right)\right] \\ & + \Delta t k_{N-1/2}^n \frac{T_{w,N-1}^n - T_{w,N}^n + \zeta\left(\Delta T_{w,N-1}^{n+1} - \Delta T_{w,N}^{n+1}\right)}{\Delta z} + \Delta t\; q''' \Delta z\end{aligned} \tag{4.2-4}$$

4.2.3 One-Dimensional Heat Conduction in Cylindrical Coordinates

The 1-D heat conduction equation in cylindrical coordinates is given by Equation (4.1-7). The cylindrical slab is divided into N nodes, as shown in Figure 4-2.

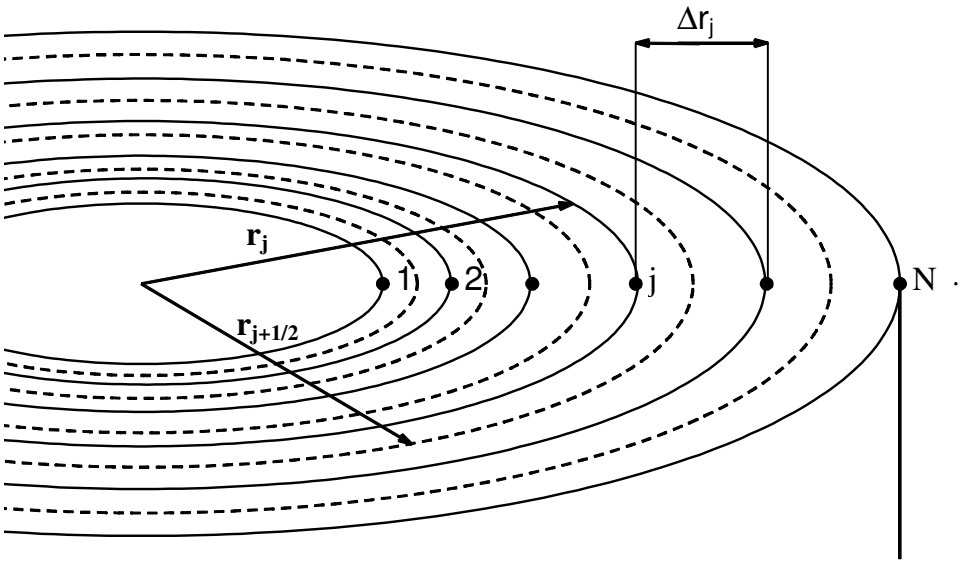

Figure 4-2. One-Dimensional Wall Geometry in Cylindrical Coordinates

For the first node, j = 1, the linearized heat conduction equation becomes:

$$\left(r_1\Delta r_1+\frac{\Delta r_1^2}{4}\right)\rho_1 C_{p1}^n\Delta T_{w,1}^{n+1}=$$

$$-2r_1\Delta th_{w\ell i}^n\left[T_{w,1}^n-T_{\ell i}^n+\theta\left(\Delta T_{w,1}^{n+1}-\Delta T_{\ell i}^{n+1}\right)\right]$$

$$-2r_1\Delta th_{wvi}^n\left[T_{w,1}^n-T_{vi}^n+\theta\left(\Delta T_{w,1}^{n+1}-\Delta T_{vi}^{n+1}\right)\right] \qquad (4.2\text{-}5)$$

$$+2r_{1+1/2}\Delta tk_{1+1/2}^n\frac{T_{w,2}^n-T_{w,1}^n+\zeta\left(\Delta T_{w,2}^{n+1}-\Delta T_{w,1}^{n+1}\right)}{\Delta r_1}$$

$$+\left(r_1\Delta r_1+\frac{\Delta r_1^2}{4}\right)\Delta tq'''$$

where:

$$r_{j+1/2}=\frac{r_j+r_{j+1}}{2};\ \Delta r_j=r_{j+1}-r_j \qquad (4.2\text{-}6)$$

In this equation, θ=0 corresponds to an explicit integration of the hydraulic model, while θ=1 corresponds to an implicit integration. ζ=0 corresponds to an explicit integration of the heat conduction model, while ζ=1 corresponds to an implicit integration.

For a fuel rod as shown by the schematic in Figure 4-3, the inner radius for the first node is $r_1 = 0$ and the boundary conditions are $h_{wv1} = 0$ and $h_{w\ell 1} = 0$.

For the subsequent nodes, $1 < j < N$, the linearized heat conduction equation becomes:

$$\begin{aligned}
&\left(r_{j+1/2}^2 - r_{j-1/2}^2\right)\rho_j C_{pj}^n \Delta T_{w,j}^{n+1} = \\
&\quad + 2r_{j+1/2}\Delta tk_{j+1/2}^n \frac{T_{w,j+1}^n - T_{w,j}^n + \zeta\left(\Delta T_{w,j+1}^{n+1} - \Delta T_{w,j}^{n+1}\right)}{\Delta r_j} \\
&\quad + 2r_{j-1/2}\Delta tk_{j-1/2}^n \frac{T_{w,j-1}^n - T_{w,j}^n + \zeta\left(\Delta T_{w,j-1}^{n+1} - \Delta T_{w,j}^{n+1}\right)}{\Delta r_{j\text{-}1}} \\
&\quad + \Delta t\ q'''\left(r_{j+1/2}^2 - r_{j\text{-}1/2}^2\right)
\end{aligned} \tag{4.2-7}$$

For the last node, $j = N$, the linearized heat conduction equation becomes:

$$\begin{aligned}
&\left(r_N \Delta r_{N-1} - \frac{\Delta r_{N-1}^2}{4}\right)\rho_N C_{pN}^n \Delta T_{w,N}^{n+1} = \\
&\quad - 2r_N \Delta th_{w\ell o}^n \left[T_{w,N}^n - T_{\ell o}^n + \theta\left(\Delta T_{w,N}^{n+1} - \Delta T_{\ell o}^{n+1}\right)\right] \\
&\quad - 2r_N \Delta th_{wvo}^n \left[T_{w,N}^n - T_{vo}^n + \theta\left(\Delta T_{w,N}^{n+1} - \Delta T_{vo}^{n+1}\right)\right] \\
&\quad + 2r_{N-1/2}\Delta tk_{N-1/2}^n \frac{T_{w,N-1}^n - T_{w,N}^n + \zeta\left(\Delta T_{w,N-1}^{n+1} - \Delta T_{w,N}^{n+1}\right)}{\Delta r_{N-1}} \\
&\quad + \Delta t\ q'''\left(r_N \Delta r_{N-1} - \frac{\Delta r_{N-1}^2}{4}\right)
\end{aligned} \tag{4.2-8}$$

For a fuel rod (Figure 4-3), special considerations need to be given to the gap between the fuel pellet and the cladding. For the last node (M) in the fuel, the linearized heat conduction equation becomes:

$$\left(r_M \Delta r_{M-1} - \frac{\Delta r_{M-1}^2}{4} \right) \rho_M C_{pM}^n \Delta T_{w,M}^{n+1} =$$

$$+ 2 r_{M+1/2} \Delta th_{gap}^n \left[T_{w,M+1}^n - T_{w,M}^n + \zeta \left(\Delta T_{w,M+1}^{n+1} - \Delta T_{w,M}^{n+1} \right) \right]$$

$$+ 2 r_{M-1/2} \Delta t \, k_{M-1/2}^n \frac{T_{w,M-1}^n - T_{w,M}^n + \zeta \left(\Delta T_{w,M-1}^{n+1} - \Delta T_{w,M}^{n+1} \right)}{\Delta r_{M-1}} \qquad (4.2\text{-}9)$$

$$+ \Delta t \; q''' \left(r_M \Delta r_{M-1} - \frac{\Delta r_{M-1}^2}{4} \right)$$

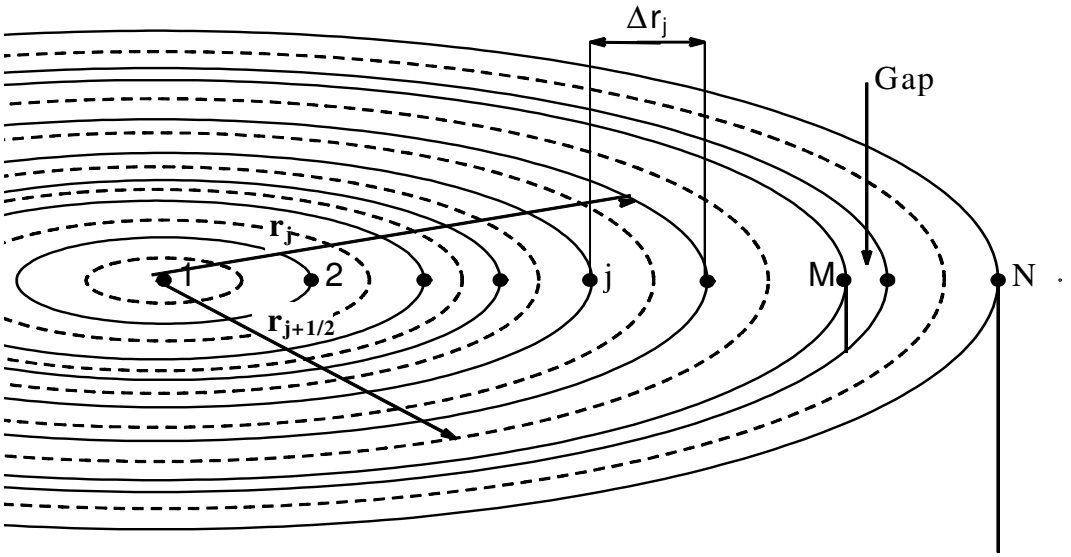

Figure 4-3. One-Dimensional Fuel Rod Geometry

For the first node in the cladding (M+1), the linearized heat conduction equation becomes:

$$\left(r_{M+1}\Delta r_{M+1} + \frac{\Delta r_M^2}{4} \right) \rho_{M+1} C_{pM+1}^n \Delta T_{w,M}^{n+1} =$$

$$+ 2r_{M+3/2}\Delta t k_{M+3/2}^n \frac{T_{w,M+2}^n - T_{w,M+1}^n + \zeta\left(\Delta T_{w,M+2}^{n+1} - \Delta T_{w,M+1}^{n+1}\right)}{\Delta r_{M+1}}$$

$$+ 2r_{M+1/2}\Delta t \; h_{gap}^n \left[T_{w,M}^n - T_{w,M+1}^n + \zeta\left(\Delta T_{w,M}^{n+1} - \Delta T_{w,M+1}^{n+1}\right) \right] \qquad (4.2\text{-}10)$$

$$+ \Delta t \; q''' \left(r_{M+1}\Delta r_{M+1} + \frac{\Delta r_{M+1}^2}{4} \right)$$

5.0 FLOW REGIME MAP

The two-fluid model used in TRACG requires the use of auxiliary relations for the constitutive correlations in the basic conservation equations. The constitutive correlations express the rates of exchange of mass, momentum, and energy between each phase and its surroundings. These correlations take on different forms for different flow patterns. As an example, two-phase flow patterns affect the rate of vapor generation in direct contact with the walls, and this term is important in determining mass exchange between liquid and vapor. Both the exchange of energy and momentum at the interface between vapor and liquid depend on the interfacial area per unit volume and the topology of the two-phase flow. For these reasons, it is important to identify the flow regime in each hydraulic cell before proceeding with the solution of the flow equations for that cell.

The nomenclature used in this section is given below:

Nomenclature

Item	*Description*
A	cross-sectional area
C_o	distribution parameter
D	diameter
D_h	hydraulic diameter
E	entrainment
E_f	fraction of wall in boiling transition
g	acceleration of gravity
G	mass flux
g_T	component of gravity perpendicular to flow axis
h	height of liquid in pipe
j	volumetric flux
P	pressure
Re	Reynolds number
S	perimeter
v	velocity
v_{gj}	drift flux velocity
Greek Symbols	
α	void fraction
ρ	density
σ	surface tension
θ	inclination angle of flow axis relative to gravity vector

Nomenclature

Item	*Description*
μ	dynamic viscosity
Subscripts	
a	annular flow
bc	bubbly/churn flow
ℓ	liquid
tran	transition to annular flow
v	vapor
w	wetted
Superscript	
*	Superficial velocity (e.g., j_v^*)

5.1 Basis for Flow Regime Map in TRACG

The constitutive correlations for shear and heat transfer in TRACG use a relatively simple flow regime map, which consists basically of two distinct patterns: (a) liquid-continuous at low void fractions and (b) vapor-continuous at high void fractions with a transition zone in between. The liquid-continuous regime applies to the single-phase liquid flow, bubbly/churn and inverted annular flows. The vapor-continuous regime applies to the annular, dispersed droplet flow and single-phase vapor flow regimes. The transition regime involves churn to annular and churn to droplet; depending on the void fraction, flow rate and other variables.

The criterion for transition from the liquid-continuous zone is defined in terms of a transition void fraction, α_{tran} that is a function of flow conditions and geometry.

This flow regime map is based on one that was originally suggested by Ishii[44] in his derivations of the drift-flux model. Ishii suggested two simple flow regime transition criteria that, in his words, "are based on the relative motion between phases and are consistent with the concept of drift-flux model."

Transition between bubbly/churn and annular flow takes place when the liquid in the film (or entrained droplets) can be lifted relative to the liquid velocity in the bubbly/churn flow regime. Transition between annular flow and dispersed droplet flow is given by the onset of entrainment. For low vapor flow, annular flow will exist and, as the vapor flux is increased, more and more entrainment will occur, causing a gradual transition to droplet flow.

The flow regime map (Figure 5-1) that was originally developed for vertical flow is assumed to be usable for both vertical and horizontal flow components. For horizontal flow with low velocities, however, stratification can occur. Transition to stratified flow is based on a critical Froude number.

5.1.1 Churn to Annular Transition

5.1.1.1 Technical Basis and Assumptions

The transition between churn flow and annular flow has been widely analyzed. See References [44] through [47]. The criterion for transition is when the liquid in the film can be lifted by the vapor flow relative to the liquid in the churn flow regime. This criterion is satisfied at the void fraction where the same velocity is predicted for churn flow as for annular flow. Using the drift flux model, the vapor velocity for churn flow is given by:

$$v_{v,bc} = C_{o,bc} j + \bar{v}_{gj,bc} \tag{5.1-1}$$

Similarly, for annular flow, the vapor velocity is given by:

$$v_{v,a} = C_{o,a} j + \bar{v}_{gj,a} \tag{5.1-2}$$

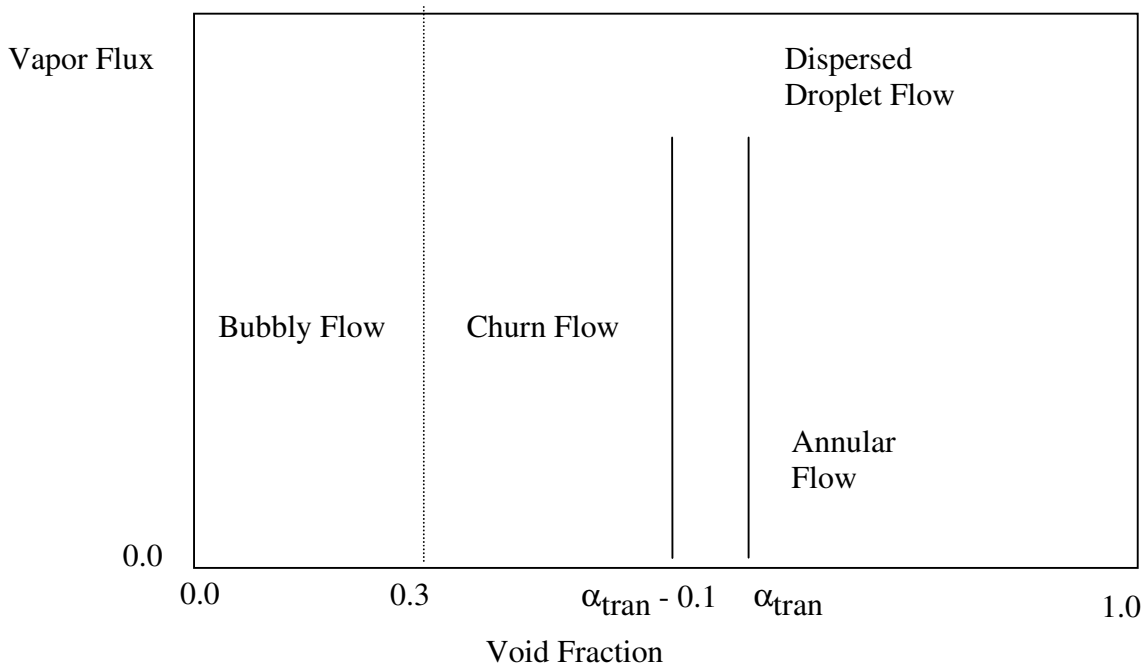

Figure 5-1. Flow Regime Map in terms of Void Fraction

The intersection of the two correlations or the condition where the velocity is the same in the two flow regimes is given by:

$$C_{o,bc} j + \bar{v}_{gj,bc} = C_{o,a} j + \bar{v}_{gj,a} \tag{5.1-3}$$

For annular flow, C_o is given by the following expression from Section 6.1.4:

$$C_{o,a} = 1 + \frac{1-\alpha}{\alpha + \left(\frac{1+75(1-\alpha)}{\sqrt{\alpha}} \frac{\rho_v}{\rho_\ell} \right)^{0.5}} \tag{5.1-4}$$

which, according to Ishii[44], can be approximated to:

$$C_{o,a} = 1 + \frac{1-\alpha}{\alpha + 4\sqrt{\frac{\rho_v}{\rho_\ell}}} \tag{5.1-5}$$

Inserting this expression in Equation (5.1-3) and solving for the void fraction, one gets:

$$\alpha_{tran} = \frac{j + 4\sqrt{\frac{\rho_v}{\rho_\ell}} \left[(1 - C_{o,bc}) j + (\bar{v}_{gj,a} - \bar{v}_{gj,bc}) \right]}{C_{o,bc} j - (\bar{v}_{gj,a} - \bar{v}_{gj,bc})} \tag{5.1-6}$$

where $C_{o,bc}$ is given by the following expression from Section 6.1.3. See Equation (6.1-43).

$$C_{o,bc} = C_{\infty,bc} - \left(C_{\infty,bc} - 1 \right) \sqrt{\frac{\rho_v}{\rho_\ell}} \tag{5.1-7}$$

where:

$$C_{\infty,bc} = 1.288 + 0.105 \left[4.5 \sqrt{\frac{\rho_v}{\rho_\ell}} \right] - 0.015 \log_e \left(Re_\ell \right) \tag{5.1-8}$$

$$Re_\ell = \frac{G D_h}{\mu_\ell} \tag{5.1-9}$$

5.1.1.2 Model as Coded

The calculation of the transition void fraction to annular flow is encoded as described by Equations (5.1-6) through (5.1-9) in Section 5.1.1.1, with the limitations on $C_{o,bc}$ as described in Section 6.1.3.2.

In order to avoid discontinuities in the interfacial shear at the transition to annular flow, the transition is implemented to take place over a void fraction interval of 0.1:

$$\{\alpha_{tran} - 0.1, \alpha_{tran}\} \tag{5.1-10}$$

Churn flow exists for $\alpha < \alpha_{tran}$ - 0.1 and annular flow exists for $\alpha > \alpha_{tran}$. A linear interpolation is performed for the constitutive correlations for shear and heat transfer over this interval between the correlations for churn flow and the correlations for annular flow.

5.1.1.3 Applicability

Several criteria for transition to annular flow have been proposed. Mishima and Ishii[46] proposed two criteria: (a) flow reversal in the liquid film section along large bubbles, and (b) destruction of liquid slugs or large waves by entrainment. A simpler criterion was proposed by Wallis[40], in which the transition to annular flow is given in terms of the superficial velocities:

$$j_v^* > 0.4 + 0.6 j_\ell^* \qquad (5.1\text{-}11)$$

where:

$$j_v^* = \frac{j_v \sqrt{\rho_v}}{(g D_h \Delta\rho)^{0.5}} \quad \text{and} \quad j_\ell^* = \frac{j_\ell \sqrt{\rho_\ell}}{(g D_h \Delta\rho)^{0.5}} \qquad (5.1\text{-}12), (5.1\text{-}13)$$

The TRACG criterion (Equation (5.1-6)) and the Wallis criterion (Equation (5.1-11)) have been compared to data by Bergles and Suo[47] in Figure 5-2.

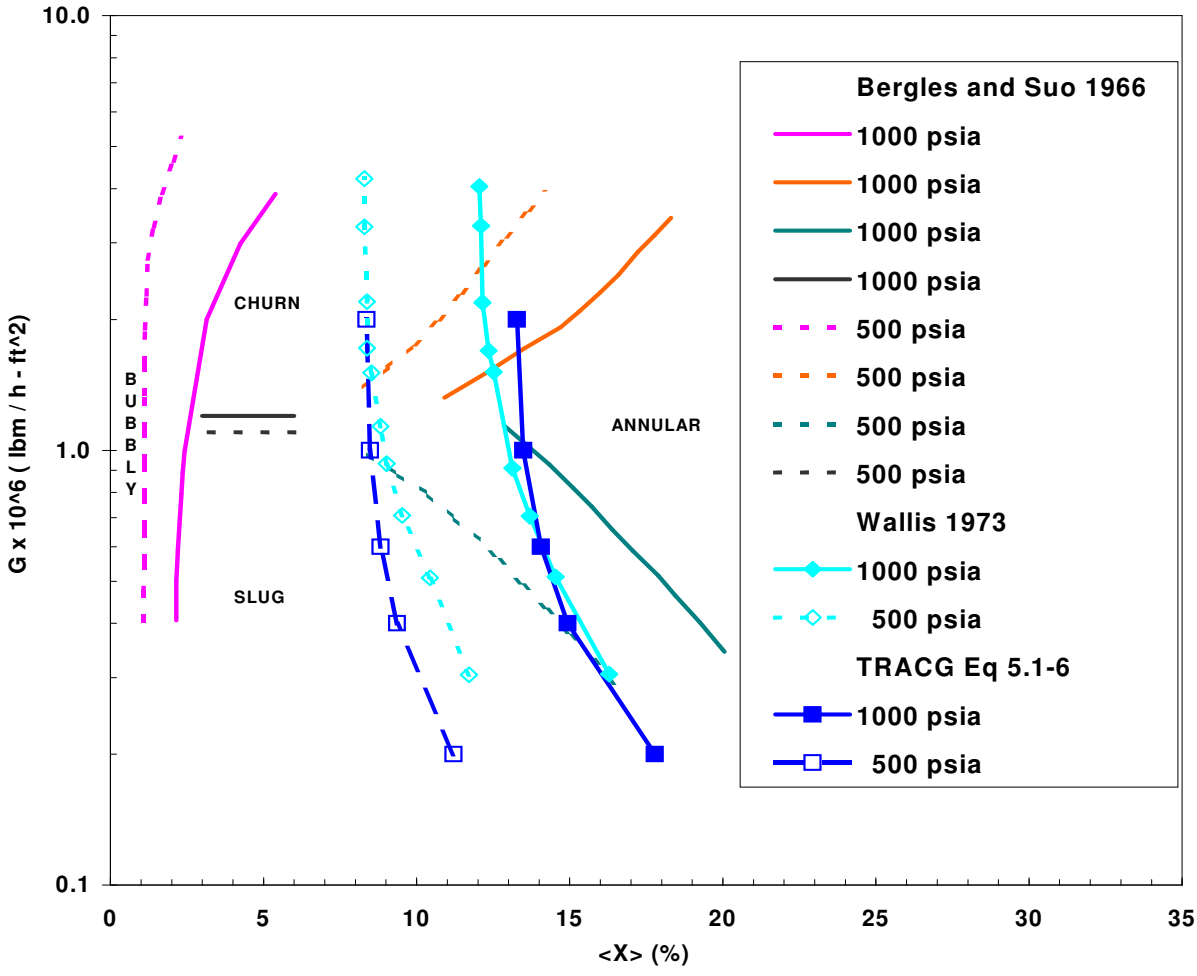

Figure 5-2. Flow Regime Map in terms of Quality

The lower bound of the transition regime (Equation (5.1-6)), where the transition to annular flow is initiated, is in good agreement with the data and the Wallis criterion from Equation (5.1-11). It should be kept in mind that flow regime maps are based on visual interpretation of test data, which tend to be fairly subjective. The main assessment of the flow regime map should be done in connection with the interfacial shear model and based on the accuracy of void fraction prediction. As will be shown in Section 6.1, the void fraction is predicted quite accurately, generally to within a few percent.

5.1.2 Entrainment

The transition from a purely annular flow regime to an annular flow with dispersed droplets is given by the onset of entrainment.

5.1.2.1 Technical Basis and Assumptions

The entrainment correlation proposed by Mishima and Ishii[46] has been adopted:

$$E = \mathrm{tgh}(\eta) = \mathrm{tgh}\left(7.5\cdot 10^{-7}\left(j_v^*\right)^{2.5}\left(D^*\right)^{1.25}\mathrm{Re}_\ell^{0.25}\right) \tag{5.1-14}$$

where:

$$j_v^* = \frac{j_v}{\left[\frac{\sigma\Delta\rho g}{\rho_v^2}\left(\frac{\rho_v}{\Delta\rho}\right)^{0.667}\right]^{0.25}} \tag{5.1-15}$$

$$D^* = D_{h\ell}\sqrt{\frac{g\Delta\rho}{\sigma}} \tag{5.1-16}$$

$$\mathrm{Re}_\ell = \frac{\rho_\ell j_\ell D_{h\ell}}{\mu_\ell} \tag{5.1-17}$$

It is assumed that the liquid will only flow on the fraction of the wall that has not experienced boiling transition and therefore can be wetted. Therefore, the film thickness and the corresponding hydraulic diameter for the liquid ($D_{h\ell}$) is defined based on the wetted wall perimeter (S_w) as

$$D_{h\ell} = \frac{4A}{S_w} \tag{5.1-18}$$

For example, if all the rods in a fuel bundle are in post boiling transition while the channel box is wetted, then S_w is given by the perimeter of the channel box. It is also seen that the entrainment becomes 1.0 for the condition where the entire wall perimeter is in post boiling transition and S_w approaches 0.0.

5.1.2.2 Model as Coded

Ishii's correlation has been slightly modified in the TRACG implementation. When TRACG was assessed against void fraction data, it was observed that the void fraction was over predicted for conditions where a large entrainment fraction, close to 1, was predicted. This was attributed to the asymptotic behavior of tgh(η) in Ishii's correlation; tgh(η) approaches 1 too fast for large values of η, leading to the over prediction of the void fraction due to the much lower relative velocity for droplet flow than for annular flow. In order to correct this deficiency, a modification was introduced to Ishii's correlation. The dimensionless property groups in the correlation were retained, but the functional form was modified from tgh(η) to:

$$E = \begin{cases} \dfrac{\max\left((\eta_l - 0.03), 0.0\right)}{\sqrt{1+(\eta_l + 0.1)^2}}, & \eta_l < 10^6 \\ 1 - \dfrac{0.13}{\eta_l}, & \eta_l \geq 10^6 \end{cases} \qquad (5.1\text{-}19)$$

where

$$\eta_l = 10^{-6}\left(j_v^*\right)^{2.5}\left(D^*\right)^{1.25}\mathrm{Re}_\ell^{0.25} \qquad (5.1\text{-}20)$$

The calculated entrainment values from Equation (5.1-19) compared to values from Equation (5.1-14) are shown in Figure 5-3. The calculated values from the revised expression relative to the original are: lower at very low values of η, slightly higher for intermediate values of η, and slightly lower for the highest values of η.

When a surface experiences boiling transition less liquid is available for entrainment, but the fraction of that liquid that becomes entrained actually increases so that in the limit as all surfaces dry out the entrainment fraction approaches unity. This effect is accounted by defining the liquid hydraulic diameter from Equation (5.1-18). As the wetted perimeter decreases the hydraulic diameter for the liquid increases, the Reynolds number for the liquid from Equation (5.1-17) increases, and the value of D^* from Equation (5.1-16) increases. These increases all cause η_l in Equation (5.1-20) to increase so that in the limit as η_l becomes very large and the entrainment fraction predicted from Equation (5.1-19) approaches unity.

5.1.2.3 Applicability

Ishii's correlation has been compared to many experimental data[48] for air-water systems covering the ranges:

$0.1 < P < 0.4$ MPa

$0.0095 < D_h < 0.032$ m

$370 < \mathrm{Re}_\ell < 6400$

$j_v < 100$ m/sec

An example on this qualification is shown in Figure 5-3. This figure also shows the difference between Ishii's original correlation from Equation (5.1-14) and the modified correlation given by Equation (5.1-19). Relative to the 187 data points, the average error in the calculated entrainment from Equation (5.1-19) is +0.008 with a standard deviation of 0.056. As expected, less than 5% of the data points fall outside the ±2-sigma bands as depicted by the eight solid-colored data points compared to the colored lines in Figure 5-3.

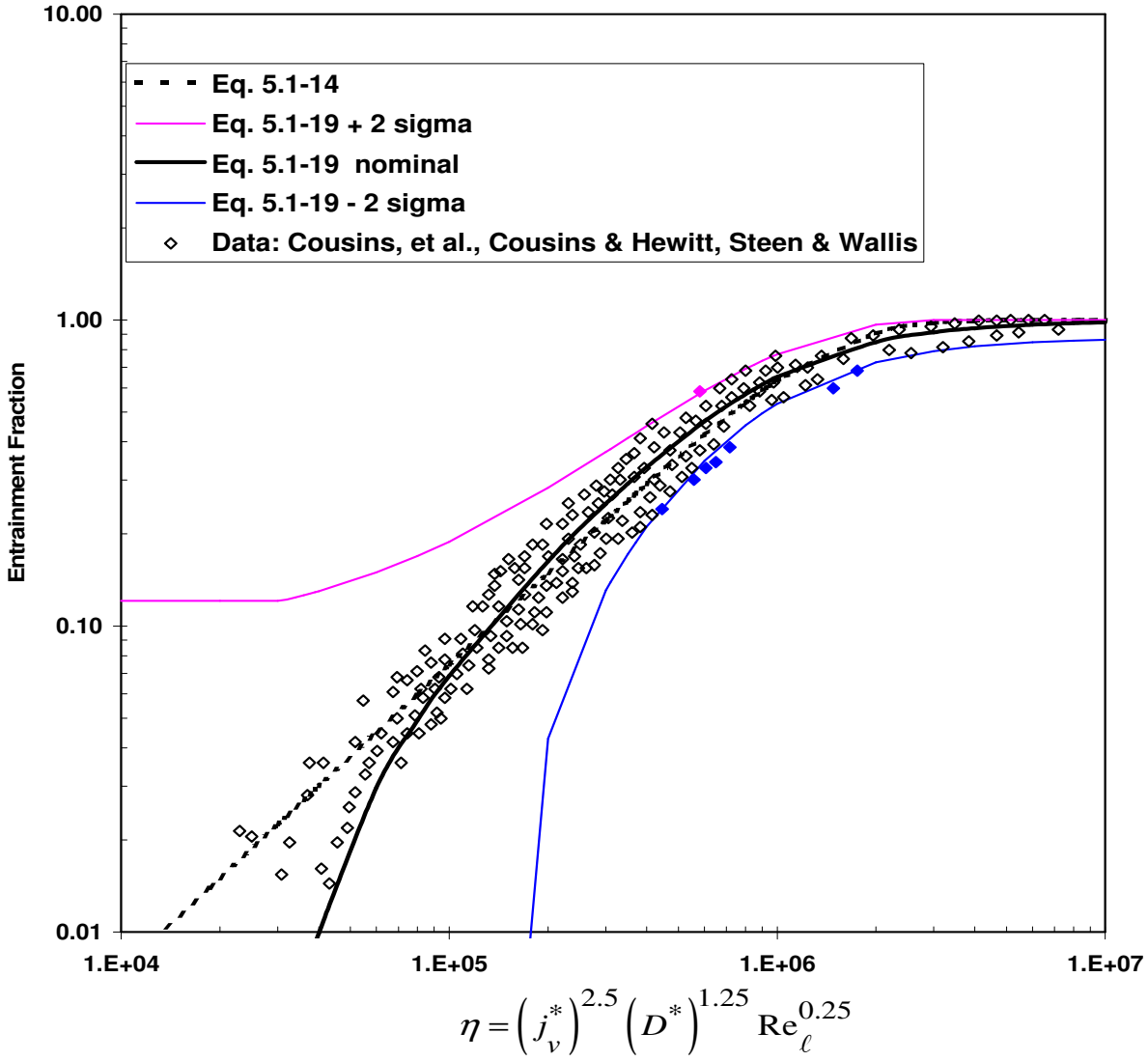

Figure 5-3. Comparison of Equilibrium Entrainment Correlation to Various Data

The main shortcoming for Ishii's entrainment correlation is the relatively limited pressure range near atmospheric pressure of the database used to develop the correlation. This is not believed to limit the correlation's applicability because pressure (and other fluid properties) are

implicitly included in the dimensionless parameters from Equations (5.1-15) through (5.1-17) that are used to develop the correlation. For higher pressures approaching BWR operating pressures, the entrainment correlation as implemented in Equation (5.1-19) has been indirectly validated through comparisons to void fraction data (Section 6.1.8). For annular flow especially, the relationship between void fraction and entrainment is very strong as indicated in Sections 6.1.4 and 6.1.6. For the intermediate pressures, additional qualification using Toshiba void fraction data has been added as indicated in Section 3.1.6 of Reference [6]. The excellent prediction of the void fraction data (±2%) for pipes and rod bundles over the entire range of pressures justifies the use of Ishii's entrainment correlation for pressures over the entire range of BWR operating pressures.

5.1.3 Horizontal Flow

For horizontal pipes, a transition from bubbly flow to stratified flow is introduced. The transition is similar to the transition to annular flow in the sense that it represents a transition from dispersed flow to separated flow. The transition from stratified to dispersed flow is derived from the condition where an instability will develop for the free surface in stratified flow based on a critical Froude number.

5.1.3.1 Technical Basis and Assumptions

For vapor flowing over a free surface, an instability will develop if the perturbation in the vapor pressure as predicted by Bernoulli's equation due to a small perturbation in the liquid level, δ, exceeds the static head corresponding to the level perturbation:

$$\rho_v v_v^2 \frac{\delta}{\alpha D_h} > \delta \Delta\rho g_T \tag{5.1-21}$$

where g_T is the component of the gravity vector perpendicular to the pipe. For a horizontal pipe $g_T = g$, while $g_T = 0$ for a vertical pipe. In general, $g_T = g \cos(\theta)$, where θ is the inclination of the pipe.

The condition for instability of the free surface is thus given by:

$$\frac{\rho_v v_v^2}{\alpha D_h \Delta\rho g_T} = 1 \tag{5.1-22}$$

or

$$\alpha_{strat} = \frac{\rho_v v_v^2}{\Delta\rho g_T D_h} \tag{5.1-23}$$

5.1.3.2 Model as Coded

Analogous to the transition to annular flow, a transition region is implemented to avoid discontinuities in the constitutive correlations. The transition is implemented to take place over a void fraction interval of 0.1.

$$\{\alpha_{strat}, \alpha_{strat} + 0.1\} \tag{5.1-24}$$

Dispersed flow exists for $\alpha < \alpha_{strat}$ and stratified flow exists for $\alpha > \alpha_{strat}+0.1$. A linear interpolation is performed for the constitutive correlations for shear and heat transfer over this interval between the correlations for bubbly/churn flow and the correlations for stratified flow.

5.1.3.3 Applicability

Mishima and Ishii[50] have compared various modified Helmholz models with data for predicting the transition between stratified and dispersed flow. The current TRACG model is a simplification of the term for the critical gas velocity recommended by Taitel and Dukler[49], where the following subsitutions are made:

$$\left(1-\frac{h_\ell}{D}\right) \equiv \alpha \tag{5.1-25}$$

$$\frac{dA_\ell}{dh_\ell} \equiv \frac{\pi}{4} D \tag{5.1-26}$$

Figure 5-4 shows a comparison of the TRACG model given by Equations (5.1-23) and (5.1-24) to Ishii's theory and the data of Wallis and Dobson[51]. The model is seen to bracket the data for low flow rates and slightly under-predict the data by about 0.2 for high flow rates. It should be noted that horizontal two-phase flow is not very significant for BWR applications, and, considering the reasonably good comparison to data, it can be concluded that the correlation for transition to stratified flow is applicable to BWRs.

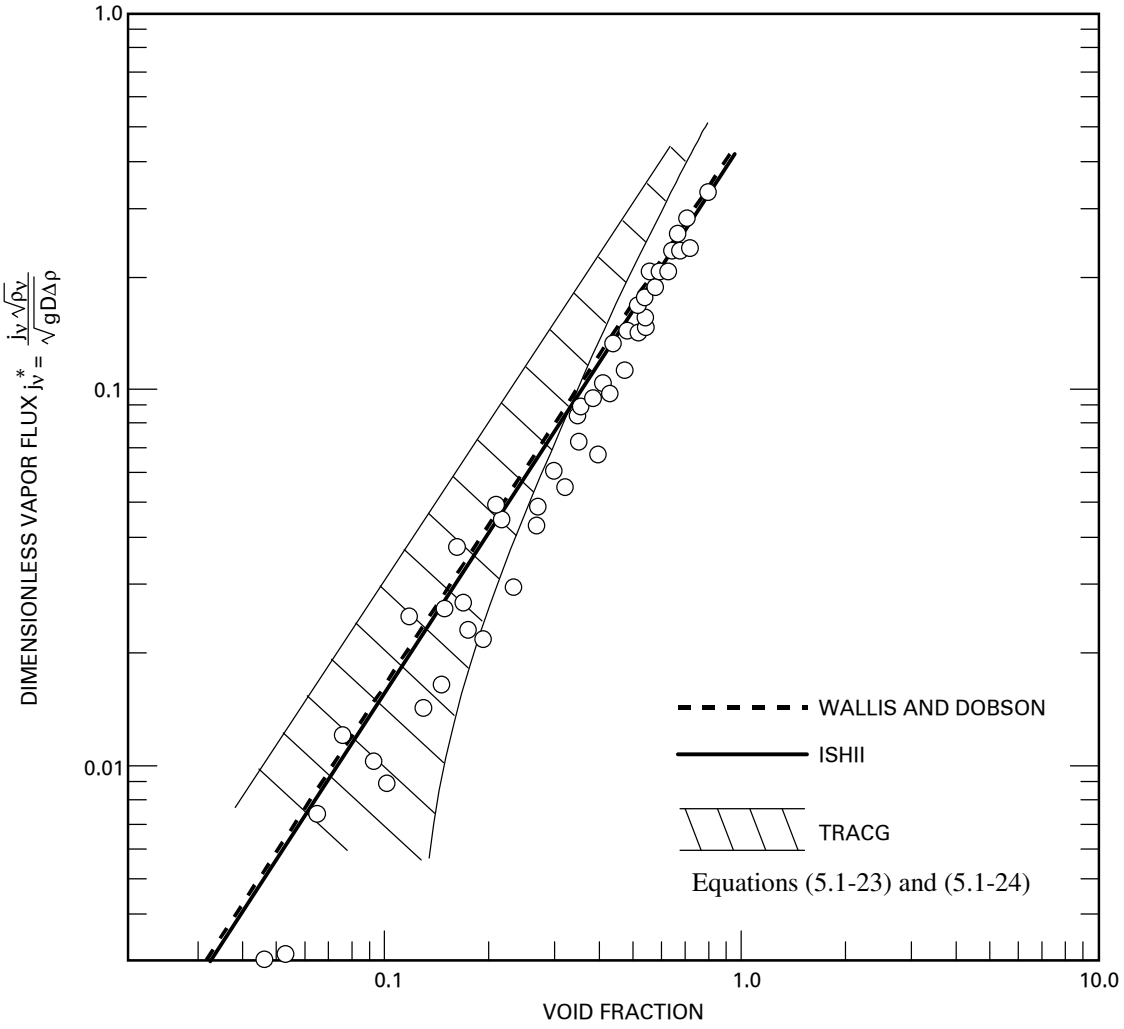

Figure 5-4. Transition to Stratified Flow

5.2 Assessment and BWR Applicability

Numerous flow regime maps exist in the literature that could be used for comparisons. Many are not mechanistic and are based on subjective observations or simply based on correlations of data, often in terms of j_ℓ and j_v. Assumptions about the interfacial drag or relative velocity are required to convert this type of map to the type of map used in TRACG. Some assessments have been given in Sections 5.1.1.3, 5.1.2.3, and 5.1.3.3. The trends are generally correct, and, due to the subjective nature of determining the transition boundaries, reasonably accurate.

It is important to note that the flow regime *per se* is not used by the field equations, but rather the values for the interfacial parameters. The main assessment of the flow regime map should be done in connection with the interfacial shear model and based on the accuracy of the void fraction prediction.

In Section 6.1, it is shown that the void fraction is predicted very accurately, generally within 2-5%. Consequently, the applicability of the flow regime map is identical to the applicability of the interfacial shear model:

$0.1 < P < 10$ MPa

$0 < G <$ greater than 2000 kg/m^2-sec

Onset of sub-cooled boiling $< T_\ell < T_{sat}$

$0.01 < D_h < 1.2^+$m

6.0 MODELS AND CORRELATIONS

To close the set of basic equations described in Section 3.0, a set of constitutive correlations describing interfacial shear and heat transfer, wall friction and heat transfer is needed. These correlations define the rates of exchange of mass, momentum and energy between the phases and their surroundings. The correlations depend on the flow regime, as they take on different forms for the different flow patterns. The flow regime map defining the flow patterns as a function of the thermal-hydraulic conditions was described in Section 5.0. This section describes the constitutive correlations for interfacial shear and heat transfer, wall friction and heat transfer for the individual flow patterns.

The ultimate objective of the TRACG code is to analyze a wide variety of BWR transients and LOCAs. The models and correlations described in this section must be adequate for this purpose over the range of expected conditions. Table 6-1 provides the desired range of applicability for the various BWR regions in the reactor vessel. These ranges were derived by considering reactor startup conditions (at criticality) for the lower bound for the flow rates in the reactor vessel. The upper bound flow rates generally correspond to the reactor operation at rated conditions. Break flow following a LOCA can also result in the highest flow rate in the region of the break. For the containment, the steamline break provides an upper bound on flow rates. The void fraction range considers depressurization during a LOCA and possible uncovery because of loss of inventory.

Later in this section, the ranges for each group of models will be compared with the desired ranges given in Table 6-1. This is done in Table 6-2 for interfacial shear, Table 6-3 for pressure drop, Table 6-10 for interfacial heat transfer and Table 6-18 for wall heat transfer. The entries in these four tables refer to the suitability of the models and correlations to predict the particular phenomenon in the ranges given for each component in Table 6-1. The entries do not indicate whether or not a model was developed specifically for that component or region. So, for example, if the models for single phase convection to liquid and two-phase convection cover the Reynolds number range of 1400 to 200,000 then the Reynolds number column for Bypass in Table 6-18 would be marked with a "C".

Table 6-1. Range of Parameters for BWR Regions

Range of Parameters for BWR Regions								
Region	**Flow Regimes**	**Wall HT Regimes**	**Size (m)**	**Range of Conditions**				**Noncondensable Concentration in Vapor Phase**
				P (MPa)	**G(kg/m^2-s)**	**Void**	**Reynolds No.**	
Lower Plenum	SPL, BC	SPCL, TPC	3D cells; O (1 m)	[[				
CRD Guide Tubes	SPL, BC	SPCL, TPC	D_h~0.3, L~4.0					
Core	All	SPCL, NB, BT, FB	D_h~0.01, L~2.7 – 3.7					
Bypass	SPL, BC, SPV	SPCL, TPC	D_h~0.04, L~4.0					
Upper Plenum	SPL, BC, DD, SPV	SPCL, TPC, SPCV	3D cells; O (1 m)					
Mixing Region	SPL, BC, DD, SPV	SPCL, TPC, SPCV	3D cells; O (1 m)					
Steam Dome	DD, SPV	SPCV	O (1 m)					
Steam Line	DD, SPV	SPCV	D_h~0.8					
Downcomer	SPL, BC, SPV	SPCL, TPC, SPCV	3D cells; O (1 m)					
Recirculation Loop	SPL, BC	SPCL, TPC	D_h~0.5 m					
Drywell	SPV, DD	SPVC, COND	3D cells; O (2 m)					
Wetwell Air Space	SPV, DD	SPVC, COND	3D cells; O (2 m)					
Suppression Pool	SPL, bubbly	SPCL	3D cells; O (2 m)					
Main vents	SPL, large buble, stratified	SPCL, TPC	D_h~0.7, L~0.7					
Steam Seperator	SPL,BC,DD,SPV	SPCC,TPC,SPCV	D_h~0.15, L~4.0					
ESBWR Chimney	SPL, BC, DD, SPV	SPCL, TP, C, SPCV	D_h~0.6, L~7.0					]]

Range of Parameters for BWR Regions	
Flow Regimes:	
SPL	Single Phase Liquid
BC	Bubbly – Churn
Transition	Transition from bubbly to annular flow
Annular	Annular Flow
DD	Droplet Flow
SPV	Single-Phase Vapor
Wall Heat Transfer Regimes:	
SPCL	Single-Phase Convection to Liquid
TPC	Two-Phase Convection (small amount of condensation or boiling based on wall temperature)
NB	Sub-cooled and Nucleate Boiling
SPCV	Single-Phase convection to Vapor
BT	Boiling Transition from Nucleate to Film Boiling
FB	Film Boiling
COND	Condensation

In the nomenclature, the term gas implies a general mixture of steam and noncondensable gases. The subscript "v" will denote a property or parameter applying to the gas mixture; the subscript "s" indicates a quantity applying specifically to steam, and the subscript "a" signifies the summation of all noncondensable gases. The subscripts "f" and "g" signify saturated liquid and steam, respectively. The following list of nomenclature applies to Section 6.0.

Nomenclature

Item	***Description***
a	constant; absorption coefficient; sonic velocity
A	area; constant
B	Constant
B	Radiosity
C	Constant
C_D	drag coefficient
C_o	drift flux model distribution parameter
C_p	specific heat at constant pressure
C_v	specific heat at constant volume
CHF	critical heat flux
d_i	interfacial area per unit volume
D	Diameter
D_Q	thermal diameter
e	specific total energy
E	Entrainment
ECPR	experimental critical power ratio
F	wall shear; factor in Chen correlation; radiation view factor
$f_{\ell v}$	drag force per unit volume between gas and liquid phase
f_1	correlation factor for pure steam
f_2	correlation factor for noncondensable gas
f_R	friction factor
F_s	Sub-cooled correction factor for modified Zuber correlation
g	acceleration of gravity
G	mass flux
Gr	Grashof number = $\rho^2 g \beta L^3 \Delta T / \mu^2$
h	heat transfer coefficient; specific enthalpy
H	incoming radiation
h_L	dynamic head loss term
h_{fg}	$h_g - h_f$

Nomenclature

Item	*Description*
I	Bessel function
j^*	superficial velocity
k	thermal conductivity; constant
L	length
M_v	interfacial drag between the two phases due to difference in velocity
n	constant; variable
Nu	Nusselt number = h D / k
P	pressure
PCT	peak cladding temperature
Pe	Peclet number = G D C_p / k
Pr	Prandtl number = μ C_p / k
q"	heat flux
q"'	volumetric heat generation rate
R	local peaking pattern parameter; gas constant
Re	Reynolds number = G D / μ or as defined in text
s	thickness of oxide layer
S	suppression factor in Chen correlation; specific entropy
t	time
T	temperature
v	velocity
v_{gj}	drift flux velocity
V	variable in GEXL correlation
W	molecular weight
We	Weber number = ρ v^2 L / σ
x	flow quality; noncondensable mass fraction
X	variable defined in text
Y	mole fraction; variable used in model as coded sections
z	coordinate direction
Greek Symbols	
α	void fraction
β	heat transfer coefficient from steam to droplets; volumetric coefficient of thermal expansion
χ	inverse of the Lockhart-Martinelli parameter
δ	film thickness

Nomenclature

Item	*Description*
ε	pumping factor; emissivity
$\phi^2_{\ell o}$	two-phase multiplier
$\Phi^2_{\ell o\ hom}$	homogeneous two-phase multiplier
γ	specific heat ratio = C_p / C_v; variable in Section 6.6.8
Γ_g	volumetric vapor generation rate
Γ	mass flow of condensate per unit circumference
μ	viscosity; bias; anisotropic correction factor
ρ	density
σ	surface tension; standard deviation; Stefan-Boltzmann constant
τ	shear; transmissivity

Subscripts

a	all noncondensable gases
A	annular
air	air
b	bubbly
B	bulk
BER	Berenson
c	critical
d	droplet
e	equilibrium
E	entrainment fraction
evap	evaporation
f	saturated liquid
FB	film boiling
free	free or natural convection
g	saturated steam
h	hydraulic
He	helium
HE	HEM critical flow model
i	interface
L	level
ℓ	liquid (sub-cooled)

Nomenclature

Item	*Description*
ℓd	liquid departure
lam	laminar
m	mixture
mac	macroscopic
mic	microscopic
min	minimum
n	specific noncondensable gas component
NB	nucleate boiling
NC	nucleate boiling at CHF
r	relative
ref	reference
s	steam
sat	saturated
t	throat
TB	transition boiling
TP	two phase
tran	transition
turb	turbulent
u	universal
v	vapor
w	wall
Zr	Zirconium
Superscripts	
I	isotropic
A	anisotropic

6.1 Interfacial Shear

Calculation of interfacial shear and momentum exchange across the interface is a necessary part of the two-fluid equation system solution. In specific terms, the interfacial shear model calculates the variable $f_{\ell v}$ in the equations of motion for vapor and liquid (Section 3.1.2). $f_{\ell v}$ represents the drag force, per unit volume, between the phases; and it is expressed in terms of average phasic velocity difference:

$$f_{\ell v} = c_i \left|\overline{v}_r\right| \overline{v}_r \qquad (6.1\text{-}1)$$

where c_i is the local average interfacial drag coefficient between phases (per unit volume) and $\overline{v}_r$ is the void-weighted average velocity difference between vapor and liquid. The local values of c_i and $\overline{v}_r$ are dependent on flow regime, void fraction and properties of vapor and liquid (c_i is a function of $\overline{v}_r$). Equation (6.1-1) gives only the generic form of $f_{\ell v}$ (its specific forms are described later). The basic principle of these calculations is to identify the prevailing flow pattern at each hydraulic junction and then apply specific correlations for relative phasic velocity and interfacial drag to determine the momentum exchange across the interface at that junction.

6.1.1 Background

The bulk of the data available for the evaluation of the interfacial shear and the wall friction are void fraction and pressure drop data. These are also the parameters that are important and must be described accurately in a best-estimate analysis of the two-phase flow in a BWR. More fundamental data are available for the shear and the interfacial forces, and extensive basic research is continuing. However, a comprehensive set of models for the shear and interfacial forces for all flow regimes does not presently exist, and the models that do exist are primarily for idealized flow regimes. For these reasons, the development of the constitutive correlations for the interfacial shear is based on the very large database that exists for void fractions and pressure drop. The correlations are based on the following:

For adiabatic and steady state conditions, the two-fluid model and the drift flux model are equivalent, and drift flux parameters can be used to characterize the relative velocity, and the phase and flow distributions.

The correlations for the interfacial shear and drag, as well as wall friction, as derived from adiabatic steady-state conditions, are applicable for transient conditions.

The interfacial shear correlations are based on the set of drift flux correlations developed by Ishii[44] from void fraction data available in literature. These models for the interfacial shear are validated through the qualification against steady state and transient void fraction data described in the TRACG qualification reports[4],[5],[6].

6.1.2 Relation to Drift Flux Parameters

The relation between interfacial forces and drift flux parameters is discussed in detail in Reference [52]. A brief summary will be given in the following sections.

6.1.2.1 Shear and Wall Friction

The presence of wall friction creates a shear field in the two-phase flow. This shear field will interact with both phases, and thus create an interfacial force, which has its origin in the wall friction. For example, for steady-state bubbly flow, the momentum equations can be written as:

$$0 = -\alpha\frac{\partial P}{\partial x} - \alpha\rho_v g - f_{\ell v} \qquad \text{[for the vapor phase]}^1 \qquad (6.1\text{-}2)$$

$$0 = -(1-\alpha)\frac{\partial P}{\partial x} - (1-\alpha)\rho_\ell g + f_{\ell v} - F_w \qquad \text{[for the liquid phase]} \qquad (6.1\text{-}3)$$

where $f_{\ell v}$ represents the shear at the interface, and F_W represents the shear between the wall and the liquid. If the pressure gradient is eliminated from the above equations, one obtains:

$$f_{\ell v} = \Delta\rho g\alpha(1-\alpha) + \alpha F_w \qquad (6.1\text{-}4)$$

Consequently, if the interfacial shear above was a function only of the relative velocity between the phases, the relative velocity would be dependent upon the wall friction or the Reynolds number. This, however, is not the case. Data[44],[53] indicate that the drift velocity is virtually independent of the flow rate. The interfacial shear, therefore, consists of another term with its origin in the wall friction besides a term that is a function of the relative velocity.

Following Ishii's notation[44], the local time-averaged momentum equations for the vapor and liquid phases are:

$$\alpha\rho_v\left(\frac{\partial \bar{v}_v}{\partial t} + \bar{v}_v\cdot\nabla\bar{v}_v\right) = -\alpha\nabla P + \alpha\nabla\cdot\bar{\bar{\tau}} - \alpha\rho_v\bar{g} - \bar{M}_v \qquad (6.1\text{-}5)$$

$$(1-\alpha)\rho_\ell\left(\frac{\partial \bar{v}_\ell}{\partial t} + \bar{v}_\ell\cdot\nabla\bar{v}_\ell\right) = -(1-\alpha)\nabla P + (1-\alpha)\nabla\cdot\bar{\bar{\tau}} - (1-\alpha)\rho_\ell\bar{g} + \bar{M}_v \qquad (6.1\text{-}6)$$

Here the interfacial mass transfer has been neglected and it has been assumed that each phase, as well as the interface, has the same pressure.

For one-dimensional flow, Equations (6.1-2) and (6.1-3) degenerate to:

$$\alpha\rho_v\left(\frac{\partial v_v}{\partial t} + v_v\cdot\nabla v_v\right) = -\alpha\frac{\partial P}{\partial z} + \alpha\nabla\cdot\bar{\tau}_z - \alpha\rho_v g - M_v \qquad (6.1\text{-}7)$$

$$(1-\alpha)\rho_\ell\left(\frac{\partial v_\ell}{\partial t} + v_\ell\cdot\nabla v_\ell\right) = -(1-\alpha)\frac{\partial P}{\partial z} + (1-\alpha)\nabla\cdot\bar{\tau}_z - (1-\alpha)\rho_\ell g + M_v \qquad (6.1\text{-}8)$$

An interpretation of the various terms on the right-hand side of Equations (6.1-7) and (6.1-8) can be obtained from Figure 6-1.

For the gas equation, the interpretation of the various terms is as follows:

[1] A general formulation is applied for the gravitational force in the momentum equations in Section 3. For the 3D equations, the gravitational force is introduced as a vector $\vec{g}$ and for the 1D equations; the gravitational force is introduced as a parameter g that can range from –9.81 to +9.81 m/sec^2 dependent on the orientation of the pipe. In this Section 6.1 the momentum equation is formulated for a vertical pipe with the positive direction up and g=9.81. Since the force of gravity is downwards, the force is $-g\alpha\rho_g$ for the liquid momentum equation and $-(1-\alpha)\rho_\ell g$ for the liquid momentum equation.

$-\alpha\frac{\partial P}{\partial z}$ = the force on the gas due to the pressure gradient in the z-direction (the pressure is assumed to be the same for each phase)

$\alpha\nabla\cdot\bar{\tau}_z$ = the force on the gas due to the shear at the surface of the incremental volume. It is assumed that the averaged shear tension is the same for each phase, which is reasonable, because, except for surface tension and mass transfer effects, the shear is a continuous function.

$-\alpha\rho_v g$ = the body force, due to gravity, on the gas.

M_v = the interfacial drag between the phases inside the incremental volume due to a local difference in the phase velocities.

For a dispersed two-phase flow regime such as bubbly or droplet flow, it is a good assumption that the fraction of the surface of the control volume occupied by the gas phase is equal to void fraction. For other flow regimes such as pure annular flow, i.e., no entrainment, the model assumption is less accurate. The assumption however was adopted for all flow regimes for consistency. The excellent comparison to void fraction data shown in Section 3.1 of the *TRACG Qualification LTR*[4],[5],[6] demonstrates the applicability of the model.

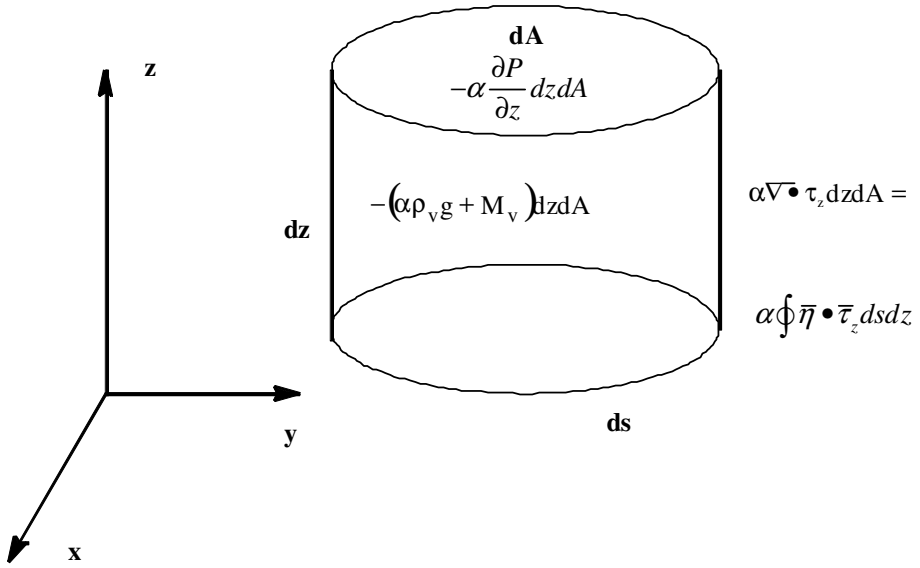

Figure 6-1. Right-Hand Side of Vapor Momentum Equation

The bases for the interfacial shear model are stated in Section 6.1.1. For adiabatic and steady state conditions in a straight fluid channel without any area changes, there is no acceleration of the fluid and the $\frac{\partial}{\partial t}$ as well as the $\frac{\partial}{\partial x}$ terms are zero. Therefore, for adiabatic steady-state conditions, Equations (6.1-7) and (6.1-8) reduce to:

$$\alpha\frac{\partial P}{\partial z} - \alpha\nabla\cdot\bar{\tau}_z + \alpha\rho_v g + M_v = 0 \qquad (6.1\text{-}9)$$

$$(1-\alpha)\frac{\partial P}{\partial z} - (1-\alpha)\nabla\cdot\bar{\tau}_z + (1-\alpha)\rho_\ell g - M_v = 0 \qquad (6.1\text{-}10)$$

When Equations (6.1-9) and (6.1-10) are added,

$$\frac{\partial P}{\partial z} - \nabla\cdot\bar{\tau}_z + \left((1-\alpha)\rho_\ell + \alpha\rho_v\right)g = 0 \qquad (6.1\text{-}11)$$

The integration of this equation over the cross section, assuming that the densities and the pressure gradient are constant across the flow area, results in:

$$A\frac{\partial P}{\partial z}-\int_S \bar{\eta}\cdot\bar{\tau}_z ds + A\left(\langle 1-\alpha\rangle \rho_\ell + \langle\alpha\rangle\rho_v\right)g = 0 \tag{6.1-12}$$

The integral is along the boundary (S), $\bar{\eta}$ is the normal to the boundary, and Gauss's theorem has been used. When Equations (6.1-11) and (6.1-12) are combined,

$$\nabla\cdot\bar{\tau}_z = \frac{1}{A}\int \bar{\eta}\cdot\bar{\tau}_z ds - \Delta\rho g\left(\alpha-\langle\alpha\rangle\right) \tag{6.1-13}$$

Integrating the momentum equation for the gas over the cross section results in:

$$\langle\alpha\rangle A\frac{\partial P}{\partial z}-\int_A \alpha\nabla\cdot\bar{\tau}_z dA + \langle\alpha\rangle A\rho_v g + \int_A M_v dA = 0 \tag{6.1-14}$$

The second term in this equation can be evaluated using Equation (6.1-13):

$$\int_A \alpha\nabla\cdot\bar{\tau}_z dA = \langle\alpha\rangle\int\bar{\eta}\cdot\bar{\tau}_z ds - A\Delta\rho g\left\langle\left(\alpha-\langle\alpha\rangle\right)^2\right\rangle \tag{6.1-15}$$

The left side of Equation (6.1-15) is the total amount of shear on the vapor phase. The first term on the right side is the void fraction times the wall friction. The second term is an induced shear stress due to the variance of the void fraction across the flow area:

$$f_i = A\Delta\rho g\left\langle\left(\alpha-\langle\alpha\rangle\right)^2\right\rangle \tag{6.1-16}$$

and from which

$$\int_A \alpha\nabla\cdot\bar{\tau}_z dA = -\langle\alpha\rangle F_w - f_i \tag{6.1-17}$$

Inserting this into Equation (6.1-14) gives:

$$\langle\alpha\rangle A\frac{\partial P}{\partial z}+\langle\alpha\rangle F_w + f_i + \langle\alpha\rangle A\rho_v g + \int_A M_v dA = 0 \tag{6.1-18}$$

Similarly, for the liquid momentum equation,

$$\langle 1-\alpha\rangle A\frac{\partial P}{\partial z}+\langle 1-\alpha\rangle F_w - f_i + \langle 1-\alpha\rangle A\rho_\ell g - \int_A M_v dA = 0 \tag{6.1-19}$$

The various terms in the integrated momentum equation for the gas have the following physical interpretations:

$\langle\alpha\rangle A\frac{\partial P}{\partial z}$ = the force due to the pressure gradient

$\langle\alpha\rangle F_w$ = induced shear stress due to the shear created by the wall friction

$\langle\alpha\rangle A\rho_v g$ = the body force due to gravity

$\int_A M_v dA$ = the drag force between the phases due to local velocity differences

f_i = induced shear stress due to the radial phase distribution

The terms in the integrated liquid momentum equation can, of course, be interpreted in the same way.

Consequently, if the liquid phase alone is in contact with the wall, the wall friction acts alone on the liquid, giving:

$$F_{wv} = 0 \tag{6.1-20}$$

$$F_{w\ell} = F_w \tag{6.1-21}$$

The induced shear, however, caused by the wall friction, creates an interfacial force between the phases given by $\langle\alpha\rangle F_w$ where the net forces on the phases due to the wall friction become $\langle\alpha\rangle F_w$ for the gas phase and $\langle 1-\alpha\rangle F_w$ for the liquid phase. Similarly, if the gas phase is in contact with the wall,

$$F_{wv} = F_w \tag{6.1-22}$$

$$F_{w\ell} = 0 \tag{6.1-23}$$

and the interfacial force, due to the wall friction, becomes $\langle 1-\alpha\rangle F_w$. Again, the net forces on the phases due to the wall friction become $\langle\alpha\rangle F_w$ for the gas phase and $\langle 1-\alpha\rangle F_w$ for the liquid phase.

It is significant to realize that the distribution of the wall shear between the phases has no impact on the pressure drop, as the total momentum equation is not affected. The distribution, however, affects the interaction between the phases and is in agreement with the experimental observation[44],[53] that the relative velocity is insensitive to flow rate.

6.1.2.2 Interfacial Drag and Phase Distribution

In Section 6.1.2.1, the interfacial force due to the wall friction was derived. The remaining interfacial forces then become a function of the interfacial drag due to the difference in the phase velocities, the buoyancy due to the gravity, and a force that is due to the phase distribution.

When $\frac{\partial P}{\partial z}$ and τ are eliminated from Equations (6.1-9) and (6.1-10),

$$M_v = \alpha(1-\alpha)\Delta\rho g \tag{6.1-24}$$

The physical interpretation of this equation is that, locally, the drag is equal to the buoyancy. Integrating this equation over the cross section gives:

$$\int_A M_v dA = A\Delta\rho g\langle\alpha(1-\alpha)\rangle \tag{6.1-25}$$

This equation, combined with Equation (6.1-16), gives the total interaction between the phases due to drag or shear:

$$\langle f_{\ell v}\rangle = f_i + \int_A M_v dA = A\Delta\rho\langle\alpha\rangle\langle 1-\alpha\rangle \tag{6.1-26}$$

The interfacial force must be related to the velocity difference between the phases. It is conventional to define:

$$f_{\ell v} = c_i |v_r| v_r \tag{6.1-27}$$

Integrating Equation (6.1-27) over the cross section yields:

$$A\langle f_{\ell v}\rangle = \int_A f_{\ell v} dA = A\bar{c}_i |\bar{v}_r| \bar{v}_r \tag{6.1-28}$$

Where:

$$\bar{c}_i = \frac{\langle c_i |v_r| v_r\rangle}{|\langle v_r\rangle|\langle v_r\rangle} \tag{6.1-29}$$

In this equation, $\bar{v}_r$ is a weighted average value for the relative velocity. It is important to note that $\bar{v}_r \neq \bar{v}_v - \bar{v}_\ell$, since $\bar{v}_v = \langle\alpha v_v\rangle/\langle\alpha\rangle$ and $\bar{v}_\ell = \langle(1-\alpha)v_\ell\rangle/\langle 1-\alpha\rangle$ have different weight functions. We will only have $\bar{v}_r = \bar{v}_v - \bar{v}_\ell$ for a uniform phase or velocity distribution.

Locally, the drift flux velocity is related to the relative velocity by:

$$v_r = \frac{v_{gj}}{1-\alpha} \tag{6.1-30}$$

and, consequently, an average relative velocity can be defined by:

$$\bar{v}_r = \frac{\bar{v}_{gj}}{\langle 1-\alpha\rangle} \tag{6.1-31}$$

where

$$\bar{v}_{gj} = \langle \alpha v_{gj} \rangle / \langle \alpha \rangle \tag{6.1-32}$$

Eliminating $\bar{v}_{gj}$ using the drift flux correlation:

$$\bar{v}_v = C_o \langle j \rangle + \bar{v}_{gj} \tag{6.1-33}$$

where

$$C_o = \langle \alpha j \rangle / \left(\langle \alpha \rangle \langle j \rangle \right) \tag{6.1-34}$$

yields:

$$\bar{v}_r = \frac{1 - \langle \alpha \rangle C_o}{\langle 1 - \alpha \rangle} \bar{v}_v - C_o \bar{v}_\ell \tag{6.1-35}$$

This expression, combined with Equation (6.1-28), results in:

$$\langle f_{\ell v} \rangle = \bar{c}_i \left| \frac{1 - \langle \alpha \rangle C_o}{\langle 1 - \alpha \rangle} \bar{v}_v - C_o \bar{v}_\ell \right| \left(\frac{1 - \langle \alpha \rangle C_o}{\langle 1 - \alpha \rangle} \bar{v}_v - C_o \bar{v}_\ell \right) \tag{6.1-36}$$

Thus, using Equation (6.1-26) and with C_o and $\bar{v}_{gj}$ correlated from void fraction data, the interfacial interaction can be evaluated by:

$$\bar{c}_i \left| \frac{1 - \langle \alpha \rangle C_o}{\langle 1 - \alpha \rangle} \bar{v}_v - C_o \bar{v}_\ell \right| \left(\frac{1 - \langle \alpha \rangle C_o}{\langle 1 - \alpha \rangle} \bar{v}_v - C_o \bar{v}_\ell \right) = \Delta \rho g \langle \alpha \rangle \langle 1 - \alpha \rangle \tag{6.1-37}$$

6.1.3 Bubbly/Churn Flow

6.1.3.1 Technical Basis and Assumptions

For bubbly flow, it is convenient to introduce:

$$\bar{c}_i = \frac{1}{8} \frac{C_D}{d_i} \rho_\ell \tag{6.1-38}$$

where C_D is the drag coefficient for the bubbles and d_i is the interfacial area per unit volume.

The interfacial area per unit volume can be given in terms of a critical Weber number:

$$\frac{1}{d_i} = 6\alpha \frac{\rho_\ell \bar{v}_{gj}^2}{\sigma \, We_c (1-\alpha)^2} \tag{6.1-39}$$

Combining Equations (6.1-37), (6.1-38) and (6.1-35) gives:

$$\frac{3}{4} \alpha \frac{C_D}{We_c} \frac{\rho_\ell^2}{\sigma} \frac{\bar{v}_{gj}^{\,4}}{(1-\alpha)^4} = \Delta \rho \, g \, \alpha (1-\alpha) \tag{6.1-40}$$

Many expressions for $\bar{v}_{gj}$ for co-current flow have been reported in the literature by References [40] and [53]. Most expressions for $\bar{v}_{gj}$ are of the form:

$$\bar{v}_{gj} = k \left\{ \frac{\Delta\rho g\sigma}{\rho_\ell^2} \right\}^{0.25} \tag{6.1-41}$$

where k ranges from 1.18 to 1.53. A value for k of 1.53 fits a wide range of data. Inserting Equation (6.1-41) into Equation (6.1-40) results in:

$$\frac{C_D}{We_c} = 0.2433\ (1-\alpha)^5 \tag{6.1-42}$$

In order to specify the interfacial shear, the exact value of We_c is not needed; only the ratio C_D/We_c matters.

For co-current flow, the distribution parameter will range from 0 for sub-cooled boiling to 1.333 as a maximum value for parabolic profiles. For high flow rates or high pressure $(\rho_v \approx \rho_\ell)$, the distribution parameter should approach one. Ishii[44] recommends:

$$C_o = C_\infty - (C_\infty - 1)\sqrt{\frac{\rho_v}{\rho_\ell}} \tag{6.1-43}$$

where C_∞ as given by Nikuradse[55] has been modified to extend it to lower pressures by defining:

$$C_\infty = 1.288 + 0.105 * \sqrt{\frac{\rho_\ell}{\rho_v}}\bigg|_{P_{ref}} \sqrt{\frac{\rho_v}{\rho_\ell}}\bigg|_{P} - 0.015 \log_e\left(Re_\ell\right) \tag{6.1-44}$$

In this expression the first density ratio is evaluated at the reference pressure of P_{ref} = 7.0 MPa and the second density ratio is evaluated at the pressure of interest.

For low flow rates in large geometries, such as bubbles rising in a pool[56],[57], Equations (6.1-41) and (6.1-44) lead to an over prediction of the void fraction data. The primary reason for this is that rising bubbles tend to induce a natural circulation in large geometries with local regions of two-phase co-current up flow separated by local regions of single-phase liquid down flow. This effect is not included in the above correlations.

Assuming the local drift to be given by Equation (6.1-41), the constant k can be correlated from Wilson's data[56], and one obtains:

$$k = 0.73\ \left(D^*\right)^{0.121}\ \left(\frac{\Delta\rho}{\rho_v}\right)^{0.203}\ \left(j_v^*\right)^{0.635} - C_o\ j_v^* \tag{6.1-45}$$

where:

$$D^* = D_h \sqrt{\frac{\Delta\rho\, g}{\sigma}} \tag{6.1-46}$$

$$j_v^* = \frac{j_v \sqrt{\rho_\ell}}{(\Delta\rho g\sigma)^{0.25}} \tag{6.1-47}$$

For large hydraulic diameters and low values of the volumetric flux, Equation (6.1-45) gives larger values than 1.53. TRACG uses the larger of 1.53 and the value of k predicted by Equation (6.1-45).

6.1.3.2 Model as Coded

The model for the interfacial shear for bubbly/churn flow is encoded as described by the above equations with the following limitations:

- C_o is not allowed to exceed a value of 1.333 or $1/\alpha$. The latter limit is imposed, as a value larger than this limit would cause the coefficient to the vapor velocity in Equation (6.1-35) to become negative.
- When calculating the interfacial shear from Equations (6.1-40) and (6.1-42), an expression of the following form is obtained: $\langle f_{\ell v} \rangle = \bar{c}_i' v_r |v_r|^3$. The last term in this equation is limited to a lower value of 0.2; i.e., $\langle f_{\ell v} \rangle = \bar{c}_i' v_r \max\left(0.2, |v_r|\right)^3$. This is a smaller value than what would be expected from Equation (6.1-41) for a wide range of pressures and thus will have no impact on the solution. This limit is implemented on the relative velocity to prevent the derivative of the interfacial shear with respect to the relative velocity from approaching zero, which would cause numerical problems.

6.1.3.3 Applicability

The correlations for the interfacial shear for bubbly flow are based on Ishii's recommendations[44]. In his database, Ishii considered data covering a wide range of parameters:

$0.1 < P < 12$ MPa

$0.01 < D_h < 0.17$m

$-30 < j < 20$ m/sec.

The correlation has been extended using Wilson's bubble rise data[56] to cover hydraulic diameters up to 0.48 m. Further qualification using the EBWR void fraction data (Section 3.1.4 of References [4], [5] and [6]) shows that the correlation can be applied for hydraulic diameters on the order of 1.5 meters without significant error. For even larger diameters the shear along the wall has progressively less importance in determining the average interfacial shear of the bulk fluid so the void fraction can be predicted by models that assume bubbles in an infinite medium.

6.1.4 Annular Flow

6.1.4.1 Technical Basis and Assumptions

For annular flow, c_i will be expressed as:

$$\overline{c}_i = \frac{1}{8}\frac{C_D}{d_i}\rho_\ell \tag{6.1-48}$$

with the interfacial area per unit volume given by:

$$\frac{1}{d_i} = \frac{4}{D_h}\sqrt{\alpha} \tag{6.1-49}$$

This equation holds only for a smooth film. For a rough film, the interfacial area will be increased; however, this effect of surface roughness is included in C_D.

Combining Equations (6.1-37), (6.1-48) and (6.1-49) gives:

$$\frac{1}{2}\sqrt{\alpha}C_D\ \frac{\rho_\ell}{D_h}\ \frac{\overline{v}_{gj}^2}{(1-\alpha)^2} = \Delta\rho\ g\ \alpha(1-\alpha) \tag{6.1-50}$$

Ishii[44] has analyzed the annular flow regime, using Wallis' expression[40] for the interfacial shear, and recommends:

$$\overline{v}_{gj} = \frac{(1-\alpha)^{3/2}}{\alpha + a}\sqrt{\frac{\Delta\rho\ gD_h}{0.015\ \rho_\ell}} \tag{6.1-51}$$

where:

$$a = \sqrt{\frac{1 + 75(1-\alpha)}{\sqrt{\alpha}}}\sqrt{\frac{\rho_v}{\rho_\ell}} \tag{6.1-52}$$

Inserting Equation (6.1-51) into Equation (6.1-50) gives:

$$C_D = 0.03\sqrt{\alpha}\ (\alpha + a)^2 \tag{6.1-53}$$

For the distribution parameter, Ishii[44] recommends:

$$C_o = 1 + \frac{1-\alpha}{\alpha + a} \tag{6.1-54}$$

6.1.4.2 Model as Coded

The model for the interfacial shear for annular flow is encoded as described by the above equations with the following limitations:

- The expression for the interfacial area given by Equation (6.1-49) assumes that the wall is covered by a film no matter how thin the film is. In reality, this will not

happen; at some point, the film will break up and only cover a fraction of the surface. This effect is approximated by applying a multiplier of $10(1-\alpha)$ for void fractions greater than 0.9. The purpose of this multiplier is not to model this phenomenon in great detail, but to prevent the numerical difficulty that would arise, if the interfacial shear were allowed to remain finite in the limit of α approaching 1.0

- When calculating the interfacial shear from Equations (6.1-50) and (6.1-51), an expression of the following form is obtained: $\langle f_{\ell v} \rangle = \overline{c}_i' v_r |v_r|$. The last term in this equation is limited to a lower value of 0.1; i.e., $\langle f_{\ell v} \rangle = \overline{c}_i' v_r \max(0.1, |v_r|)$. This is a smaller value than what would be expected from Equation (6.1-51) for a wide range of pressures and thus will have no impact on the solution. This limit is implemented on the relative velocity to prevent the derivative of the interfacial shear with respect to the relative velocity from approaching zero, which would cause numerical problems.

6.1.4.3 Applicability

The correlations for the interfacial shear for annular flow are based in Ishii's recommendations[44]. In his database, Ishii considered data covering a wide range of parameters, including laminar and turbulent flow and relative velocities covering a range from 0.2 to 4 m/sec.

6.1.5 Droplet Flow

6.1.5.1 Technical Basis and Assumptions

For droplet flow, it is convenient to introduce:

$$\bar{c}_i = \frac{1}{8}\frac{C_D}{d_i}\rho_v \tag{6.1-55}$$

with interface area per unit volume given in terms of a critical Weber number:

$$\frac{1}{d_i} = 6(1-\alpha)\frac{\rho_v \bar{v}_{gj}^2}{\sigma\, We_c\, (1-\alpha)^2} \tag{6.1-56}$$

Combining Equations (6.1-37), (6.1-55), and (6.1-56) results in:

$$\frac{3}{4}(1-\alpha)\frac{C_D}{We_c}\frac{\rho_v^{\,2}}{\sigma}\frac{\bar{v}_{gj}^4}{(1-\alpha)^4} = \Delta\rho\, g\, \alpha(1-\alpha) \tag{6.1-57}$$

Many expressions for $\bar{v}_{gj}$ are reported in the literature[40], and most are of the form:

$$\bar{v}_{gj} = k\,(1-\alpha)\left\{\frac{\Delta\rho g\sigma}{\rho_v^{\,2}}\right\}^{0.25} \tag{6.1-58}$$

Ishii[44] recommends k = 1.41.

Using Equation (6.1-58) and $k = 1.41 = \sqrt{2}$, Equation (6.1-57) gives:

$$\frac{C_D}{We_c} = \frac{1}{3}\,\alpha \tag{6.1-59}$$

Since the droplets can be assumed uniformly distributed due to the turbulence, the distribution parameter is defined as:

$$C_o = 1 \tag{6.1-60}$$

For large flow rates where the droplets are created by entrainment from the film, the droplet size will be determined by the initial relative velocity as they are entrained from the film on the wall. Since the film velocity is much smaller than the vapor velocity and the void fraction is high, the initial relative velocity can be approximated by the total flux. Thus, assuming a critical Weber number of 12, this is in agreement with Ishii's recommendations and leads to:

$$\frac{1}{d_i} = \frac{1}{2}(1-\alpha)\frac{\rho_v\, j^2}{\sigma} \tag{6.1-61}$$

The droplets produced by the entrainment process can mainly be characterized as undistorted particles outside the Stokes regime, and an approximation[44] for the drag coefficient is:

$$C_D = 1.07\ \alpha\ Re_d^{-0.5} \tag{6.1-62}$$

where:

$$Re_d = \frac{\rho_v\ d_d\ v_r}{\mu_v} \tag{6.1-63}$$

6.1.5.2 Model as Coded

The model for the interfacial shear for droplet flow is encoded as described by the above equations with the following limitations:

When calculating the interfacial shear from Equations (6.1-58) and (6.1-59), an expression of the following form is obtained: $\langle f_{\ell v} \rangle = \overline{c}_i^{'}\ v_r \left| v_r \right|^3$. The last term in this equation is limited to a lower value of 0.5; i.e., $\langle f_{\ell v} \rangle = \overline{c}_i^{'}\ v_r \max\left(0.5, \left| v_r \right|\right)^3$. This is a smaller value than what would be expected from Equation (6.1-58) for a wide range of pressures and thus will have no impact on the solution. This limit is implemented on the relative velocity to prevent the derivative of the interfacial shear with respect to the relative velocity from approaching zero, which would cause numerical problems. For high flow, the corresponding limitation is: $\langle f_{\ell v} \rangle = \overline{c}_i^{'}\ v_r \max\left(0.1, \left| v_r \right|\right)$.

6.1.5.3 Applicability

The correlations for interfacial shear for droplet flow are based on Ishii's recommendations[44]. For distorted particles, the model for the drift flux velocity is equivalent to the drift flux velocity for bubbly flow and the range of applicability of the model is similar. The model is consistent with the recommendations of Wallis[40]. No specific range of applicability is given by Ishii[44] and Wallis[40] and the applicability of the model is determined by the assessment (Section 6.1.8).

6.1.6 Annular/Droplet Flow

6.1.6.1 Technical Basis and Assumptions

For dispersed annular flow, the drift flux parameters as recommended by Ishii[44] are interpolated between the annular and the droplet drift flux parameters based on the entrainment fraction:

$$\bar{v}_{gj} = \frac{(1-\alpha)(1-E)}{\sqrt{\frac{1+75(1-\alpha)}{\sqrt{\alpha}}\frac{\rho_v}{\rho_\ell}}}\sqrt{\frac{\Delta\rho g D_h (1-\alpha)(1-E)}{0.015\rho_\ell}} + \frac{E(1-\alpha)}{\alpha+E(1-\alpha)}\ \min\left[\sqrt{2}\left(\frac{\Delta\rho g\sigma}{\rho_v^2}\right)^{0.25}, \frac{3\sigma}{\rho_v}\left(\frac{(\Delta\rho g)^2}{\mu_v\rho_v}\right)^{1/3}\frac{1}{j^2}\right] \quad (6.1\text{-}64)$$

The distribution parameter C_o is given by:

$$C_o = 1 + \frac{(1-\alpha)\ (1-E)}{\alpha + \sqrt{\frac{1+75(1-\alpha)}{\sqrt{\alpha}}\frac{\rho_v}{\rho_\ell}}} \quad (6.1\text{-}65)$$

where E is the entrainment fraction defined by Equation (5.1-19).

6.1.6.2 Model as Coded

In TRACG, the entrainment fraction is defined by Equation (5.1-19). It is assumed that the fraction (1-α) E of the liquid exists as entrained droplets and that the fraction (1-α) (1-E) exists as an annular film on the wall. For the entrained droplets, the shear is calculated as described in Section 6.1.5, and for the annular film the shear is calculated as described in Section 6.1.4. The two contributions are then added to form the total interfacial shear.

6.1.6.3 Applicability

The applicability of the correlations for the annular/droplet flow regime is given by the applicability of the correlation for the annular (Section 6.1.4) and droplet (Section 6.1.5) flow regimes, as well as the applicability of the entrainment correlation.

In TRACG, as in other system codes, an additional complication arises from the use of the two-fluid model. The droplets and the film will not have the same velocity. However, when a two-fluid model is used, the interfacial shear is calculated based on the average liquid velocity.

Given the above comments, the applicability of the interfacial shear model for the annular/droplet flow regime will be determined by the assessment (Section 6.1.8).

6.1.7 Modifications to Interfacial Shear

6.1.7.1 Sub-cooled Boiling

For sub-cooled boiling, the vapor is concentrated at the wall, where the liquid velocity approaches zero. Consequently, for sub-cooled boiling, the distribution parameter should also approach zero, and become zero at the point of net vapor generation. A modification to C_o for sub-cooled boiling that has the right limits was suggested by Findlay and Dix[58]:

[[ ]] (6.1-66)

where $h_{\ell d}$ is the liquid enthalpy at the point of net vapor generation (for details on $h_{\ell d}$, see Section 6.6.4). (If local subcooling occurs because of a pressure increase rather than sub-cooled boiling, the above modification to C_o will not be appropriate. In that case, the unmodified C_o is used).

6.1.7.2 Counter-Current Flow Limitations

Very few data for the void fraction exist for counter-current flow; however, a large database for counter-current flow limitation (CCFL) exists. From the drift flux correlation one gets:

$$j_v = \frac{\alpha C_o}{1-\alpha C_o} j_\ell + \frac{\alpha \bar{v}_{gj}}{1-\alpha C_o} \tag{6.1-67}$$

The general form for CCFL correlations[41] is given by:

$$\sqrt{\frac{j_v}{j_{vo}}} + \sqrt{\frac{j_\ell}{j_{\ell o}}} = 1 \tag{6.1-68}$$

where j_{vo} and $j_{\ell o}$ represent the intercepts with the axes. Because the drift flux correlation should describe all possible flow situations at or below the CCFL curve (Figure 6-2), the line given by Equation (6.1-67) for constant void fraction should be tangent to the CCFL curve.

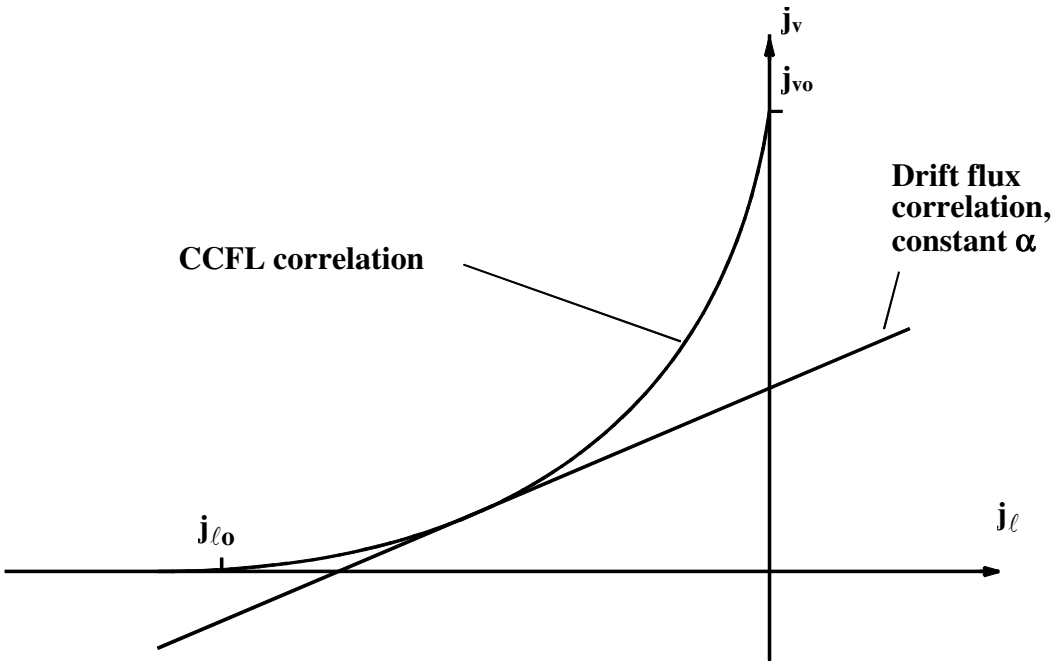

Figure 6-2. Drift Flux Correlation and CCFL

This puts a constraint on C_o and $\bar{v}_{gj}$. By requiring that Equation (6.1-67) be tangent to Equation (6.1-68), we get:

$$\frac{\bar{v}_{gj}}{-j_{\ell o}} = \frac{C_o\ (1-\alpha C_o)}{\frac{-j_{\ell o}}{j_{vo}}\ \alpha\ C_o + 1-\alpha\ C_o} \tag{6.1-69}$$

The CCFL correlation in TRACG utilizes the Kutateladze numbers,

$$\sqrt{K_v} + m\sqrt{-K_\ell} = \sqrt{K} \tag{6.1-70}$$

where:

$$K_v = \frac{j_v\ \sqrt{\rho_v}}{(\Delta\rho g\sigma)^{1/4}} \tag{6.1-71}$$

$$K_\ell = \frac{j_\ell\ \sqrt{\rho_\ell}}{(\Delta\rho g\sigma)^{1/4}} \tag{6.1-72}$$

For counter-current flow, C_o is not very well defined (e.g., C_o has a singularity for j = 0). Consequently, $\bar{v}_{gj}$ is determined as described in Sections 6.1.5, 6.1.6, and 6.1.7 and C_o is determined from Equation (6.1-69).

Even though the interfacial shear is fitted to match the CCFL correlation for counter-current flow, TRACG will check the flow rates to make sure the CCFL correlation is not exceeded (Section 3.3.2). The primary reason for this additional check is the discontinuity in the void fraction that often will exist at the CCFL location. This discontinuity, coupled with the use of donor-celled void fractions, can lead to an over prediction of the liquid down flow. The additional check against the CCFL correlation prevents this from happening.

6.1.7.3 Virtual Mass

The virtual mass is normally a small term compared to the other terms in the momentum equation. It is of importance only for bubbly flow and for critical flow or sudden accelerations due to abrupt area changes. The inclusion of virtual mass has a positive effect on the stability of the numerical method used for the integration of the conservation equations.

The virtual mass terms in the momentum equations in Section 3.2.2.1 are defined by:

$$k = \begin{cases} 0.5\alpha\dfrac{1+2\alpha}{1-\alpha} & \text{for } 0 \le \alpha < \alpha_{tran} \\ \\ 0.5(1-\alpha)\dfrac{3-2\alpha}{\alpha} & \text{for } \alpha_{tran} \le \alpha < 1 \end{cases} \tag{6.1-73}$$

$$\rho_c = \begin{cases} \rho_\ell & \text{for } 0 \le \alpha < \alpha_{tran} \\ \rho_v & \text{for } \alpha_{tran} \le \alpha < 1 \end{cases} \tag{6.1-74}$$

where α_{tran} = 0.65, represents the transition to annular flow. For horizontal flow, Equation **(5.1-23)** is used if it produces a lower value.

The velocity of the dispersed phase is approximated by:

$$v_d = (1-\alpha)v_v + \alpha v_\ell \tag{6.1-75}$$

The virtual mass is characterized by the velocity of the dispersed phase. The velocity of the dispersed phase is vv for α approaching 0 and vℓ for α approaching 1. It should be noted that the virtual mass term is only significant for bubbly flow. Thus, the calculations are not sensitive to the definition of the velocity of the dispersed phase for larger values of the void fraction. Equation (6.1-74) is chosen as a simple formulation which has the right limits.

The virtual mass term accounts for the fact that the relative velocity on which the interfacial force depends can vary with time. The term is introduced on page 3-5. It is represented in the simplified momentum expressions in Equations **(3.1-10)**, **(3.1-11)**, **(3.1-30)** and **(3.1-31)** by f_{VM}. It is correlated as indicated in Equation **(3.2-9)**. The expressions for k and ρ_c are in agreement with those recommended by Zuber[59].

6.1.7.4 Applicability

The applicability of the modifications to the interfacial shear is addressed through the assessment (Section 6.1.8). Sub-cooled boiling is present in all the heated void fraction tests, and the applicability of the modification to C_o is covered by this assessment.

The CCFL correlation is based on data from prototypical full-scale BWR components[41] and thus the correlation is directly applicable to BWR locations such as upper tie plates and bundle inlet orifices. Assessment of the CCFL correlation is covered in the *TRACG Qualification LTR*[6], and an example is shown in Figure 6-3.

The phenomenon of CCFL in the downcomer region (ECC bypass) is not of importance to BWRs because of the milder depressurization and large downcomer flow area. The low-pressure injection systems will be enabled after the reactor vessel has been depressurized. There has been no evidence of any CCFL in the downcomer in any BWR LOCA test simulations. For these reasons, the TRACG interfacial shear model has not been assessed against PWR ECC bypass data. The empirical Kutateladze correlation discussed earlier is also used in the downcomer cells. This correlation is used to limit the maximum down flow of liquid corresponding to the vapor up flow rate in the cell.

Calculations performed using a Kutateladze constant of 3.2, i.e.,

$$\sqrt{K_g} + \sqrt{K_\ell} = \sqrt{3.2} \tag{6.1-76}$$

have confirmed that CCFL will not occur in the downcomer during a typical LOCA transient in a BWR, and that it is not necessary to develop accurate models for this phenomenon. The justification for using this correlation is provided below.

Data related to ECC bypass have been collected at various test facilities as summarized in Reference [18]. These include the Creare 1/30, 1/15 and 1/5 scale facilities, BCL 1/15 and 2/15 scale facilities, etc. Data obtained from these facilities were correlated in the form of a Wallis[40] correlation:

$$\sqrt{j_g^*} + m\sqrt{j_\ell^*} = C \tag{6.1-77}$$

where

$$j_g^* = \left[\frac{\rho_g j_g^2}{gD\left(\rho_\ell - \rho_g\right)}\right]^{1/2} ; \; j_\ell^* = \left[\frac{\rho_\ell j_\ell^2}{gD\left(\rho_\ell - \rho_g\right)}\right]^{1/2} \tag{6.1-78}$$

These data are bounded by using m=1 and C=0.38 in the above correlation, as shown in Figure 6-3. Using a typical downcomer annulus hydraulic diameter of 0.985m, and at a pressure of 15 to 20 bar, the Wallis correlation above is equivalent to the Kutateladze correlation with a constant of 3.2. Further comparison of this correlation with the UPTF data[61] is shown in Figure 6-4. The figure shows two best-fit correlations to the data, one for injection to Loop 1 only and the other for ECC injection to three loops. The latter is more representative of injection into a BWR downcomer through several loops. Use of the Wallis correlation with a constant of 0.38 (corresponding to the Kutateladze correlation with a constant of 3.2) would be conservative at

the limiting conditions of high steam flow. In the region where large down flow of liquid occurs, the correlation is non-conservative, but the effects are inconsequential.

The virtual mass model has been used for all the assessment studies, and the range of applicability given by the assessment of the interfacial shear applies to the combined model.

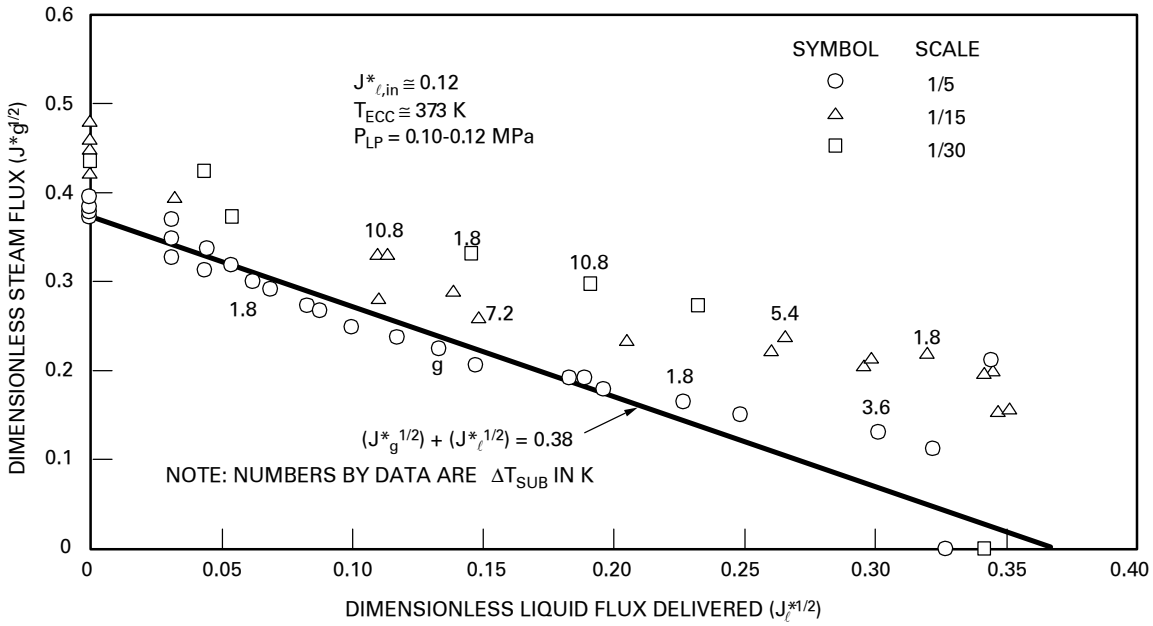

Figure 6-3. Comparison of CCFL Data[60] at 1/5, 1/15 and 1/30 scale

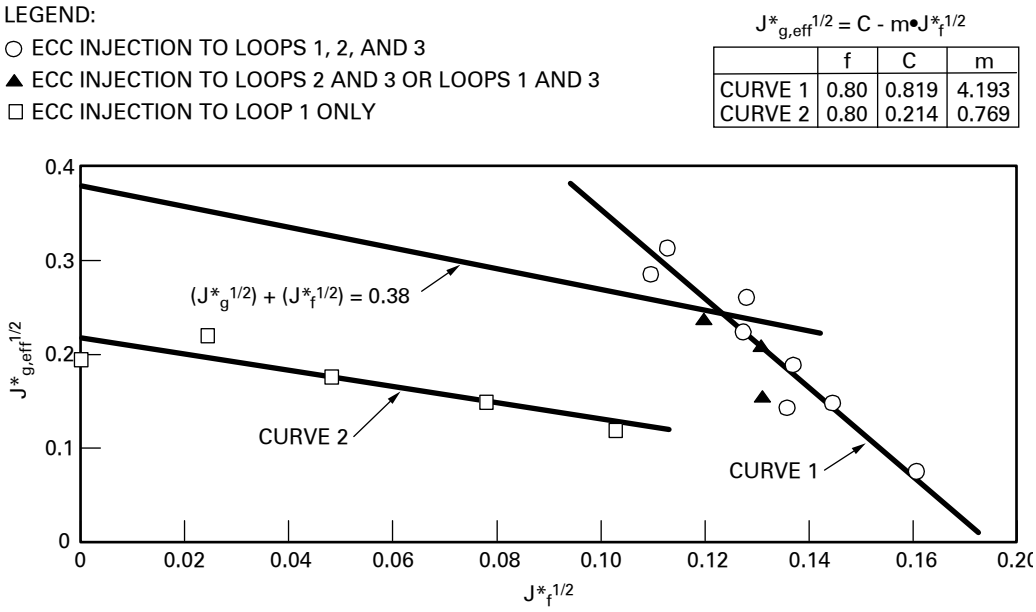

Figure 6-4. Best-Fit of Dimensionless Steam and Delivery Rates for UPTF Cold Leg Injection Tests[61]

6.1.8 Assessment and Applicability to BWR

The interfacial shear model as described in the previous section has been extensively tested against void fraction data. This assessment is documented in the *TRACG Qualification LTR*[4],[5],[6].

This assessment covers a wide range of parameters typical of reactor applications:

Pressure: [[ ]]

Mass flow: [[ ]]

Inlet subcooling: [[ ]]

Hydraulic diameter: [[ ]]

Void Fraction: [[ ]]

The void fraction data in the core is typically predicted with an accuracy of [[ ]]. An example of this assessment is shown in Figure 6-5. In large diameter pipes, the void fraction is predicted within [[ ]].

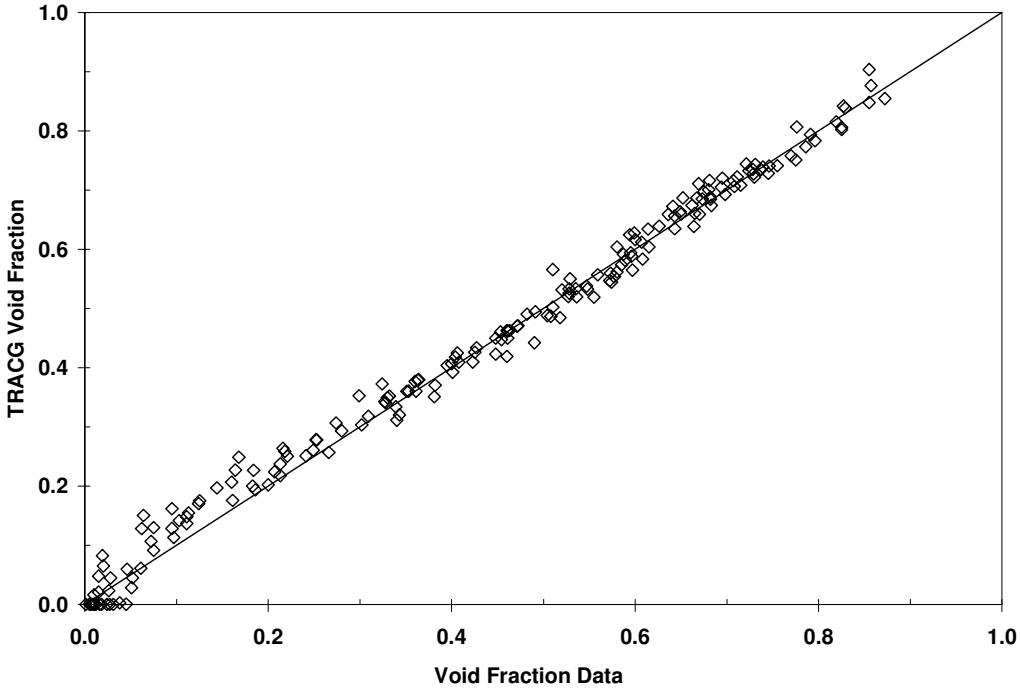

Figure 6-5. Calculated Versus Measured Void Fraction for an 8x8 BWR Fuel Bundle, at 6.8 MPa

When combining the assessment as reported in Reference [6] with the applicability and theoretical basis of the individual models, the following range of applicability can be defined:

Pressure: [[ ]]

Mass Flow: [[ ]]

[[

]]

Inlet Subcooling: [[ ]]

In the assessment of the interfacial shear for sub-cooled boiling[6], the subcooling exceeds the departure enthalpy for net vapor generation.

Hydraulic Diameter: [[ ]]

The assessment covers hydraulic diameters up to [[ ]]. For large diameters, however, C_o will approach 1.0, and thus the relative velocity will be determined primarily by

$\overline{v}_{gj}$. As $\overline{v}_{gj}$ for bubbly and droplet flow is determined based on first principle models for single particles in an infinite medium it is justifiable to apply these models for large hydraulic diameters. It is more difficult to extrapolate the annular flow model to large hydraulic diameters; however, for large hydraulic diameters a large entrainment fraction will be calculated and, consequently, the interfacial shear model is applicable for large hydraulic diameters.

Flow Regimes: The assessment covers flow regimes identified in Section 5.0. For LOCA applications, inverted annular flow may also exist. This flow regime is not specifically modeled in TRACG; instead, it is treated as churn flow. This is justifiable, as only a thin vapor film will exist at the wall and the major part of the vapor will be entrained into the bulk flow. This flow regime is primarily significant for the core region.

Assessment against LOCA tests from the TLTA and FIST test facilities[6] has shown that the core pressure drop is well predicted. Since the pressure drop during the re-flood phase of a LOCA is primarily dominated by static head, it is concluded that the core void fraction is adequately predicted.

The required range of parameters for analysis of BWR transients and accidents is summarized by region inTable 6-1. Given the above applicability range, the applicability of the interfacial shear model to the various BWR components can be summarized in Table 6-2.

Table 6-2. Applicability of Interfacial Shear Models to BWR Regions

Region	Flow Regimes	Size (m)	Range of Conditions		
			P (MPa)	G (kg/m^2-sec)	Void
Lower Plenum	C	CA/CE	CA	C	C
GT	C	C	CA	C	C
Core	C	C	CA	C	C
Bypass	C	C	CA	C	C
Upper Plenum	C	CA/CE	CA	C	C
Mixing Region	C	CA/CE	CA	C	C
Steam Dome	C	CA/CE	CA	C	C
Steam Line	C	CA	CA	C	C
Downcomer	C	CA	CA	C	C
Recirculation Loop	C	CA	CA	CA	C
Drywell	C	CE	CA	C	C
Wetwell Air Space	C	CE	CA	C	C
Suppression Pool	CA	CA/CE	CA	C	C
Main Vents	CA/CE	C	CA/CE	C	C
ESBWR Chimney	C	C	CA	C	C

Legend:

C = Correlation database and separate effects tests cover range

CA = Correlation supplemented by assessment covers range

CE = Correlation supplemented by reasonable physical basis

CA/CE = Assessed against geometrically scaled data

CN = Correlation range limited but phenomenon not significant

N/A = Correlation not applicable over range

6.2 Wall Friction and Form Losses

6.2.1 Wall Friction

6.2.1.1 Technical Basis and Assumptions

The major assumption in the calculation of wall friction is that the friction factors based on steady-state data are applicable for transients. Also, correlations for fully developed flow are utilized. These assumptions are reasonable for BWR transients as long as passages being analyzed have L/D > 10. This is generally true for BWR regions, except where large 3D cells are used. The errors in the use of fully developed correlations could be larger in these regions. This is discussed later in the section.

The field equations for conservation of momentum for the vapor and liquid phases contain terms resulting from the wall friction Equations (3.1-30) and (3.1-31). These terms appear as $F_{wv}/\alpha\rho_v$ and $F_{w\ell}/(1-\alpha)\rho_\ell$, respectively. As discussed in Section 6.1, the net force on the vapor phase due to wall friction is αF_w; thus, the term $F_{wv}/\alpha\rho_v$ reduces to F_w/ρ_v. Similarly, the term in the liquid momentum equation reduces to F_w/ρ_ℓ. Here, F_w is the total wall shear. In this section, the basis for calculation of the wall shear F_w is described. The total wall shear is calculated using a two-phase multiplier approach as:

$$F_w = \frac{f_\ell}{2D_h}\frac{G^2}{\rho_\ell}\phi_{\ell o}^2, \tag{6.2-1}$$

where $\phi_{\ell o}^2$ is the two-phase multiplier, and "f_ℓ" is the single-phase friction factor.

6.2.1.2 Single-Phase Friction Factor

The single-phase friction factor is calculated from a fit to the Moody curves given by Waggener[64]:

$$f_k = \begin{cases} \dfrac{64}{Re_k} & ,Re < 1084 \\ 0.0055\left[1+\left(2x10^4\dfrac{\varepsilon}{D_h}+\dfrac{10^6}{Re_k}\right)^{1/3}\right] & ,Re \geq 1084 \end{cases} \tag{6.2-2}$$

where:

$$Re_k = \frac{GD_h}{\mu_k} \tag{6.2-3}$$

and k can be liquid (ℓ) or vapor (v).

The form of the single-phase friction factor is well established[64]. For laminar flow, the friction factor results from the exact solution for fully developed flow in circular pipes. For

turbulent flow in smooth pipes, Blasius and McAdams proposed correlations that approximate the Prandtl - Von Karman - Nikuradse line over a wide range of Reynolds numbers. In 1939, Colebrook extended the expression for turbulent flow in a smooth pipe to include roughness of the pipe wall in the so-called transition region between smooth pipe flow and flow for which f is constant. Moody, in 1941, presented the Colebrook function in the well-known Moody diagram. An approximation to Colebrook's function, which includes the effect of roughness, was proposed in 1947 by Moody as the above Equation (6.2-2).

6.2.1.3 Two-Phase Multiplier

The frictional pressure drop in two-phase flow is conventionally correlated by means of a two-phase multiplier, which relates the overall frictional pressure drop to a reference frictional pressure drop for an equivalent single-phase flow. These models were originally motivated by the "separate cylinders" model for two-phase flow, which provided a rationale for the correlating parameters. In the Lockhart-Martinelli model[62], the reference pressure gradient is that due to the liquid flowing alone in the total cross section; the Martinelli-Nelson correlation[63] considers a 'liquid only' pressure gradient resulting from a liquid flow equal to the total two-phase flow rate. The two-phase multiplier is correlated in terms of the ratio of the pressure gradients for liquid and vapor flowing alone.

TRACG employs a two-phase multiplier, $\phi^2_{\ell o}$, which is of the Martinelli-Nelson type. The two-phase frictional multiplier used in TRACG is based on a modification to the Chisholm correlation[65]. Following a traditional separated flow approach, Chisholm proposed a correlation of the form:

$$\frac{\Delta P_{TP}}{\Delta P_{\ell o}} = \Phi^2_{\ell o} = (1-x)^2\left(1+\frac{C}{X}+\frac{1}{X^2}\right) \tag{6.2-4}$$

where X is the Lockhart-Martinelli parameter given by:

$$1/X^2 = \frac{f_v x^2}{\rho_v}\Bigg/\frac{f_\ell (1-x)^2}{\rho_\ell} = \varsigma\frac{x^2}{(1-x)^2} \tag{6.2-5}$$

where:

$$\varsigma = \frac{\rho_\ell f_v}{\rho_v f_\ell} \tag{6.2-6}$$

The correlation used in TRACG is of the form:

[[ ]] (6.2-7)

where:

[[ ]] (6.2-8)

The modifications to the Chisholm correlation are based on extensive comparisons to rod bundle pressure drop data[66] from BWR bundles with 7x7 and 8x8 lattices.

6.2.1.4 Model As Coded

The calculation of the wall friction is encoded as described by Equations (6.2-1), (6.2-2) and (6.2-7). However, there are some limitations on specific variables that should be noted. A minimum value of 10^{-5} is used for the hydraulic diameter whenever the input value is less than this minimum value for evaluating the Reynolds number. A minimum value of the absolute value of the mass flux used in the Reynolds number is obtained by calculating the mass flux with a mixture velocity of 0.1 m/s. In Equation (6.2-2), the friction factor is limited to a maximum value of 0.1. When applying Equation (6.2-2) at low Reynolds numbers (< 1084), the maximum friction factor calculated by the two expressions is used to avoid a discontinuity between the two values; 1084 is the intercept for ε=0. In calculating the flow quality used in Equation (6.2-7), a minimum value of 0.001 is used for the total mass flux to avoid discontinuities as $G \rightarrow 0$. These imposed lower limits do not adversely affect the application of TRACG. They prevent division by zero for low flow where the frictional pressure drop is insignificant.

The evaluation of the wall friction requires a combination of cell-edged and cell-centered quantities. The cell-edged quantities of phase velocity, hydraulic diameter and surface roughness are used as is. The mass fluxes are donor-celled based on the phase velocity. The densities and viscosities are linearly interpolated based on the lengths of the adjacent cells as follows:

$$\rho = \frac{\Delta x_i \rho_i + \Delta x_{i+1} \rho_{i+1}}{\Delta x_i + \Delta x_{i+1}} \tag{6.2-9}$$

The wall friction from cell-center to cell-center is calculated assuming two pipe segments, each of a length equal to one half the cell length:

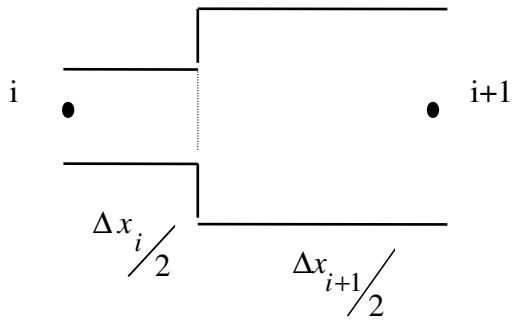

For the left half-cell, the average mass flux is

$$G^{i}_{i+1/2} = G_{i+1/2}\frac{A_{i+1/2}}{Vol_i / \Delta x_i} \tag{6.2-10}$$

and similarly for the right half-cell, the average mass flux is

$$G^{i+1}_{i+1/2} = G_{i+1/2}\frac{A_{i+1/2}}{Vol_{i+1} / \Delta x_{i+1}} \tag{6.2-11}$$

For a pipe with constant cross section, $G^{i}_{i+1/2} = G_{i+1/2}$, a linear interpolated mass flux based on the cell length is used for the calculation of the wall friction:

$$\bar{G} = \frac{\Delta x_i}{\Delta x_i + \Delta x_{i+1}} G^{i}_{i+1/2} + \frac{\Delta x_{i+1}}{\Delta x_i + \Delta x_{i+1}} G^{i+1}_{i+1/2} \tag{6.2-12}$$

The wall friction is applied to one-dimensional and three-dimensional components in a consistent manner.

6.2.1.5 Applicability

The single-phase friction factor represented by the Moody diagram has a tolerance of ±5% for values of Re from 4000 to 10^7, and for values of f up to 0.05. Below 4000, the range of Reynolds numbers is covered by laminar flow and a transition region with a slightly higher uncertainty. The uncertainty is of the order of 10% for non-smooth pipe data. Data for non-circular channels are also well predicted with the concept of the hydraulic diameter. Data[67] for triangular channels fall about 3% under the Moody smooth line, and for square channels about 10% under the Moody line for Reynolds numbers between 10,000 and 200,000.

For two-phase flow, the majority of the comparisons with the modified Chisholm correlation have been made for rod bundle data. It should be noted that the measured pressure drop will include both frictional and static head components for vertical flow. Thus, it is

important to use a consistent set of void fraction and frictional pressure drop models in analyzing such data. The void correlation used in the data reduction produces almost identical results as TRACG. The pressure range for the comparisons was from [[ ]][66]. The mass flux range was from [[ ]], while the steam quality ranged from [[ ]]. For a total of [[ ]] points for the [[ ]] lattice, the mean error was [[ ]] with a standard deviation of [[ ]]. For the [[ ]] data, [[ ]] points of comparison yielded a mean error of [[ ]] with a standard deviation of [[ ]]. Over this range of pressure, the prediction error was fairly uniform, with the lowest standard deviation at the lowest pressure.

Idsinga, Todreas and Bowring[68] tested 18 two-phase friction pressure drop models and correlations against 2200 experimental steam-water pressure drop measurements under adiabatic conditions and 1230 in diabatic flow conditions. The data represented several geometries and had the following property ranges:

Pressure:	1.7 - 10.3 MPa
Mass flux:	270 - 4340 kg/m^2/s
Quality:	Sub-cooled to 100%
Hydraulic diameter:	2.3 - 33 mm

The Chisholm correlation was among those tested. The authors concluded that the correlation performed better for low-pressure data (1.7 - 6.2 MPa) than for the high-pressure data (6.2 - 10.3 MPa). While these conclusions are not directly applicable to the modified Chisholm correlation, it is reasonable to assume that its application at lower pressures will not lead to large errors.

Applicability to Containment Volumes

The correlations are applicable to containment flow paths such as Passive Containment Cooling Condensers (PCC) piping, headers and tubes, and the main vents which are adequately represented by pipes. The range of applicability is as quoted earlier. These are the flow paths of importance in the containment. Frictional pressure drops in the large open areas of the drywell and wetwell are small after the initial blowdown. However, they do determine the global flow patterns and natural circulation flows in these regions. The application of the friction factors and two-phase multipliers, which are based on fully developed flows in pipes, will have larger margin for error for large 3-D cells.

The containment is nodalized such that at least one surface of each cell is in contact with a wall. For cells which have a wall on both sides, the flow is similar to one-dimensional duct flow and the pressure drop correlations in conjunction with the hydraulic diameter concept will be applicable with the same degree of accuracy. Two possible situations where the wall is in contact with one side of the cell are shown in Figure 6-6 below. Scene (a) on the left side of Figure 6-6 shows a situation with a dominant flow through the duct formed by the two adjacent cells. Here, the free stream velocity is similar in the two cells, and an appropriate hydraulic diameter is closer to D1+D2 for both cells. Scene (b) on the right side of Figure 6-6 depicts the other situation where there is a circulating flow pattern, with the average velocities in the opposite directions in the two cells. Here the actual velocity at the cell interface will be small, and the velocity profile in each cell is closer to that in a duct with an intermediate wall. The

appropriate hydraulic diameter is then D1 for the left cell and D2 for the right cell. Assuming cells of approximately equal size, these two different flow patterns result in a possible error of a factor of 2 in the hydraulic diameter and Reynolds number used in the friction factor calculations. In the turbulent flow regime, $f \sim Re^{-0.2}$. Thus, the possible error in the friction factor is of the order of 13%.

It should be noted that the friction factors are used in the same way in TRACG as in other codes such as GOTHIC[69], which are specifically meant for containment analysis, and have been extensively qualified for these applications.

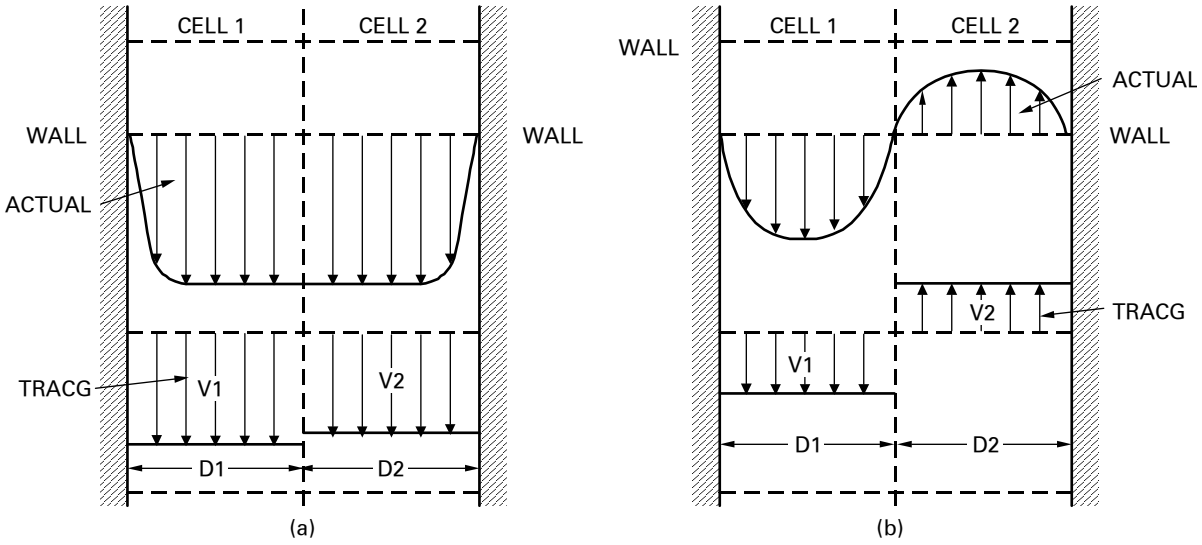

Figure 6-6. Velocity Profiles in 3-D Cells

6.2.2 Form Losses at Abrupt Expansions and Contractions

6.2.2.1 Technical Basis and Assumptions

The basic assumption underlying the formulation of local form losses at abrupt expansions and contractions is that the transient flow process can be approximated as a quasi-steady flow process that is instantaneously satisfied by the upstream and downstream conditions (i.e., transient inertia, mass and energy storage are neglected at abrupt area changes). However, the upstream and downstream flows are treated as fully transient flows.

The quasi-steady approach can be justified on the grounds that available loss correlations are based on data taken during steady processes, but transient investigations[70] have verified the adequacy of the assumption. The volume of fluid and associated mass, energy and inertia at points of abrupt area change is generally small compared with the volume of upstream and downstream fluid regions. These transient effects are approximated by lumping them into the upstream and downstream volumes. In general, the quasi-steady approach is consistent with modeling of other important phenomena in transient codes (i.e., heat transfer, pumps and valves).

6.2.2.2 Single-Phase Flows

In steady, incompressible flow, losses at an area change are modeled by the inclusion of an appropriate dynamic head loss term, h_L, in the one-dimensional modified Bernoulli equation:

$$\left(v^2/2+P/\rho\right)_1=\left(v^2/2+P/\rho\right)_2+h_L \tag{6.2-13}$$

$$h_L=Cv^2/2 \tag{6.2-14}$$

The particular form of the dynamic head loss is obtained by employing the Bourda-Carnot[71] assumption for calculating losses associated with the expansion part of the flow process. For a contraction, the loss corresponds to an expansion from the vena contracta. TRACG does not compute these local loss coefficients. The loss coefficient C is input by the user based on the geometry of the flow. In the absence of an input loss, TRACG will calculate the reversible pressure change given by the Bernoulli equation. (TRACG does estimate these losses, but this is only used as an input check.)

6.2.2.3 Two-Phase Flows

The flow through an abrupt area change can be visualized by considering each phase to be flowing in a phasic stream tube. The velocities and volume fractions are calculated from the transient flow equations in the upstream and downstream regions. Within the area change region, the phases are coupled through the interphase drag and a common pressure gradient. The gradient in relative velocity can be large at points of abrupt area changes. Since each phase is governed by a modified Bernoulli type of equation, it is reasonable to assume that losses associated with changes in phasic flow area can be modeled by separate dynamic pressure loss terms for both the liquid and gas phases. However, the interfacial drag effects are important at abrupt area changes. These will affect the local slip between the phases and the effective phasic areas. [[

]] (6.2-15)

[[

]] (6.2-16)

This pressure drop is apportioned to each phase in proportion to the volume fraction of the phase. The [[ ]] is used to partition the form losses applied between the two cell centers. The [[ ]] is also used to partition the wall friction between the phases as indicated in Section 6.2.1.1. The single-phase loss coefficient C must be input by the user. In the absence of an input loss, TRACG will calculate a 'reversible' pressure change consistent with the momentum equations.

6.2.2.4 Model as Coded

The calculation of the singular losses is encoded as described by Equations (6.2-15) and (6.2-16). A minimum value of the mass flux used in Equation (6.2-15) is obtained by calculating the mass flux with a mixture velocity of 0.1. This imposed lower limit should not adversely affect the intended application of TRACG.

The single-phase loss coefficient is input separately for forward and reverse flow directions. The sign of the total mass flux will determine which loss coefficient is applied:

$$C_{i+1/2} = \begin{cases} C_{forward} & ,G'_{i+1/2} \geq 1.0 \\ 0.5[(1- G'_{i+1/2})C_{reverse} + (1+ G'_{i+1/2})C_{forward}] & ,-1.0 < G'_{i+1/2} < 1.0 \\ C_{reverse} & ,G'_{i+1/2} < -1.0 \end{cases} \quad (6.2\text{-}17)$$

where G' is based on the volumetric fluxes normalized to a Kutateladze number (i.e., an interpolation is performed for mass fluxes where counter-current flow is possible). The frictional pressure drop is generally insignificant for counter-current flow.

6.2.2.5 Applicability

The model used in TRACG has been extensively tested for pressure drop across spacers and bundle upper tie plates. The range of conditions is similar to that for the frictional pressure drop data. This data covered a pressure range from [[ ]], mass flux range from [[ ]], and a steam quality to [[ ]]. For typical grid spacers, the standard deviation of the error in the prediction of the two-phase multiplier was about [[ ]][74]. For typical upper tie-plates[75], the standard deviation of the prediction error in pressure drop was [[ ]] and ranged from [[ ]] over the pressure range of [[ ]].

Husain, Choe and Weisman[72] have made extensive comparisons of pressure drop across abrupt area changes with separated flow and homogeneous flow models. They quote the following statistics:

For Abrupt Expansions:

Mass Flux	**Homogeneous Model**		**Slip Flow**	
(kg/m2-s)	**Mean Error**	**σ**	**Mean Error**	**σ**
<680	0.60	0.94	-0.02	0.64
<1360	0.49	0.82	-0.03	0.54
>1360	0.05	0.11	-0.08	0.09
>2720	0.10	0.06	-0.00	0.08
All	0.42	0.77	-0.04	0.49

For Abrupt Contractions:

Mass Flux	Homogeneous Model		Slip Flow	
(kg/m2-s)	Mean Error	σ	Mean Error	σ
<680	-0.075	0.30	-0.09	0.28
<1360	-0.16	0.09	-0.17	0.12
> 2040	-0.05	0.01	-0.17	0.02
>2720	-0.05	0.00	-0.16	0.00
All	0.03	0.27	-0.00	0.25

The error statistics in the tables above are expressed as fractions of the mean value. A comparison of the two tables reveals that the homogeneous flow model works well for contractions, but not as well for expansions. The statistics do not apply to the TRACG model, which uses the homogeneous multiplier only for the irreversible pressure drop; but they indicate the likely errors in its application to expansions, which are in the acceptable range.

Applicability to Containment Volumes

The formulations for form losses at abrupt expansions and contractions are applicable to pipe geometries in the containment such as the PCC inlet piping, headers and tubes, and the vent pipes and horizontal vents. These involve inlet and exit losses and losses at bends in the piping. Form losses are not as important in the large three-dimensional cells, where large changes in area are not common. The same formulation is applied in these regions.

6.2.3 Assessment and Applicability to BWR

The models for wall friction and form losses have been assessed against experimental data and other correlations. Extensive sets of comparisons have been performed against pressure drop data over the active, heated length of rod bundles. These comparisons were made at the BWR operating pressure of 6.9 MPa and a range of mass fluxes from [[ ]]. The data were obtained over a length of 4m and included seven spacers distributed over the heated length. For an advanced BWR fuel design[73], the mean and standard deviation of the calculated minus measured bundle pressure drop were [[ ]], respectively. For reference, the absolute value of the pressure drop ranged from [[ ]]. For an 8x8 bundle, the corresponding mean error and standard deviation were [[ ]][66].

Reactor data at natural circulation for the Hatch 2 and LaSalle 2 plants have been analyzed with TRACG. The two comparisons are shown in Reference [6]. Flow rate through the core is predicted accurately in all these cases, indicative of the adequacy of the wall friction correlation for a wide range of geometries.

For conditions typical of a LOCA, there are numerous comparisons against integral system data that bear out the adequacy of the wall friction correlations. Comparisons have been made with LOCA simulations in TLTA, FIST and GIST. The results are shown in Sections 5.1, 5.2, and 5.3 of Reference [6]. Flow rates through the core and bypass regions are predicted

accurately in all these cases. This demonstrates adequacy of the wall friction correlation over a wide range of pressures and qualities.

Applicability for BWR applications is summarized by a comparison against the table of desired ranges for various reactor regions (Table 6-1).

Flow Regimes: The range of test data covers all relevant flow regimes, ranging from single-phase liquid to single-phase vapor. Qualities as high as [[ ]] (void fractions greater than [[ ]]) are included in the database. The only exception is the inverted annular flow regime in low flow film boiling, where the frictional pressure drop is secondary to the density head. Flow regimes representative of bubbly flow in large pools (lower plenum, suppression pool) are not as well covered, but the frictional pressure drop is very small in these regimes.

Hydraulic Diameter: The correlations are valid for the desired range of hydraulic diameter for pipe flows. For containment volumes, the correlations are valid with the use of the equivalent hydraulic diameter concept, but with larger uncertainty (by about [[ ]]).

Mass Flux/Reynolds Number: The friction factor correlation is applicable from laminar flow to highly turbulent flows ([[ ]]). Two-phase pressure drop data encompass the required range of mass flux.

Pressure: The correlation for the two-phase multiplier is based primarily on data at pressures greater than [[ ]], though a similar correlation has been tested against data down to [[ ]]. Other low-pressure assessment includes that for the horizontal vent and LOCA tests mentioned above.

Void Fraction: This is covered by the flow regime and quality ranges discussed above.

It should be noted that the frictional pressure drop in the core is the dominant pressure drop in the BWR. Pressure drop in the separators is discussed later in Section 7.7. Frictional pressure drop is negligible in the upper plenum and downcomer. In the core bypass region, the leakage flow is controlled by the resistance of the leakage paths as described in Section 7.5.1.

Based on the above evaluation, Table 6-3 has been constructed to summarize how the requirements for the pressure drop models in TRACG are satisfied. The pressure drop in all the important reactor vessel and containment regions is adequately predicted.

Table 6-3. Applicability of Pressure Drop Models to BWR Regions

Region	Flow Regimes	Size (m)	Range of Conditions			
			P (MPa)	G (kg/m^2-s)	Void	Reynolds No.
Lower Plenum	C	CN	CA	C	C	C
GT	C	C	CA	C	C	C
Core	C	C	CA	C	C	C
Bypass	C	C	CA	C	C	C
Upper Plenum	C	CN	CA	C	C	C
Mixing Region	C	CN	CA	C	C	C
Steam Dome	C	CN	CA	C	C	C
Steam Line	C	C	CA	C	C	C
Downcomer	C	CN	CA	C	C	C
Recirculation Loop	C	C	CA	C	C	C
Drywell	C	CE	CA	C	C	C
Wetwell Air Space	C	CE	CA	C	C	C
Suppression Pool	CN	CN	CA	C	C	C
Main Vents	CA	C	CA	C	C	C
ESBWR Chimney	C	C	CA	C	C	C

Legend:

C = Correlation database and separate effects tests cover range

CA = Correlation supplemented by assessment covers range

CE = Correlation supplemented by reasonable physical basis

CA/CE = Assessed against geometrically scaled data

CN = Correlation range limited but phenomenon not significant

N/A = Correlation not applicable over range

6.3 Critical Flow

This section details the equilibrium critical flow model employed in the TRACG computer code. The critical flow model used in TRACG is applicable for a coarse-mesh nodalization and is based on a semi-empirical approximation of the choking criteria derived from the general one-dimensional, two-phase fluid field equations. The critical flow model also allows for the simulation of choking when noncondensable gases are present. The principal motivation for using a choked flow limitation model was to improve code efficiency and run times. In the past, it was found that modeling choked flow using the finite-difference approximation to the basic conservation equations required extremely fine cell nodalization in the vicinity of the break plane. As a consequence, simulating break transients generally led to prohibitively costly calculations. The choked flow model was developed in several stages by a number of individuals as indicated by the progression in References [76], [77], [78], and [79].

The remainder of this section is organized as follows. Section 6.3.1 documents the technical basis and assumptions used to formulate the choking criteria in TRACG. Section 6.3.2 documents the general methodology and implementation details for calculating the thermodynamic properties at the choke plane. Sections 6.3.3.1, 6.3.3.2, and 6.3.3.3 document the two-phase/two-component, single-phase/two-component vapor, and single-phase liquid flow models, respectively. Section 6.3.4 documents the closure relations needed to calculate the choke plane phasic velocities. Section 6.3.5 discusses the applicability of the TRACG choking model.

6.3.1 Technical Basis and Assumptions

Choking occurs when the mass flow in a pipe becomes independent of the downstream conditions. Therefore, a further reduction in the downstream pressure will not change the mass flow rate. The reason choking occurs is that acoustic signals can no longer propagate upstream to affect the properties that determine the mass flow rate at the choke plane. The choking model employs a flow-limiting scheme that uses a linear function of the cell junction phasic velocities and compares this expression to the calculated local sonic velocity for the junction. If this linear function exceeds the local sound speed, the choking model is employed to limit flow at that particular junction. The quantitative details of how this is done will be identified later in this section. The choking model used in TRACG is similar to that used in TRAC-BF1/MOD1[97], which is based on the RELAP5/MOD1 model originally developed by Ransom and Trapp (see References [80], [81], [82], and [83]).

Originally, the TRACG choking model was based on a characteristic analysis of the partial differential equations governing the flow response. However, it has been found empirically that a much-simplified criterion relating the throat Homogenous Equilibrium Mixture (HEM) sonic velocity and throat phasic velocities, void fractions, and densities may be used in place of the detailed theoretical expression and still yield good code/data comparisons. The simplified criterion that indicates choked flow is:

$$\left| \frac{\alpha_v \rho_\ell v_v + \alpha_\ell \rho_v v_\ell}{\alpha_v \rho_\ell + \alpha_\ell \rho_v} \right| \geq a_{HE} \qquad (6.3\text{-}1)$$

The choking model consists of five different regimes, identified in Table 6-4. These regimes are based on cell-centered void conditions immediately upstream of the choke plane.

Each of these regimes is simulated in the TRACG. In each case, the method used to calculate the homogeneous sound speed a_{HE} is slightly different. The presence of noncondensable gases introduces an additional degree of complexity in the approximation of a_{HE}. The presence of noncondensable gases is accounted for in all of the break flow regimes with one exception. Noncondensable gases at the break choke plane are ignored for the low void regime (Table 6-4) when the Alamgir-Jones-Lienhard (AJL) correlation is used. In the sub-cooled blow-down regime, the effects of noncondensables on the local sonic speed are assumed to be small and are therefore ignored.

6.3.2 Implementation Details

This section summarizes how the choking model is implemented in TRACG. The choking model is implemented in only one-dimensional components. The critical flow model is called by the subroutine TF1DE, which is the subroutine to solve the governing equations for one-dimensional TRACG components. TF1DE passes donor cell parameters based on new-time velocities to CHOKE. Table 6-5 and Table 6-6 summarize the principal variables passed to CHOKE and the calculated output variables. The alphanumeric identifiers in Table 6-5 and Table 6-6 should not be necessarily interpreted as subroutine call arguments. After CHOKE has been entered, control is passed to a particular model, depending on the void conditions defined in Table 6-4. Each model that is invoked follows the same computational sequence:

1. The throat pressure and temperature conditions are calculated. The subroutine THERMO is called to calculate additional thermodynamic properties at the throat conditions.
2. The throat sonic speed is calculated and the choking criteria evaluated to determine if the flow is choked.
3. If the flow is not choked, control is returned to TF1DE.
4. If choking criteria are met, new-time throat velocities and derivatives are recalculated. To calculate the derivatives, the throat pressure is perturbed by 1% and a second pass is made to calculate the liquid and vapor velocities. The choked derivatives are calculated by dividing the change in the choked velocity calculated between passes by the pressure perturbation.
5. Control is returned to TF1DE with the new calculated junction phasic velocities and derivatives.
6. The following sections detail how CHOKE calculates the throat conditions, the details of particular models that are invoked, and how they are implemented in the code.

Table 6-4. Equilibrium Critical Flow Regimes

Void Fraction	Regime	Correlation
$\alpha \leq 0.01$	liquid	Alamgir-Jones-Lienhard
$0.01 < \alpha < 0.1$	transition	Interpolate between liquid and two-phase
$0.1 < \alpha < 0.95$	two-phase	Homogeneous equilibrium sound speed
$0.95 < \alpha < 1.0$	transition	Interpolate between two-phase and gas only
1.0	gas only	HEM with adiabatic gas approximation

6.3.2.1 Methodology for the Calculation of Choke Plane Thermodynamic Properties

This section details the principal method used to calculate choke plane thermodynamic properties and how this method is implemented in the TRACG code. In order to calculate a_{HE}, the cell break plane conditions must first be approximated. In the TRACG finite-differencing scheme, fluid properties are calculated as cell-centered quantities. As a consequence, approximation techniques must be employed to estimate gradients in fluid conditions between the cell center and cell edge choke plane. In TRACG, a half-cell momentum (Figure 6-7) balance approximation is used to estimate the junction pressure. It is assumed that the area change from the cell center to the cell face is not too abrupt. Hence, form loss effects are not accounted for in the approximation. The throat pressure is evaluated using Bernoulli's theorem, and accounting for the wall friction in the half-cell:

$$P_t = P_c - \frac{\rho_{mt}\, v_{mt}^2}{2} + \frac{1}{2}\left[\rho_{mc} - \left(\alpha_{vc}\rho_{vc} + \alpha_{\ell c}\rho_{\ell c}\right) f \frac{L}{D_H}\right] v_{mc}^2 \qquad (6.3\text{-}2)$$

where the subscripts t and c designate cell throat and center locations. The subscript m designates mixture conditions. The parameters V_{mc}, V_{mt}, ρ_{mc}, and ρ_{mt} are mixture velocities and densities at the cell center and throat, respectively (Figure 6-7). The parameter f is friction factor. The L and D_H parameters are the upstream cell half length and throat hydraulic diameter, respectively.

The Bernoulli equation, Equation (6.3-2), was evaluated by assuming that the mixture velocities rather than the phasic velocities are sufficient to calculate throat properties. The mixture densities and velocities in Equation (6.3-2) are defined in Equations (6.3-3) to (6.3-8). The details for each type of flow are provided in Sections 6.3.3.1, 6.3.3.2, and 6.3.3.3.

Table 6-5. Input Call Parameters to CHOKE Subroutine

Variable	Parameter
DXC	Donor cell length
HD	Hydraulic diameter
WFL	Wall friction factor, liquid
WFV	Wall friction factor, vapor
ALP	Donor cell void fraction
PC	Donor cell upstream pressure
PD	Donor cell downstream pressure
RL	Donor cell density, liquid
RV	Donor cell density, vapor
SIGMA	Donor cell surface tension
TL	Donor cell temperature, liquid
TV	Donor cell temperature, vapor
VMC	Donor cell mixture velocity
VMO	Old-time mixture velocity
VL	Throat junction velocity, liquid
VV	Throat junction velocity, vapor
DFLDP	Derivative of VL with respect to pressure
DFVDP	Derivative of VV with respect to pressure
ICHOKE	Choking flag
ROAX	Donor cell total noncondensable density
IEOS	Gaseous phase equation-of-state flag
AVMO	Old-time HE sonic velocity

Table 6-6. Outputs from Subroutine CHOKE

Variable	Parameter
VL	Throat liquid velocity
VV	Throat vapor velocity
DFLDP	Derivative of VL with respect to pressure
DFVDP	Derivative of VV with respect to pressure
ICHOKE	Choking status flag

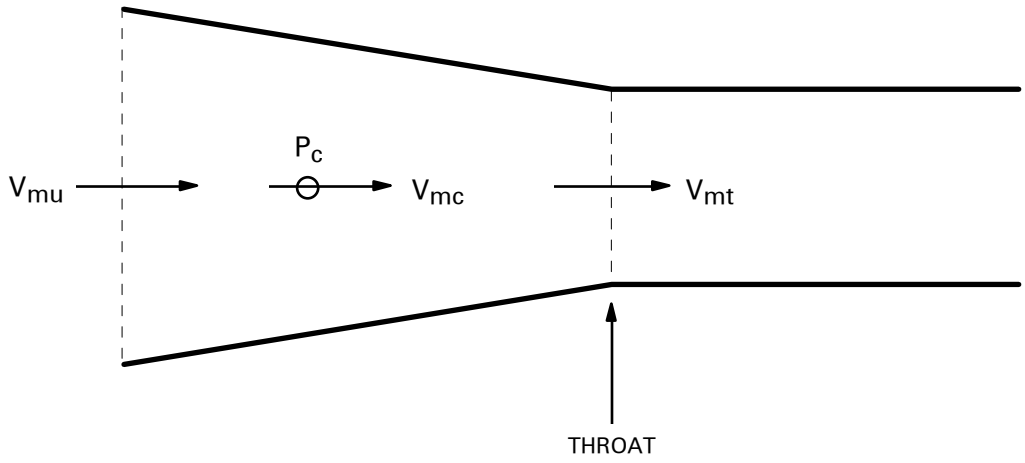

Figure 6-7. Choking Cell Configuration

Because of inherent limitations in the TRACG finite-difference solution scheme, additional approximations have been made to evaluate V_{mc}, V_{mt} and ρ_{mt}. In particular, the finite-difference scheme solves the field equations so that the phasic velocities are calculated only at cell edges. Cell-donored quantities, including the pressure, phase densities, temperatures and void fractions, are calculated only as cell-centered parameters. The mixture densities and velocities in Equation (6.3-2) are calculated as follows:

$$\rho_{mc} = \alpha_{vc}\rho_{vc} + \alpha_{\ell c}\rho_{\ell c} \tag{6.3-3}$$

$$v^{*}_{mt} = \frac{\alpha_{vc}\rho_{vc}v_{vt} + \alpha_{\ell c}\rho_{\ell c}v_{\ell t}}{\alpha_{vc}\rho_{vc} + \alpha_{\ell c}\rho_{\ell c}} \tag{6.3-4}$$

$$v_{mt} = \frac{v^{*}_{mt}}{c_{vena}} \tag{6.3-5}$$

The throat area is the minimum of the actual throat area and a vena contracta in the throat. The loss coefficient in the throat is related to the vena contracta through the following approximation:

$$c_{vena} = \frac{1}{\frac{A_t}{Vol_d/\Delta x_d} + \sqrt{c_{loss}}} \tag{6.3-6}$$

This is equivalent to basing the loss coefficient on an abrupt expansion from $A_t\, c_{vena}$ to the downstream area $Vol_d/\Delta x_d$. The vena contracta is limited to a minimum value of 0.75.

$$v_{mc} = v^{*}_{mt} \frac{A_t}{Vol_c / \Delta x_c} \tag{6.3-7}$$

The cell edge velocities, cell-centered densities and void fractions are quantities calculated at the previous computational time step that are passed to the CHOKE subroutine. The quantities from Equations (6.3-3) through (6.3-7) are calculated and used to evaluate Equation (6.3-2). The density ratio ρ_{mt}/ρ_{mc} is calculated at the previous time step, with ρ_{mt}, being estimated using CHOKE. The expression for the throat mixture velocity V_{mt} is a logical consequence of the code finite-differencing scheme. The approximation for V_{mt} is done by equating the mass fluxes with cell and throat-donored densities so that $\rho_{mc}\ V^{*}_{mt} = \rho_{mt} V_{mt}$. The mixture velocity V^{*}_{mt} is the effective velocity weighted with the cell-centered mixture density, whereas V_{mt} is weighted with the throat mixture density. Use of V_{mt} improves the accuracy of the throat pressure P_t calculation when compressibility effects are important.

The expression used to approximate the cell-centered mixture velocity V_{mc} is based on the assumption (Figure 6-7) that the flow area at the cell center upstream of the choke plane is given by Vol/Δx. By assuming constant volumetric flow, we have the following relationship between the cell-centered and upstream mixture velocities:

$$A_c\ v_{mc} = A_t\ v^{*}_{mt} \tag{6.3-8}$$

where

$$A_c = \frac{Vol_c}{\Delta x_c} \tag{6.3-9}$$

Equation (6.3-9) is substituted into Equation (6.3-8) and the result is rearranged to get Equation (6.3-7).

Once P_t has been calculated at the choke plane, the phasic temperatures at this location are calculated using assumptions dependent on the break upstream void fraction conditions and whether noncondensables are present. The choking model assumes that the throat void fraction is equal to the calculated void fraction of the cell immediately upstream of the choke plane. Once the phasic temperatures and throat pressure have been calculated at the break plane, they are used to evaluate the remaining thermodynamic properties needed to calculate the sonic speed. Once a_{HE} is calculated, the appropriate tests for choking using Equation (6.3-1) are performed.

Table 6-7 summarizes the assumptions used to calculate the key throat parameters (pressure and phasic temperatures) and the associated sonic models used in the code. This table also makes reference to the presence of noncondensable gases, which will be discussed in later sections. Additional details of the assumptions used to calculate the break plane thermodynamic conditions and corresponding sonic velocity for different types of flow are presented in the following sections.

6.3.3 Calculation of Local Sonic Velocity

6.3.3.1 Two-Component/Two-Phase Flow

The two-component/two-phase (TCTP) HEM critical flow model used in TRACG was developed primarily by Phillips[78] with extensions and modifications attributed to Ransom[82]. This model is based exclusively on theoretical grounds and employs several simplifying assumptions to enable one to derive an expression for the equilibrium sonic mixture velocity. This section will deal with several variations of the TCTP model employed in the TRACG code. The variations include the following:

Noncondensables/water mixture for $\alpha_v \leq 0.01$.

Steam/water mixture for $\alpha_v \leq 0.01$.

General TCTP model with steam/water/noncondensables mixture applied to void fraction regimes:

- $0.01 \leq \alpha_v \leq 0.1$
- $0.1 \leq \alpha_v \leq 0.95$
- $0.95 \leq \alpha_v \leq 1.0$

Noncondensables /steam mixture formulation covers void regime $\alpha_v \geq 0.9999$.

Table 6-7. Summary of TRACG Choking Correlations and Throat Conditions

Void Fraction Range	Two-Phase Liquid Steam Throat Conditions	Two-Phase Two-Component Throat Conditions	Water With Noncondensable Throat Conditions	Steam With or Without Noncondensable Throat Conditions	Sonic Velocity Correlation
Case 1 $\alpha_v \le 0.01$	P_T = SATPRS ($T_{\ell c}$) T_ℓ = TSAT (P_T) $T_g = T_\ell$	Noncondensable gas effects ignored; throat conditions same as left box.	Noncondensable gas effects ignored; throat conditions same as left box.	N/A	Use maximum of AJL and HEM correlation. See Section 6.3.3.3.
Case 2 $0.01 \le \alpha_v \le 0.1$	Throat conditions based on information in box above or box below.	Throat conditions based on information in box above or box below.	Throat conditions based on information in box above or box below.	N/A	Interpolate with cubic spline between cases 1 and 3.
Case 3 $0.1 \le \alpha_v \le 0.95$	P_T calculated from Bernoulli equation; T_g = TSAT(P_T) $T_g = T_\ell$ Assume $\frac{d\alpha_v}{dP} \neq 0$	P_T calculated from Bernoulli equation; equilibrium throat temperature T_{EQ} calculated with Taylor series approximation $T_{EQ}=T_\ell=T_{NC}=T_g$ Assume $\frac{d\alpha_v}{dP} \neq 0$	P_T calculated from Bernoulli equation; liquid throat temperature set equal to cell center liquid temperature $T_{NC} = T_\ell$ Assume $\frac{d\alpha_a}{dP} = 0$	N/A	HEM sonic velocity model.
Case 4 $0.95 < \alpha_v < 1.0$	Throat conditions based on information in box above or box below.	Throat conditions based on information in box above or box below.	Throat conditions based on information in box above or box below.	N/A	Interpolate between cases 3 and 5.
Case 5 $\alpha_v = 1.0$	N/A	N/A	N/A	For perfect gas P_T and T_v are calculated from adiabatic law $T_v = T_a$. For HEM case, P_T has same value but, $T_v=T_a$=TSAT(P_T)	$\text{Max}\left[\begin{array}{c}\text{HEM model}\\ \text{with } \frac{d\alpha_v}{dP}=0,\\ \text{HEM model}\\ \text{with } \frac{d\alpha_v}{dP}\neq 0,\end{array}\right]$

The general expression for the local HEM sonic velocity is:

$$a_{HE} = \left(\frac{\partial P}{\partial \rho} \right)_S^{1/2} \tag{6.3-10}$$

where the subscript S corresponds to constant entropy of the derivative P with respect to ρ. In order to derive a tractable expression for a_{HE} in terms of thermodynamic quantities and derivatives, a number of simplifying assumptions have been made:

1. Each fluid component is in thermal equilibrium with itself, i.e., there are no temperature gradients.
2. The flow process is isentropic. Non-equilibrium interfacial heat and mass transfer are not directly considered.
3. Noncondensable gases occupy the same volume as the steam and they obey the Gibbs-Dalton law of partial pressures.
4. The noncondensable gases are chemically and mechanically inert, i.e., they do not dissolve into or evolve from the liquid, or form new compounds with water molecules.
5. The noncondensable gases are ideal gases.
6. Multi-dimensional and turbulence effects are not considered.
7. The fluid is homogenous. Stratification and/or other flow-map-dependent phenomena that could affect the sonic velocity are precluded. For critical flow, the velocities are so large that stratification will not occur.

The above assumptions, with some exceptions, also apply to the critical flow models documented in Sections 6.3.3.2 and 6.3.3.3. With regard to assumptions 1 and 2, TRACG assumes a mixture equilibrium temperature at the choke plane that is calculated according to which break flow regime (Table 6-7) is considered. Under certain circumstances, the equilibrium assumption may break down[76],[77],[78]. In particular, for break assemblies of very short length, non-equilibrium transport behavior may be important. This occurs when the liquid and vapor phase at the choke plane have not had adequate time to relax to thermal equilibrium. However, it was judged that, in most cases, the equilibrium assumption is reasonable except in the low liquid void regime (Table 6-4). Modifications to assumption 2 under these circumstances are detailed in Section 6.3.3.3.

With respect to assumptions 3 through 5, the class of problems is confined to situations where noncondensable gases cannot interact with the liquid-steam mixture. This may not produce accurate results for certain classes of problems where significant quantities of dissolved gases are hypothesized to come out of solution as the liquid decompresses at the choke plane[84]. Assumption 6 may require code input adjustments to account for break flow geometry effects. The effects of break geometry near the choke plane are discussed by a number a authors (see References [84] through [91]). In general, the use of a one-dimensional critical flow model approximation requires that a discharge coefficient be employed to account for two- or three-dimensional geometry effects[85]. Since there is a wide range of possible break flow geometries, there is no particular universal discharge coefficient that is applicable to all situations.

Using the formulations detailed in APPENDIX D and APPENDIX E, the following equations show how the HEM sonic speed is derived for either a steam-liquid or noncondensable-steam-liquid mixture. The general form of the isentropic derivative for the reciprocal of the sonic velocity squared is:

$$a_{HE}^{-2} = \left(\frac{\partial \rho}{\partial P}\right)_S = \alpha_v \left(\frac{\partial \rho_a}{\partial P}\right)_S + \alpha_v \left(\frac{\partial \rho_s}{\partial P}\right)_S + \alpha_\ell \left(\frac{\partial \rho_\ell}{\partial P}\right)_S - \left(\rho_a + \rho_s - \rho_\ell\right)\left(\frac{\partial \alpha_v}{\partial P}\right)_S \tag{6.3-11}$$

In the liquid/noncondensable regime, $\left\{\frac{\partial \alpha_v}{\partial P}\right\}_S = 0$, so that Equation (6.3-11) reduces to:

$$a_{HE} = \left[\alpha_v \left(\frac{\partial \rho_a}{\partial P}\right)_S + \alpha_v \left(\frac{\partial \rho_s}{\partial P}\right)_S + \alpha_\ell \left(\frac{\partial \rho_\ell}{\partial P}\right)_S\right]^{-1/2} \tag{6.3-12}$$

The individual isentropic derivatives in Equation (6.3-12) are given by the general formula for a pure substance derived in APPENDIX D as:

$$\left(\frac{\partial \rho}{\partial P}\right)_S = \left(\frac{\partial \rho}{\partial P}\right)_T - \frac{T\left(\frac{\partial \rho}{\partial T}\right)_P^2}{\rho^2\left[\left(\frac{\partial e}{\partial T}\right)_P - \frac{P}{\rho^2}\left(\frac{\partial \rho}{\partial T}\right)_P\right]} \tag{6.3-13}$$

where the state variables, such as ρ, are for the liquid or noncondensable . In the case where we are modeling a single-phase vapor/noncondensable mixture ($\alpha_v \approx 1$), Equation (6.3-12) becomes:

$$a_{HE} = \left[\left(\frac{\partial \rho_a}{\partial P}\right)_S + \left(\frac{\partial \rho_s}{\partial P}\right)_S\right]^{-1/2} \tag{6.3-14}$$

where the individual isentropic derivatives are again evaluated using Equation (6.3-13) and the appropriate values for ρ and e.

In situations where the steam/liquid phases coexist, the general expression for the homogenous sound speed can be expanded using Equation (6.3-11). In this situation, the isentropic derivative $\left\{\frac{\partial \alpha_v}{\partial P}\right\}_S \neq 0$; and we have a significantly more complex expression. The expansion of the individual isentropic derivatives into algebraic expressions containing non-isentropic derivatives is somewhat long and is detailed in APPENDIX E. In the limit where the noncondensable gas density becomes zero, Equation (6.3-11) can be expressed as:

$$a_{HE} = \left(\frac{\partial \rho}{\partial P}\right)_S^{-1/2} = \left(\frac{\rho}{\rho_\ell \rho_g}\Omega\right)^{-1/2} \tag{6.3-15}$$

where

$$\Omega = \alpha_v \rho_\ell \left(\frac{\partial \rho_s}{\partial P} \right)_S + \alpha_\ell \rho_s \left(\frac{\partial \rho_\ell}{\partial P} \right)_S - \Lambda \tag{6.3-16}$$

$$\Lambda = \frac{\rho_s - \rho_\ell}{S_s - S_\ell} \left[\alpha_v \rho_g \left(\frac{\partial S_s}{\partial P} \right)_S + \alpha_\ell \rho_\ell \left(\frac{\partial S_\ell}{\partial P} \right)_S \right]. \tag{6.3-17}$$

Prior to calculating the value of the sonic velocity, the throat thermodynamic conditions must be evaluated. The general outline for calculating the throat pressure was given in Section 6.3.2.1, using Equation (6.3-2). This section describes further details as to how the throat temperature and partial pressures are calculated. The methodology used depends on the particular break flow regime. This section considers cases 1 through 3 in Table 6-7. Case 4 is documented separately in Section 6.3.3.2. Table 6-7 summarizes how the throat conditions are calculated for Cases 1 through 4.

Relative to the steam-water case, P_t is calculated with Equation (6.3-2). The throat temperature of the liquid is assumed to be the upstream cell-centered liquid temperature ($T_{\ell c}$). The noncondensable gas throat temperature is set equal to the liquid temperature. In the situation where there is a steam-liquid mixture at the cell center upstream of the break plane, Equation (6.3-2) is again used; and the steam-liquid mixture is assumed to be in equilibrium with the throat steam and liquid temperatures set equal to the saturation temperature at the throat pressure, P_t.

For the steam-liquid-noncondensable situation, the total throat pressure P_t is again calculated with Equation (6.3-2). However, the effect due to partial pressure complicates matters for estimating the throat temperature. The steam-liquid-noncondensable temperature is calculated using a Taylor series approximation to account for the steam partial pressure as is done in Reference [78]. Given the cell-centered pressure P_c, which is the sum of the vapor and noncondensable partial pressures, the steam partial pressure P_s at the throat is expanded as:

$$P_{st}\left(P_c + \Delta P\right) = P_s\left(P_c\right) + \Delta P \left(\frac{\partial P_s}{\partial P} \right)_{P=P_c} \tag{6.3-18}$$

where from Dalton's law, the cell-centered pressure upstream of the throat is

$$P_c = P_a + P_s \tag{6.3-19}$$

and the pressure increment to the throat is

$$\Delta P = P_t - P_c. \tag{6.3-20}$$

In the above expansion, the steam throat partial pressure is calculated with a Taylor series expansion, where P_s is the dependent variable and P_c is the independent variable. The derivative of P_s with respect to P evaluated at $P = P_c$ is given by:

$$\left(\frac{\partial P_s}{\partial P}\right)_{P=P_c} = \left(\frac{\partial T}{\partial P}\right)_S \left(\frac{dP_s}{dT}\right)_{\substack{P=P_c \\ T=T_{sat(P_c)}}} \tag{6.3-21}$$

The isentropic part of the derivative $\left(\frac{\partial T}{\partial P}\right)_S$ is a fairly complex expression. Its expansion into its basic components is detailed in APPENDIX E. The equilibrium throat steam-liquid-noncondensable temperature is then

$$T = TSAT\ (P_{st}) \tag{6.3-22}$$

where TSAT is the saturation temperature evaluated at the throat pressure P_{st}.

6.3.3.2 Single-Phase One- or Two-Component Vapor Flow

The seven principal simplifying assumptions employed in Section 6.3.3.1 to calculate a_{HE} are also employed in the single-phase, one/two-component vapor choking formulation. This choking model presently employs two methods for calculating the sonic speed. The first approximation models the steam as a "perfect gas" (in the sense that there is no potential for vapor condensation). This is a valid approximation when the throat temperature of the steam is well above saturation conditions so that the isentropic derivative $\left\{\frac{\partial \alpha_v}{\partial P}\right\}_S = 0$. The second approximation employs the generalized HE formulation from Section 6.3.3.1. In this formulation, the isentropic derivative $\left\{\frac{\partial \alpha_v}{\partial P}\right\}_S$ is not equal to zero. This formulation fully accounts for the vapor equation of state deviations from the "perfect gas" approximation when the calculated throat temperature is near saturation conditions.

In the first approximation, the steam and noncondensable mixture are assumed to approximate a perfect gas with zero friction losses between the cell center and downstream choke plane. Under these conditions, the cell-centered total pressure, temperature, and density are approximated within the adiabatic choked flow perfect gas formulation[92] which gives:

$$P_t = P_c^* \left(1 + \frac{\gamma - 1}{2}\right)^{-\left(\frac{\gamma}{\gamma - 1}\right)} \tag{6.3-23}$$

$$P_c^* = P_c + \frac{\rho_c V_c^2}{2} \tag{6.3-24}$$

$$T_t = T_c \left(1 + \frac{\gamma - 1}{2}\right)^{-1} \tag{6.3-25}$$

$$\rho_t = \rho_c \left(1 + \frac{\gamma - 1}{2}\right)^{-\left(\frac{\gamma}{\gamma - 1}\right)} \tag{6.3-26}$$

where the specific heat ratio is density-averaged

$$\gamma = \frac{\bar{C}_P}{\bar{C}_V} = \frac{X_a C_{P_a} + (1 - X_a) C_{P_s}}{X_a C_{V_a} + (1 - X_a) C_{V_s}} \tag{6.3-27}$$

$$X_a = \frac{\rho_a}{\rho_t} . \tag{6.3-28}$$

Assuming constant noncondensable mass fraction X_a gives a noncondensable throat density

$$\rho_{at} = X_a \rho_t . \tag{6.3-29}$$

The throat partial pressure of the steam becomes:

$$P_{st} = P_t - \rho_{at} R T_a . \tag{6.3-30}$$

The conditions at the throat are thus completely specified.

The above throat pressure and temperature conditions are then used by THERMO to calculate the remaining thermodynamic parameters and derivatives to evaluate the equations for the isentropic sound speed. In the limit $\alpha_v = 1$, Equation (6.3-11) reduces to:

$$a_{HE} = \left[\left(\frac{\partial \rho_a}{\partial P} \right)_S + \left(\frac{\partial \rho_s}{\partial P} \right)_S \right]^{-1/2} \tag{6.3-31}$$

where the individual isentropic derivatives are evaluated at $T_t = T_a = T_s$.

In the second formulation of the sonic speed, the vapor and noncondensable temperature are set equal to TSAT (P_{st}), or the saturation temperature at the throat partial steam pressure. Since the vapor state is now on the saturation curve, the isentropic derivative $\left\{ \frac{\partial \alpha_v}{\partial P} \right\}_S$ is not equal to zero even though $\alpha_\ell = 0$. From APPENDIX E, the generalized HEM sonic velocity in the limit $\alpha_v = 1$ reduces to:

$$a_{HE}^{-2} = \frac{\rho}{\rho_\ell \rho_s} \left\{ \rho_s \left(\frac{\partial \rho_a}{\partial P} \right)_S + (\rho_\ell - \rho_a) \left(\frac{\partial \rho_s}{\partial P} \right)_S \right.$$

$$\left. - \frac{\rho_a + \rho_s - \rho_\ell}{S_s - S_\ell} \left[\rho_a \left(\frac{\partial S_a}{\partial P} \right)_S + \rho_s \left(\frac{\partial S_s}{\partial P} \right)_S \right] \right\} . \tag{6.3-32}$$

TRACG calculates the sonic speed using both Equations (6.3-31) and (6.3-32) and uses the maximum value in the criteria for choking.

6.3.3.3 Single-Phase Liquid Flow

This section documents the single-phase liquid critical flow model used in TRACG. The terminology single-phase liquid is used in the sense that the vapor and/or noncondensable void fraction is either negligible or nonexistent. The single-phase liquid critical flow model employs two approximations for calculating the sonic velocity. The first method uses the approach developed by Alamgir, Jones and Lienhard (AJL)[93],[94],[95] to correlate the sonic velocity. This approach is called the AJL model or correlation. The second method employs a modified HEM approximation. After the sonic speed for each scheme is calculated, the maximum value is used in the choking criterion formulation. The single-phase liquid model is activated when the cell vapor void fraction immediately upstream of the break plane satisfies the criteria $\alpha \le 0.01$.

The seven principal assumptions employed to calculate the choke plane a_{HE} in Sections 6.3.3.1 and 6.3.3.2 are modified for the single-phase liquid critical flow model. These modifications are:

- Vapor or noncondensables immediately upstream of the break plane are assumed to be insignificant and are not donored to the cell choke plane.
- The AJL model quantifies turbulent fluctuations and non-equilibrium nucleation phenomena at the choke plane.

When high-pressure, high-temperature water is suddenly decompressed, it transitions from a sub-cooled or saturated state to a superheated state. As a consequence, the throat pressure of the flashing liquid can be much lower than the choke plane saturation pressure. Such enhanced depressurization can be driven by turbulent fluctuations or by bubble nucleation effects as the liquid exits the choke plane. The pressure undershoot $\Delta P(a_s)$ at the throat is related to the sonic speed via the correlation:

$$P_{sat}\left(T_\ell\right) - P_t = \Delta P(a_s) \tag{6.3-33}$$

$$\Delta P(a_s) = \left(CA + CB\, a_S^{2.4}\right)^{1/2} - CC\, a_s^2 \tag{6.3-34}$$

where:

$$CA = \frac{0.258\,\sigma^{3/2}\left(\dfrac{T_\ell}{T_{crit}}\right)^{13.76}}{(kT_{crit})^{1/2}\left(1-\dfrac{\rho_g}{\rho_\ell}\right)} \tag{6.3-35}$$

$$CB = \left[\frac{(13.25)\,(9.866\times10^{-12})\,\rho_\ell\left(\dfrac{dA}{dx}\right)_t}{A_t}\right]^{0.8} \tag{6.3-36}$$

$$CC = 0.072\,\rho_\ell \left(\frac{A_t}{A_u}\right)^2 \tag{6.3-37}$$

σ	=	surface tension
k	=	Boltzmann constant
$\left(\frac{dA}{dx}\right)_t$	=	rate of area change
T_{crit}	=	critical fluid temperature
$P_{sat}\,(T_\ell)$	=	saturation pressure at the liquid temperature in the cell adjacent to the choking plane

The first term in Equation (6.3-34) represents the depressurization driven by nucleation effects formulated by Alamgir and Lienhard[93] The second term developed by Jones[94],[95] represents the additional pressure losses because of increased turbulence due to flashing. In the formulation implemented in TRACG, turbulence driven by acceleration effects (break geometry area gradients) is assumed to be much larger than wall friction effects. As a consequence, wall friction is ignored in the implementation of the AJL correlation in TRACG. The 0.072 coefficient is a best estimate of the turbulent intensity index in Equation (6.3-34). This number is recommended unless there is a clear and substantially different value known *a priori* for a particular break geometry.

For closure, the second equation used to relate the throat pressure with the sonic speed is:

$$P_c + \frac{\rho_m V_{mc}^2}{2} = P_t + \frac{\rho_m a_s^2}{2}. \tag{6.3-38}$$

Equation (6.3-38) is obtained by applying the Bernoulli equation (Equation (6.3-32)) assuming no wall friction and sonic velocity in the throat. Equations (6.3-34) and (6.3-38) are solved in the TRACG solution scheme by eliminating P_t and finding a_s from the transcendental equation:

$$a_s - \sqrt{\frac{2}{\rho_\ell}\left[DPP + \Delta P\left(a_s\right)\right] + V_{mc}^2} = 0 \tag{6.3-39}$$

where:

$$DPP = \max\,[0,\ P_c - P_{sat}\,(T_\ell)] \tag{6.3-40}$$

Equation (6.3-39) is solved iteratively using a standard Newton-Raphson technique.

The sonic speed is calculated using a second approximation with Equation (6.3-13). Here, the throat temperature is set equal to T_ℓ and the pressure is set equal to $P_{sat}(T_\ell)$, where T_ℓ, is the cell-centered liquid temperature upstream of the throat. In the second approximation, it is assumed that the liquid has decompressed to a saturated state at the break plane. The final sonic velocity becomes Max [a_S, a_{HE}], where a_{HE} is the liquid single-phase homogenous sound speed from Equation (6.3-14).

In the course of doing simulations with early versions of the TRACG choking model, numerical oscillations in the break mass flow rate were observed when the throat conditions were near the sub-cooled sonic regime[79]. If the conditions upstream of the break plane transition from sub-cooled to saturated conditions, large reductions in the throat sonic velocity will occur. To prevent large discontinuous changes in the sonic velocity, a cubic spline interpolation scheme has been employed in the transition region $0.01 \le \alpha_v \le 0.1$. In this α_v range, both the TCTP homogeneous equilibrium and single-phase liquid models are separately used to calculate the break plane sonic speed. The cubic spline interpolation yields the transition sonic speed:

$$a_t = Wa_{HE} + (1 - W)a_s \tag{6.3-41}$$

where:

$$W = 3\alpha_T^2 - 2\alpha_T^3 \tag{6.3-42}$$

$$\alpha_T = \frac{\alpha_v - 0.01}{0.1 - 0.01} \tag{6.3-43}$$

6.3.4 Determination of Choked Flow Phasic Velocities

Once a particular regime has been picked and the corresponding sonic speed calculated, Equation (6.3-1) is employed to test for choking conditions. Because of the half-cell donoring scheme, Equation (6.3-1) is implemented in TRACG with the following modifications.

The sonic speed calculated from cell edge throat properties is first multiplied by the throat mixture density ratio so that:

$$a_s^* = a_s \left(\frac{\rho_{mt}}{\rho_{mc}} \right) \tag{6.3-44}$$

This modification was used to partially account for the difference in throat mass flux used in the cell continuity equation (due to cell-centered donoring) and the velocity that would exist if the throat density were used instead. If the choking criteria are satisfied, the new-time throat mixture velocity is set equal to the sonic velocity and then calculated using a relaxation scheme:

$$a_s^{*n+1} = a_s^{*n} + \mathrm{RELAX}\left(a_s^{*n} - a_s^{*n+1}\right) \tag{6.3-45}$$

where:

$$\mathrm{RELAX} = \max\{0.1,\ 1\text{-}\exp(-20\,\Delta t)\} \tag{6.3-46}$$

where n and n+1 refer to old and new times, respectively. The relaxation algorithm is used to ensure numerical stability. Calculating the throat sonic velocity is not sufficient to advance the momentum solution to the next time step, since the two throat edge velocities must first be specified.

Two equations are needed to solve for the two unknown throat edge velocities. The solution scheme (except for single-phase vapor choking) uses the following two equations:

$$a_s^* = \frac{\alpha_v \rho_\ell v_v + \alpha_\ell \rho_v v_\ell}{\alpha_v \rho_\ell + \alpha_\ell \rho_v} \tag{6.3-47}$$

and

$$C_v v_v + C_\ell v_\ell = RHS \tag{6.3-48}$$

where:

a_s^* = calculated sonic speed

v_ℓ, v_v = choke plane cell edge liquid and vapor velocities

C_ℓ, C_v, RHS = TRACG momentum equation solution constants calculated from TF1DE.

For single-phase one- or two-component vapor choking, Equations (6.3-47) and (6.3-48) are replaced by the simple relationships:

$$v_\ell = v_v = a_s^* . \tag{6.3-49}$$

In general, the above formulation allows for slip between the phases at the choke plane. In order to advance the TRACG momentum solution scheme in time, the velocity derivatives with respect to pressure must be calculated. The derivatives are calculated by perturbing the previously calculated throat pressure by 1% in the subroutine CHOKE. The sonic speed and junction velocities are then recalculated. The phasic velocity derivatives are then calculated as follows:

$$\frac{\Delta v_\ell}{\Delta P_t} = \frac{v_\ell (P_t + \Delta P_t) - v_\ell (P_t)}{\Delta P_t} \tag{6.3-50}$$

$$\frac{\Delta v_v}{\Delta P_t} = \frac{v_v (P_t + \Delta P_t) - v_v (P_t)}{\Delta P_t} \tag{6.3-51}$$

where (ΔP_t) is the 1% throat pressure variation. It should be noted that the phasic velocities, calculated by CHOKE and passed back to TF1DE when the flow is choked, are calculated at P_t and not at ($P_t + \Delta P_t$).

6.3.5 Applicability

The two-phase critical flow models described in Sections 6.3.1 through 6.3.4 contain a number of simplifying assumptions. The most important limitation is that the TRACG choking model is inherently one-dimensional. Break flow geometry must be considered as a factor in simulating a particular scenario. If the modeled break configuration is strongly affected by multi-dimensional hydrodynamic phenomena, a discharge coefficient may have to be used.

The TRACG sonic speed formulation (with the exception of the AJL correlation, which considers turbulence and nucleation) assumes that non-homogeneous or non-equilibrium

processes are not significant. As a consequence, the sonic speed at the choke plane is derived with the assumption that the liquid and vapor phases have relaxed to thermodynamic equilibrium. In reality, the degree of break plane non-homogeneity is dependent on the flow map, while the degree of non-equilibrium is determined by interfacial transport processes and the time needed to relax to equilibrium. The primary dependence on flow regimes is accounted for by using the void fraction to select which model and corresponding simplifications are most appropriate together with use of the individual component densities in evaluating the sonic velocity. This simple approach and the assumption of thermodynamic equilibrium are justified by assessing the calculated results against data.

6.3.6 Assessment and Applicability to BWR

Assessment work using the TRACG critical flow model has generally yielded very good results. The methodology for calculating the choke plane phasic velocities has generally yielded accurate comparisons versus experimental data with regard to calculated mass flow rates and system depressurization responses. See References [76], [77], [78], [79], and [96] for the details.

Break flow studies based on the TRACG predictions versus data from 11 tests in five different test facilities (PSTF, TLTA, FIST, FIX, Marviken) show that the TRACG over-predicts the data, on a mean value basis, by [[ ]], with standard deviation of [[ ]] for the liquid blow-down phase and under-predicts the data by [[ ]] for the two-phase blow-down phase. For the Marviken tests (full scale), in the liquid blow-down period TRACG over-predicted the average break flow by about [[ ]] for Test 15 (L/D=3.6) and under-predicted the break flow by about [[ ]] for Test 24 (L/D=0.33). These results show that the TRACG break flow model has no strong bias for different values of the ratio of discharge pipe length (L) to pipe diameter (D). The comparisons to data include choked flow for both smooth and abrupt area changes, i.e., orifices.

6.4 Two-Phase Level Model

In the normal TRACG solution of the fluid flow equations, the mean cell void fraction is assumed to exist uniformly throughout each hydrodynamic fluid cell. If a phase boundary or liquid level exists in the cell, the numerical solution to the fluid flow equations results in an artificially high diffusion of vapor in one direction and liquid in the other. To minimize this artificial diffusion, it is necessary to accurately predict the existence of two-phase levels that may occur in vertically oriented cells and to take proper account for this in the numerical solution of the flow equations. The TRACG two-phase level-tracking model was developed for this purpose. The model provides the capability of maintaining the sharp void fraction discontinuity across a two-phase level that occurs in vertical components.

The TRACG level tracking model consists of two parts:

1. Detection of two-phase levels plus calculation of their positions, velocities, and void fractions above and below the phase boundaries.
2. Appropriate modification to the equations governing the flow when a two-phase level is present.

Part 2 above is discussed in Section 6.4.3. Part 1 may be further divided into two sections: (1) detection of two-phase levels and (2) calculation of the parameters necessary to describe the propagation of fluid above and below the phase boundaries.

6.4.1 Level Detection

The first step in detecting a two-phase level is the determination of the type of vertical void profile existing around a particular cell. The level detection logic required for a normal (increasing in the vertical direction) void profile is not the same as the logic required for an inverted (decreasing in the vertical direction) void profile. Once the type of void profile has been established, the model must determine if the conditions in the cell indicate the existence of a two-phase level. Although different logic is used depending on the void profile, the use of cell average void fraction differences to initiate the level calculations is common to all conditions. Generally, a level is assumed to exist in cell j if (Figure 6-8):

$$(\alpha_{j+1} - \alpha_j) \geq \Delta\alpha_{cut} \quad \text{and} \quad \alpha_{j+1} \geq \alpha_{cut} \qquad (6.4\text{-}1), (6.4\text{-}2)$$

provided that no level exists in cell (j+1) or cell (j-1). Here, $\Delta\alpha_{cut}$ is a predetermined cutoff value. A value of 0.2 is recommended for $\Delta\alpha_{cut}$ and 0.9 is recommended for α_{cut}. Once a level has been established in a cell, these criteria are not used. The level calculation is therefore not sensitive to the precise value of $\Delta\alpha_{cut}$ as long as a reasonable value is chosen. The value of α_{cut} is used to prevent spurious level indications when the $\Delta\alpha_{cut}$ criteria are satisfied. The recommended value has been used for all TRACG qualification cases.

An inverted void profile is detected when the decrease in void fraction from cell (j) to cell (j+1) is greater than a predetermined cutoff value similar to $\Delta\alpha_{cut}$. The recommended value for the inverted level $\Delta\alpha_{cut}$ is 0.1. If a void inversion is detected, the normal void profile level criterion (Equation (6.4-1)) is applied to the cells above and below the inversion boundary. For cells below a void inversion, the α_{cut} criterion is not applied.

6.4.2 Calculation of Level Parameters

The parameters necessary to describe a two-phase level are (1) the position and velocity of the level and (2) the void fractions above and below the level. Figure 6-8 shows a simplified diagram of a two-phase level established in a normal void profile situation.

For a normal void profile $(\alpha_{j+1} \geq \alpha_j \geq \alpha_{j-1})$ the two-phase level parameters in cell j can be obtained from the conditions in the vessel cells above and below cell j. The position of the level in cell j can be described by the equation:

$$\Delta z_{Lj} = \Delta z_j \left(\frac{\alpha_j^+ - \alpha_j}{\alpha_j^+ - \alpha_j^-} \right) \qquad (6.4\text{-}3)$$

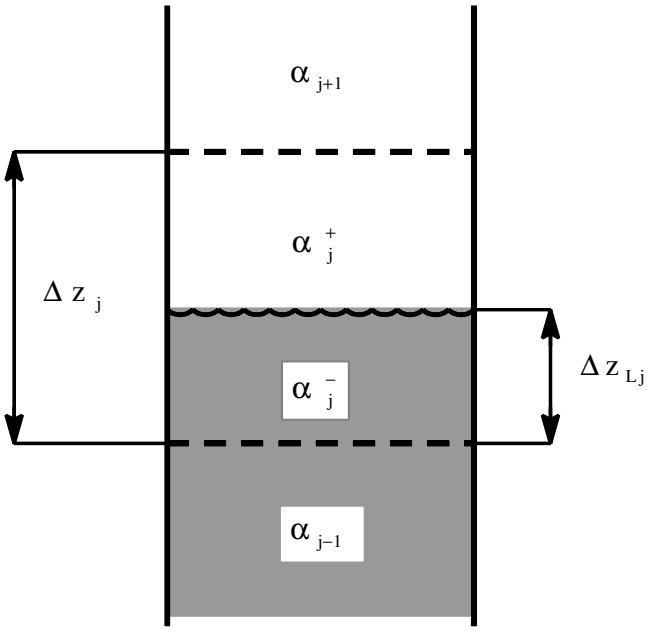

Figure 6-8. Two-Phase Level with Normal Void Profile

where α^+ and α^- are the void fractions above and below the level. For normal void profile conditions, the void fraction below the level α_j^- is assumed to be equal to the void fraction in the cell below, i.e.:

$$\alpha_j^- = \alpha_{j-1} \tag{6.4-4}$$

In the absence of entrainment of liquid from below the level, the void fraction above the level, α_j^+, is assumed to be equal to the void fraction in the cell above:

$$\alpha_j^+ = \alpha_{j+1} \tag{6.4-5}$$

Entrainment lowers the void fraction given by Equation (6.4-5). The mass flux of entrained liquid ($G_{\ell ent}$) is calculated from the correlation of Rosen[98] as:

$$G_{\ell ent} = \left[3 \cdot 10^{-5} (C_K^{0.5} + 530.0\, C_K^{2.1}) \left(\frac{\rho_\ell - \rho_v}{\rho_v} \right)^{0.5} \right] j_v \rho_v \tag{6.4-6}$$

$$C_K = \frac{2\, D_{max}\, j_v}{v_{crit} \left(\frac{\sigma}{g\,(\rho_\ell - \rho_v)} \right)^{0.5}} \tag{6.4-7}$$

$$v_{crit} = 2 \left(\frac{\sigma g (\rho_\ell - \rho_v)}{\rho_v^2} \right)^{0.25} \quad (6.4\text{-}8)$$

$$D_{max} = 0.3375 \frac{\rho_v v_v^2}{g (\rho_\ell - \rho_v)} \quad (6.4\text{-}9)$$

In these expressions, all fluid properties are for the cell in question and j_v and v_v are for the upper cell boundary. For positive liquid velocity at the top of the cell, the liquid mass flux may also be represented as:

$$G_{\ell ent} = (1-\alpha_j^+) \rho_\ell v_\ell \quad (6.4\text{-}10)$$

from which the above-level void fraction, α_j^+, is computed to be:

$$\alpha_j^+ = 1 - \frac{G_{\ell ent}}{\rho_\ell v_\ell} \quad (6.4\text{-}11)$$

For negative liquid velocity at the top of the cell, the entrainment is assumed to be zero and α_j^+ is assumed equal to the void fraction in the cell above (Equation (6.4-5)).

The level velocity, v_{Lj}, is calculated as the time derivative of the level position:

$$v_{Lj} = \frac{\Delta z_j \left(\frac{\Delta \alpha_j}{\Delta t}\right) - \Delta z_{Lj} \left(\frac{\Delta \alpha_j^-}{\Delta t}\right) - (\Delta z_j - \Delta z_{Lj}) \left(\frac{\Delta \alpha_j^+}{\Delta t}\right)}{\alpha_j^- - \alpha_j^+} \quad (6.4\text{-}12)$$

The level velocity is used to predict when a two-phase level will leave a cell. In the event the level does exit a cell, the level velocity is used to predict the new velocity conditions at the boundary the level has crossed.

For a normal void profile, the two-phase level is completely described by Equations (6.4-3) through (6.4-12). However, if the two-phase level is in a cell below a void profile inversion ($\alpha_{j+1} < \alpha_j$) or flow area reduction, Equations (6.4-5) and (6.4-11) cannot be used to determine the void fraction above the level without modification. In this situation, it is assumed that:

$$\alpha_j^+ = 0.999 \quad (6.4\text{-}13)$$

and the two-phase level can be described by Equations (6.4-3), (6.4-4), (6.4-11) and (6.4-12). For a two-phase level occurring above a void fraction inversion ($\alpha_j < \alpha_{j-1}$) or flow area reduction, the void fraction below the level is evaluated using the drift flux model:

$$\alpha_j^- = \frac{j_v^-}{C_o\, j^- + \overline{v}_{gj}} \tag{6.4-14}$$

where C_o and $\overline{v}_{gj}$ are determined assuming bubbly/churn flow (Section 6.1.3), and j_v^- and j^- are the vapor and mixture volumetric flux below the level, respectively.

6.4.3 Model As Coded

The two-phase level model is available for both three-dimensional and one-dimensional components. There are differences in the implementation for the two component types. For this reason, the as-coded details of the model will be described separately.

6.4.3.1 Three-Dimensional Component

The discretized governing equations described in Section 3.2 are impacted by the presence of a level through the void fraction axial donor celling as follows:

$$\phi^d_{i+1/2} = \begin{cases} \phi_i & \text{if } v_{i+1/2} \geq 0 \text{ and no level exists in cell i} \\ \phi_i^+ & \text{if } v_{i+1/2} \geq 0 \text{ and a level exists in cell i} \\ \phi_{i+1} & \text{if } v_{i+1/2} < 0 \text{ and no level exists in cell i+1} \\ \phi_{i+1}^- & \text{if } v_{i+1/2} < 0 \text{ and a level exists in cell i+1} \end{cases} \tag{6.4-15}$$

If an average property is required at a cell boundary, the above or below level void fraction is used for interpolation if a level exists.

The donor celling for source connections to the vessel for flow from vessel cell i is impacted in a similar fashion as follows:

$$\phi^d_s = \begin{cases} \phi_i & \text{if no level exists in cell i} \\ \phi_i^+ & \text{if level position is below connection} \\ \phi_i^- & \text{if level position is above connection} \end{cases} \tag{6.4-16}$$

The donor-celled property is interpolated between the above and below values as a level crosses the source connection area. Old time step values are used for the above level or below level properties, i.e., the level is tracked explicitely.

The pressure drop from cell center to cell center in the momentum equation is also adjusted to account for a level in the cell. The pressure difference is modified to reflect the fluid conditions that exist at the cell boundary. In Figure 6-8, the hydrostatic head between cells j and j+1 is modified by adjusting the cell j pressure used in the momentum equation as follows:

$$P_j^* = P_j + (\rho_\ell - \rho_v)(\alpha^+ - \alpha^-) g \left(\Delta z_{Lj} - \frac{\Delta z_j}{2} \right) \tag{6.4-17}$$

This modification, together with the use of averaged void fractions as discussed above for the cell boundary, gives both the correct static head between cells and the correct pressure gradient and relative velocity at the cell boundary.

The interfacial heat transfer and shear are also impacted by a two-phase level. Above and below level heat transfer coefficients are calculated and volume weighted using the level position. A free surface convection component is added to account for free surface heat transfer. Interfacial heat transfer is described in Section 6.5. The interfacial shear is evaluated at the conditions present at the cell boundary when a level exists.

When a level crosses a boundary, there is a discontinuity in the void fraction and phase velocity at the boundary. To account for this, the phase velocities are modified when a level crosses a cell boundary using the jump conditions:

$$v_L = \begin{cases} \dfrac{-j_v^- + j_v^+}{\alpha^+ - \alpha^-} & ,v_L < 0 \\ \dfrac{j_\ell^- - j_\ell^+}{\alpha^+ - \alpha^-} & ,v_L > 0 \end{cases} \tag{6.4-18}$$

For a falling level, the modified old time vapor velocity becomes:

$$(v_v)_{j-1} = \frac{\alpha_j^-(v_v)_{j-1} - (\alpha_j^- - \alpha_j^+)v_{Lj}}{\alpha_j^+} \tag{6.4-19}$$

The liquid velocity at the boundary is adjusted using the above vapor velocity and the drift flux correlation with parameters appropriate for droplet flow as described in Section 6.1.5. For the falling level:

$$(v_\ell)_{j-1} = (v_v)_{j-1} - 1.41\left(\frac{\Delta\rho g\sigma}{\rho_v^2}\right)^{0.25} \tag{6.4-20}$$

The evaluation of a rising level is handled in the same manner. In this case, the vapor velocity is adjusted using the liquid velocity modified using the jump condition and the drift flux correlation with parameters appropriate for bubbly flow (Section 6.1.3).

6.4.3.2 One-Dimensional Component

The level model is available in a one-dimensional (1-D) component cell that is vertically oriented. The level detection and calculation of level parameters are consistent with the three-dimensional (3-D) component. The major difference between the implementation is that, unlike the 3-D component, the 1-D component model does not affect the donor celling of void fraction at cell boundaries. For the 1-D component, the level model impact is limited to the interfacial heat transfer calculation within the cell. Above and below level heat transfer coefficients are calculated and volume weighted using the level position. A free surface convection component is added to account for free surface heat transfer. The absence of any special treatment for the convected void fraction in the presence of a level can be accounted for through nodalization. The 1-D component will require a finer nodalization in the vicinity of a two-phase level.

Assessment regarding appliation of the level model to 1-D components is discussed in Section 7.11.7.

6.4.4 Applicability

The applicability of the level model is controlled by the assumptions used in the model development, in particular, the assumptions regarding the setting of the above and below void fractions. It is assumed that these values can be assigned the values of adjacent cells. Implicit in this assumption is that there is no significant change in void fraction for cells below or above the level position. An adjustment is made for entrainment for the above level void fraction but there is no provision for the existence of a void profile below the level. In situations where a significant void profile exists below the two-phase level, the nodalization must be sufficient to provide the necessary below level detail to avoid discontinuities in the level position. In addition to the model assumptions, the model applicability depends on the applicability of the interfacial shear and heat transfer models used to determine the void fraction.

6.4.5 Assessment

Assessment of the level model is provided by the PSTF level swell tests[99]. The PSTF facility consists of a 4.27m tall vessel with an internal diameter of 1.19m. A blow-down pipe is connected to the bottom of the vessel and could be fitted with different nozzles. In some tests, the blow-down pipe contained a vertical section with its inlet in the upper portion of the vessel at an elevation of 3.2m. In all cases, the vessel was partially filled with water, heated and pressurized to 7.2 MPa. A rupture disk at the end of the blow-down pipe was broken, allowing the system to depressurize. A complete description of the test facility, nodalization and individual test initial conditions is provided in Section 3 of the *TRACG Qualification LTR*[6].

For the cases where the blow-down pipe contained the vertical section, the break flow was primarily steam flow and the system depressurized quickly. In these tests, the liquid in the vessel flashed, causing the liquid level to rise initially and subsequently subside toward the end of the depressurization. Comparisons of the level predictions for two steam blow-down cases (5801-13 and 5801-15) are provided in Figure 6-9 and Figure 6-10. The level swell is generally well predicted for these tests. The primary cause of the difference between the measured and calculated void fractions and the corresponding level positions is the uncertainty in the cross-sectional distribution of the vapor resulting from the flashing of liquid during the rapid depressurization.

For cases where the vertical section was omitted, the system initially depressurized slowly as the break flow was primarily liquid and two-phase flow. During this period, the level dropped slowly. When the level uncovered the entrance to the blow-down pipe, the depressurization rate increased. The increased depressurization rate caused increased flashing of the liquid and the level drop subsided. Comparisons of the level predictions for two liquid blow-down cases (5803-01 and 5803-02) are provided in Figure 6-9 and Figure 6-10. The level movement is well predicted for these tests, indicating a good prediction of the void fraction. In these tests, the slower depressurization results in less uncertainty in the cross-sectional vapor distribution.

Visible in the TRACG level predictions are small discontinuities in the level position. These discontinuities result from the change in below level void fraction that occurs when a level crosses a cell boundary. Whenever a void profile exists below the level, the nodalization must

provide sufficient detail below the level to minimize these discontinuities. The impact on the results for these tests is insignificant, indicating an acceptable nodalization.

The above separate effects assessment of the level model is supplemented by integral system testing and plant data comparisons provided in Sections 5 and 7 of the *TRACG Qualification LTR*[6].

[[

]]

Figure 6-9. PSTF 5801-13 Level Prediction

[[

]]

Figure 6-10. PSTF 5801-15 Level Prediction

[[

]]

Figure 6-11. PSTF 5803-01 Level Prediction

[[

]]

Figure 6-12. PSTF 5803-02 Level Prediction

6.5 Interfacial Heat Transfer

Interfacial heat transfer models are needed for the closure and solution of the system of two-phase equations (Section 3.1). Interfacial heat transfer rates are part of the vapor and liquid conservation energy equations and determine the interfacial mass exchange rate Γ_g, which appears in the vapor and liquid mass and energy conservation equations. This section describes models and correlations incorporated into the TRACG interfacial heat transfer model, their technical bases and limitations.

6.5.1 Background

The TRACG interfacial heat transfer model is based on the assumption that the liquid-vapor interface is always at saturation temperature corresponding to the local partial steam pressure. Energy exchange rate at the interface provides the necessary mass exchange to maintain the interface at saturation temperature. The total heat exchange and mass transfer at the interface are functions of the volume-averaged liquid-interface heat transfer rate $q_{\ell i}$ and vapor-interface heat transfer rate q_{vi}:

$$q_{\ell i} = A_i h_{i\ell} \left(T_\ell - T_{sat} \right) \; ; \quad q_{vi} = A_i h_{iv} \left(T_v - T_{sat} \right) , \tag{6.5-1}$$

where A_i is the interfacial area per unit volume and $h_{i\ell}$ and h_{iv} are liquid-interface and vapor-interface convective heat transfer coefficients. Energy exchange at the vapor-liquid interface leads to mass exchange at the interface Γ_g due to evaporation ($\Gamma_g > 0$) or condensation ($\Gamma_g < 0$) processes at the interface:

$$\Gamma_g = \frac{q_{\ell i} + q_{vi}}{h_{fg}} \tag{6.5-2}$$

Equations (6.5-1) and (6.5-2) represent the energy and mass exchange between phases at the interface and appear in the mass and energy conservation equations (Section 3.1). According to Equation (6.5-1), interfacial area A_i and interfacial heat transfer coefficients $h_{i\ell}$ and h_{iv} have to be defined (based on the flow regime) to calculate energy and mass exchange at the interface and to close the thermal-hydraulic system of equations.

The interfacial heat transfer model described below is closely related to the interfacial shear model (Section 6.1) and incorporates the same flow regime map (Section 5.1.1.1). The entrainment model described in Section 5.1.2 is used to determine the fraction of the entrained liquid.

6.5.2 Interfacial Area

The calculations of the interfacial heat transfer require the specification of the interfacial area A_i and heat transfer coefficients $h_{i\ell}$ and h_{iv}. The experimental data will generally lead only to information about their product. The models for the interfacial area described in the following

sections are mostly based on the models proposed by Ishii[44], which were used to determine the interfacial shear[100],[101] (Section 6.1). For this reason, the database that was used to confirm the drift flux parameters for the interfacial shear model is applicable to the interfacial heat transfer model (interfacial area calculations). For some flow regimes (bubbly-churn flow, droplet flow), the interfacial area is defined by a maximum stable particle size, which is a function of a critical Weber number. In the calculation of the interfacial shear, only the ratio of the drag coefficient C_D and critical Weber number We_c have to be correlated (Section 6.1), and there is no need to calculate interfacial area A_i. This is not the case in the interfacial heat transfer calculations, where the value of the interfacial area A_i has to be defined for all the flow regimes to calculate interfacial heat flux (Equation (6.5-1)).

6.5.3 Bubbly/Churn Flow

A staggered mesh is used, where the mass and energy equations are integrated over a cell, and the equation of motion is integrated from cell center to cell center. The cell average void fraction is used for the interfacial heat and mass transfer. The upstream void fraction is applied between two cell centers to calculate the interfacial shear between the phases.

6.5.3.1 Technical Basis and Assumptions

The interfacial area in bubbly flow regime depends on the number of bubbles and average bubble diameter:

$$A_{ib} = N_b \pi d_b^2 \tag{6.5-3}$$

The number of bubbles N_b is related to the void fraction:

$$N_b = \frac{6\alpha}{\pi d_b^3} \tag{6.5-4}$$

Substituting Equation (6.5-4) into Equation (6.5-3), one obtains the expression for the interfacial area:

$$A_{ib} = \frac{6\alpha}{d_b} \tag{6.5-5}$$

The bubble diameter is calculated from critical Weber number:

$$d_b = \frac{\sigma We_c}{\rho_\ell v_{rb}^2} \tag{6.5-6}$$

A maximum critical Weber number for stable spherical particles is typically 12-13 (see References [40] and [44]). In reality, a spectrum of bubbles will exist with a critical Weber number of 13 representing the maximum bubble diameter. A value of half the maximum bubble size is chosen for the average bubble diameter d_b.

The relative phasic velocity is calculated similar to Section 6.1:

$$v_{rb} = \frac{\overline{v}_{gj}}{1-\alpha} \tag{6.5-7}$$

The same correlation for the cross-sectional average vapor drift velocity $\overline{v}_{gj}$ is used in the interfacial heat transfer and interfacial shear models (Section 6.1):

$$\overline{v}_{gj} = k\left\{\frac{\Delta\rho g\sigma}{\rho_\ell^2}\right\}^{0.25}, \quad \text{where } k = 1.53 \tag{6.5-8}$$

The heat transfer coefficient $h_{i\ell,b}$ between the continuous liquid phase and bubbly interface is calculated based on modified Lee-Ryley model and the corresponding correlation for the Nusselt number. (See References [100], [101], [102], [103], and [105].) The Nusselt number is correlated as:

$$Nu_{\ell,b} = 2 + 0.74\sqrt{Re_b}; \qquad Re_b = \frac{\rho_\ell v_{rb} d_b}{\mu_\ell} \tag{6.5-9),(6.5-10}$$

The original correlation is based on measurements of the evaporation rate of small droplets[103]. The vapor properties in the original correlation are replaced with liquid properties and a factor of $Pr^{1/3}$ that is a part of the original correlation is omitted[102],[105]. This has no significant impact, since $Pr \approx 1$ for water. The heat transfer coefficient $h_{i\ell,b}$ corresponding to the liquid side is given by:

$$h_{i\ell,b} = \frac{Nu_{\ell,b} k_\ell}{d_b} \tag{6.5-11}$$

The correlation for the heat transfer coefficient between vapor and bubble interface is based on the solution of the heat conduction equation for a spherical solid particle. For the fully developed temperature profile, this solution leads to $h_{iv,b} = 2\pi^2 k_v/3d_b$ as indicated in Reference [104]. Due to relative motion between the bubbles and liquid, internal circulation will occur. The empirical factor $2.7\mu_\ell/\mu_v$ is applied[114] to account for this circulation and the final form for the $h_{iv,b}$ is:

$$h_{iv,b} = \frac{2}{3}\pi^2 \frac{k_v}{d_b}\left[2.7\frac{\mu_\ell}{\mu_v}\right] \tag{6.5-12}$$

6.5.3.2 Model as Coded

Bubbly churn flow is realized when the criteria for the liquid continuous flow regime $\alpha < \alpha_{tran} - 0.1$ are satisfied (Section 5.1). Calculation of the heat transfer factors $(Ah)_{i\ell,b}$ and

$(Ah)_{iv,b}$ is based on equations described in Section 6.5.3.1 with the following limitations. The minimum number of bubbles per unit volume is limited to 10^7. The limitation on bubble diameter is $0.0005\ m < d_b < 0.5D_h$.

The limits on the bubble sizes for the calculation of the interfacial heat transfer are chosen to keep the bubble size and the interfacial heat transfer within reasonable bounds. The upper boundary is given by the geometry. Theoretically the maximum bubble size would be given by the hydraulic diameter, however due to the fact that the spacers will break up the bubbles in a fuel channel an upper limit of half the hydraulic diameter was chosen. For a fuel channel, which has the smallest hydraulic diameter of the BWR components, this would lead to an upper limit of 0.006 m. The lower limit of 0.0005 m was chosen to prevent the interfacial heat transfer from becoming too large, which can lead to numerical difficulties. For very large interfacial heat transfer rate, the phases will be in thermal equilibrium and the results are not very sensitive to the exact value of the interfacial heat transfer. For typical operating conditions, the bubble sizes will be in the range of 0.002 – 0.004 m, and the number density will be in the range of 1.0E7 – 5.0E7, and are therefore not affected by the limits. Similar arguments are applied for droplet flow, in order to keep the interfacial heat transfer within reasonable bounds. The good comparison to the void fraction and heat transfer data shows that these limits do not adversely affect the results.

6.5.3.3 Applicability

Because the calculation of the interfacial area is based on flow-regime, and is closely related to the interfacial shear model, the applicability of these calculations corresponds to the range of data described in Sections 5.0 and 6.1. The original Lee-Ryley correlation, which provides the basis for calculations of the heat transfer coefficient between the liquid and bubble interface, was developed based on data on measured evaporation rates of small droplets, due to heat transfer from hot air or superheated steam. Because this correlation has been developed for small spherical particles, it is reasonable to apply it for small bubbles. Assessments presented in Reference [105] and Section 6.5.8 provide the justification for this correlation.

While a detailed discussion on derivation of the heat transfer factor on the vapor side has been presented in the previous section, it should be noted that, because of the small bubble diameter and low heat capacity of the vapor, the vapor temperature is very close to saturation temperature and the interfacial heat transfer model is insensitive to the value of the vapor side heat transfer coefficient.

6.5.4 Annular Flow

6.5.4.1 Technical Basis and Assumptions

In this flow regime, interfacial heat transfer and mass exchange occur at the surface of the liquid film on the walls. The interfacial area per unit volume in the annular film flow regime is a function of the average film thickness δ. The volume fraction α_f, which is occupied by liquid film, is:

$$\alpha_f = 1 - \alpha \qquad (6.5\text{-}13)$$

The average film thickness δ and vapor-film interfacial area A_{if} per unit volume are given by the film fraction α_f and hydraulic diameter D_h. Assuming a tubular cross section, one obtains:

$$\delta = \frac{D_h}{2}\left(1-\sqrt{\alpha}\right); \quad A_{if} = \frac{4}{D_h}\sqrt{\alpha} \qquad (6.5\text{-}14), (6.5\text{-}15)$$

Equation (6.5-15) predicts a non-zero interfacial area

$$A_i = \frac{4}{D_h} \qquad (6.5\text{-}16)$$

as the void fraction approaches one and Equation (6.5-14) predicts a film thickness approaching zero as the void fraction approaches one. In reality, at some point the film will break up and not cover the entire surface. TRACG uses a model for the minimum stable film thickness to model this breakup. The average film thickness δ is limited by the minimum film thickness δ_{min}:

$$\delta = \max\{\delta, \delta_{min}\} \qquad (6.5\text{-}17)$$

The expression for δ_{min} is derived from the theory of minimum stable film flow[102] and defined as:

$$\delta_{min} = \min\left\{C\cdot\left[\frac{18\sigma\mu_\ell^2}{g^2\rho_\ell^3}\right]^{0.2}, \left[\frac{6\sigma\mu_\ell^2}{\rho_\ell\tau^2}\right]^{1/3}\right\} \qquad (6.5\text{-}18)$$

where the interfacial shear stress is approximated by:

$$\tau = 0.005\,\frac{\rho_v v_v^2}{2} \qquad (6.5\text{-}19)$$

The original correlation for the minimum film thickness[102] has the form:

$$\delta_{min} = \left[\frac{18\sigma\mu_\ell^2}{g^2\rho_\ell^3}\right]^{0.2} \qquad (6.5\text{-}20)$$

The empirical factor "C" is set to 0.5 based on comparisons with the boiling transition correlations described in Section 6.6.6.

The corresponding value for α_f is:

$$\alpha_{f,min} = 1-\left(1-2\,\frac{\delta_{min}}{D_h}\right)^2 \qquad (6.5\text{-}21)$$

The film thickness δ will decrease as α_f decreases but remains constant after it reaches the minimum thickness δ_{min}. When $\alpha_f < \alpha_{f,min}$, the vapor-film interfacial area is defined as:

$$A_{if} = \frac{4}{D_h}\sqrt{1-\alpha_{f,min}}\left[\frac{\alpha_f}{\alpha_{f,min}}\right] \tag{6.5-22}$$

which is consistent with Equations (6.5-14) and (6.5-15) when $\alpha_f = \alpha_{f,min}$ and provides the right trend ($A_{if} = 0$ when $\alpha_f = 0$).

Combining Equation (6.5-14), (6.5-15) and (6.5-22), one obtains:

$$A_{if} = \begin{cases} \frac{4}{D_h}\sqrt{1-\alpha_f} & \text{for } \alpha_f > \alpha_{f,min} \\ \frac{4}{D_h}\sqrt{1-\alpha_{f,min}}\left[\frac{\alpha_f}{\alpha_{f,min}}\right] & \text{for } \alpha_f < \alpha_{f,min} \end{cases} \tag{6.5-23}$$

The heat transfer coefficient $h_{iv,f}$ between the vapor phase and film interface is calculated according to Reference [105] and based on Theofanous' model[106]. The original model has the form:

$$St = 0.02\sqrt{L/D} \tag{6.5-24}$$

As suggested in Reference [105], the modified version does not include the shape factor $\sqrt{L/D}$ and has the following form:

$$St = \frac{h_{i\ell}}{\rho_\ell C_{p\ell} v_\ell} = 0.02 \tag{6.5-25}$$

The heat transfer coefficient on the vapor side is obtained from Equation (6.5-25) by substituting corresponding vapor properties to produce:

$$h_{iv,f} = 0.02\rho_v C_{P,v} v_v \tag{6.5-26}$$

For the liquid side, the heat transfer coefficient is given by the analytical solution of the heat conduction equation across a thin liquid film[100], assuming a linear temperature profile:

$$h_{i\ell,f} = 2\frac{k_\ell}{\delta} \tag{6.5-27}$$

The presence of noncondensables affects the interfacial heat transfer calculations in several ways. First, the saturation temperature T_{sat} in Equation (6.5-1) is calculated based on

steam partial pressure. Second, the heat transfer coefficient on the liquid side is multiplied by a factor C_{ncg} to reduce the overall heat transfer at the interface[114]:

$$C_{ncg} = \min \left\{ 1.0 \, , \, 0.168 \left(\frac{\alpha \rho_s^2}{(1-\alpha)\rho_a \rho_\ell} \right)^{0.1} \right\} \qquad (6.5\text{-}28)$$

6.5.4.2 Model as Coded

Calculation of the heat transfer factors $(Ah)_{i\ell,f}$ and $(Ah)_{iv,f}$ is based on equations described in Section 6.5.4.1 with the following limitations for the interfacial heat transfer coefficients: $h_{i\ell,f} > h_{i\ell,free}$, $h_{iv,f} > h_{iv,free}$, where the heat transfer coefficients at free surface $h_{i\ell,free}$, $h_{iv,free}$ are defined according to Section 6.5.8.

The maximum value of the heat transfer coefficient on the liquid side is based on the constant Stanton number criteria (Section 6.5.4.1):

$$h_{i\ell f} < 0.02 \, \rho_\ell C_{P,\ell} v_f \, , \qquad v_f = \frac{\delta^2 g \Delta\rho}{3\mu_\ell} \qquad (6.5\text{-}29),(6.5\text{-}30)$$

where v_f is the film velocity derived from a simple force balance on a falling film, assuming viscous flow and a linear velocity distribution in the film. The minimum values of $\alpha\rho_s^2$ and $C_{ncg}\,(1\text{-}\alpha)\,\rho_a\,\rho_\ell$ are limited to 10^{-8}.

6.5.4.3 Applicability

The constant Stanton number criterion is frequently used to calculate the heat transfer coefficients. A constant Stanton number approach was suggested by various investigators for predicting the condensation rates on highly turbulent sub-cooled liquid jets. A comprehensive review of these studies is presented in Reference [106]. Some of these models, such as Theofanous' model, include a correction factor. The Theofanous model, which is based upon the diffusion of turbulent eddies, covers a wide range of Reynolds numbers:

$$4.5 \times 10^3 < Re < 5 \times 10^5$$

and was originally suggested for the highly turbulent liquid jets. Because the correction factor L/D is based upon the shape factor of the jet, this factor is ignored in TRACG[105]. Assessments presented in Reference [105] and Section 6.5.8 provide the justification for this correlation.

The heat transfer coefficient for the liquid side is based on the analytical solution of the heat conduction equation for the thin liquid film. It should be noted that, because the film is very thin (10^{-4} – 10^{-5}m for typical BWR conditions) the heat capacity is low and the temperature will be very close to saturation temperature. Consequently, the interfacial heat transfer factor model is insensitive to the exact value of the heat transfer coefficient on the liquid side. Similarly, when the wall is covered by a film, the vapor core will be close to thermal equilibrium with the interface. Therefore, the vapor temperature is not sensitive to the exact value of the heat transfer coefficient on the vapor side.

6.5.5 Droplet Flow

6.5.5.1 Technical Basis and Assumptions

In this regime, interfacial heat transfer and mass exchange occur at the vapor-to-droplet interface. The interfacial area in the droplet flow regime depends on the number of droplets and average droplet diameter. The volume fraction α_d occupied by a droplet is:

$$\alpha_d = 1 - \alpha \tag{6.5-31}$$

The interfacial area in the droplet flow regime depends on the number of droplets and average droplet diameter:

$$A_{id} = N_d \pi d_d^2 \tag{6.5-32}$$

The number of droplets N_d is related to the droplet fraction:

$$N_d = \frac{6\alpha_d}{\pi d_d^3} \tag{6.5-33}$$

Substituting Equation (6.5-32) into Equation (6.5-31), one obtains the expression for the interfacial flow area:

$$A_{id} = \frac{6\alpha_d}{d_d} \tag{6.5-34}$$

Droplet diameter is calculated from the critical Weber number[44]. For low flow rates, the relative vapor-liquid velocity is used:

$$d_d = \frac{\sigma We_c}{\rho_v v_{rd}^2}; \qquad v_{rd} = \frac{\bar{v}_{gj}}{1-\alpha} \tag{6.5-35),(6.5-36}$$

For large flow rates where the droplets are created by entrainment from the film, the droplet size will be determined by the initial relative velocity as they are entrained from the film on the wall. Since the film velocity is much smaller than the vapor velocity and the void fraction is high, the initial relative velocity can be approximated by the total flux (Section 6.1), and the droplet diameter is defined as:

$$d_d = \frac{\sigma We_c}{\rho_v j^2} \tag{6.5-37}$$

Combining these two expressions, the final equation for the droplet diameter is:

$$d_d = \frac{\sigma We_c}{\rho_v \max\left(v_{rd}^2, j^2\right)} \tag{6.5-38}$$

As is usually the case[40], the relative velocity v_{rd} is related to the vapor drift velocity $\bar{v}_{gj}$ by:

$$v_{rd} = \frac{\bar{v}_{gj}}{1-\alpha} = 1.41 \left\{ \frac{\Delta\rho g \sigma}{\rho_v^2} \right\}^{0.25} \tag{6.5-39}$$

A maximum critical Weber number for the droplets is typically in the range from 12 to13 (see References [40] and [44]). In reality, a spectrum of droplets will exist with a critical Weber number of 13 representing the maximum droplet diameter. The critical Weber number defines the maximum stable droplet size; the actual droplet size will therefore be smaller. A droplet size based on half the critical Weber number was chosen as a representative size for the average droplet size. The excellent comparison to void fraction data shown in NEDE-32177P demonstrate the applicability of the model. Comparisons to integral effects LOCA tests such as TLTA and FIST as shown in NEDE-32177P also demonstrates the adequacy of the model. It should furthermore be kept in mind, that TRACG is not intended to be conservative but best estimate. Conservative estimates for the critical safety parameters are obtained as described in the application methodology LTR.

Similar to bubbly flow, the Lee-Ryley correlation[103] is used to calculate the interfacial heat transfer coefficient at the vapor-to-droplet interface:

$$Nu_{v,d} = 2 + 0.74\sqrt{Re_d}\, Pr_v^{1/3}; \quad Re_d = \frac{\rho_v v_{rd} d_d}{\mu_v} \tag{6.5-40), (6.5-41}$$

$$h_{iv,d} = \frac{Nu_{v,d} k_v}{d_d} \tag{6.5-42}$$

The heat transfer coefficient on the liquid side is defined[104] as:

$$h_{i\ell,d} = \frac{2}{3}\pi^2 \frac{k_\ell}{d_d} \cdot 2.7 \tag{6.5-43}$$

Equation (6.5-43) is similar to Equation (6.5-12) and is based on the analytical solution of the heat conduction equation for a spherical solid particle. The empirical factor 2.7 is applied to account for internal circulation (Section 6.5.3.1). In the presence of noncondensables, the heat transfer coefficient on the liquid side is modified as for the annular flow regime (Section 6.5.4.1).

6.5.5.2 Model as Coded

Calculation of the heat transfer factors $(Ah)_{i\ell,d}$ and $(Ah)_{iv,d}$ is based on equations described in Section 6.5.5.1 and implemented with the following limitation for the droplet diameter:

$$2 \bullet 10^{-4}\, m \le d_d \le \frac{D_h}{4}. \tag{6.5-44}$$

6.5.5.3 Applicability

The Lee-Ryley correlation is based on measurements of evaporation of a water droplet for the following range of variables: droplet diameter 0.006–0.03m, droplet Reynolds number 64–250. The Lee-Ryley correlation is very consistent with the correlation reported in Reference [115], where the heat transfer to spheres is considered over a wide range of conditions: sphere diameter 0.013–0.04m, Reynolds number 20–2000. A comprehensive review of heat transfer data for spheres is also presented in Reference [115]. It is noted in References [103] and [115] that the form:

$$Nu = 2 + B \bullet Re^{0.5} Pr^{1/3} \tag{6.5-45}$$

has been firmly established by a number of authors for heat transfer to spherical particles under forced convection conditions. All the available data in the range $20 < Re < 2000$ has been best fit to obtain the resulting coefficient: $B = 0.63$ (heat transfer in air), $B = 0.79$ (heat transfer in water). The correlation suggested in Reference [115], which covers heat transfer in air and water and predicts the data with an error no greater than 10%, has the form:

$$Nu = 2 + 0.72 \bullet Re^{0.5} Pr^{1/3} \tag{6.5-46}$$

This correlation is almost identical to the Lee-Ryley correlation (the difference is within 4%). Based on results presented in References [103] and [115], it can be concluded that Lee-Ryley correlation is applicable over the wide range of conditions that would be present in the reactor vessel.

Because of the small droplet diameter, the liquid temperature is very close to saturation temperature. Thus, the interfacial heat transfer model is relatively insensitive to the liquid side heat transfer coefficient.

6.5.6 Annular/Droplet Flow

In the annular/droplet flow regime, liquid is distributed between the liquid film and droplets based on the entrainment model (Section 5.1.1.2). The total vapor-liquid interfacial area is the sum of the vapor-to-liquid film interfacial area and vapor-to-droplet interfacial area. The fraction of the entrained liquid is defined by entrainment coefficient E. The volume fractions occupied by liquid film α_f and droplets α_d are:

$$\alpha_f = (1-\alpha)\,(1-E), \qquad \alpha_d = (1-\alpha)E \tag{6.5-47}$$

If the vapor continuous flow regime exists ($\alpha > \alpha_{tran}$), the heat transfer factors $(Ah)_{i\ell,fd}$ and $(Ah)_{iv,fd}$ are defined as:

$$(Ah)_{i\ell,fd} = (Ah)_{i\ell,f} + (Ah)_{i\ell,d} \tag{6.5-48}$$

$$(Ah)_{iv,fd} = (Ah)_{iv,f} + (Ah)_{iv,d} \tag{6.5-49}$$

where heat transfer factors for the film and droplet regimes are defined in Section 6.5.3.1 and 6.5.4.1.

In the presence of noncondensables, the heat transfer coefficient on the liquid side is modified as for the annular flow regime (Section 6.5.4.1).

6.5.7 Transition to Annular Flow

In the transition region ($\alpha_{tran} - 0.1 < \alpha < \alpha_{tran}$), linear interpolation for the heat transfer factors is applied to provide smooth transition from the liquid continuous to vapor continuous flow regime.

6.5.8 Free Surface in Vertical Pipes or 3D Cells

6.5.8.1 Technical Basis and Assumptions

When a level is established in a vertical pipe or 3D cells, natural, or free, convection is observed in the vicinity of the level. TRACG provides the capability to calculate heat and mass exchange at the free surface. Free-convection heat-transfer coefficients can generally be represented as a function of Grashof and Prandtl numbers for a variety of circumstances:

$$Nu = Nu\ (Gr \cdot Pr) \tag{6.5-50}$$

For flat plates, McAdams[134] proposes the general form

$$Nu = k_1 \left(Gr \cdot Pr\right)^{k_2} \tag{6.5-51}$$

where the constants k_1 and k_2 depend on the value of ($Gr \cdot Pr$) and whether the plate is heated or cooled from above or below. For applications to plates, the characteristic length (L) is taken to be the average of the length and the width and the heat transfer coefficient is calculated as:

$$h = \frac{Nu \cdot k}{L} \tag{6.5-52}$$

Holman's correlation for the average heat transfer coefficient for horizontal plates obtained from Table 7-2 of Reference [107] is a specialized application of Equations (6.5-50) and (6.5-52). In SI units, Holman's expression is

$$h = 1.43(\Delta T)^{1/3} \tag{6.5-53}$$

This correlation was modified to simulate natural free convection in a medium other than air by multiplying by the ratio of the conductivities:

$$h = 1.43 \frac{k_v}{k_{air}} (\Delta T)^{1/3} \tag{6.5-54}$$

Using a value of 0.03175 for the conductivity of air at 373K, the above expression becomes:

$$h = 1.43 \frac{k_v}{0.03175} (\Delta T)^{1/3} = 45.04 k_v (\Delta T)^{1/3} \tag{6.5-55}$$

A similar expression for the heat transfer coefficient to the liquid is obtained by substituting the liquid thermal conductivity for the vapor thermal conductivity. The following two simple expressions are obtained for the heat transfer coefficient at a free surface:

$$H_{iv} = 45.04 k_v \left|T_v - T_{sat}\right|^{0.3333} \; ; \quad H_{i\ell} = 45.04 k_\ell \left|T_{sat} - T_\ell\right|^{0.3333} \qquad (6.5\text{-}56),(6.5\text{-}57)$$

Further discussion of the simplistic correlation attributed to Holman is not warranted since it has been replaced as the default model by McAdams' more general form indicated in Equation (6.5-51).

Once the heat transfer coefficient is determined for steam and water, the Sparrow-Uchida degradation factors are applied to account for how the pressence of noncondensable gases reduces the interfacial heat transfer. The Sparrow-Uchida degradation factors are a blending of the degradation factors due to Sparrow at low concentrations of noncondensable gases to the degradation factors due to Uchida at high noncondensable gas concentrations.

The Sparrow-Uchida degradation factors are tabulated in the code versus the ratio of air-to-steam density and are presented graphically in Figure 6-13 together with the curves of the degradation factors attributed individually to Uchida and Sparrow. The curve marked "Sparrow 100" in Figure 6-13 is obtained from Figure 10.4 from Collier[147]. Collier attributes this and 3 other curves shown in his Figure 10.4 to Minkowycz and Sparrow. The "Sparrow 100" curve that is shown here is the forced convection curve corresponding to a bulk mixture temperature of 100 C. It is clear that all four of the "Sparrow" curves shown by Collier are for relatively low mass fractions for air in steam over the range from 0.0 to 0.1.

The Uchida correlation for the overall heat transfer coefficient is defined by (6.6-106). It cannot apply for relatively low air mass fractions because it obviously predicts the wrong trend as the mass of air approaches zero and in fact is undefined in the limit of zero air mass. For Uchida, the functional form of the degradation factor is obvious but the composite heat transfer coefficient (HTC) must be divided by the undegraded heat transfer coefficient (HTCo) to obtain the degradation function. Appropriate values for HTCo are in the range from around 40 to 70 ($W/m^2/K$). The plots presented in Figure 6-13 use HTCo = 64.19 to covert the Uchida heat transfer coefficient expression into the degradation function because this value causes the Uchida degradation factor to match the Sparrow factor for the higher ratios of air mass to steam mass.

6.5.8.2 Model as Coded

Calculations of the interfacial heat transfer at a free surface are encoded as described in Section 6.5.8.1. Holman's simplistic expression may still be selected via user input; however, the default model has been changed to evaluate the heat transfer coefficient directly from Equation (6.5-52) where the Nusselt number is evaluated from Equation (6.5-51). This change provides for a wider applicability to other fluids because the fluid properties are reflected in the calculation of the of Grashof and Prandtl numbers.

The Sparrow-Uchida degradation factors are tabulated in the code versus the ratio of air-to-steam density. Linear interpolation between the tabulated values is used to determine the degradation factors for air-to-steam density ratios not explicitly given in the table.

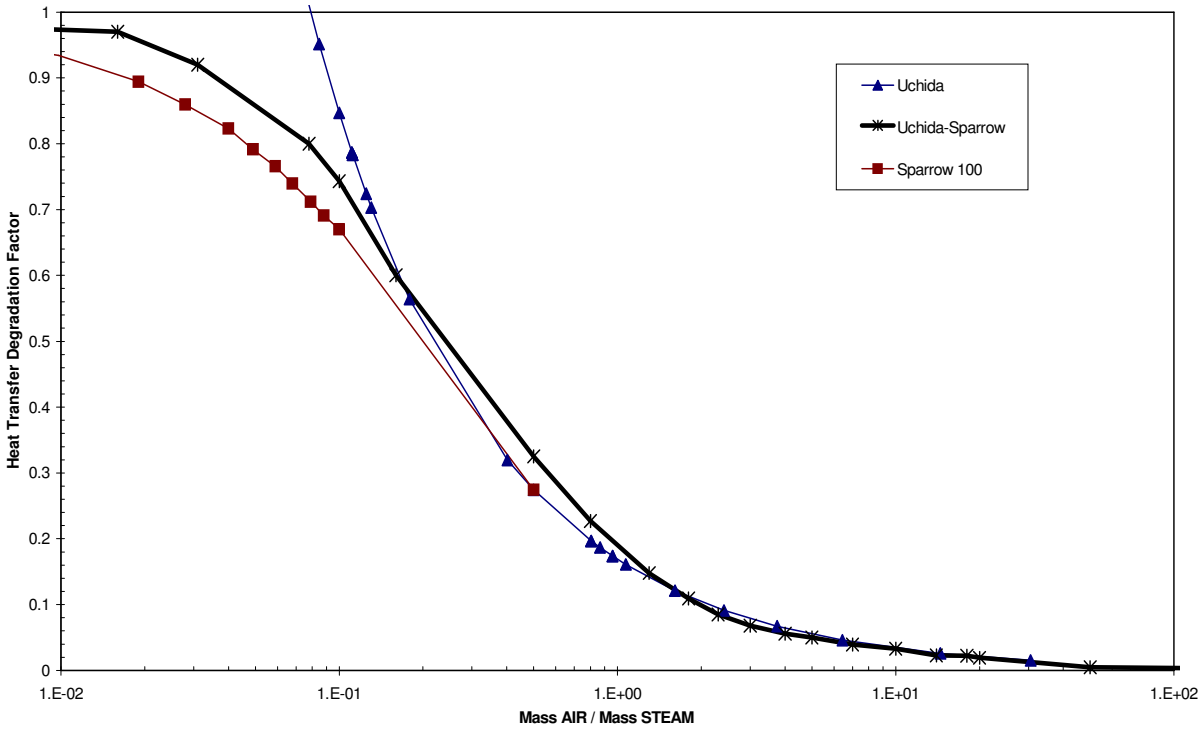

Figure 6-13. Sparrow-Uchida Degradation Factor

6.5.8.3 Applicability

Holman's correlation (Equations (6.5-56) and (6.5-57)) has been derived for turbulent flow with $Gr \cdot Pr > 10^9$. McAdams considers the range $10^5 < Gr \cdot Pr < 3x10^{10}$ by applying different values for the constants k_1 and k_2 in Equation (6.5-51). The main limitation is that these correlations derived from heated and/or cooled plates are being applied for modeling the interfacial heat transfer on a stratified surface where the effective heat transfer can be enhanced by several orders of magnitude because of the effect of ripples at the surface. Fortunately, even with these enhancements the interfacial heat transfer at a stratified surface is typically small relative to the interfacial heat transfer for drops and bubbles where the heat transfer area can be many orders of magnitude larger. The applicability is evaluated through the qualifciation of the models against relevant data. For containment applications in particular, TRACG is seen to grossly underestimate the interfacial heat transfer on a stratified surface; nevertheless, this deficiency does not significantly impact the pressures and temperatures.

The Uchida-Sparrow degradation factors are intended for use as a best-estimate (unbiased) model for heat transfer degradation due to noncondensable gases at a stratified mixture-vapor surfaces corresponding to a water level. The uncertainty for the Uchida-Sparrow degradation factors is estimated to be bounded by the uncertainty for the heat transfer coefficients determined from the K-S-P correlation. Since K-S-P has an overall uncertainty of 17.6% for steam-air tests but only 7.4% for pure steam tests, the RMS difference attributed to the

degradation factor is estimated to be 16%. A value of 20% is suggested in Section 6.6.11.3 as an appropriate uncertainty for the degradation in the heat transfer coefficient due to the presence of noncondensable gases. An uncertainty of this magnitude is also supported based on a comparison of the overall heat transfer coefficient as shown in Figure 6-37. Most of the work that has been done to determine the degradation due to noncondensable gases has been done at relatively low pressures. At higher pressures degradation becomes less important; therefore, the heat transfer coefficient is conservatively under-estimated by using expressions developed based on data at lower pressures.

6.5.9 Horizontal Stratified Flow in a Pipe

6.5.9.1 Technical Basis and Assumptions

In a horizontal pipe stratified flow will exist if the void fraction is greater than a critical void fraction given by a critical Froude number (Section 5.1.3).

For horizontal stratified flow the interfacial area per unit volume is approximated from the void fraction by:

$$A_i = \frac{16\sqrt{\alpha(1-\alpha)}}{\pi D_h} \tag{6.5-58}$$

The interfacial heat transfer is calculated using the same correlations as for annular flow.

Equation (6.5-58) is based on the following assumptions. When stratified flow exists in a horizontal pipe and the pipe is either almost empty or almost full, the surface will either be very close to the bottom of the pipe or very close to the top. For these conditions, it is assumed that the surface is smooth. When the pipe is half full, it is assumed that surface waves exist and that the impact of the surface waves is to double the surface area. Figure 6-14 shows the void fraction, the surface area per unit volume assuming a smooth surface, the surface area per unit volume assuming a wavy surface and Equation (6.5-29) as function of the liquid height.

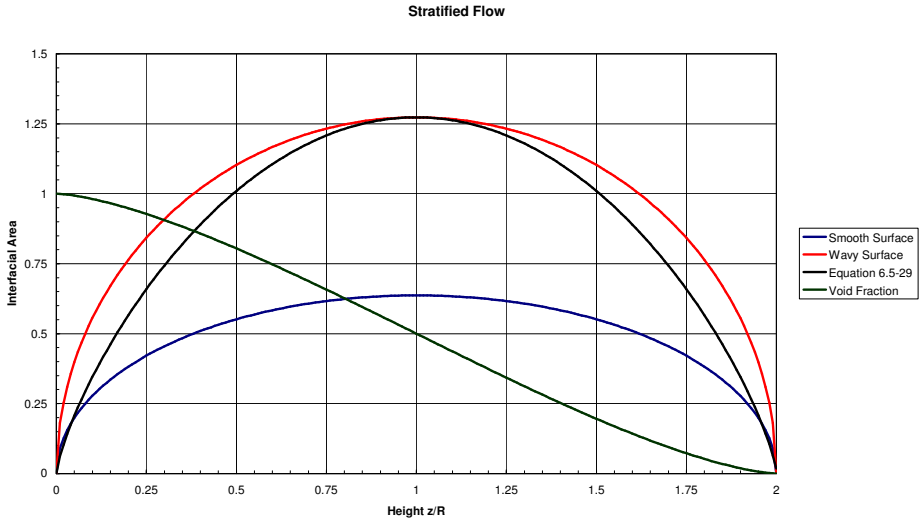

Figure 6-14. Surface Area for Stratified Flow

It is seen that Equation (6.5-58) approaches the smooth surface area for α approaching either 0.0 or 1.0 and that Equation (6.5-58) approaches the wavy surface for α=0.5.

6.5.9.2 Model as Coded

The calculation of the interfacial heat transfer for horizontal stratified flow is encoded as described in Section 6.5.9.1.

6.5.9.3 Applicability

The applicability of the interfacial heat transfer for horizontal stratified flow is assumed to be the same as the applicability for annular flow, and evaluated through assessment.

6.5.10 Upper and Lower Limits for the Interfacial Heat Transfer

In order to avoid numerical difficulties, upper and lower limits have been implemented for the interfacial heat transfer. A lower limit has been implemented to maintain some coupling (mass and energy) between the liquid and vapor field for all conditions. The lower limits are given by:

$$A_i \, h_{iv} > 2.0 \bullet 10^{-3} \, \rho_v$$

$$A_i \, h_{i\ell} > 2.0 \bullet 10^{-4} \, \rho_\ell$$

Upper limits have been implemented to prevent the partial differential equations from becoming stiff:

$$A_i \, h_{i\ell} < 5.5 \bullet 10^{6} \, \rho_v \, \alpha(1-\alpha)$$

$$A_i \, h_{iv} < 10^{8} \, \rho_v \, \alpha(1-\alpha)$$

It is recognized that there is no physical basis for these limits; they have been implemented strictly for numerical reasons. The limits, however, have been chosen such that there is no impact on the heat transfer for all reasonable scenarios for BWRs.

6.5.11 Assessment and Application to BWR

Separate assessment of all the models and correlations incorporated into the interfacial heat transfer model is not possible because of the limited range of test data. Test data for the separate effects are described in the previous sections. The overall assessments of the TRACG interfacial heat transfer model can be performed by selecting a set of steady state and transient regimes with a strong dependency on the interfacial heat transfer. This approach is typical and has been used by TRAC-PF1[105] developers by selecting the test cases with ECC injection to qualify the interfacial heat transfer model. The assessments include examples of sub-cooled boiling and film boiling where interfacial heat transfer effects are significant.

To assess the interfacial heat transfer model for the bubbly flow regime, the Christensen data[109] have been used. In Christensen's tests, sub-cooled single-phase liquid was fed into a heated tube with a rectangular cross section. The void fraction was measured at various axial locations along the channel. Two tests were chosen for the comparisons, and the test conditions are summarized in Table 6-8.

The controlling phenomena in these tests are interfacial heat transfer, interfacial shear and sub-cooled boiling heat transfer.

Table 6-8. Christensen Test Conditions

	Test 1	Test 2
Hydraulic Diameter	0.018 m	0.018 m
Pressure	5.51 MPa	6.89 MPa
Inlet Mass Flux	882 kg/(m^2-s)	873 kg/(m^2-s)
Inlet Equilibrium Quality	-0.04	-0.04
Heat Flux	495 kW/m^2	495 kW/m^2

The comparisons between the measured and calculated void fractions as a function of the equilibrium quality are given in Figure 6-15 and Figure 6-16. The agreement is seen to be excellent. The rate of vapor generation substantially depends on interfacial heat transfer. The void fraction in the sub-cooled (interfacial heat transfer between bubbles and sub-cooled liquid) and saturated boiling (interfacial heat transfer between bubbles and saturated liquid) regions is well predicted. The good agreement with the data demonstrates the adequacy of TRACG models.

To assess the interfacial heat transfer model for the droplet flow regime, the experimental test data from the Thermal Hydraulic Test Facility (THTF)[110] at Oak Ridge National Laboratory have been used. The THTF is an experimental test loop designed to represent typical Pressurized Water Reactor (PWR) fuel bundles. Although the initial pressure is significantly higher than that encompassed in typical BWR transients, it has many of the features, which are important to film boiling. It is also a well-instrumented heated bundle experiment, which includes a sustained period of forced convection film boiling heat transfer over a wide range of conditions. The test

section consists of a 3.66 meter fuel channel with 60 heated and 4 unheated rods. The axial power profile is flat. The channel inlet flow and system pressure, as well as heater rod temperatures, were measured in the tests. To measure in-bundle fluid temperature, thermocouples that extend a short distance from the rod surface into the fluid were used. In-bundle fluid temperatures were measured using thermocouples mounted on the spacer grid and at the bundle exit.

[[

]]

Figure 6-15. Comparison of TRACG with Christensen Test, 5.5 MPa

[[

]]

Figure 6-16. Comparison of TRACG with Christensen Test, 6.9 MPa

Test 3.08.6C from Reference [110] was chosen for the comparisons. In this test, the power was maintained at 2.4 MW for the first 7 seconds. It was then raised to 7.8 MW over a period of 1.5 seconds, and then held at that level until 27.6 seconds and then decreased to 3.2 MW at 32 seconds. Following the power increase, boiling transition occurred, and the rods underwent a rapid temperature increase. The temperature peaked and turned over at the time the power was reduced. During film boiling heat transfer heat flux at the rod surface is a function of vapor temperature. The vapor temperature is a strong function of the interfacial heat transfer between vapor and liquid droplets. Therefore, the controlling phenomena in this test are film boiling and interfacial heat transfer (droplet regime).

Comparisons between the calculated and measured rod surface temperatures for two different elevations and calculated vapor temperature and measured in-bundle temperature at the channel exit are given in Figure 6-17. It is seen that the initial temperature increase is very well predicted, indicating that wall heat transfer is accurately calculated during this time. Beyond 15 seconds the calculated temperature continues to increase after the measured temperature has stopped increasing and has begun to decrease for the 2.4m location. As a result, TRACG overpredicts the measurement by [[ ]], respectively, at the two elevations. These are not systematic errors because the comparisons for THTF test 3.06.06B in Section 3.2.1 of Reference [6] reveals the opposite trend. In the comparisons for test 3.06.06B, a reduction in the calculated rate of temperature increase occurring 2 seconds earlier than the data causes the peak temperatures to be underpredicted by [[ ]], respectively, at the 2.4m and 3.6m measurement locations.

The calculated vapor temperature at the channel exit for THTF test 3.08.6C starts to superheat slightly when the power is increased whereas the measurement continues to follow the saturation line until the pump is shut off at around 30 seconds. The superheat transient following pump shutoff is well predicted by TRACG. The calculation shows a peak in the vapor superheating consistent with data. Generally, the calculated superheat is consistent with data, demonstrating the adequacy of the interfacial heat transfer model. The difference between the calculated and measured vapor superheat could be caused by either an under-prediction of the interfacial heat transfer, or the impact of droplets on the thermocouples.

[[

]]

Figure 6-17. Comparison of TRACG with THTF Test 3.08.06C

To further assess the interfacial heat transfer model, data from the PSTF test facility[99] (LOCA transient) have been used. The PSTF facility consists of a 4.27m tall vessel with an internal diameter of 1.19m. A blow-down pipe is connected to the bottom of the vessel at an elevation of 0.76m and could be fitted with nozzles of various diameters ranging from 0.054 to

0.092m. In some of the tests, the blow-down pipe contained a vertical section with a diameter of 0.25m, and the inlet to the pipe was in the upper part of the vessel at an elevation of 3.2m. For the cases where the blow-down pipe contained the vertical section, the break flow was primarily steam flow, and the system depressurized quickly, depending on the size of the nozzle. In these tests, the liquid in the vessel flashed, causing liquid level to rise initially and subsequently subside again toward the end of the depressurization. Test 5801-15 from Reference [99] was chosen for the comparisons and the test conditions are summarized in Table 6-9.

Figure 6-18 shows a comparison between the measured and calculated pressure. The depressurization, including the initial undershoot, is very well predicted by TRACG. This pressure undershoot due to delayed flashing depends mostly on interfacial heat transfer. The good agreement with data indicates the adequacy of the heat transfer model.

Table 6-9. PSTF Test Conditions

Test	Nozzle Size (m)	Initial Pressure (MPa)	Initial Level (m)
5801-15	0.0635	7.3	1.67

[[

]]

Figure 6-18. PSTF Test 5801-15, Pressure

To show the adequacy of the interfacial heat transfer model during rapid depressurization transients, the Edwards blow-down test[113] has been simulated with TRACG. This test is considered as a standard for these kinds of transients. The test section consists of a 4.096m long horizontal pipe with an inner diameter of 0.073m. The test section is filled with liquid, heated and pressurized to 7.0 MPa. During the transient, the pipe is depressurized through the open end

in approximately 0.6 sec. Similar to PSTF test, the pressure undershoot observed in the test depends mostly on interfacial heat transfer. Comparison between pressure calculated by TRACG and measured is shown in Figure 6-19. It is seen that the initial pressure drop is very well predicted.

[[

]]

Figure 6-19. Edwards Test, Pressure

Sub-cooled CCFL tests are indicative of the applicability of the interfacial heat transfer model. A comparison to data from the CSHT[145] test facility is used. The CSHT test section consists of a single, full-scale 8x8 fuel channel made up of 64 simulated fuel rods. The tests performed to examine the effect of liquid subcooling were run at zero bundle power with injection water temperatures varying from near saturation to subcoolings in excess of 60 K. The injected liquid flow was fixed at a nominal value of 0.63 kg/s (10 gpm). Each test run consisted of between 20 and 30 individual tests with increasing inlet steam flows between 0 and 0.113 kg/s at a prescribed nominal subcooling of the injected liquid. Over the entire range of liquid subcoolings and inlet steam flows tested, the system pressures ranged from atmospheric to approximately 1.6 atm. The system pressure increased with increasing steam flow and decreasing liquid subcooling because of the pressure loss in the vent that conveyed steam from the upper plenum to the atmosphere.

When the steam flow exceeds the condensation capacity of the injected liquid flow, a pool of saturated liquid forms above the UTP and the system behavior becomes the same as for saturated liquid injection. The saturated liquid injection data can be fitted[112] by the Kutateladze correlation curve:

$$\sqrt{K_v} + m\sqrt{-K_\ell} = \sqrt{K} \tag{6.5-59}$$

The liquid down-flow for the sub-cooled liquid injection case is also given by the same equation, when the steam flow exceeds the condensation capacity of the liquid, W_{cond}, which is given by:

$$W_{cond} = W_\ell \; C_{p\ell} \frac{\Delta T_\ell}{h_{fg}} \tag{6.5-60}$$

When the steam flow is less than the condensation capacity of the liquid, all the steam is condensed and the drainage is equal to the sum of the liquid and the steam flow as follows:

$$W_{drain} = W_\ell + W_g \tag{6.5-61}$$

Figure 6-20 shows the liquid drain flow plotted against the injected steam flow with the subcooling of the injected liquid as a parameter. The loci shown in the figure fall along three paths: (1) a straight line representing the linear increase in condensation corresponding to Equation (6.5-60) as the liquid subcooling increases; (2) a vertical line representing the cutoff where the steam flow is just equal to the condensing capacity (0.074 kg/s) of the injected liquid flow at the maximum subcooling of 63.1 K; and (3) a curve representing Equation (6.5-59) [[ ]]. The calculated results shown by the solid curve and the dashed lines show excellent agreement with the data along the CCFL curve for saturated liquid and sub-cooled liquid lines with the steam flow exceeding the condensation capacity of the liquid. For sub-cooled liquid and steam flow rates less than the condensation capacity, the liquid drainage is seen to match the sum of the liquid and steam injection. In conclusion, the TRACG interfacial heat transfer models provide the right condensation rate for saturated CCFL, as well as sub-cooled CCFL breakdown.

On combining the theoretical basis and applicability of the individual models for the interfacial heat transfer with the assessment, the following range of applicability can be defined:

Bubbly/Churn Flow

Pressure	[[ ]]
Flow rate	[[ ]]
Dimension	[[ ]]
Void fraction	[[ ]]

where $\alpha_{tran} \approx 0.65$ represent the transition to annular flow.

[[

]]

Figure 6-20. TRACG Prediction of CCFL

The liquid side heat transfer has been evaluated from sub-cooled boiling, flashing, and sub-cooled CCFL. The liquid side heat transfer coefficient can be justified from [[ ]] and [[ ]]. Since the model is based on first principle models for flow around a spherical particle in an infinite medium it is reasonable to extend the model for pressure to [[ ]] and hydraulic diameter to [[ ]] as indicated above. For the vapor side, the model is not sensitive to the exact value of the heat transfer. The vapor will be very close to thermal equilibrium with the interface at saturation temperature, as a result of the relatively large value of the heat transfer coefficient and low heat capacity of the bubbles. Combining this with the first principle model for the conductive and convective heat transfer in the bubble justifies the above application range.

Dispersed Annular Flow

Pressure	[[ ]]
Flow rate	[[ ]]
Dimension	[[ ]]
Void fraction	[[ ]]

For this flow regime, the liquid will be very close to thermal equilibrium with the interface at saturation temperature and the model is not sensitive to the exact value of the heat

transfer coefficient. Using similar arguments as for the vapor side heat transfer coefficient for bubbly flow, the above application range can be justified. For the vapor side only the heat transfer to droplets for film boiling is significant. If the wall is covered with a film, the vapor will be close to thermal equilibrium with the interface at the saturation temperature and the results are not sensitive to the value of the heat transfer coefficient.

For film boiling the vapor side heat transfer coefficient has been tested extensively using the THTF tests for high pressure and flow and the core spray heat transfer (CSHT[145]) tests for low pressure and flow. The THTF and CSHT testing is for small hydraulic diameters; however, given the first principle model based on flow over a spherical particle in an infinite medium it is reasonable to extrapolate the model to large hydraulic diameters.

Stratified Annular Flow

Stratified horizontal flow is generally not important in a BWR. The only location where this flow regime is significant is for the vent pipe in containments with horizontal vents. For horizontal vents the flow is virtually adiabatic and the two phase flow will be close to thermal equilibrium. The simulation of the vent in TRACG has been tested extensively as part of TRACG qualification against PSTF, GIRAFFE and PANDA test data (see References [6] and [7]). This justifies the following application range for horizontal stratified flow:

Pressure	[[ ]]
Mass flow	[[ ]]
Dimension	[[ ]]
Void fraction	[[ ]]

Free Surfaces

Free surfaces will occur in a BWR in the mixing region during normal operation, in various regions of the vessel during the refill/reflood phase of a LOCA and in the containment suppression pool. Free surfaces will also exist for the GDCS, PCC and ICC pool in an ESBWR containment.

Generally, the heat transfer at free surfaces is small and has negligible impact on the overall system performance. Testing involving free surface heat transfer has been conducted for the TLTA, FIST, and SSTF integral test facilities, Peach Bottom and Hatch plant tests as described in the *TRACG Qualification LTR*[6]. Additional testing that is applicable to the ESBWR includes tests from the GIST[7], GIRAFFE and PSTF integral test facilities and the PSTF and PANDA[7] containment test facilities. This testing justifies using the same application range as for bubbly and dispersed annular flow.

Given the above ranges the applicability of interfacial heat transfer models to BWR regions are summarized in Table 6-10.

Table 6-10. Applicability of Interfacial Heat Transfer Models to BWR Regions

Region	Flow Regimes	Size (m)	Range of Conditions		
			P (MPa)	G (kg/m^2-sec)	Void
Lower Plenum	C	CA/CE	CA	C	C
GT	C	CA	CA	C	C
Core	CA	C	CA	C	C
Bypass	C	C	CA	C	C
Upper Plenum	CA	CA/CE	CA	CA	CA
Mixing Region	C	CA/CE	CA	C	C
Steam Dome	C	CA/CE	CA	C	C
Steam Line	C	CA	CA	C	C
Downcomer	C	CA	CA	C	C
Recirculation Loop	C	CA	CA	CA	C
Drywell	C	CE	CA	C	C
Wetwell Air Space	C	CA/CE	CA	C	C
Suppression Pool	CA	CA/CE	CA	C	CA
Main Vents	CN	C	CA	CN	CN
ESBWR Chimney	CA	CA/CE	CA	CA	CA

Legend:

C	=	Correlation database and separate effects tests cover range
CA	=	Correlation supplemented by assessment covers range
CE	=	Correlation supplemented by reasonable physical basis
CA/CE	=	Assessed against geometrically scaled data
CN	=	Correlation range limited but phenomenon not significant
N/A	=	Correlation not applicable over range

6.6 Wall Heat Transfer

This section describes all models used in TRACG for the exchange of energy between the fluid and the solid walls of each hydraulic volume. The basis for the correlations, the situations to which they apply, and their implementations are discussed.

6.6.1 Background

Wall heat transfer encompasses many different regimes, including (1) single-phase heat transfer (liquid or gas, forced or natural circulation), (2) two-phase heat transfer (nucleate boiling, film boiling, condensation) and (3) thermal radiation. Most of these are contained in what is referred to as the boiling curve shown in Figure 6-21. Actually, a single curve in the figure is representative of a family of curves that depend on the flow rate with higher curves corresponding to higher flow rates.

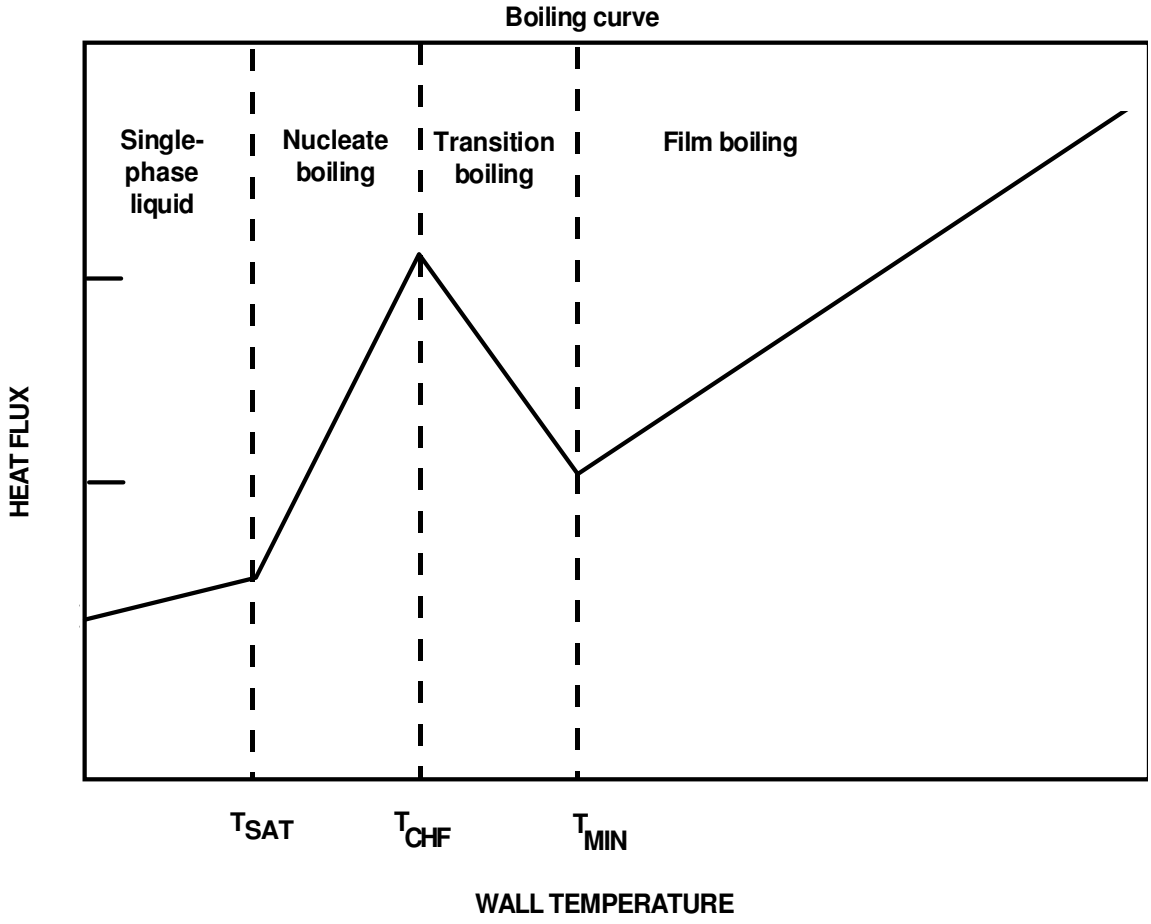

Figure 6-21. Boiling Curve

- The left most part of the curve represents single-phase convection to liquid in which the fluid motion can result from an imposed pressure difference or can result from density differences (natural convection).

- As the wall temperature rises sufficiently above the saturated conditions, nucleate boiling occurs. Initially, the bulk liquid may still be sub-cooled. This regime is also called the isolated bubble regime and is characterized by high heat transfer rates. Bulk saturated nucleate boiling and forced convection vaporization are other boiling regimes.
- The critical heat flux (CHF) occurs when the heat flux reaches a maximum prior to degradation in heat transfer.
- As the wall temperature increases past the point of the CHF, transition boiling occurs. At low vapor content, this phenomenon is known as Departure from Nucleate Boiling (DNB). In this regime, the local vapor generation is so great that the drag on the liquid moving toward the surface prevents it from completely wetting the surface. As a result, the heat transfer decreases. For BWRs, high quality CHF is more relevant. This corresponds to the dryout of the liquid film at the wall, resulting in reduced heat transfer. In an increasing heat flux experiment, transition boiling would not be encountered. The local minimum at the end of the transition-boiling regime is termed the minimum heat flux or the minimum stable film boiling temperature.
- When the entire boiling surface becomes blanketed with vapor, the regime is the film-boiling regime. The heat flux then begins to increase with increasing superheat, and radiation effects become more important.
- Convection to single-phase (super-heated) steam.

The heat transfer in each of these boiling regimes or the transition points between regimes are predicted by correlations developed specifically for a particular regime. For a given set of local thermal-hydraulic conditions, a unique wall heat transfer mode is assigned. In a similar manner to the boiling curve, the heat transfer at the wall is divided into the following modes:

- Single-phase liquid convection mode
- Sub-cooled and nucleate boiling mode
- Transition boiling mode
- Film boiling mode
- Single-phase vapor convection

Additionally, the following modes of heat transfer are considered:

- Condensation
- Thermal radiation
- Quenching heat transfer

Each mode has a correlation to predict the amount of heat transfer. Sections 6.6.3 through 6.6.13 discuss each correlation along with its implementation and applicability. Section 6.6.2 discusses the logic selection and Section 6.6.15 assesses the correlations.

6.6.2 Heat Transfer Selection Logic

The wall heat transfer coefficient depends on the fluid condition and the wall conditions (Table 6-11 and Figure 6-22):

For single-phase liquid ($\alpha = 0$), convective heat transfer will exist up to the point of net vapor generation for sub-cooled boiling ($h_\ell = h_{\ell d}$).

For two-phase flow with void fractions below the transition to annular flow (Section 5.1.1), several heat transfer regimes can exist. For sub-cooled wall temperatures, liquid convection will exist at the wall while condensation will take place at the bubble interface if $T_\ell < T_{sat}$. For superheated wall temperatures up to the point of boiling transition, either sub-cooled ($x_e<0$) or nucleate boiling ($x_e>0$) will exist dependent on the equilibrium quality. Nucleate boiling will exist up to the point where boiling transition occurs ($x_e < x_c$ and $T_w < T_{CHF}$ dependent on the boiling transition correlation). If boiling transition has occurred, transition boiling will exist if the wall temperature is less than the minimum point on the boiling curve ($T_w < T_{min}$) and sufficient liquid is present for rewet ($x_e < x_c$); otherwise, film boiling will exist.

For two-phase flow conditions with void fractions above the transition to annular flow, several heat transfer regimes can exist. For sub-cooled wall temperatures, film condensation will occur. For superheated wall temperatures up to the point of boiling transition, forced convection vaporization will exist. Forced convection vaporization will exist up to the point where boiling

Table 6-11. Selection Logic for Wall Heat Transfer

	Wall Conditions			
Fluid Condition	**No Boiling Transition**		**Boiling Transition**	
Flow Regime	$T_w < T_{sat}$	$T_{sat} < T_w < T_{CHF}$	$T_{CHF} < T_w < T_{min}$	$T_{min} < T_w$
$\alpha = 0$	Liquid Convection	Liquid Convection	N/A	N/A
$0 < \alpha < \alpha_{tran}$	Liquid Convection	Sub-cooled/ Nucleate Boiling	Transition Boiling	Film Boiling
$\alpha_{tran} < \alpha < 1$	Condensation	Forced Convection Vaporization	Transition Boiling	Film Boiling
$\alpha = 1$	N/A	Vapor Convection	Vapor Convection	Vapor Convection

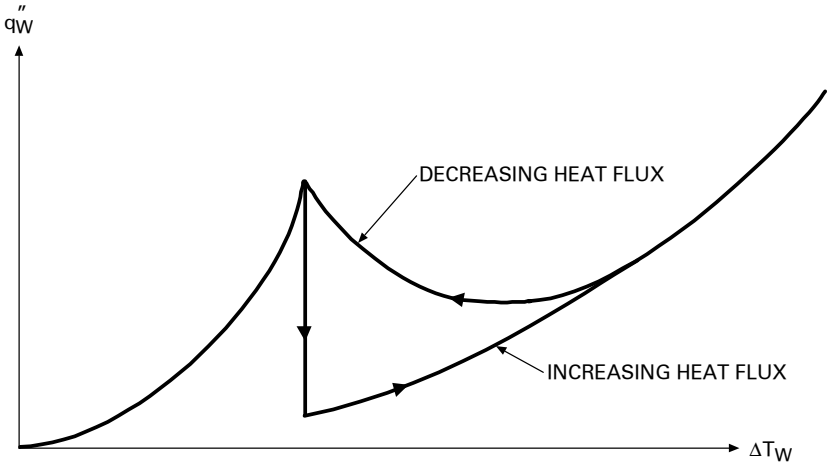

Figure 6-22. Selection Logic for Wall Heat Transfer Coefficient

transition occurs ($x_e < x_c$ and $T_w < T_{CHF}$ dependent on the boiling transition correlation). If boiling transition has occurred, transition boiling will exist if the wall temperature is less than the minimum point on the boiling curve ($T_w < T_{min}$) and sufficient liquid is present for rewet ($x_e < x_c$); otherwise, film boiling or vapor convection will exist.

The partitioning of the wall heat transfer between the phases is based on the fraction of the surface area in contact with the respective phase. For the heat transfer regimes indicated in Table 6-11 and for most flow regimes, the heat transfer is either entirely to the liquid or to the vapor. For the liquid continuous flow regimes, all the heat transfer is to the liquid. For the vapor continuous flow regimes, the energy is deposited in the vapor phase. Only for transition boiling during rewet, the wall heat transfer is weighted between heat transfer to the vapor and heat transfer to the liquid as described in Section 6.6.8.

For single-phase vapor (α=1), convective heat transfer will exist for all wall temperatures above the saturation temperature ($T_w > T_{sat}$).

When the wall goes into boiling transition ($x_e > x_c$ and $T_w > T_{CHF}$ dependent on the boiling transition correlation), the heat transfer regime will change from nucleate boiling to film boiling. Transition boiling will only be entered from the film-boiling mode if two criteria are met: (1) the wall temperature is sufficiently low ($T_w < T_{min}$) and (2) there is sufficient liquid to allow rewet ($x_e > x_c$ and $T_w > T_{CHF}$).

6.6.3 Single-Phase Convection to Liquid

Liquid single-phase wall heat transfer is broken down into three different categories: (1) laminar forced convection; (2) turbulent forced convection, and (3) natural convection.

6.6.3.1 Technical Basis and Assumptions

The heat transfer to liquid is given by the maximum heat transfer coefficient calculated by the liquid laminar; natural convection and turbulent heat transfer correlations:

$$h_\ell = \max\left\{h_{\ell,\text{turb}}\ ,\ h_{\ell,\text{1am}}\ ,\ h_{\ell,\text{free}}\right\} \tag{6.6-1}$$

Laminar flow heat transfer is given by the Rohsenow-Choi[118] equation:

$$h_{\ell,\text{1am}} = 4.0\ \frac{k_\ell}{D_h} \tag{6.6-2}$$

This represents a compromise between the analytical solutions for uniform wall heat flux (Nu = 4.364) and for constant surface temperature (Nu = 3.658). The solutions were developed for a fully developed parabolic profile and therefore are suitable for only laminar flow.

For turbulent flow, the heat transfer is given by the Dittus-Boelter[119] correlation:

$$h_{\ell,\text{turb}} = 0.023\ \frac{k_\ell}{D_h}\left(\frac{G_\ell D_h}{\mu_\ell}\right)^{0.8}\left(\frac{C_{p,\ell}\mu_\ell}{k_\ell}\right)^{0.4} \tag{6.6-3}$$

For natural convection flows, both laminar and turbulent, the heat transfer is given by Reference [120]:

$$h_{\ell,\text{free}} = 0.12\ k_\ell\left\{\frac{-g\ \rho_\ell\ \frac{\partial \rho_\ell}{\partial T_\ell}\ C_{p,\ell}\ \left|T_w - T_\ell\right|}{\mu_\ell\ k_\ell}\right\}^{0.333} \tag{6.6-4}$$

6.6.3.2 Model as Coded

Calculations of the heat transfer coefficient to the liquid h_ℓ are based on equations described in Section 6.6.3.1. The Chen correlation (Section 6.6.4.1) is used to calculate heat transfer coefficient for the turbulent flow $h_{\ell,\text{turb}}$. The value of the Chen F-factor is set equal to one and the microscopic term is set to zero. Under these conditions, the Chen correlation transforms into Dittus-Boelter correlation.

6.6.3.3 Applicability

As stated above, the Rohsenow-Choi correlation was derived analytically for laminar, parabolic flow in a circular tube. The analytic solutions for noncircular cross-sectional geometries are similar to Rohsenow-Choi for aspect ratios not greater than 3. For aspect ratios greater than 3, Rohsenow-Choi will under-predict heat transfer; up to 50% for very large aspect ratios. At low flow rates, natural convection forces may distort the parabolic profile assumed in Rohsenow-Choi. This will likely cause Rohsenow-Choi to under-predict heat transfer. If Equation (6.6-4) predicts a higher heat transfer coefficient, then TRACG will use that value.

A large database exists for single-phase turbulent heat transfer. Figure 6-23 shows a comparison of Dittus-Boelter with data from Reference [121]. Typically, the Dittus-Boelter correlation represents the data within ±25%. The correlation has been successfully and widely used for over 50 years for both nuclear and non-nuclear applications. It was originally developed for turbulent flow in smooth tubes for application to automobile radiators. For moderate temperature differences, the correlation is valid for forced flows[122] within the following ranges:

$0.7 < Pr < 160$

$Re > 6000$

$L/D > 60$

For moderate to high temperature differences, Dittus-Boelter appears to over-predict heat transfer for gases[123] by 10 to 25%. The correlation uses the bulk temperature of the fluid to determine the thermodynamic properties. Some authors recommend a property correction for wide temperature differences[124]. However, the correlation for many practical cases of interest can be used without any property correction to yield reasonably accurate estimation of the single-phase heat transfer coefficients in rod bundles[112].

In the development of the correlation, the entrance effect was neglected and is similarly neglected in the application in the code. For turbulent flow, the effects of the entrance flow are generally small. For flows over small lengths, the entrance region will have a more pronounced effect and the correlation will under-predict the actual heat transfer.

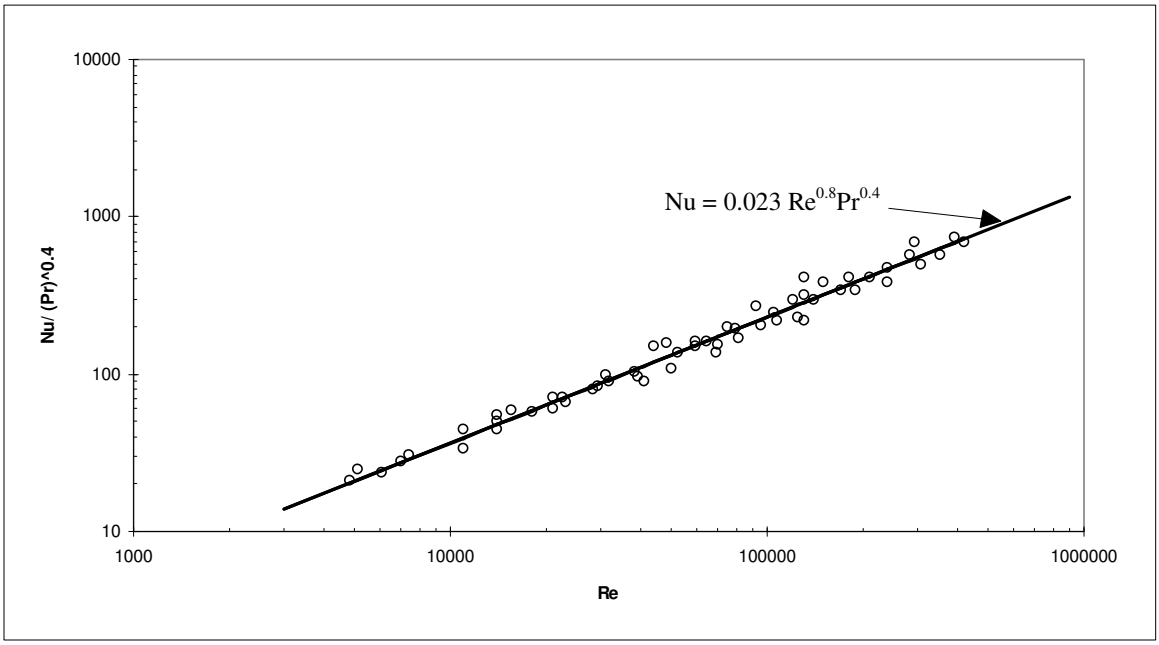

Figure 6-23. Dittus-Boelter Correlation Plotted Along with Data for Forced, Turbulent Convection in Tubes

Transition from laminar flow in pipes to turbulent flow in pipes is generally viewed to occur at Re = 2300. Laminar flows can be maintained to Reynolds numbers an order of magnitude larger than 2300 if the surfaces are smooth and there are no disturbances. Flows in

the range 2300 < Re < 6000 often oscillate between laminar and turbulent flow. As a result the spread in experimental data in this range is large and no known correlations exist in this transition region. However, for practical applications, pipes will not be smooth or will be of a varying shape or diameter. This will tend to cause laminar flows near or greater than Re = 2300 to become turbulent. For this reason, a sensible approach is to take the maximum of the laminar and turbulent correlations.

The natural convection correlation used in TRACG was developed for use for turbulent natural convection for values of GrPr greater than 10^8. The form of this correlation, $(GrPr)^{0.33}$, was analytically derived by Bailey[128] using a turbulent integral analysis. Figure 6-24 shows that the correlation agrees well with data for GrPr greater than 10^7. As GrPr decreases, the correlation will under-predict the data by an increasing amount. The code logic is to pick the largest heat transfer coefficients predicted by the turbulent, laminar and natural convection correlations. Below GrPr = 4.1 x 10^4, the heat transfer coefficient is based on Nu = 4.0 because the value predicted by Equation (6.6-4) will be less than Nu = 4.0. The correlation agrees with the data in Figure 6-24 above GrPr = 4.1 x 10^4 to approximately 65%. This is the recommended value to be used in any sensitivity studies. It should be noted that results of turbulent correlations at identical conditions can vary by 100% (see Reference [125]).

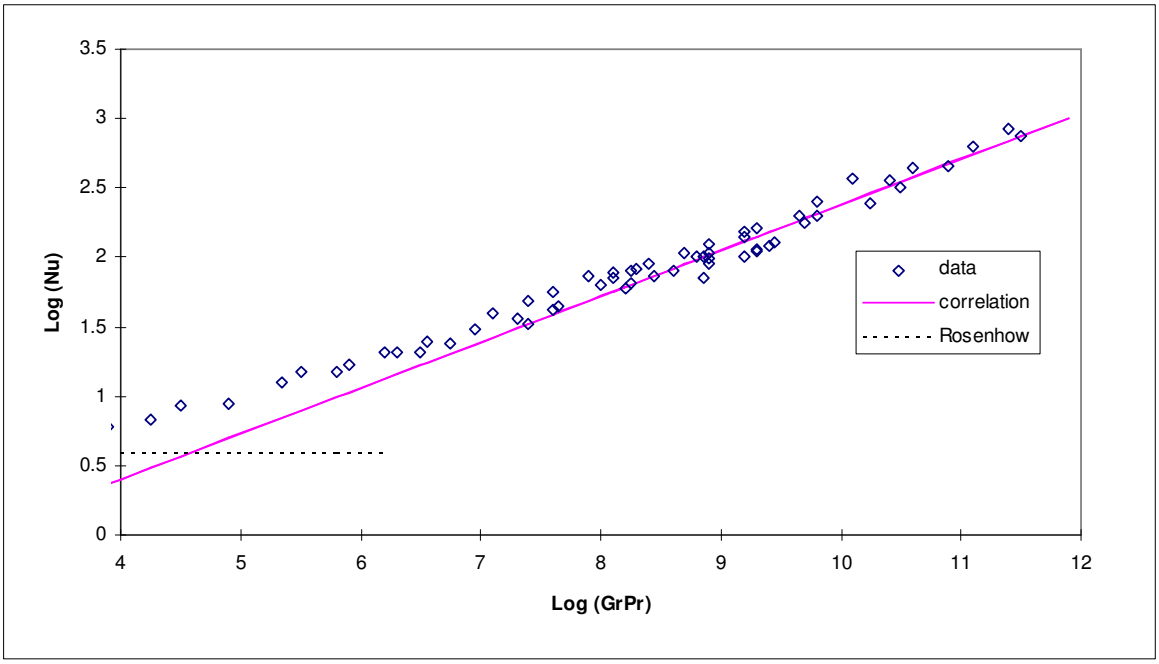

Figure 6-24. Fishenden and Saunders Correlation (Equation (6.6-4)) Plotted against Natural Convection Data for Vertical Surfaces

Equation (6.6-4) was developed for vertical flat plate natural convection. According to Gebhart[126], the error in applying it to vertical cylinders is less than 5% when

$$\frac{D}{L} \geq 35 \cdot (Gr)^{-0.25} \tag{6.6-5}$$

While there is no known experimental basis for applying this correlation to internal flow, RELAP5/MOD2[139] applied a similar correlation to internal flow with apparent success. The form of the equation, $(GrPr)^{0.33}$, makes the heat transfer coefficient independent of the chosen characteristic length.

6.6.4 Sub-cooled and Nucleate Boiling

For sub-cooled boiling and nucleate boiling, the heat transfer is given by Chen's correlation[129]. The technical basis for the Chen correlation is discussed by Carey[127]. An option is available to use the Forster-Zuber correlation[130] for pool boiling in the IC and PCC pools.

6.6.4.1 Technical Basis and Assumptions

Chen argued that the heat transfer coefficient for saturated convective boiling is equal to the sum of the macroscopic (bulk convective) contribution h_{mac} and the microscopic (nucleate boiling) contribution h_{mic}:

$$q''_{w,\ell} = F\, h_{mac}\, (T_w - T_\ell) + h_{mic}\, (T_w - T_s(P)) \tag{6.6-6}$$

where F is a factor that modifies the convective part to account for increased heat transfer due to agitation caused by vapor bubble formation.

The macroscopic or convective portion is represented by the Dittus-Boelter correlation (Equation (6.6-3)). The microscopic contribution to the overall heat transfer coefficient is given by a modified version of the Forster and Zuber[130] relation for the heat transfer coefficient for nucleate pool boiling:

$$h_{mic} = 0.00122 \frac{k_\ell^{0.79} C_{p,\ell}^{0.45} \rho_\ell^{0.49}}{\sigma^{0.5} \mu_\ell^{0.29} h_{fg}^{0.24} \rho_g^{0.24}} (\Delta T_w)^{0.24} (\Delta P_w)^{0.75} S \tag{6.6-7}$$

where S corrects the fully developed nucleate boiling prediction in h_{mic} to account for the fact that as the macroscopic convective effect increases in strength, nucleation is more strongly suppressed.

The factors F and S are given by Reference [9] as:

$$F = \begin{cases} 1.0 & \text{if } \chi_{tt} \leq 0.10 \\ 2.35(\chi_{tt} + 0.213)^{0.736} & \text{if } \chi_{tt} > 0.10 \end{cases} \tag{6.6-8}$$

where χ_{tt} is the inverse of the Lockhart-Martinelli parameter and is defined by:

$$\chi_{tt} = \left(\frac{x}{1-x}\right)^{0.9}\left(\frac{\rho_\ell}{\rho_g}\right)^{0.5}\left(\frac{\mu_g}{\mu_\ell}\right)^{0.1} \tag{6.6-9}$$

The other quantities needed to evaluate Equation (6.6-7) are given by:

$$\Delta T_w = T_w - T_{sat} \tag{6.6-10}$$

$$\Delta P_w = P_{sat}(T_w) - P_{sat} \tag{6.6-11}$$

$$S = \begin{cases} (1+0.12\,Re_{TP}^{1.14})^{-1} & \text{if } Re_{TP} < 32.5 \\ (1+0.42\,Re_{TP}^{0.78})^{-1} & \text{if } 32.5 \le Re_{TP} < 50.9 \\ 0.1 & \text{if } Re_{TP} \ge 50.9 \end{cases} \tag{6.6-12}$$

$$Re_{TP} = \frac{G_\ell D_h}{\mu_\ell} F^{1.25} 10^{-4} \tag{6.6-13}$$

During sub-cooled boiling, vaporization may occur at the heated surface before the mean temperature of the cooling liquid reaches the saturation point. This phenomenon is caused by a non-uniform temperature distribution in the liquid.

Each computational cell is assumed to have a uniform temperature distribution and the volumetric vaporization rate is given by:

$$\Gamma_g = - \frac{q'''_{i\ell} + q'''_{iv}}{h_{fg}} \tag{6.6-14}$$

where:

$$q'''_{i\ell} = h_{i\ell}\,(T_{sat} - T_\ell)\,\frac{A_i}{V} \tag{6.6-15}$$

$$q'''_{iv} = h_{iv}\,(T_{sat} - T_v)\,\frac{A_i}{V} \tag{6.6-16}$$

This means that no vapor will be generated until the liquid reaches its saturation point and the void fraction will not be correctly predicted during sub-cooled boiling, unless specific models are introduced for sub-cooled boiling.

The Rouhani-Bowring model as described in Reference [131] for sub-cooled boiling energy distribution, along with the Saha-Zuber model[132] for sub-cooled boiling initiation, has been implemented. The models are summarized by the following equations:

$$q''_w = q''_\ell + q''_{evap} \tag{6.6-17}$$

where q''_w is the wall heat flux, which goes to heat up the liquid

$$q''_\ell = \begin{cases} q''_w & \text{if } h_\ell \le h_{\ell d} \\ q''_w \dfrac{h_f - h_\ell}{h_f - h_{\ell d}} \left(1 + \dfrac{h_\ell - h_{\ell d}}{h_f - h_\ell} \dfrac{\varepsilon}{1+\varepsilon} \right) & \text{if } h > h_{\ell d} \end{cases} \tag{6.6-18}$$

and q''_{evap} is the liquid side heat flux which goes to vaporize the liquid.

The pumping factor is given by:

$$\varepsilon = \frac{\rho_\ell (h_f - h_\ell)}{\rho_g \, h_{fg}} \tag{6.6-19}$$

The sub-cooled departure enthalpy is given by:

$$h_{\ell d} = \begin{cases} h_f - 154 \dfrac{q''_w}{\rho_\ell v_\ell} & \text{if Pe} > 70000 \\ h_f - 0.0022 \dfrac{q''_w D_h C_{p,\ell}}{k_\ell} & \text{if Pe} < 70000 \end{cases} \tag{6.6-20}$$

where:

$$Pe = \frac{G_\ell D_h \, C_{p,\ell}}{k_\ell} \tag{6.6-21}$$

The expression for $q_{i,\ell}$ is then modified to:

$$q_{i\ell} = A_i h_{i\ell} (T_s - T_\ell) - A_w q''_{evap} \tag{6.6-22}$$

Hence, vapor can be generated even if the liquid temperature is below saturation.

TRACG also has an option to simulate pool boiling whereby "F" in Equation (6.6-6) is set to zero and "S" is set to 1. This is used only in the IC and PCC pools. The correlation then becomes the modified Forster-Zuber correlation. In this situation, the value that is selected is the maximum value obtained from the Forster-Zuber correlation

$$h_{F-Z} = 0.00122 \frac{k_\ell^{0.79} C_{p,\ell}^{0.45} \rho_\ell^{0.49}}{\sigma^{0.5} \mu_\ell^{0.29} h_{fg}^{0.24} \rho_g^{0.24}} (\Delta T_w)^{0.24} (\Delta P_w)^{0.75} \tag{6.6-23}$$

and the Dittus-Boelter correlation

$$h_{\ell,turb} = 0.023 \, \frac{k_\ell}{D_h} \left(\frac{\rho_\ell v_\ell D_h}{\mu_\ell} \right)^{0.8} \left(\frac{C_{p,\ell} \mu_\ell}{k_\ell} \right)^{0.4} \tag{6.6-24}$$

6.6.4.2 Model as Coded

Calculations of the heat transfer coefficient to the liquid h_ℓ are based on equations described in Section 6.6.4.1. The suppression factor, S, should approach zero as $\alpha \to 1$. To ensure the right trend the following internal procedure is used. When void fraction exceeds 0.95, the calculated suppression factor is modified according to the following equations:

$$S = f_\alpha \bullet S, \text{ where } f_\alpha = X_\alpha^2 (3 - X_\alpha),\ X_\alpha = 20 * (1 - \alpha) \qquad (6.6\text{-}25),(6.6\text{-}26)$$

For annular flow, the heat transfer coefficient is reduced if the film thickness is less than the minimum film thickness (Section 6.5.4) and only a fraction (W_f) of the wall is wetted. This is accomplished by the following multiplier to the wall area in contact with the liquid.

$$h_{mult} = (1 - x_2) + x_2 W_f \qquad (6.6\text{-}27)$$

where $x_2 = 0$ for bubbly/churn flow and $x_2 = 1$ for annular flow. x_2 is linearly interpolated from 0 to 1 at the transition to annular flow.

6.6.4.3 Applicability

The original database for the Chen correlation covered the following ranges:

Pressure: 0.09 to 3.48 MPa

Mass Flow: 54 to 4070 kg/(m^2-s)

Quality: 0.0 to 0.7

The pressure range has been extended up to 6.9 MPa[133]. The specific experimental geometries and conditions for the database are shown in Table 6-12. The results of the comparison of the Chen correlation with previous correlations is shown in Table 6-13. Both tables are shown in Reference [133] where they are attributed to Collier[147]. The combined average for all comparisons to data in Table 6-13 show that the Chen correlation has by far the lowest average percentage deviations. A standard deviation of 11.0% is appropriate to use for sensitivity studies for convective boiling.

Table 6-12. Range of Conditions for Data Used in Testing Correlations

Fluid	Geometry	Flow	Pressure (Pa x 10^{-5})	Liquid inlet velocity (m/s)	Quality (wt%)	Heat flux (kW/m^2)
Water	Tube	Up	0.55-2.76	0.06-1.45	15-71	88-630
Water	Tube	Up	2.9-34.8	0.24-4.5	3-50	205-2400
Water	Tube	Down	1.1-2.1	0.24-0.82	2-14	44-158
Water	Annulus	Up	1	0.06-0.27	1-59	100-500
Methanol	Tube	Up	1	0.3-0.76	1-4	22-54
Cyclohexane	Tube	Up	1	0.4-0.85	2-10	9.5-41
Pentane	Tube	Up	1	0.27-0.67	2-12	9.5-38
Heptane	Tube	Up	1	0.3-0.73	2-10	6.2-28
Benzene	Tube	Up	1	0.3-0.73	2-9	12.5-41

Table 6-13. Comparison of Correlations

Average Percentage Deviations for Correlations					
Data	**Dengler and Addoms**	**Guerriei and Talty**	**Bennett, et al.**	**Schrock and Grossman**	**Chen**
Dengler and Addoms (water)	30.5	62.3	20.0	20.3	14.7
Schrock and Grossman (water)	89.5	16.4	24.9	20.0	15.1
Sani (water)	26.9	70.3	26.5	48.6	8.5
Bennet, et al. (water)	17.9	61.8	11.9	14.6	10.8
Guerrieri and Talty (methanol)	42.5	9.5	64.8	62.5	11.3
Guerrieri and Talty (cyclohexane)	39.8	11.1	65.9	50.7	13.6
Guerrieri and Talty (benzene)	65.1	8.6	56.4	40.1	6.3
Guerrieri and Talty (heptane)	61.2	12.3	58.0	31.8	11.0
Guerrieri and Talty (pentane)	66.6	9.4	59.2	35.8	11.9
Combined average for all data	38.1	42.6	32.6	31.7	11.0

For situations such as the PCC and IC pool where the boiling is known to be pool boiling, the Forster-Zuber correlation is used (Equation (6.6-7) with F = 0 and S = 1). The Forster-Zuber correlation was developed for pool boiling heat transfer and is one of the most frequently quoted pool-boiling correlations. The pressure range of the data used in the Forster-Zuber correlation was 1 to 50 bar.

Figure 6-25 shows a comparison at 1.0 MPa provided by Carey[127] of the Forster-Zuber correlation with two other pool boiling correlations - - Rohsenow and Stephan-Abdelsalam. The heat transfer coefficient predicted by Forster-Zuber falls between the other two correlations over a majority of the values of superheat. As the wall superheat approaches the value at the critical heat flux, Forster-Zuber predicts less heat transfer than both of the other correlations.

Regarding sub-cooled boiling and differing geometries, Carey in his book[127] writes: "First, because the subcooling of the liquid pool has virtually no effect on the resulting heat transfer rate, the pool boiling correlations are generally regarded as being valid for both sub-cooled and saturated nucleate boiling. Second, it has also been observed that a pool boiling heat transfer correlation developed for one heated surface geometry in one specific orientation often works reasonably well for other geometries and/or other orientations. Hence, although a correlation was developed for a specific geometry and orientation, it may often be used, at least as a good approximation, for others as well."

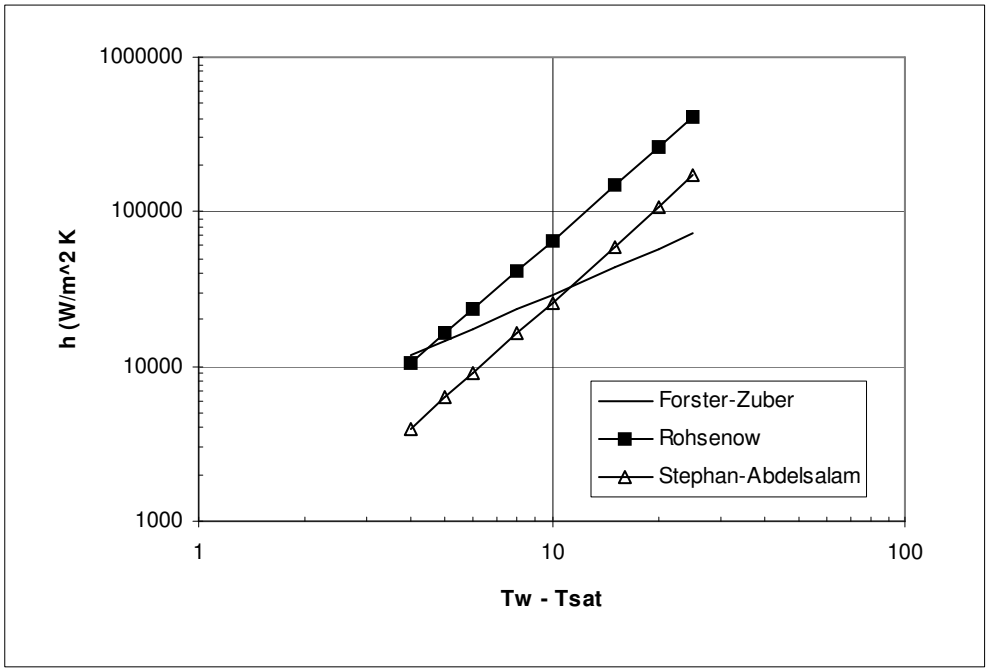

Figure 6-25. Heat Transfer Coefficients Predicted by Three Pool Boiling Correlations vs. Wall Superheat

6.6.5 Single-Phase Convection to Vapor

In a similar manner as liquid single-phase wall heat transfer, single-phase convection to vapor is broken down into three different categories: (1) laminar forced convection, (2) turbulent forced convection, and (3) natural convection.

6.6.5.1 Technical Basis and Assumptions

The heat transfer is calculated using the maximum heat transfer coefficient calculated by the laminar, turbulent or natural convection correlations:

$$h_v = \max \{h_{v,lam}, h_{v,free}, h_{v,turb}\} \tag{6.6-28}$$

The natural convection correlation is given by McAdams[134]:

$$h_v = 0.13 \frac{k_v}{D_h} \left[\frac{D_h^3 \rho_v^2 g |T_w - T_v|}{\mu_v^2 T_v} \right]^{1/3} \left(\frac{C_{p,v} \mu_v}{k_v} \right)^{1/3} \tag{6.6-29}$$

The Rohsenow-Choi equation (Equation (6.6-1)) is used for laminar forced convection. The Dittus-Boelter correlation (Equation (6.6-3)) is used for the turbulent forced convection, $h_{v,\,turb}$. The vapor properties are used in Equations (6.6-1) and (6.6-3) instead of the liquid properties. When $T_w > T_v$, the heat transfer coefficient predicted by Dittus-Boelter is multiplied by a factor $\sqrt{T_v/T_w}$ to account for variation in vapor properties.

6.6.5.2 Model as Coded

Calculations of the heat transfer coefficient to vapor are encoded as described in Section 6.6.5.1.

6.6.5.3 Applicability

There is no fundamental difference between heat transfer to a single-phase vapor and heat transfer to a single-phase liquid. Most correlations apply to both vapors and liquids. The Dittus-Boelter correlation and the Rohsenow-Choi equation are exactly the same as that used in Section 6.6.3. The McAdams correlation (Equation (6.6-22)) is almost identical to the Fishenden and Saunders correlation (Equation (6.6-4)). The heat transfer coefficient differs by the choice of constants, 0.13 versus 0.12. The fact that there are two natural convection correlations, rather than one, relates to historical, not technical, reasons of the way the code was developed. The applicability and accuracy can be considered equal to what was presented in Section 6.6.3.3.

6.6.6 Boiling Transition Criteria

Boiling curves generally exhibit a maximum or critical heat flux at the transition between nucleate and transition boiling. The correlations presented in this section define the point where a shift is made from the nucleate boiling correlations to the transition boiling correlations, or vice-versa.

The channel component uses a combination of the GEXL correlation for dryout in annular flow, the Biasi correlation for departure from nucleate boiling and the Modified Zuber pool boiling critical heat flux correlation for low flow conditions. The GEXL correlation is determined from full-scale test data for co-current up flow in a channel. It correlates film dryout for the annular flow regime. The GEXL correlation is therefore only used for co-current up-flow and for relatively long boiling lengths consistent with the flow having transitioned to annular flow. The GEXL correlation does not apply for: (1) counter-current flow, (2) co-current down-flow, or (3) co-current up-flow with a short boiling length and prior to the transition to annular flow. For these conditions in the fuel channel, boiling transition is evaluated from the modified Zuber correlation for very low flows and the Biasi correlation for higher flows.

The GEXL correlation is only used for the channel component. For other components such as the pipe and vessel components the Biasi and the modified Zuber correlations are used. The modified Zuber correlation is used for mass fluxes less than 100 kg/m^2-sec in absolute value and the Biasi correlation is used for mass fluxes greater than 200 kg/m^2-sec in absolute value. An interpolation between the two correlations is performed for mass fluxes between 100 and 200 kg/m^2-sec.

6.6.6.1 Technical Basis and Assumptions

There are four options for the boiling transition criteria:

(1) Modified Zuber and Biasi correlations

(2) CISE-GE and modified Zuber critical quality correlations

(3) Modified CISE-GE critical quality and modified Zuber correlations

(4) GEXL correlations

For Option 1, which is used for all components except the channel component, the critical heat flux is given by the modified Zuber correlation in low and counter-current flow conditions, while in high flow conditions, it is given by the Biasi correlation. The cutoff value for low and high flow conditions is 100-kg/m^2-s for up-flow and 240-kg/m^2-s for down-flow.

The modified Zuber correlation[135],[136] is given by:

$$q''_{CHF} = 0.1179(1-\alpha)\rho_g h_{fg}\left[\frac{\sigma g \Delta\rho}{\rho_g^2}\right]^{1/4} + (1-\alpha)\ 0.696 F_s [\rho_\ell c_{p,\ell} k_\ell]^{1/2}\left[\frac{g\Delta\rho}{\sigma}\right]^{1/4}\left[\frac{\sigma g\Delta\rho}{\rho_g^2}\right]^{1/8} \quad (6.6\text{-}30)$$

where F_s is a sub-cooled correction factor given by:

$$F_s = \begin{cases} T_s - T_\ell & \text{if } T_\ell < T_s \\ 0 & \text{if } T_\ell > T_s \end{cases} \quad (6.6\text{-}31)$$

The Biasi correlation[143] is given by:

$$q''_{CHF} = \max(q_1, q_2) \quad (6.6\text{-}32)$$

$$q_1 = \frac{3.78\times10^7}{(100D_h)^n \left(\frac{G}{10}\right)^{0.6}} h_p (1-x) \quad (6.6\text{-}33)$$

$$q_2 = \frac{1.883\times10^7}{(100D_h)^n \left(\frac{G}{10}\right)^{1/6}}\left[\frac{f_p}{\left(\frac{G}{10}\right)^{1/6}} - x\right]^{1/4} \quad (6.6\text{-}34)$$

$$h_p = -1.159 + 0.149P\cdot e^{-0.019P} + \frac{8.99P}{10+P^2} \quad (6.6\text{-}35)$$

$$f_p = 0.7249 + 0.099P\cdot e^{-0.032P} \quad (6.6\text{-}36)$$

where P is pressure in bars and:

$$n = \begin{cases} 0.4 \text{ for } D_h \geq 0.01 \text{ m} \\ 0.6 \text{ for } D_h < 0.01 \text{ m} \end{cases} \tag{6.6-37}$$

The temperature at critical heat flux, T_{CHF}, is obtained by solving the following equation:

$$q''_{CHF} = h_{Chen}(T_{CHF} - T_{sat}) \tag{6.6-38}$$

Onset of boiling transition will take place when the wall temperature is higher than T_{CHF}.

In Options 2 or 3, the departure from nucleate boiling is defined by the critical quality instead of critical heat flux as in the Zuber and Biasi Correlations. As indicated in Reference [131], the critical quality is given by the CISE-GE or modified CISE-GE correlation and has the form:

$$x_c = C \frac{A L_{B1}}{B + L_{B1}} \tag{6.6-39}$$

where:

$$A = 1.055 - 0.013\left(\frac{P - 4.137\times10^6}{2.758\times10^6}\right)^2 - 0.909\left(\frac{G}{10^3}\right) + 0.493\left(\frac{G}{10^3}\right)^2 - 0.114\left(\frac{G}{10^3}\right)^3 \tag{6.6-40}$$

$$B = 0.457 + 1.476\left(\frac{G}{10^3}\right) - 0.489\left(\frac{G}{10^3}\right)^2 \tag{6.6-41}$$

$$C = \begin{cases} 1.24/F_L & \text{for Option 3} \\ (1.24/F_L)^{1/2} & \text{for Option 2} \end{cases} \tag{6.6-42}$$

in which:

$$L_{B1} = \begin{cases} L_B & \text{for Option 2} \\ (P_h / P_{h,7})L_B & \text{for Option 3} \end{cases} \tag{6.6-43}$$

$P_{h,7}$ = Heated perimeter of a 7x7 bundle

F_L = Relative rod power

L_B = the heated length over which the steam quality is greater than zero

During co-current flow, the heat transfer mode at the wall will change from nucleate boiling mode to film boiling mode whenever the local equilibrium quality exceeds the critical quality. The CISE-GE and the modified CISE-GE correlations are rarely used in TRACG.

The GEXL correlation, which is recommended for applications to BWR fuel bundles, is applied for Option 4. The correlation is described in detail in Reference [137] and has been approved by the NRC. A summary is included here.

The correlation, expressed in the most general terms, is:

$$x_c = x_c(L_B, D_Q, G, P, R, L_A, L_H) \quad (6.6\text{-}44)$$

where:

x_c = Bundle average critical quality

L_B = Distance from the initiation of bulk boiling to the boiling transition point

D_Q = Thermal diameter (four times the ratio of total flow area to total rod perimeter, including unheated rods when any are present)

G = Mass flux (kg/m2-s)

P = System pressure (MPa)

R = A parameter which characterizes the local peaking pattern with respect to the most limiting rod

L_A = Annular length

L_H = Heated length

A more specific form of the GEXL correlation is:

$$x_c = \sum_{I=1}^{26} A(I) \times V(I) \quad (6.6\text{-}45)$$

where A(I) is a set of constants which are fuel type specific. The correlating variables V(I) are listed in Table 6-14.

Table 6-14. GEXL V(I) Expressions

[[

]]

6.6.6.2 Model as Coded

Calculations of the boiling transition criteria are based on equations described in Section 6.6.6.1. If Option 1 is chosen, then the Biasi correlation is used for high flow rate ($G > G_2$) and the Zuber correlation is used for low flow rates ($G_1 < G$). Linear interpolation for critical heat flux is applied within the region $G_1 < G < G_2$. The cutoff values for G_1 and G_2 are:

G_1 = 100 kg/(m^{2}s) for up-flow and G_1 = 240 kg/(m^{2}s) for down-flow

G_2 = 200 kg/(m^{2}s) for up-flow and G_2 = 440 kg/(m^{2}s) for down-flow

The Biasi correlation is modified for high void fraction to satisfy the trend $q_{CHF} \rightarrow 0$, when $\alpha \rightarrow 1$. When $\alpha > 0.9$, the Biasi critical heat flux is multiplied by factor $10.0 \cdot (1 - \alpha)$.

To obtain the critical flux temperature,

$$q_{CHF} = h_{chen} (T_{CHF} - T_{sat})$$

is solved for T_{CHF} where $h_{chen} = h_{mic} + h_{mac}$.

If options 2–4 are used, boiling transition is realized when two conditions are satisfied: $x > x_c$ and $T_w > T_{CHF}^{Zuber,G=0}$, where $T_{CHF}^{Zuber,G=0}$ is the critical heat flux temperature calculated based on the Zuber correlation for the pool conditions (G = 0).

6.6.6.3 Applicability

The form of the modified Zuber equation for critical heat flux in pool boiling was developed analytically in a number of different ways (with different constants)[153]. The Zuber equation becomes the modified Zuber equation by multiplying by 0.9. The factor 0.9 was recommended by Walkush[135] after he compared his counter-current critical heat flux data with pool boiling critical heat flux data.

The constant in the similar equation developed in Reference [135] is 0.149, whereas Zuber's constant was 0.131. Whalley reports that the equation works well for predicting critical heat flux from long horizontal plates as long as two conditions are satisfied:

(1) Liquid is prevented from entering around the sides of the plate. This can be ensured by adding sides to the flat plate.

(2) The test section should be reasonably large. If the test section dimensions become small, then the number of vapor jets to be fitted in becomes important. The predicted critical heat flux varies significantly when the length is less than three times the distance between vapor jets. If the test section is reasonably large, then the impact of liquid entering around the sides of the plate is small.

The Biasi correlation[143] was developed for vertical up-flow boiling of water in uniformly heated tubes. The equations were developed from a database with the following ranges of parameters [127]:

Data points:	over 4500
Mass flow rate:	100 to 6000 kg/m^2-s
Pressure:	0.27 to 14.0 MPa
Diameter:	0.003 to 0.0375 m
Quality at CHF:	$\rho_v / (\rho_\ell - \rho_v)$ to 1
Axial power:	uniform distribution

The RMS error of this correlation against the database was reported to be 7.3%. The Biasi correlation has been compared[138] to other data banks. Table 6-15 shows data that fall into different error bounds for the data, which is in the range of the experimental conditions listed above. As explained previously, the correlation is only used for non-channel components for mass flow rates greater than 300 or 440 kg/m^2-s, depending on the flow direction.

Table 6-15. Biasi Correlation Compared to Chalk River Data Bank

	Data Within the Error Bound (%)						
	Constant Dryout Quality			Constant Inlet Subcooling			No. Of
	+10%	+20%	+30%	+10%	+20%	+30%	Data Points
Valid data	21.32	41.12	73.04	77.60	96.60	99.91	9936

According to Reference [139], the correlation has also been compared to 1928 data points from a Harwell round-tube data bank. All the data essentially fell within +40% and -50% of the correlation. On average, the correlation was 8% below the data and the standard deviation was 17%.

The GEXL correlation is actually a series of correlations, each with its own set of constants, which were tested and developed for a specific GEH BWR fuel design. The GEXL correlations have been well qualified for predictions of critical quality in BWR fuel bundles and should only be used for predicting the critical power quality for BWR fuel. The GEXL correlations have been reviewed and approved by the NRC for application to GEH fuel. The correlations are based on experimental data that cover the following ranges:

[[

]]

The overwhelming portion of the experimental data used for the correlations for GE2 through GE14 fuel was obtained from the ATLAS loop and the remainder were obtained from the Columbia University test loop. The total number of data points was greater than [[ ]], and were obtained with full size 7x7 through 10x10 rod bundles.

[[

]]

GEXL correlations have been developed for a variety of bundle geometries. The process is generically applicable and can be extended to new geometries. The following serves as an example of how the correlation bias and uncertainty are determined for each correlation. For example, the GEXL correlation for GE9 fuel was qualified against 1091 data points of ATLAS data. The Experimental Critical Power Ratio (ECPR) is defined by:

$$\text{ECPR} = \frac{\text{Predicted Critical Power}}{\text{Measured Critical Power}} \tag{6.6-46}$$

For the GE9 database, the overall mean of the ECPR is [[ ]] and the standard deviation is [[ ]]. A histogram of ECPR for the database used to qualify the GEXL correlation for GE9 is shown in Figure 6-26. The correlation statistics for the various fuel types are listed in Table 6-16. As new geometries are introduced, new GEXL correlations can be introduced and modeled in TRACG because the code allows the GEXL coefficients to be provided as input. The code also includes internal sets of coeefficients for many GEH fuel products that can be selected via user input.

[[

]]

Figure 6-26. ECPR Histogram for GE9 Fuel

Table 6-16. Example of Statistics for the GEXL Correlations

Fuel Type	ECPR	Standard Deviation
[[		]]

6.6.7 Minimum Stable Film Boiling Temperature

The boundary between the transition boiling regime and the film boiling regime corresponds to a minimum in the boiling curve. The boundary point is defined by the minimum stable film boiling temperature.

6.6.7.1 Technical Basis and Assumptions

The transition point from film boiling to transition boiling will occur only after the wall temperature drops below the minimum stable film boiling temperature, T_{min}. If Option 1 from Section 6.6.6 is chosen, then transition boiling is defined to begin when the wall temperature drops below T_{min}. For Options 2, 3 or 4, an additional condition has to be met before the wall rewets. This condition requires that the local equilibrium quality has to be lower than 97% of the critical quality described in Section 6.6.6. This ensures that there is sufficient liquid at the wall to keep the wall covered by a liquid film, which helps to minimize oscillations. Qualification[6] against ATLAS test data has shown that a factor of 0.97 fits the data.

Three options for calculating T_{min} are incorporated in TRACG: (1) the Iloeje correlation option, (2) the homogeneous nucleation correlation option and (3) the Shumway correlation.

The Iloeje correlation[154] has been used in past TRACG applications. The Shumway correlation[23], however, has a larger data base and captures the flow and pressure dependence better than the Iloeje correlation.

For the Iloeje correlation, T_{min} is given by:

$$T_{min} = \max\left(T_{min,\ Iloeje},\ T_{min,\ homogeneous\ nucleation}\right) \tag{6.6-47}$$

where $T_{min,\ Iloeje}$ is given by Equation (6.6-49) and $T_{min,\ homogeneous\ nucleation}$ is given by Equation (6.6-51). For the homogeneous nucleation option, T_{min} is given by:

$$T_{min} = T_{min,\ homogeneous\ nucleation} \tag{6.6-48}$$

The Iloeje correlation is based on Berenson's minimum pool film boiling temperature correlation and extended to provide the effects of mass flux and equilibrium quality. The correlation is given by:

$$\begin{aligned}\Delta T_{min} &= T_{min} - T_{sat} \\ &= 0.29\Delta T_{BER}\left(1-0.295x_e^{2.45}\right)\left[1+\left(7.37\cdot 10^{-2}G\right)^{0.49}\right]\end{aligned} \tag{6.6-49}$$

where:

$$\Delta T_{BER} = 0.127\frac{\rho_g h_{fg}}{k_g}\left[\frac{g\Delta\rho}{\rho_\ell+\rho_g}\right]^{2/3}\left[\frac{\sigma}{g\Delta\rho}\right]^{1/2}\left[\frac{\mu_g}{g\Delta\rho}\right]^{1/3} \tag{6.6-50}$$

The mass flow rate, G, is limited to the range $54.4 \le G \le 135.9$ kg/s-m^2. The equilibrium quality is limited to the range of $0.3 \le x_e \le 0.8$.

For the homogeneous nucleation correlation[155], the minimum stable film temperature, T_{min}, is given by

$$T_{min} = T_c + (T_c - T_\ell)\left(\frac{\rho_\ell k_\ell C_{p,\ell}}{\rho_w k_w C_{p,w}}\right)^{1/2} \tag{6.6-51}$$

where T_c is the critical temperature for water.

For the Shumway correlation, T_{min} is given by:

$$T_{min} = T_{sat} + 3.7\frac{\rho_\ell + \rho_v}{\Delta\rho}\frac{h_{fg}}{C_{p\ell}\,Pr_\ell}\left(1+(1-\alpha)^2\right)\left(1+1.5\cdot 10^{-5}\,Re_\ell\right)^{0.15} \left(1-\frac{P}{P_{crit}}\right)^{0.1}\left(\frac{\rho_\ell k_\ell C_{p,\ell}}{\rho_w k_w C_{p,w}}\right)^{1/2} \tag{6.6-52}$$

6.6.7.2 Model as Coded

Calculations of the minimum stable film boiling temperature are based on equations described in Section 6.6.7.1. The following limitations for the mass flux G and equilibrium flow quality x_e are applied to the Iloeje correlation:

$54.25 \text{ kg/m}^2\text{s} < G < 135.63 \text{ kg/m}^2\text{s}$

$0.3 < x_e < 0.8$

The are no limitations applied to the Shumway correlation.

6.6.7.3 Applicability

The database for the Iloeje correlation was obtained from a transient boiling experiment in a 1.25 cm ID Inconel X-750 tube at mass fluxes of 68, 136, and 340 kg/s-m^2, quality range of 30-100% and a single pressure of 6.9 MPa. The correlation was based on Berenson's minimum pool film boiling temperature difference correlation in order to provide a technique for extrapolating to different pressures.

For the Iloeje correlation, the estimated error for conditions near those of the database is 10% for (T_{min} - T_{sat}). For conditions outside the mass flux and quality ranges and significantly different from 6.9 MPa, 20% is the recommended value to use for the uncertainty.

Comparisons of the Iloeje correlation to other minimum stable film boiling temperature correlations are shown in Figure 6-27 and Figure 6-28. Figure 6-27 shows the comparison of Iloeje (TRACG) to the correlations of Cheng, et al.[156] and Groeneveld and Stewart[157] and also to the correlation in TRAC-PF1/MOD1[133]. The Cheng and the Groeneveld correlations utilize different parameters and cover different ranges of qualities, but are still useful for comparison. A similar comparison at higher pressures is shown in Figure 6-28.

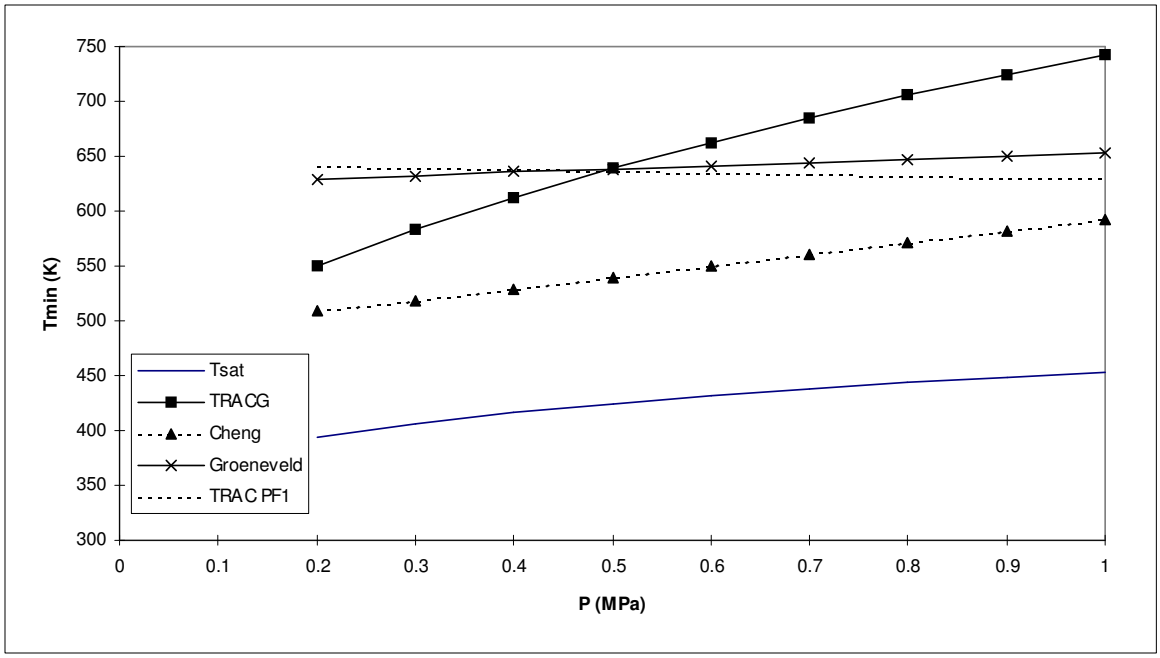

Figure 6-27. Comparison of the TRACG Correlation for Minimum Stable Film Boiling Temperature at Low Pressures

NOTE: The mass flux is 100 kg/m^2-s, the liquid subcooling is 10K and the quality < 0.3.

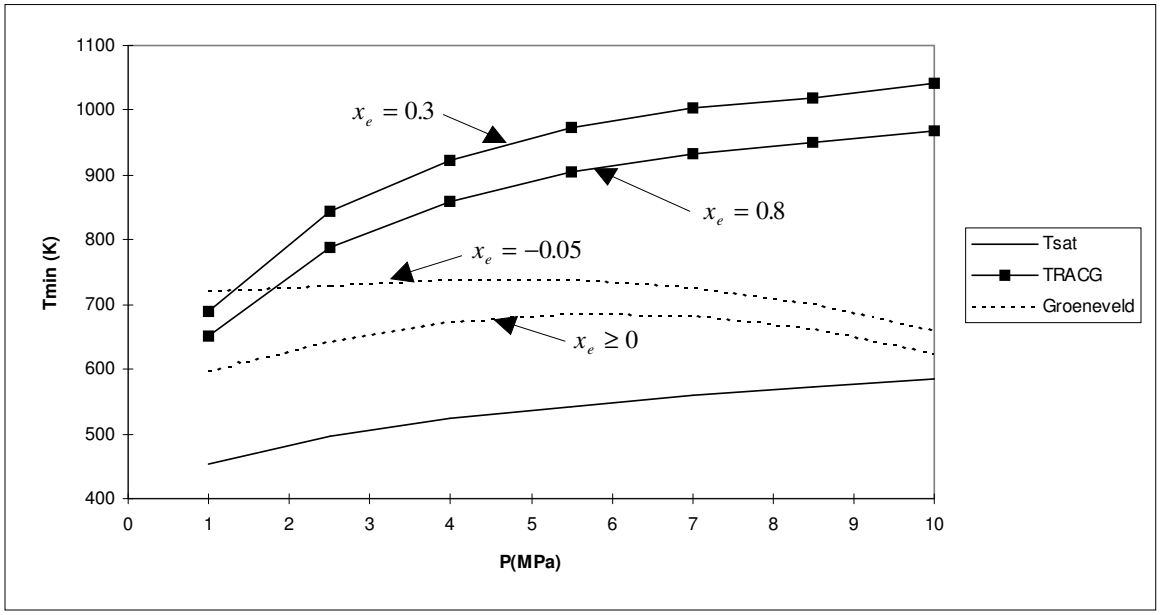

Figure 6-28. Comparison of the TRACG Correlation for Minimum Stable Film Boiling Temperature at High Pressures to those Predicted by Groeneveld

NOTE: The mass flux is 50 kg/m2-s, the subcooling is 0 K.

As can be seen in the figures, TRACG (and the Iloeje experiment) tends to predict a higher minimum stable film boiling temperature than do the other correlations. This was

explained in Reference [154] to be caused by scale deposits, axial conduction and roughness of the test surface. Since BWR fuel will normally have oxidized surfaces, the data and correlation are applicable to BWR LOCA evaluations.

The database for the Shumway[23] correlation covers a wider range. Pressures range from 0.4 to 9 MPa and Reynolds numbers range from $0.1 \cdot 10^5$ to $6.7 \cdot 10^5$. The Shumway correlation predicts the data with a mean error of –30K and a standard deviation of 35K (rounded off to the nearest 5K) as depicted in Figure 6-29.

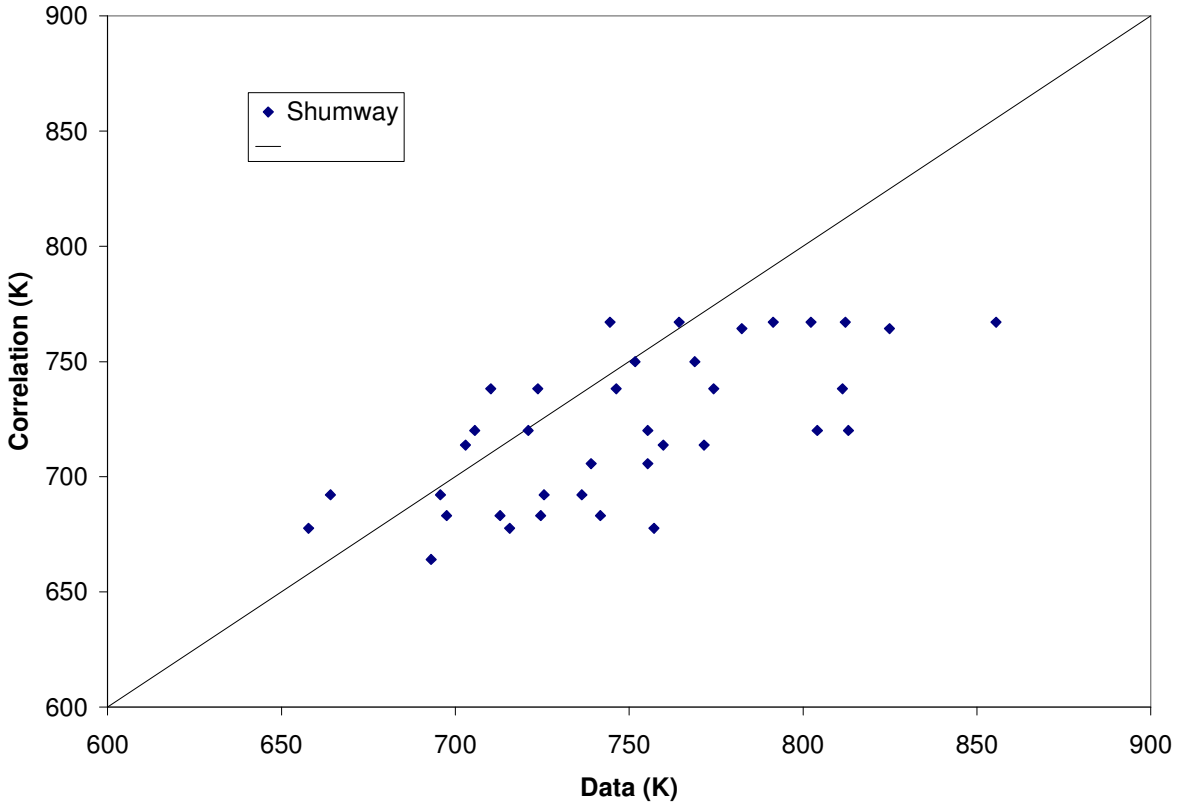

Figure 6-29. Comparison of the Shumway Correlation for the Minimum Stable Film Boiling Temperature to Data

6.6.8 Transition Boiling

Transition boiling is characterized by a wall heat flux that decreases with increasing wall superheat. Physically, this is caused by dryout of the liquid film over portions of the surface, which adds to the thermal resistance.

6.6.8.1 Technical Basis and Assumptions

As is done in Reference [9], the heat transfer coefficient in the transition-boiling mode is obtained by interpolating the values of the heat transfer coefficients in the nucleate and film boiling modes as follows:

$$h_{TB} = \gamma h_{NB}(T_{CHF}) + (1-\gamma) h_{FB}(T_{min}) \tag{6.6-53}$$

where the interpolation parameter from Reference [152] takes the form

$$\gamma = \left(\frac{T_w - T_{min}}{T_{CHF} - T_{min}} \right)^2 \tag{6.6-54}$$

and:

$h_{NB}(T_{CHF})$ = Nucleate boiling heat transfer coefficient evaluated at T_{CHF}

$h_{FB}(T_{min})$ = Film boiling heat transfer coefficient evaluated at T_{min}.

6.6.8.2 Model as Coded

Calculations of the heat transfer coefficients in the transition boiling region are based on equations described in Section 6.6.8 and include several interpolation procedures to provide smooth flow regime transition and smooth transition from wetted to un-wetted wall. Calculations of the heat transfer coefficients at the critical heat flux temperature are based on the nucleate boiling correlation as described in Section 6.6.4. Calculation of the heat transfer coefficient at T_{min} is based on the film boiling heat transfer correlations as described in Sections 6.6.9 and 6.6.10.

6.6.8.3 Applicability

In order to operate in the transition boiling regime, the wall temperature of the passage must be controlled in the physical system so that it remains in the transition-boiling regime. This may occur during re-flood following a loss-of-coolant accident (LOCA) scenario. Compared with nucleate boiling and film boiling, relatively fewer investigations of transition boiling have been conducted. The data that do exist are relatively scarce and generally cover only narrow ranges of conditions. The few correlations that have been developed for transition boiling are not well established or accepted. Also, no steady-state transition boiling data for rod bundles are available.

Transition boiling has traditionally been interpreted as a combination of nucleate and film boiling occurring alternately over the heated surface. The variation in the heat flux in the regime

is due to the varying fractions of time that the two boiling regimes exist at a given location. This interpretation led to the assumption made that transition boiling could be represented by an interpolation between nucleate boiling at the critical heat flux and film boiling at the minimum stable film boiling temperature. Since transition boiling occurs for a relatively short transient period on a fuel rod, such an interpolation is deemed to be acceptable and the model will be insensitive to the value of the heat transfer coefficient.

The form of the interpolation in Equation (6.6-54) was selected for its simplicity and physical basis. According to Reference [152], the exponent of 2 gave the best agreement with data.

The interpolation endpoints (CHF and the minimum film-boiling heat flux) and the associated uncertainties have been discussed in detail in Sections 6.6.6 and 6.6.7. The CHF is particularly well defined for fuel bundles. An appropriate and conservative uncertainty for sensitivity studies in this short duration transient heat transfer regime is to add the uncertainties of 11% (Chen) and 35% (Tien-Gonzalez, Section 6.6.10.3).

6.6.9 Film Boiling - Low Void Fraction

The assumption is made that film-boiling can be adequately described as being in one of three forms. At low void fractions, the flow will take on the so-called inverted annular flow configuration where a thin vapor film covers the tube wall and a two-phase mixture flows in the center of the tube or channel. At high void fractions, the liquid is in the form of dispersed drops in a vapor. The third form is a transition between the two regimes where the liquid is in the form of slugs and drops. The convective heat transfer correlations are presented in this section for inverted annular flow and in Section 6.6.10 for dispersed droplet flow.

6.6.9.1 Technical Basis and Assumptions

In the liquid continuous flow regime the heat transfer from the wall surface to the vapor-liquid interface is largely by thermal radiation, depending on the wall temperature. The heat transfer coefficient to liquid is based on radiation heat exchange between two parallel planes, one at wall temperature and the other at saturation temperature:

$$h_{w\ell} = \varepsilon_w \frac{\sigma (T_w^4 - T_s^4)}{T_w - T_\ell} \tag{6.6-55}$$

where ε_w is the wall emissivity and σ is the Stefan-Boltzmann constant.

The heat transfer to vapor and from the vapor to the liquid is by convection and is given by the modified Bromley correlation. In this flow regime, TRACG applies a large value for the interfacial heat transfer from the vapor to the interface, such that the net resistance for convective heat transfers between the wall and the liquid is:

$$\frac{1}{h_{wv}} + \frac{1}{h_{iv}} \approx \frac{1}{h_{wv}} \tag{6.6-56}$$

where h_{wv} or h_v is given by Equation (6.6-57).

The (unmodified) Bromley correlation is described in Reference [140] as:

$$h_v = 0.62 \left(\frac{k_v^3 h_{fg} \rho_v (\rho_\ell - \rho_v) g}{\mu_v (T_w - T_s) L_H} \right)^{1/4} \quad (6.6\text{-}57)$$

where L_H is the characteristic length. This length is determined using the Helmholtz instability criteria[140]. The effect of the liquid velocity is thereby included in this derivation, and the modified Bromley correlation is:

$$h_v = C \left(\frac{k_v^9 \, h_{fg}^2 \, \rho_v^3 \, (\rho_\ell - \rho_v)^4 \, g^4}{\mu_v^4 \, (T_w - T_s)^2 \, \sigma} \right)^{1/11} \quad (6.6\text{-}58)$$

where σ in this equation is surface tension and:

$$C = \frac{4}{3} \left\{ \frac{\left(\frac{3n-1}{8} \right)^4}{\left(\frac{3\pi\sqrt{3}}{2} \right)^2} \right\}^{1/11} \quad (6.6\text{-}59)$$

and n is determined from

$$\frac{v_\ell}{v_m} = \frac{2n-1}{(3n-1)^{8/11}} \quad (6.6\text{-}60)$$

$$v_m = \frac{8}{2^{8/11}} \left(\frac{3\pi\sqrt{2}}{2} \right)^{4/11} \left(\frac{(\rho_\ell - \rho_v)^3 k_v^4 (T_w - T_s)^4 \sigma^2}{\mu_v^3 h_{fg}^4 \rho_v^6} \right)^{1/11} \quad (6.6\text{-}61)$$

6.6.9.2 Model as Coded

Calculations of the heat transfer coefficients for the film boiling at low void fraction conditions are based on equations described in Section 6.5.9.1. For low void fractions, the modified Bromley correlation determines the net conductive resistance across the thin vapor film and the modified Bromley heat transfer coefficient is applied to the wall to liquid heat transfer coefficient. For high void fractions close to the transition to annular flow, the modified Bromley heat transfer coefficient is applied to the wall to vapor heat transfer coefficient. This is done to allow a continuous transition to annular flow film boiling. This interpolation is done linearly from a void fraction of 0.1 to 0.5. It should be noted that the impact of this implementation is small, since $T_v \approx T_{sat}$ for this condition.

6.6.9.3 Applicability

Equation (6.6-55) represents the heat transfer from the wall surface to the vapor-liquid interface and is a straightforward application of the Stefan-Boltzmann law. It is applicable for situations where the optically thin assumption is valid.

The Bromley correlation is widely used for inverted annular-flow film boiling and was developed from data for boiling in a horizontal tube. The modified Bromley correlation was developed for vertical geometries and is derived from theoretical considerations and compared to experimental data over a sufficiently wide range to verify the correlation. The range of applicability as reported in NEDO-20566-1[140] is for wall temperatures less than 1260°C and pressures less than 8.3 MPa. Figure 6-30 shows a plot of KWU re-flood data compared to the modified Bromley. The agreement is excellent in the film-boiling regime. Further comparison to data can be found in Reference [140]. This methodology was successfully applied in the approved code SAFER[116].

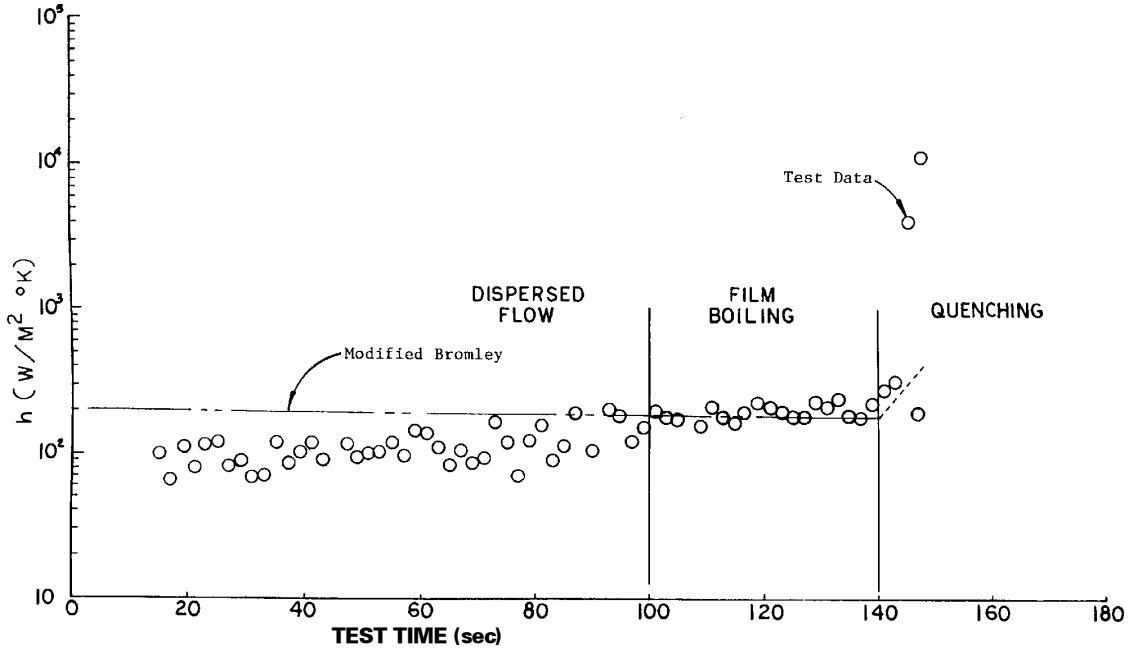

Figure 6-30. Comparison of Modified Bromley with Data during Re-flood Test

6.6.10 Film Boiling - High Void Fraction

In this flow regime, both radiation and convection play important roles in the heat transfer. Radiative heat transfer is treated in Section 6.6.12. This section covers convection heat transfer in the dispersed droplet flow regime.

6.6.10.1 Technical Basis and Assumptions

Due to steam superheat, there will be a temperature difference between steam and the interface between the steam and the droplets and, thus, a net heat transfer. Reference [141] provides a good correlation for the convective heat transfer coefficient from the steam to droplets of the form:

$$\beta = Nu_d \; k_v \; N_d \pi \; d_d \tag{6.6-62}$$

where N_d is the droplet number density given by:

$$N_d = \frac{6(1-\alpha)}{\pi \; d_d^{\;3}} \tag{6.6-63}$$

and the droplet Nusselt number is given by (Section 6.5.5)

$$Nu_d = 2 + 0.74 \left(\frac{d_d \; \rho_v \; v_R}{\mu_v} \right)^{0.5} \; Pr_v^{\;1/3} \tag{6.6-64}$$

The presence of droplets in a steam atmosphere has two effects on the convection wall-to-steam heat transfer: (1) the bulk steam temperature will be lowered toward the saturation temperature, thus increasing the heat transfer, and (2) the temperature profile of the steam will be changed, causing a steeper temperature gradient close to the wall. This effect will also enhance the heat transfer. Sun, Gonzalez and Tien[142] solved the continuity and energy equation for the temperature profile of the steam. If a parabolic velocity profile for the steam is assumed, the Nusselt number is given by:

$$Nu_v = \frac{2X I_1(X)}{I_0(X) - \frac{8}{x^2} I_2(X)} \tag{6.6-65}$$

where:

$$X = \frac{D_h}{2} \sqrt{\frac{\beta \; h_v}{k_v \; h_{fg}}} \tag{6.6-66}$$

Equation (6.6-65) was derived from the assumption that the temperature profile of the steam is determined from a balance between heat transfer from the wall and heat transfer to the droplets. Hence, the terms $\partial/\partial z$ were neglected in the continuity and energy equations. This is valid only for large droplet concentrations. For zero droplet concentration, the single-phase

Nusselt number for a tube is calculated as described in Section 6.6.5. For laminar flow, a value of 4.0 is obtained, whereas the limiting value of Equation (6.6-65) is 6.0.

For large droplet concentrations, an asymptotic approximation to Equation (6.6-65) is:

$$Nu_v \approx 2X - 1 \text{ for } x \rightarrow \infty \tag{6.6-67}$$

An expression having this behavior and having the appropriate limit for $x \rightarrow 0$ ($\alpha = 1$) is given by:

$$h_v = \frac{k_v}{D_h}\left(2X\text{-}1 + \frac{(Nu_s + 1)^2}{Nu_s + 1 + 2X}\right) \tag{6.6-68}$$

where

$$Nu_s = \frac{D_h}{k_v} h_{g,\text{ single phase}} \tag{6.6-69}$$

Equation (6.6-68) is known as the modified Tien-Gonzalez correlation.

6.6.10.2 Model as Coded

Calculations of the heat transfer coefficients for the film boiling at high void fraction conditions are based on equations described in Section 6.6.10.1. Droplet diameter and number of droplets are input parameters and have been defined during interfacial heat transfer calculations (see Section 6.5.5) for the heat transfer coefficients. An interpolation procedure is included to provide smooth changes to the modified Bromley correlation:

$$h_v = (1 - x_2)\, h_{MB} + x_2\, h_{SGT} \tag{6.6-70}$$

where MB designates modified Bromley and SGT designates Sun-Gonzalez-Tien. Values for x_2 are zero for low void fractions and one for dispersed flow. x_2 is interpolated linearly from 0 to 1 over the transition region to dispersed annular flow.

6.6.10.3 Applicability

The Tien-Gonzalez correlation was developed especially for convection heat transfer in rod bundles under emergency cooling conditions. The modified Tien-Gonzalez correlation was developed to yield correct heat transfer behavior as the droplet concentration approached zero. This correlation was successfully used in the CORECOOL[144] code. An example of the CORECOOL comparison to data was provided as Figure 6.6-10 in Revision 2 of this LTR. A similar example showing the TRACG comparison to data from the same series of tests is shown here in Figure 6-31. These CSHT tests[145] simulate a full-scale fuel channel. The TRACG calculated peak cladding temperatures agree well with the data. In these tests the heat transfer is by both radiation and convection; therfore, it is important to isolate one effect so that "compensating errors" can be ruled out as the reason for good prediction.

[[

]]

Figure 6-31. Peak Cladding Temperature for a BWR Fuel Element

Figure 6-32 shows the CORECOOL prediction of the temperature profile within an 8x8 bundle compared to test results for three steady state tests selected from the GEH and AB Atomenergi CSHT (Core Spray Heat Transfer) experiments. For the steady-state tests, no liquid was injected at the top of the fuel bundle and the bundle contained only stagnant air. Under these conditions, the convective heat transfer is minimized and radiation heat transfer is the dominant mode. A constant power of 25 kW was applied to the bundle, while the outside of the channel box was cooled by water at a temperature of 311 K. The tests were conducted until equilibrium conditions were obtained. A single calculation was made for these comparison because the conditions for the three steady-state tests were essentially identical. The symbols in Figure 6-32 indicate different rod locations, moving inward from the corner position. Except for the

peripheral rods, where a considerable amount of conduction/convection existed across the narrow gap to the cold channel, the cooling of the rods was primarily by thermal radiation. The CORECOOL calculations are in good agreement with the data.

Figure 6-33 shows the TRACG prediction of the same three steady state CSHT tests used for the CORECOOL qualification. (Note the different temperature units for Figure 6-32 and Figure 6-33.) The TRACG calculations shown in Figure 6-33 are in good agreement with the data. In particular, the average of the peak temperatures for interior rods in the bundle from the three tests is predicted within 2K, which is within the measurement uncertainty of ±4K. On the other hand, the temperatures of the two corner rods on the exterior of the bundle are overpredicted by about 90K. The main reason for this is that a one-dimensional hydraulic model cannot simulate the cross-sectional variation of the vapor temperature in the bundle.

[[

]]

[[

]]

Figure 6-32. CORECOOL Compared to "Radiation Only" Experiments

[[

]]

Figure 6-33. TRACG Compared to "Radiation Only" Experiments

For transient testing, TRACG was compared to a subset consisting of six of the transient CSHT experiments also used in the CORECOOL qualification. The mean and standard deviation for the error in predicting the peak clad temperatures from these tests are shown in Table 6-17 for both TRACG and CORECOOL. It is seen that the uncertainty is similar while TRACG is slightly conservative compared to the data and to CORECOOL.

Table 6-17. TRACG and CORECOOL Qualification for the CSHT Experiments

	TRACG	CORECOOL
Mean Error (Calculation – Data), K	[[	
Standard deviation, K		]]

The details for the six transient CSHT tests are provided in Section 3.2 of the *TRACG Qualification LTR*[4],[5],[6]. The parameters varied for the individual tests were the power, spray flow rate and the peak rod temperature at which the spray flow was initiated. To start the test, the power was held constant with no spray until the average rod temperature at some instrumented elevation in one of the rod groups reached an elevated temperature near 1000 K with the precise value varying from test to test. Spray was then initiated and the bundle power was decreased to simulate decay heat Immediately following the initiation of the spray, the rod temperature continues to increase and the primary effect of the spray is to reduce the vapor superheat. Droplets form within the vapor but they are unable to reach the wall. Subsequently, the spray begins to form a film on the inside and outside of the channel walls and the channel is quenched as the film front advances downward. The channel wall then becomes an effective radiation sink for the peripheral rods and the peripheral rods, in turn, become radiation sinks for the interior rods. Rod heat transfer is now about equally divided between convection and radiation and the combination of these two heat transfer modes is sufficient to turn the rod temperatures downward. Eventually, the rods are cooled sufficiently to allow the spray droplets to migrate to the rod wall and form a quench front. When the quench front reaches the elevation of the temperature measurement, the temperature drops to close to the spray temperature.

In the six transient experiments used to construct Table 6-17, TRACG predicts that near the time of the peak clad temperature approximately half of the heat transfer is from convection and half is from radiation. By assuming that the standard deviation of [[ ]] in predicting the PCT is entirely attributed to the convection model, one can bound the uncertainty from Equation (6.6-68).

6.6.11 Condensation Heat Transfer in the Presence of Noncondensable Gases

Condensation heat transfer will occur when the wall temperature is less than the saturation temperature and the flow regime is vapor continuous.

6.6.11.1 Technical Basis and Assumptions

Steam Condensation in Tubes

A modified version of the Vierow-Schrock (V-S) condensation correlation[146] has been used in TRACG. The correlation is based on a two-part correction to a reference local heat transfer coefficient termed the "Nusselt" heat transfer coefficient. This reference value is calculated by dividing the condensate thermal conductivity by the local liquid film thickness:

$$h_{condensation} = f_1 \, f_2 \, h_{ref} \tag{6.6-71}$$

$$h_{ref} = k_\ell/\delta \tag{6.6-72}$$

The factor f_1 is greater than or equal to unity since it accounts for increased heat transfer due to shearing (thinning) of the condensate film layer. The factor f_2 is less than unity and accounts for the decrease in heat transfer resulting from the presence of noncondensable (NC) gases. NC gases tend to accumulate at the condensation site where they lower the steam partial pressure resulting in a reduction in the steam saturation temperature. Because of how f_2 is obtained, it accounts for other mechanisms that have not been explicitly considered in getting f_1. Section 6.3 of Reference [149] indicates how f_2 is correlated from the data for air and helium after accounting for the other effects already considered in f_{1shear} and f_{1other}. One mechanism that is not explicitly considered is the change in buoyancy of the vaporous mixture because of the NC gases. This effect is implicit in the value of f_2 and will change as the NC gas composition changes; however, it is doubtful that the subtle effects of buoyancy are significant when compared to the strong impact of shear.

The local condensate film thickness is defined in Reference [147] as:

$$\delta=\left(\frac{3\mu_\ell\Gamma}{g\rho_\ell(\rho_\ell-\rho_v)}\right)^{1/3} \quad \text{or} \quad \delta=\left(\frac{3\mu_\ell^2 Re_\ell}{4g\rho_\ell\Delta\rho}\right)^{1/3} \tag{6.6-73),(6.6-74}$$

for laminar condensate film flow ($Re_l < 1000$) where

$$Re_\ell = \frac{4\Gamma}{\mu_\ell} \tag{6.6-75}$$

For turbulent condensate film flow, Burmeister[148] presents

$$\frac{Re_\ell}{4} = 0.003\left[\frac{g^{1/3}\rho_\ell^{2/3}k_\ell(T_s-T_w)z}{h_{fg}\mu_\ell^{5/3}}\right]^{3/2} \tag{6.6-76}$$

Re-arranging and differentiating yields:

$$d(Re_\ell^{2/3}) = 0.052\left[\frac{g^{1/3}\rho_\ell^{2/3}k_\ell(T_s - T_w)}{h_{fg}\mu_\ell^{5/3}}\right]dz \tag{6.6-77}$$

A simple energy balance yields:

$$\Gamma(z) = \frac{\bar{h}(z)}{h_{fg}}(T_s - T_w)z \tag{6.6-78}$$

Combining Equations (6.6-75) and (6.6-78) and differentiating produces

$$d(Re_\ell) = \frac{4h}{\mu_\ell h_{fg}}(T_s - T_w)dz \tag{6.6-79}$$

Now, combining Equations (6.6-77) and (6.6-79)

$$\tfrac{2}{3}Re_\ell^{-1/3} = 0.052\frac{g^{1/3}\rho_\ell^{2/3}k_\ell}{\mu_\ell^{2/3}}\cdot\frac{1}{4h} \tag{6.6-80}$$

Using Equations (6.6-72) and (6.6-80) and solving for δ gives the turbulent film thickness

$$\delta = 51.3\left(\frac{\mu_\ell^2}{\rho_\ell^2 g\, Re_\ell}\right)^{1/3} \quad \text{or} \quad \delta = 32.3\left(\frac{\mu_\ell^3}{\rho_\ell^2 g\Gamma}\right)^{1/3} \tag{6.6-81),(6.6-82}$$

for $Re_\ell > 2000$.

As stated above, the two-part correction takes the form:

$$h_{condensation} = f_1\ f_2\ h_{ref} \tag{6.6-83}$$

When $Re_\ell \le 1000$, which indicates a smooth liquid film, the factor f_1 is given by:

$$f_1 = \min\left[\ 1 + 2.88 \times 10^{-5} Re_m^{1.18}\ ,\ \ 3.0\ \right] \tag{6.6-84}$$

where

$$Re_m = \frac{G_m d}{\mu_m} \tag{6.6-85}$$

When $Re_\ell > 2000$,

$$f_1 = 1 \tag{6.6-86}$$

Note: The "m" subscript denotes the mixture of gases.

The factor f_2 is correlated in terms of the density ratio for air by:

$$f_2 = \begin{cases} 1.0 - 10.0\, x_{air} & x_{air} < 0.066 \\ 1.0 - 0.938\, x_{air}^{0.13} & 0.066 < x_{air} < 0.49 \\ 1.0 - x_{air}^{0.22} & 0.49 < x_{air} < 1.0 \end{cases} \quad (6.6\text{-}87)$$

$$x_{air} = \frac{\rho_{air}}{\rho_m} \quad (6.6\text{-}88)$$

The density of the gas mixture (ρ_m) is the sum of the partial densities for the gases.

Incorporating the film thickness into Equation (6.6-72), the reference (or Nusselt) condensation heat transfer coefficient becomes:

$$h_{Nusselt} = \begin{cases} 1.1\, k_\ell \left(\dfrac{\rho_\ell \Delta\rho g}{\mu_\ell^{\,2}\, Re_\ell} \right)^{1/3} & \text{for } Re_\ell < 1000 \\ \\ 0.0195\, k_\ell \left(\dfrac{\rho_\ell^{\,2} g\, Re_\ell}{\mu_\ell^{\,2}} \right)^{1/3} & \text{for } Re_\ell > 2000 \end{cases} \quad (6.6\text{-}89)$$

A cubic spline interpolation is used for $1000 < Re_\ell < 2000$.

The Vierow-Schrock correlation has been included in this description for historical reasons. It has been supplanted by a more recent correlation, which has a wider database and is recommended by the developers at U. C. Berkeley. This correlation, referred to as the K-S-P (Kuhn-Schrock-Peterson) correlation[149],[146], is the default and recommended correlation and was also developed at U. C. Berkeley for condensation in the presence of noncondensable gases inside tubes. The correlation takes the same form as Equations (6.6-71) and (6.6-72). However, f_1 is split up into two parts:

$$f_1 = f_{1shear} \cdot f_{1other} \quad (6.6\text{-}90)$$

where

$$f_{1other} = 1 + 1.83 \times 10^{-4}\, Re_\ell \quad \text{where again} \quad \left(Re_\ell = \frac{4\Gamma}{\mu} \right) \quad (6.6\text{-}91),(6.6\text{-}92)$$

and $f_{1\ shear}$ is:

$$f_{1shear} = \frac{\delta_1}{\delta_2} \quad (6.6\text{-}93)$$

Reference [146] states: "The f_{1other} factor accounts for other influences such as interfacial disturbances, deviations from linear temperature profiles, and temperature dependent properties, etc." In effect, f_{1other} is a correction factor to bring the theoretical approximation derived from

smooth interface laminar film theory with interfacial shear as represented by f_{1shear} into better agreement with the data.

δ_1 is equivalent to δ from Equation (6.6-73) and is the film thickness without shear. δ_2 is the film thickness with shear. With interfacial shear the predicted film thickness, δ_2 is given implicitly by:

$$\Gamma = \frac{g}{\mu_f}\rho_f(\rho_f - \rho_g)\frac{\delta_2^{\,3}}{3} + \frac{\rho_f \tau_i \delta_2^{\,2}}{2\mu_f} \tag{6.6-94}$$

where:

$$\tau_i = \frac{1}{2} f_R \rho_g V_g^2 \tag{6.6-95}$$

$$f_R = 0.046\,Re_m^{\,-0.2} \tag{6.6-96}$$

leading to the interfacial shear prediction

$$\tau_i = \frac{0.023}{\rho_g}\left(\frac{\mu_m}{D_i}\right)^2 Re_g^{\,1.8} \tag{6.6-97}$$

The f_2 degradation function has been correlated in the form

$$f_2 = \left(1 - cx^b\right) \tag{6.6-98}$$

for both air and helium. For air x becomes x_{air} where

$$x_{air} = \frac{\rho_{air}}{\rho_m} \tag{6.6-99}$$

and

$$f_{2,air} = \begin{cases} 1.0 - 2.601\,x_{air}^{0.708}, & x_{air} < 0.1005 \\ 1.0 - x_{air}^{0.292}, & x_{air} \geq 0.1005 \end{cases} \tag{6.6-100}$$

For helium x becomes x_{He} where

$$x_{He} = \frac{\rho_{He}}{\rho_m} \tag{6.6-101}$$

and

$$f_{2,He} = \begin{cases} 1.0 - 35.81\, x_{He}^{1.074}, & x_{He} < 0.010005 \\ 1.0 - 2.09\, x_{He}^{0.457}, & 0.010005 \le x_{He} < 0.099895 \\ 1.0 - x_{He}^{0.137}, & 0.099895 \le x_{He} \le 1.0 \end{cases} \quad (6.6\text{-}102)$$

Given the appropriate value for f_2 (see Section 6.6.11.2) the Kuhn-Schrock-Petersen correlation is formulated as

$$h = f_l f_2\, h_{Nusselt} = f_{l_{shear}} \cdot f_{l_{other}} \cdot f_2 \cdot h_{Nusselt} \quad (6.6\text{-}103)$$

or

$$h = f_2 \left(1 + 1.83 \times 10^{-4}\, Re_\ell\right) \frac{k_\ell}{\delta_2} \quad (6.6\text{-}104)$$

The K-S-P correlation[149] has a database for Re_ℓ extending to 2000. For turbulent films, a turbulent correlation is needed. The Burmeister correlation[148] was used in conjunction with Vierow-Schrock. Further review of correlations in the literature indicated that the correlation of Colburn and models developed by Dukler and Seban were better accepted. These models agree with Burmeister only at high Prandtl number and predict lower heat transfer coefficients for water. TRACG incorporates a correlation, which is proportional to $Re_\ell^{1/3}$ (similar to Burmeister), but with a coefficient of 0.01, which puts it in the same range as the Dukler, Seban, Colburn models (see Figure 6-37). The coefficient was chosen so that the correlation merges smoothly with the K-S-P correlation.

The heat transfer coefficient for turbulent condensate flow ($Re_\ell > 2000$) is calculated as:

$$h = 0.01\, f_2\, k_\ell \left(\frac{\rho_\ell^{\,2} g\, Re_\ell}{\mu_\ell^{\,2}} \right)^{1/3} \quad \text{for } Re_\ell > 2000 \quad (6.6\text{-}105)$$

A cubic spline interpolation is used for $1000 < Re_\ell < 2000$.

Steam Condensation in Containment

The formulation of the local condensate film thickness in Equation (6.6-73) was derived for flat plates and is therefore suitable for use for steam condensation in the containment. The default application for condensation is to use the K-S-P correlation (Equation (6.6-104)) with the f_{1shear} factor set equal to 1, or $\delta_2 = \delta_1$. This is appropriate, since velocities in the containment will be small compared to the tubes and the f_{1shear} factor was developed specifically for tubes. The f_2 factors will remain the same.

Another option is to use the "Uchida" correlation for condensation in the containment. The "Uchida" correlation is:

$$\bar{h} = 380\left(\frac{1-x_{air}}{x_{air}}\right)^{0.7}\frac{Watts}{m^2K} \tag{6.6-106}$$

Equation (6.6-106) is undefined when $x_{air} = 0$. As a result, TRACG takes the minimum of the heat transfer coefficients predicted by Equation (6.6-106) and the K-S-P correlation with $f_{1shear} = 1$.

An option to use the Vierow-Schrock correlation with the f_1 factor set equal to 1 is also available.

6.6.11.2 Model as Coded

The f_2 degradation functions for both the V-S and K-S-P correlations are correlated by piecewise functions where the independent variable x is a density ratio. Only air and helium have been considered in developing these correlations. To accommodate a wide range of different gases, the equivalent density ratios x_{air} for air and x_{He} for helium are determined as follows.

First, the mole fraction of noncondensable gas molecules to total gas molecules is approximated by the ratio of the partial pressure ratio of all noncondensable gases to the total pressure. Because all gases are assumed to be at the same temperature, this pressure ratio is equivalent to the mole ratio, provided the mixture of all the noncondensable gases with steam is assumed to also be an ideal gas. Such an approximation is appropriate in a condensing environment because steam exhibits ideal gas behavior as its partial pressure is reduced in the presence of accumulating noncondensables.

The mole fraction Y_a of all condensable gases to the total combined gas reduces to:

$$Y_a = \frac{\rho_a / W_a}{\rho / W} = \frac{\rho_a}{\rho}\frac{W}{W_a} \tag{6.6-107}$$

since Avogadro's number and the common volume used to convert from mass to density cancel out in the ratio. The ideal gas state relationship provides that

$$\rho = \frac{P}{RT_v} = \frac{PW}{R_u T_v} \tag{6.6-108}$$

Application of this state relationship to both the noncondensable gas density and the combined total gas density in Equation (6.6-107) leads to elimination of the molecular weights and the presumed common temperatures and results in:

$$Y_a = \frac{P_a W_a}{R_u T_a W_a}\cdot\frac{R_u T_v W}{PW} = \frac{P_a}{P} \tag{6.6-109}$$

The mole fraction is specified locally by the local pressure ratio, which, in turn, reflects the local concentration and composition of the noncondensable gases, whatever they may be.

The effective molecular weight for the local noncondensable gas mixture is calculated by rearranging Equation (6.6-108) and applying it using the pressure and density for the mixture of all noncondensable gases to get

$$W_a = \frac{\rho_a R_u T_v}{P_a} \tag{6.6-110}$$

In general, the total noncondensable gas (subscript a) cannot be expected to have the properties for air unless air is the only gas being modeled (the same is true for helium). Consequently, to evaluate $f_{2,air}$, it is necessary to determine the density ratio x_{air} as if the aggregate gas were replaced by an equivalent amount of air. A similar transformation is needed to obtain the equivalent value for x_{HE} needed to evaluate $f_{2,He}$. An equivalent mass fraction x_n for a particular gas n is defined as that value for x_n that will yield the same mole ratio as for the general aggregate gas. Mathematically, the requirement is:

$$\frac{P_n}{P} \equiv Y_n(x_n) \overset{\text{must}}{=\!=} Y_a(x_a) \equiv \frac{P_a}{P} \tag{6.6-111}$$

The mass ratio and mole ratios for a noncondensable gas n with a molecular weight of W_n coexisting with steam are related by:

$$x_n = \frac{Y_n W_n}{Y_s W_s + Y_n W_n} = Y_n \left[(1 - Y_n) \frac{W_s}{W_n} + Y_n \right]^{-1} \tag{6.6-112}$$

where W_s is the molecular weight of steam. Use has been made of the fact that

$$Y_s + Y_n = 1.0 \tag{6.6-113}$$

Apply the requirement from Equation (6.6-111) to rewrite Equation (6.6-112) as:

$$x_n = \frac{P_a}{P} \left[\left(1 - \frac{P_a}{P} \right) \frac{W_s}{W_n} + \frac{P_a}{P} \right]^{-1} \tag{6.6-114}$$

Using Equation (6.6-89), the local mole ratio for the total noncondensable gas, as characterized by its pressure ratio P_a/P, is transformed to an equivalent mass ratio for gas n. Thus, x_{air} and x_{He} can be calculated and used to evaluate $f_{2,air}$ and $f_{2,He}$. This approach is justified by the fact that, when applied in this way, the degradation functions $f_{2,air}$ and $f_{2,He}$ produce similar results for a given input of P_a/P. The similarities can be seen in Figure 6-34. The $f_{2,air}$ function from Equation (6.6-87) used in the Vierow-Schrock correlation also produces similar results. These similarities are obtained in spite of the fact that the equivalent mass ratios for air and helium are quite different. The implication is that the mole ratio or pressure ratio (not

the mass ratio) is the natural choice of independent variable for extension of the f_2 degradation functions to a wide range of noncondensable gases.

Because $f_{2,air}$ and $f_{2,He}$ for the K-S-P correlation yield similar but not identical results, linear interpolation between them is used for a total noncondensable gas with a molecular weight between the molecular weights of helium and air. The interpolation variable is calculated as:

$$Z = \begin{cases} 0.0 & , \quad W_a < W_{He} \\ (W_a - W_{He})/(W_{air} - W_{He}) & , \quad W_{He} < W_a < W_{air} \\ 1.0 & , \quad W_a > W_{air} \end{cases} \tag{6.6-115}$$

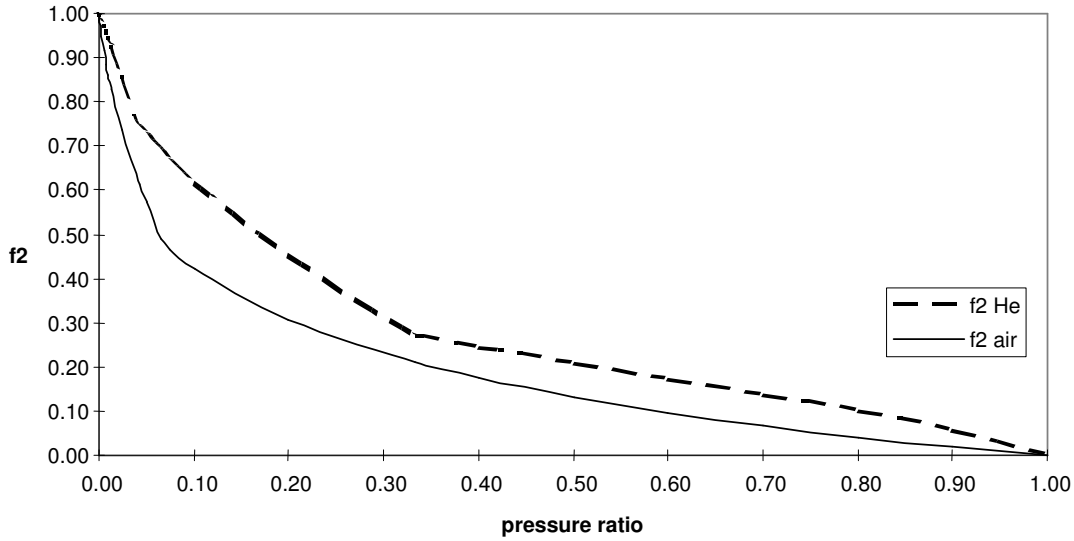

Figure 6-34. Degradation Factor f_2 Plotted versus Ratio of Noncondensable Partial Pressure to Total Pressure

The generalized f_2 function for the total noncondensable gas is then calculated for the K-S-P correlation using:

$$\left[f_{2,a}\right]_{KSP} = \left[Z \cdot f_{2,air}\left(x_{air}\right) + (1-Z) \cdot f_{2,He}\left(x_{He}\right)\right]_{KSP} \tag{6.6-116}$$

The values for x_{air} and x_{He} are those obtained from Equation (6.6-114). Note that for the case where the total noncondensable gas is either all air or all helium the general form given above reduces to the original forms provided in the K-S-P correlation.

For the Vierow-Schrock f_2 function, where only air was considered, we use by default:

$$\left[f_{2,a}\right]_{VS} = \left[f_{2,air}\left(x_{air}\right)\right]_{VS} \tag{6.6-117}$$

For assessment purposes, the code user may elect via input to substitute the more general form of $[f_{2,a}]_{KSP}$ from Equation (6.6-116) for $[f_{2,a}]_{VS}$ or vice-versa when using the K-S-P and V-S correlations.

For the K-S-P correlation, values of Re_ℓ are limited to 100,000. The gravity vector, g, is equal to 9.8 cos θ.

In the K-S-P correlation, the factor f_2 accounts for the degradation due to noncondensable gases. It is obtained by correlating the ratio of the condensation heat transfer coefficient with noncondensable gases to the heat transfer coefficient without noncondensable gases. It is intended to be a best fit to the data.

6.6.11.3 Applicability

Steam Condensation in Tubes

The Vierow-Schrock correlation was developed for condensation of steam inside a tube in the presence of noncondensable gas. Subsequent experiments have shown that the Vierow-Schrock correlation is accurate over the range of conditions of the Vierow experiment, but needs some care in extrapolation beyond that range. Kuhn[149] reports the standard deviation of the correlation with the data is approximately 30%. The ranges and physical dimensions of the experiment were:

Inlet pressure:	0.03 - 0.45 MPa
Inlet temperature:	343 - 419 K
Inlet steam flow rate:	0.0022 - 0.0083 kg/s
Inlet air mass fraction:	0 - 0.14
Local air mass fraction:	0 - ~1
Tube dimensions:	
Length:	1.8 m
Outside diameter:	25.4 mm
Tube thickness:	1.65 mm

The limit of $f_1 \leq 3$ was added to the model due to the rapid increase in f_1 that occurs when the mixture Re exceeds the conditions of the Vierow experiment. Even with this limit, the V-S correlation still over-predicts the Kuhn heat transfer data by more than 100% at high mixture Re inside of tubes. However, as shown in Figure 6-35, the K-S-P correlation agrees well with the (unmodified) Vierow-Schrock correlation over the range of data in the Vierow experiment.

Although the V-S correlation over-predicts the heat transfer coefficients overall, it predicts more degradation from noncondensable gases (lower heat transfer coefficients) than does the K-S-P correlation, as shown in Figure 6-36. It is the f_1 factor, which causes the over-prediction of the modified Vierow-Schrock correlation.

The K-S-P correlation has a standard deviation of 7.4% when compared to the pure steam data and a standard deviation of 17.6% when compared to the 70 steam-air tests of Kuhn. The Kuhn experiment benefited from the experience of previous researchers and, as a result, provided the best set of data.

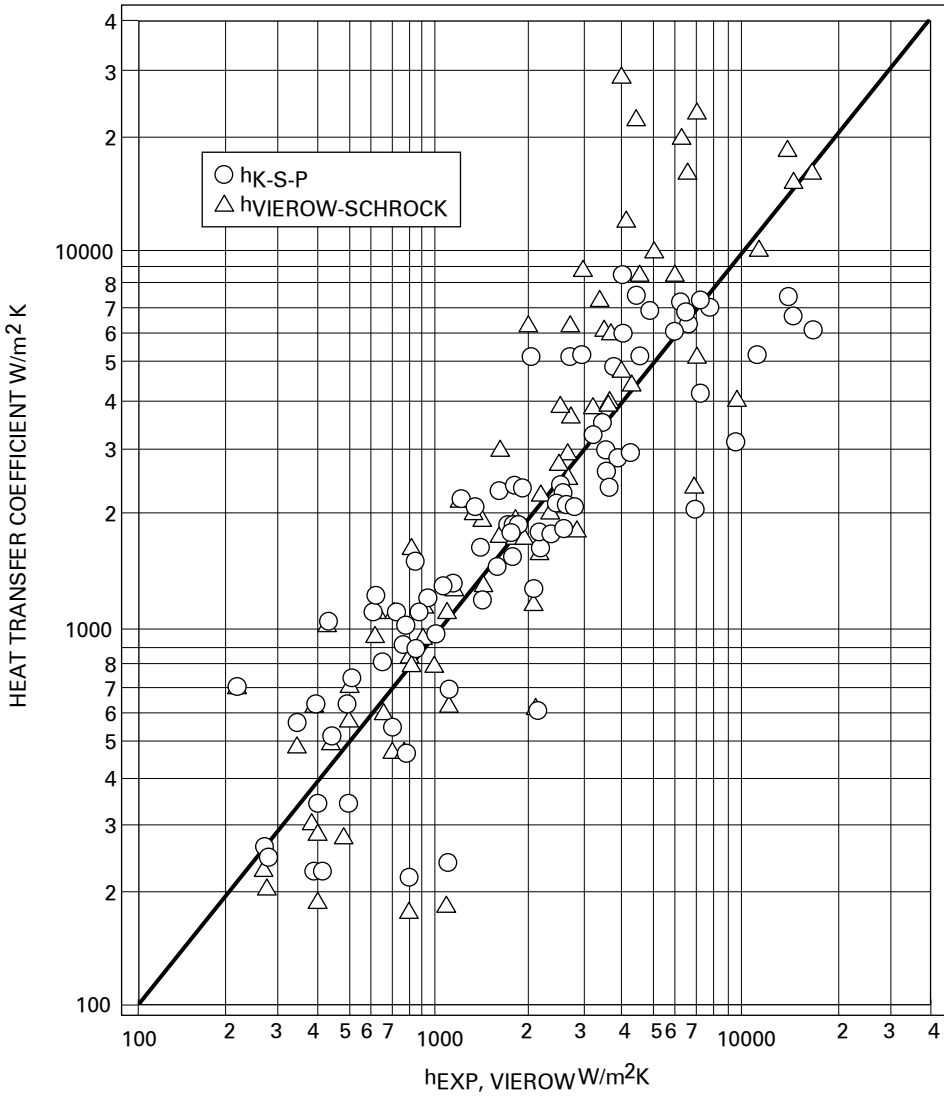

Figure 6-35. Heat Transfer Coefficients Predicted by K-S-P and Vierow-Schrock Correlations versus Vierow's Experimental Data

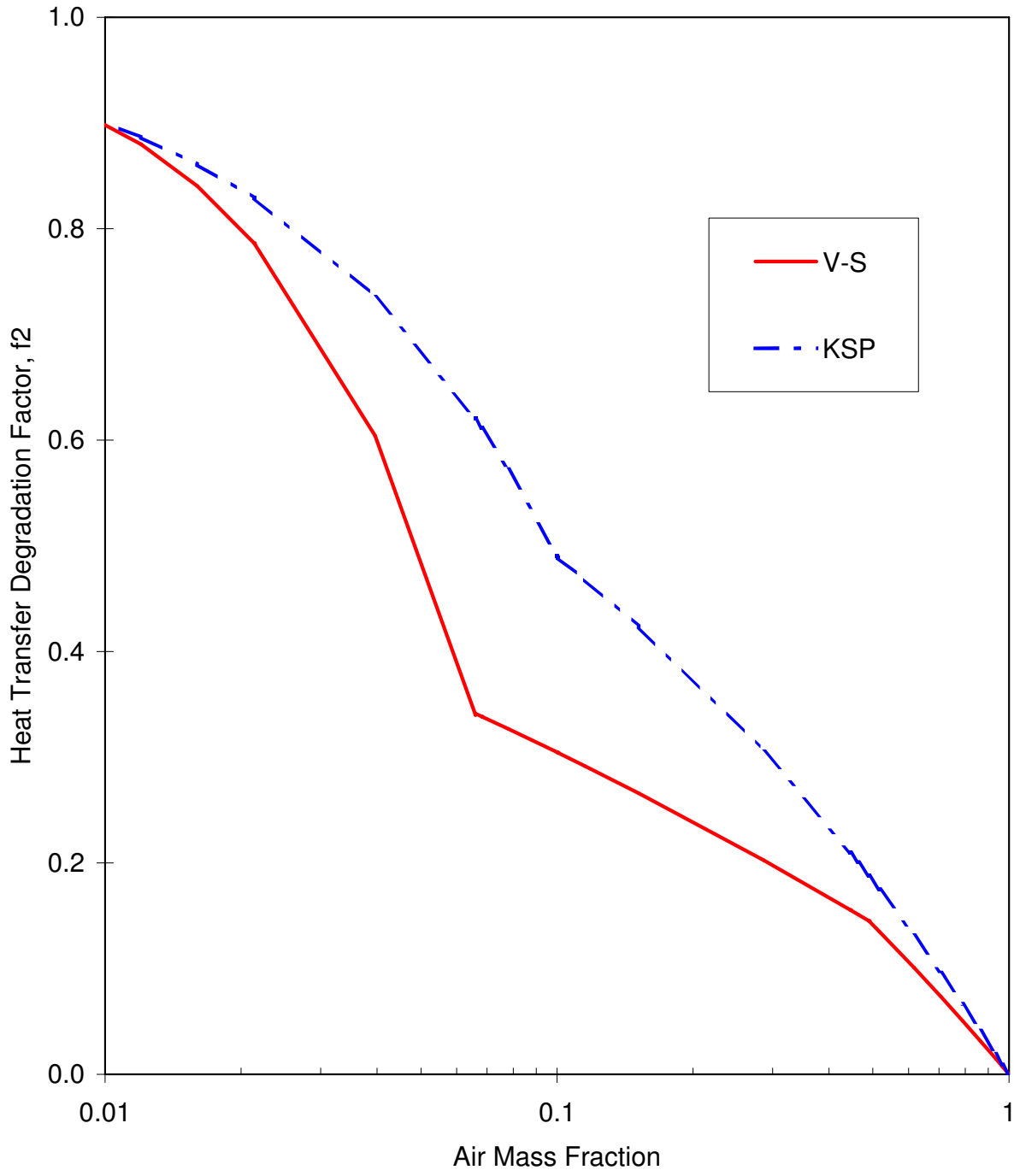

Figure 6-36. Comparison of the V-S and K-S-P Predictions of Heat Transfer Degradation Due to the Presence of Air

Figure 6-37 shows a plot of the normalized average heat transfer coefficient predicted by the recommended correlations (K-S-P for laminar flow, Equation (6.6-105) for turbulent flow) versus the condensate liquid Reynolds number for a case with a gas mixture Reynolds number of zero. This is plotted against other correlations found in Collier[147] for flat plate condensation.

TRACG agrees well with Dukler in both the laminar and low-end turbulent range and the Seban analytical equation in the low-end turbulent range (Pr = 1). Above Re_ℓ = 20,000 TRACG predicts lower heat transfer than Colburn and higher heat transfer than both Seban and Dukler. The slope is the same as the Colburn slope ($Re^{1/3}$). Equation (6.6-105) was chosen because it has the same slope as Colburn and also because it falls in between the well-established turbulent condensation expressions for Pr = 1. Because the spread in these expressions is large, an appropriate uncertainty to use in sensitivity analysis for condensation in the turbulent regime is 20%.

Steam Condensation in Containment

As shown in Figure 6-37, the TRACG correlation is in good agreement with correlations designed for vertical plate condensation. Most of the condensation in the containment will be similar to this situation. Thus, TRACG should provide a good estimate of the condensation heat transfer coefficient. If the containment contains significant amounts of horizontal surface area, care should be taken to model this area with a non-horizontal equivalent area since no condensation heat transfer will be predicted using $g \cos(0^o) = 0$.

Comparison of the K-S-P correlation[149] with tube data has shown a standard deviation of 7% with pure steam data, 18% with steam-air data and 13% for helium/air. [[

]]

A comparison of the normalized average heat transfer coefficient predicted by TRACG with three commonly used models for flat plates. Figure 6-37 also shows that the TRACG model agrees well with the Dukler model for laminar and low-end turbulent flow conditions. For film Reynolds numbers larger than 20,000, TRACG predictions fall between the predictions by the Seban and Colburn models. It should be noted that at such high Reynolds numbers, the heat transfer quickly becomes conduction controlled and the condensation heat transfer coefficient has a very small effect on the overall heat transfer rate. Considering the fact that TRACG predictions fall between the predictions by two flat plate condensation models, and since the distribution and the deviations for these models are not known, it was decided to increase the maximum standard deviation for the tube data by [[ ]] to account for the spread of the flat plate correlations, [[ ]].

[[

]]

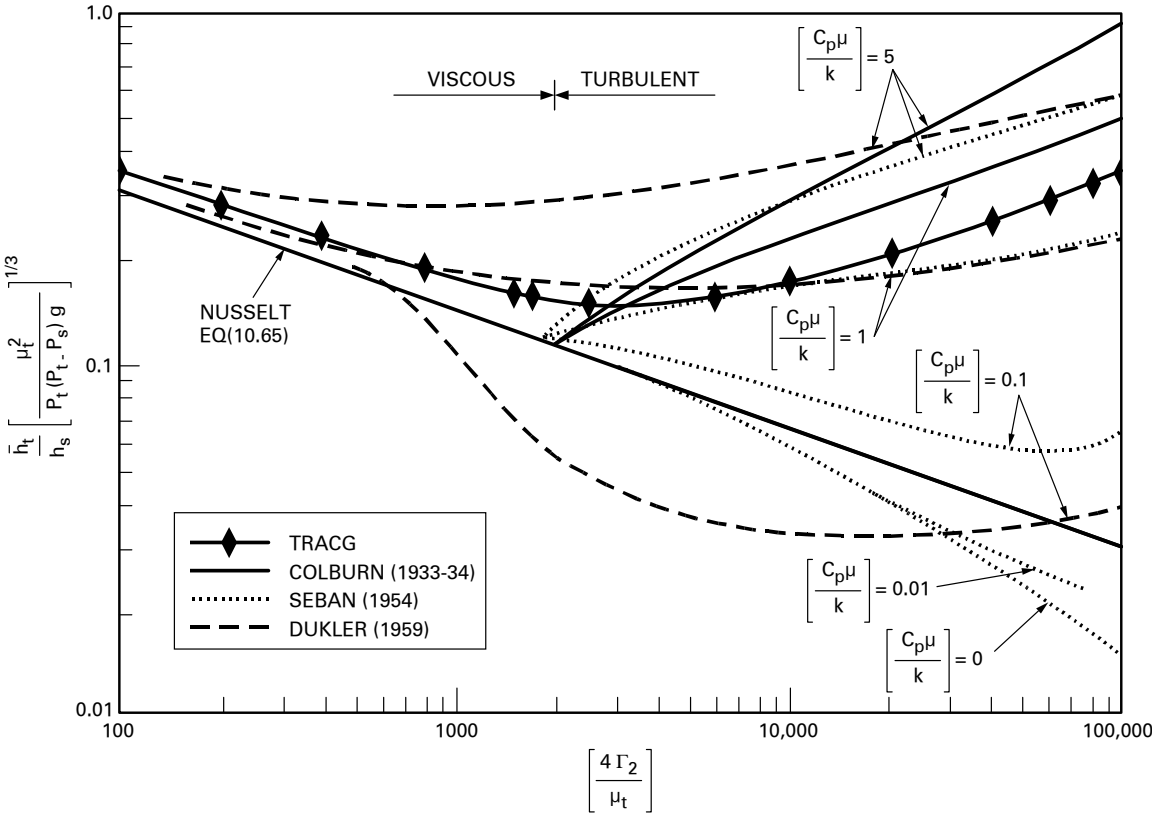

Figure 6-37. Comparison of the Average Heat Transfer Coefficients versus Film Reynolds Number

The Uchida correlation was based on data obtained from a vertical flat plate of 300 mm in height. Figure 6-38 shows a comparison of the K-S-P, V-S, Dehbi[150] and Uchida correlations. The comparison is made by averaging over a vertical slab of 5 meters in height. All four of the correlations are in reasonable agreement for air mass fractions less than 0.1. As the air mass fraction increases, the Uchida correlation predicts less heat transfer than the other three correlations. The Vierow-Schrock correlation predicts lower heat transfer than K-S-P due to the lower f_2 factor. The Uchida correlation, while widely used, has the least physical basis of any of the correlations. The only parameter is the air mass fraction. Thus, it does not take into account pressure or large vertical condensing surfaces, which may be present in a containment. It is useful, however, in obtaining the effect on containment performance of a low condensation heat transfer coefficient. Typically, though, the long-term heat transfer is dominated by conduction through the wall. Any error in the heat transfer coefficient will affect the rate of condensation, but will have only a minimal effect on the total amount of steam condensed in the drywell. This is due to the heat transfer from bodies of high thermal mass in the containment eventually being controlled by conduction. The total steam condensed will be nearly identical using any of the four correlations.

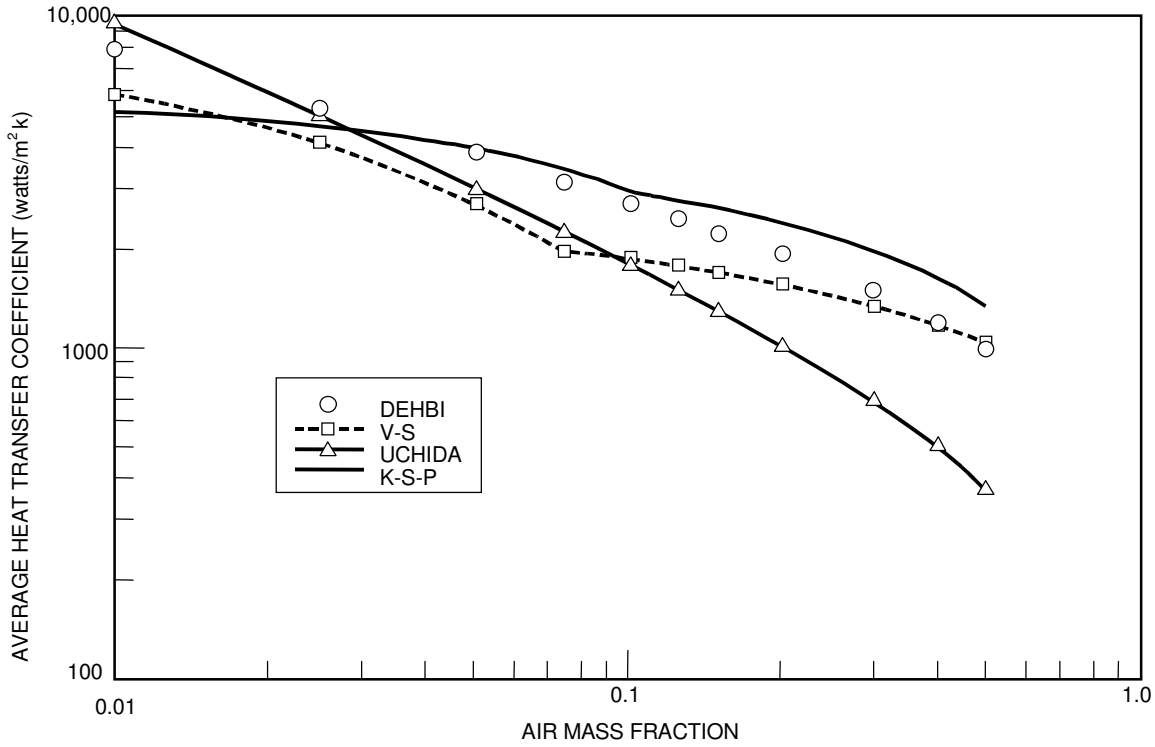

Figure 6-38. Comparison of Average Heat Transfer Coefficients Predicted by Four Correlations under Containment Conditions

6.6.12 Thermal Radiation

During a BWR loss-of-coolant accident (LOCA), radiation heat transfer may account for a significant amount of the total heat transfer in the fuel bundle. An analytical model for calculating radiation heat transfer in a BWR fuel bundle was established and implemented into TRACG. The model considers surface-to-surface radiation and the interaction between radiation and the two-phase mixture in the bundle. The surface-to-surface radiation model contains a first-order anisotropic transport correction, and the interaction with the two-phase mixture consists of absorption and emission.

6.6.12.1 Radiation Heat Transfer Model - Technical Basis and Assumptions

The radiation heat transfer model is similar to the model in References [104] and [116]. The model is based on the following assumptions:

- All surfaces are gray.
- All surfaces have uniform temperatures.
- All surfaces emit radiation diffusely.
- The two-phase fluid between surfaces has uniform temperature, and it absorbs and emits radiation.
- The semi-gray radiation model is applied for the two-phase mixture (i.e., absorption is based on the wall temperature, while emission is based on the temperature of the

two-phase mixture).

- A first-order anisotropic transport correction is applied for surface reflections. For large and/or curved surfaces, there is generally a tendency for radiation to be reflected backwards towards the origin of the incident radiation. Hence, the assumption that a fraction, μ, of the incident radiation is reflected backwards toward the origin, whereas the rest, $1-\mu$, is reflected uniformly in all directions, is a significant improvement over the assumption of isotropic reflection.

The radiosity of surface i, B_i can be expressed as the sum of the emitted and reflected radiation (Figure 6-39):

$$B_i = \varepsilon_i S_i + (1-\varepsilon_i) H_i \tag{6.6-118}$$

where:

$$S_i = \sigma T_i^4 \tag{6.6-119}$$

$$H_i = \sum_j H_{ji} \tag{6.6-120}$$

and H_{ji} is the incident radiation of surface i coming from surface j.

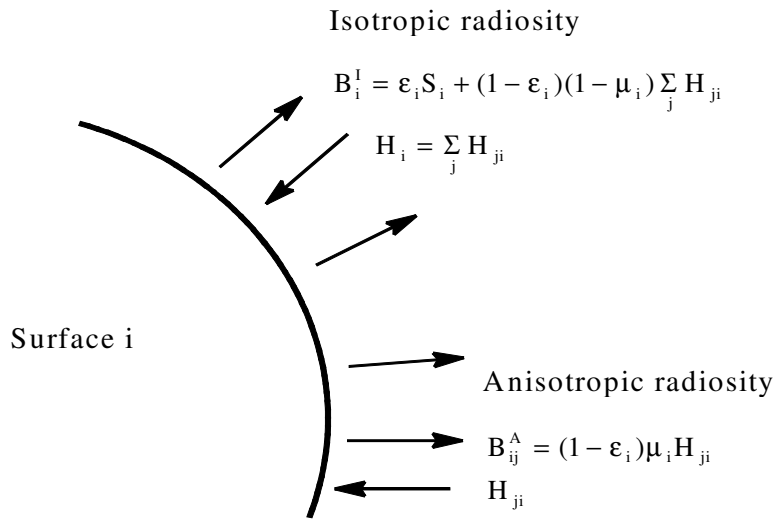

Figure 6-39. Radiation Heat Transfer at a Surface

The isotropic part of the radiosity of surface i, B_i^I, is given by:

$$B_i^I = \varepsilon_i S_i + (1-\varepsilon_i)(1-\mu_i) H_i \tag{6.6-121}$$

and the anisotropic part, B_{ij}^{A}, which is reflected back to surface j, is:

$$B_{ij}^{A} = \mu_i \ (1-\varepsilon_i) \ H_{ji} \tag{6.6-122}$$

The incident radiation from the direction of surface j is the sum of the radiation leaving surface j in the direction of surface i reduced by the transmissivity of the medium plus what is emitted by the medium:

$$H_{ji} = \frac{1}{A_i} \left(A_j \ B_j^{I} \ F_{ji} + A_j \ B_{ji}^{A} \right) \tau_{ji} + \varepsilon_{mij} \ F_{ij} \ S_{mij} \tag{6.6-123}$$

After simple algebraic manipulations, the following expression is obtained:

$$B_{ij}^{A} = (a_{ij} \ B_i^{I} + b_{ij} \ B_j^{I} + c_{ij} \ ) \ F_{ij} \tag{6.6-124}$$

where:

$$a_{ij} = \frac{X_i \ X_i \ \tau_{ij} \ \tau_{ji}}{1-X_i \ X_j \ \tau_{ij} \ \tau_{ji}} \tag{6.6-125}$$

$$b_{ij} = \frac{X_i \ \tau_{ji}}{1-X_i \ X_j \ \tau_{ij} \ \tau_{ji}} \tag{6.6-126}$$

$$c_{ij} = \frac{X_i \ (\varepsilon_{mij} \ S_{mij} + X_j \ \tau_{ji} \ \varepsilon_{mji} \ S_{mji})}{1-X_i \ X_j \ \tau_{ij} \ \tau_{ji}} \tag{6.6-127}$$

$$X_i = \mu_i \ (1-\varepsilon_i) \tag{6.6-128}$$

$$\tau_{ij} = e^{-(a_{\ell ij} + a_{vij}) R_{ij}} \tag{6.6-129}$$

$$\varepsilon_{mij} = \varepsilon_{\ell ij} + \varepsilon_{vij} \tag{6.6-130}$$

$$S_{mij} = \frac{\varepsilon_{\ell ig} \ S_\ell + \varepsilon_{vij} \ S_v}{\varepsilon_{\ell ij} + \varepsilon_{vij}} \tag{6.6-131}$$

$$S_\ell = \sigma \ T_\ell^{4} \tag{6.6-132}$$

$$S_v = \sigma \ T_v^{4} \tag{6.6-133}$$

$$\varepsilon_{\ell ij} = \frac{a_\ell}{a_\ell + a_v} \left[1-e^{-(a_\ell + a_v) R_{ij}} \right] \tag{6.6-134}$$

$$\varepsilon_{vij} = \frac{a_v}{a_\ell + a_v}\left[1-e^{-(a_\ell + a_v)R_{ij}}\right] \tag{6.6-135}$$

$$a_{\ell ij} = \frac{a_{\ell,i}\ S_i + a_{\ell,j}\ S_j}{S_i + S_j} \tag{6.6-136}$$

$$a_{vij} = \frac{a_{v,i}\ S_i + a_{v,j}\ S_j}{S_i + S_j} \tag{6.6-137}$$

a_{vi} and $a_{\ell i}$ are the vapor and liquid absorption coefficients, respectively. For absorption, these coefficients are evaluated at the temperature of the surface, while the temperature of the vapor is used for emission from the vapor.

Combine Equations (6.6-119), (6.6-121), (6.6-122) and (6.6-124) to obtain the following expression:

$$B_i^I = \varepsilon_i S_i + \frac{1-\mu_i}{\mu_i}\sum_j \left(a_{ij}B_i^I + b_{ij}B_j^I + c_{ij}\right) F_{ij} \tag{6.6-138}$$

Equation (6.6-138) describes a system of linear equations that can be solved for B_i^I.

The heat flux of surface i, is the difference between the radiosity and incident radiation:

$$q_i = B_i - H_i \tag{6.6-139}$$

Combining Equations (6.6-118), (6.6-121) and (6.6-139) yields:

$$q_i = \frac{\varepsilon_i}{1-\varepsilon_i}\ \frac{S_i\ [1-\mu_i\ (1-\varepsilon_i\ )] - B_i^I}{1-\mu_i} \tag{6.6-140}$$

The energy absorbed and emitted by vapor is given by the following equations:

$$Q_{abs,v} = \sum_i \sum_j A_i \left(F_{ij}\ B_i^I + B_{ij}^A\right)\left(1-\tau_{ij}\right)\frac{a_{vij}}{a_{vij} + a_{\ell ij}} \tag{6.6-141}$$

and:

$$Q_{emit,v} = \sum_i \sum_j A_i\ \varepsilon_{mij}\ \frac{\varepsilon_{vij}S_v}{\varepsilon_{vij} + \varepsilon_{\ell ij}}\ F_{ij} \tag{6.6-142}$$

Similar expressions can be written for the absorption and emission for the liquid. Energy conservation can be shown by:

$$\sum_i\ Q_i = Q_{abs,\ell} + Q_{abs,v} - Q_{emit,v} - Q_{emit,\ell} \tag{6.6-143}$$

after simple algebraic manipulations.

Net heat fluxes for surface i to either vapor or liquid can be derived from Equations (6.6-141) and (6.6-142), as follows:

$$q_{i,v} = \sum_j \left\{ \left(F_{ij} B_i^I + B_{ij}^A \right) \left(1 - \tau_{ij} \right) \frac{a_{vij}}{a_{\ell ij} + a_{vij}} - F_{ij} \varepsilon_{vij} S_v \right\} \tag{6.6-144}$$

$$q_{i,\ell} = \sum_j \left\{ \left(F_{ij} B_i^I + B_{ij}^A \right) \left(1 - \tau_{ij} \right) \frac{a_{\ell ij}}{a_{\ell ij} + a_{vij}} - F_{ij} \varepsilon_{\ell ij} S_\ell \right\} \tag{6.6-145}$$

6.6.12.2 Model as Coded

The equations for the isotropic radiosities as given by Equation (6.6-138) constitute a system of linear equations and are solved by direct inversion.

The view factors and the beam lengths are dependent on the geometry only and are given by the general expressions[160]:

$$F_{ij} = \frac{\int_{A_i} \int_{A_j} \frac{\cos\beta_i \cos\beta_j}{\pi R^2} dA_j dA_i}{A_i} \tag{6.6-146}$$

and

$$R_{ij} = \frac{\int_{A_i} \int_{A_j} \frac{\cos\beta_i \cos\beta_j}{\pi R} dA_j dA_i}{A_i} \tag{6.6-147}$$

where R is the distance between two points on surface i and j, and β_i and β_j are the angles between the line R and the normals to surface i and j respectively. For elongated surfaces, as radiation in the axial direction is neglected, Equations (6.6-146) and (6.6-147) reduce as indicated in Reference [159] to:

$$F_{ij} = \frac{\int_{S_i} \int_{S_j} \frac{\cos\beta_i \cos\beta_j}{2R} dS_j dS_i}{S_i} \tag{6.6-148}$$

and

$$R_{ij} = \frac{\int_{S_i} \int_{S_j} \frac{\cos\beta_i \cos\beta_j}{2} dS_j dS_i}{S_i} \tag{6.6-149}$$

where R is the distance between two points along the perimeter of surface i and j, and β_i and β_j are the angles between the line R and the normals to perimeter i and j, respectively. Equations (6.6-136) and (6.6-137) are integrated directly by numerical integration.

The interaction of the thermal radiation with steam and droplets is based on the semi-grey radiation model, and the assumption that the medium is optically thin. For the droplets it can be shown[142] that, when the medium is optically thin, scattering can be neglected and the absorption coefficient will be given by:

$$a_\ell = 1.11 \frac{\alpha_d}{d_d} \qquad (6.6\text{-}150)$$

Reference [159] indicates that the absorption coefficient for the steam is a function of the temperature and pressure. A good polynomial fit is given by:

$$a_v = P \cdot 10^{-5} \left(5.2 \cdot 10^{-4} - 9 \cdot 10^{-7} T + 5.6 \cdot 10^{-10} T^2 - 1.2 \cdot 10^{-13} T^3\right) \qquad (6.6\text{-}151)$$

6.6.12.3 Applicability

The ranges of parameters in which the assumptions are valid include low pressures and high temperatures. This is the range where core spray heat transfer applies for BWR LOCA conditions. The radiation heat transfer model is identical to the radiation heat transfer model in CORECOOL[142], and has been extensively tested as part of the SAFER/CORECOOL[116] models. CORECOOL was found to accurately predict core spray heat transfer and peak cladding temperatures[116] for the following ranges:

$0.1 < P < 7.0$ MPa

$T_{sat} < T < 1420$ K

Peak cladding temperatures were predicted with an average error of [[ ]] and standard deviation of [[ ]].

6.6.13 Quenching Heat Transfer

Experimental studies simulating the re-flood stage of a postulated loss-of-coolant accident for a BWR indicate that cladding temperature history can reasonably be characterized by the boiling curve with rewet being controlled by the transition boiling model. Details are provided in Sections 6.6.6 through 6.6.8 of this document and References [116] and [153]. An optional model for conduction controlled quenching existed in prior versions of TRACG but had been deactivated. This model has been enhanced and is recommended for use for LOCA simulations. The quench model is described briefly below.

6.6.13.1 Technical Basis and Assumptions

The re-flood initialization consists of a search to locate quench fronts. Rather than assume that the core is dry at the beginning of re-flood, which may not be the case, a pattern search of each average rod is made for the combined condition of clad surface temperature less than the quench front temperature and sufficient liquid available to form a film on the rod. Two quench fronts per rod group or channel box surface are accounted for: (1) a falling film from the top and (2) a bottom quench front.

The motion of a quench front on a hot surface is a complex function of axial conduction, radial convection both ahead and behind the front, internal heat generation, and heat transfer. Since axial conduction of heat from ahead of the front to the quenched side occurs on a length scale of a centimeter or less, and typical fuel rods are several meters long, analytical methods have been developed to approximate quench front motion without resorting to costly two-dimensional conduction solutions[160],[161]. A correlation, which approximates the one- and two-dimensional solutions of References [116] and [153], is used for the quench front velocity v_q:

$$v_q = \frac{k_w}{\rho_w \, C_{pw} \, d_w} \left(\overline{Bi} \, (1+0.40\overline{Bi}) \right)^{0.5} \tag{6.6-152}$$

where:

$$\overline{Bi} = \frac{Bi}{\overline{T}^2} \tag{6.6-153}$$

$$Bi = \frac{h_q d_w}{k_w} \tag{6.6-154}$$

$$\overline{T} = \frac{\sqrt{\Theta}}{1-\Theta} \tag{6.6-155}$$

$$\Theta = \frac{T_w^+ - T_o}{T_w^+ - T_{sat}} \tag{6.6-156}$$

and:

h_q = Heat transfer coefficient just behind the quench front

T_o = Quench front temperature

T_w^+ = Wall temperature just ahead of the quench front

d_W = Wall thickness

There is considerable ambiguity as to the proper definition of the quench front temperature. The value used in TRACG is the same as in the SAFER[116] model:

$$T_o = T_s + 65 \text{ K} \tag{6.6-157}$$

The value of the heat transfer coefficient used in Equation (6.6-154) in the quench front correlation is the maximum of either the heat transfer coefficient just behind the quench front, h_ℓ^-, or an experimentally determined value. For quenching from the top by a falling film on the surfaces a value of [[ ]] is used. This value is correlated from quench front propagation data and validated for core spray heat transfer data in Reference [116]. For reflooding from below, the value is based on an empirical correlation developed for TRACC-P1A based on FLECHT reflood data[162]:

$$h_q = \begin{cases} 4.2 \cdot 10^8 V_r^{0.992} (T_o - T_{sat})^{-0.308} & \text{for} \quad V_r > 0.0092 \\ 1.9 \cdot 10^9 V_r^{2.3} (T_o - T_{sat}) & \text{for} \quad V_r < 0.0092 \end{cases} \tag{6.6-158}$$

where V_r is the reflood velocity obtained from the liquid velocity upstream of the quench front.

The volumetric heat removal rate due to the advancement of the quench front is:

$$q'''_w = \rho_w \; C_{pw} \; v_q \; (T_w^+ - T_{sat}) \tag{6.6-159}$$

6.6.13.2 Model as Coded

The model has been encoded as described by Equations (6.6-152) through (6.6-159) with the following limitations:

- An upper limit on the quench front velocity of 0.5 m/sec. is applied.
- For re-flooding from the bottom, a multiplier is applied to the quench front velocity for high void fractions forcing the quench front velocity to 0.0 as the void fraction approaches 1.0. The multiplier is given by: 1.0 for $\alpha < 0.85$ and $\frac{0.995 - \alpha}{0.145}$ for $0.85 < \alpha < 0.995$.
- For quenching due a falling film due to the overhead core spray sparger in the BWR, a multiplier is applied to the quench front velocity for high void fractions forcing the quench front velocity to 0.0 as the void fraction approaches 1.0. The multiplier is given by: 1.0 for $\alpha < 0.975$ and $\frac{0.995 - \alpha}{0.020}$ for $0.975 < \alpha < 0.995$.

6.6.13.3 Applicability

The quench front model is primarily applicable to film front quenching and re-flood quenching for conditions, where the heat transfer coefficient ahead of the quench front is small compared to the quench front heat transfer coefficient. For conditions where a significant precursory cooling exists, the quench front model will conservatively under-predict the quench front velocity.

6.6.14 Metal-Water Reaction

At high temperatures, the zirconium used for the fuel rod cladding and the fuel channel box will react chemically with the steam:

$$Zr + 2\,H_2O \rightarrow ZrO_2 + 2\,H_2 + Q \tag{6.6-160}$$

6.6.14.1 Technical Basis and Assumptions

The reaction rate is a function of the temperature and is given by Cathcart[163]:

$$\frac{ds}{dt} = \frac{3.473\ 10^{-6}}{s} \exp\left(-\frac{2.010\ 10^4}{T}\right) \tag{6.6-161}$$

where s is the thickness of the oxide layer.

The heat generation rate is given by:

$$Q = 6.45 \text{ MJ/kg}_{Zr} \quad (6.6\text{-}162)$$

6.6.14.2 Model as Coded

The metal-water reaction is calculated by direct integration of Equation (6.6-161).

6.6.14.3 Applicability

The metal-water reaction rate is calculated by the Cathcart correlation[163] assuming that the reaction rate is limited by diffusion through the Zirconium-oxide layer. For severe conditions with large hydrogen generation, the reaction rate can be limited by vapor diffusion through a hydrogen film at the surface. This process is not modeled and will lead to an over-prediction of the reaction rate for this condition.

6.6.15 Assessment and Application to BWR

The technical basis for the wall heat transfer correlations and their applicability were discussed in Sections 6.6.3 through 6.6.11. Those sections discussed the ranges of applicability of the specific correlations and also compared the correlations to other data or other correlations. This section discusses the performance of TRACG in situations where the wall heat transfer correlations are used. The *TRACG Qualification LTR*[6] discusses in detail many comparisons of calcualted results to experimental data. Some of those comparisons will be highlighted here.

A comparison of heat transfer coefficients directly evaluated from the specific correlations to those calculated by TRACG for single-phase water flow in a pipe at a pressure of 0.5 MPa is shown in Figure 6-40. From left to right (low to high flow) the correlation changes from natural convection to turbulent flow. In both regimes, the heat transfer value from the alternate calculation agrees well with the heat transfer coefficient calculated by TRACG. This provides assurance that the correlations have been correctly implemented into TRACG.

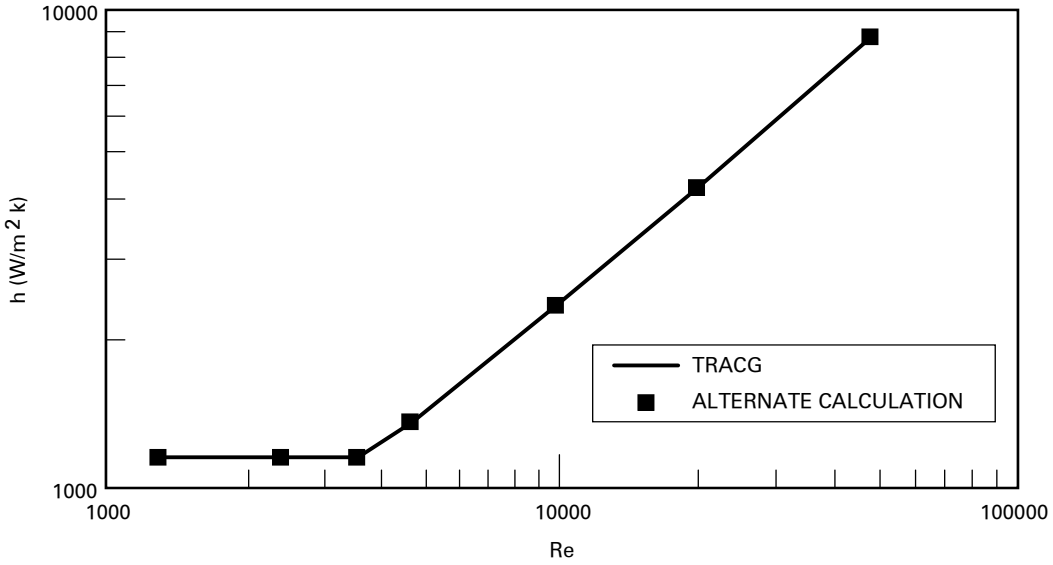

Figure 6-40. Comparison of TRACG Calculated Heat Transfer Coefficients and Alternate Calculations for Single Phase Flow

Comparisons of TRACG predictions of nucleate boiling are made in Section 6.5.11. That section shows comparisons of the void fraction predicted by TRACG to the data from the Christensen sub-cooled boiling tests. The calculations are in good agreement with the data. This provides an assessment of the split of energy from the wall that goes into vapor generation versus heating up the bulk sub-cooled liquid. Figure 6-41 is a comparison of heat transfer coefficients evaluated directly from the correlations with those made by TRACG for a heated 12 mm diameter pipe at 7.2 MPa with an inlet flow velocity of 0.8 m/sec. At the bottom of the pipe, the heat transfer is by turbulent single-phase heat transfer using the Dittus-Boelter correlation. As more heat is added to the liquid, it transitions into sub-cooled and then saturated nucleate boiling. The independent calculations of the correlations (based on ASME physical properties) agree well with the TRACG generated coefficients. The heat transfer coefficients plotted for the Chen correlation (nucleate boiling) are the sum of the macroscopic and microscopic heat transfer coefficients. This was done for comparison purposes. In TRACG, the two-heat transfer coefficients are multiplied by different temperature differences as detailed in Section 6.6.4.

The ability of TRACG to predict boiling transition in a BWR fuel bundle was shown in Section 3.6 of References [4], [5] and [6]. That section describes flow oscillation tests on a GE11 bundle and transient tests for a GE9 bundle in the ATLAS thermal-hydraulic test facility. The flow rates for the oscillation tests were selected such that the bundle had dryout-rewet behavior. The tests show that TRACG, using the GEXL correlation accurately predicts transient critical power behavior. The calculated ΔCPR values compare well with the experimental values as do the calculated time to the onset of boiling transition for the transient tests.

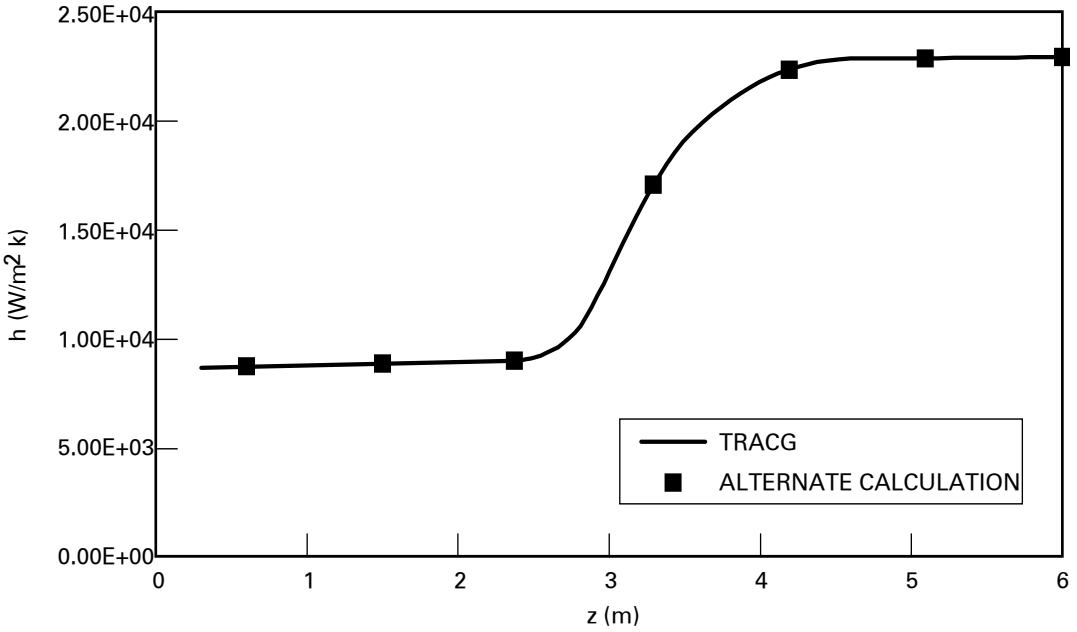

Figure 6-41. Heat Transfer Coefficient from Heated Vertical Pipe Flow

The ability of TRACG to predict correct heat transfer for conditions of low void fraction film boiling is shown in Section 5.4 of Reference [6]. TRACG was used to predict the system response of the SSTF test facility during refill-re-flood transients of a BWR/6 large break LOCA. TRACG predicts the overall system performance well.

TRACG was also used to predict film boiling at high void fraction in the THTF test facility. The results are shown in Sections 6.5.11 and 3.2.1 of the *TRACG Qualification LTR*[6].

Applicability of the wall heat transfer correlations for BWRs is summarized by a comparison against the table of desired ranges for various reactor and containment regions (Table 6-18). The desired ranges are shown in Table 6-1. The most important regions from the standpoint of wall heat transfer are the core, the drywell, and, to a lesser extent, the wetwell air space. The PCC and IC components are covered in Section 6.6.11.

Wall Heat Transfer Regimes: There are specific correlations for all wall heat transfer regimes encountered in the core, the drywell and the wetwell air space. These are listed and discussed in Sections 6.6.1 through 6.6.14.

Hydraulic Diameter: The correlations are valid for the desired range of hydraulic diameter for the core region. For containment volumes, the correlations are valid with the use of the equivalent hydraulic diameter concept, but with larger uncertainty. The major heat transfer regime of importance is condensation. Film condensation on walls is not dependent on the hydraulic diameter.

Mass Flux/Reynolds Number: The wall heat transfer correlations are validated over the range of mass flux and Re data encountered in the core. In the wetwell airspace and drywell, the range of mass fluxes and Re are well covered. The liquid Re number for condensate flow can become quite large. This has been well assessed in Section 6.6.11 and several conditions exist in the literature up to $Re_\ell = 100{,}000$.

Pressure: The correlations applicable for the drywell and wetwell air space were developed within the pressure ranges of these compartments. The correlations for the core were typically developed for pressures up to 7 MPa. Extension to higher pressures is based on assessment of pertinent parameters (CHF, film boiling, rewet) for pressurization transient.

Void Fraction: The void fraction ranges are covered in all the regions.

Table 6-18. Applicability of Wall Heat Transfer Models to BWR Regions

Region	Wall HT Regimes	Size (m)	Range of Conditions			
			P (MPa)	G (kg/m^2-s)	Void	Reynolds No.
				CN	C	CE
GT	C	CE	CA	C	C	C
Core	C	C	CA	C	C	C
Bypass	C	C	CA	C	C	C
Upper Plenum	C	CN	CA	C	C	CE
Mixing Region	C	CN	CA	C	C	CE
Steam Dome	C	CN	CA	C	C	C
Steam Line	C	CN	CA	CE	C	CE
Down-comer	C	CE	CA	CE	C	CE
Recirculation Loop	C	CE	CA	CE	C	CE
Drywell	C	CE	C	C	C	CA
Wetwell Air Space	C	CE	C	C	C	CA
Suppression Pool	C	CE	C	CE	C	CE
Main Vents	C	CA	C	C	C	C
ESBWR Chimney	C	CN	CA	C	C	C

Legend:

C	Correlation database and separate effects tests cover range
CA	Correlation supplemented by assessment covers range
CE	Correlation supplemented by reasonable physical basis
CA/CE	Assessed against geometrically scaled data
CN	Correlation range limited but phenomenon not significant
N/A	Correlation not applicable over range

6.7 Turbulent and Molecular Mixing Models

Single- and two-phase fluid mixing models have been formulated to account for mixing due to molecular and turbulent diffusion. These optional models are selectable via user input. The formulation focuses on describing the local mixing velocity j* separately, first for turbulent diffusion and then for molecular diffusion.

During turbulent flow, volumes of fluids are exchanged laterally among adjacent locations leading to transport of mass, momentum and energy. These mixing effects alter local axial mass flux, quality, void fraction and enthalpy distributions.

A mixing model has been incorporated to account for this turbulent flow behavior. The model accounts for exchange of mass, momentum, and energy laterally. This exchange is caused by turbulent shear and eddy interchange. It is able to account for the void profile, pressure drop characteristics, and enthalpy distribution more accurately than a model which ignores these phenomena.

Typical applications may include turbulent mixing phenomena in the upper plenum, containment, and molecular diffusion/convection for boron mixing.

6.7.1 Technical Basis and Assumptions

As a part of the two-phase turbulent mixing model development, an extensive study of existing literature has been made. The study identified fundamental measurements for phenomena such as jet and plume mixing, two-phase recirculation flow, and subchannel mixing. From these measurements, information has been obtained on local mixing velocities dependent on local thermodynamic and flow conditions[164],[165].

The mixing process (Figure 6-42) assumes equal volume exchange of two-phase mixture (eddies). This volume exchange is caused by turbulence of the flow field. The molecular diffusion process can also be shown to be an equal volume exchange process.

The lateral transport rates are functions of the cross flow area, lateral mixing velocities, and the fluid properties of the adjacent participating locations. The lateral cross flow area for turbulent exchange in the fluid continuum is typically larger than the axial flow area. Thus, even for small mixing velocities, the lateral exchange rates may be significant compared to the axial flow rates. Therefore, a model for "mixing velocity" (referred to as j* in the following formulation) is required for realistic evaluation of the two-phase conditions.

The following assumptions are made to model turbulent mixing and molecular diffusion:

- Equal volumes of two-phase mixture are exchanged among adjacent regions.
- In each computational cell, the properties of the incoming fluid volume and the resident fluids are perfectly mixed.
- Both vapor and liquid travel with the same lateral mixing velocity.

The mixing model is formulated as a net "outflow rate" due to mixing across the boundaries of a fluid control volume (node). The general formulation is applicable to mass, momentum, and energy exchange for both vapor and liquid transport due to mixing.

The general mathematical formulation of the two-phase mixing model is adapted from the model of Kazimi and Kelley[166]. The net outflow rate per unit volume due to mixing interaction among adjacent fluid regions, i and j, may be written as:

$$W_{ki} = \sum_j A_{ij}\, j^*[(\phi_k \rho_k)_i - (\phi_k \rho_k)_j] \qquad (6.7\text{-}1)$$

where

j	=	Index for surrounding cells
k	=	Liquid phase or vapor phase
A_{ij}	=	Inter–cell area per unit volume
ϕ_k	=	Unity for mass exchange Axial velocity, u_k for momentum exchange Enthalpy, h_k for energy exchange
ρ_k	=	Macroscopic density of phase k
j^*	=	Two-phase mixing velocity

The local single-phase or two-phase mixing velocity, j*, which is assumed to be equal for both the phases, is formulated to be proportional to the local mixture superficial velocity:

$$j^* = c\, j \qquad (6.7\text{-}2)$$

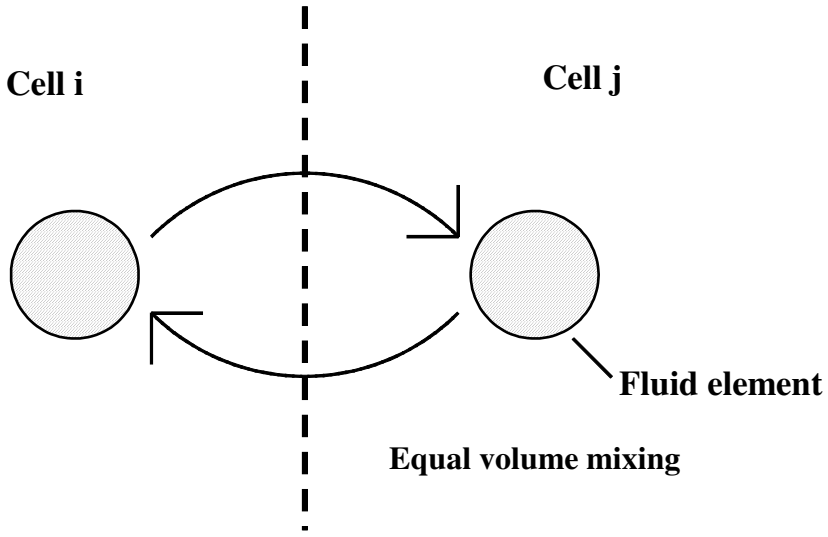

Figure 6-42. Turbulent Mixing in a Two-Phase Mixture

This formulation is based on observations of mixing behavior in jet, plume, and subchannel type mixing described in References [164] and [165]. From these references, a value of:

$$c = 0.1 \tag{6.7-3}$$

describes the turbulent mixing velocity in these tests. This value has been implemented into the TRACG mixing model. Qualification of the mixing model, along with sensitivity studies that vary the value of C to reflect the degree of mixing, are included in the following sections.

For molecular mixing, Fick's Law of Diffusion leads to:

$$j^* = \frac{D}{L} \quad \text{(molecular mixing)} \tag{6.7-4}$$

where D is the molecular diffusivity of the fluid mixture or solution and L is the typical mixing length. In the linearization scheme of TRACG, the lateral distance between node centers participating in the mixing process is chosen as the value for L.

6.7.2 Applicability

The mixing model described in the previous section is relatively simple, but has produced good results for a number of applications. Section 3.8 of References [4], [5] and [6] shows comparisons for void fraction distribution for the chimney regions of the Experimental Boiling Water Reactor (EBWR) and the VK-50 reactor. The predictions were generally within 0.1 of the measurements. Calculations made without the mixing term showed a larger variation between the central and peripheral regions, with less favorable agreement with the data. In both cases, the geometry was cylindrical with diameters from 1 to 2m. The pressure ranged from 4.6 to 6.4 MPa.

The model is based on data that includes low pressure conditions, and has been assessed against subchannel and plume mixing data over a range of pressures. The main limitation in the model is the use of a length scale which is not well defined. Because the length scale is typically the cell size, the results will be dependent on the nodalization, and empirical confirmation is needed at different scales.

The main applications where a mixing model is needed is for ECCS mixing in the upper plenum, for the distribution of noncondensable gases in the drywell, and for thermal stratification in the suppression pool.

For the upper plenum, a specific model has been developed based on the tracking of spray trajectories and submerged jet mixing. This model is described in Section 7.8.2.

The mixing model described in this section is not currently being used for containment applications. In the drywell, flows are calculated by application of the momentum equation (Section 3.1), with the mixing terms set to zero. Thus, the flows are dependent only on wall friction and buoyancy. The calculated noncondensable distributions provide a measure of the adequacy of the model. Comparisons[151] with the data obtained in the PANDA facility at the Paul Scherrer Institute show that the trends are reasonably predicted. In this context, the mixing

model is only being used for sensitivity studies. An alternate bounding approach will address the effects of the noncondensable distribution on containment performance.

Stratification in the suppression pool is being modeled empirically with TRACG. In this model, the portion of the pool below the lowest source of thermal energy is assumed to be stratified. The portion above the source will be well mixed. These phenomena are not sensitive to the mixing model used. The validity of the TRACG model has been demonstrated by comparison against a variety of large-scale data as summarized in Figure 7-44.

7.0 COMPONENT MODELS

Descriptions of the various component models included in TRACG are given in this section. A physical description of each component is presented with a typical noding diagram showing the conventions used to model the component. Mathematical models, including finite-difference approximations, are given only for those aspects of the component that are not covered in the basic hydrodynamics and heat-transfer descriptions. User options, restrictions on the use of the component and input/output information are also given. Specialized models for pumps, jet pumps, fuel channels, steam separators, and heat exchangers are described. Models for the steam dryer and the upper plenum regions of the vessel are also described.

The terminology and nomenclature in this section are generally consistent with the terminology and nomenclature defined previously in Sections 3.0 through 6.0. Symbols specific to a particular model are defined in the individual sections that follow.

7.1 Pipe

The pipe (PIPE) component models the flow in a one-dimensional (1-D) duct or pipe. The pipe component can be used alone in a simulation or it can be used as a connector between components to model a reactor system. Capability is provided to model area changes, wall heat sources, and heat transfer across the inner and outer wall surfaces. A wide selection of pipe materials is available to represent the wall material in the wall conduction calculation.

Figure 7-1 shows a typical noding diagram for a pipe containing a Venturi tube and an abrupt area change. The numbers within the pipe indicate fluid cell numbers. The positive sense for flow is the direction of increasing cell numbers. The geometry is specified by providing a volume and length for each cell and a flow area, hydraulic diameter and loss coefficient at each cell boundary. The junction variables, JUN1 and JUN2, provide reference numbers for connecting a pipe to other components. The numerical methods used to treat the thermal-hydraulics in the pipe are described in Section 8.2.

Input options are available to allow for wall heat transfer and to select correlations for CHF. Wall heat transfer can be omitted by setting the number of heat-transfer nodes (NODES) to zero. Generalized heat-transfer capability allows the user to specify heat exchange between any pipe cell and any other component fluid cell or wall node in the model. The generalized heat-transfer option is activated through the IHTS and IWT input parameters. The CHF calculation can be bypassed by setting the input parameter, ICHF, to a negative value.

Calculation of pressure drop due to wall friction losses for the pipe component described in Section 6.2.1 requires a wall roughness input by the user. An abrupt area change can be modeled by input of additional pressure loss factors. Because of central differencing, any irreversible losses must be modeled with an appropriate pressure loss factor.

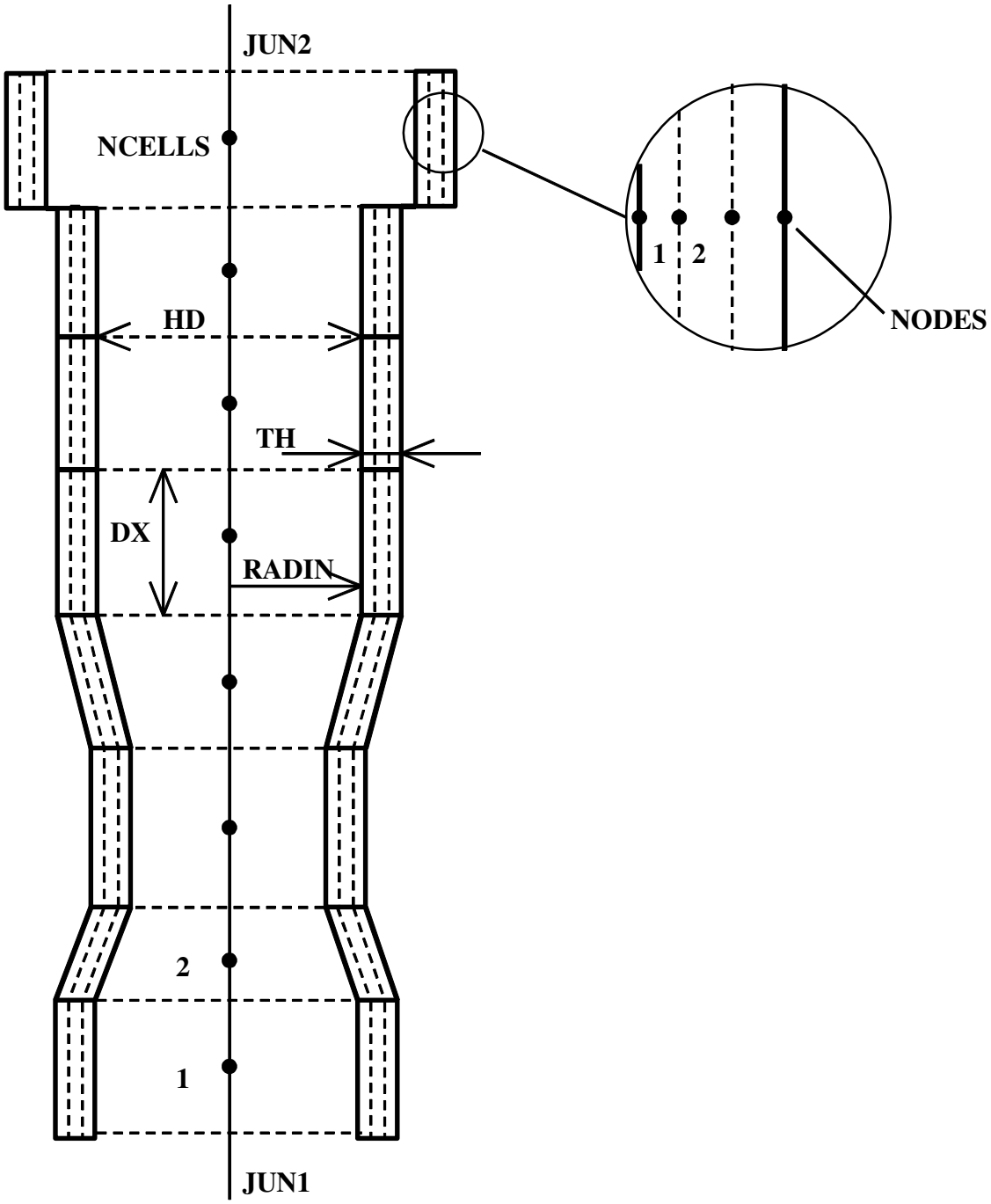

Figure 7-1. PIPE Noding Diagram

Pipe components may be connected to any other component. However, computational expense increases rapidly with the number of component junctions and the users are cautioned to minimize the number of components used in their models. In addition, 1-D cells of grossly different length should not be placed together, as this can cause computational difficulties, particularly when area changes also occur.

Output for a pipe consists of mass flow rate in and out of the pipe, mass flux in and out of the pipe, and nodal values of pressure, void fraction, liquid and vapor velocities, saturation temperature, liquid and vapor temperatures, liquid and vapor density, cell-to-cell pressure drop, choking, and CCFL indicators. If wall heat transfer is included, information on the heat-transfer regime, liquid and vapor HTC on inner and outer surfaces, surface heat fluxes to liquid and vapor on the inner wall surface, heat sources and wall temperatures for each radial node are printed for each axial cell.

7.2 Pump

The pump (PUMP) component is represented by a 1-D component with N cells (N > 1). Figure 7-2 shows a typical noding diagram for the pump component. The pump momentum is modeled as a source, called SMOM. SMOM is required to act between Cells 1 and 2; therefore, it is necessary to construct the cell noding such that the cell numbers increase in the normal flow direction.

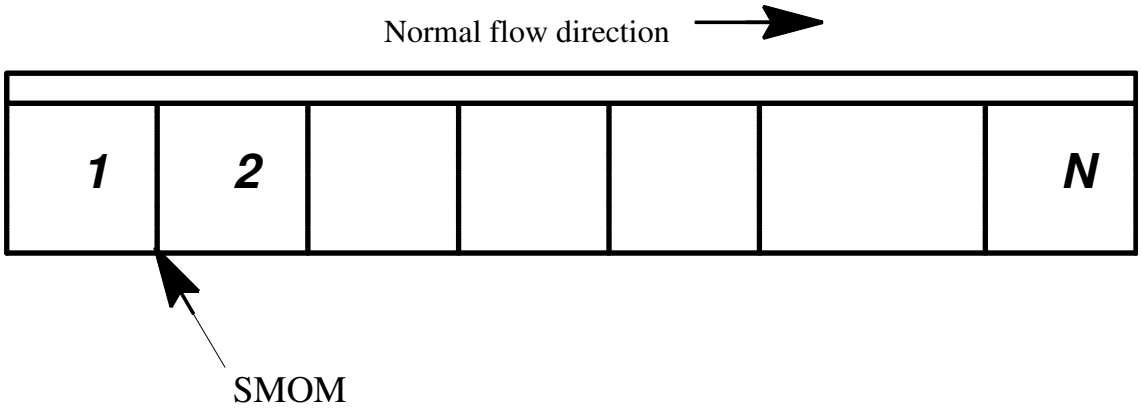

Figure 7-2. PUMP Noding

7.2.1 Pump Governing Equations

The pump component combines the PIPE component with pump correlations. The pump model is identical to the 1-D pipe model except that the momentum equations at the SMOM face are rewritten as:

$$\frac{v_\ell^{n+1} - v_\ell^{n}}{\Delta t} = \frac{P_1^{n+1} - P_2^{n+1} + \Delta P_p^{n+1}}{\rho_m \Delta x} - g\cos\theta \qquad (7.2\text{-}1)$$

where

$$\Delta P_p^{n+1} = \Delta P_p^{n} + \left(\frac{\partial \Delta P_p}{\partial v}\right)^n \left(v_\ell^{n+1} - v_\ell^{n}\right) + \left(\frac{\partial \Delta P_p}{\partial \Omega}\right)^n \left(\Omega^{n+1} - \Omega^{n}\right) \qquad (7.2\text{-}2)$$

and

$$v_v = v_\ell \qquad (7.2\text{-}3)$$

ΔP_p is the pressure rise through the pump evaluated from the pump correlation. The steady-state solution of Equation (7.2-1) is:

$$\Delta P_p = P_2 - P_1 + g\cos\theta\, \rho_m \Delta x \qquad (7.2\text{-}4)$$

which is the desired result. Friction does not enter explicitly into the pump motion equation. Therefore, additive friction is not allowed at the SMOM face.

The pump model describes the interaction of the system fluid with a centrifugal pump. The model calculates the pressure differential across the pump and its angular velocity as a function of the fluid flow rate and the fluid properties. The model can treat any centrifugal pump and allows for inclusion of head degradation caused by two-phase effects.

Pump characteristic curves describe the pump head and torque response as a function of fluid volumetric flow rate and pump speed. Homologous curves (one curve segment represents a family of curves) are used for this description because of their simplicity. These curves describe, in a compact manner, all operating states of the pump obtained by combining positive or negative impeller velocities with positive or negative flow rates.

To account for two-phase effects on pump performance, the pump curves are divided into two separate regimes. Data indicate that two-phase pump performance in the vapor fraction range of 20% to 80% is degraded significantly in comparison with its performance at vapor fractions outside of this range. One set of curves describes the pump performance for single-phase fluid (void fraction 0.0 or 1.0), and another set describes it for two-phase fluid. The pump head at any vapor fraction is calculated from the relationship:

$$H = H_1 - m(\alpha)\,(H_1 - H_2) \qquad (7.2\text{-}5)$$

where

H = Total pump head
H_1 = Pump head from the single-phase homologous curves
H_2 = Pump head from the fully degraded homologous curves
m = Pump degradation multiplier
α = Vapor fraction

The two-phase hydraulic torque is treated similarly. The following definitions are used in the subsequent development:

H = Pump head = $\Delta Pp/\rho$
Q = Pump volumetric flow rate
Ω = Pump impeller angular velocity

where ΔP_p is the pump differential pressure and ρ is the pump inlet density. To allow one set of curves to be used for a variety of pumps, the following normalized quantities are used:

$$h = \frac{H}{H_r} \tag{7.2-6}$$

$$q = \frac{Q}{Q_r} \tag{7.2-7}$$

$$w = \frac{\Omega}{\Omega_r} \tag{7.2-8}$$

where the subscript, r, denotes the rated condition. The pump similarity relations given in Reference [167] show:

$$\frac{h}{w^2} = f\left(\frac{q}{w}\right). \tag{7.2-9}$$

For small w, this correlation is not satisfactory and the following combination of variables is used:

$$\frac{h}{q^2} = f\left(\frac{w}{q}\right). \tag{7.2-10}$$

The first correlation is used in the range $0 \le |q/w| \le 1$ and the second is used in the range of $0 \le |w/q| \le 1$. The four resulting curve segments, as well as the curve selection logic used in TRACG, are shown in Table 7-1.

The dimensionless hydraulic torque is defined by:

$$\beta = \frac{T/\rho}{T_r/\rho_r} \tag{7.2-11}$$

where

T = Hydraulic torque
T_r = Rated torque
ρ = Pump inlet density
ρ_r = Rated density

The single-phase torque, T, is dependent on the fluid density and is calculated from:

$$T = \beta T_r\left(\frac{\rho}{\rho_r}\right) \tag{7.2-12}$$

The density ratio multiplier is needed to correct for the density difference between the pumped fluid and the rated condition. For two-phase conditions, the impeller torque is calculated from:

$$T = T_1 - N(\alpha)\ (T_1 - T_2) \tag{7.2-13}$$

where

T = Total impeller torque
T_1 = Impeller torque from the single-phase homologous curves
T_2 = Impeller torque from the fully degraded homologous curves
$N(\alpha)$ = Torque degradation multiplier

The homologous, normalized, torque curve segments for β are correlated in the same manner as the head curve segments shown in Table 7-1.

In addition to the homologous head and torque curves, the head and torque degradation multipliers defined in Equations (7.2-5) and (7.2-14) are needed. These functions are usually nonzero only in the vapor fraction range where the pump head and torque are either partially or fully degraded.

The pump model can either specify the pump angular velocity or the motor torque while its motor is energized. When the torque is specified, the time rate of change for the pump motor assembly is proportional to the sum of the moments acting on it, and is calculated from:

$$I\ \frac{d\Omega}{dt} = \sum_i\ T_i = T_m - (T + T_f + T_b) \tag{7.2-14}$$

where

I = Pump motor assembly moment of inertia
T = Impeller torque
T_f = Torque caused by friction (constant)
T_b = Bearing and windage torque
T_m = Applied motor torque

The bearing and windage torque (T_b) is modeled as a fraction of the rated torque by:

$$T_b = T_r\ C_b\ \frac{\Omega^{n+1}\left|\Omega^n\right|}{\Omega_r^2} \tag{7.2-15}$$

where C_b is an input constant (TFR2) and Ω_r is the rated impeller angular velocity.

The torque due to friction (T_f) is modeled as a fraction of the rated torque by:

$$T_f = T_r\ C_f\ \frac{\Omega^{n+1}}{\left|\Omega^n\right|} \tag{7.2-16}$$

where C_f is an input constant (TFR1). The impeller torque is evaluated using the homologous torque curves and Equation (7.2-14); it is a function of the fluid density and flow rate as well as the pump angular velocity. T_m is defined through the control system. It is initially set to zero and retains that value unless the control system changes it to a nonzero value. For time step (n+1), Equation (7.2-15) is solved implicitly with respect to pump speed using:

[[ ]] (7.2-17)

Equation (7.2-17) is substituted into Equations (7.2-1) and (7.2-2), which are solved together with the thermal-hydraulic equations as described in Section 3.0 for the new fluid velocities. The new pump speed is then obtained by back substitution into Equation (7.2-17).

The pump work, which is added to the fluid energy equation, is calculated as:

$$E_p = \Omega T \qquad (7.2\text{-}18)$$

The wall heat transfer, wall friction, CHF calculation and implicit hydrodynamics options are the same for the pump component as for the pipe component. In addition, the following options are specified: pump type, motor action, reverse speed, two-phase, and pump curve. The input variables, IPMPTR and NPMPTX, specify the trip identifier for the pump trip initiation and the number of pairs of points in the pump-speed table (SPTBL), respectively. If IPMPTR = 0, no pump trip action occurs (a constant speed pump).

If the pump motor is energized, its angular velocity is assumed to be the constant value specified. If the motor is not energized, a pump coast down calculation is performed using the specified initial pump speed.

There are three pump options available (IPMPTY = 1, 2, or 3). For pump option 1 (IPMPTY = 1), the pump speed variation is specified by input. Pump option 2 (IPMPTY =2) is similar to option 1 except the pump speed is calculated from Equation (7.2-17) after a trip has occurred. Pump option 3 (IPMPTY = 3) allows the motor torque and its partial derivative with respect to speed to be calculated by the control system. For IPMPTY = 3 the pump speed is calculated using Equation (7.2-17).

If the reverse speed option is turned off (IRP = 0), the pump is allowed to rotate in the forward direction only. For this case, if negative rotation is calculated (after trip with pump Option 2), its speed will be set to zero.

If the two-phase option is turned on (IPM = 1), the degraded pump head and torque are calculated from Equations (7.2-5) and (7.2-13). If the two-phase option is turned off (IPM = 0), only the single-phase head and torque homologous curves are used.

There are several restrictions and limitations in the pump component. Because there is no pump motor torque-versus-speed model, the pump speed is assumed to be input if the motor is energized. Pump noding is restricted such that the pump momentum source is located between

Cells 1 and 2 of the pump model. Finally, the head degradation multiplier, M(α), and the torque degradation multiplier, N(α), are assumed to apply to all operating states of the pump.

7.2.2 Pump Head and Torque Homologous Curves

The user may specify pump homologous curves in the input or alternatively choose between two sets of built-in pump curves. In earlier versions of TRACG, the built-in default set of pump curves were based on the MOD-1 Semi-scale system pump[168],[169],[170]. These curves have been retained as "set 1". Another built-in set of curves more typical of large centrifugal pumps has been incorporated as "set 2". The curves for set 2 are similar to the Bingham pump curves built into RETRAN-02 and the default RELAP/5-MOD1 curve set. For either of the TRACG curve sets, the single-phase head (HSP), fully degraded two-phase head (HTP), head degradation multiplier (M), single-phase torque (TSP), fully degraded two-phase torque (TTP), and torque degradation multiplier (N) curves are provided. Figure 7-3 through Figure 7-8 depict the built-in curves. The dark blue lines with the solid symbols correspond to "set 1" and the red lines with the open symbols correspond to "set 2". The curves are numbered corresponding to the conditions provided in Table 7-1 where "z" is the either the dimensionless head "h" or the dimensionless hydraulic torque "β". Because these homologous curves are dimensionless, they can describe a variety of pumps of different sizes using the pump similarity relations and the rated values for fluid density, head, torque, flow and angular velocity provided via input as the scaling parameters.

The last column of Table 7-1 is provided to indicate how the head curve numbers used by RELAP and RETRAN can be related to the curve numbering used in TRACG. To get the corresponding torque curve numbers for RELAP and RETRAN simply add eight to these numbers. There are two RELAP and RETRAN curve numbers for each TRACG curve because both RELAP and RETRAN use a different number depending on whether the independent axis is positive or negative.

Table 7-1. Definitions of the Four Curve Segments that Describe the Homologous Pump Curves

TRACG Curve Segment	Selection Criteria	Correlation of $z = h$ or β	RELAP & RETRAN Head Curves
1	$\lvert q/w \rvert \le 1$ and $w > 0$	$\frac{z}{w^2} = f_1\left(\frac{q}{w}\right)$	3, 1
4	$\lvert q/w \rvert \le 1$ and $w < 0$	$\frac{z}{w^2} = f_4\left(\frac{q}{w}\right)$	7, 5
3	$\lvert w/q \rvert \le 1$ and $q < 0$	$\frac{z}{q^2} = f_3\left(\frac{w}{q}\right)$	4, 6
2	$\lvert w/q \rvert \le 1$ and $q > 0$	$\frac{z}{q^2} = f_2\left(\frac{w}{q}\right)$	8, 2
Static State	$w = 0$ and $q = 0$	$z = 0$	

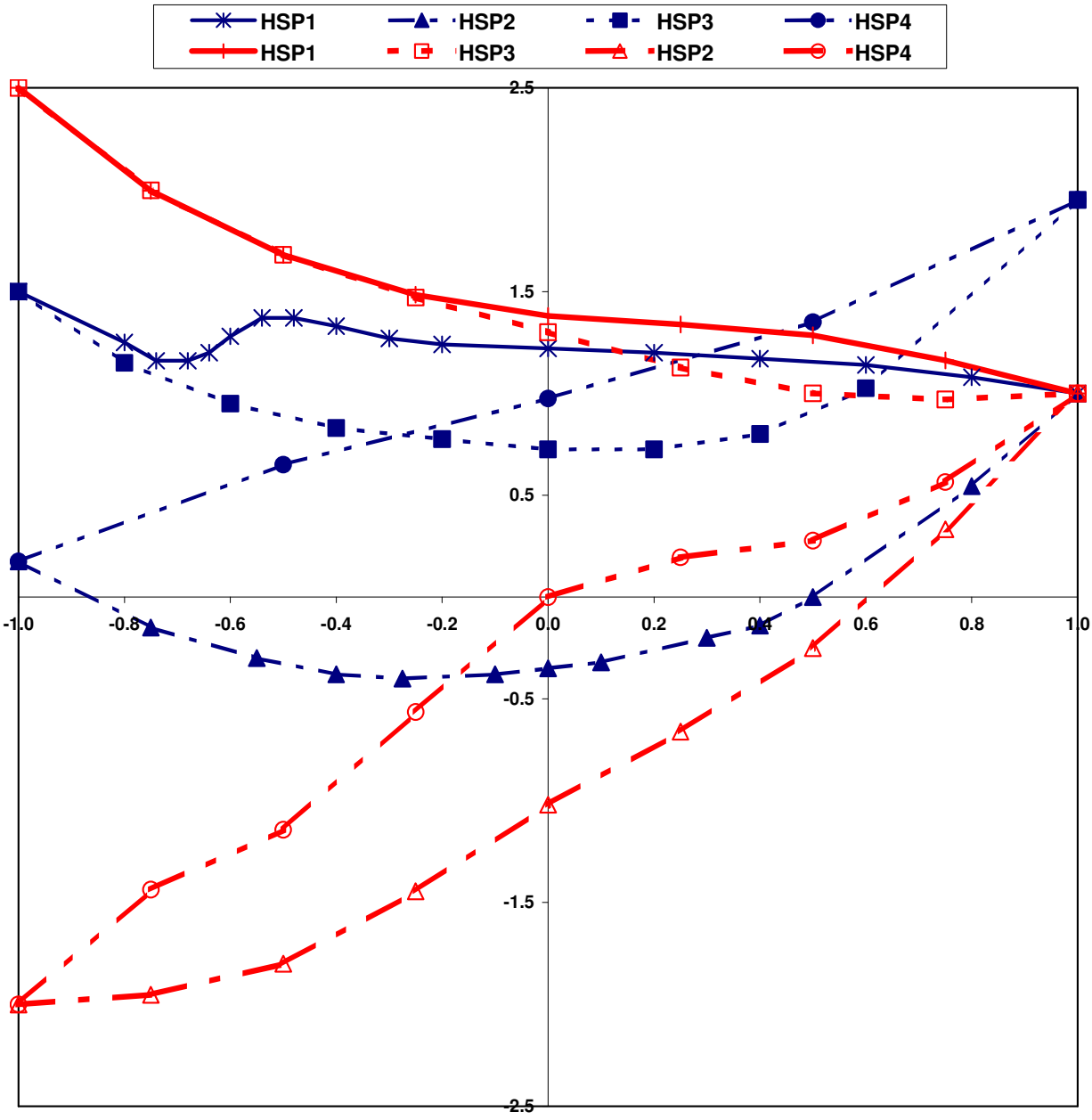

$$(x, y) = \begin{cases} \left(\frac{w}{q}, \frac{h}{q^2}\right) & \text{, HSP2 and HSP3} \\ \left(\frac{q}{w}, \frac{h}{w^2}\right) & \text{, HSP1 and HSP4} \end{cases}$$

Figure 7-3. Single-Phase Homologous Head

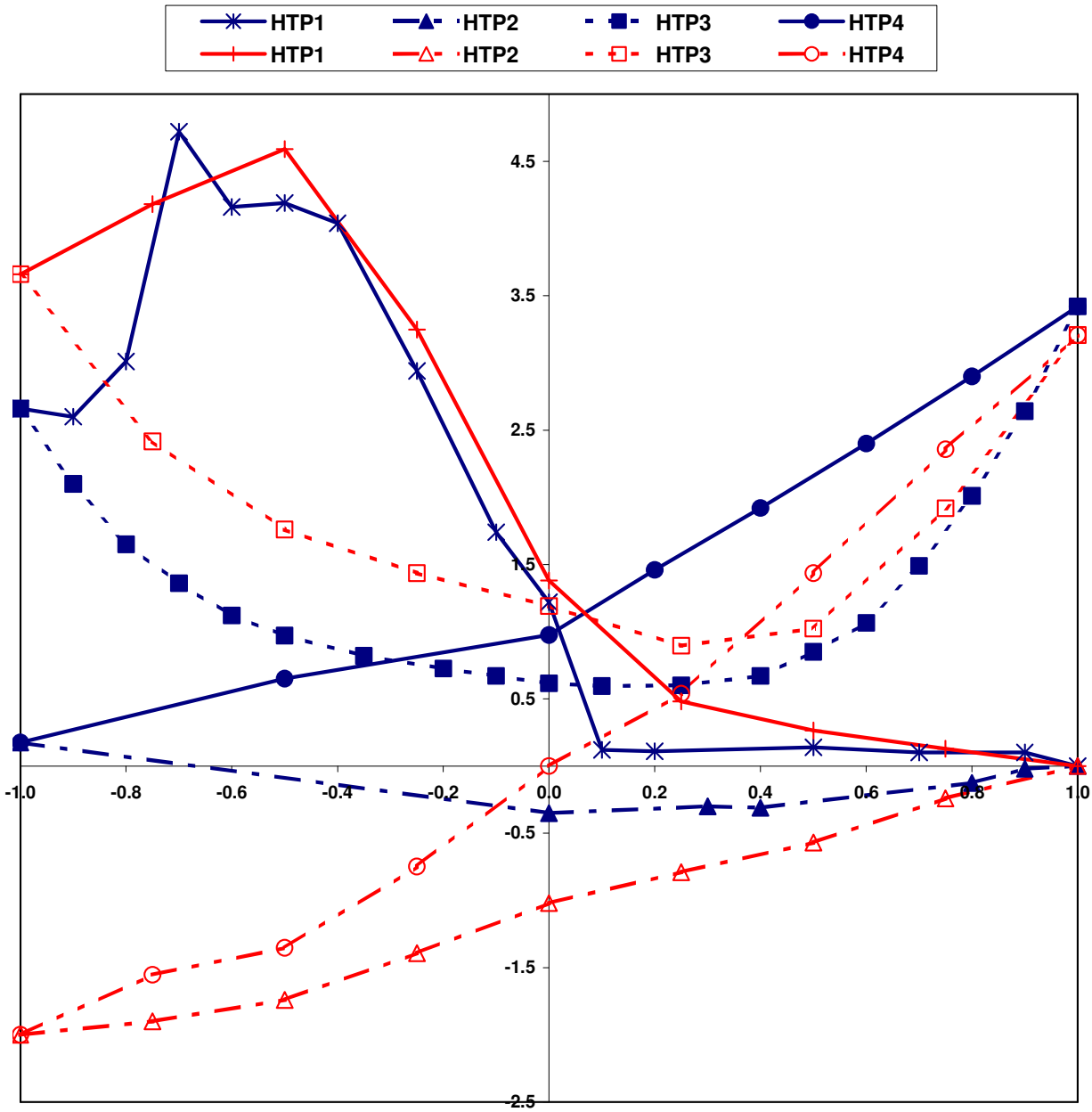

$$(x,y)=\begin{cases}\left(\dfrac{w}{q},\dfrac{h}{q^2}\right) & \text{, HTP2 and HTP3}\\ \left(\dfrac{q}{w},\dfrac{h}{w^2}\right) & \text{, HTP1 and HTP4}\end{cases}$$

Figure 7-4. Fully Degraded Homologous Head Curves

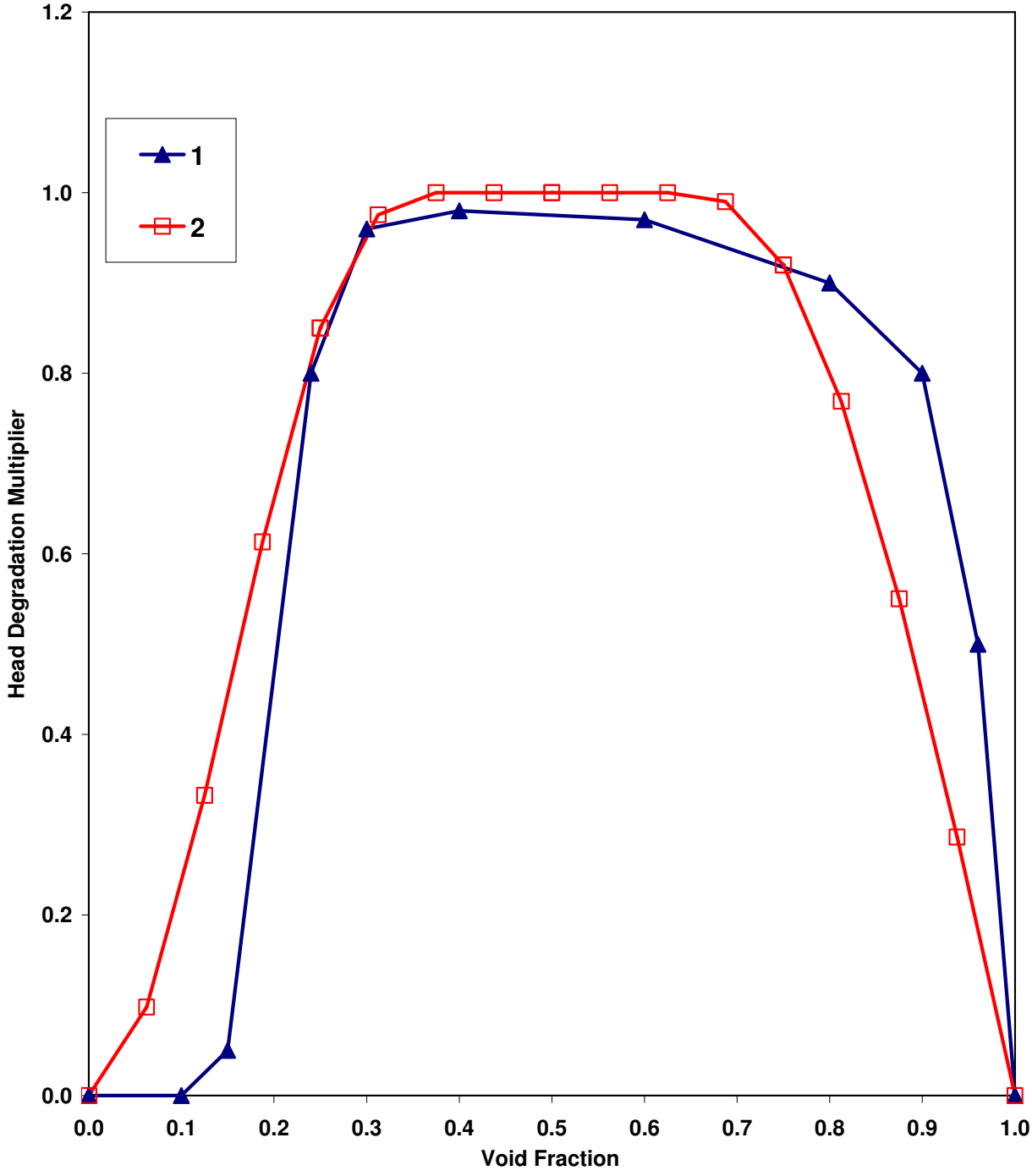

Figure 7-5. Head Degradation Multiplier

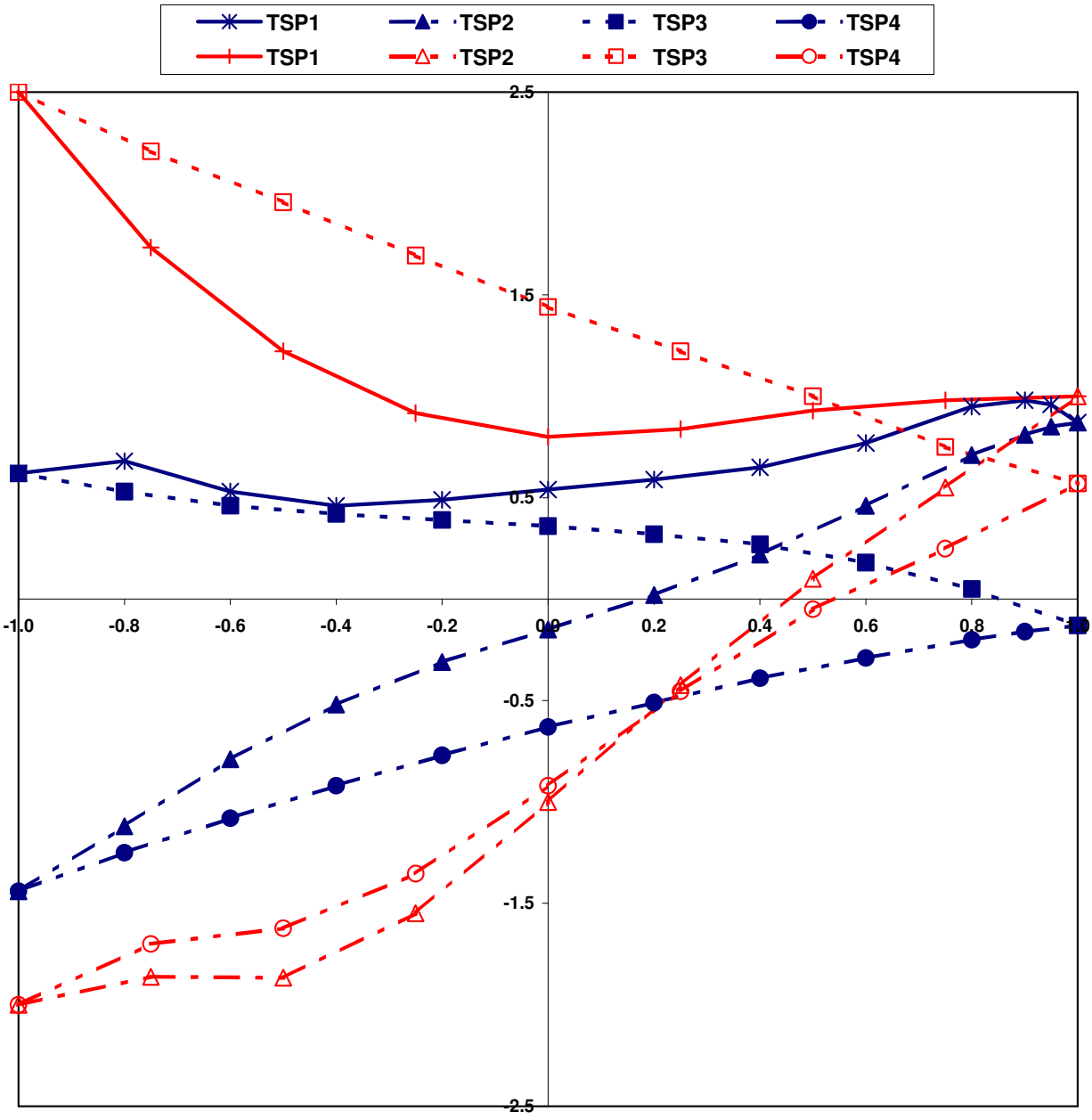

$$(x, y) = \begin{cases} \left(\frac{w}{q}, \frac{\beta}{q^2}\right) & \text{, TSP2 and TSP3} \\ \left(\frac{q}{w}, \frac{\beta}{w^2}\right) & \text{, TSP1 and TSP4} \end{cases}$$

Figure 7-6. Single-Phase Homologous Torque Curves

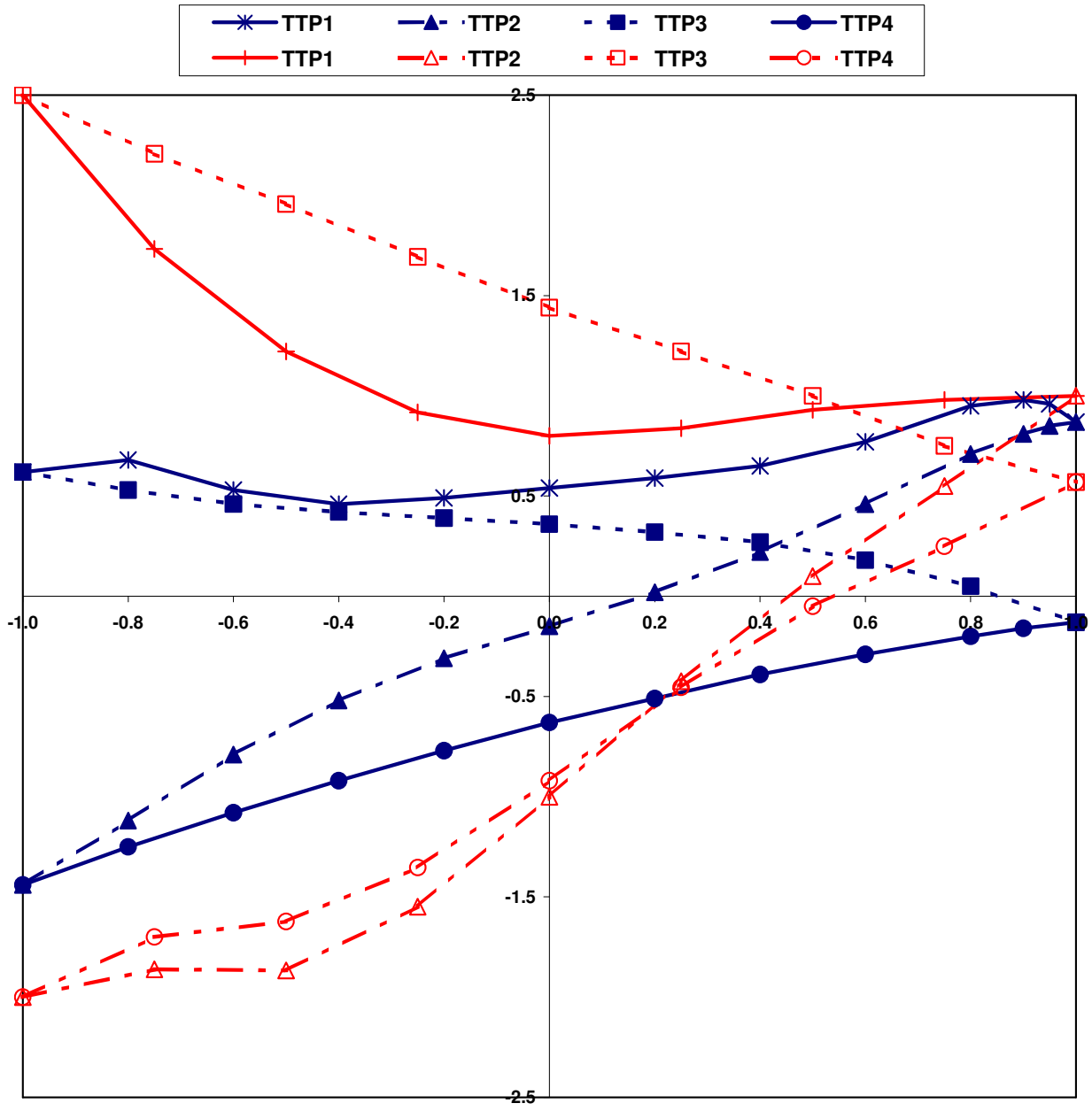

$$(x, y) = \begin{cases} \left(\frac{w}{q}, \frac{\beta}{q^2}\right) & \text{, TTP2 and TTP3} \\ \left(\frac{q}{w}, \frac{\beta}{w^2}\right) & \text{, TTP1 and TTP4} \end{cases}$$

Figure 7-7. Fully Degraded Homologous Torque Curves

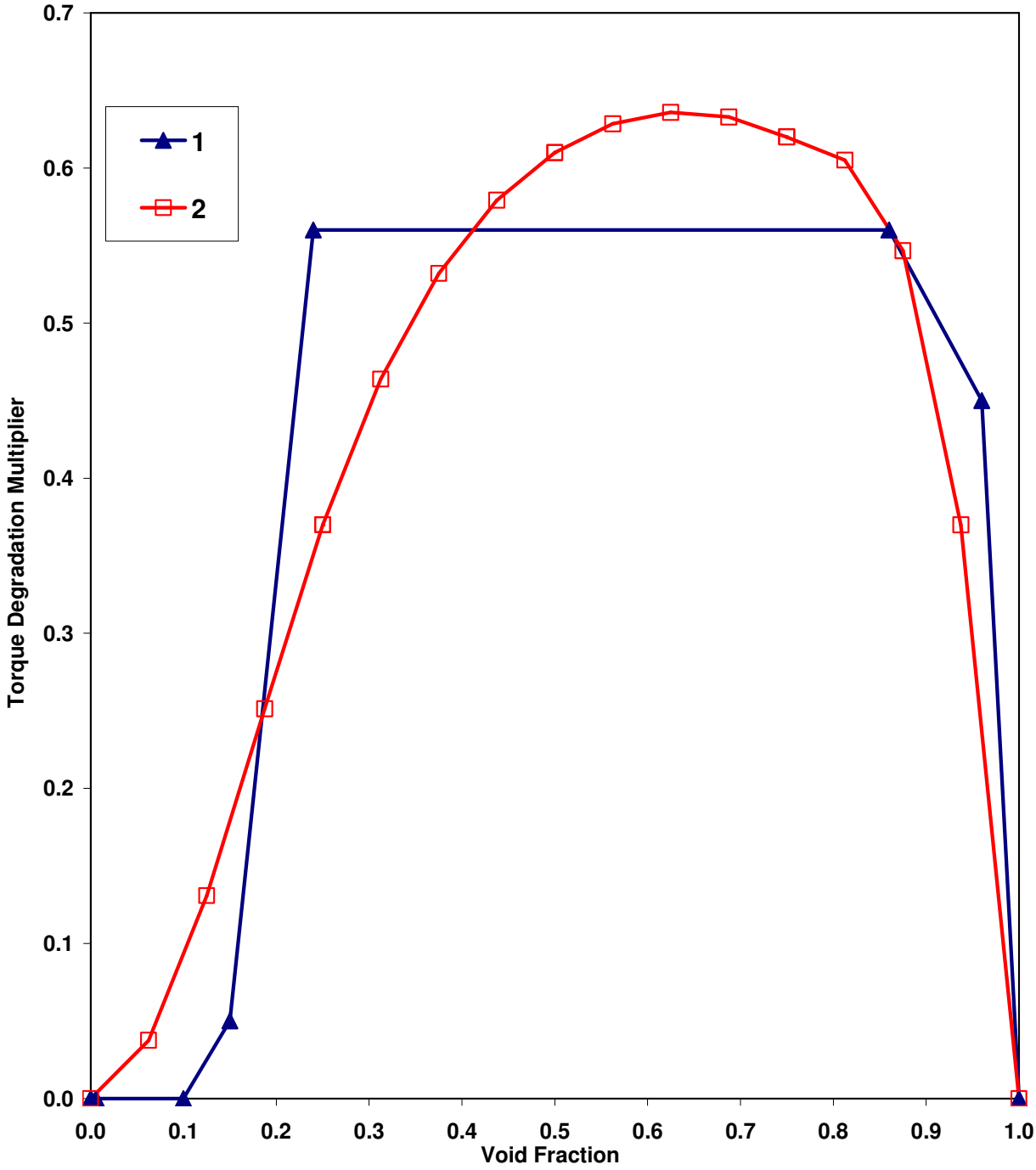

Figure 7-8. Torque Degradation Multiplier

7.3 Valve

The valve (VLVE) component models the flow in a valve. A valve is modeled as a one-dimensional component, as shown in Figure 7-9. The heat-transfer and fluid-dynamics models used in a valve calculation are identical to those of a pipe (Section 7.1).

Modeling valve action is achieved by controlling the flow area and associated local loss coefficient between two fluid cells. The expressions used for this purpose are:

flow area = AVLVE x FRACT

and

K_{LOSS} = f (FRACT)

where:

AVLVE = Fully open valve flow area

FRACT = Fraction of the valve that is open

f = A user-defined table of loss coefficient versus valve area fraction

Eight user options are provided for controlling the valve action by setting the value of IVTY (see Table 7-2). Choosing IVTY = -1 allows the valve area to be set by the control system. Setting IVTY to a value from 1 to 4 allows trip control, with the valve opening or closing instantly or as a function of time. Setting IVTY = 5 models a check valve where an open or closed condition is determined by a pressure differential between the specified cells and two setpoints. Setting IVTY = 6 models a motor-operated valve, while choosing IVTY = 7 simulates a relief valve with multiple setpoints.

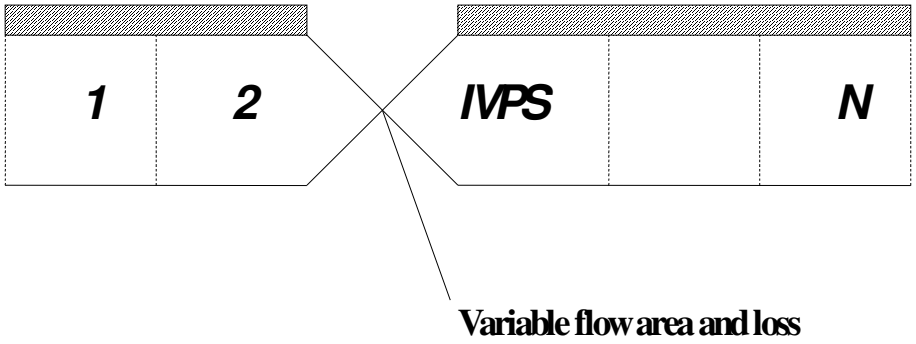

Figure 7-9. VLVE Noding Diagram

Table 7-2. Control Options for VLVE	
IVTY	**Option**
-1	Valve area is controlled by a control system.
1	Valve is normally open and is closed instantly on a trip signal.
2	Valve is normally closed and is opened instantly on a trip signal.
3	Valve is normally open and is closed on a trip signal according to a time-dependent valve table.
4	Valve is normally closed and is opened on a trip signal according to a time-dependent valve table.
5	Check valve is controlled by a static pressure gradient. IVPG is the gradient option. IVPS defines the cell face where the valve orifice is located.
	If IVPG = 1, DP = P(IVPS - 1) – P (IVPS). If IVPG = 2, DP = P(IVPS) - P (IVPS - 1). If DP + PVC1 ≥ 0, valve opens instantly. If DP + PVC2 < 0, valve closes instantly.
6	Power-operated valve that opens or closes at fixed rates based on pressure setpoints.
7	Relief valve with multiple setpoints.

7.4 Tee

The tee (TEE) component models the thermal-hydraulics of three piping branches, two of which lie along a common line. The third enters at some angle from the main axis of the other two as shown in Figure 7-10. In the code, the tee is treated as two pipes, as indicated in Figure 7-10 and Figure 7-11. Beta is defined as the angle from the low-numbered end of PIPE1 to PIPE2. The low-numbered end of PIPE2 always connects to PIPE1. The first pipe extends from Cell 1 to Cell NCELL1 and connects to PIPE2 at Cell JCELL. The second pipe begins at Cell 1 and ends at Cell NCELL2.

The connection is effected through mass, momentum, and energy source terms in PIPE1. PIPE2 sees the connection as boundary conditions from Cell JCELL in PIPE1. The time differencing and iteration procedures are such that conservation of the scalar qualities is preserved (within a convergence tolerance) and the level of implicitness at the connection ensures that no additional stability limitations apply at a tee. Phase separation at the junction is not implemented. The void fraction from cell JCELL in PIPE1 is used when donor-celling the boundary conditions of Cell 1 in PIPE2.

The momentum equation in the TRACG solution scheme depends on noding and flow direction. Considering the simple nodalization shown in Figure 7-11, the momentum source is derived for the liquid phase momentum equation. The results will also be applicable to the vapor momentum equation. The calculated pressure change for a single-phase steady-state flow with positive velocity and without sources, friction loss and gravity from Cell 1 to Cell 2 is given by:

$$\frac{P_2 - P_1}{\rho_\ell} = -v_2 \left(v_2 - v_1 \frac{A_1}{A_2}\right) + B_{1\text{-}2} \qquad (7.4\text{-}1)$$

where

$v\frac{\partial v}{\partial x}$ is calculated according to Equation (3.2-2) (for simplicity D and E are set to unity)

and $B_{1\text{-}2}$ is a source term.

In the derivation of Equation (3.2-2), a side branch was not accounted for. To get the correct pressure drop for two streams mixing (with D=E=1) Equation (7.4-1) should read:

$$\frac{P_2 - P_1}{\rho_\ell} = -v_2\ (v_2 - v') \tag{7.4-2}$$

where v′ is an estimate for the velocity at the center of Cell 1. Neglecting compressibility effects, this velocity is given by the merging of the two streams:

$$v' = \frac{A_1}{A_2} v_1 - \frac{A_3}{A_2} v_3 \tag{7.4-3}$$

Combining Equations (7.4-1), (7.4-2) and (7.4-3) gives:

$$B_{1\text{-}2} = -\frac{A_3}{A_2} v_3\ v_2 \tag{7.4-4}$$

This source term is applied in TRACG for both positive and negative source flow. In the case of negative primary flow (v_1), the momentum source term, $B_{1\text{-}0}$, is calculated to be:

$$B_{1\text{-}0} = -\frac{A_3}{A_1} v_3\ v_1 \tag{7.4-5}$$

In most applications of interest, the error incurred by ignoring the effect of the source momentum is small. In cases where this is not true, however, the user may use the jet pump (JETP) component in place of the tee. This component is a special type of tee in which certain assumptions have been made regarding the normal flow direction and in which the momentum source term in PIPE 1 is not neglected (see JETP description).

Because the tee is modeled as essentially two interconnected pipes, the pipe model description in Section 7.1 should be referenced for additional information.

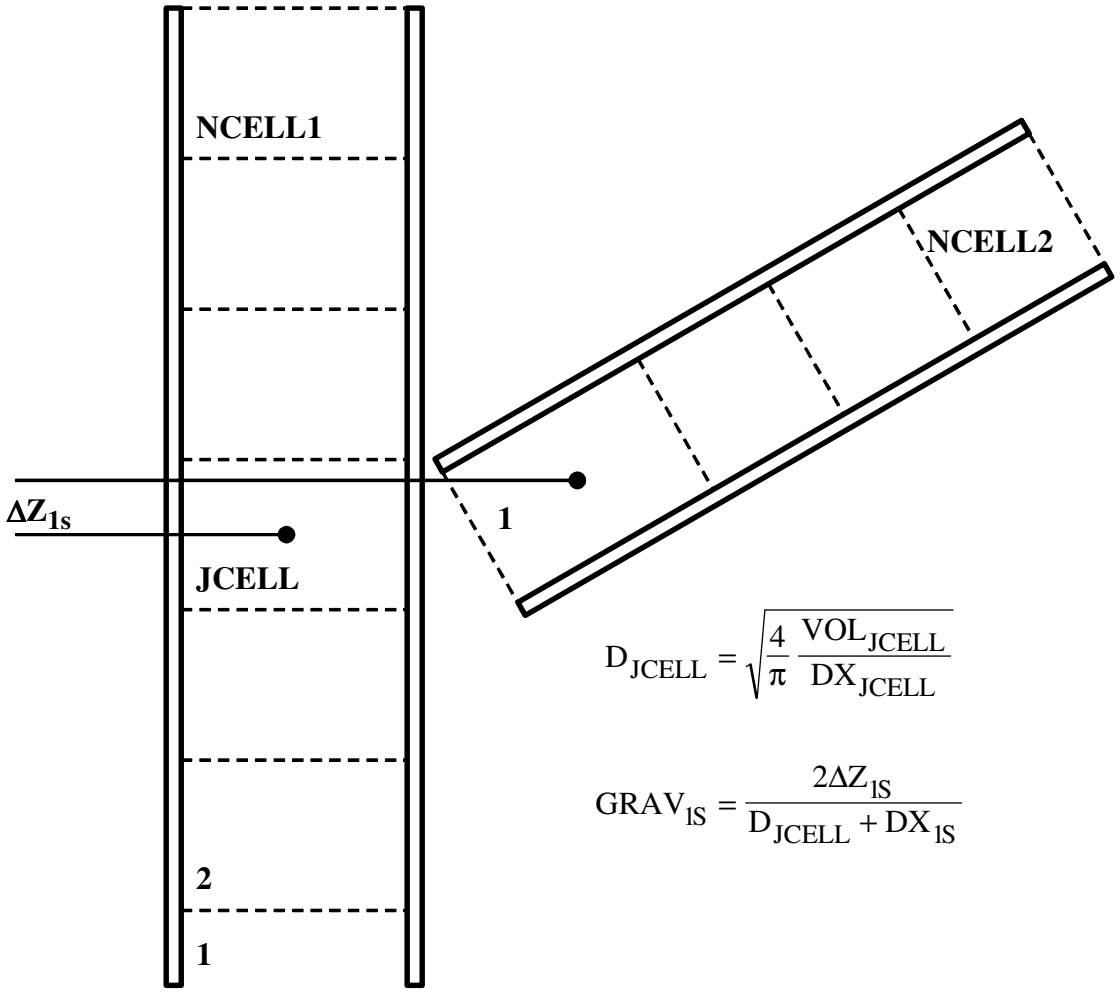

Figure 7-10. TEE Noding Diagram

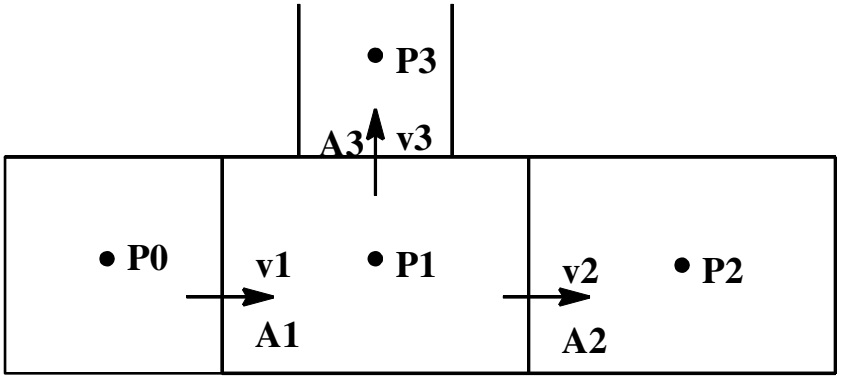

Figure 7-11. Sample Noding Scheme for Tee Component

7.5 Fuel Channel

The fuel channel (CHAN) component has been developed to simulate one or more BWR fuel rod bundles and channel walls. The channel is a tee component (Section 7.4) to which fuel rod heat transfer and channel wall heat transfer models have been added. The channel can be used to simulate a single bundle or several bundles in a stand-alone mode in which boundary conditions to the channel are supplied by break and fill components. This capability is quite useful for performing hot bundle analysis or for investigating single bundle experiments. The channel component can also be used to simulate rod bundles in a BWR core region.

Basing the channel component on the tee structure provides an implicit coupling of all flow paths, including the leakage paths. Junction 1 of the channel component represents the channel inlet connection to the lower plenum. The end of the primary section of the channel (JUN2) is the channel exit to the upper plenum. The secondary section of the channel is used to model the leakage path from the channel to core bypass region. The channel utilizes a zero cell secondary pipe as shown in Figure 7-12 The secondary function (JUN3) provides a connection from JCELL directly to another component.

The leakage flow calculation makes use of GEH design correlations that express leakage flow as functions of pressure drop, fluid conditions, and geometry for all possible leakage paths. The calculated leakage flow is based on an effective loss coefficient applied at the leakage junction (JUN3). A similar process is used in the vessel component to model leakage flow from the lower plenum to the core bypass region. Details of the leakage calculation are provided in Section 7.5.1.

Each channel component is assigned a fraction of the total core power. The axial and rod group distributions of power provide the power deposition in each fuel rod axial node. The radial distribution of power within the fuel rod is also specified. Details of the fuel rod radial conduction solution are provided in Section 4.2.3. Direct heating of the channel fluid and structure is also available as described in Section 9.4.

An option to model water rod flow is available for the channel component. The water rod model (Section 7.5.6) allows the modeling of a flow path between two channel cells. The geometry of this internal pipe connection is user specified. Heat transfer through the water rod and direct energy deposition are modeled.

To model a BWR core, channel components are connected across the usual core region of the vessel component. The connections are made with standard vessel sources (see vessel component in Section 7.8). The 3-D hydrodynamics solution in the core region of the vessel component is used for the flow in the region outside the BWR channels but inside the core barrel. A simplified noding scheme for a BWR vessel is illustrated in Figure 7-13. For this nodalization, three channel components are used to simulate all fuel bundles in the BWR core region. Within each channel component, five-rod groups are chosen to model radiation heat transfer. This noding scheme allows for fine nodalization in the radial direction of the core without increasing the number of vessel nodes.

In addition to the heat transfer options available for other components, the fuel rod and channel wall heat transfer models include detailed radiation heat transfer (Section 6.6.12), and bottom-up and top-down quench fronts (Section 6.6.13) for each rod group as well as for the inside of the channel wall. Heat transfer on the outside of the channel wall is coupled to the vessel hydrodynamics solution.

Nomenclature

Item	*Description*
A	area
A_o	an empirical constant representing the mean radius of the contact spots
A_{vi}	empirical constant for the i^{th} component (Equation (7.5-12))
C	coefficient in leakage flow correlation (Section 7.5.1)
C	contact pressure constant (Section 7.5.2)
C_{g1}	perforated rod gap conductivity equation constant (Equation (7.5-13))
C_{g2}	perforated rod gap conductivity equation exponent (Equation (7.5-13))
C_{R1}	=0.2, constant defined by the GESTR-LOCA empirical relocation model
C_{R2}	=0.5, constant defined by the GESTR-LOCA empirical relocation model
CPR	critical power ratio
D_Q	thermal diameter
E	modulus of elasticity
F_r	fraction of additional fission gas released
F_{kx}	the ratio of krypton to xenon in the fission gas
G	mass flux
(g_1+g_2)	fuel rod gas gap temperature jump distance
h	heat transfer coefficient
h	enthalpy
Δh_s	subcooling at channel inlet
h_g	total gap conductance
h_s	heat transfer coefficient for conduction through fuel/cladding contact spots
h_f	heat transfer coefficient for conduction through the gas layer at fuel/cladding interface
h_r	radiant heat transfer coefficient
H_m	Meyer hardness of the cladding
I	radial pellet/cladding interaction
k_{fg}	thermal conductivity of the fuel rod gas
K	loss coefficient
L	rod heated length
L_A	annular length
L_B	boiling length
M_i	molecular weight of the i^{th} component
n	total amount of gap gas (gm-mol)
n_i	empirical constant for the i^{th} component (Equation (7.5-12))
N	number of radial nodes in the fuel
N_{fgr}	total moles of gaseous fission products released from the fuel
N_{fgf}	total moles of gaseous fission products remaining in the fuel
N_{He}	total moles of filler gas in the rod
N_{Xe}	total moles of xenon

Nomenclature

Item	Description
N_{Kr}	total moles of krypton
P	system coolant pressure
P	power
P_c	fuel/cladding contact pressure (Section 7.5.2.3)
P_c	critical power
P_g	fuel rod internal gas pressure
P_Y	fuel/cladding contact pressure corresponding to cladding yield
ΔP	pressure difference
q	heat transfer per unit volume
Q	bundle power
Q_c	bundle critical power
Δr_i	reference (cold) radial dimension of the i^{th} fuel node
r_{fo}	fuel nominal (cold dimension) outer radius
r_{ci}	cladding nominal (cold dimension) inner radius
r_{co}	cladding nominal (cold dimension) outer radius
R	GEXL R-factor
R	nominal radial gap size
R	universal gas constant
R_1	fuel pellet surface roughness
R_2	cladding surface roughness
R_4	mean roughness (Equation (7.5-16))
R_{eff}	effective hot radial thermal gap between the fuel pellet and cladding
R_{ci}	hot cladding inner radius
R_{fo}	hot outer fuel radius
ΔR_f	fuel thermal expansion
s	clad oxide thickness
t	cladding thickness
T	temperature
T_c	cladding average temperature
T_f	gas temperature in the fuel rod volume
T_p	plenum gas temperature
T_{fi}	fuel temperature of the i^{th} fuel node
$\overline{T}_c$	cladding average temperature at the maximum LHGR axial position
$\overline{T}_{pellet,max}$	volume-weighted fuel pellet temperature at the maximum LGHR axial position
TM	thermal margin
V_f	fuel rod volume
V_p	plenum volume
W	flow

Nomenclature

Item	*Description*
x_c	node instantaneous critical quality
x_e	node instantaneous equilibrium quality
X	fuel exposure (GWd/MTU)
X_i	gm-moles of the i^{th} component
Greek	
α_{fi}	thermal expansion coefficient of the i^{th} fuel node
α_c	thermal expansion coefficient of cladding
α	void fraction
ρ	density
ε	thermal emissivity
ε	cladding strain
ε_E	cladding elastic strain
$\sigma\beta$	Stefan-Boltzman constant
σ_c	cladding hoop stress
σ_Y	cladding yield stress
ν	Poisson's ratio for the cladding
Subscript	
csp	core support plate leakage path
B	channel-lower tie plate leakage path
c	cladding
f	fuel pellet
f	saturated liquid
g	gas gap
g	saturated steam
FS	fuel support leakage path
i	inner
i	initial
i	ith component
ℓ	liquid
LEAK	leakage
LTPH	lower tie plate hole
o	outer
p	plenum
r	reference
ref	reference
sat	saturated condition
sg	spring/getter
v	vapor
w	wall
Superscript	
H	hot rod

7.5.1 Leakage Flows

The bypass flow rate is the summation of the leakage flows through several paths. The flow rate across each leakage path is represented as a function of the pressure difference across the path. These leakage flow expressions are correlated from test data (see References [171] and [172]). The leakage paths are shown in Figure 7-14. There are two different types of leakage paths. The first category consists of the paths in which the flow rates are functions of the core support plate pressure difference (ΔP_{csp}). There are seven different paths of this type represented by W_{csp} in Figure 7-14. The second type of leakage path depends on the fuel assembly type and is dependent on the pressure distribution in the fuel assembly. There are three leakage paths of this type.

7.5.1.1 Leakage Flow Paths

The seven core support plate leakage paths, which are modeled, are as follows:

- Fuel support casting – control rod guide tube (upper)
- Fuel support casting – control rod guide tube (lower)
- Core support plate – control rod guide tube
- Control rod guide tube – control rod drive housing
- Core support plate – in-core instrument guide tube
- Core support plate holes
- Core support plate – shroud

The data for the various core support plate leakage flow rates have been correlated in the following form:

[[ ]] (7.5-1)

where the C's depend on the particular path being calculated. The flow rate from each individual path is multiplied by the number of paths of that type in the core.

The other leakage paths are from the fuel bundle to the bottom of the bypass region. The driving pressures for these paths are dependent upon the pressure distribution within each fuel assembly type. Three separate paths are considered in the leakage modeling as described below.

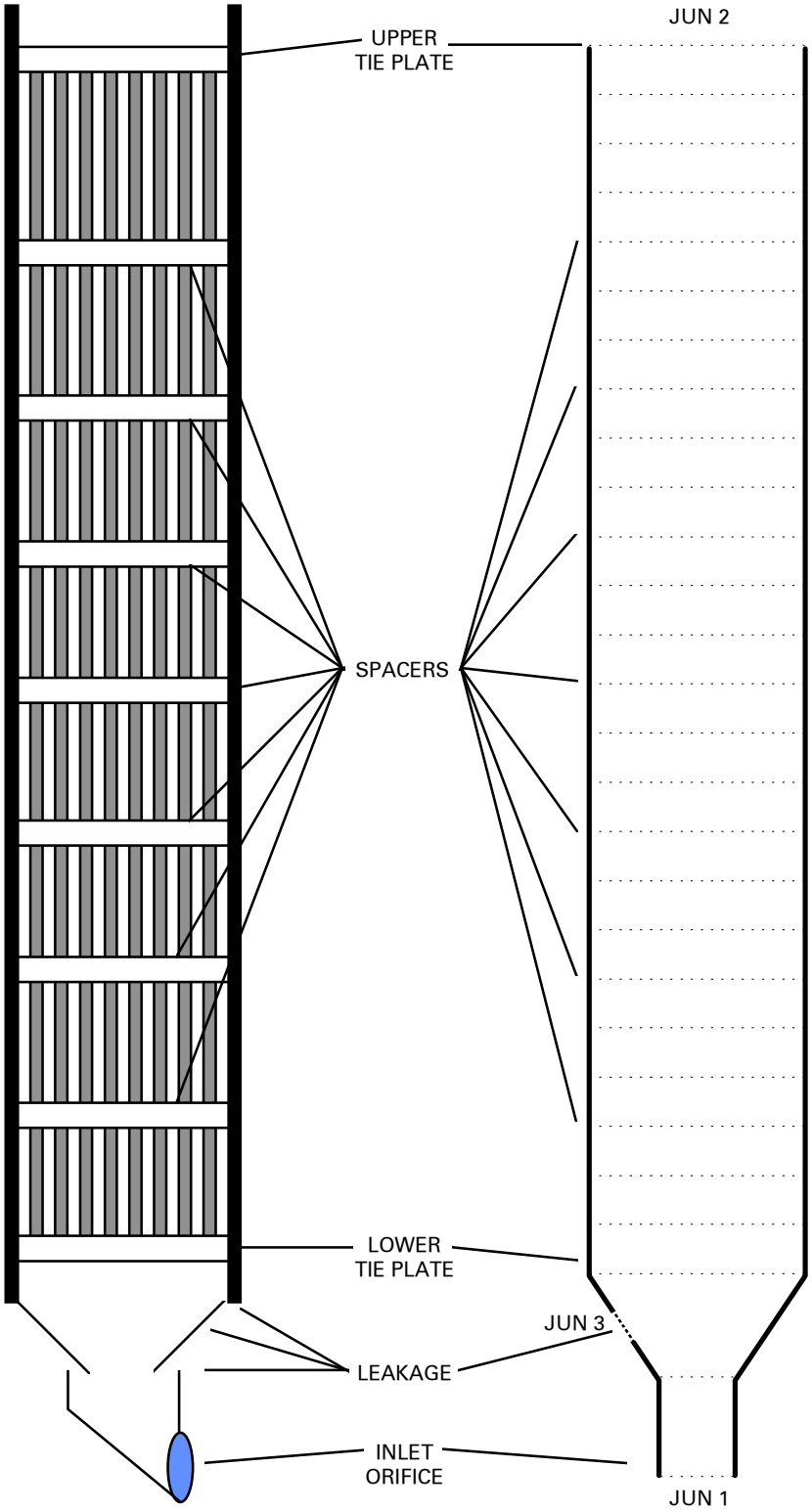

Figure 7-12. Channel Noding Diagram

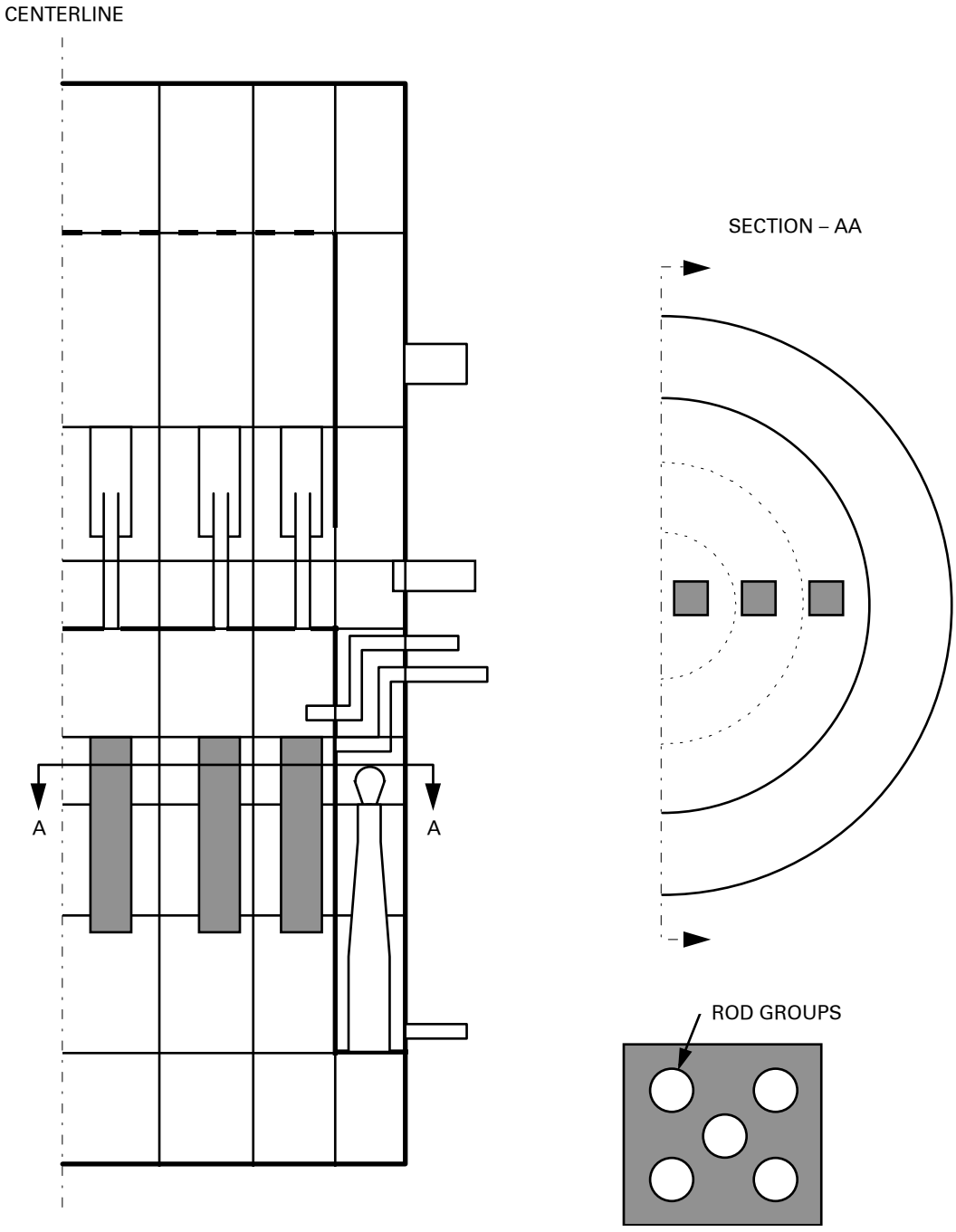

Figure 7-13. Simplified Reactor Nodalization Showing CHAN Components

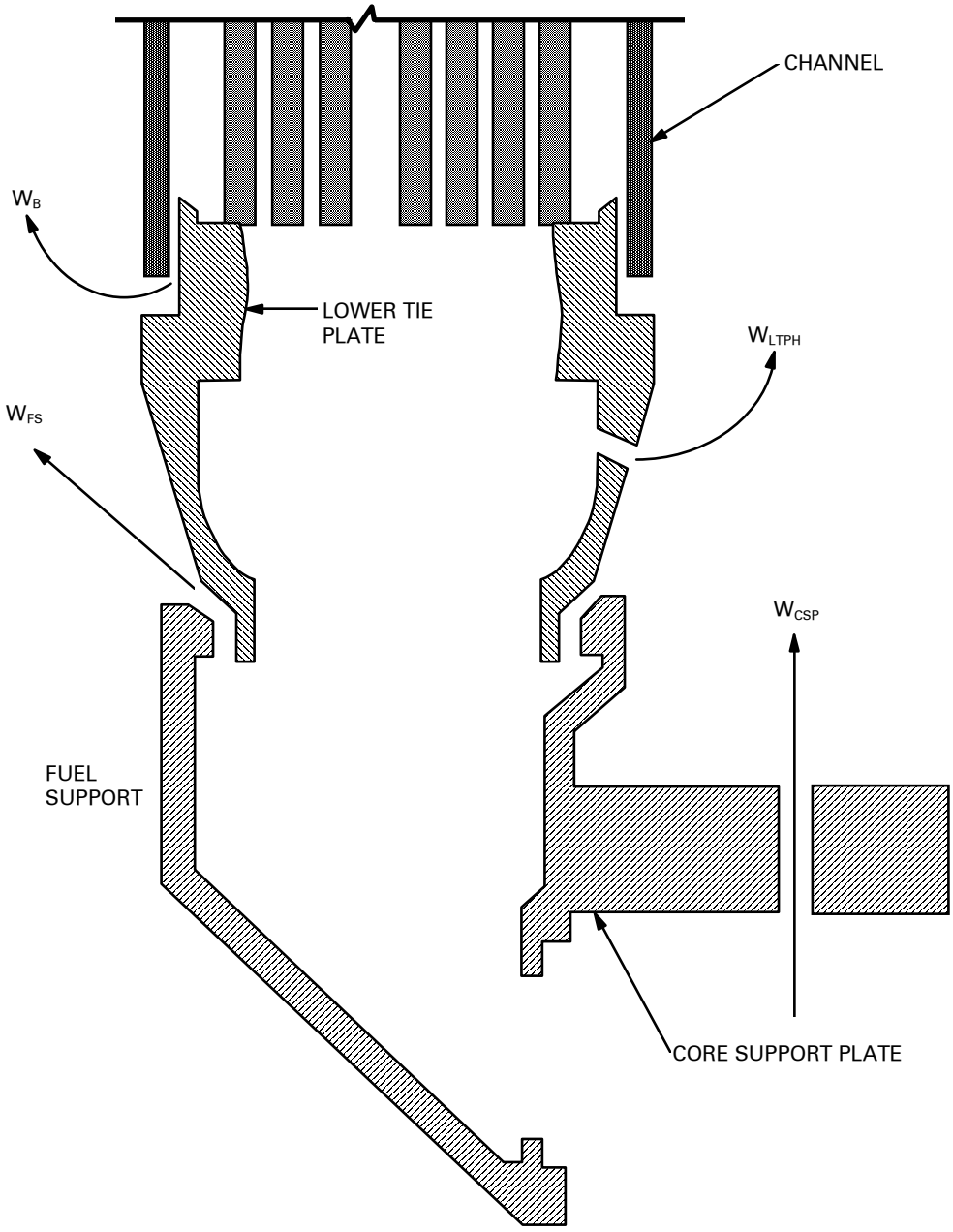

Figure 7-14. Leakage Flow Paths

The fuel support-lower tie plate leakage flow rate is channel type dependent and is of the form:

[[ ]] (7.5-2)

The lower tie plate hole leakage flow rate is channel type dependent and is of the form:

[[ ]] (7.5-3)

The channel-lower tie plate leakage flow rate is channel type dependent and is of the form:

[[ ]] (7.5-4)

The above correlations (Equations (7.5-1) through (7.5-4)) are employed for the calculation of forward leakage flow.

Different sets of equations are used for the two directions to account for direction dependent flow losses and the possible effect of the pressure differential on flow area in certain paths. The individual leakage flows are calculated for backflow using correlations of the form:

[[ ]] (7.5-5)

The constants are empirically fitted to experimental data[173]. Hot wall effects are considered in backflow to account for a lag in the metal temperature with respect to the fluid saturation temperature during a blow-down. Steam generation in the smaller paths has the potential for increasing the pressure drop because of two-phase losses and reducing the net liquid leakage.

7.5.1.2 Model Formulation

The leakage flow correlations described above are implemented into the TRACG solution scheme by defining effective loss coefficients as follows:

$$K_{LEAK} = \frac{2A_{LEAK}^2 \rho \Delta P}{W_{LEAK}^2} \quad (7.5\text{-}6)$$

where

W_{LEAK} = Simulation of all applicable leakage flows
A_{LEAK} = Leakage area
ρ = Fluid density
ΔP = Driving pressure drop

When two-phase conditions are predicted, K_{LEAK} is modified by a two-phase multiplier. Effective loss coefficients are defined for each channel type and each vessel cell at the bottom of the bypass region.

7.5.1.3 Assessment

The GEH design correlations for the leakage flow as described in Equations (7.5-1) to (7.5-6) are implemented into TRACG. The flow and ΔP dependence for each type of leakage paths is simulated through the user input for the coefficients. The TRACG calculated flow rates agree very well with those calculated by ISCOR[171] for identical boundary conditions. The uncertainty and applicability of the TRACG leakage flow model are the same as the coefficients correlated from data[173]. The standard deviations are [[ ]] for W_{LTPH} and [[ ]] for W_B. The correlations cover a wide range of pressure differentials ranging from forward to reverse flow.

7.5.2 Fuel Pellet Gap Conductance

The gap between the fuel pellet and the surrounding cladding of a fuel rod causes a local thermal resistance, which must be included in an accurate model of the fuel cladding radial temperature distribution. The gap contains a mixture of helium fuel rod filler gas and xenon and krypton gaseous fission products released from the fuel. The gap can be characterized by assuming that it has negligible thermal capacitance and a thermal conductance which is calculated from a rather complex model that considers such phenomena as relative fuel cladding thermal expansion, fuel cladding creep and plasticity, fuel relocation, densification, irradiation swelling, and fission gas release.

The GESTR-LOCA gap conductance model[174] developed by General Electric Company is similar to the Ross and Stoute model, which considers the overall gap conductance as the sum of three separate components. These components represent radiation heat transfer between fuel and cladding, conduction across the gas gap, and conduction through points of contact between the fuel and cladding. TRACG contains gap conductance models, which are consistent with the GESTR-LOCA model, and which are comparable to the models used in SAFER[172]. [[

]]

The gap conductance model as formulated by Ross and Stoute and used in GESTR and TRACG is:

$$h_g = h_s + h_f + h_r \qquad (7.5\text{-}7)$$

where

h_g = Total gap conductance
h_s = Heat transfer coefficient for conduction through fuel/cladding contact spots
h_f = Heat transfer coefficient for conduction through the gas layer at the fuel/cladding interface
h_r = Radiant heat transfer coefficient

The total gap conductance, h_g, is used in the heat conduction model to describe the heat flux from fuel to cladding.

The remainder of this section is outlined as follows. Sections 7.5.2.1 through 7.5.2.3 document the formulations for the radiation heat transfer (h_r), gap gas conductance heat transfer (h_f), and fuel/cladding contact heat transfer (h_s), respectively. The gap gas conductance and contact heat transfer depend on the gap size, and the fuel and cladding thermal expansion. Sections 7.5.2.4 and 7.5.2.5 document these calculations. The implementation and initialization of this conductance model in TRACG are documented in Section 7.5.2.6. Section 7.5.2.7 gives the assessment of the conductance model in TRACG.

7.5.2.1 Radiation Heat Transfer

An equivalent radiation heat transfer coefficient is used to model radiation heat transfer between the fuel pellet and cladding:

$$h_r = \frac{\sigma_\beta \left(T_{fo}{}^4 - T_{ci}{}^4 \right)}{\left(T_{fo} - T_{ci} \right)} \left(\frac{1}{\varepsilon_c} + \frac{1}{\varepsilon_f} - 1 \right)^{-1} \tag{7.5-8}$$

where T_{fo} and T_{ci} are the fuel pellet outer surface temperature and the cladding inner surface temperature in K and ε_c and ε_f are the cladding and fuel thermal emissivities, and σ_β is the Stefan-Boltzman constant.

7.5.2.2 Gap Gas Conductance Heat Transfer

The conductance across the gas gap, h_f, is modeled assuming that the fuel pellet has cracked into wedge-like segments which have non-uniform radial displacements:

[[

]]

The gas gap thermal conductivity is calculated as a function of gas composition and temperature:

[[

]]

Helium, xenon and krypton are considered in the calculation. [[
]]

If a fuel rod perforation occurs, the gap conductance is adjusted to reflect the presence of steam and hydrogen rather than a fission product gas mixture inside the fuel rod. The model for

composition of the gases in the gap after perforation is the same model that also approved by the NRC in 1981[180]. The thermal conductivity is simply modeled as:

$$k_{fg} = C_{g1}\left(T_g\right)^{C_{g2}} \qquad (7.5\text{-}13)$$

where

C_{g1} = Perforated rod gap conductivity equation constant

C_{g2} = Perforated rod gap conductivity equation exponent

[[

]]

The gases that are considered are those that are prevalent in the gap. Helium is important because of the initial backfilling of helium. [[

]]

The fission gas production of some isotopes of xenon (Xe) and krypton (Kr) are important because their fission yield rates compared to the decay times are large enough that these gases exist in sufficient amounts and for long enough times that they can be released from the UO2 pellet into the gap.

The fission yields and the half-lives are not the only consideration. For example, cesium is produced in large amounts but is not present as a gas in the gap in any appreciable amounts because it readily reacts chemically and is effectively removed as a gas by a number of processes. Olander discusses these processes in Chapter 12 of Reference [177]. Chapter 13 of Olander's book discusses fission gas production in the fuel pellet and the release mechanisms are

discussed in Chapter 15. Ultimately, the only fission gases that accumulate in the gap in any appreciable amounts are the stable (or longer half-life) isotopes of Xe and Kr as stated in Section 15.3.6 of Olander's book[177]. In terms of the total number of fission gas atoms in the gap, the GESTR model assumes [[ ]] is krypton and [[ ]] is xenon (page 3-9 of Reference [174]). This composition is representative of the ratios that one would expect from accumulated fission gas yields for the stable and longer half-life isotopes of Kr and Xe due to thermal fissions in U-235 and Pu-239 and fast fissions in U-238.

[[

]]

7.5.2.3 Fuel/Cladding Contact Heat Transfer

The fuel/cladding contact conduction term (h_s) depends on fuel/cladding contact at some contact pressure (P_c). Conduction through points of contact between the fuel and cladding is modeled as:

[[

]]

7.5.2.4 Gap Size Calculation

Several factors affect the size of the fuel-cladding gap. The change of gap size during the transient is partially due to the thermal expansion or contraction of the fuel pellet and the cladding. The change of fuel and system pressure during the transient can affect the cladding hoop stress and, therefore, change the gap size. During some transients, the cladding plastic strain may increase the gap size and may develop through-wall cracks.

The effective gap size in Equation (7.5-9) is determined as follows:

[[

]]

7.5.2.5 Fuel and Cladding Thermal Expansion

In general, the fuel pellet is cracked into pie-shaped segments during operation. [[

]]

The cladding plastic strain model is described in Section 7.5.3.3.

7.5.2.6 Implementation and Initialization

The preceding sections describe the transient gap conductance model, which must be initialized to reflect the steady-state operating condition. [[

]]

7.5.2.6.1 *Gap Gas Composition*

From the gap conductance data files, generated by GESTR, TRACG obtains the following:

[[

]]

[[

]]

7.5.2.6.2 *Initial Gap Size*

[[

]]

7.5.2.7 Assessment

The gap conductance models implemented into TRACG are consistent with the GESTR-LOCA model[174] and are comparable to the models in SAFER[172]. The TRACG calculated transient gap responses agree very well with those calculated by SAFER for the identical boundary conditions as shown in Figure 7-15. The comparison was done for a small break LOCA case. The initial values agreed perfectly and small differences developed during the transient due to differences between the TRACG and SAFER hydraulic models.

[[

]]

Figure 7-15. TRACG to SAFER/GESTR Gap Conductance Comparison

The uncertainty in the total fuel heat transfer is assessed in terms of the calculated temperature difference (fuel centerline-moderator). For 1σ value in gap conductance, the change in temperature difference is [[ ]].

7.5.3 Cladding Perforation

The cladding swelling and rupture model calculates the cladding hoop stress, strain (elastic and plastic) and the conditions of cladding perforation. The cladding hoop stress is calculated from the differential pressure (internal gas pressure – system coolant pressure) across the cladding. This hoop stress is then compared to the stress at which perforation will occur, which decreases as the cladding temperature increases. The transient internal gas pressure is calculated from the perfect gas law, which requires calculation of the transient gas temperature in the fuel rod plenum and in the fuel column.

The remainder of this section is organized as follows. Section 7.5.3.1 documents the calculation for the cladding hoop stress and the internal gas pressure. Section 7.5.3.2 documents the calculation for the plenum gas temperature, and Section 7.5.3.3 describes the perforation model. Section 7.5.3.4 gives the assessment of the cladding swelling and rupture model in TRACG.

The perforation model applies to any point along the fuel rod. Normally perforation would be expected to occur at the point of peak LHGR, but perforation could occur for an LHGR less than the PLHGR, if the temperature is higher at that location.

7.5.3.1 Cladding Stress and Internal Gas Pressure

The transient fuel rod cladding hoop stress is a function of the difference between the fuel rod internal gas pressure (P_g) and the external coolant pressure (P) and is calculated for a thin walled tube as:

$$\sigma_c = \left(\frac{r_{ci}}{r_{co} - r_{ci}} \right) \left(P_g - P \right) \tag{7.5-30}$$

where

P_g = Fuel rod internal gas pressure

P = System coolant pressure

The fuel rod internal gas pressure is calculated using the perfect gas law [[

]]

7.5.3.2 Plenum Gas Temperature

The transient plenum temperature, T_p (t), is calculated by solving a set of coupled ordinary differential equations for the spring/getter, unheated cladding and plenum gas temperatures as described here (and shown as Figure 7-16):

[[

]]

These results are used to determine the transient fuel rod internal gas pressure and the transient cladding hoop stress.

7.5.3.3 Rod Perforation Model

The transient fuel rod cladding hoop stress (Equation (7.5-30)) is used with the perforation model to determine the onset of cladding plastic yielding and fuel rod perforation.

[[

]]

7.5.3.4 Assessment

The gap perforation models implemented into TRACG are comparable to the models in SAFER[172]. The cladding rupture stress and plastic strain are based on experimental data[175]. The TRACG calculated transient gap responses agree very well with those calculated by SAFER[172] for identical boundary conditions.

7.5.4 Thermal Radiation Heat Transfer

In addition to heat transfer options available for other components, the fuel rod and channel wall heat transfer models include detailed radiation heat transfer for each rod group as well as for the inside of the channel wall. Section 6.6.12 describes the thermal radiation model used in TRACG.

[[

]]

Figure 7-16. Plenum Gas Temperature Model

[[

]]

Figure 7-17. Cladding Rupture Stress vs. Temperature

[[

]]

Figure 7-18. Cladding Plastic Strain vs. Temperature

7.5.5 Critical Power

The critical power is calculated from the GEXL correlation. The GEXL correlation calculates the critical quality as function of pressure (P), mass flux (G), boiling length (L_B), annular length (L_A), R-factor (R), and thermal diameter (D_Q):

$$x_c = x_c(P, G, L_B, L_A, R, D_Q) \tag{7.5-38}$$

Critical power or boiling transition is then determined as the condition where the equilibrium quality (x_e) equals the critical quality (x_c):

$$x_e = x_c \tag{7.5-39}$$

For a bundle with a power Q, a typical equilibrium quality and critical quality as function of axial elevation may look as shown in Figure 7-19.

[[

]]

Figure 7-19. Typical Equilibrium Quality and Critical Quality for a Fuel Bundle

The critical power is then determined by increasing the power or heat flow to the fluid while all other parameters such as pressure, inlet fluid conditions and power shapes are kept constant. The equilibrium quality will increase as the heat flow to the fluid is increased. As a result of the increased quality, the boiling boundary, defined as the point where the equilibrium quality equals zero (x_e = 0.0) is reached at a lower elevation in the bundle. Similarly, the

transition to annular flow, which is determined from the [[ ]] correlation, will move downwards in the bundle as the heat flow and equilibrium quality is increased. Consequently, for a given elevation z, the boiling and annular lengths will increase, and there will be a corresponding increase in the critical quality. The power or heat flow to the fluid is increased until, at some point in the bundle, the equilibrium quality equals the critical quality. The power Q_c at this condition is the critical power. For a bundle with a critical power of Q_c, a typical equilibrium quality and critical quality as function of axial elevation may look as shown in Figure 7-20.

[[

]]

Figure 7-20. Typical Equilibrium Quality and Critical Quality at Critical Power

[[

]]

It is convenient to introduce the following parameters: critical power ratio (CPR) and thermal margin (TM):

$$CPR = \frac{Q_c}{Q} \tag{7.5-41}$$

$$TM = \frac{x_c + \frac{\Delta h_s}{h_{fg}}}{x_e + \frac{\Delta h_s}{h_{fg}}} \tag{7.5-42}$$

where Δh_s is the inlet subcooling. Note:

$$x_{inlet} = -\frac{\Delta h_s}{h_{fg}} \tag{7.5-43}$$

From the above equations it is seen that critical power corresponds to CPR=1 and TM=1. Two options exist for the calculation of the CPR for transient conditions. [[

]]:

Option 1. [[

———— ————]] (7.5-44)

Option 2. [[

]]

The assessment of the critical power calculation can be found in Section 3.6 of the *TRACG Qualification LTR*[6].

7.5.6 Water Rod Model

An option to model water rod flow is available for the channel component. The water rod model allows the modeling of a flow path between any two channel cells. The geometry of this internal pipe connection is user specified as part of the channel input. The geometry specification is consistent with any pipe component with the added restriction that the cell boundaries in the water rod must match cell boundaries in the channel. This requirement facilitates the calculation of heat transfer through the water rod clad and direct energy deposition to the water rod fluid. The heat transfer connection between the channel and the water rod is specified using the component-to-component heat transfer logic. The solution of the water rod is handled in the same manner as that used for the secondary branch of the tee component. In the water rod, both end junctions are internal, whereas in the secondary tee branch only one end is an internal junction. This formulation allows for an implicit coupling of the water rod flow.

7.5.7 Hot Rod Model

TRACG uses a one-dimensional thermal hydraulic model for the fuel channel as well as the other one-dimensional components. Experience from the qualification of TRACG has shown that TRACG calculates the average fuel rod temperatures very well based on the average hydraulic conditions. Cross-sectional variations in the hydraulic conditions, however, can lead to variations in the in the heat transfer and fuel temperatures. This is particularly the case for high void fractions where the flow is in the annular flow regime and where the rods are in film boiling heat transfer. This is typically only important for the reflood phase of a LOCA prior to the quenching of the fuel rods. An optional hot rod model has been implemented into TRACG to account for this phenomenon. [[

]]

[[

]]

Figure 7-21. Hot Region Void Fraction

7.5.8 Cladding Oxidation

Cladding oxidation during events with high cladding temperatures are calculated using the Cathcart correlation[163] as described in Section 6.6.14. The initial oxidation thickness can be specified through input to TRACG. This allows the user the flexibility to specify either a nominal or bounding initial oxide thickness. In addition, TRACG also contains an optional model determined from plant data where the oxide thickness is determined as function of exposure. The nominal oxide thickness as function of exposure is given by:

[[ ]] (7.5-45)

where X is the exposure in GWd/MTU.

The uncertainty in the initial thickness is given by:

[[ ]] (7.5-46)

7.6 Jet Pump

This model is based on the tee component; however, modifications have been made to include the momentum source term for the junction in order to conserve momentum for the mixing process. Furthermore, losses have been included to account for inefficient mixing and for smooth and abrupt flow area changes.

7.6.1 Jet Pump Momentum Source

The momentum source term to be applied to the momentum equation for primary tube flow (Figure 7-22) is obtained by considering the momentum balance for the different flow configurations that can occur in the jet pump (Figure 7-24).

Considering the simple nodalization shown in Figure 7-23, the momentum source is derived for the liquid phase momentum equations. The results will also be applicable to the vapor momentum equation. The steady-state pressure changes due to the merging of two liquid flows (Figure 7-23) are for normal operating conditions ($V_1 > 0$, $V_2 > 0$, $V_3 < 0$):

$$\frac{P_1 - P_o}{\rho_\ell} = 0 \tag{7.6-1}$$

$$\frac{P_2 - P_1}{\rho_\ell} = v_2(v_1 - v_2) + v_3(v_1 + v_3)\frac{A_3}{A_2} \tag{7.6-2}$$

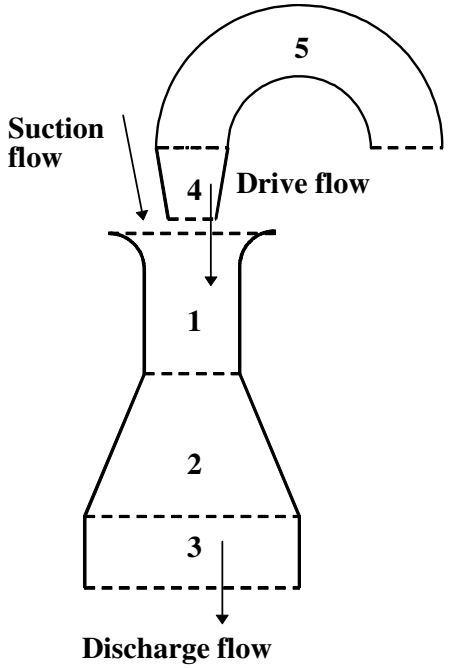

Figure 7-22. Jet Pump Nodalization

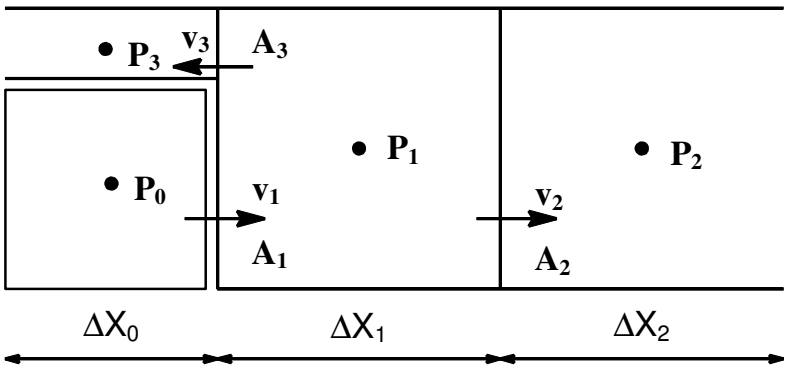

Figure 7-23. Simple Noding Scheme for Jet Pump Component

The momentum equation in the TRACG solution scheme depends on noding and flow direction. The calculated pressure change for a single-phase steady-state flow without sources, friction loss and gravity from the suction inlet to Cell 1 is given by:

$$\frac{P_1 - P_o}{\rho_\ell} = -\frac{1}{2}\,(v_1 + v_1\,\frac{A_1}{A_2})(v_1\,\frac{A_1}{A_2} - v_1) = \frac{1}{2}\,v_1^{\,2}\,(1 + \frac{A_1}{A_2})\,\frac{A_3}{A_2} \tag{7.6-3}$$

This pressure increase is the pressure recovery given by Bernoulli's equation for a stream expanding from an area of A_1 to A_2. This pressure gain will not occur in the jet pump and is compensated for by a simple loss coefficient.

From Cell 1 to Cell 2, the pressure change is given by:

$$\frac{P_2 - P_1}{\rho_\ell} = -v_2\,(v_2 - v_1\frac{A_1}{A_2}) + B \tag{7.6-4}$$

By combining Equations 7.6-2 and 7.6-4, the momentum source term is calculated to be:

$$B = \frac{A_3}{A_2}v_3\,(v_3 + v_1) + \frac{A_3}{A_2}v_1v_2 \tag{7.6-5}$$

This source term is applied in TRACG for positive drive flow. In the case of negative source flow (positive side tube velocity), the flow in the primary tube may not be accelerated by the source flow. Therefore, the momentum source term is set to zero; nevertheless, there is an irreversible loss due to the flow splitting similar to the flow with sudden expansion.

Two loss coefficients have been implemented into TRACG to account for incomplete mixing of the fluid stream. The losses are the nozzle loss applied at face 3 in Figure 7-23, and the mixing loss applied at face 2 in Figure 7-23. These losses have been correlated against data

from the 1/6 scale jet pump test performed at INEL. The losses depend on the flow regime, and are given in Table 7-3 and Table 7-4.

Table 7-3. Jet Pump Mixing Losses

Regime	Drive flow	M	$\frac{\Delta P}{\rho_\ell}$
1	$v > 0$	$0 < M$	$\max\left[0,\ 0.065\left(1-\frac{M_o}{M}\right)\right] c^*\ v_1^2$
2	$v > 0$	$-1 < M < 0$	0.0
3	$v > 0$	$M < -1$	0.0
4	$v < 0$	$0 < M$	0.0
5	$v < 0$	$-1 < M < 0$	$0.065\ c^*\ v_1^2$
6	$v < 0$	$M < -1$	$0.065\ c^*\ v_1^2$

Table 7-4. Jet Pump Nozzle Losses

Regime	Drive flow	M	$\frac{\Delta P}{\rho_\ell}$
1	$v > 0$	$0 < M$	0
2	$v > 0$	$-1 < M < 0$	$\min [2.5, M (0.08M - 0.06)]\ v_3^2$
3	$v > 0$	$M < -1$	$\min [2.5, M (0.08M - 0.06)]\ v_3^2$
4	$v < 0$	$0 < M$	$\max [0, 0.48 (1 - M/M_o)]\ v_3^2$
5	$v < 0$	$-1 < M < 0$	$[0.48 - M(0.33 - 1.74M)]\ v_3^2$
6	$v < 0$	$M < -1$	$2.55\ v_3^2$

where:

$$M=\frac{W_1}{-W_3}=\frac{A_1 v_1}{-A_3 v_3} \tag{7.6-6}$$

$$M_0 = \frac{A_2 - A_3}{A_3} \tag{7.6-7}$$

$$c^* = \max\left[1 , \left(\frac{A_1}{A_2 - A_3}\right)^2\right] \tag{7.6-8}$$

7.6.2 Jet Pump Form Loss Coefficients

Additional losses are included in the jet pump model. These losses account for inlet and exit losses as well as form losses in converging or diverging flow areas.

7.6.2.1 Diffuser (Expansion) Losses

The irreversible pressure loss coefficient through a diffuser is given by Idelchik[181] as:

$$K = C_e \, (\tan\beta)^{1.5} \, (1-A^*)^2 \tag{7.6-9}$$

where:

β = Diffuser angle

A^* = Area ratio of outlet to inlet

C_e = Constant

The recommended value of C_e is 0.0 and is the default value in TRACG. Users may input the value of C_e if they so desire.

This pressure loss coefficient is used at every cell face of the jet pump where the flow areas at the cell centers on either side of the face increase in the direction of flow.

7.6.2.2 Nozzle (Contraction) Losses

The irreversible pressure loss coefficient through a nozzle is due to the contraction is given by Idelchik[181] as:

$$K = C_o \, \sin\beta \, (1-A^*) \tag{7.6-10}$$

where:

β = Contraction angle

A^* = Area ratio of outlet to inlet of contraction

C_o = Constant

The default value of C_O is 0.38 in TRACG. The user can optionally input their own value of C_O. This pressure loss coefficient is used at every face in the jet pump where the flow area at the cell centers on either side of the face decrease in the direction of flow.

7.6.2.3 Inlet Losses

There is an irreversible pressure loss at the jet pump suction inlet due to the contraction of the suction flow from the down-comer to the jet pump. The loss coefficient for this loss has been estimated to be 0.02 from data obtained at INEL using 1/6 scale jet pumps[182]. When flow at the jet pump diffuser outlet reverses, there is a contraction loss from the lower plenum into the jet pump diffuser. The loss coefficient for this loss has been estimated from data to be 0.38. These values are in TRACG as default values, but the user may change them.

7.6.2.4 Outlet Losses

There is a loss at the diffuser outlet due to the flow expansion from the diffuser outlet into the lower plenum for normal operating conditions in the jet pump. The loss coefficient for this loss is estimated to be 1.0 and is implemented into TRACG at the diffuser outlet for forward flow in the diffuser.

7.6.3 Applicability

The jet pump model was developed based on 1/6 scale jet pump data[182],[184] from Idaho National Engineering Laboratory. The test data included a range of drive flow from $-4.2 \cdot 10^{-3}$ to $4.2 \cdot 10^{-3}$ m^3/sec covering typical operating conditions of a BWR jet pump and covering all six flow regimes indicated in Figure 7-24.

7.6.4 Assessment

Assessment against the 1/6 scale jet pump data is shown in Figure 7-25. In this figure the data are plotted in terms of M and N ratios defined as follows:

$$M = \frac{W_{Suction}}{W_{Drive}} \tag{7.6-11}$$

$$N = \frac{P_{Discharge} - P_{Suction}}{P_{Drive} - P_{Discharge}} \tag{7.6-12}$$

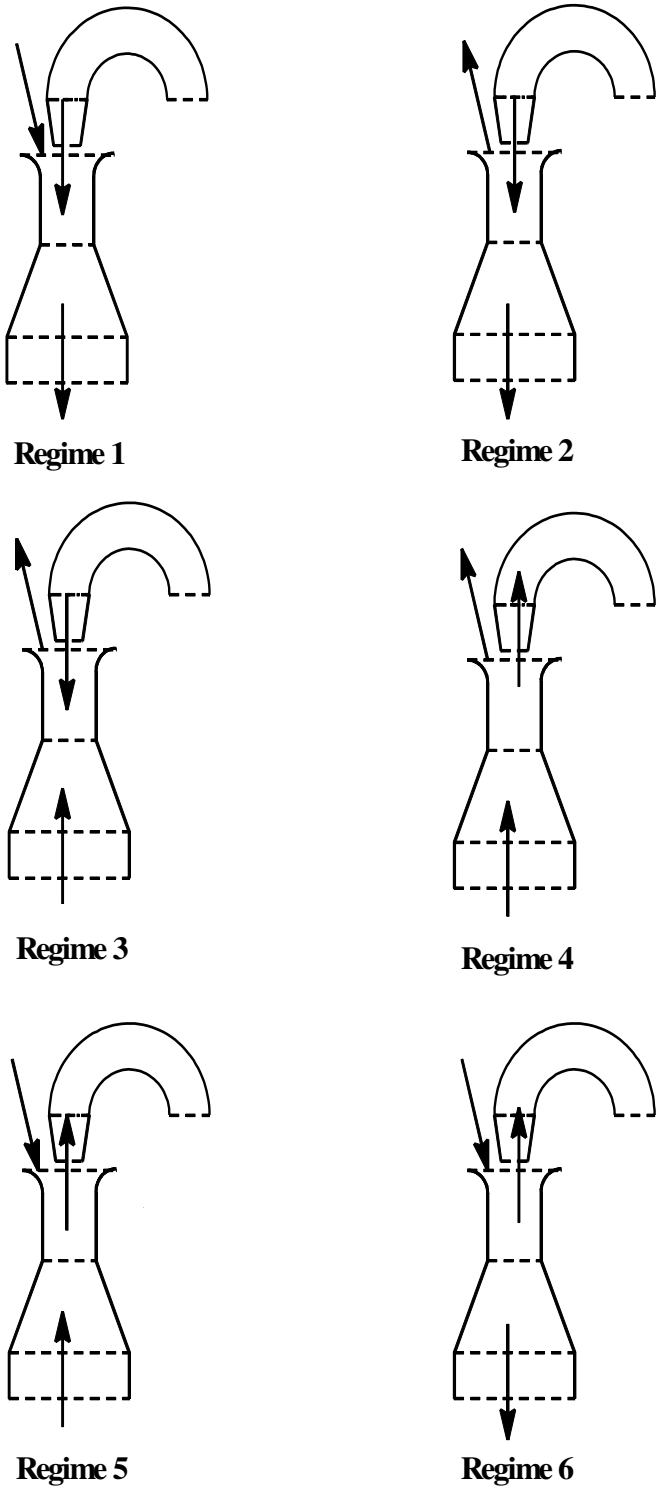

Figure 7-24. Jet Pump Flow Regimes

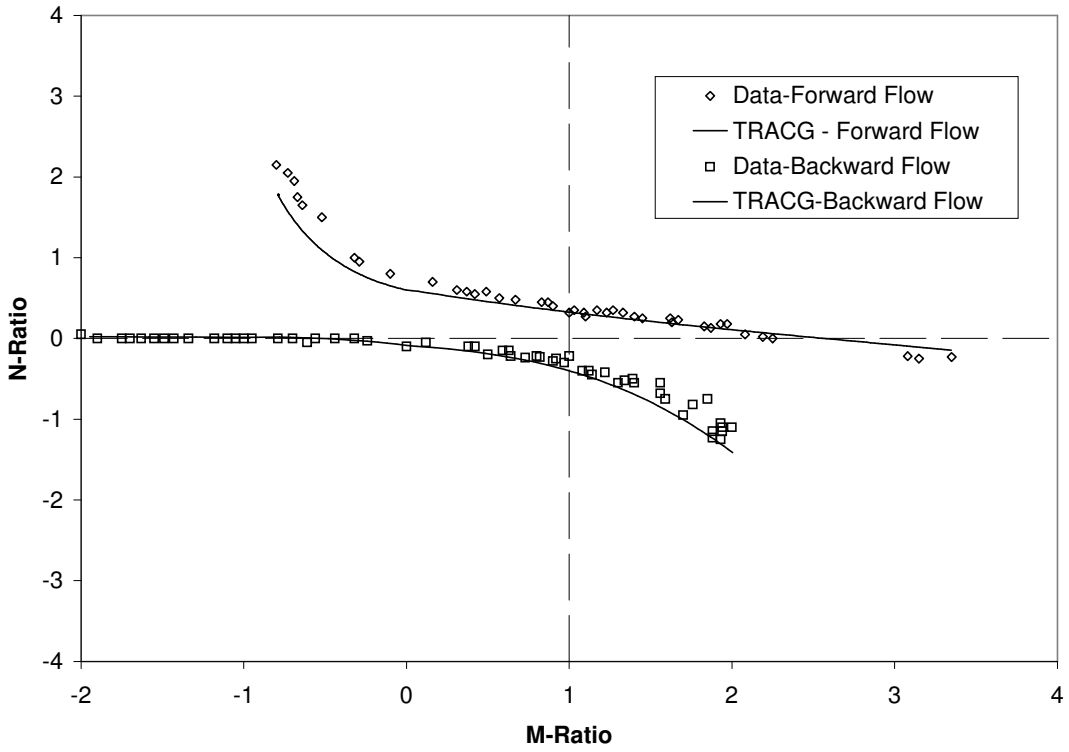

Figure 7-25. Comparison to 1/6 Scale Jet Pump Data

The agreement between TRACG and the data is seen to be very good for both positive (Curve 1) and negative drive flow (Curve 2). Only for negative drive flow and large M-ratios, where the suction velocity exceeds the drive velocity, is some deviation from the data observed. Except for negative drive flow and large M-ratios, which is not a typical operating condition, the N-ratio is seen to be predicted with a typical accuracy of 0.1.

7.7 Steam Separator

The performance characteristics of the steam separator are measured in terms of the pressure drop across the separator, carryover, which is the amount of liquid entrained in the steam leaving the separator, and carryunder, which is the amount of steam entrained into the liquid leaving the separator. These quantities have important effects on plant transient performance. The separator pressure drop is one of the resistances for the flow circulating through the reactor core. The carryover affects the steam dryer pressure drop and dryer efficiency. The carryunder affects the water subcooling in the downcomer and at the reactor core inlet. Core inlet subcooling, in turn, affects the thermal-hydraulic performance of the fuel bundles, and the moderator-to-fuel ratio in the core. The following sections describe the assumptions and formulation of a mechanistic based model for internal steam separators in BWRs.

Nomenclature

Item	*Description*
A	void profile function in water layer (Equation 7.7-4)
A	area
AA	constant parameter used in void profile function “a”
A_I	standpipe flow area
A_N	exit flow area of the swirl vane passage
b	void profile function in vapor core (Equation 7.7-3)
BB	constant parameter used in void profile function “b”
C	proportional constant used in Equation 7.7-1
CC	proportional constant
C_F	frictional coefficient
C_{NOZ}	contraction loss coefficient
DD	proportional constant
D_D	hydraulic diameter of the discharge passage
E_{LD}	equivalent L/D coefficient at the pickoff ring
F	frictional force
F_f	resultant frictional force
g	acceleration of gravity
h_{12}	distance from pickoff ring to discharge exit
H_D	barrel length
P_o	vapor core pressure
P	pressure
r	radius
r_f	inner radius of the water layer (Figure 7-27)
r_w	inner radius of the separator barrel (Figure 7-27)
Re	Reynolds number
v	velocity
W	flow rate
x	quality
Greek Symbols	

Nomenclature

Item	***Description***
α	void fraction
ρ	density
$\rho_{M,D}$	mean discharge density
π	Constant = 3.14159
μ	viscosity
θ	swirl vane angle
Subscripts	
a	axial
cu	carryunder
co	carryover
D	discharge
f	water layer
g	vapor
i	inlet
m	mixture
n	swirl vane exit
t	tangential
w	separator barrel

7.7.1 Technical Basis and Assumptions

Under normal operating conditions, the steam-water mixture enters the separator from the standpipe, and passes through a set of stationary swirl vanes into the separating barrel. The swirl vanes are physically similar to a set of stationary turbine blades with blade tip angle of θ to the horizontal at the blade channel exit. These vanes produce a high rotational velocity component in the fluid flowing through the separating barrel. The resultant centrifugal force separates the steam-water mixture into a water layer on the wall and a steam vortex core. Figure 7-26 shows two typical types of steam separators used in General Electric BWRs. Figure 7-27 depicts the geometries and flows in the separator model. In this model, consideration is focused on the conservation of mass and momentum in the water layer region and vapor core region. Integral formulations are used for the conservation equations. The following assumptions are made at the axial locations near the pickoff ring:

- A mean (or uniform) axial velocity is assumed in each flow region, i.e.:
  $0 < r < r_f$: $v_a = v_{ag}$. Uniform in vapor core
  $r_f < r < r_w$: $v_a = v_{af}$. Uniform in water layer
  where r_f is the inner radius of the water layer. Velocity slip conditions exist at the interface and at the wall.
- It is assumed that the tangential velocity in each region is proportional to a quantity C that is related to the vortex strength or angular momentum. For the radial distribution of tangential velocity, it would be reasonable to expect a tangential velocity profile with zero at the vapor core center, a peak value at the interface between the two regions, and a somewhat lower velocity in the water

layer region due to wall effects. In the following, it is assumed that there is solid rotation in the vapor core region and the tangential velocity decays with $1/\sqrt{r}$ in the water layer region, as follows:

$$0 < r < r_f \ : \ v_t = \frac{rC}{r_f^{3/2}} \text{ in vapor core} \tag{7.7-1}$$

$$r_f \le r < r_w \ : \ v_t = \frac{C}{\sqrt{r}} \text{ in water layer} \tag{7.7-2}$$

The inertia is small in the high void fraction core region. The assumption of solid body rotation is therefore made for the core with the angular velocity given by the velocity of the film surface. For the film, the angular velocity will decrease approaching the wall. In this region the assumption of zero vorticity is made, except for a thin boundary layer next to the wall.

The radial distributions of void fraction in each region are affected mainly by the vortex strength and the inlet quality. For higher vortex strength and inlet quality, it is expected that the void fraction profile in the vapor core region would get closer to 1.0. For higher vortex strength and lower inlet quality, it is expected that the void fraction profile in the water layer region would get closer to 0.0. With these expected characteristics, the void fraction profiles in each region are assumed to have the following functional forms:

$$0 < r < r_f \ : \ \alpha = 1 - b\frac{r}{r_w} \text{ in vapor core} \tag{7.7-3}$$

$$r_f < r < r_w \ : \ \alpha = a\left[\frac{r_w}{r} - 1\right] \text{ in water layer} \tag{7.7-4}$$

and

$$a = AA\left[\frac{\sqrt{gr_w^2}}{C}\right]^{0.5} x_i^2 \tag{7.7-5}$$

$$b = BB\left[\frac{\sqrt{gr_w^2}}{C}\right]^{0.5} (1 - x_i)^3 \tag{7.7-6}$$

- Where x_i is the inlet quality, AA and BB are parameters to be determined from data.
- Since the vapor density is relatively small, it is reasonable to expect the pressure variation in the vapor core to be small. In the model, the vapor core pressure (P_o) is assumed to be uniform radially and axially. The pressure at the separator wall (P_w) is related to P_o by centrifugal force across the water layer.

7.7.2 Model Formulations

For the first stage of the separator, a total of six unknowns are introduced in this model: v_{ag}, v_{af}, C, r_f, P_o, and P_w. The required equations are formulated from conservation of water mass, vapor mass, axial momentum, and angular momentum for the fluid entering and leaving the separating barrel, from centrifugal pressure drop across the water layer, and from pressure drop in the discharge passage. The above unknowns can then be solved for given conditions of pressure P_i, total flow rate W_i, and quality x_i at the nozzle inlet.

The mass and momentum conservation equations for flows entering the separating barrel at the swirl vane exit and leaving the separating barrel at the pickoff ring are as follows:

Water Mass

$$(1-x_i)\,W_i = \int_0^{r_w} \rho_f v_a (1-\alpha)\, 2\pi r dr$$

$$= 2\pi\rho_f v_{ag} \left(\frac{1}{3}\frac{r_f}{r_w} b\right) r_f^2 \qquad (7.7\text{-}7)$$

$$+ 2\pi\rho_f v_{af} \left[\left(\frac{1+a}{2}\right)\left(r_w^2 - r_f^2\right) - a\, r_w \left(r_w - r_f\right)\right]$$

Vapor Mass

$$x_i W_i = \int_0^{r_w} \rho_g v_a\, \alpha\, 2\pi r dr$$

$$= 2\pi\rho_g v_{ag} \left(\frac{1}{2} - \frac{1}{3}\frac{r_f}{r_w} b\right) r_f^2 \qquad (7.7\text{-}8)$$

$$+ \pi\rho_g v_{af}\, a \left(r_w - r_f\right)^2$$

Angular Momentum

$$\int_{r_h}^{r_w} v_{tn} r \left(2\pi r dr \rho_{mi} v_{an}\right) = \int_0^{r_w} v_t r \left(2\pi r dr \rho v_a\right) + F_t r_w \qquad (7.7\text{-}9)$$

The integrated equation is as follows:

$$\frac{2}{3}\pi\rho_{mi}v_{tn}v_{an}\left(r_w^3-r_h^3\right)$$

$$=2\pi v_{ag}C\left[\frac{1}{4}\rho_g r_f^{5/2}+\frac{1}{5}\frac{b}{r_w}\left(\rho_f-\rho_g\right)r_f^{7/2}\right]$$

$$+2\pi v_{af}C\left[\rho_f+a\left(\rho_f-\rho_g\right)\right]\frac{2}{5}\left(r_w^{5/2}-r_f^{5/2}\right) \qquad (7.7\text{-}10)$$

$$-2\pi v_{af}Cr_w a\left(\rho_f-\rho_g\right)\frac{2}{3}\left(r_w^{3/2}-r_f^{3/2}\right)+F_t r_w$$

Axial Momentum

$$\pi r_h^2 P_o+\int_{r_h}^{r_w}\left(\rho_{mi}v_{an}^2+P_n\right)2\pi r dr=\int_0^{r_w}\left(\rho v_a^2+P\right)2\pi r dr+F_a \qquad (7.7\text{-}11)$$

The integrated equation is as follows:

$$\pi r_h^2 P_o\left(\rho_{mi}v_{an}^2+P_n\right)\pi\left(r_w^2-r_h^2\right)=$$

$$\left(\rho_g v_{ag}^2+P_o\right)\pi r_f^2+\frac{2}{3}\pi b\left(\rho_f-\rho_g\right)v_{ag}^2\frac{r_f^3}{r_w}$$

$$+2\pi v_{af}^2\left[\left(\rho_f+a\left(\rho_f-\rho_g\right)\right)\frac{1}{2}\left(r_w^2-r_f^2\right)\right.$$

$$\left.-a\left(\rho_f-\rho_g\right)r_w\left(r_w-r_f\right)\right]+F_a$$

$$+2\pi\left[\frac{1}{2}P_w\left(r_w^2-r_f^2\right)-\frac{1}{2r_w}\left(\rho_f+a\left(\rho_f-\rho_g\right)\right)C^2\left(r_w-r_f\right)^2\right.$$

$$\left.+\frac{1}{4}a\left(\rho_f-\rho_g\right)C^2\left(2r_w\log\left(\frac{r_w}{r_f}\right)-\frac{1}{r_w}\left(r_w^2-r_f^2\right)\right)\right] \qquad (7.7\text{-}12)$$

Assuming that the flow through the swirl vane passage is homogeneous, the pressure and velocity entering the separating barrel are related to the conditions at the standpipe as follows:

$$W_i = \rho_{mi} v_i A_i = \rho_{mi} v_{an} A_n \tag{7.7-13}$$

$$P_i + \frac{1}{2}\rho_{mi} v_i^2 = P_n + \frac{1}{2}\rho_{mi}\left(v_{an}^2 + v_{tn}^2\right)\left(1 + C_{NOZ}\right) \tag{7.7-14}$$

and

$$\frac{v_{an}}{v_{tn}} = \tan\theta \tag{7.7-15}$$

where θ is the angle between the swirl vane and a horizontal plane, and C_{NOZ} is the contraction loss coefficient (Reference [185]) defined as:

$$C_{NOZ} = 0.5\left(1 - \frac{A_N}{A_I}\right) \tag{7.7-16}$$

A_N is the exit flow area of the swirl vane passages and A_I is the standpipe flow area.

F_a in Equation (7.7-11) is the axial component and F_t in Equation (7.7-9) is the tangential component of the frictional force on the swirling water layer:

$$F_a = F_f \frac{v_{af}}{v_w} \tag{7.7-17}$$

$$F_t = F_f \frac{v_{tw}}{v_w} \tag{7.7-18}$$

where v_{tw} is the tangential velocity on the wall,

$$v_{tw} = \frac{C}{\sqrt{r_w}} \tag{7.7-19}$$

and v_w is the resultant swirling velocity on the wall,

$$v_w = \sqrt{v_{tw}^2 + v_{af}^2} \tag{7.7-20}$$

F_f is the resultant frictional force,

$$F_f = \frac{1}{2}\rho_f C_F v_w^2 \left(2\pi r_w\right) H_D \tag{7.7-21}$$

For turbulent flow over a flat plate (Reference [183]),

$$C_F = \frac{0.455}{\left(\log Re_L\right)^{2.58}} \tag{7.7-22}$$

where Re_L is defined as:

$$Re_L = \frac{\rho v_w}{\mu}\left(\frac{H_D v_w}{v_{af}}\right) \tag{7.7-23}$$

The term ($H_D\ v_w/v_{af}$) represents the linear distance that a water particle will travel inside the separator barrel.

The radial pressure drop across the water layer due to centrifugal force is:

$$\int_{P_o}^{P_w} dP = \int_{r_f}^{r_w} \rho \frac{v_t^2}{r} dr \tag{7.7-24}$$

or

$$P_o = P_w - \left[\rho_f + a\left(\rho_f - \rho_g\right)\right]C^2\left(\frac{1}{r_f} - \frac{1}{r_w}\right) + \frac{1}{2}a\left(\rho_f - \rho_g\right)C^2\left(\frac{r_w}{r_f r_f} - \frac{1}{r_w}\right) \tag{7.7-25}$$

The pressure drop in the discharge passage is:

$$\int_{r_r}^{r_w}\left(\frac{\rho}{2}v_a^2 + P\right)dA\left[\int_{r_r}^{r_w} dA\right]^{-1}$$

$$= \frac{1}{2}\rho_{M,D}v_D^2\left[1 + 4C_F\left(\frac{H_D}{D_D} + E_{LD}\right) + C_K\right] \tag{7.7-26}$$

$$+\left(P_o + \rho_f h_{sub} g - \rho_D h_{12} g\right)$$

where $\rho_{M,\,D}$ and v_D are the mean discharge density and velocity to be defined. H_D and D_D are the length of the separator barrel and hydraulic diameter of the discharge passage, h_{12} is the distance from pickoff ring to discharge exit. E_{LD} is the equivalent L/D coefficient at the pickoff ring, and C_K is the total loss coefficient in the discharge passage.

The left-hand side of Equation (7.7-26) can be integrated as follows:

For $r_f < r_r$:

$$\int_{r_r}^{r_w} \left(\frac{\rho}{2} v_a^2 + P\right) dA \left[\int_{r_r}^{r_w} dA\right]^{-1} =$$

$$\frac{1}{\left(r_w^2 - r_r^2\right)} \left\{ \frac{1}{2} v_{af}^2 \left[\left(\rho_f + a\left(\rho_f - \rho_g\right)\right)\left(r_w^2 - r_r^2\right) - 2a\left(\rho_f - \rho_g\right) r_w \left(r_w - r_r\right)\right] \right.$$

$$+ P_w \left(r_w^2 - r_r^2\right) - \left[\rho_f + a\left(\rho_f - \rho_g\right)\right] C^2 \frac{\left(r_w - r_r\right)^2}{r_w} \qquad (7.7\text{-}27)$$

$$\left. + \frac{1}{2} a\left(\rho_f - \rho_g\right) C^2 \left[2 r_w \log\left(\frac{r_w}{r_r}\right) - \frac{\left(r_w^2 - r_r^2\right)}{r_w}\right] \right\}$$

for $r_f \geq r_r$

$$\int_{r_r}^{r_w} \left(\frac{\rho}{2} v_a^2 + P\right) dA \left[\int_{r_r}^{r_w} dA\right]^{-1} =$$

$$\frac{1}{\left(r_w^2 - r_r^2\right)} \left\{ \left(\frac{1}{2} \rho_g v_{ag}^2 + P_o\right)\left(r_f^2 - r_r^2\right) + \frac{1}{3 r_w} b\left(\rho_f - \rho_g\right) v_{ag}^2 \left(r_f^3 - r_r^3\right) \right\}$$

$$+ \frac{1}{\left(r_w^2 - r_r^2\right)} \left\{ \frac{1}{2} v_{af}^2 \left[\left(\rho_f + a\left(\rho_f - \rho_g\right)\right)\left(r_w^2 - r_f^2\right) - 2a\left(\rho_f - \rho_g\right) r_w \left(r_w - r_f\right)\right] \right.$$

$$+ P_w \left(r_w^2 - r_f^2\right) - \left[\rho_f + a\left(\rho_f - \rho_g\right)\right] C^2 \frac{\left(r_w - r_f\right)^2}{r_w}$$

$$\left. + \frac{1}{2} a\left(\rho_f - \rho_g\right) C^2 \left[2 r_w \log\left(\frac{r_w}{r_f}\right) - \frac{\left(r_w^2 - r_f^2\right)}{r_w}\right] \right\} \qquad (7.7\text{-}28)$$

For the discharge passage Reference [183] gives:

$$C_F = \frac{0.079}{Re^{0.25}} \tag{7.7-29}$$

The steam and water flows discharged through the discharge passage are calculated as follows:

$$W_{g,cu} = \int_{r_r}^{r_w} \alpha \rho_g v_a \, 2\pi r dr \tag{7.7-30}$$

$$W_{f,cu} = \int_{r_r}^{r_w} (1-\alpha) \rho_f v_a \, 2\pi r dr \tag{7.7-31}$$

for $r_f < r_r$

$$W_{g,cu} = \pi \rho_g v_{af} a \left(r_w - r_r\right)^2 \tag{7.7-32}$$

$$W_{f,cu} = \pi \rho_f v_{af} \left[\left(r_w^2 - r_r^2\right) - a \left(r_w - r_r\right)^2 \right] \tag{7.7-33}$$

For $r_r < r_f$:

$$W_{g,cu} = x_i w_i - 2\pi \rho_g v_{ag} \left(\frac{1}{2} - \frac{1}{3} b \frac{r_r}{r_w} \right) r_r^2 \tag{7.7-34}$$

$$W_{f,cu} = \left(1 - x_i\right) w_i - 2\pi \rho_f v_{ag} \left(\frac{1}{3} b \frac{r_r}{r_w} \right) r_r^2 \tag{7.7-35}$$

The steam and water flows leaving the present stage and entering the next stage are:

$$W_{g,co} = (\text{steam flow})in - W_{g,cu} \tag{7.7-36}$$

$$W_{f,co} = (\text{water flow})in - W_{f,cu} \tag{7.7-37}$$

The total discharge flow is:

$$W_D = W_{g,cu} + W_{f,cu} \tag{7.7-38}$$

Assuming homogeneous flow in the discharge passage, the mean void fraction is:

$$\alpha_{cu} = \frac{W_{g,cu}}{W_{g,cu} + W_{f,cu} \left(\rho_g / \rho_f\right)} \tag{7.7-39}$$

the mean discharge density is:

$$\rho_{m,D} = \alpha_{cu} \rho_g + \left(1 - \alpha_{cu}\right) \rho_f \tag{7.7-40}$$

and the mean discharge velocity is:

$$v_D = \frac{W_D}{\rho_{m,D} A_D} \tag{7.7-41}$$

In summary, for given nozzle inlet conditions (P_i, x_i, and W_i) the unknowns (v_{ag}, v_{af}, C, r_f, P_o, and P_w) are calculated by solving Equations (7.7-7) to (7.7-26) simultaneously.

Similar equations can be written for the second and third stages. It is assumed that P_o is uniform axially (i.e., the vapor core pressure drop in the axial direction is small); therefore, the axial momentum equations can be neglected in the calculations. For these stages, the unknowns are reduced to v_{ag}, v_{af}, C, r_f, and P_w, and the equations are the conservation of liquid mass, vapor mass, and angular momentum, the pressure drop across the water layer, and the pressure drop in the discharge passage.

The right-hand sides of Equations (7.7-7), (7.7-8), and (7.7-9) represent the water flow, vapor flow and angular momentum, respectively, entering the separating barrel. For the second and third stages, these terms are modified as follows:

$$(\text{Water flow})_{in} = \left[W_{f,co} \right]_{\text{previous stage}} \tag{7.7-42}$$

$$(\text{Steam flow})_{in} = \left[W_{g,co} \right]_{\text{previous stage}} \tag{7.7-43}$$

$$(\text{Angular momentum})_{in} = \left[\int_0^{r_r} v_t r \left(2\pi r dr \rho v_a \right) \right]_{\text{previous stage}} \tag{7.7-44}$$

7.7.3 Carryunder and Carryover

The total vapor flow that is carried under consists of two parts. The first part is the steam flow through the first discharge passage with exit below the surface of the water pool surrounding the separators. The second part is the steam entrained by the total downward water flow, which is discharged from second and higher stages with exit above the surface of the water pool surrounding the separators. The amount entrained is proportional to the drag force, which is proportional to the square of the downward water velocity (or water flow). It is assumed that the second part is proportional to the square of the total water flow discharged from the second and higher stages, i.e.:

$$\left(W_{g,cu} \right)_{total} = \left[W_{g,cu} \right]_1 + CC \left[\sum_{i=2}^{N} \left(W_{f,cu} \right)_i \right]^2 \tag{7.7-45}$$

where:

N = 2 for 2-stage separator

= 3 for 3-stage separator

and CC is a proportional constants to be determined from data.

The total water that is carried over consists of two parts. The first part is the water flow through the last stage. The second part is the water flow entrained by the upward steam flow discharged from the second and higher stages through the discharge passage. Similarly, the second part is assumed to be proportional to the square of the total steam flow discharged from higher stages, i.e.:

$$\left(W_{f,co}\right)_{total} = \left[W_{f,co}\right]_N + DD\left[\sum_{i=2}^{N}\left(W_{g,co}\right)_i\right]^2 \tag{7.7-46}$$

where DD is a proportionality constant determined from data.

The carryunder and carryover are defined as follows:

$$CU = \frac{\left[W_{g,cu}\right]_{total}}{\text{Total Downward Water Flow}} \tag{7.7-47}$$

$$CO = \frac{\left[W_{f,co}\right]_{total}}{\text{Total Upward Steam Flow}} \tag{7.7-48}$$

Full scale performance test data for two-stage and three-stage steam separators are reported in References [186], [187], and [188]. In calculating these test conditions, it was determined that the parameters AA, BB, CC and DD with values summarized in Table 7-5 would yield good predictions.

[[

]]

7.7.4 Assessment

Full-scale performance test data for two-stage and three-stage steam separators are reported in References [186], [187], and [188]. These tests were performed at full scale conditions and provided carryunder, carryover and pressure drop data for a wide range of inlet conditions. Predictions of these test data by the TRACG model are presented in Figure 7-28 through Figure 7-32. These results are examples from the larger set of qualification cases that are documented in Section 4.2 of the *TRACG Qualification LTR*[6].

Figure 7-28 and Figure 7-29 show the comparison of the test data[186] with values calculated by the model for carryunder and carryover from a two-stage separator used in BWR/4 and BWR/5 reactors. The carryunder and carryover versus inlet quality are shown for three separator inlet flows that span the range of normal operation. The curves for different separator flows are offset by 0.2% in carryunder and 20% in carryover so the results for all the inlet flows can be shown in one figure. The data and predictions are for a separator skirt submergence of [[ ]], typical of normal operation.

Figure 7-30 compares the measured[187] and calculated pressure drop for a two-stage separator. These data are for a two-stage separator with an inlet flow of [[ ]]. The separator pressure drop is plotted versus the square of the volumetric flow rate to remove the inlet quality dependence from the data. It is seen that the separator pressure drop varies as the square of the volumetric flow in a manner similar to other irreversible loss elements. The plot shows the data best-fit line and parallel lines representing the best fit plus and minus one standard deviation. For this separator, the standard deviation is less than [[ ]] of mixture level. Similar fits to pressure drop data, developed for all of the BWR separator designs, are incorporated in the TRACG separator component model.

Figure 7-31 and Figure 7-32 compare the measured[188] and calculated carryunder and carryover for three-stage separators. The figures show carryunder and carryover versus inlet quality for three separator inlet flows at a separator skirt submergence of [[ ]]. This submergence is at the lower extreme of the range for normal operation. Again, the curves for different separator flows are offset by 0.2% in carryunder and 20% in carryover so the results for the three inlet flows can be shown in one figure.

The steam separators are designed to have the best performance under normal operating conditions, in the range of [[ ]] inlet quality for two-stage and [[ ]] inlet quality for three-stage separators. As indicated by the data shown in Figure 7-28 through Figure 7-32, both carryunder and carryover are at their minimum values around the normal operating conditions for two-stage and three-stage separators.

At lower inlet qualities, carryover increases significantly. This is because the water flowing into the separator, and hence the water layer thickness, increases as the inlet quality reduces. [[

]] Figure 7-29 and Figure 7-32 show that these carryover characteristics are well predicted by the model. As the inlet quality increases from the normal operating point, the water layer thickness reduces and, therefore, more steam from the vapor core is captured by the pickoff rings. Consequently, the carryunder increases as the inlet quality increases. Figure 7-28 and Figure 7-31 show that these carryunder characteristics are well predicted by the model.

In summary, results of these comparisons indicate that the mechanistic model adequately predicts the performance characteristics of steam separators for a wide range of inlet conditions and different inlet flow rates.

Table 7-5. Summary of Parameters Used in the Separator Model

2-Stage Separator			3-Stage Separator		
Parameter	**1st**	**2nd**	**1st**	**2nd**	**3rd**
AA	110.	20.	110.	20.	20.
BB	0.5	0.25	0.5	0.25	0.55
CC	0.0004	Not used	0.0004	Not used	Not used
DD	0.009	Not used	0.11	Not used	Not used

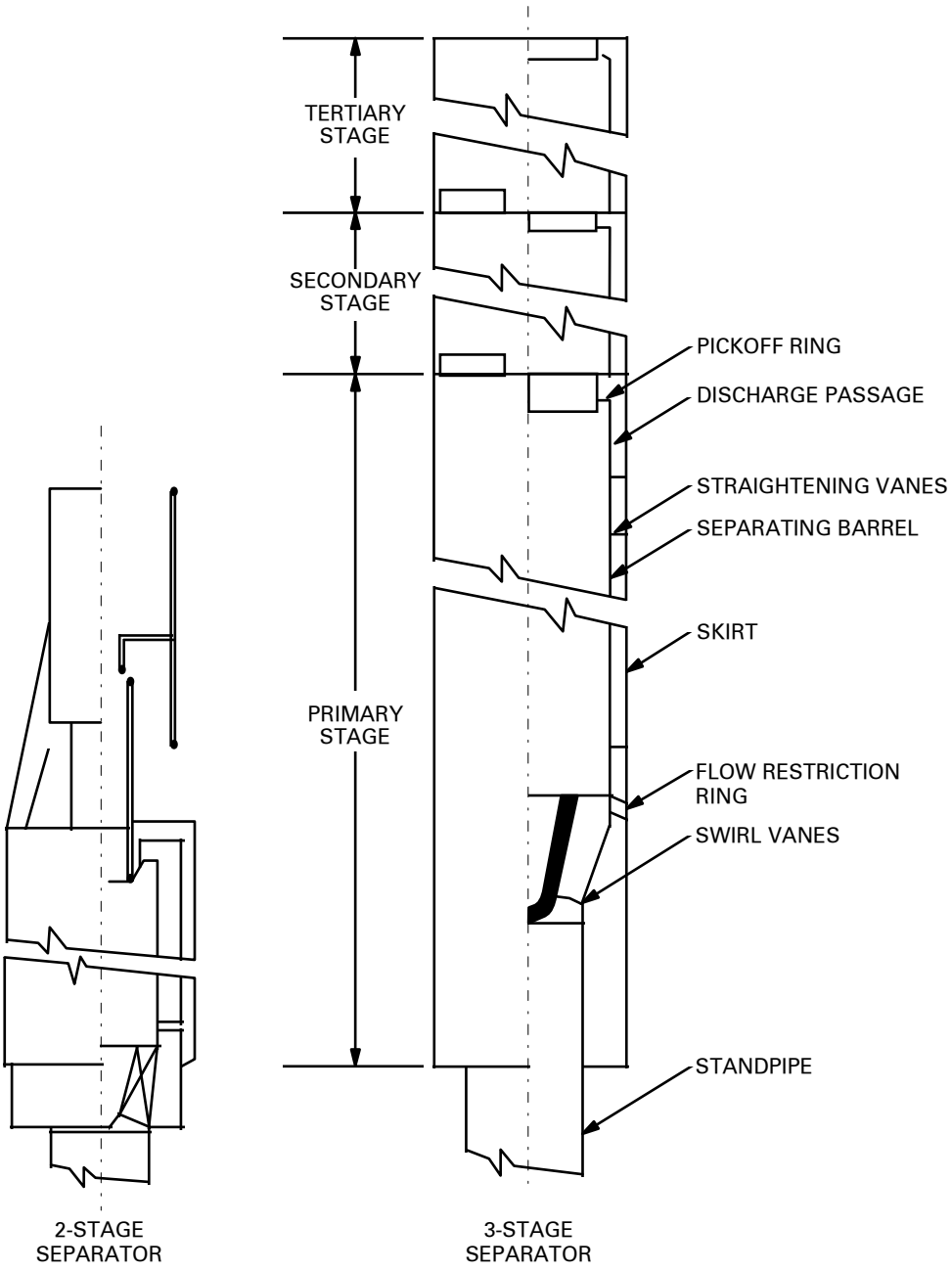

Figure 7-26. Typical Types of Steam Separators

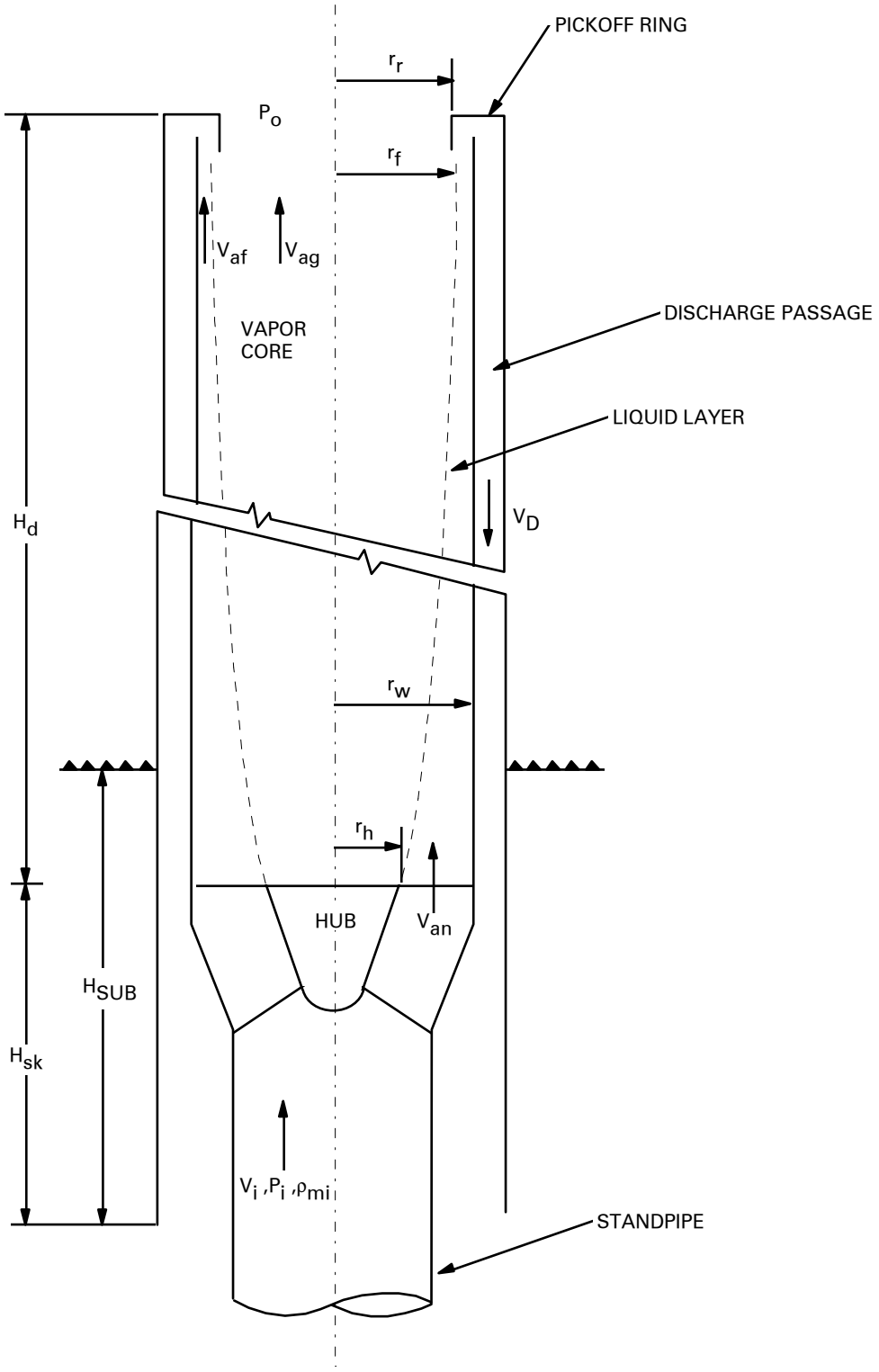

Figure 7-27. Schematic of the Separator Model

[[

]]

Figure 7-28. Comparison of Test Data and Mechanistic Model Prediction of Carryunder for Two-Stage Separator

[[

]]

Figure 7-29. Comparison of Test Data and Mechanistic Model Prediction of Carryover for Two-Stage Separator

[[

]]

Figure 7-30. Comparison of Test Data and Mechanistic Model Prediction of Separator Pressure Drop for Two-Stage Separator

[[

]]

Figure 7-31. Comparison of Test Data and Mechanistic Model Prediction of Carryunder for Three-Stage Separator

[[

]]

Figure 7-32. Comparison of Test Data and Mechanistic Model Prediction of Carryover for Three-Stage Separator

7.8 Vessel

The vessel (VSSL) component employs a three-dimensional, two-fluid, thermal-hydraulic model in cylindrical coordinates to describe the vessel flow. For modeling a BWR reactor vessel, a regular cylindrical mesh, with variable mesh spacings in all three directions, encompasses the downcomer, core bypass and upper and lower plenums of the vessel. The user describes the mesh by specifying the radial, angular, and axial coordinate of the mesh-cell boundaries:

R_i i = ,...NRSX

θ_j j = 1,...NTSX

and

z_k k = 1,...NASX

where NRSX is the number of rings, NTSX is the number of angular segments, and NASX is the number of axial levels. The point (R_i, θ_j, z_k) is a vertex in the coordinate mesh. Mesh cells are constructed and identified by an axial level number and a cell number as shown in Figure 7-33. For each axial level, the cell number is determined by counting the cells radially outward starting with the first angular segment and the innermost ring of cells. Figure 7-33 shows the relative face-numbering convention for an individual cell that is used in connecting other components to the vessel.

NOTE: Only three faces must be identified per mesh cell because the other faces will be defined by neighboring cells.

All fluid flow areas (on cell faces) and all fluid volumes are dimensioned so that the internal structure within the vessel can be modeled. Flow areas and fluid volumes are computed based on the geometric mesh spacings and scaled according to factors supplied as input. The scaled volumes and flow area are then used in the fluid dynamics and heat-transfer calculations. Flow restrictions and the volume occupied by the structure within each mesh cell are modeled through use of these scale factors. For example, the downcomer walls are modeled by setting the appropriate flow area scale factors to zero. Flow restrictions such as the top and bottom core support plates require scale factors between zero and one. Figure 7-34 shows the cell faces scaled to model the downcomer and core support plate flow restrictions.

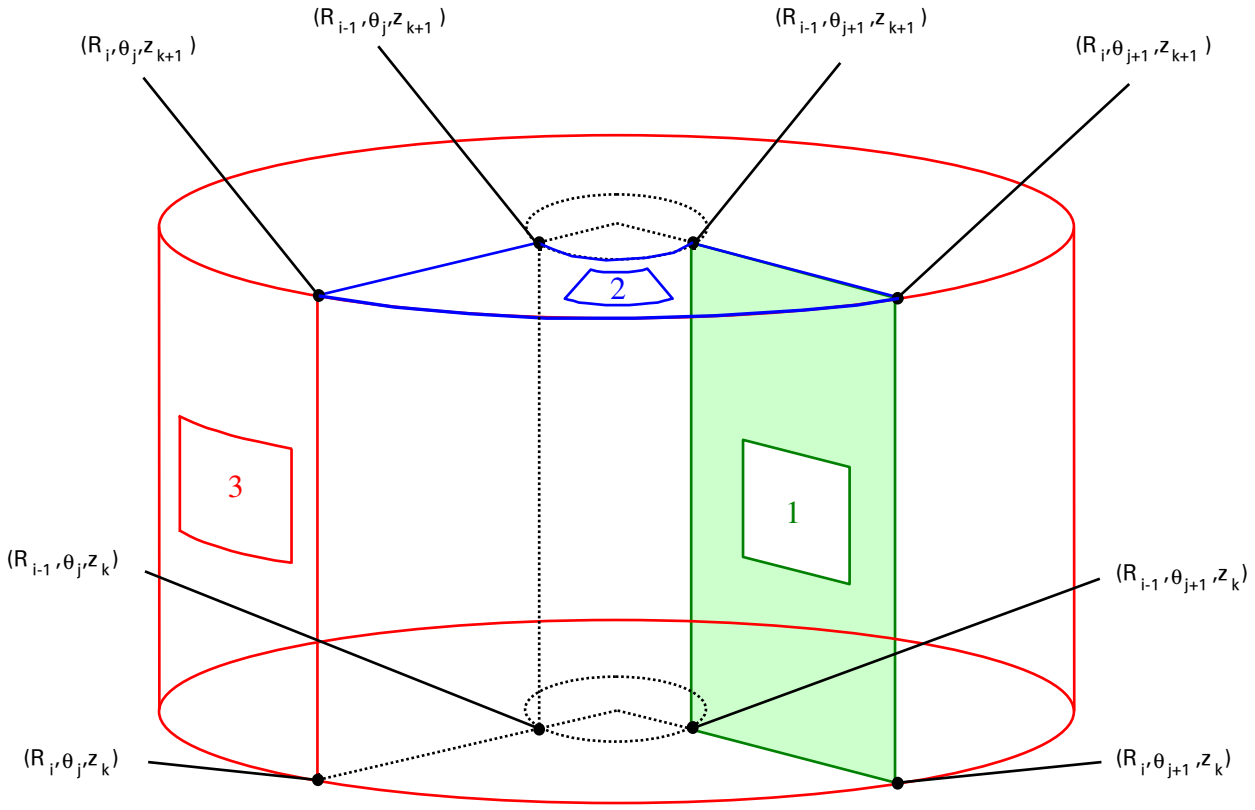

Face numbering convention is: 1=azimuthal=θ, 2=axial=z, and 3=radial=R.

Figure 7-33. Boundaries of a Three-Dimensional Mesh Cell

Plumbing connections from other components to the vessel are made on the faces of the mesh cells. Any number of connections may be made to the vessel; in fact, any mesh cell in the vessel can have one component or more connected to it. Five input parameters are used to describe a connection: ISRL, ISRC, ISRF, JUNS and ZJUN. The parameter ISRL defines the axial level in which the connection is made; ISRC is the mesh-cell number, as defined above; and ISRF is the face number, as defined in Figure 7-33. If ISRF is positive, the connection is made on the face shown in the figure with the direction of positive flow into the cell. The parameter JUNS is the system function number used to identify this function. The parameter ZJUN specifies the axial location of the connection expressed as a fraction of the level height. Figure 7-35 shows several vessel, pipe and jet pump connections. Internal and external connections are allowed. The user is cautioned against connecting to the vessel any component with a flow area that differs greatly from the flow area of the mesh-cell face to which it is connected because this can cause anomalous pressure gradients. Such a situation can be avoided by proper adjustment of the vessel geometry coordinate spacings and/or the use of taper or expansion sections on one-dimensional components prior to the vessel connections.

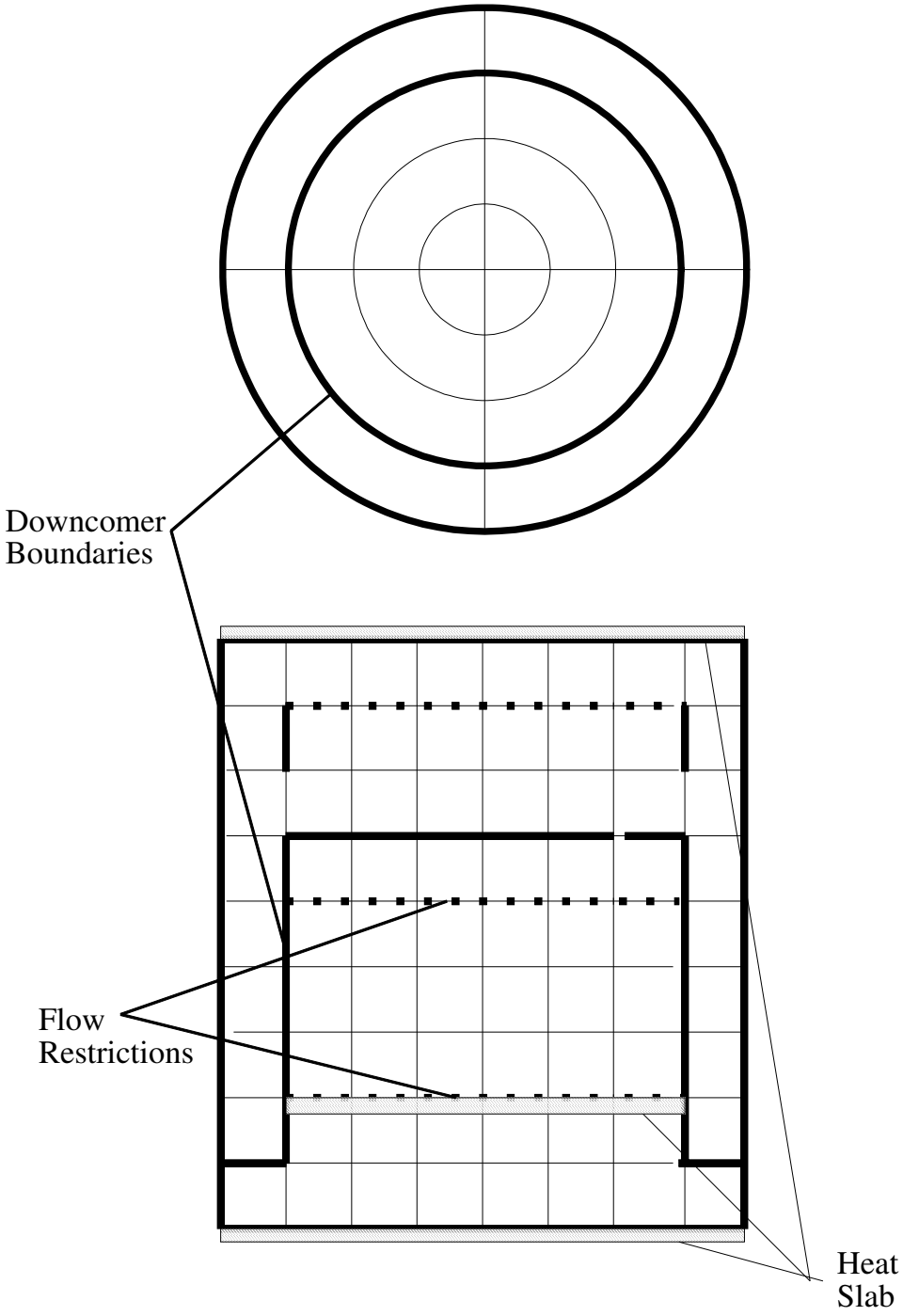

Figure 7-34. Flow Restrictions and Downcomer Modeling

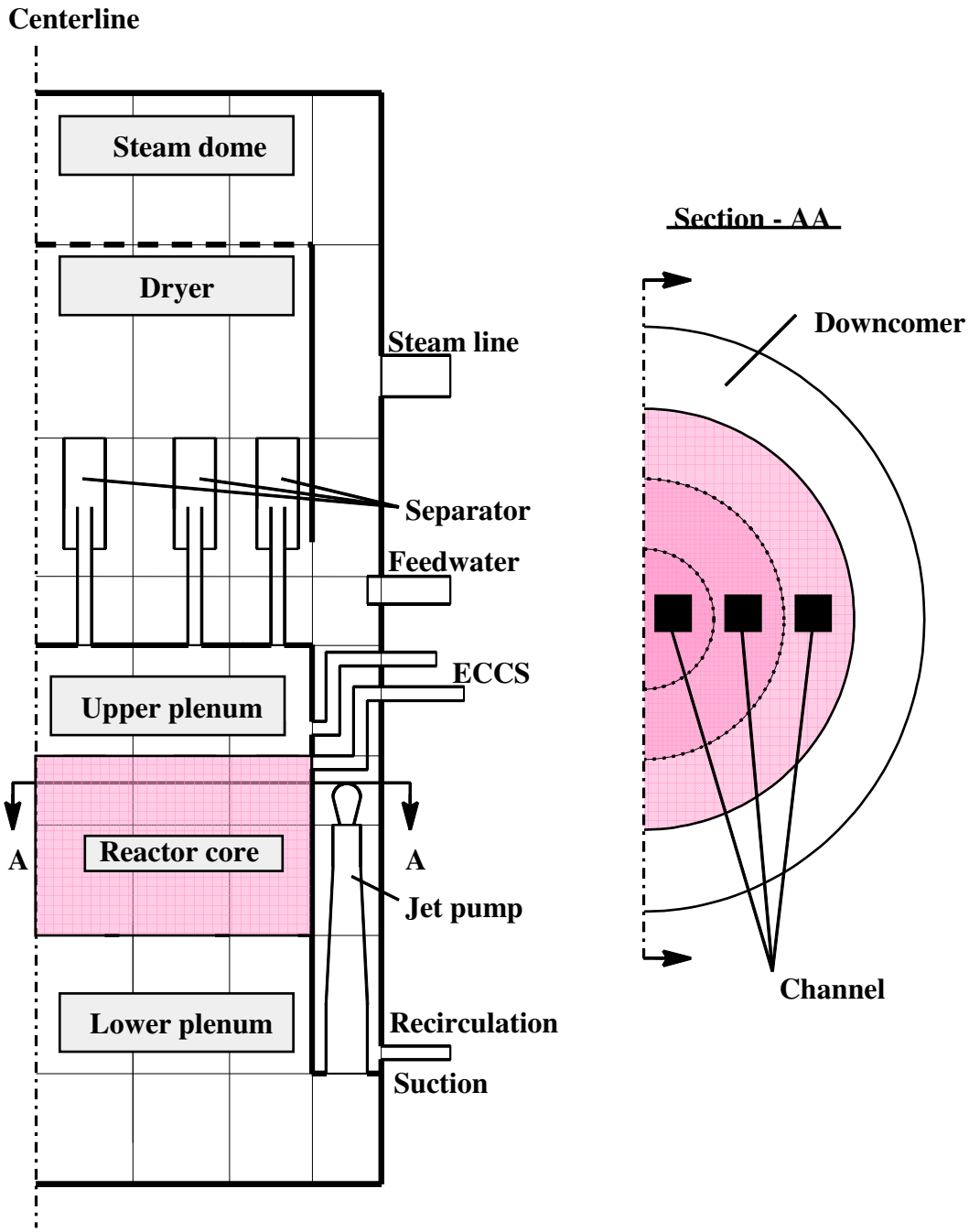

Figure 7-35. A Simplified Vessel Nodalization

The reactor core region in the vessel is specified by the upper, lower and radial core positional parameters (ICRU, ICRL, and ICRR). These parameters define, respectively, the upper, lower and radial boundaries of the cylindrical core region. The example provided in Figure 7-35 shows a possible configuration in which ICRU = 4, ICRL = 2, and ICRR = 3. Each mesh cell stack in the core region contains a channel component to simulate the fuel bundles in that core region. The flow into this core bypass region is calculated based on the leakage flow model described in Section 7.5.1. The bypass fluid properties associated with each channel are used in the kinetics calculations as described in Section 9.4.

A very important aspect of this three-dimensional vessel component is that it results in a multidimensional hydraulic model of regions within a BWR vessel in which multidimensional effects may be important. For example, an important aspect of BWR LOCA analysis is the emergency core coolant spray (ECCS) into the upper plenum. The noding diagram in Figure 7-35 results in a model in which the radial distribution of ECCS water in the upper plenum is represented by three vessel radial rings. The solution to the conservation equations in that region plus the coupled solutions for the conservation equations in the core bypass, channels, separators, and in ECC spray connections results in a radial distribution of ECC water in the upper plenum.

Heat slabs of arbitrary masses and volumes can be defined in any mesh cell (including core regions) to model that heat capacity of structures within the vessel. A heat transfer coefficient is computed for each slab using the local fluid conditions. The temperature calculation is based on a lumped-parameter model (Sections 4.1.1 and 4.2.1).

In addition to the lumped-parameter heat model, a double-sided heat slab model is available to permit accurate modeling of heat conduction through cylindrical structures found within a BWR vessel. The double-sided heat slab (double slab) model will allow the user to model heat conduction through a surface separating two different vessel radial or axial regions. Double slabs may also be used to model the release of stored energy from the reactor vessel wall. In this case, the outside surface of the double slab will not connect to a vessel region but will use boundary conditions specified by the user.

Two double-sided heat slabs may be associated with each fluid cell on each vessel axial level. These double slabs are considered to lie on the outside radial surface and upper axial surface of their associated fluid cell, as shown in Figure 7-36. In this figure, the outside surface of the double-sided heat slab associated with fluid Cell 2 is actually in contact with fluid Cell 6. A double-sided slab on the axial surface of Cell 2 would be in contact with fluid Cell 2 in the level above. Heat transfer coefficients for both sides of a double-sided heat slab are calculated, using the appropriate old-time fluid conditions from the fluid cells on each side of the heat slab. The liquid and vapor temperatures from the appropriate fluid cells are used in calculating the heat flux on each surface of the double slab. If the double slab lies on the outside surface of the vessel, the external heat transfers coefficients and fluid temperatures are set equal to values supplied by the user. Energy source terms are included in the energy equation for the fluid cells on each side of the double slab to account for energy transfer from the slab.

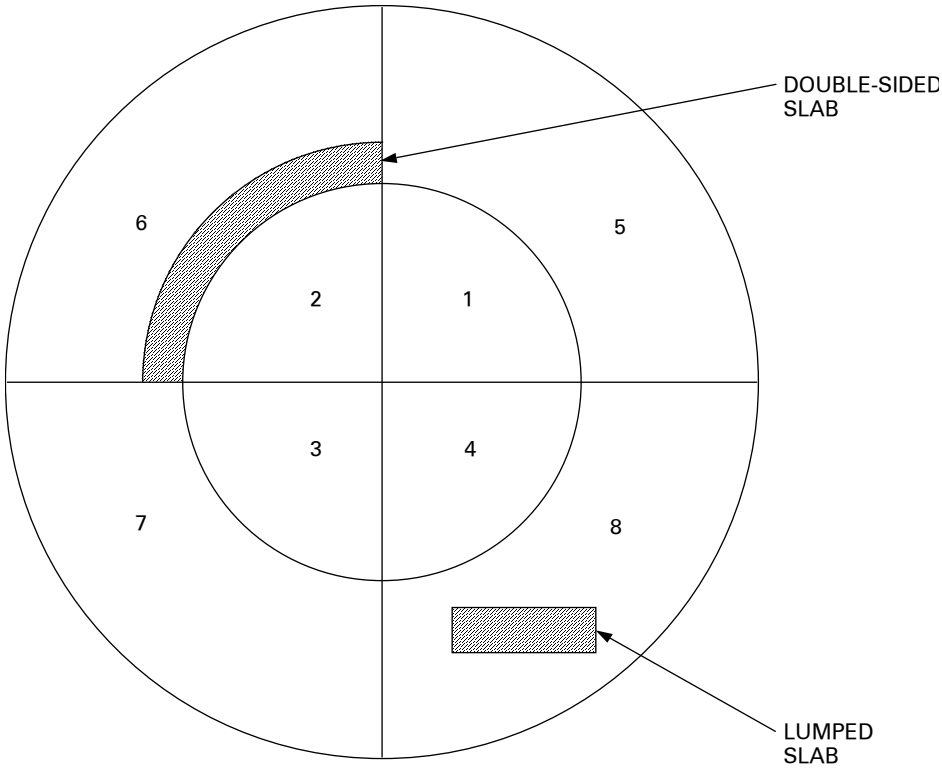

Figure 7-36. Sample Geometry for Double-Sided Heat Slab

The user specifies the inside surface area, thickness, and material type for the double slab associated with each vessel cell. If the double slab area for a particular cell is input as zero, no double slab is assumed to exist for that cell. The double slab material properties (density, specific heat, and thermal conductivity) are evaluated separately for each conduction heat transfer node within a double slab, these properties being evaluated at the mean temperature for each node. The number of conduction heat transfer nodes within the double slabs is specified by the user, and the same value is used for all double slabs.

7.8.1 Steam Dryer

The steam dryer is structured as an integral part of the pressure vessel. The characteristics of the steam dryer to be modeled are the dryer pressure drop and further separation of moisture in the steam flow from the steam separator.

The pressure drop is simulated by a flow resistance to the steam flow at the cell boundary between the steam dome and dryer. By imposing the appropriate loss factor on the vapor phase in the axial direction, the pressure drop in the dryer is correctly determined. The loss factor K_{SD} for the dryer is defined as:

$$K_{SD} = \frac{2\rho_v \Delta P_{SD}}{\left(\frac{W_v}{A_{SD}}\right)^2} \tag{7.8-1}$$

where:

ρ_v = Vapor density

W_v = Steam flow through the dryer

A_{SD} = Dryer flow area

ΔP_{SD} = Pressure drop in the dryer

The separation of moisture from the steam flow in the dryer is simulated by imposing a large liquid resistance in the axial direction at the cell boundary between the steam dome and the dryer.

The separation efficiency of the dryer depends on the vapor velocity and the moisture content of the steam flow entering the dryer (Figure 7-37). For a given inlet vapor velocity, there corresponds a critical dryer inlet quality. Good moisture separation is achieved if the dryer inlet quality is below the critical value. If the inlet moisture is above the critical value, the dryer capacity is exceeded and the moisture would pass through the dryer.

The dryer efficiency is computed by comparing the dryer inlet moisture to a critical dryer inlet moisture. The dryer efficiency is 100% if the dryer inlet moisture is below the critical dryer inlet moisture and is zero if the dryer inlet moisture exceeds the critical inlet moisture by a user-defined amount, $\Delta\beta_d$. The dryer efficiency is linearly interpolated between these two extremes based on the dryer inlet moisture. The dryer efficiency is given by:

$$\eta_D = \begin{cases} 1.0 & ,\beta_i < \beta_{i,crit} \\ 1.0 + \dfrac{\beta_{i,crit} - \beta_i}{\Delta\beta_d} & ,\beta_{i,crit} < \beta_i < \beta_{i,crit} + \Delta\beta_d \\ 0.0 & ,\beta_i > \beta_{i,crit} + \Delta\beta_d \end{cases} \tag{7.8-2}$$

where:

η_D = Dryer efficiency

β_i = Dryer inlet moisture

$\beta_{i,crit}$ = Critical dryer inlet moisture

$\Delta\beta_d$ = Range of dryer inlet moisture over which efficiency degrades from 100% to 0%

The range of dryer inlet moisture over which the dryer efficiency degrades is a user input constant. The default value of $\Delta\beta_d$ is 0.05 in TRACG.

The dryer inlet moisture is determined from the donor void fraction assuming homogeneous flow at the dryer face and is given by:

$$\beta_i = 1 - \frac{\alpha}{\alpha + (1-\alpha)\left[\frac{\rho_\ell}{\rho_v}\right]} \tag{7.8-3}$$

where ρ_ℓ and ρ_V are the donor liquid and vapor densities, respectively.

Finally, the critical dryer inlet moisture is given as a linear function of the vapor velocity at the dryer face and is given by:

$$\beta_{i,crit} = \begin{cases} 1.0 & , v_{vd} < v_{vd,\ell} \\ 1.0 - \dfrac{v_{vd} - v_{vd,\ell}}{v_{vd,u} - v_{vd,\ell}} & , v_{vd,\ell} < v_{vd} < v_{vd,u} \\ 0.0 & , v_{vd,u} < v_{vd} \end{cases} \tag{7.8-4}$$

where:

v_{vd} = Vapor velocity at dryer face

$v_{vd,\ell}$ = Lower dryer vapor velocity (Figure 7-37)

$v_{vd,u}$ = Upper dryer vapor velocity (Figure 7-37)

The lower dryer vapor velocity is the dryer inlet vapor velocity below which the dryer efficiency is 100% regardless of dryer inlet moisture. The upper dryer vapor velocity is the dryer inlet vapor velocity above which the dryer efficiency is less than 100% regardless of dryer inlet moisture. The dryer efficiency relationships are summarized in Figure 7-37.

The lower and upper dryer velocities are estimated from data[186] as 0.25 and 1.2 m/s, respectively. Dryer performance tests were performed at normal operating pressure with flow rates covering from 25 kg/sec to 51 kg/sec per separator.

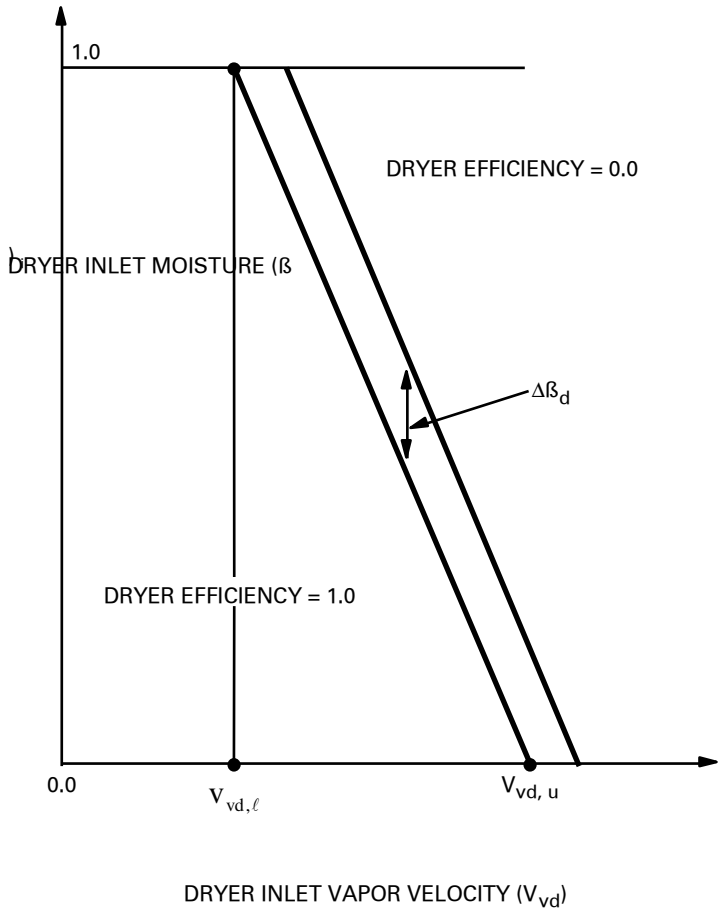

Figure 7-37. Dryer Efficiency Summary

7.8.2 Upper Plenum Model

One of the means of mitigating the severity of a postulated LOCA in a BWR is to inject sub-cooled water through the Emergency Core Cooling System (ECCS). Depending on the design, the emergency core cooling systems can include both the High Pressure Core Spray System (HPCS) and the Low Pressure Core Spray System (LPCS). This section describes a model for the HPCS and the LPCS, which are injected into the upper plenum.

At the time of core spray initiation, the core spray nozzles could be submerged in a two-phase mixture, in which case the injected liquid forms a submerged jet. If the two-phase mixture is below the nozzle elevation, then a spray forms downstream of the nozzles. The physical processes underlying spray and jet formation are different and are thus formulated separately.

For a realistic system transient calculation by TRACG, there is a practical upper limit for the system nodalization. The upper plenum, being a three-dimensional component in the system, would be nodalized rather coarsely in comparison with the size of the nozzles. For an accurate calculation of the jets and sprays, one needs a fine mesh size along the trajectory of the jet and

normal to it. Prediction of the gross motion in the plenum requires cylindrical noding coordinates. The jets and sprays cannot be described adequately by this system of coordinates. In this sense, the analysis carried out in this work resembles that of singular perturbation analysis in a boundary layer for which the theory is well developed[189]. In analysis of this type, a fine grid is adopted for the boundary layer scaled by the local boundary layer thickness, and a coarse grid is adopted for the external flow scaled by the main geometric dimensions. The two flows are then matched asymptotically at their boundaries. In the present analysis, a similar approach is undertaken.

In the present model, the entrainment of vapor by the spray is neglected. The effect of this may be an under-prediction of the spray penetration for high pressure. In the submerged regime where the liquid phase is continuous, the gross motion of the liquid in the upper plenum is modeled taking into account turbulence mixing and jet entrainment[190]. After calculating the submerged jet regime, the entrainment of the ambient liquid due to the injected jet is calculated for each TRACG node. The upper plenum liquid motion is then calculated with the jet entrainment treated as a line sink.

The spray nozzles are mounted on a sparger pipe, located at the periphery of the upper plenum, usually in two or three sets each aimed at a particular angle so as to more evenly distribute the liquid spray over the core. It is assumed in the model that the injected liquid from any one set of nozzles will coalesce downstream of the nozzles and form a sheet or ring jet. Any interaction between the different ring jets formed by nozzle sets aimed at different angles is assumed to be negligible in the present model.

In the spray regime, the motion of droplets in the upper plenum is predicted. An empirical correlation for the mean droplet size is utilized. Depending on the initial spray velocity, the trajectories of mean, outer and innermost droplets are calculated for each nozzle. Between the outer and inner extremities of the spray, Gaussian distribution for the flux profile is utilized. With this profile and the calculated spray width, the source distribution at the upper tie plate or the two-phase level is calculated as a function of radius from the center. From this distribution, the mass source for each TRACG node at the upper tie plate or the two-phase level is calculated. The spray reaches saturation temperature in a short distance from the nozzle exit, usually a few nozzle diameters[191]; therefore, the spray is assumed to be saturated at the time it reaches the upper tie plate or the two-phase level.

In the submerged jet regime, the basic conservation equations of mass, momentum and energy are written in an integral form[192] in an orthogonal system of coordinates coinciding with the jet trajectory and normal to it. The jet-spread rate is assumed to be the same as an un-deflected jet. The properties of the jet such as entrainment, velocity and enthalpy distribution and the jet trajectory are also simultaneously calculated. The location at which the jet terminates at the upper tie plate and the mass source distribution at the tie plate is calculated.

The motion generated in the ambient fluid is mainly due to the entrainment effects of the injected liquid. As described, the ambient upper plenum is analyzed using the entrainment as a line sink. Where the jet terminates on the upper tie plate, the calculated jet mass distribution is added as a source distribution. Thus, the effects of the injected jet are treated by a system of distributed sources and sinks, which, when summed together, gives the total mass of the injected liquid. Turbulence can be modeled by a simple mixing length hypothesis. This is appropriate due to the uncertainty of the more sophisticated models in two-phase flows, and the coarse

nodalization. Descriptions of the spray, jet and the gross motion of the upper plenum pool are described in the following section.

7.8.2.1 Spray Model

If the liquid level in the upper plenum falls below the spray level, the injected liquid from the nozzles form a spray. Spray systems are complex to analyze, but single sprays have been studied extensively in the literature both by experimental and analytical techniques. Most analytical studies confine themselves to the study of individual spray drops of a uniform size. In a real spray, particles vary in size and either an average diameter or Sauter Mean Diameter (SMD) is used to describe the spray characteristics[193]. Heat transfer to spray drops is analyzed based on conduction heat transfer. There are also some studies following a field approach where droplets are assumed to form a continuum with the ambient liquid. Preliminary work undertaken with this approach proved to be very inconvenient because of a need to describe the jet growth and the prediction of a distorted trajectory. Consequently, this approach was abandoned in favor of the droplet approach.

7.8.2.1.1 *Droplet Size*

In the referenced literature, several empirical correlations are available for describing the mean droplet size[193]. Since these empirical correlations are fitted to specific nozzle geometries, a more general correlation based on the critical Weber number criterion is used in TRACG for the droplet size "d" where the Weber number is calculated from:

$$We = \frac{\rho_v \, v_r^2 \, d}{\sigma} \tag{7.8-5}$$

7.8.2.1.2 *Spray Trajectory*

The spray trajectory is determined by the paths of droplets emanating at the extremities of the distribution. If the nozzle inclination to the horizontal is θ_0, and the initial spray cone angle, ϕ_0, then the outer, middle and inner extremity droplets are aimed at $\theta_o - \phi_0/2$, θ_o, and $\theta_o + \phi_o/2$, respectively, to the horizontal. The spray emanating from all nozzles aimed at a particular angle θ_0 is combined to form a ring spray source.

The relevant equations of motion of a droplet in terms of coordinates parallel to the trajectory and normal to it are:

$$v \frac{dv}{ds} = -g \sin\psi - C_D \frac{3}{4} \frac{|v| \, v}{d} \frac{\rho_v}{\rho_\ell} \tag{7.8-6}$$

$$v^2 \frac{d\psi}{ds} = -g \cos\psi \tag{7.8-7}$$

where "s" is the distance along the trajectory for the droplet.

Ψ is the inclination of the droplet trajectory relative to the horizontal.

The initial conditions are:

$v = v_O$ for $s = 0$

$\psi = \theta_o - \phi_o/2$ for the outer trajectory

$\psi = \phi_o$ for the middle trajectory

$\psi = \theta_o + \phi_o/2$ for the inner trajectory

It is assumed implicitly here that the injected liquid shatters in the form of uniform sized droplets at a short distant from the nozzle exit.

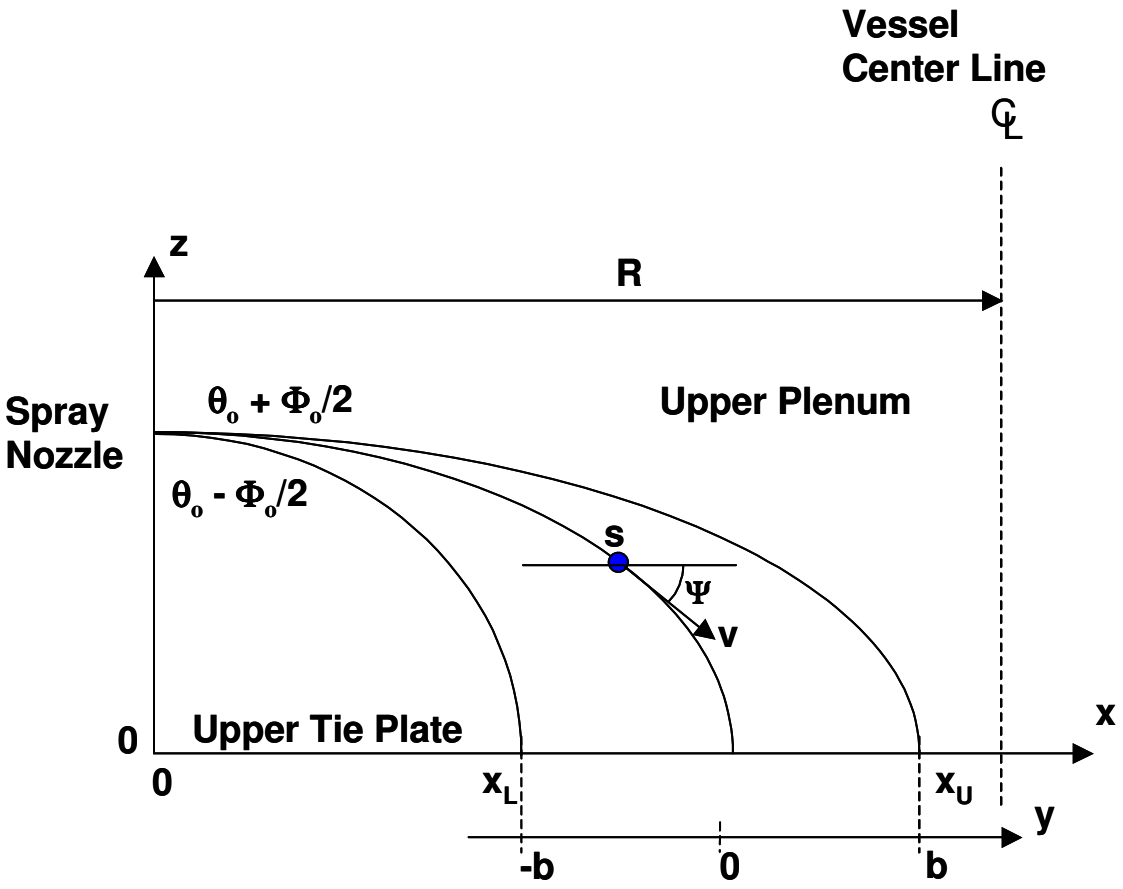

Figure 7-38. Coordinates for Spray Trajectory

The above ordinary differential equations are integrated along the trajectory to give the velocity and trajectory angle at every spatial location. However, in order to determine the location at which the trajectory terminates on the upper tie plate, the following equations are solved:

$$\frac{dz}{ds} = \sin\psi \tag{7.8-8}$$

$$\frac{dx}{ds} = \cos\psi \tag{7.8-9}$$

where "s" is the horizontal coordinate as indicated in Figure 7-38 and "z" is the elevation above the upper tie plate. The initial conditions are $z = z_N$ and $\beta = 0$ for $s = 0$ where z_N is the elevation of the nozzle. Thus the trajectory starts at the nozzle exit. A combined solution of the equations defined by Equations (7.8-6) to (7.8-9) gives the location of the trajectory above the tie plate. Each trajectory is terminated when y=0. The β coordinate at the upper tie plate or two-phase level determines the spray width. Between the spray extremities, the mass flow per unit length along the radius is modeled as a Gaussian distribution. Since a Gaussian distribution extends to infinity, for the purpose of calculation this was replaced with a cosine fit given by:

$$\frac{q}{q_m} = \begin{cases} \frac{1}{2}\left(1 + \cos\left(\frac{\pi y}{b}\right)\right) & \text{for } -b < y < b \\ 0 & \text{for } |y| > b \end{cases} \tag{7.8-10}$$

where as indicated in Figure 7-38: $b = (x_U - x_L)/2$, "y" is the location along the mid trajectory and "b" the corresponding spray width, and "q" is the spray flow rate at a location. The boundary conditions of $q=q_m$ at y=0 and q=0 at y=b are automatically satisfied.

7.8.2.1.3 *Spray Distribution*

The above spray distribution define by Equation (7.8-10) must satisfy the total spray rate plus the condensed liquid. Thus:

$$\int \frac{q_m}{2}\left(1 + \cos\left(\frac{\pi y}{b}\right)\right) dy = W + W_c \tag{7.8-11}$$

7.8.2.1.4 *Heat Transfer*

Tests indicate that spray drops reach saturation temperature within five to six nozzle diameters. Thus, in the analysis spray drops are assumed to reach saturation temperature in the first node, since the TRACG node is generally much larger than the nozzle diameter. It is also assumed that sufficient steam is available for the droplets to reach saturation temperature.

7.8.2.1.5 *Source Calculation*

The steam condensed can be calculated by bringing the total injected liquid from inlet enthalpy to saturation. Thus:

$$W_c = \frac{W\,(h_f - h_{\ell o})}{h_{fg}} \tag{7.8-12}$$

This is treated as a vapor sink at the node where spray is injected. The total mass of injected liquid plus the condensed mass is now distributed at the upper tie plate by Equation (7.8-10). Then the source for a particular TRACG node i from a set of spray nozzles j above the tie plate or a two-phase level between r coordinate given by r_i and r_{i+1} is:

$$S_{ij} = \int_{r_i}^{r_{i+1}} q_m \left(1 + \cos\left(\frac{\pi y}{b}\right)\right) dr \tag{7.8-13}$$

The sources from various ring jets are now combined:

$$S_i = \sum_j S_{ij} \tag{7.8-14}$$

In case the spray overshoots the centerline, a reflection with respect to the central plane gives the distribution. Mathematically,

$$S_i' = S_i + S_{-i} \tag{7.8-15}$$

The distribution of spray beyond the centerline is symmetrically reflected and added. In case of a solid wall, like in the sector test hardware, the distributions beyond the centerline are added and input in the central node.

If the level of the liquid rises above the nozzles, the injected liquid forms a submerged jet. The transition between submerged jet and spray is modeled as a linear interpolation in the model. This is done to avoid discontinuities.

$z_L < z_N - 1.1d_N$ Spray Distribution

$z_L > z_N + 1.1d_N$ Jet Distribution

Here z_L is the two-phase mixture level, z_N is the nozzle elevation and d_N is the nozzle diameter. In between these two, a linear interpolation in distribution is obtained. Thus:

$$S = S_{jet}\,\frac{z_L - z_N + 1.1d_N}{2.2\,d_N} + S_{spray}\,\frac{z_N - z_L + 1.1d_N}{2.2\,d_N} \tag{7.8-16}$$

If a two-phase level is not calculated, a similar criterion is arrived at using the void fraction. The transition is fixed at $\alpha = 0.75$ at the sparger elevation.

7.8.2.2 Submerged Jet Model

If the liquid level in the upper plenum rises above the sparger level, the injected liquid from the nozzles forms a submerged jet. The submerged jet model is analyzed by utilizing the basic conservation equations of motion written in an orthogonal system of coordinates along and normal to the trajectory. These are integrated over the jet width using an assumed velocity profile. A jet-spread rate is also assumed. The location at which the jet from a set of nozzles

terminates on the upper tie plate is then calculated. Knowing the jet width, the angle at which it hits the tie plate and the profiles of velocity and enthalpy, one can calculate the distribution due to a set of spray nozzles. The source S due to different sets is then linearly superimposed.

The method of analysis closely follows that outlined by Abromovich[192]. The integral methods are reasonably accurate and very fast compared to the differential methods, and are deemed to be sufficiently accurate for this analysis.

7.8.2.2.1 *Basic Conservation Equations*

The basic conservation equations of mass continuity, momentum and energy for a submerged jet are in (steady-state) integral form[194].

Mass:

$$\frac{d}{dx}\left[\int_0^b \rho\ v\, dy\right] = dQ \tag{7.8-17}$$

Momentum:

$$\frac{d}{dx}\left[\int_0^b \rho\ v^2\, dy\right] = \int_0^b (\rho-\rho_\infty)\, g\, dy \tag{7.8-18}$$

Energy:

$$\frac{d}{dx}\left[\int_0^b \rho\ v\, h\, dy\right] = h_\infty \frac{d}{dx}\left[\int_0^b \rho\ v\, dy\right] \tag{7.8-19}$$

Writing this in a system of coordinates along and normal to the trajectory we have

Mass:

$$\frac{d}{ds}\left[\int_0^b \rho\ v\ dy\right] = dQ \tag{7.8-20}$$

Momentum s:

$$\frac{d}{ds}\left[\int_0^b \rho\ v^2\ dy\right] = \int_0^b (\rho-\rho_\infty)\ g\ \sin\psi\ dy \tag{7.8-21}$$

Momentum ψ:

$$\frac{d\psi}{ds}\left[\int_0^b \rho\ v^2\ dy\right] = \int_0^b (\rho-\rho_\infty)\ g\ \cos\psi\ dy \tag{7.8-22}$$

Energy:

$$\frac{d}{ds}\left[\int_0^b \rho\ v\,h\ dy\right] = h_\infty\ \frac{d}{ds}\left[\int_0^b \rho\ v\ dy\right] \tag{7.8-23}$$

7.8.2.2.2 *Solution Procedure*

The solution to the above set is sought by assuming known velocity, density and enthalpy profiles of the form:

$$\frac{\rho-\rho_\infty}{\rho_m-\rho_\infty} = \eta\left(\frac{y}{b}\right) \tag{7.8-24}$$

$$\frac{v}{v_m} = f\left(\frac{y}{b}\right) \tag{7.8-25}$$

$$\frac{h-h_\infty}{h_m-h_\infty} = \phi\left(\frac{y}{b}\right) \tag{7.8-26}$$

Substituting these in the above momentum equations gives

Mass:

$$\frac{d}{ds}\left[v_m(\rho_m-\rho_\infty)b\int_0^1 \eta f dy^* + v_m\rho_\infty b\int_0^1 f dy^*\right] = dQ \tag{7.8-27}$$

Momentum s:

$$\frac{d}{ds}\left[v_m^{\,2}\,(\rho_m-\rho_\infty)\,b\int_0^1 \eta\; f^2\; dy^* + v_m^{\,2}\,\rho_\infty\; b\int_0^1 f^2\; dy^* \right] = (\rho_m-\rho_\infty)\,g\,\sin\psi\int_0^1 \eta\; dy^* \tag{7.8-28}$$

Momentum ψ:

$$\frac{d\psi}{ds}\left[v_m^{\,2}\,(\rho_m-\rho_\infty)\,b\int_0^1 \eta\; f^2\; dy^* + v_m^{\,2}\,\rho_\infty\; b\int_0^1 f^2\; dy^* \right] = (\rho_m-\rho_\infty)\,g\,\cos\psi\int_0^1 \eta\; dy^* \tag{7.8-29}$$

Energy:

$$\begin{aligned} &\frac{d}{ds}\left[v_m\,(\rho_m-\rho_\infty)(h_m-h_\infty)\,b\int_0^1 \eta\; f\,\phi\; dy^* \right] \\ &+\frac{d}{ds}\left[v_m\,(\rho_m-\rho_\infty)\,h_\infty\; b\int_0^1 \eta\; f\; dy^* \right] \\ &+\frac{d}{ds}\left[v_m\,(h_m-h_\infty)\rho_\infty\; b\int_0^1 \phi\; f\; dy^* \right] \\ &+\frac{d}{ds}\left[v_m\,\rho_\infty\; h_\infty\; b\int_0^1 f\; dy^* \right] = dQ\,h_\infty \end{aligned} \tag{7.8-30}$$

where

$$y^* = \frac{y}{b} \tag{7.8-31}$$

Denoting these integrals as A_1, A_2, A_3, A_4, A_5, A_6, and A_7, one gets:

Mass:

$$\frac{d}{ds}\left[v_m\,(\rho_m-\rho_\infty)bA_5+v_m\,\rho_\infty\,bA_6\right]=dQ \tag{7.8-32}$$

Momentum s:

$$\frac{d}{ds}\left[v_m^{\,2}\,(\rho_m-\rho_\infty)bA_1+v_m^{\,2}\,\rho_\infty\,bA_2\right]=(\rho_m-\rho_\infty)g\cdot\sin\psi\cdot A_3 \tag{7.8-33}$$

Momentum ψ:

$$\frac{d\psi}{ds}\left[v_m^{\,2}\,(\rho_m-\rho_\infty)bA_1+v_m^{\,2}\,\rho_\infty\,bA_2\right]=(\rho_m-\rho_\infty)g\cdot\cos\psi\cdot A_3 \tag{7.8-34}$$

Energy:

$$\begin{aligned}&\frac{d}{ds}\left[v_m\,(\rho_m-\rho_\infty)\,(h_m-h_\infty)bA_4+v_m\,h_\infty\,(\rho_m-\rho_\infty)bA_5\right]\\&+\frac{d}{ds}\left[v_m\,\rho_\infty\,(h_m-h_\infty)bA_7+v_m\,h_\infty\,\rho_\infty bA_6\right]\qquad=dQ\,h_\infty\end{aligned} \tag{7.8-35}$$

The above set of non-linear ordinary differential equations in ψ_m, h_m, b, ψ can be solved by numerical integration.

7.8.2.2.3 *Initial Region*

At the nozzle exit, the velocity and enthalpy profiles are uniform. Shear layers originating at the edges of the nozzle consume the inner core of uniform properties. These regions are difficult to evaluate because, to some extent, pressure gradients also exist in them. In the traditional analysis, assumptions are made regarding the growth of boundary layer in the initial region that gives the location at which the initial region terminates. Beyond the initial region, there is a transition region after which the fully developed region prevails. In the fully developed region, self-similar profiles for velocity and enthalpy are obtained given by the profiles of the previous section. It is a common observation in heated jets[192] that the constant velocity core vanishes first and then the constant enthalpy core. This is due to the turbulent mixing length for momentum exchange being larger then the energy exchange. The mixing length for energy exchange is roughly the square root of the Prandtl number times that of momentum exchange. The initial region is thus defined as the point where the constant enthalpy core disappears. This can be determined from the above set of equations by setting $h_m = h_o$, the initial sub-cooled enthalpy. For the purposes of computation, the buoyancy terms are ignored in the initial region. Thus, the momentum in the tangential direction is ignored completely giving the conservation equations in the form:

Momentum:

$$\rho_o\ v_o^{\ 2}\ b = v_m^{\ 2}\ (\rho_o-\rho_\infty)\ b\ A_1 + v_m^{\ 2}\ \rho_\infty\ b\ A_2 \tag{7.8-36}$$

Energy:

$$\rho_o\ v_o\ h_o\ b = v_m\ (\rho_o-\rho_\infty)\ b\ (h_o-h_\infty)A_4$$

$$+ v_m\ h_\infty\ (\rho_o-\rho_\infty)\ b\ A_5 + v_m\ \rho_\infty\ (h_o-h_\infty)\ b\ A_7 \tag{7.8-37}$$

$$+ v_m\ h_\infty\ \rho_\infty\ b\ A_6$$

These sets of equations give the value v_m and b at the location where the constant enthalpy core disappears. Assuming a spread rate of $b=k\beta$, then the length of the initial region can be determined when b is calculated.

7.8.2.2.4 *Jet Trajectory*

The jet trajectory is now determined by the transformation of s,ψ coordinates to β, z, coordinates, where β and y are measured from the nozzle plane:

$$\frac{d\beta}{ds} = \cos\psi \tag{7.8-38}$$

$$\frac{dz}{ds} = \sin\psi \tag{7.8-39}$$

with the initial condition $s=0$, $\beta=0$, and $z=z_N$, the nozzle elevation.

Integration of the conservation equations is carried out until the jet hits the upper tie plate ($y=0$). At that location, the mass and energy source for TRACG are calculated. The β coordinates of the outer and inner edge of the jet are calculated to give the jet width.

$$b_x = \frac{b}{\sin\psi} \tag{7.8-40}$$

where b is the normal jet width given by

$$\frac{db}{ds} = k \tag{7.8-41}$$

and k is the assumed spread rate. Within this jet width, the assumed profiles for velocity and enthalpy now give the mass distribution at the upper tie plate.

7.8.2.2.5 *Jet Distribution*

The jets formed by several nozzles all aimed at a particular angle are assumed to form a ring jet enveloped between the extreme trajectories. The assumed velocity distribution now gives the mass distribution at the upper tie plate.

7.8.2.2.6 *Ambient Fluid Interaction*

The submerged jet interacts with the ambient fluid in which it is discharged. The interaction can be obtained if one writes the jet conservation equations along and normal to the jet trajectory. For the purposes of calculation, the jet is assumed to be in a stagnant environment. The ambient fluid, however, is treated with a line sink along the jet trajectory.

7.8.2.2.7 *Source Calculation*

For the ambient fluid, the jet forms a line sink. Thus, the jet entrainment is calculated for a TRACG node and used as a mass sink. At the upper tie plate, the assumed distribution is applied to the total mass flow rate $W_o + \Sigma W_{ent}$, where W_o is the injected mass and ΣW_{ent} is the entrained mass. The energy sink and source are calculated as $w_{ent} h_{node}$, where h_{node} is the nodal enthalpy and w_{ent} is the entrainment by the jet within a given node. The energy source at the upper tie plate is obtained by calculating $W_o h_o + \Sigma W_{ent} h_{node}$, which is the sum of the energy of the injected fluid and the entrained fluid, and distributing it according to the assumed function.

In case the jet overshoots the centerline, the amount of liquid overshooting the central line is added to the central node.

7.8.3 Nozzle Model

A special condensation source connection is available for the VESSEL component. This optional condensation model applies when subcooled fluid is injected into the vessel cell either above the mixture level or into a vessel cell where the void fraction is greater than the void fraction for transition to annular flow.

The calculated condensation rate (W_c) for subcooled flow (W_{liq}) into the vessel is:

$$W_c = -W_{liq} \frac{(h_{liq} - h_f)}{h_{fg}} * C_{ncg} * CLEV \qquad (7.8\text{-}42)$$

The multiplier C_{ncg} allows for incomplete condensation in the presence of noncondensable gases. The degradation factor is calculated in the same way as in Equation (6.5-28) from Section 6.5.4:

$$C_{ncg} = \min \left\{ 1.0 , 0.168 \left(\frac{\alpha \rho_s^2}{(1-\alpha)\rho_a \rho_\ell} \right)^{0.1} \right\} \qquad (7.8\text{-}43)$$

The multiplier CLEV decreases condensation as the water level approaches the source elevation. If the two-phase level covers the source, no condensation is calculated. If the level is

1 ft or more below the source, complete condensation is calculated. Between these two limits, the degradation is calculated using a spline as follows:

$$CLEV = aux^2(3 - 2aux) \tag{7.8-44}$$

where

$$aux = \max(0, \min(1, (\frac{Z_{source} - Z_{level}}{0.3048}))) \tag{7.8-45}$$

If the level model is not active in the vessel cell, condensation begins at the transition to annular flow and reaches 100% when the cell void fraction is unity.

Making the following adjustments to the liquid and vapor source terms for the connection preserves mass and energy conservation:

Liquid Mass: $M_{s\ell} = M_{s\ell} + W_c$ (7.8-46)

Vapor Mass: $M_{sv} = M_{sv} - W_c$ (7.8-47)

Liquid Energy: $E_{s\ell} = E_{s\ell} + W_c h_g$ (7.8-48)

Vapor Energy: $E_{sv} = E_{sv} - W_c h_g$ (7.8-49)

7.9 Heat Exchanger

The modeling of heat exchangers (heaters or condensers) can be accomplished using a combination of standard TRACG components without the use of the specialized heat exchanger component. A pipe component is typically used to simulate the tube bank. Multiple pipes with the associated manifold tees can also be used to represent the tubes if additional detail is required. The nodalization within the simulated tube(s) is flexible and as such can be customized for a particular application. The shell side of the heat exchanger can be simulated using either the vessel component, which allows multi-dimensional flow or the one-dimensional tee component. In either case, the level of modeling detail can be specified to match the individual application. The heat transfer between the tube and shell utilizes the generalized component-to-component heat transfer capability of TRACG. This feature allows for heat transfer from the wall of any one-dimensional component cell to the fluid in any other component cell, including the vessel component. The correlations used to evaluate the wall heat transfer are described in Section 6.6.

The modeling flexibility using a combination of standard TRACG components makes this the recommended approach for most applications. However, for some applications, the use of a simplified heat exchanger component may be desirable. The heat exchanger component allows the user to simulate typical heat exchangers with a minimum number of cells. To accomplish this, the model requires that the details of the shell side geometry be provided as a function of shell average void fraction. The user-supplied tables of shell liquid level versus void fraction and fraction of tubes covered by liquid versus liquid level provide the basis for determining the detailed shell internal conditions. The heat exchanger component is recommended only if the assumptions and input requirements of the component are appropriate for a particular application.

7.9.1 Model Assumptions

The heat exchanger is based on the tee component and includes changes to the heat transfer correlation package and special treatment of the momentum and mass flow in the primary tube. A typical heat exchanger component is shown in Figure 7-39. Included in the figure is a pipe component that represents the heat transfer tubes within the heater. The combination of the heat exchanger and pipe represents a typical tube-in-shell heat exchanger, with attached drain-cooler region. The steam enters the shell (Cell 1), condenses, enters the drain cooler (Cell 2) as single-phase liquid (normally), undergoes further cooling and, finally, exits the heat exchanger. The side arm is included and attached to the steam shell cell, since high-pressure saturated liquid (from turbine separators or higher-pressure feedwater heaters) is frequently input to the heater shells in a separate flow path. Typical shell void fractions are about 0.5, while the drain cooler normally receives only liquid from the cell. The user must specify the drain cooler inlet height and a table of shell liquid level versus void fraction. The assumption is made that only liquid is present below the position of the liquid level and only vapor is present above the level. With this assumption, the donor cell void fraction α_{DC} for flow from the shell to the drain cooler is:

$$\alpha_{DC} = \begin{cases} 0.0 \text{ if liquid level } \geq \text{ drain cooler height} \\ 1.0 \text{ if liquid level } \leq \text{ drain cooler height - 0.05m} \\ 20.0 \text{ x (drain cooler height - liquid level) otherwise} \end{cases} \quad (7.9\text{-}1)$$

The 5 cm for linear interpolation of the donor celled void fraction provides a gradual change in α_{DC} as the drain cooler inlet is uncovered.

The validity of the α_{DC} modeling is dependent on an accurate user specification of the shell liquid level versus void fraction and the applicability of the above and below void fraction assumptions. If the assumptions or input requirements are not appropriate for a particular application, the user has the option to use other components to model the shell side of the heat exchanger in more detail. The generalized component-to-component heat transfer is then used to model the heat transfer between the tubes and shell.

Another change to the hydrodynamic equations was forced by the normally high inlet steam velocities found in the main condenser. Momentum flux was eliminated at the drain cooler inlet interface. This was done to prevent V•∇V induced pressurization of the first cell in the drain cooler.

Some special features of tees that are used as heat exchangers are:

- Side arm input is simplified — the pipe arrays do not have to be input for the side arm.
- Heat transfer from the walls of the shell is not modeled (NODES = 0).
- The shell must consist of only one cell, but the drain cooler may contain as many cells as required. The side-arm always connects to the first cell (shell).
- The heat transfer pipe may contain as many cells as needed. U-tubes may be represented by appropriate assignment of the heat transfer connections.

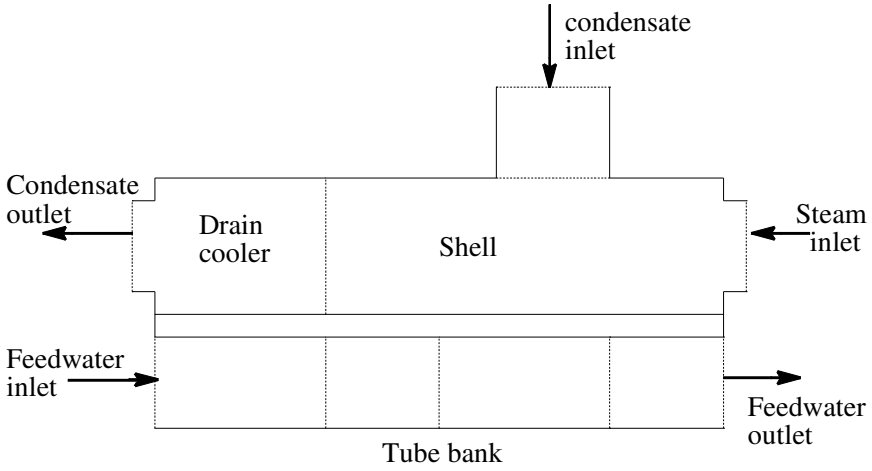

Figure 7-39. Model of Feedwater Heater Using a HEAT Component (modified TEE) and PIPE Component for the Tube Bank

7.9.2 Heat Transfer Correlations

Correlations appropriate to flow condensation on horizontal and vertical tube banks[195] have been introduced. In addition, a correlation for single-phase (liquid) convection across tube banks[196] has been implemented in order to better describe the behavior in the liquid-filled regions of the heat exchanger. These correlations are presently available in the code for heat exchangers only. Models for convection and condensation described in Section 6.6 are used for other components. The correlations used are:

For condensing flow on horizontal tube banks,

$$h_v = X_f \frac{k_\ell}{D_t} Re_\ell^{1/2} \left(1 + \frac{0.276}{X_f{}^4 Fr H_f}\right)^{1/4} \tag{7.9-2}$$

For condensing flow on vertical tube banks,

$$h_v = X_f \frac{k_\ell Re_\ell^{1/2}}{D_t} + 0.943 \left[\frac{h_{fg} k_\ell{}^3 \rho_\ell{}^2 g}{\mu_\ell D_B (T_{sat} - T_w)}\right]^{1/4} \tag{7.9-3}$$

For liquid cross-flow across tube banks,

$$h_\ell = 0.36 \frac{k_\ell}{D_t} \left(\frac{D_h \rho_\ell v_\ell}{\mu_\ell}\right)^{0.55} \left(\frac{C_{P_\ell} \mu_\ell}{k_\ell}\right)^{1/3} \tag{7.9-4}$$

X_f, H_f, R_f, Re_ℓ (liquid film Reynolds number) and Fr (Froude number) are dimensionless parameters defined as:

$$X_f = 0.9 \left(1 + \frac{1}{R_f H_f}\right)^{1/3} \tag{7.9-5}$$

$$H_f = \frac{k_\ell (T_{sat} - T_w)}{\mu_\ell h_{fg}} \tag{7.9-6}$$

$$R_f = \left(\frac{\rho_\ell \mu_\ell}{\rho_g \mu_g}\right)^{1/2} \tag{7.9-7}$$

$$Re_\ell = \frac{\rho_\ell v_v D_t}{\mu_\ell} \tag{7.9-8}$$

$$Fr = \frac{v_v{}^2}{g D_t}. \tag{7.9-9}$$

In the above equations, the heat exchanger geometry is specified by the following parameters:

D_h = Shell hydraulic diameter

D_t = Individual tube outer diameter

D_B = Distance between tube bank baffles

The method for handling condensation requires that all the energy be taken out of the liquid phase; condensation then occurs due to interfacial heat transfer. This being the case, the liquid and vapor coefficients must be adjusted accordingly:

$$h_\ell = \text{FRACL}\, h_\ell + \left(1 - \text{FRACL} \right) h_v \left(\frac{T_{sat} - T_w}{T_\ell - T_w} \right) \tag{7.9-10}$$

$$h_v = 0.0 \tag{7.9-11}$$

where h_ℓ and h_v are the heat transfer coefficients. FRACL is the fraction of the heat transfer tubes that is covered by liquid. This is determined by user input of two tables: (1) shell liquid level versus shell void fraction and (2) FRACL versus liquid level.

7.10 Boundary Conditions

The break (BREK) and fill (FILL) components are used to impose boundary conditions at any one-dimensional component terminal junction. Consequently, these components differ from the other components in that they do not model any system component per se or perform hydrodynamic or heat-transfer calculations. However, they are treated like any other component with respect to input, initialization and identification procedures.

It is recommended that the cell volume and length in these components be identical to those for the neighboring cell of the adjacent component. The void fraction and fluid temperatures specified in the fill and break determines the properties of fluid convected into the adjacent component if an inflow condition should occur. By convention, inflow corresponds to a positive fill velocity and a negative break velocity. The break components may not be connected directly to the vessel component for the purpose of imposing a boundary condition. The connection of the fill directly to the vessel is allowed.

7.10.1 Velocity Specified Boundary Conditions

The fill component imposes a velocity boundary condition at the junction to its adjacent component, as shown in Figure 7-40. Fill boundary conditions of velocity, void fraction, and phase temperatures may be constant, user-specified time-dependent, or they may be set by the control system. In addition, the fill velocity condition may be specified as a function of adjacent component pressure. In this case, the pressure functions are imposed in an approximate manner that avoids numerical difficulties caused by instabilities.

7.10.2 Pressure Specified Boundary Conditions

The break component implies a pressure boundary condition one cell away from its adjacent component, as shown in Figure 7-41. Like the fill component, this boundary condition may be constant, user-specified time-dependent, or it may be set by the control system. The break component also specifies the boundary conditions of void fraction and phase temperatures at the terminal junctions of one-dimensional components.

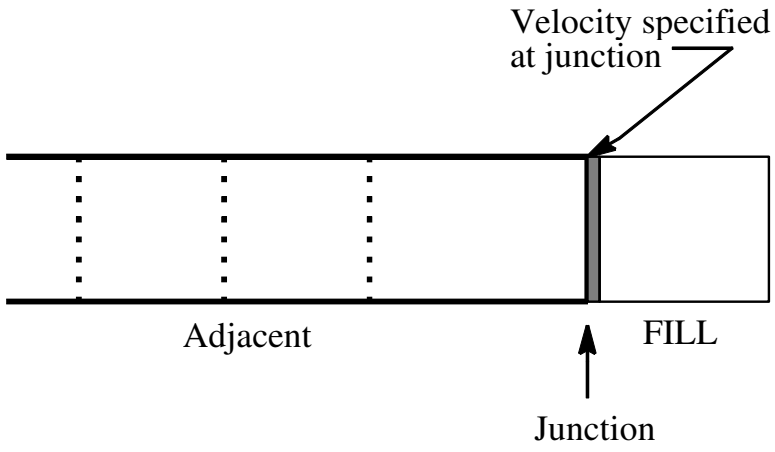

Figure 7-40. FILL Noding Diagram

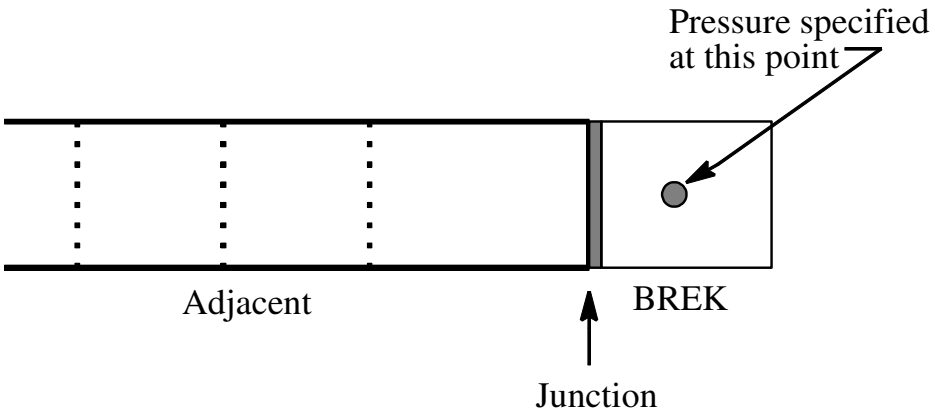

Figure 7-41. BREK Noding Diagram

7.11 Containment Components

The containment is modeled with TRACG as a combination of a three-dimensional vessel component in conjunction with one-dimensional components such as pipes, tees and valves. All these components utilize the same conservation equations and constitutive correlations. The set of conservation equations is described in Section 3.1. The correlations for wall heat transfer, interfacial heat transfer, wall shear and interfacial shear are described in Section 6.0.

BWR containments utilizing the pressure suppression principle have similar components. The specific example referred to in this section is for the ESBWR The ESBWR containment is similar in concept to the Mark III and ABWR containments, in that a horizontal vent system is employed to transfer blowdown energy from the drywell to the suppression pool. In addition, the ESBWR is equipped with a Passive Containment Cooling System (PCCS) for long-term decay heat removal.

Figure 7-42 shows a schematic of the ESBWR containment and reactor pressure vessel (RPV). Figure 7-43 shows the corresponding TRACG representation and the major components used for modeling the containment. The three-dimensional vessel (VSSL) component simulates the drywell, wetwell, reactor vessel and the IC and PCC pools.

7.11.1 Drywell

The drywell is composed of an upper drywell, bounded by the drywell head, top slab, containment walls, and the diaphragm floor separating it from the wetwell. The upper drywell (indicated by 1 in Figure 7-42) constitutes the largest portion of the drywell volume. A break in the main steam line as well as the opening of the depressurization valves (DPVs) would discharge flow into this region. The annulus region of the drywell (indicated by 2) comprises the region between the RPV and the inner wall of the wetwell horizontal vent duct system. A break in the Gravity-Driven Cooling System (GDCS) line would be expected to discharge flow into this region. The lower drywell (3) is a separate region that is connected to the drywell annulus by multiple vents. Liquid discharged into the upper drywell or the annulus region (e.g., from a broken GDCS line connected to a GDCS pool) will drain into the lower drywell. A break in the bottom drain line could discharge flow to the lower drywell.

The drywell is modeled as a two-dimensional (axisymmetric) region, with four radial rings in the upper drywell and two radial rings in the annular and lower drywell regions (Figure 7-43). This allows natural circulation patterns to develop, if calculated, with upflow in one ring and downflow in another. The three-dimensional conservation equations for mass, momentum and energy given in Section 3.1 are applied in this region. Discretization of the equations is shown in Section 3.2.

Specific models are discussed below.

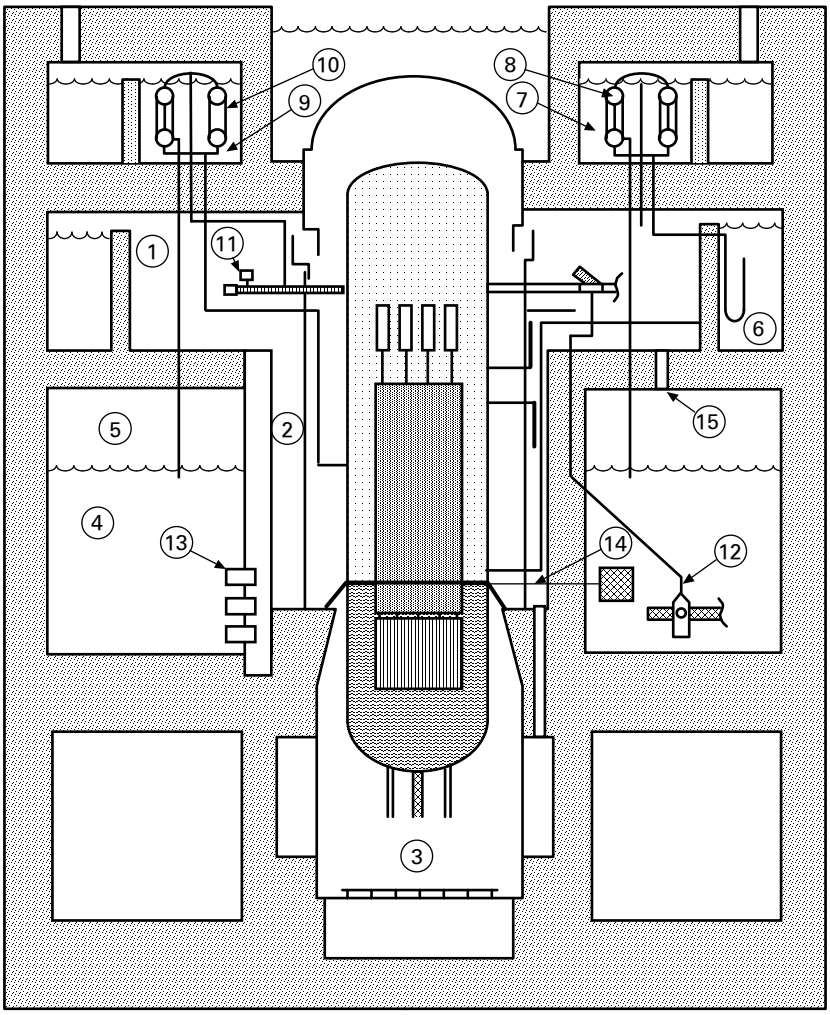

Figure 7-42. ESBWR Containment

[[

]]

Figure 7-43. Simulation of ESBWR Containment

7.11.1.1 Turbulent Shear Between Cells

The TRACG model for turbulent shear between cells at cell boundaries is not being used. Thus, there is no shear between adjacent cells. All flows in the drywell are driven by buoyancy and wall shear. The nodalization employed ensures the presence of a wall surface in every cell.

7.11.1.2 Noncondensable Distribution

TRACG has mass continuity equations for multiple species of noncondensables in addition to steam. See Equations (3.1-23) through (3.1-27). A noncondensable species is treated as a perfect gas and its properties are specified in terms of the gas constant, R and the specific heat c_{pg} (Section 6.6.11). The noncondensable gas (or mixture of gases) has the same temperature and velocity as the steam in a given cell. The partial pressure of the noncondensable gas is calculated based on the temperature and mass of the gas in a cell (Perfect Gas Law). Dalton's law (Equation (3.1-26)) relates the partial pressures of steam and noncondensables to the total pressure. Note that there are no requirements for the steam to be at saturation conditions corresponding to its partial pressure.

The TRACG model for molecular diffusion of noncondensables driven by concentration gradients is not used. Noncondensables are transported solely by bulk convection. Diffusion effects will be small for nitrogen and air. Transport by diffusion could be more significant for hydrogen. Buoyancy effects are not treated at a local level (i.e., steam and noncondensables have the same velocity in a cell). However, buoyancy effects will be accounted for on a global level. For example, if a light noncondensable is injected into a cell, a natural circulation pattern will develop between adjacent rings, and lighter fluid will rise to the upper regions. The distribution of noncondensables calculated by TRACG has been assessed through comparisons against data from the GIRAFFE and PANDA facilities. Based on these comparisons, a bounding analysis approach has been developed in the SBWR qualification report[7].

7.11.1.3 Wall Friction Correlations

The flow regime in the drywell is mostly single-phase vapor. In some cells, a dispersed droplet high void fraction regime may exist. This corresponds to cells where liquid from the break or from the GDCS pool with a broken line is falling to the lower regions of the drywell. In some cells, a liquid film can form on the wall because of condensation. The single-phase friction factor is obtained from Equation (6.2-2). The Reynolds number is calculated based on the axial velocity in the cell adjacent to the wall and the hydraulic diameter of the cell in the direction of the wall. In case a two-phase flow regime is present, a two-phase multiplier will be applied as shown in Equation (6.2-7).

7.11.1.4 Interfacial Shear Correlations

For the droplet flow regime, the models described in Section 6.1.5 will be employed to calculate the interfacial shear between vapor and droplets. For cells with wall liquid films, the annular flow correlations in Section 6.1.4 are used.

7.11.1.5 Wall Heat Transfer

The important modes of wall heat transfer in the drywell include forced and free convection to vapor and condensation heat transfer.

For forced convection, TRACG uses the Dittus-Boelter correlation (Equation (6.6-3)), based on the cell velocities and properties. The hydraulic diameter of the cell in the direction of the wall is used in the correlation. The vapor properties are calculated at the cell fluid temperature.

For free convection, the McAdams correlation (Equation (6.6-29)) is used. Again, the cell temperature is used for the calculation of vapor properties and the cell hydraulic diameter for the calculation of the Grashof number. (The heat transfer coefficient is independent of the hydraulic diameter when correlations of the form $h \sim G_r^{1/3}$ are used.)

These equations and their application are similar to those in other containment codes such as GOTHIC[69]. TRACG will evaluate both the free and forced convection correlations and use the higher of the two calculated values. The same correlations are used for horizontal surfaces.

The condensation correlations are discussed in Section 6.6.11. A Nusselt condensation correlation is used with multiplicative factors for shear enhancement and degradation by noncondensables. The Nusselt correlation is expressed in Equation (6.6-89). In this equation, the liquid film Reynolds number Re_ℓ is defined as $Re_\ell = 4\Gamma/\mu_\ell$, where Γ is the condensate flow rate per unit perimeter of surface and μ_ℓ is the liquid viscosity. The recommended method is to use the Kuhn-Schrock-Peterson (K-S-P) correlation[149] with the shear enhancement factor set to 1. The minimum of the Uchida and K-S-P correlations is used in the calculations.

7.11.1.6 Fogging of Drywell Vapor

Heat transfer from the vapor in a cell will result in cooling of the vapor. If the temperature drops below the saturation temperature of the steam corresponding to its partial pressure, condensation will occur. Generally, in this situation a cold wall will be present in the cell. A liquid film will form on the surface because of condensation. This will be typically the dominant form of condensation in the cell. If the temperature drops below saturation in a cell that has no heat transfer surfaces, liquid droplets will form (fogging) by condensation of steam. In this situation, a droplet flow regime will exist. Interfacial heat transfer between droplets and vapor will be calculated as per Section 6.5.5. Interfacial shear between the droplets and steam is calculated using the models in Section 6.1.5.

In general, heat transfer from the vapor is more likely to lead to condensation on the walls. Fogging is more likely to occur as a result of adiabatic expansion of steam from pressures higher than 30 bar.

7.11.2 Wetwell

The wetwell consists of the suppression pool (4) and the wetwell vapor space (5) in Figure 7-42. The wetwell is bounded by the diaphragm floor on top, containment outer wall and wetwell inner wall on the sides and the floor of the containment. During blowdown, flow from the safety/relief valves (SRVs) is directed to the suppression pool and quenched via the SRV discharge lines. Flow from the LOCA break and DPVs is directed from the drywell to the suppression pool and quenched via the suppression pool horizontal vent system. Any flow through the Passive Cooling Condenser (PCC) vents is also discharged to the suppression pool.

7.11.2.1 Wetwell Vapor Space

The wetwell vapor space is also represented by multi-dimensional cells as shown in Figure 7-43. Typically, two rings and two axial levels are employed in the TRACG model. This allows for natural circulation in this region. The flow regimes in this region will be the same as in the drywell: single-phase vapor, dispersed droplets resulting from entrainment from the suppression pool, and a condensate film on the walls. The models discussed in the preceding section for the drywell for turbulent shear between cells, noncondensable distribution, wall friction, interfacial friction, wall heat transfer, fogging and interfacial heat transfer apply also in the wetwell vapor space. One other model is important for this region; namely, the heat transfer at the suppression pool interface.

Test data from PANDA [7] show that the top of the wetwell gas space which receivers leakage flow from the drywell through the vacuum breakers is at a higher temperature than the lower part of the gas space due to thermal stratification. In the TRACG nodalization of the wetwell gas space, stratification is forced by restricting the flow between cells in the top two levels of the gas space by specifying an irreversible frictional loss. This approach produces conservatively high local gas space temperatures in the vicinity of the leakage.

7.11.2.2 Interfacial Heat Transfer at Pool Interface

The interfacial heat transfer coefficients on the vapor and liquid sides of the interface are defined by Equation (6.5-52) with the Nusselt number defined by Equation (6.5-51). The Sparrow-Uchida correlation shown in Figure 6-13 is used to calculate degradation of heat transfer at the pool surface due to noncondensable gases.

7.11.2.3 Suppression Pool

The suppression pool is represented by multi-dimensional cells as shown in Figure 7-43. At least two rings are used to represent the pool. The major phenomena of interest for the suppression pool include condensation of vapor bubbles, temperature distribution / thermal stratification and pool two-phase level.

7.11.2.4 Condensation of Vapor Bubbles

In the presence of noncondensables, the bubbles will include steam and noncondensables. The partial pressure of steam and noncondensables will be calculated as stated earlier. The interfacial heat transfer from the liquid to the vapor is calculated according to Equations (6.5-11) and (6.5-12). There is no degradation in heat transfer due to the presence of noncondensables. This is based on large-scale data showing complete condensation of steam in the bubbles.

7.11.2.5 Pool Temperature Distribution

An empirical model is used to force thermal stratification below the lowest thermal source to the pool. This is done by effectively limiting the amount of water that participates in the absorption of energy to that above the lowest discharge location (i.e., lowest active horizontal vent, SRV quencher or PCC vent). Above this elevation, TRACG will calculate circulation velocities which produce a well mixed region. Figure 7-44 shows the results from a number of large scale tests. The measured temperature at the top of the pool has been compared with

calculations using the empirical model described above. All data are predicted either well or conservatively.

7.11.2.6 Pool Level

The two-phase level model described in Section 6.4 is used to calculate the pool level. The liquid and vapor side interfacial heat transfer coefficients are calculated by Equation (6.5-52) with the Nusselt number defined by Equation (6.5-51). When the liquid surface is subcooled relative to the partial pressure of steam, the condensation at the surface is reduced by a degradation factor based on the Sparrow-Uchida correlation (see Figure 6-13).

7.11.3 GDCS Pools

Three GDCS pools (6) are located in the upper drywell (Figure 7-42). During the GDCS phase of the post-LOCA transient, the GDCS pools discharge into the RPV downcomer, following the opening of squib valves and check valves in the three divisionally separated GDCS lines. During the intermediate and long-term phases of the post-LOCA transient, the GDCS pools receive condensate from the PCC units. Each PCC unit condensate return line is designed with a loop seal to prevent reverse flow of steam or noncondensables in the condensate return line.

The GDCS pools are also modeled as part of the multi-dimensional containment model (Figure 7-43). In practice, two pools are represented, with one accounting for the volume of two of the three pools. The representation is essentially one-dimensional, with each pool being characterized by one ring. The main phenomenon of interest for the GDCS pool is the pool level and the associated inventory of water in the pool. The two-phase level model referred to earlier is also applicable here. Heat transfer at the pool surface is modeled analogously to that for the suppression pool.

[[

]]

Figure 7-44. Suppression Pool Stratification (TRACG Model vs. Horizontal Vent Stratification)

7.11.4 Isolation Condenser (IC)/Passive Containment Condenser (PCC)Pools

The IC pools (9) are located outside (above) the containment (Figure 7-42). Each contains an IC unit. The pools are interconnected.

The PCC pools (7) are located outside (above) the containment. Each contains a PCC unit. The pools are interconnected with each other and with the IC pools.

As shown in Figure 7-43, the pools are represented as part of the 3-D TRACG region, partitioned into the IC and PCC pools. The pools are allowed to communicate with each other at the bottom and the top. The pools are modeled with two rings each and with several axial levels. Heat transfer occurs from the PCC and IC headers and tubes to the water in the pools. Pool side heat transfer is calculated by the Forster-Zuber[130] correlation for boiling heat transfer (see Equation (6.6-7)).

7.11.5 PCC/IC Units

The ESBWR has four PCC heat exchanger units (8). Each is comprised of two modules with inlet and outlet headers and 248 tubes in parallel. The PCC units are connected to the top of the upper drywell and discharge condensate into the GDCS pools. Noncondensables and uncondensed steam are vented to the suppression pool. The vent submergence is 0.9m less than that of the top horizontal LOCA vent. Thus, drywell noncondensables and uncondensed steam are purged preferentially through the PCC vent line following the early blowdown phase.

The ESBWR has six IC heat exchanger units (10) (Figure 7-42). Each consists of two modules with inlet and outlet headers and 248 tubes in parallel. The IC units are connected to stub tubes, which are attached to the RPV steam dome. Condensate is discharged into the downcomer of the RPV. Noncondensables can be vented from the upper and lower IC headers to the suppression pool.

The IC and PCC units are represented by one-dimensional components simulating the inlet piping, headers, condenser tubes, condensate discharge lines and vent lines. One-dimensional forms of the mass, momentum and energy equations in Section 3.1 are applicable. Heat is transferred through the walls of the tubes and headers to the respective pools.

7.11.5.1 Wall Friction Correlations

The flow regime in the PCC and IC is single-phase vapor at the inlet. Due to condensation, a liquid film forms on the walls. The exit conditions consist of a draining liquid film, and a gas mixture that is rich in noncondensables. The single-phase friction factor is obtained from Equation (6.2-2). The Reynolds number is calculated based on the axial velocity in the cell adjacent and the hydraulic diameter of the cell. In the condensing region, a two-phase multiplier will be applied as shown in Equation (6.2-7).

7.11.5.2 Interfacial Shear Correlations

For cells with wall liquid films, the annular flow correlations in Section 6.1.4 are used.

7.11.5.3 Wall Heat Transfer

The important mode of wall heat transfer in the PCC and IC is condensation heat transfer. Under conditions where condensation heat transfer is severely degraded by a large amount of noncondensables, forced convection from the vapor to the wall will become the mode of heat transfer.

The condensation correlations are discussed in Section 6.6.11. A Nusselt condensation correlation is used with multiplicative factors for shear enhancement and degradation by noncondensables. The Nusselt correlation is expressed in Equation (6.6-89). In this equation, the liquid film Reynolds number Re_ℓ is defined as $Re_\ell = 4\Gamma/\mu_\ell$, where Γ is the condensate flow rate per unit perimeter of surface and μ_ℓ is the liquid viscosity. The Kuhn-Schrock-Peterson correlation[149] is used for the calculation of condensation heat transfer in the presence of noncondensable gases. Extensive comparisons have been made against prototypical data from the PANTHERS test facility with excellent results[7].

For forced convection, TRACG uses the Dittus-Boelter correlation (Equation (6.6-3)), based on the cell velocities and properties. The hydraulic diameter of the cell is used in the correlation. The vapor properties are calculated at the cell fluid temperature.

7.11.6 Depressurization Valves

There are 8 DPVs (11) in the ESBWR. Four DPVs are on the RPV stub tubes. (The steam supply lines for the three IC units are also connected to three of these stub tubes.) The other four DPVs are on the main steam lines. The DPVs discharge into the upper drywell.

The DPVs are modeled using the VLVE component, which is a one-dimensional component. The TRACG control system will trigger the DPVs to open based on the sensed level in the RPV downcomer. The primary TRACG model associated with the DPV is that of critical flow, which is discussed in Section 7.11.9 in connection with the break.

Critical flow is calculated using the model described in Section 6.3. This model has been extensively qualified. The critical flow is calculated based on the upstream pressure, enthalpy and void fraction. Correlations used in the calculation of interfacial shear in the RPV are given in Section 6.1. The void fraction will depend on the position of the two-phase level in the downcomer. The two-phase level model is described in Section 6.4. Validation of the void fraction and two-phase level models is performed in Section 3.1 of the *TRACG Qualificiation LTR*[4],[5],[6].

7.11.7 Safety/Relief Valves (SRVs) and Quenchers

SRVs (12) relieve RPV pressure by discharging steam into the suppression pool. Steam is discharged though quenchers to minimize chugging and condensation loads. The quencher submergence is greater than that of the top row of horizontal vents.

The SRVs and associated piping are represented by one-dimensional components. TRACG will trigger the opening of the SRVs based on pressure or downcomer level. The quenchers are not modeled in detail. Condensation and chugging loads will not be calculated with TRACG. Critical flow models used for the SRVs have been discussed for the break and

DPVs. Models for the condensation of SRV discharge were referred to in the section on the suppression pool.

7.11.7.1 Horizontal Vent System

The ESBWR has multiple sets of horizontal vents between the drywell and the suppression pool. Each set of three vents consists of three horizontal vents (13) attached to a vertical vent pipe (Figure 7-42). The top row of horizontal vents is approximately 0.9m below the bottom of the PCC vents.

The horizontal vents are represented by one-dimensional TEE components. The vent component is shown in more detail in Figure 7-45.

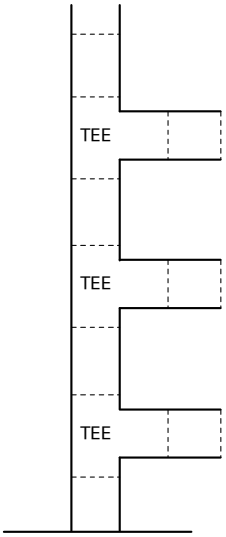

Figure 7-45. Horizontal Vent Component

7.11.7.2 Vent Clearing Model

As the level drops in the pipe to "uncover" the horizontal vent, the vent will be opened to two-phase flow to the suppression pool. This phenomenon is referred to as "vent clearing". Vent clearing terminates the initial pressure rise of the drywell, as the pressure is relieved by the vent discharge to the suppression pool. The top two rows of vents can clear during the early blowdown. As the blowdown flow rate decreases, the water level in the vertical pipes will rise to cover the second row of vents. Eventually, the top row is also covered and only flow through the PCC vents, which have a lower submergence, will persist. Following vent clearing, the wetwell gas space pressurizes as the noncondensables from the drywell are purged into that volume. The drywell pressure is maintained higher than the wetwell by an amount corresponding to the submergence of the open vents.

In the prediction of vent clearing and the associated drywell and wetwell pressure histories, the important phenomena are those discussed in Sections 7.11.7.3 through 7.11.7.6.

7.11.7.3 Level Tracking in the Vertical Vent Pipes

The one dimensional component level tracking model described in Section 6.4 is employed in the vertical pipe that is connected to the three horizontal vents.

7.11.7.4 Vent Flow Regime

The flow regime in the vents is single-phase liquid, until the vent begins to uncover when it transitions rapidly to bubbly flow. The flow to the vent is "donor celled" at the upstream conditions in the vertical pipe. TRACG calculates a transition from stratified to dispersed flow based on the instability of the interface. The expression for the instability is solved to obtain the void fraction at which the transition from stratified flow to dispersed flow is expected to occur (see Equation (5.1-23)).

7.11.7.5 Pressure Drop Correlations

The single-phase friction factor is obtained from Equation (6.2-2). The Reynolds number is calculated based on the axial velocity in the cell and the hydraulic diameter of the cell. The pressure drop in the vent is actually dominated by the inlet and exit form loss coefficients. A two-phase multiplier will be applied for wall friction as shown in Equation (6.2-7). For singular losses, Equations (6.2-15) and (6.2-16) are applicable.

7.11.7.6 Vent Back Pressure

As the vent discharges vapor into the suppression pool, it will tend to move the liquid in the pool above the vent upwards as it expands. The inertia of this liquid tends to create a back-pressure effect, reducing the discharge flow, and affecting the drywell pressure after vent clearing. This effect is accounted for in the TRACG momentum equation. However, the nodalization in the wetwell precludes an accurate modeling of the virtual mass effect. The liquid mass in the inner ring immediately above the discharge location will have to be accelerated upwards as the vapor expands into the pool.

7.11.7.7 Model Applicability

The vent clearing model in TRACG has been assessed in Reference [7] by comparison against data from the Pressure Suppression Test Facility (PSTF). TRACG calculated the initial pressure rise and time of vent clearing accurately. Following the onset of vent clearing, TRACG undercalculates the vent flow, and the drywell pressure increases to a higher value than seen in the data. The discrepancy is due to large vapor bubbles rapidly transiting through the top part of the vent at the inception of vent uncovery. This flow regime is not captured by TRACG and results in a conservative response for the vent clearing transient. Subsequent to this period, the transient is captured adequately by TRACG. The oscillatory response and slight undershoot in the drywell pressure, as well as the final pressure and vent flow are predicted accurately. This indicates that the pressure drop correlation is accurate after the initial vent-clearing transient.

7.11.7.8 GDCS Equalizing Lines

Three GDCS equalizing lines (14) connect the suppression pool to the RPV downcomer. During the long-term portion of the post-LOCA transient, the squib valves in these lines will open if the level in the downcomer drops to 1m above the top of the active fuel and a time delay of 30 minutes has elapsed.

The equalizing lines are represented by a one-dimensional VLVE component. The correlations used for wall friction and singular losses are the same as described in the previous paragraph for the horizontal vents.

7.11.8 Vacuum Breakers

The SBWR has three vacuum breakers (15) connecting the upper drywell to the wetwell vapor space. The vacuum breakers will open to relieve a negative pressure difference between the drywell and the wetwell.

The vacuum breakers (VB) are represented by one-dimensional VLVE components. Two VBs are lumped together as one component. The VBs are triggered open at a set negative pressure differential between the drywell and wetwell. They will close at a lower value of the pressure differential. The VBs transport flow from the wetwell vapor space to the drywell at conditions corresponding to the cell in the wetwell vapor space to which they are connected. The correlations used for the singular losses are the same as described previously for the horizontal vents.

7.11.9 Break

Critical flow through the break is calculated using the model described in Section 6.3 of this report. This model has been extensively qualified. Comparisons with data are shown in Section 3.4 of the *TRACG Qualificiation LTR*[4],[5],[6]. The critical flow is calculated based on the upstream pressure, enthalpy and void fraction. Correlations used in the calculation of interfacial shear in the RPV are given in Section 6.1 of this report. The void fraction will depend on the position of the two-phase level in the downcomer. The two-phase level model is described in Section 6.4. Validation of the void fraction and two-phase level models is performed in Section 3.1 of the *TRACG Qualificiation LTR*[4],[5],[6].

In many thermal-hydraulic codes (RELAP, other versions of TRAC), the kinetic energy terms in the energy equation are eliminated by using the momentum equation. This leads to a form of the energy equation which is nonconserving when discretized (i.e., the energy leaving the RPV is not exactly equal to that deposited in the containment). In TRACG, the kinetic energy terms have been retained in the energy equation (Section 3.1), and the discretization is in a conserving form (Section 3.2).

Later in the transient, the flow through the break will no longer be choked. TRACG effectively calculates the minimum of the Bernoulli flow from the momentum equation and critical flow. The flow calculated from the momentum equation cannot exceed the critical flow. At low pressures, the flow will not be limited by critical flow.

8.0 NUMERICAL METHOD

TRACG uses a fully implicit integration technique for the heat conduction and hydraulic equations. For certain specialized calculations, primarily time domain stability calculations, an optional explicit integration technique can be employed. The fully implicit technique is the default option.

The heat transfer coupling between the structures and the hydraulics is treated implicitly, when the implicit integration technique is used. For this purpose, the heat conduction equation is solved in two steps, and thus integration of the combined equations involves the following steps:

1. The heat conduction equation for structures is linearized with respect to fluid temperatures. The result of this step is a system of linear equations for structure temperatures and surface heat flow as functions of the fluid temperatures.
2. The hydraulic equations are solved using an iterative technique. This step results in new values for the fluid pressures, void fraction, temperatures and velocities.
3. A corrector step is utilized for the hydraulic solution. Due to use of an iterative solution technique, the conservation of the properties is affected by the convergence. The corrector step is employed to correct any lack of conservation due to imperfect convergence.
4. Back-substitution into the heat conduction equation is performed to obtain new temperatures for structures.

The linearization of the heat conduction equation and subsequent back-substitution (Steps 1 and 4) are described in Section 8.1. The hydraulic solution (Steps 2 and 3) are described in Section 8.2.

The nomenclature used in this section is given below:

Nomenclature

Item	***Description***
A	flow area between mesh cells
A	surface area
$\underline{\underline{A}}$	coefficient matrix
$\vec{B}$	vector of sources or forcing functions
B_s	source term in momentum equation
c	concentration (boron)
c_p	specific heat of a fluid at constant pressure
c_v	specific heat of a fluid at constant volume
C_p	specific heat of a solid
C	coefficient
$\vec{C}$	coefficient vector
e	internal energy
E_s	source term in energy equation
F_w	wall shear

Nomenclature

Item	***Description***
$\vec{F}'$	vector of functions
f	interfacial shear
g	acceleration of gravity
h	heat transfer coefficient
h	internal enthalpy, $h = e + P/\rho$
h_{fg}	latent heat of vaporatization, $h_{fg} = h_g - h_f$
k	constant in virtual mass term in momentum equation
k	conductivity
M	mass
M_d	interface shear
M_s	source term in mass equation
P	pressure
q	heat transfer rate
r	radial dimension
R	Radial dimension for 3-D components
R	gas constant
R	acceptable rate-of-change (Equations (8.2-76) through (8.2-83))
$\vec{S}$	source vector
T	temperature
t	time
V	cell volume
v	velocity
x	dimension for 1-D component
z	axial dimension for 3-D components
Greek Symbols	
α	gas volume fraction
Δ	change
ε	user-specified convergence criterion, usually 10^{-3} - 10^{-4}
ζ	rate-of-change ratio (Equations (8.2-76) through (8.2-84))
Γ_g	interfacial mass transfer rate
η	convergence ratio
ρ	microscopic density
$\wp$	neutronics nodal power
σ	Surface tension
τ	shear tensor
θ	azimuthal dimension for 3-D components
θ	indicator for implicit/explicit integration (hydraulic model)
Subscript	
a	all noncondensable gases
b	boron
c	continuous phase
d	dispersed phase

Nomenclature

Item	*Description*
f	face of a fluid cell
f	saturated liquid
g	saturated steam
i	inner surface
i	fluid node number
IJK	a particular fluid cell IJK
kij	a particular neutronics node
ℓ	liquid phase
max	maximum
min	minimum
n	noncondensable gas
o	outer surface
p	constant pressure
r	relative (vapor-liquid)
s	source connection
s	steam
sat	saturation
v	constant volume
v	gas phase (mixture)
w	wall
Superscript	
d	donor celled
n	time step number
m	iteration number

8.1 Finite Difference Formulation of Heat Conduction Equation

The heat conduction equation for the fuel rods and heat slabs is solved using either a lumped slab model or a one-dimensional model. The one-dimensional model can be formulated either in Cartesian coordinates or in cylindrical coordinates. The lumped slab model is used for heat slabs completely internal to a single cell in the vessel component. The one-dimensional model using Cartesian coordinates is used for heat slabs in the vessel component situated between two axial levels. The one-dimensional model using cylindrical coordinates is used for the fuel rods, the walls of a one-dimensional component, and for heat slabs in the vessel component situated between two radial rings.

8.1.1 Lumped Slab Heat Conduction

The lumped slab heat conduction model is given by Equation (4.2-1).

Introducing

$$\Delta T^{n+1} = T^{n+1} - T^{n} \tag{8.1-1}$$

$$q_{w\ell} = A_w h_{w\ell} (T_w - T_\ell) \tag{8.1-2}$$

and

$$q_{wv} = A_w h_{wv} (T_w - T_v) \tag{8.1-3}$$

Equations (8.1-2) and (8.1-3) can be linearized as:

$$q_{w\ell}^{n+1} = q_{w\ell}^{n} - \theta \frac{\partial q_{w\ell}}{\partial T_\ell} (\Delta T_w^{n+1} - \Delta T_\ell^{n+1}) \tag{8.1-4}$$

and

$$q_{wv}^{n+1} = q_{wv}^{n} - \theta \frac{\partial q_{wv}}{\partial T_v} (\Delta T_w^{n+1} - \Delta T_v^{n+1}) \tag{8.1-5}$$

Using these results Equation (4.2-1) from Section 4.2 can be written as:

$$\begin{aligned} M_w C_{pw}^{n} \Delta T_w^{n+1} = &-\Delta t \left[q_{w\ell}^{n} - \theta \frac{\partial q_{w\ell}}{\partial T_\ell} (\Delta T_w^{n+1} - \Delta T_\ell^{n+1}) \right] \\ &-\Delta t \left[q_{wv}^{n} - \theta \frac{\partial q_{wv}}{\partial T_v} (\Delta T_w^{n+1} - \Delta T_v^{n+1}) \right] \end{aligned} \tag{8.1-6}$$

This equation can be rewritten as:

$$\Delta T_w^{n+1} = \Delta \tilde{T}_w^{n+1} + \frac{\partial T_w}{\partial T_\ell} \Delta T_\ell^{n+1} + \frac{\partial T_w}{\partial T_v} \Delta T_v^{n+1} \tag{8.1-7}$$

where

$$\Delta\tilde{T}_w^{n+1} = \frac{-\Delta t\,(q_{w\ell}^n + q_{wv}^n)}{MC_{pw}^n - \Delta t\theta\left(\frac{\partial q_{w\ell}}{\partial T_\ell} + \frac{\partial q_{wv}}{\partial T_v}\right)} \tag{8.1-8}$$

$$\frac{\partial T_w}{\partial T_\ell} = \frac{-\Delta t\theta\,\frac{\partial q_{w\ell}}{\partial T_\ell}}{MC_{pw}^n - \Delta t\theta\left(\frac{\partial q_{w\ell}}{\partial T_\ell} + \frac{\partial q_{wv}}{\partial T_v}\right)} \tag{8.1-9}$$

$$\frac{\partial T_w}{\partial T_v} = \frac{-\Delta t\theta\,\frac{\partial q_{wv}}{\partial T_v}}{MC_{pw}^n - \Delta t\theta\left(\frac{\partial q_{w\ell}}{\partial T_\ell} + \frac{\partial q_{wv}}{\partial T_v}\right)} \tag{8.1-10}$$

Substitute Equation (8.1-7) into Equation (8.1-4) to get the following expression for heat transfer rate to the liquid:

$$q_{w\ell}^{n+1} = q_{w\ell}^n - \theta\frac{\partial q_{w\ell}}{\partial T_\ell}\left[\Delta\tilde{T}_w^{n+1} + \left(\frac{\partial T_w}{\partial T_\ell} - 1\right)\Delta T_\ell^{n+1} + \left(\frac{\partial T_w}{\partial T_v}\right)\Delta T_v^{n+1}\right] \tag{8.1-11}$$

Similarly, substitute Equation (8.1-7) into Equation (8.1-5) to get the following expression for heat transfer rate to the vapor:

$$q_{wv}^{n+1} = q_{wv}^n - \theta\frac{\partial q_{wv}}{\partial T_v}\left[\Delta\tilde{T}_w^{n+1} + \left(\frac{\partial T_w}{\partial T_\ell}\right)\Delta T_\ell^{n+1} + \left(\frac{\partial T_w}{\partial T_v} - 1\right)\Delta T_v^{n+1}\right] \tag{8.1-12}$$

At the back-substitution step, after the final fluid temperatures have been obtained, the final wall temperatures are obtained by back-substitution into Equation (8.1-7).

8.1.2 One-Dimensional Heat Conduction in Cartesian Coordinates

The one-dimensional heat conduction equation in Cartesian coordinates is given by Equations (4.2-2) through (4.2-4) of Section 4.2.

These equations represent a system of linear equations, [[

]] (8.1-13)

Equation (8.1-13) can be solved to give:

[[ ]] (8.1-14)

where

[[ ]] (8.1-15)

[[ ]] (8.1-16),(8.1-17)

[[ ]] (8.1-18),(8.1-19)

Similar to Equation (8.1-4) for the lumped slab, for the one-dimensional problem the heat transfer rate to the liquid at the inner surface is given by:

$$q_{w\ell i}^{n+1} = q_{w\ell i}^{n} - \theta \frac{\partial q_{w\ell i}}{\partial T_{\ell i}} (\Delta T_{wi}^{n+1} - \Delta T_{\ell i}^{n+1}) \quad (8.1\text{-}20)$$

Applying Equation (8.1-14), the heat transfer rate to the liquid at the inner surface can be expressed as:

[[ ]] (8.1-21)

[[

]] (8.1-22)

A similar expression can be obtained for the heat transfer rate to the vapor at the inside of the slab:

[[ ]] (8.1-23)

Similar expressions are easily obtained for the heat transfer rates to the liquid and the vapor at the outer surface:

[[ ]] (8.1-24)

[[ ]] (8.1-25)

[[
]]

8.1.3 One-Dimensional Heat Conduction in Cylindrical Coordinates

The one-dimensional heat conduction equation in cylindrical coordinates is given by Equations (4.2-5) through (4.2-10) of Section 4.2.3.

These equations represent a system of linear equations, which can be written as:

[[ ]] (8.1-26)

These equations are solved exactly as the system of one-dimensional equations for heat conduction in Cartesian coordinates as described in Section 8.1.2.

8.2 Discretization of Hydraulic Equations

TRACG solves the conservation equations for mass, momentum, and energy for the vapor and liquid phases. The vapor phase can be a mixture of steam and noncondensable gases. Dissolved noncondensable gases in the liquid are not considered.

8.2.1 Predictor Step

The spatial discretization of the 3-D conservation equations was shown in Section 3.2.2. In this section the discretization in time is developed. The modification to the existing semi-implicit integration technique to generate the predictor step only affects the temporal discretization.

8.2.1.1 Momentum Equations

The spatial discretization of the momentum equations was shown in Section 3.2.2.1. In developing the temporal discretization, let us consider vapor and liquid momentum equations for the axial direction (Equations (3.2-21) and (3.2-26)). As mentioned earlier, the main modification affects the convective terms. In the convective terms the diagonal terms will be calculated using a combination of old and new time properties, such that outflow is given by the

new time properties and inflow by the old time properties. The off-diagonal terms will be based strictly on old time properties as before. The interfacial shear and wall friction will be based on the new velocities using a Taylor expansion around the old velocities. The fully discretized axial momentum equations then become:

Vapor

$$v^{n+1}_{vz,I+1/2,J,K} - v^{n}_{vz,I+1/2,J,K} + \Delta t\, v^{n}_{vz,I+1/2,J,K} \begin{cases} \dfrac{v^{n+1}_{vz,I+1/2,J,K} - v^{n}_{vz,I-1/2,J,K}}{\Delta z_I} & \text{if } v^{n}_{vz,I+1/2,J,K} \geq 0 \\ \dfrac{v^{n}_{vz,I+3/2,J,K} - v^{n+1}_{vz,I+1/2,J,K}}{\Delta z_{I+1}} & \text{if } v^{n}_{vz,I+1/2,J,K} < 0 \end{cases}$$

$$+ \Delta t \left[v_{vR} \left(\frac{\partial v_{vz}}{\partial R} \right)^{d} + \frac{v_{v\theta}}{R} \left(\frac{\partial v_{vz}}{\partial \theta} \right)^{d} \right]^{n}_{I+1/2,J,K}$$

$$+ \left(\frac{k\rho_c}{\alpha\rho_v} \right)^{n}_{I+1/2,J,K} \left[v^{n+1}_{rz} - v^{n}_{rz} + \Delta t v^{n}_{dz} \begin{cases} \dfrac{v^{n+1}_{rz,I+1/2,J,K} - v^{n}_{rz,I-1/2,J,K}}{\Delta z_I} & \text{if } v^{n}_{dz} \geq 0 \\ \dfrac{v^{n}_{rz,I+3/2,J,K} - v^{n+1}_{rz,I+1/2,J,K}}{\Delta z_{I+1}} & \text{if } v^{n}_{dz} < 0 \end{cases} \right]_{I+1/2,J,K} =$$

$$- \frac{\Delta t}{\rho_{v,I+1/2,J,K}} \frac{P^{n+1}_{I+1,J,K} - P^{n+1}_{I,J,K}}{\Delta z_{I+1/2}} - g\Delta t + B^{n}_{vz,I+1/2,J,K}\, \Delta t \qquad (8.2\text{-}1)$$

$$- \frac{\Delta t}{(\alpha\rho_v)_{I+1/2,J,K}} \left[f^{n}_{\ell v} + \frac{\partial f^{n}_{\ell v}}{\partial v_{vz}} \left(v^{n+1}_{vz} - v^{n}_{vz} \right) + \frac{\partial f^{n}_{\ell v}}{\partial v_{\ell z}} \left(v^{n+1}_{\ell z} - v^{n}_{\ell z} \right) \right]_{z,I+1/2,J,K}$$

$$- \frac{\Delta t}{\rho_{v,I+1/2,J,K}} \left[F^{n}_{w} + \frac{\partial F^{n}_{w}}{\partial v_{vz}} \left(v^{n+1}_{vz} - v^{n}_{vz} \right) + \frac{\partial F^{n}_{w}}{\partial v_{\ell z}} \left(v^{n}_{\ell z} - v^{n}_{\ell z} \right) \right]_{z,I+1/2,J,K}$$

where B_v includes both source terms and mixing terms.

Liquid:

$$v^{n+1}_{\ell z,I+1/2,J,K} - v^{n}_{\ell z,I+1/2,J,K} + \Delta t\, v^{n}_{\ell z,I+1/2,J,K} \begin{cases} \dfrac{v^{n+1}_{\ell z,I+1/2,J,K} - v^{n}_{\ell z,I-1/2,J,K}}{\Delta z_I} & \text{if } v^{n}_{\ell z,I+1/2,J,K} \geq 0 \\ \dfrac{v^{n}_{\ell z,I+3/2,J,K} - v^{n+1}_{\ell z,I-1/2,J,K}}{\Delta z_{I+1}} & \text{if } v^{n}_{\ell z,I+1/2,J,K} < 0 \end{cases}$$

$$+ \Delta t \left[v_{\ell R} \left(\frac{\partial v_{\ell z}}{\partial R} \right)^{d} + \frac{v_{\ell \theta}}{R} \left(\frac{\partial v_{\ell z}}{\partial \theta} \right)^{d} \right]^{n}_{I+1/2,J,K}$$

$$- \left(\frac{k\rho_c}{(1-\alpha)\rho_\ell} \right)^{n}_{I+1/2,J,K} \left[v^{n+1}_{rz} - v^{n}_{rz} + \Delta t v^{n}_{dz} \begin{cases} \dfrac{v^{n+1}_{rz,I+1/2,J,K} - v^{n}_{rz,I-1/2,J,K}}{\Delta z_I} & \text{if } v^{n}_{dz} \geq 0 \\ \dfrac{v^{n}_{rz,I+3/2,J,K} - v^{n+1}_{rz,I-1/2,J,K}}{\Delta z_{I+1}} & \text{if } v^{n}_{dz} < 0 \end{cases} \right]_{I+1/2,J,K} =$$

$$- \frac{\Delta t}{\rho_{\ell,I+1/2,J,K}} \frac{P^{n+1}_{I+1,J,K} - P^{n+1}_{I,J,K}}{\Delta z_{I+1/2}} - g\Delta t + B^{n}_{\ell z,I+1/2,J,K}\, \Delta t \qquad (8.2\text{-}2)$$

$$+ \frac{\Delta t}{\left[(1-\alpha)\rho_\ell\right]_{I+1/2,J,K}} \left[f^{n}_{\ell v} + \frac{\partial f^{n}_{\ell v}}{\partial v_{vz}} \left(v^{n+1}_{vz} - v^{n}_{vz} \right) + \frac{\partial f^{n}_{\ell v}}{\partial v_{\ell z}} \left(v^{n+1}_{\ell z} - v^{n}_{\ell z} \right) \right]_{z,I+1/2,J,K}$$

$$- \frac{\Delta t}{\rho_{\ell,I+1/2,J,K}} \left[F^{n}_{w} + \frac{\partial F^{n}_{w}}{\partial v_{vz}} \left(v^{n+1}_{vz} - v^{n}_{vz} \right) + \frac{\partial F^{n}_{w}}{\partial v_{\ell z}} \left(v^{n+1}_{\ell z} - v^{n}_{\ell z} \right) \right]_{z,I+1/2,J,K}$$

Examination of these equations reveals that they are linear equations in $v^{n+1}_{vz,\,I+1/2,J,K}$, $v^{n+1}_{\ell z,\,I+1/2,J,K}$, $P^{n+1}_{I,J,K}$, and $P^{n+1}_{I+1,J,K}$. Consequently, the velocities at time n+1 can be expressed implicitly as a function of the pressures at time n+1:

$$v^{n+1}_{vz,\,I+1/2,J,K} = \tilde{v}_{vz,\,I+1/2,J,K} + C_{vz,I+1/2,J,K} \left(P^{n+1}_{I,J,K} - P^{n+1}_{I+1,J,K} \right) \qquad (8.2\text{-}3)$$

$$v^{n+1}_{\ell z,\,I+1/2,J,K} = \tilde{v}_{\ell z,\,I+1/2,J,K} + C_{\ell z,I+1/2,\,J,\,K} \left(P^{n+1}_{I,J,K} - P^{n+1}_{I+1,J,K} \right) \qquad (8.2\text{-}4)$$

Similar equations can be generated for the radial and azimuthal directions, and for any source connection to the cell. These equations are used as shown in the next section to eliminate the velocities from the convective terms in the mass and energy equations.

8.2.1.2 Mass and Energy Equations

The spatial discretization of the mass and energy equations was shown in Section 3.2.2.2.
[[

]] The heat transfer rates (Equations (8.1-11), (8.1-12), (8.1-22) – (8.1-25)) and the vapor generation rate are based on fluid properties at time n+1. The fully discretized mass and energy equations then become:

Vapor Mass:

[[

]]

Mixture Mass:

[[

]]

Total Noncondensable Mass:

[[

]]

Note that the noncondensable gas components that are summed to form the total noncondensable gas have exactly the same mass equation form as Equation (8.2-7), except the "a" subscript is replaced by an "n" subscript for noncondensable gas component "n".

Vapor Energy:

[[

]]

Mixture Energy:

[[

]]

Examination of these equations reveals that they are equations in $P_{IJK}^{n+1,m}$, $\alpha_{IJK}^{n+1,m}$, $T_{v,IJK}^{n+1,m}$, $T_{\ell,IJK}^{n+1,m}$, $P_{a,IJK}^{n+1,m}$ and the new velocities at the faces of cell IJK. Here the following relationships have been used:

$$\rho_v^{n+1,m} = \rho_v\left(P^{n+1,m}, T_v^{n+1,m}, P_a^{n+1,m}\right) \tag{8.2-10}$$

$$e_v^{n+1,m} = e_v\left(P^{n+1,m}, T_v^{n+1,m}, P_a^{n+1,m}\right) \tag{8.2-11}$$

$$\rho_\ell^{n+1,m} = \rho_\ell\left(P^{n+1,m}, T_\ell^{n+1,m}\right) \tag{8.2-12}$$

$$e_{\ell}^{n+1,m} = e_{\ell}\left(P^{n+1,m}, T_{\ell}^{n+1,m}\right) \tag{8.2-13}$$

Using Equations (8.2-3) and (8.2-4) and the equivalent expressions for the radial and azimuthal directions, the updated face velocities at time n+1 can be eliminated from the mass and energy conservation equations (Equations (8.2-5) through (8.2-9)). The resulting set of conservation equations is of the form:

$$\vec{F}'\left(\begin{Bmatrix} P \\ \alpha \\ T_v \\ T_{\ell} \\ P_a \end{Bmatrix}_{IJK}^{n+1,m}\right)_{IJK} + \sum_{j=1}^{N_f} \vec{F}'_{fj,IJK}\left(P_{IJK}^{n+1,m} - P_{j,IJK}^{n+1,m}\right) = \vec{S}_{IJK}^{n+1,m} \tag{8.2-14}$$

where $\vec{F}'$ and $\vec{F}'_{fj,IJK}$ are vector functions, and $\vec{S}_{IJK}$ represents the source terms:

$$\vec{S}_{IJK}^{n+1,m} = \begin{Bmatrix} M_v \\ M_m \\ M_a \\ E_v \\ E_m \end{Bmatrix}_{IJK}^{n+1,m} V_{IJK} \bullet \Delta t \tag{8.2-15}$$

For the purpose of setting up and solving the pressure network in the predictor step, it is not necessary to consider the noncondensable gas components individually. Because all the noncondensable gases are assumed to be ideal gases and are assumed to have the same temperature node by node, the combined impact on the pressure network is accounted for by the response of the total noncondensable gas provided the properties of the total gas are properly determined. This is achieved by specifying for each node the total noncondensable gas properties as:

$$\rho_a = \sum_{n=1}^{NC} \rho_n \tag{8.2-16}$$

$$P_a = \sum_{n=1}^{NC} P_n \tag{8.2-17}$$

$$R_a = \frac{1}{\rho_a} \sum_{n=1}^{NC} \rho_n R_n \tag{8.2-18}$$

$$c_{va} = \frac{1}{\rho_a} \sum_{n=1}^{NC} \rho_n c_{vn} \tag{8.2-19}$$

where NC is the number of noncondensable gas components. Sections B.2.4, B.3.2, and B.3.3 of APPENDIX B provide additional details of how these properties, their derivatives, and the transport properties are defined and combined with the properties for steam. Note that in the predictor step and the network solution that the fluid properties for noncondensable gases do not appear individually; however, they do appear individually in the mass corrector step.

A source term exists for the vessel cell whenever a 1-D component is connected to the cell or for an 1-D cell in a TEE component, where the side branch is connected. Using the same discretization technique as for the cell faces, the source terms can be expressed as:

[[ ]] (8.2-20)

where the source velocity is measured positive going out and the "s,IJK" subscript represents the property in the 1-D source cell that is connected to cell IJK.

[[

]]

Substituting Equations (8.2-20) through (8.2-24) into Equation (8.2-14), and expressing the source velocities in terms of the pressure difference using expressions equivalent to Equations (8.2-3) and (8.2-4), gives:

$$\vec{F}'\left(\left\{\begin{matrix}P\\ \alpha\\ T_v\\ T_\ell\\ P_a\end{matrix}\right\}_{IJK}^{n+1,m}\right)_{IJK} + \sum_{j=1}^{N_f}\vec{F}'_{fj,IJK}\left(P_{IJK}^{n+1,m} - P_{j,IJK}^{n+1,m}\right) + \sum_{j=1}^{N_s}\vec{F}'_{sj,IJK}\left(P_{IJK}^{n+1,m} - P_{sj,IJK}^{n+1,m}\right) = 0 \qquad (8.2\text{-}25)$$

Here a summation over the N_s sources has been introduced for the case that more than one 1-D component is connected to vessel cell IJK.

In solving Equation (8.2-25) it is convenient to combine the term $\vec{F}'_{fj,IJK}P_{IJK}^{n+1,m}$ from the second term involving the summation over N_f faces of cell IJK with the first term. This gives the final form of the discretized mass and energy equations:

$$\vec{F}\left(\left\{\begin{matrix}P\\ \alpha\\ T_v\\ T_\ell\\ P_a\end{matrix}\right\}_{IJK}^{n+1,m}\right)_{IJK} + \sum_{j=1}^{N_f}\vec{F}_{fj,IJK}\left(P_{j,IJK}^{n+1,m}\right) + \sum_{j=1}^{N_s}\vec{F}'_{sj,IJK}\left(P_{IJK}^{n+1,m} - P_{sj,IJK}^{n+1,m}\right) = 0 \qquad (8.2\text{-}26)$$

where for convenience the following changes in nomenclature are defined

$$\vec{F}_{IJK}^{n+1,m} = \vec{F}'_{IJK} - \sum_{j=1}^{N_f}\vec{F}'_{fj,IJK}P_{IJK}^{n+1,m} \qquad (8.2\text{-}27)$$

$$\vec{F}_{fj,IJK} = -\vec{F}'_{fj,IJK} \qquad (8.2\text{-}28)$$

$$\vec{F}_{sj,IJK} \equiv \vec{F}'_{sj,IJK} \qquad (8.2\text{-}29)$$

The fully discretized mass and energy equations are non-linear equations and are solved using a standard Newton iteration technique:

$$\underline{\underline{A}}_{IJK}^{n+1,m}\begin{Bmatrix}\Delta P\\ \Delta\alpha\\ \Delta T_v\\ \Delta T_\ell\\ \Delta P_a\end{Bmatrix}_{IJK}^{n+1,m} = \vec{B}_{IJK}^{n+1,m} + \sum_{j=1}^{N_f}\vec{C}_{j,IJK}^{n+1,m}\Delta P_{j,IJK}^{n+1,m} + \sum_{j=1}^{N_s}\vec{S}_{j,IJK}^{n+1,m}\left(\Delta P_{IJK}^{n+1,m} - \Delta P_{sj,IJK}^{n+1,m}\right) \tag{8.2-30}$$

where m is the iteration number (this iteration is called the outer iteration). Here $\underline{\underline{A}}_{IJK}^{n+1,m}$ is the Jacobian matrix of $\vec{F}$:

$$\underline{\underline{A}}_{IJK}^{n+1,m} = \underline{\underline{Ja}}\left(\vec{F}_{IJK}^{n+1,m}\right) \tag{8.2-31}$$

and

$$\vec{C}_{j,IJK}^{n+1,m} = -\frac{\partial\vec{F}_{fj,IJK}^{n+1,m}}{\partial P_{j,IJK}^{n+1,m}} \tag{8.2-32}$$

$$\vec{S}_{j,IJK}^{n+1,m} = -\frac{\partial\vec{F}_{sj,IJK}^{n+1,m}}{\partial\left(P_{IJK}^{n+1,m} - P_{sj,IJK}^{n+1,m}\right)} \tag{8.2-33}$$

$$\vec{B}_{IJK}^{n+1,m} = -\vec{F}\left(\begin{Bmatrix}P\\ \alpha\\ T_v\\ T_\ell\\ P_a\end{Bmatrix}_{IJK}^{n+1,m-1}\right)_{IJK} - \sum_{j=1}^{N_f}\vec{F}_{fj,IJK}\left(P_{j,IJK}^{n+1,m}\right) - \sum_{j=1}^{N_s}\vec{F}_{sj,IJK}\left(P_{j,IJK}^{n+1,m} - P_{sj,IJK}^{n+1,m}\right) \tag{8.2-34}$$

and the change in the nodal quantities during the iteration is defined by

$$\begin{Bmatrix}\Delta P\\ \Delta\alpha\\ \Delta T_v\\ \Delta T_\ell\\ \Delta P_a\end{Bmatrix}_{IJK}^{n+1,m} = \begin{Bmatrix}P^{n+1,m} - P^{n+1,m-1}\\ \alpha^{n+1,m} - \alpha^{n+1,m-1}\\ T_v^{n+1,m} - T_v^{n+1,m-1}\\ T_\ell^{n+1,m} - T_\ell^{n+1,m-1}\\ P_a^{n+1,m} - P_a^{n+1,m-1}\end{Bmatrix}_{IJK} \tag{8.2-35}$$

Equation (8.2-30) is the final form of the discretized continuity equations. The solution of this equation will be described in Section 8.2.2.

8.2.2 Network Solution

In the previous section, the final discretized form of the conservation equations was developed for the fast implicit numerics. A key feature of this equation, Equation (8.2-30), is that its basic form is unchanged from the previous semi-implicit formulation in TRACG and only the elements in the equation have been modified (i.e., no new elements have been added and none deleted). Consequently, the existing network solution can be applied without any change. For the sake of completeness, the network solution will be reviewed here.

Multiplying Equation (8.2-30) by $(\underline{\underline{A}}_{IJK})^{-1}$ and omitting the superscript, one gets:

$$\begin{Bmatrix} \Delta P \\ \Delta\alpha \\ \Delta T_v \\ \Delta T_\ell \\ \Delta P_a \end{Bmatrix}^{n+1,m}_{IJK} = \vec{B}'_{IJK} + \sum_{j=1}^{N_f} \vec{C}'_{j,IJK} \Delta P_{j,IJK} + \sum_{j=1}^{N_s} \vec{S}'_{j,IJK} \left(\Delta P_{IJK} - \Delta P_{sj,IJK} \right) \tag{8.2-36}$$

where:

$$\vec{B}'_{IJK} = (\underline{\underline{A}}_{IJK})^{-1} \bullet \vec{B}_{IJK} \tag{8.2-37}$$

$$\vec{C}'_{j,IJK} = (\underline{\underline{A}}_{IJK})^{-1} \bullet \vec{C}_{j,IJK} \tag{8.2-38}$$

$$\vec{S}'_{j,IJK} = (\underline{\underline{A}}_{IJK})^{-1} \bullet \vec{S}_{j,IJK} \tag{8.2-39}$$

Examination of Equation (8.2-36) reveals that once the set of all ΔP values are known, $\Delta\alpha$, ΔT_v, ΔT_ℓ, and ΔP_a can be obtained for each IJK node through back-substitution. Consequently, the task in the network solution reduces to the calculation of the change in total pressure, ΔP. The first row in Equation (8.2-36) is:

$$\Delta P_{IJK} = \left\{ B'_{IJK} \right\}_1 + \sum_{j=1}^{N_f} \left\{ C'_{j,IJK} \right\} \Delta P_{j,IJK} + \sum_{j=1}^{N_s} \left\{ \vec{S}'_{j,IJK} \right\}_1 \left(\Delta P_{IJK} - \Delta P_{sj,IJK} \right) \tag{8.2-40}$$

This is the pressure equation that is solved in the network solution. For a 1-D component, the equation that is equivalent to Equation (8.2-40) reduces to:

$$\Delta P_i = \left\{ b'_i \right\}_1 + \sum_{j=1}^{N_n} \left\{ c'_{j,i} \right\}_1 \Delta P_{j,i} + \sum_{j=1}^{N_s} \left\{ s_{j,i} \right\}_1 \left(\Delta P_i - \Delta P_{sj,i} \right) \tag{8.2-41}$$

where N_n is the number of neighboring cells and N_S is the number of sources to any given cell of the 1-D component. In the context of a 1-D component, a source is a junction to another component so that

$$N_s = \begin{cases} 0, & \text{for an internal cell of a PIPE} \\ 1, & \text{for an end cell of a PIPE} \end{cases} \tag{8.2-42}$$

$$N_n = \begin{cases} 2, & \text{for an internal cell of a PIPE} \\ 1, & \text{for an end cell of a PIPE} \end{cases} \tag{8.2-43}$$

A value of $N_s' = N_s + 1$ and $N_n' = N_n + 1$ is possible for components that are based on a tee such as the TEE, JETP, CHAN and SSEP components. For a CHAN component where the dynamic water rod is applied, the cells where the water rod connects appear as though they have an additional connection.

Rearranging Equation (8.2-41) to:

$$\Delta P_i - \sum_{j=1}^{N_n} \left\{c'_{j,i}\right\}_1 \Delta P_{j,i} = \left\{b'_i\right\}_1 + \sum_{j=1}^{N_s} \left\{s'_{j,i}\right\}_1 \left(\Delta P_i - \Delta P_{sj,i}\right) \tag{8.2-44}$$

and remembering that $\left\{s'_{j,i}\right\}_1$ is only non-zero for an end cell, the system of linear equations can be solved to give:

$$\Delta P_i = d_i + \sum_{s=1}^{N_{st}} e_{i,s} \Delta^2 P_{j_s} \tag{8.2-45}$$

where N_{st} is the total number of source junctions and $\Delta^2 P_{j_s}$ is the change in ΔP across the source junction "s" corresponding to junction "j_{ik}" that connects component "i" cell "1" to component "k" cell "m" as shown in Figure 8-1. For example,

$$\Delta^2 P_{j_{ik}} = \Delta P_{k_m} - \Delta P_{i_1} \tag{8.2-46}$$

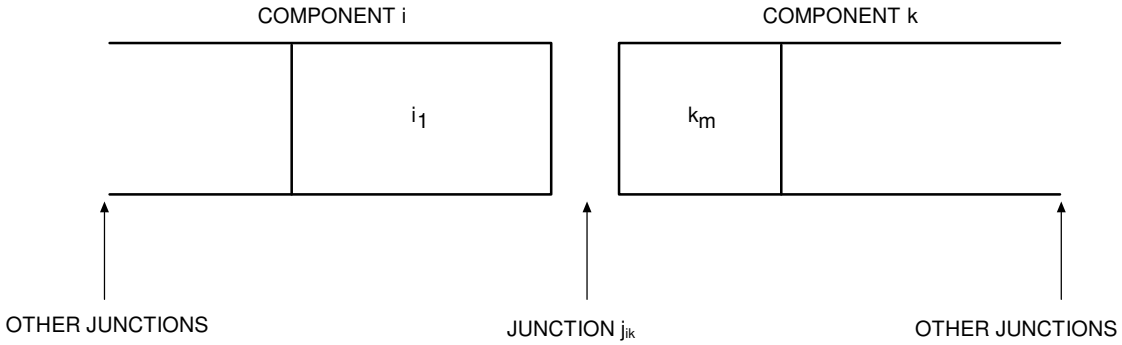

Figure 8-1. Junction of 1-D Components

Let $\Delta^2\vec{P}_j$ be a vector describing the change in ΔP across all junctions in the system including 1D-1D and 1D-3D junctions. For cell i_1, Equation (8.2-45) can be written as:

$$\Delta P_{i_1} = d_{i_1} + \vec{e}_{i_1} \bullet \Delta^2\vec{P}_j \tag{8.2-47}$$

Similarly, for cell k_m, Equation (8.2-45) can be written as:

$$\Delta P_{k_m} = d_{k_m} + \vec{e}_{k_m} \bullet \Delta^2\vec{P}_j \tag{8.2-48}$$

Subtracting Equation (8.2-47) from Equation (8.2-48) and applying

$$\Delta^2 P_{j_{ik}} = \Delta P_{k_m} - \Delta P_{i_1} \tag{8.2-49}$$

one gets:

$$\Delta^2 P_{j_{ik}} = d_{k_m} - d_{i_1} + \left(\vec{e}_{k_m} - \vec{e}_{i_1}\right) \bullet \Delta^2\vec{P}_j \tag{8.2-50}$$

Consider the example where a 1-D component is connected to a 3-D component by junction "j_{i3}" as shown in Figure 8-2.

For cell i_1 in the 1-D component, Equation (8.2-45) can be written as:

$$\Delta P_{i_1} = d_{i_1} + \vec{e}_{i_1} \bullet \Delta^2\vec{P}_j \tag{8.2-51}$$

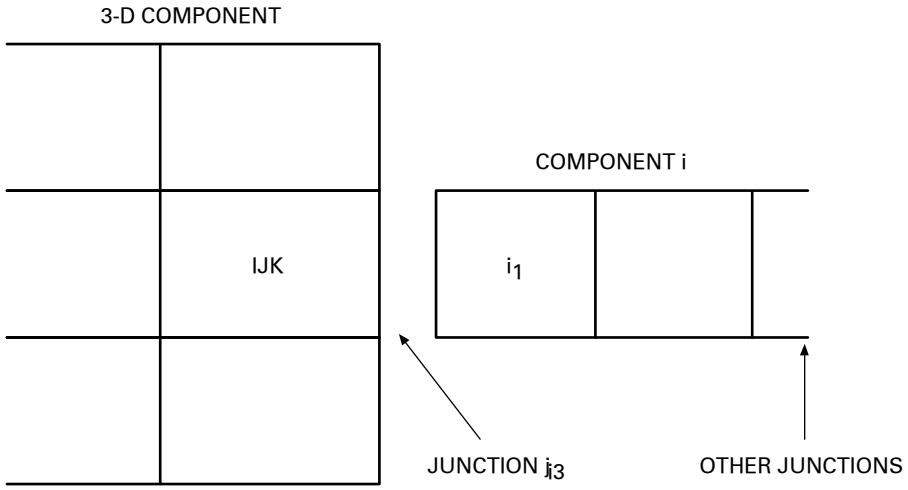

Figure 8-2. Junction of 1-D and 3-D Components

Subtracting ΔP_{IJK} from this equation and remembering that:

$$\Delta^2 P_{j_{i3}} = \Delta P_{i_1} - \Delta P_{IJK} \tag{8.2-52}$$

one gets:

$$\Delta^2 P_{j_{i3}} = d_{i_1} + \vec{e}_{i_1} \bullet \Delta^2 \vec{P}_J - \Delta P_{IJK} \tag{8.2-53}$$

For all junctions, Equations (8.2-50)and (8.2-53) will thus form a system of linear equations:

$$\underline{\underline{E}} \bullet \Delta^2 \vec{P}_j = \vec{D} + \underline{\underline{F}} \bullet \Delta \vec{P}_{3D} \tag{8.2-54}$$

where $\Delta \vec{P}_{3D}$ is a vector of all the pressure changes for the 3-D component. Solving Equation (8.2-54) produces:

$$\Delta^2 \vec{P}_j = \vec{D}' + \underline{\underline{F}}' \bullet \Delta \vec{P}_{3D} \qquad \text{where} \tag{8.2-55}$$

$$\vec{D}' = \left(\underline{\underline{E}}\right)^{-1} \bullet \vec{D} \tag{8.2-56}$$

$$\underline{\underline{F}}' = \left(\underline{\underline{E}}\right)^{-1} \bullet \underline{\underline{F}} \tag{8.2-57}$$

In Equation (8.2-40), $\Delta P_{IJK} - \Delta P_{sj,IJK}$ is $\Delta^2 P_j$ across a junction "j" connecting a 1-D component to the 3-D component. Consequently, Equation (8.2-40) can be written as:

$$\underline{\underline{G}} \bullet \Delta \vec{P}_{3D} = \vec{B}_1' + \underline{\underline{S}} \bullet \Delta^2 \vec{P}_j \tag{8.2-58}$$

Substituting Equation (8.2-55) into this equation, one gets:

$$\underline{\underline{G}} \bullet \Delta \vec{P}_{3D} = \vec{B}_1' + \underline{\underline{S}} \bullet \left[\vec{D}' + \underline{\underline{F}}' \bullet \Delta \vec{P}_{3D} \right] \tag{8.2-59}$$

Equation (8.2-59) is the final equation in the network solution. It is a system of linear equations that can be solved for pressure changes in the 3-D component.

The rest of the solution consists of back-substitution. $\Delta^2 P_j$ is obtained from Equation (8.2-55), the changes in individual pressures in the 1-D components are obtained from Equation (8.2-45), and finally the changes in α, T_g, T_g, and P_a are obtained from Equation (8.2-36) and its equivalent for the 1-D components.

The total noncondensable partial pressure P_a determined from the back-substitution reflects a contribution ΔP_a due to implicit coupling of the mass, momentum, and energy equations. To achieve the same degree of coupling in the partial pressures of the individual noncondensable gas components, the implicit contribution to the total noncondensable gas is resolved into its components by applying

[[ ]] (8.2-60)

The gas constant R_a may have a different value from node to node since it depends on the nodal composition of the total noncondensable gas. The component noncondensable gas partial pressures are updated for all nodes in the same way for both 1-D and 3-D components.

8.2.3 Corrector Step

TRACG uses a fully implicit method for the mass and energy equations in the predictor step. An iterative technique is used for the predictor step. For a fully converged iteration perfect mass and energy conservation is obtained for the predictor step within the convergence criteria so the corrector step is not needed. However, the corrector step is retained because it does assure perfect mass conservation. For nodes where there is thermal equilibrium, conservation of mass is equivalent with conservation of energy for constant pressure.

8.2.3.1 Mixture Mass Conversion

$$V_{IJK}\left\{\left[(1-\alpha)\rho_\ell+\alpha\rho_v\right]^{n+1}-\left[(1-\alpha)\rho_\ell+\alpha\rho_v)\right]^{n}\right\}_{IJK}=$$

$$-\Delta t\,A_{I+1/2,J,K}\left[v^{n+1}_{\ell z,I+1/2,J,K}\begin{cases}\left[(1-\alpha)\rho_\ell\right]^{n+1}_{I,J,K} & \text{if } v^{n+1}_{\ell z,I+1/2,J,K}\geq 0\\ \left[(1-\alpha)\rho_\ell\right]^{n+1}_{I+1,J,K} & \text{if } v^{n+1}_{\ell z,I+1/2,J,K}<0\end{cases}\right.$$

$$\left.+\,v^{n+1}_{vz,I+1/2,J,K}\begin{cases}(\alpha\rho_v)^{n+1}_{I,J,K} & \text{if } v^{n+1}_{vz,I+1/2,J,K}\geq 0\\ (\alpha\rho_v)^{n+1}_{I+1,J,K} & \text{if } v^{n+1}_{vz,I+1/2,J,K}<0\end{cases}\right] \qquad (8.2\text{-}61)$$

$$-\Delta t\,A_{I-1/2,J,K}\left[v^{n+1}_{\ell z,I-1/2,J,K}\begin{cases}\left[(1-\alpha)\rho_\ell\right]^{n+1}_{I-1,J,K} & \text{if } v^{n+1}_{\ell z,I-1/2,J,K}\geq 0\\ \left[(1-\alpha)\rho_\ell\right]^{n+1}_{I,J,K} & \text{if } v^{n+1}_{\ell z,I-1/2,J,K}<0\end{cases}\right.$$

$$\left.+\,v^{n+1}_{vz,I-1/2,J,K}\begin{cases}(\alpha\rho_v)^{n+1}_{I-1,J,K} & \text{if } v^{n+1}_{vz,I-1/2,J,K}\geq 0\\ (\alpha\rho_v)^{n+1}_{I,J,K} & \text{if } v^{n+1}_{vz,I-1/2,J,K}<0\end{cases}\right]$$

Similar terms for the J and K directions

$$+V_{IJK}\left(M^{n+1}_{ms}+M^{n+1}_{mmix}\right)_{IJK}\Delta t+$$

In this equation, the densities and velocities are the fully-converged values calculated in the predictor step for time n+1. The source term is calculated as indicated in Equation (8.2-21) but using a fully implicit technique:

$$\left(V \bullet M_{ms}\right)_{IJK}^{n+1} = -A_{s,IJK}\left[v_{\ell s,IJK}^{n+1} \begin{cases} \left[(1-\alpha)\rho_{\ell}\right]_{IJK}^{n+1} & \text{if } v_{\ell s,IJK}^{n+1} \geq 0 \\ \left[(1-\alpha)\rho_{\ell}\right]_{s,IJK}^{n+1} & \text{if } v_{\ell s,IJK}^{n+1} < 0 \end{cases} \right. \tag{8.2-62}$$

$$\left. + v_{vs,IJK}^{n+1} \begin{cases} (\alpha\rho_{v})_{IJK}^{n+1} & \text{if } v_{vs,IJK}^{n+1} \geq 0 \\ (\alpha\rho_{v})_{s,IJK}^{n+1} & \text{if } v_{vs,IJK}^{n+1} < 0 \end{cases} \right]$$

Again, the densities and velocities are the fully-converged values obtained from the predictor step for time n+1. Substituting Equation (8.2-62) into Equation (8.2-61) gives an equation in only the new void fractions, which can be arranged to be of the form:

$$A_{IJK}\Delta\alpha_{IJK}^{n+1} = B_{IJK} + \sum_{j=1}^{N_f} C_{j,IJK}\Delta\alpha_{j,IJK}^{n+1} + \sum_{j=1}^{N_s} S_j\left(\Delta\alpha_{IJK}^{n+1} - \Delta\alpha_{sj,IJK}^{n+1}\right) \tag{8.2-63}$$

Dividing this equation by A_{IJK} gives an equation of exactly the same form as Equation (8.2-40) for the pressure. Once all these equations are assembled into the network, the network solver can be used to obtain the new void fractions following the same process used to calculate the nodal pressure changes. The mixture mass is conserved because Equation (8.2-61) is on a conserving form.

8.2.3.2 Noncondensable Gas Conservation

To determine the amount of total noncondensable gas relative to steam and to get perfect mass conservation, the total noncondensable mass Equation (8.2-7) is discretized using a fully implicit technique as:

$$V_{IJK}\left(m_a^{n+1} - m_a^{m}\right)_{IJK} =$$

$$-A_{I+1/2,J,K}\left[v_{vz,I+1/2,J,K}^{n+1} \begin{cases} \left(m_a\right)_{I,J,K}^{n+1} & \text{if } v_{vz,I+1/2,J,K}^{n+1} \geq 0 \\ \left(m_a\right)_{I+1,J,K}^{n+1} & \text{if } v_{vz,I+1/2,J,K}^{n+1} < 0 \end{cases} \right]\Delta t$$

$$+A_{I-1/2,J,K}\left[v_{vz,I-1/2,J,K}^{n+1} \begin{cases} \left(m_a\right)_{I-1,J,K}^{n+1} & \text{if } v_{vz,I-1/2,J,K}^{n+1} \geq 0 \\ \left(m_a\right)_{I,J,K}^{n+1} & \text{if } v_{vz,I-1/2,J,K}^{n+1} < 0 \end{cases} \right]\Delta t \tag{8.2-64}$$

+ Similar terms in J and K directions

$$+ \; V_{IJK}\left(M_{as}^{n+1} + M_{amix}^{n+1}\right)_{IJK}\Delta t$$

where $m_a = (\alpha\rho_a)$

The source term is given as:

$$V_{IJK}\, M_{as,IJK}^{n+1} = -A_{s,IJK} v_{vs,IJK}^{n+1} \begin{cases} \left(m_a\right)_{IJK}^{n+1} & \text{if } v_{vs,IJK}^{n+1} \geq 0 \\ \left(m_a\right)_{s,IJK}^{n+1} & \text{if } v_{vs,IJK}^{n+1} < 0 \end{cases} \tag{8.2-65}$$

Substituting Equation (8.2-65) into Equation (8.2-64) gives an equation in only the new total noncondensable mass concentration, which can be rearranged to be of the form:

$$A_{IJK}\Delta m_{a,IJK}^{n+1} = B_{IJK} + \sum_{j=1}^{N_f} C_{j,IJK}\Delta m_{aj,IJK}^{n+1} + \sum_{j=1}^{N_s} Sc_j\left(\Delta m_{a,IJK}^{n+1} - \Delta m_{asj,IJK}^{n+1}\right) \tag{8.2-66}$$

The mass equations for each individual noncondensable gas component are solved separately in the corrector step. The approach is identical to that described above in Equations (8.2-64), (8.2-65) and (8.2-66) except the "a" subscript is replaced by an "n" subscript. Equation (8.2-66) is of the same form as Equation (8.2-40) for the pressure so once the equations for all nodes are assembled, the network solver is used to solve for the new total noncondensable gas mass and is also used to solve for each of the individual noncondensable gas components.

8.2.3.3 Liquid Solute Conservation

To determine the amount of boron dissolved in and transported with the liquid, the boron mass equation is discretized and solved using a fully implicit technique similar to the one used for the noncondensable gas.

$$V_{IJK}\left(m_B^{n+1} - m_B^m\right) =$$

$$-A_{I+1/2,J,K}\left[v_{\ell z,I+1/2,J,K}^{n+1}\begin{cases}\left(m_B\right)_{I,J,K}^{n+1} & \text{if } v_{\ell z,I+1/2,J,K}^{n+1} \geq 0 \\ \left(m_B\right)_{I+1,J,K}^{n+1} & \text{if } v_{\ell z,I+1/2,J,K}^{n+1} < 0\end{cases}\right]\Delta t$$

$$+A_{I-1/2,J,K}\left[v_{\ell z,I-1/2,J,K}^{n+1}\begin{cases}\left(m_B\right)_{I-1,J,K}^{n+1} & \text{if } v_{\ell z,I-1/2,J,K}^{n+1} \geq 0 \\ \left(m_B\right)_{I,J,K}^{n+1} & \text{if } v_{\ell z,I-1/2,J,K}^{n+1} < 0\end{cases}\right]\Delta t \tag{8.2-67}$$

+ Similar terms in J and K directions

$$+\ V_{IJK}\left(M_{Bs}^{n+1} + M_{Bmix}^{n+1}\right)_{IJK}\Delta t$$

The source term is given as:

$$V_{IJK}\, M_{Bs,IJK}^{n+1} = -A_{s,IJK} v_{\ell s,IJK}^{n+1} \begin{cases} \left(m_B\right)_{IJK}^{n+1} & \text{if } v_{\ell s,IJK}^{n+1} \geq 0 \\ \left(m_B\right)_{sIJK}^{n+1} & \text{if } v_{\ell s,IJK}^{n+1} < 0 \end{cases} \tag{8.2-68}$$

Substituting Equation (8.2-68) into (8.2-67) gives an equation in only the new boron mass concentration, which can be rearranged to be of the form:

$$A_{IJK}\Delta m_{B,IJK}^{n+1} = B_{IJK} + \sum_{j=1}^{N_f} C_{j,IJK}\Delta m_{Bj,IJK}^{n+1} + \sum_{j=1}^{N_s} Sc_j\left(\Delta m_{B,IJK}^{n+1} - \Delta m_{Bsj,IJK}^{n+1}\right) \quad (8.2\text{-}69)$$

This equation is again of the same form as Equation (8.2-40) that was used to assemble the pressure network. Thus the mass conservation equations for the liquid solute are assembled into a network and the network solver is used to obtain the new solute masses.

8.2.3.4 Energy Conservation

In the iterative predictor step, TRACG solves the fully implicit equations for energy, thus energy is conserved for the fully-converged solution. This, coupled with the precise mass conservation assured by the corrector step, produces excellent energy conservation and does not generate the need for an extra corrector step for energy. (It should be noted that the original formulation of the energy equation in TRAC was not on a conserving form due to the elimination of the kinetic energy from the energy equation by substituting the momentum equation into the energy equation. This problem could lead to significant energy balance errors for systems involving critical flow. In TRACG the kinetic energy is included in the energy equations, thereby maintaining a conserving form of these equations.)

To demonstrate the energy conservation in TRACG, a test case using the PSTF vessel blow-down test has been evaluated for various values of the convergence criterion for the predictor step. As the convergence is tightened for the predictor step, the mass and energy balance is improved, and in the limit there is no error. Table 8-1 shows the energy error at

Table 8-1. Energy Error for PSTF Vessel Blow-down 5801-15

	Initial Mass (kg) 1.34398E3		**Initial Energy (J) 1.851458E9**	
Convergence Criterion	**Final Mass (kg)**	**Mass Conservation Error**	**Final Energy (J)**	**Relative Energy Error**
1.0E-2	1.009360E3	-4.56E-7	1.017515E9	2.9E-2
1.0E-3	1.005698E3	-1.004E-6	0.9970902E9	8.2E-3
1.0E-4	1.004096E3	-1.82E-7	0.9917846E9	2.8E-3
1.0E-5	1.003044E3	-1.82E-7	0.9897846E9	2.9E-4
1.0E-6	1.002951E3	-3.65E-7	0.9890168E9	

20 seconds which coincides approximately with the end of the depressurization of the vessel. The mass conservation is seen to be accurate for all cases. The energy error is evaluated relative to the converged case (the case with the tightest convergence is used). It is seen that there is no significant energy errors for reasonable values of the convergence criterion (1.0E-3 - 1.0E-5).

8.2.4 Time Step Control

TRACG determines the time step size in order to maximize the accuracy of the calculation and minimize the computer time. Two basic criteria are used for this purpose:

- **Convergence**. The iteration to obtain a solution to the thermal-hydraulic

equations are required to converge within a prescribed convergence criteria. If convergence is obtained with a low iteration count, the time step size is allowed to increase. On the other hand, if a high iteration count is required, the time step size will be reduced.

- **Rate-of-Change**. TRACG examines the rate of change for the primary dependent variables. If the rate of change is low, a quasi steady-state condition will exist and the time step size is allowed to increase. On the other hand, if the rate-of-change is high, the time step size will be reduced.

In practice, the time step size is normally determined by the convergence criteria. If a quasi steady-state condition exists, convergence will easily be established within a few iterations, and if a fast transient exist, where the dependent variables are changing fast, a larger iteration count will generally be required. The primary purpose of the rate-of-change criteria is to prevent excessive changes in the dependent variables during a time step to prevent excessive discretization error.

TRACG also allows the time step size to be determined based on the material Courant limit and user-specified upper and lower limits.

If the time step size is allowed to increase by all of the criteria, the time step size will be increased. However, the time step size will be reduced if a reduction is required by just one of the criteria.

8.2.4.1 Convergence

TRACG checks the convergence of the primary dependent variables for the independent hydraulic variables using the following criteria:

$$\eta_P = \max\left(\frac{\left|P_i^m - P_i^{m-1}\right|}{\max(100, \varepsilon P_i^m)}\right) \tag{8.2-70}$$

$$\eta_a = \max\left(\frac{\alpha_i^m - \alpha_i^{m-1}}{\max(0.01, 10\varepsilon)}\right) \tag{8.2-71}$$

$$\eta_{Tv} = \max\left(\frac{\left|T_{vi}^m - T_{vi}^{m-1}\right|}{\min(1.0, 10^3\varepsilon)}\right) \tag{8.2-72}$$

$$\eta_{T\ell} = \max\left(\frac{\left|T_{\ell i}^m - T_{\ell i}^{m-1}\right|}{\min(1.0, 10^3\varepsilon)}\right) \tag{8.2-73}$$

$$\eta_{Pa} = \max\left(\frac{\left|P_{ai}^m - P_{ai}^{m-1}\right|}{\max(100, \varepsilon P_i^m)}\right) \tag{8.2-74}$$

where

ε = A user-specified convergence criterion, usually 10^{-3} - 10^{-4}.

Convergence is established when:

$$\eta = \max(\eta_P, \eta_a, \eta_{Tv}, \eta_{T\ell}, \eta_{Pa}) < 1.0 \tag{8.2-75}$$

8.2.4.2 Rate-of-Change

TRACG checks the rate-of-change of the primary dependent variables using the following criteria applied for every fluid node "i":

$$\zeta_P = \max\left(\frac{\left|P_i^{n+1} - P_i^n\right|}{\max(5.0\cdot 10^4, R_1 \cdot P_i^{n+1})}\right) \tag{8.2-76}$$

$$\zeta_\alpha = \max\left(\frac{\alpha_i^{n+1} - \alpha_i^n}{R_2}\right) \tag{8.2-77}$$

$$\zeta_{Tv} = \max\left(\frac{\left|T_{vi}^{n+1} - T_{vi}^n\right|}{R_3}\right) \tag{8.2-78}$$

$$\zeta_{T\ell} = \max\left(\frac{\left|T_{\ell i}^{n+1} - T_{\ell i}^n\right|}{R_4}\right) \tag{8.2-79}$$

$$\zeta_{Pa} = \max\left(\frac{\left|P_{ai}^{n+1} - P_{ai}^n\right|}{\max(5.0\cdot 10^4, R_5 \cdot P_i^n)}\right) \tag{8.2-80}$$

where "n" is the time step number. In addition to the changes in hydraulic variables, TRACG checks the rate-of-change in three other quantities: (1) heat slab temperatures, (2) fuel rod temperatures, and (3) nodal power changes in the 3-D kinetics. For heat slabs of all kinds (point, one-sided and two-sided), the maximum absolute change in the temperature $T_{w(s)}$ for all "s" nodes in all slabs is used define the rate-of-change parameter

$$\zeta_{Tw} = \max\left(\frac{\left|T_{w(s)}^{n+1} - T_{w(s)}^n\right|}{R_6}\right) \tag{8.2-81}$$

Similarly, the maximum absolute change in fuel rod temperatures $T_{r(ik)}$ considering all "ik" nodes in all fuel rod groups of all channels defines the rate-of-change parameter

$$\zeta_{Tr} = \max\left(\frac{\left|T_r^{n+1} - T_r^n\right|}{R_7}\right) \tag{8.2-82}$$

The rate-of-change criteria for the 3-D kinetics is a complex quantity that is defined as

[[ ]] (8.2-83)

[[

]]

The rate-of-change criterion is satisfied when all eight criteria satisfy:

$$\zeta = \max(\zeta_P, \zeta_\alpha, \zeta_{Tv}, \zeta_{T\ell}, \zeta_{Pa}, \zeta_{Tw}, \zeta_{Tr}, \zeta_{\wp}) < 1.0 \quad (8.2\text{-}84)$$

The allowed rates-of-change $R_\#$ for # = {1,…,8} are set by default in the code or can be changed by optional user input.

8.2.4.3 Other Criteria

TRACG also allows the time step size to be controlled by the material Courant number:

$$\Delta t < C \cdot \min\left(\frac{\Delta x_i}{\max(|v_v|, |v_\ell|)} \right) \quad (8.2\text{-}85)$$

where

C = a user-specified multiplier

Usually a large value for the multiplier C is used, such that this is not a limiting criterion. Finally, the user has the option to specify upper and lower bounds on the time step size:

$$\Delta t_{min} < \Delta t < \Delta t_{max} \quad (8.2\text{-}86)$$

If the convergence and rate-of-change criteria cannot be satisfied using a time step size within these bounds, the calculations will abort.

9.0 THREE-DIMENSIONAL NEUTRON KINETICS MODEL

TRACG solves the three-dimensional (3-D) transient neutron diffusion equations using one neutron energy group and up to six delayed neutron precursors groups. The basic formulation and assumptions are consistent with the GEH 3-D BWR Core Simulator[3],[20]. This same one-group formulation collapsed radially to one axial dimension is the basis for the NRC-approved ODYN computer code[198]. The simplifying assumptions made in ODYN to yield a one-dimensional (1-D) transient kinetics model are not used in the TRACG three-dimensional (3-D) model. Instead, neutron flux and delayed neutron precursor concentrations at every (i,j,k) node are integrated in time in response to moderator density, fuel temperature, boron concentration or control rod changes. Exposure and xenon concentration distributions are assumed to be constant during the transient.

Nomenclature

Item	*Description*
A	miscellaneous actinides
AP	activation products
A_∞	nodal parameter defined by Equation (9.1-18)
B^2	geometric buckling
c	neutron speed
C	delayed neutron precursor concentration
C_T	Doppler coefficient
D	diffusion coefficient
DN	fission power
EX	exposure
f	decay heat fraction, $f = \sum_{k=1}^{N_d} f_k$
f	flux discontinuity factor
F	fission products
G	neutron capture effect “G-factor” defined by Equation (9.3-24)
H	total heat
I	power integral
J	current
K	multiplication constant
M^2	migration area (D/Σ)
N	total number of delayed neutron precursor groups
N_d	number of decay heat groups
P	fission power

Nomenclature

Item	***Description***
q	volumetric heat generation rate
Q	energy release/fission
r	spatial dimension
S	source term
SI	sprectral index
t	time
T	irradiation time
T	moderator temperature
TF	fuel temperature
U	relative water density
v	average neutron speed
v*	effective neutron velocity
V	volume
w	spatial weighting function
x,y	coordinates in the horizontal plane
z	axial coordinate

Greek

β	delayed neutron precursor fraction, $\beta = \sum_{n=1}^{N} \beta_n$
Φ	neutron flux
$\nu\Sigma_f$	fission neutron production cross–section
Γ	boundary condition
κ	inverse migration area
λ	decay constant
μ	initial effective multiplication factor
ρ	moderator density
ρ	reactivity
ζ	flux discontinuity factor
ν	neutrons/fission
Σ	total removal cross–section, $\Sigma = \Sigma_a + \Sigma_{s\ell}$
Σ_a	absorption cross–section
$\Sigma_{s\ell}$	slowing cross–section
τ	neutron flux logarithmic time constant

Nomenclature

Item	Description
Subscripts	
1	neutron energy group 1
2	neutron energy group 2
3	neutron energy group 3
B_{10}	boron-10
bl	control blade
ch	channel wall
d	decay
dh	decay heat
f	fission; fuel
g	neutron energy group
i	generic 3-D node
j	generic node j adjoining node i
j	fuel rod j
ij	between nodes i and j
k	decay heat group
kij	specific 3-D node
kn	channel component n, axial cell k
lib	fuel library
n	delayed neutron precursor group
o	reference value
p	prompt
s	surface
Xe	xenon
∞	infinite lattice
_	vector
Superscripts	
Dop	Doppler
m	time step index
n	time step index
r	rated power
Xe	xenon

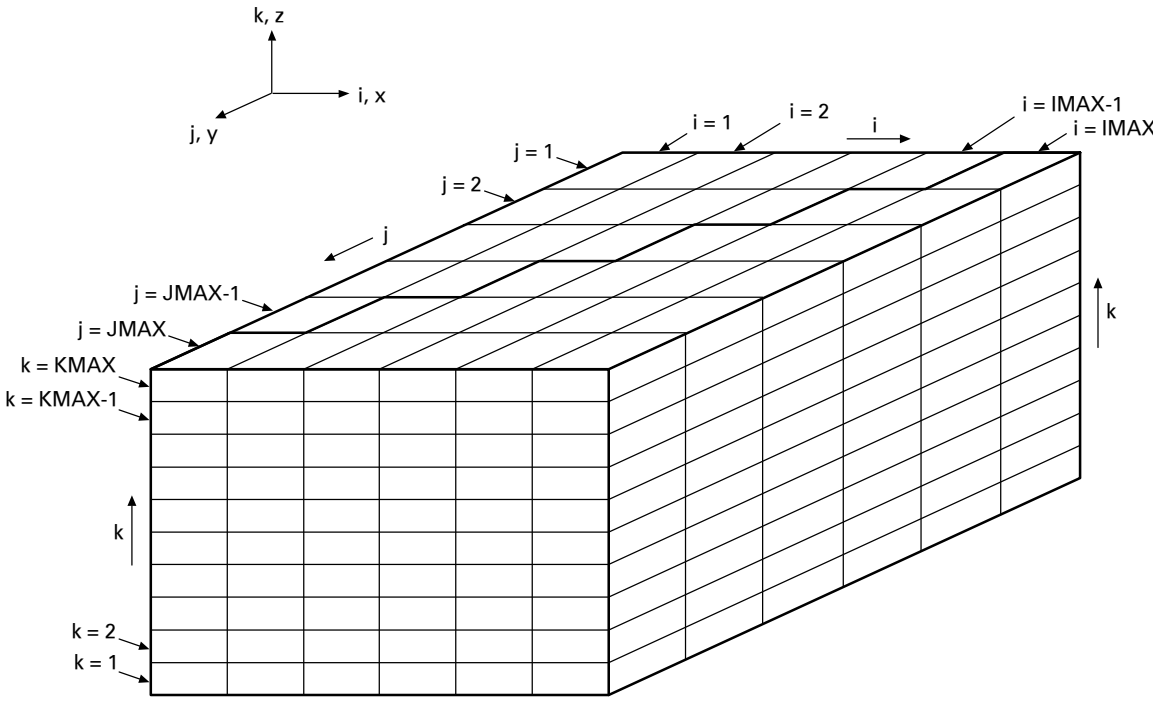

Figure 9-1. X-Y-Z View of the Core

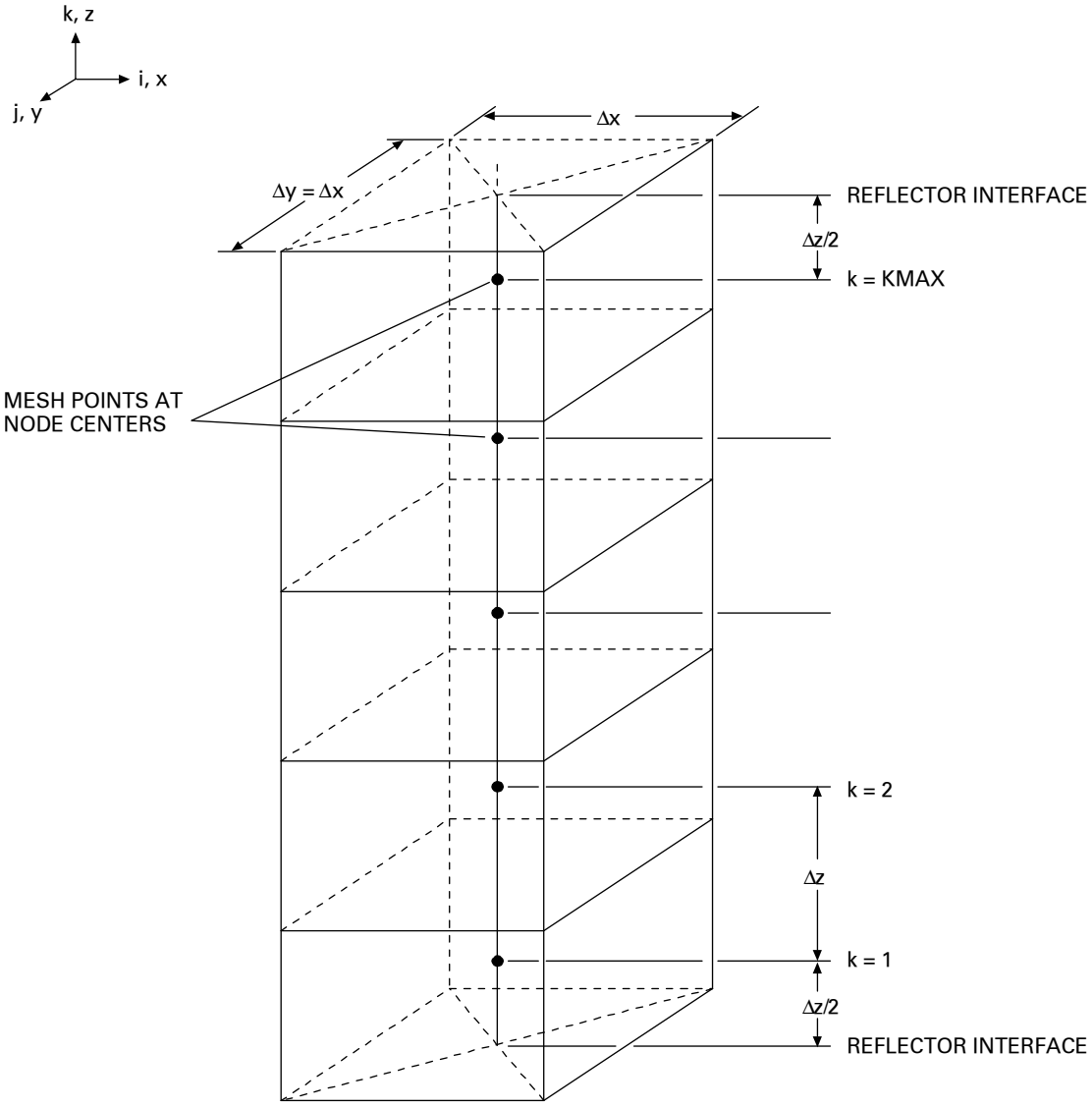

Figure 9-2. Node and Mesh Arrangement for a Given Bundle

9.1 Model Formulation and Assumptions

The mesh points are distributed within (the order of) one fast neutron mean free path, with each mesh point representing approximately a 6-inch cube. The mesh spacing is assumed to be constant. The cross sections and k_∞ s used within the physics model are derived from three-group cross sections obtained from a lattice physics code.

The core is described in X-Y-Z geometry with the restriction that there is equal mesh spacing in the X-Y directions. The x, y, z mesh is described by i, j, k nomenclature, respectively. In the horizontal planes, each fuel assembly or flow channel is described by one mesh line at the center of

the fuel assembly. Mesh line (1,1,k) is in the upper left corner of the horizontal planes as shown in Figure 9-1.

Vertically, the first point where k=1 is $\Delta z/2$ away from the bottom and the last point where k=KMAX is Δz/2 from the top as shown in Figure 9-2. The cross sections associated with the point (x,y,z) are defined to be the homogenized cross sections for the fuel, cladding, channel, interior water, exterior water, and (if applicable) control rods and/or burnable poison.

9.1.1 Theory and Formulation of the Equations

The 3-D neutron kinetics model used in TRACG04 is based on the implementation used in PANAC11. The derivation for the PANAC11 three-dimensional kinetics model begins with the assumption that the three-group transient diffusion equations with "N" delayed neutron precursors are valid:

$$\frac{1}{v_1}\frac{\partial \Phi_1}{\partial t} = \nabla \bullet D_1 \nabla \Phi_1 - \Sigma_1 \Phi_1 + \frac{(1-\beta)}{\mu_o}\sum_{g=1}^{3} \nu\Sigma_{fg} \Phi_g + \sum_{n=1}^{N} \lambda_n C_n \qquad (9.1\text{-}1)$$

$$\frac{1}{v_2}\frac{\partial \Phi_2}{\partial t} = \nabla \bullet D_2 \nabla \Phi_2 - \Sigma_2 \Phi_2 + \Sigma_{s\ell 1} \Phi_1 \qquad (9.1\text{-}2)$$

$$\frac{1}{v_3}\frac{\partial \Phi_3}{\partial t} = \nabla \bullet D_3 \nabla \Phi_3 - \Sigma_3 \Phi_3 + \Sigma_{s\ell 2} \Phi_2 \qquad (9.1\text{-}3)$$

$$\frac{\partial C_n}{\partial t} = -\lambda_n C_n + \frac{\beta_n}{\mu_o}\sum_{g=1}^{3} \nu\Sigma_{fg} \Phi_g \qquad \{n = 1,\ldots, N\} \qquad (9.1\text{-}4)$$

where

$g \equiv$ neutron energy group, g =1, 2, or 3;
$\Phi_g \equiv$ neutron flux for energy group g;
$D_g \equiv$ diffusion coefficient for energy group g;
$\Sigma_g \equiv$ removal cross section for energy group g;
$\Sigma_{s\ell g} \equiv$ slowing-down cross section for energy group g;
$\nu\Sigma_{fg} \equiv$ fission neutron production cross section for energy group g;
$\mu_o \equiv$ initial static effective multiplication factor;
$v_g \equiv$ average neutron speed in energy group g;
$C_n \equiv$ concentration of the n^{th} delayed neutron precursor
$\lambda_n \equiv$ decay constant of the n^{th} delayed neutron precursor
$\beta_n \equiv$ delayed neutron fraction of the n^{th} delayed neutron precursor

$\beta \equiv \sum_{n=1}^{N} \beta_n$ = total delayed neutron fraction

N ≡ total number of precursors (6)

In order to collapse these equations to a single energy group, the assumptions are made that the geometric bucklings of all groups are the same

$$\frac{\nabla \bullet D_3 \nabla \Phi_3}{D_3 \Phi_3} \cong \frac{\nabla \bullet D_2 \nabla \Phi_2}{D_2 \Phi_2} \cong \frac{\nabla \bullet D_1 \nabla \Phi_1}{D_1 \Phi_1} = -B^2 \qquad (9.1\text{-}5)$$

and that the logarithmic time derivatives of all groups are the same

$$\frac{1}{\Phi_3} \frac{\partial \Phi_3}{\partial t} \cong \frac{1}{\Phi_2} \frac{\partial \Phi_2}{\partial t} \cong \frac{1}{\Phi_1} \frac{\partial \Phi_1}{\partial t} \equiv \tau \qquad (9.1\text{-}6)$$

This latter assumption is equivalent to assuming that the neutron spectrum does not vary in time (unless the neutron cross sections change, in which case the spectrum is assumed to vary instantaneously).

For convenience, the following definitions are made:

$$K \equiv \sum_{g=1}^{3} \nu \Sigma_{fg} \Phi_g / \Sigma_1 \Phi_1 \qquad (9.1\text{-}7)$$

$$\dot{C}_n \equiv \frac{\partial C_n}{\partial t} \qquad (9.1\text{-}8)$$

$$M_g^2 = \frac{D_g}{\Sigma_g} \qquad (9.1\text{-}9)$$

Dividing Equations (9.1-1) through (9.1-4) by the group removal cross sections and making use of the assumptions and definitions

$$\frac{\tau}{\Sigma_1 v_1} = -M_1^2 B^2 - 1 + \frac{(1-\beta)}{\mu_o} K + \frac{\sum_{n=1}^{N} \lambda_n C_n}{\Sigma_1 \Phi_1} = -M_1^2 B^2 - 1 + \frac{K}{\mu_o} - \frac{\sum_{n=1}^{N} \dot{C}_n}{\Sigma_1 \Phi_1} \qquad (9.1\text{-}10)$$

$$\frac{\tau}{\Sigma_2 v_2} = M_2^2 B^2 - 1 + \frac{\Sigma_{s\ell 1}}{\Sigma_2} \frac{\Phi_1}{\Phi_2} \qquad (9.1\text{-}11)$$

$$\frac{\tau}{\Sigma_3 v_3} = M_3^2 B^2 - 1 + \frac{\Sigma_{s\ell 2}}{\Sigma_3} \frac{\Phi_2}{\Phi_3} \qquad (9.1\text{-}12)$$

$$\dot{C}_n = -\lambda_n C_n + \frac{\beta_n \Sigma_1 \Phi_1}{\mu_o} K \tag{9.1-13}$$

The flux ratios can now be eliminated from the group flux equations. Using the definition of "K" and eliminating the second and third group flux ratios from the fast group

$$1 + M_1^2 B^2 \frac{\tau}{\Sigma_1 v_1} = \frac{1}{\mu_o \Sigma_1} \left[\begin{array}{l} \nu\Sigma_{f1} + \nu\Sigma_{f2} \dfrac{\Sigma_{s\ell 1}/\Sigma_2}{1 + M_2^2 B^2 + \dfrac{\tau}{\Sigma_2 v_2}} \\ + \nu\Sigma_{f3} \dfrac{\Sigma_{s\ell 2}/\Sigma_3}{1 + M_3^2 B^2 + \dfrac{\tau}{\Sigma_3 v_3}} \cdot \dfrac{\Sigma_{s\ell 1}/\Sigma_2}{1 + M_2^2 B^2 + \dfrac{\tau}{\Sigma_2 v_2}} \end{array} \right] - \frac{\sum_{n=1}^{N} \dot{C}_n}{\Sigma_1 \Phi_1} \tag{9.1-14}$$

Multiplying through by the denominators of the terms in brackets [...] results in an equation which is impractical to solve since it involves powers and cross products of B^2, τ, and $\dot{C}_n$. The equation must therefore be linearized by assuming that the terms involving these powers and cross products are small and may be neglected:

$$\begin{aligned} & 1 + (M_1^2 + M_2^2 + M_3^2) B^2 + \left(\frac{1}{\Sigma_1 v_1} + \frac{1}{\Sigma_2 v_2} + \frac{1}{\Sigma_3 v_3} \right) \tau \\ & \simeq \frac{1}{\mu_o \Sigma_1} \left(\begin{array}{l} \nu\Sigma_{f1} + \nu\Sigma_{f2} \dfrac{\Sigma_{s\ell 1}}{\Sigma_2} + \nu\Sigma_{f3} \dfrac{\Sigma_{s\ell 2}}{\Sigma_3} \dfrac{\Sigma_{s\ell 1}}{\Sigma_2} \\ + \nu\Sigma_{f1} \left[(M_2^2 + M_3^2) B^2 + \left(\dfrac{1}{\Sigma_2 v_2} + \dfrac{1}{\Sigma_3 v_3} \right) \tau \right] \\ + \nu\Sigma_{f2} \dfrac{\Sigma_{s\ell 1}}{\Sigma_2} \left[M_3^2 B^2 + \dfrac{1}{\Sigma_3 v_3} \tau \right] \end{array} \right) - \frac{\sum_{n=1}^{N} \dot{C}_n}{\Sigma_1 \Phi_1} \end{aligned} \tag{9.1-15}$$

Introduce the following definitions:

$$M^2 \equiv M_1^2 + M_2^2 + M_3^2 \tag{9.1-16}$$

$$K_\infty \equiv \left[\nu\Sigma_{f1} + \nu\Sigma_{f2} \frac{\Sigma_{s\ell 1}}{\Sigma_2} + \nu\Sigma_{f3} \frac{\Sigma_{s\ell 2}}{\Sigma_3} \frac{\Sigma_{s\ell 1}}{\Sigma_2} \right] / \Sigma_1 \tag{9.1-17}$$

$$A_\infty \equiv \frac{\nu\Sigma_{f1}}{\Sigma_1} (M_2^2 + M_3^2) + \frac{\nu\Sigma_{f2}}{\Sigma_1} \frac{\Sigma_{s\ell 1}}{\Sigma_2} M_3^2 \tag{9.1-18}$$

$$\bar{v} \equiv \left[\frac{1}{v_1} + \frac{\Sigma_1}{\Sigma_2 v_2} + \frac{\Sigma_1}{\Sigma_3 v_3} \right]^{-1} \tag{9.1-19}$$

$$\bar{c} \equiv \left[\nu\Sigma_{f1} \left(\frac{1}{\Sigma_2 v_2} + \frac{1}{\Sigma_3 v_3} \right) + \nu\Sigma_{f2} \frac{\Sigma_{s\ell 1}}{\Sigma_2} \frac{1}{\Sigma_3 v_3} \right]^{-1} \tag{9.1-20}$$

$$v^* \equiv \left[\frac{1}{\bar{v}} - \frac{1}{\bar{c}\mu_o} \right]^{-1} \tag{9.1-21}$$

Apply these definitions in Equation (9.1-15) to rewrite the collapsed one group, transient diffusion equation as:

$$1 + (M^2 - A_\infty / \mu_o) B^2 + \frac{1}{\Sigma_1 v^*} \tau = \frac{K_\infty}{\mu_o} - \frac{\sum_{n=1}^{N} \dot{C}_n}{\Sigma_1 \Phi_1} \tag{9.1-22}$$

Equation (9.1-10) for the first energy group is used to eliminate the last term involving the precursors on the right hand side of Equation (9.1-22) to produce the following expression for K:

$$K = K_\infty + (A_\infty + \mu_o (M_1^2 - M^2)) B^2 + \frac{\mu_o}{\Sigma_1} \left(\frac{1}{v_1} - \frac{1}{v^*} \right) \tau \tag{9.1-23}$$

Using this expression allows the neutron precursor equations to be written as

$$\dot{C}_n = -\lambda_n C_n + \frac{\beta_n \Sigma_1 \Phi_1}{\mu_o} \left(K_\infty + (A_\infty + \mu_o (M_1^2 - M^2)) B^2 + \frac{\mu_o}{\Sigma_1} \left(\frac{1}{v_1} - \frac{1}{v^*} \right) \tau \right) \tag{9.1-24}$$

Equations (9.1-22) and (9.1-24) can be simplified further by assuming that the transient term involving τ is negligible. This assumption is justified provided that

$$\left| \frac{\mu_o}{\Sigma_1} \left(\frac{1}{v_1} - \frac{1}{v^*} \right) \tau \right| \ll K \approx 1 \tag{9.1-25}$$

This criterion is quantified by choosing an acceptable error in the value of K to be $\pm\varepsilon$ and then solving to obtain the following criteria for τ:

$$|\tau| \leq \frac{\varepsilon \Sigma_1 v^*}{\mu_o \left(1 - \frac{v^*}{v_1} \right)} \tag{9.1-26}$$

The fact that $v_1 > v^*$ has been applied to recast the quantity on the right side of the equation so that it is always positive for a positive value of ε. It is helpful to assume $\mu_o \approx 1$ and consider as an example a typical fuel bundle at an exposure of 5.0 GWd/T and 40% voids where the nuclear parameters of interest have the following representative values:

Σ_1 = 0.0298 cm^{-1}

v_1 = 5.8744 x 10^8 cm/sec

v_2 = 5.9854 x 10^6 cm/sec

v_3 = 1.6365 x 10^6 cm/sec

$\bar{v}$ = 2.4006 x 10^6 cm/sec

$\bar{c}$ = 1.2720 x 10^7 cm/sec

v^* = 2.96 x 10^6 cm/sec

As confirmed by this example, $v_1 >> v^*$ as will always be the case for a thermal reactor. Therefore, the criterion in Equation (9.1-26) can be simplified to

$$|\tau| \le \frac{\varepsilon \Sigma_1 v^*}{\mu_o \left(1 - \frac{v^*}{v_1}\right)} \approx \varepsilon \Sigma_1 v^* \approx 88 \sec^{-1} \qquad (9.1\text{-}27)$$

where the numerical value is obtained using $\varepsilon = 0.001$ and the representative values indicated above. The definition of τ in Equation (9.1-6) corresponds to the relative rate of change in the neutron fluxes. Thus it is clear that a value of τ larger than that which would result in an error in "K" greater than ε could only occur for a very short period. Such conditions if they occur at all in TRACG applications will be short-lived because of the strong nuclear feedback mechanisms inherent in a BWR. Thus it is a reasonable to neglect the term involving τ in the expression for "K' in Equation (9.1-23) and simplify the expression to

$$K = K_\infty + (A_\infty + \mu_o (M_1^2 - M^2)) B^2 \qquad (9.1\text{-}28)$$

Now substitute this simplified expression into Equation (9.1-13) to simplify Equation (9.1-24) to

$$\dot{C}_n = -\lambda_n C_n + \frac{\beta_n \Sigma_1 \Phi_1}{\mu_o} \left[K_\infty + (A_\infty + \mu_o (M_1^2 - M^2)) B^2 \right] \qquad (9.1\text{-}29)$$

This is the final form for the expression describing the neutron precursor concentrations. The final form for the flux equation is obtained by rearranging Equation (9.1-22) to produce

$$\frac{1}{\Sigma_1 v^*} \tau = -(M^2 - A_\infty / \mu_o) B^2 - 1 + \frac{K_\infty}{\mu_o} - \frac{\sum_{n=1}^{N} \dot{C}_n}{\Sigma_1 \Phi_1} \qquad (9.1\text{-}30)$$

In differential notation, Equations (9.1-30) and (9.1-29) are respectively

$$\frac{1}{v^*}\frac{\partial \Phi}{\partial t} = \Sigma_1 \left(M^2 - A_\infty / \mu_o\right)\frac{1}{D_1}\nabla \bullet D_1 \nabla \Phi + \Sigma_1 \left(\frac{K_\infty}{\mu_o} - 1\right)\Phi_1 - \sum_{n=1}^{N} \frac{\partial C_n}{\partial t} \qquad (9.1\text{-}31)$$

$$\frac{\partial C_n}{\partial t} = -\lambda_n C_n + \frac{\beta_n \Sigma_1 \Phi_1}{\mu_o}\left[K_\infty + \left(A_\infty + \mu_o \left(M_1^2 - M^2\right)\right)\cdot\left(-\frac{1}{D_1 \Phi}\nabla \bullet D_1 \nabla \Phi\right)\right] \qquad (9.1\text{-}32)$$

As in the steady state case, the macroscopic parameters in Equations (9.1-31) and (9.1-32) are evaluated by the lattice physics methods[3],[20].

9.1.2 Transient Flux and Power Calculation

The transient model is obtained by integrating Equations (9.1-31) and (9.1-32) in space and time. The spatial integration, which is performed first, assumes that the fast flux varies in a piecewise linear fashion from each surface of the node to the center as shown in Figure 9-1. Additionally, the flux is allowed to be discontinuous at the surface as follows.

In one dimension, a piecewise linear flux expansion is made:

$$\Phi(x) = \begin{cases} \phi_i + \dfrac{(x - x_i)}{\Delta x / 2}\left(\phi_{si}^{+} - \phi_i\right) & , x_i \le x \le x_i + \Delta x / 2 \\ \phi_i - \dfrac{(x - x_i)}{\Delta x / 2}\left(\phi_{si}^{-} - \phi_i\right) & , x_i - \Delta x / 2 \le x \le x_i \end{cases} \qquad (9.1\text{-}33)$$

where the surface fluxes are discontinuous:

$$f_i^{+}\phi_{si}^{+} = f_{i+1}^{-}\phi_{si+1}^{-} \qquad f_i^{-}\phi_{si}^{-} = f_{i-1}^{+}\phi_{si-1}^{+} \qquad (9.1\text{-}34),\ (9.1\text{-}35)$$

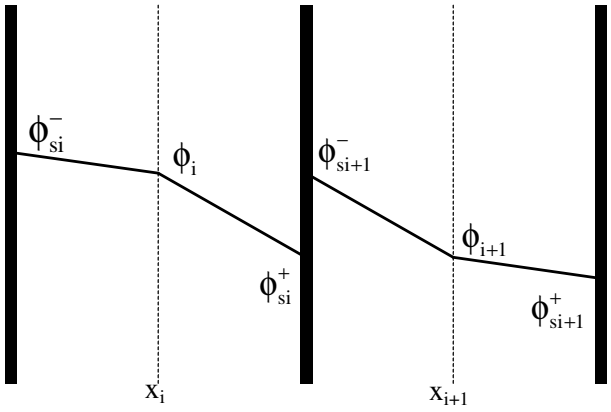

Figure 9-3. Piecewise-Linear Flux Variation

The surface fluxes are eliminated from these equations by requiring continuous current at the nodal interfaces:

$$J_{s_i} = -D_i \left.\frac{\partial\phi}{\partial x}\right|_{x=x_i+\Delta x/2} = -D_{i+1} \left.\frac{\partial\phi}{\partial x}\right|_{x=x_{i+1}-\Delta x/2} \tag{9.1-36}$$

The derivatives are approximated by finite differences.

$$-D_i \frac{(\phi_{si}^{+} - \phi_i)}{\Delta x/2} = -D_{i+1} \frac{(\phi_{i+1} - \phi_{si+1}^{-})}{\Delta x/2} \tag{9.1-37}$$

Solving for the surface fluxes:

$$\phi_{si}^{+} = \frac{D_i\phi_i + D_{i+1}\phi_{i+1}}{D_i + D_{i+1}\dfrac{f_i^{+}}{f_{i+1}^{-}}} \qquad \phi_{si}^{-} = \frac{D_i\phi_i + D_{i-1}\phi_{i-1}}{D_i + D_{i-1}\dfrac{f_i^{-}}{f_{i-1}^{+}}} \tag{9.1-38), (9.1-39}$$

The following definitions are useful.

ϕ_i ≡ flux at the center of node i;

ΔV_i ≡ volume of node i

$\bar{\phi}_i \equiv \dfrac{1}{\Delta V_i}\int \Delta V_i \, dV \, \phi_i$ = nodal average flux.

Integrating Equations (9.1-31) and (9.1-32) over ΔV_i and dividing by ΔV_i:

$$\frac{1}{v^*}\frac{\partial\bar{\phi}_i}{\partial t} = \Sigma_{1i}\left(M_i^2 - A_{\infty i}/\mu_0\right)\sum_j \frac{D_{ij}}{h_{ij}^2 D_i}\left(\phi_j\zeta_{j,i} - \phi_i\zeta_{i,j}\right) + \Sigma_{1i}\left(K_{\infty i}/\mu_0 - 1\right)\bar{\phi}_1 - \sum_{n=1}^{N}\frac{\partial\bar{C}_{ni}}{\partial t} \tag{9.1-40}$$

$$\frac{\partial\bar{C}_{ni}}{\partial t} = -\lambda_n\bar{C}_{ni} + \frac{\beta_{ni}}{\mu_0}\Sigma_{1i}\,\bar{\phi}_i\,\bar{K}_i \tag{9.1-41}$$

where the nodal coupling parameter D_{ij} is defined as:

$$D_{ij} \equiv \begin{cases} \dfrac{2D_iD_j}{D_if_j^{+} + D_jf_i^{-}} & i > j \\ \dfrac{2D_iD_j}{D_if_j^{-} + D_jf_i^{+}} & i < j \end{cases} \tag{9.1-42}$$

and $\zeta_{i,j}$ is defined as:

$$\zeta_{i,j} \equiv \begin{cases} f_i^+ & i < j \\ f_i^- & i > j \end{cases} \tag{9.1-43}$$

The nodal average flux, which is obtained by integrating the piecewise linear flux over the nodal volume and employing net current continuity conditions at the node surface, is

$$\bar{\phi}_i = \phi_i + \frac{1}{8}\sum_j \frac{D_{ij}}{D_i}\left(\phi_j \zeta_{j,i} - \phi_i \zeta_{i,j}\right). \tag{9.1-44}$$

The boundary conditions at the core/reflector interface are of the "mixed" type:

$$D\hat{n} \bullet \nabla\phi\left(\underline{r}_s\right) + \Gamma\phi\left(\underline{r}_s\right) = 0, \qquad \underline{r}_s \in \text{core boundary} \tag{9.1-45}$$

Applying a finite difference approximation for the gradient of the flux and solving for Γ:

$$\Gamma = -D_r \frac{\nabla\phi}{\phi} \cong \begin{cases} -D_r \dfrac{\left(\phi_r - \phi_{sr}\right)}{\phi_{sr}\left(\Delta x/2\right)} & \phi_r > \phi_{sr} \\ -D_r \dfrac{\left(\phi_{sr} - \phi_r\right)}{\phi_{sr}\left(\Delta x/2\right)} & \phi_r < \phi_{sr} \end{cases}. \tag{9.1-46}$$

Arbitrarily setting ϕ_r to zero and solving for the reflector diffusion coefficient:

$$D_j = \frac{\Gamma \Delta x}{2} \tag{9.1-47}$$

The value of Γ used in this model is synthesized from the reflector cross sections. A single set of reflector cross sections that vary linearly with the relative water density of the top fuel node may be provided via the wrapup file.

The integration in time assumes that the neutron precursor concentrations vary linearly from the beginning of the time step until the end. The flux on the other hand, is assumed to rise instantaneously to its final value at the beginning of the time step. This results in equations, which are fully implicit with respect to the flux, and guarantees the stability of the solution.

The following definitions are made:

$\Delta t^m \equiv t^m - t^{m-1}$ = time step m;

$\phi_i^m \equiv$ flux at the center of the node i after time step m;

$\bar{\phi}_i^m \equiv$ average flux at node i after time step m; and

$\bar{C}_{ni}^m \equiv$ average precursor concentration at node i after time step m.

Using these definitions and assumptions, Equations (9.1-40) and (9.1-41) are integrated over time step m and divided by Δt^m resulting in:

$$\frac{1}{v^* \Delta t^m}\left(\bar{\phi}_i^m - \bar{\phi}_i^{m-1}\right) = \Sigma_{1i}\left(M_i^2 - A_{\infty i}/\mu_0\right)\sum_j \frac{D_{ij}}{h_{ij}^2 D_i}\left(\phi_j^m \zeta_{j,i} - \phi_i^m \zeta_{i,j}\right) + \Sigma_{1i}\left(K_{\infty i}^m/\mu_0 - 1\right)\bar{\phi}_i^m - \sum_{n=1}^{N}\frac{1}{\Delta t^m}\left(\bar{C}_{ni}^m - \bar{C}_{ni}^{m-1}\right) \tag{9.1-48}$$

$$\frac{1}{\Delta t^m}\left(\bar{C}_{ni}^m - \bar{C}_{ni}^{m-1}\right) = -\frac{\lambda_n}{2}\left(\bar{C}_{ni}^m + \bar{C}_{ni}^{m-1}\right) + \frac{\beta_{ni}}{\mu_0}\Sigma_{1i}\,\bar{\phi}_i^m\,\bar{K}_i^m \tag{9.1-49}$$

where:

$$\bar{K}_i^m = K_{\infty i}^m + \left(A_{\infty i} + \mu_0\left(M_{1i}^2 - M_i^2\right)\right)\left(-\frac{1}{\bar{\phi}_i^m}\sum_j \frac{D_{ij}}{h_{ij}^2 D_i}\left(\phi_j^m \zeta_{j,i} - \phi_i^m \zeta_{i,j}\right)\right). \tag{9.1-50}$$

The precursor equation is solved for the precursor density after the time step:

$$\bar{C}_{ni}^m = \left[\left(\frac{1}{\Delta t^m} - \frac{\lambda_n}{2}\right)\bar{C}_{ni}^{m-1} + \frac{\beta_{ni}}{\mu_0}\Sigma_{1i}\,\bar{\phi}_i^m\,\bar{K}_i^m\right] \Big/ \left[\frac{1}{\Delta t^m} + \frac{\lambda_n}{2}\right]. \tag{9.1-51}$$

Substituting this expression into the flux Equation (9.1-48) and using the definitions of β^* and M_i^{*2}, the neutron flux model can be cast into the following form:

$$\sum_j \frac{D_{ij}}{h_{ij}^2 D_i}\left(\phi_j^m \zeta_{j,i} - \phi_i^m \zeta_{i,j}\right) + B_i^{*2}\,\bar{\phi}_i^m = \bar{S}_i^m; \tag{9.1-52}$$

$$B_i^{*2} \equiv \left[\frac{\left(1-\beta_i^*\right)}{\mu_0}K_{\infty i}^m - 1 - \frac{1}{\Sigma_{1i} v^* \Delta t^m}\right] / M_i^{*2} \tag{9.1-53}$$

$$\beta_i^* \equiv \sum_{n=1}^{N}\frac{\beta_{ni}}{1 + \Delta t^m \lambda_n/2} \tag{9.1-54}$$

$$M_i^{*2} \equiv \left(1-\beta_i^*\right)\left(M_i^2 - A_{\infty i}/\mu_0\right) + \beta_i^* M_{1i}^2 \tag{9.1-55}$$

and

$$\bar{S}_i^m \equiv -\left(\sum_{n=1}^{N}\frac{\lambda_n \bar{C}_{ni}^{m-1}}{1 + \Delta t^m \lambda_n/2} + \frac{1}{v^* \Delta t^m}\bar{\phi}_i^{m-1}\right) / \left(\Sigma_{1i} M_i^{*2}\right). \tag{9.1-56}$$

Equation (9.1-44) becomes:

$$\bar{\phi}_i^m = \phi_i^m + \frac{1}{8}\sum_j \frac{D_{ij}}{D_i}\left(\phi_j^m \zeta_{j,i} - \phi_i^m \zeta_{i,j}\right). \tag{9.1-57}$$

The equation for $\bar{K}_i^m$ can be simplified:

$$\bar{K}_i^m = K_{\infty i} + \left(A_{\infty i} + \mu_0\left(M_{li}^2 - M_i^2\right)\right)\left(B_i^{*2} - \bar{S}_i^m / \bar{\phi}_i^m\right). \tag{9.1-58}$$

The iteration procedures used to solve for the neutron flux given the source term for a given time step are the same as the procedures used for the "inner" iteration portion of the steady-state eigenvalue problem.

The un-normalized average nodal power is calculated as follows:

$$P_i = \frac{1}{\Delta V_i}\int_{\Delta V_i} d^3\underline{r}\, \varepsilon \sum_g \Sigma_{fg}\Phi_g(\underline{r}) = \varepsilon_i \sum_g \Sigma_{fgi}\,\bar{\phi}_{gi} \tag{9.1-59}$$

where ε_i is a conversion factor relating fissions to energy.

The epi-thermal flux is estimated from the infinite lattice flux ratio:

$$\frac{\bar{\Phi}_2}{\bar{\Phi}_1} = \frac{\Phi_2^\infty}{\Phi_1^\infty} = \frac{\Sigma_{sl1}}{\Sigma_2} \tag{9.1-60}$$

The thermal flux estimation starts with the thermal group equation:

$$-\nabla \bullet D_3 \nabla\phi_3(\underline{r}) + \Sigma_3\phi_3(\underline{r}) = \Sigma_{s\ell 2}\phi_2(\underline{r}) \tag{9.1-61}$$

Integrating over the volume of the node:

$$\frac{1}{V}\iiint \nabla J_3 dV + \frac{1}{V}\iiint \Sigma_3\phi_3 dV = \frac{1}{V}\iiint \Sigma_{s\ell 2}\phi_2 dV \tag{9.1-62}$$

Transforming to a surface integral using Gauss's Theorem:

$$\frac{1}{V}\iint_S J_3 \cdot \hat{n} dA + \Sigma_3\bar{\Phi}_3 = \Sigma_{s\ell 2}\bar{\Phi}_2 \tag{9.1-63}$$

The surface integral term is simply a sum of the surface currents times surface areas:

$$\frac{\bar{\Phi}_3}{\bar{\Phi}_1} = \frac{\Phi_3^\infty}{\Phi_2^\infty}\frac{\bar{\Phi}_2}{\bar{\Phi}_1} - \frac{\sum_n J_n S_n}{V\Sigma_3\bar{\Phi}_1} \tag{9.1-64}$$

where "S_n" is the surface area of node face "n".

The thermal flux estimate is simplified to:

$$\frac{\bar{\Phi}_3}{\bar{\Phi}_1} = \frac{\Phi_3^\infty}{\Phi_1^\infty} - \frac{\sum_n J_n S_n}{V\Sigma_3\bar{\Phi}_1} \tag{9.1-65}$$

The surface currents can be approximated from one-dimensional analytical solutions.

The thermal diffusion equations for this node and an adjacent node are:

$$\nabla \bullet D_3 \nabla \phi_3(\underline{r}) - \Sigma_3 \phi_3(\underline{r}) + \Sigma_{s\ell 2} \phi_2(\underline{r}) = 0 \qquad x < 0 \tag{9.1-66}$$

$$\nabla \bullet D_{3n} \nabla \phi_{3n}(\underline{r}) - \Sigma_{3n} \phi_{3n}(\underline{r}) + \Sigma_{s\ell 2n} \phi_{2n}(\underline{r}) = 0 \qquad x > 0 \tag{9.1-67}$$

where the subscript "n" denotes the adjacent node corresponding to face "n".

Assuming uniform slowing down sources the equations may be expressed as:

$$\begin{aligned} D_3 \frac{d^2\Phi_3}{dx^2} - \Sigma_3 \Phi_3(x) + S = 0 \qquad & x < 0 \\ D_{3n} \frac{d^2\Phi_{3n}}{dx^2} - \Sigma_{3n} \Phi_{3n}(x) + S_n = 0 \qquad & x > 0 \end{aligned} \tag{9.1-68}$$

where the source terms are defined as:

$$S = \Sigma_{sl2}\bar{\Phi}_2 \qquad S_n = \Sigma_{sl2n}\bar{\Phi}_{2n} \tag{9.1-69), (9.1-70}$$

The boundary conditions can be expressed as:

$$\Phi_3(-\infty) = \Phi_3^\infty = \frac{\Sigma_{sl2}\bar{\Phi}_2}{\Sigma_3} \qquad \Phi_{3n}(+\infty) = \Phi_{3n}^\infty = \frac{\Sigma_{sl2n}\bar{\Phi}_{2n}}{\Sigma_{3n}} \tag{9.1-71), (9.1-72}$$

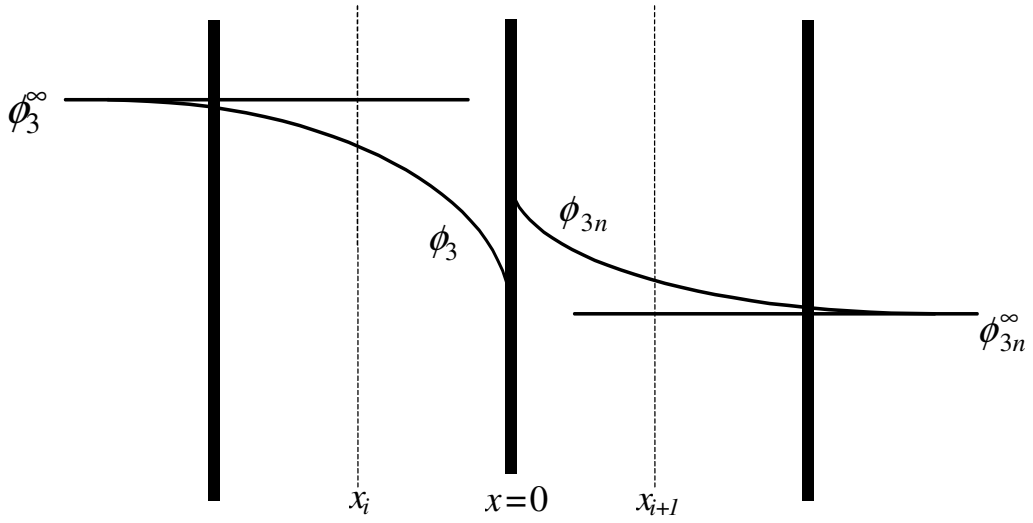

Figure 9-4. Thermal Flux Variation Within and Between Nodes

The interface conditions illustrated in Figure 9-4 can be expressed as:

$$-D_3 \left.\frac{d\Phi_3}{dx}\right|_{x=0} = -D_{3n} \left.\frac{d\Phi_{3n}}{dx}\right|_{x=0} \qquad \text{continuous current}$$
$$f_3^{\pm}\Phi_3(x=0) = f_{3n}^{\mp}\Phi_{3n}(x=0) \qquad \text{discontinuous flux} \tag{9.1-73}$$

Dropping the subscript "3", the general solutions are :

$$\Phi(x) = Ae^{-\kappa x} + Be^{+\kappa x} + \frac{S}{\Sigma} \qquad x < 0$$
$$\Phi_n(x) = A_n e^{-\kappa x} + B_n e^{+\kappa x} + \frac{S_n}{\Sigma_n} \qquad x > 0 \tag{9.1-74}$$

where "kappa" is defined as the inverse migration area:

$$\kappa^2 \equiv \frac{1}{M^2} = \frac{\Sigma}{D} \qquad \kappa_n^2 \equiv \frac{1}{M_n^2} = \frac{\Sigma_n}{D_n} \tag{9.1-75}$$

The interface currents are expressed as:

$$J_n = -D \left.\frac{d\Phi}{dx}\right|_{x=0} = D\kappa(A - B) \tag{9.1-76}$$

Applying the boundary and interface conditions the "B" coefficient is found and the thermal interface currents are:

$$J_n = -D\kappa B = \frac{\left(f^{\pm}\frac{S}{\Sigma} - f_n^{\mp}\frac{S_n}{\Sigma_n} \right)}{\left(\frac{f^{\pm}}{\kappa D} + \frac{f_n^{\mp}}{\kappa_n D_n} \right)} \qquad (9.1\text{-}77)$$

These interface currents are used to calculate the thermal flux estimate of Equation (9.1-65) which is needed in the nodal power calculation, Equation (9.1-59).

9.1.3 Overall Calculational Process

A step-by-step description of the calculational logic is as follows:

1. Obtain the initial static flux, void, fuel temperature (Doppler), exposure and xenon distribution from a converged PANACEA case. The converged case should be either a POWER (NITER=0) case or COLD (NITER=4) case.
2. Calculate steady-state nodal delayed neutron precursor concentrations.
3. Increment time by Δt and calculate TRACG thermal hydraulic response.
4. Update the void and fuel temperature distribution based on the TRACG thermal hydraulic calculation.
5. Move control rods consistent with new time.
6. Determine nuclear cross sections given the current control rod pattern and thermal hydraulic conditions. Determine source distribution given previous time step flux distributions and delayed neutron precursor concentrations.
7. Solve time step dependent neutron diffusion equation at this time step using the same procedures used for the "inner" iteration portion of the steady-state eigenvalue problem.
8. Solve delayed neutron precursor equations at this time step.
9. Determine the nodal powers at time step.
10. Calculate decay heat calculation to determine power for thermal hydraulic calculation.
11. Return to 3 to continue transient.

9.2 Nuclear Parameters

The nuclear parameters required for the 3-D kinetics model are obtained from detailed X–Y physics calculations performed for lattice cells (fuel types) normally consisting of one fuel bundle and its surrounding water. These multi-group calculations produce three-group cross sections homogenized over the lattice cell. The data are represented by polynomial fits for each fuel type. The nuclear parameters include the diffusion coefficient, absorption cross section, slowing-down cross section, fission cross section, υfission cross section and flux discontinuity factors for the fast, epi-thermal and thermal energy groups and the delayed neutron fraction.

In the solution of the coarse mesh nodal approximation of the one-group diffusion theory model, void, exposure, and fuel type conditions of a node in three-dimensional space are used in the

fits to determine nuclear properties for that node. In this way, void feedback, burn-up effects and heterogeneous fuel loading are taken into account.

Void dependence is represented by the ratio of cell average water density relative to the reference water density used in the lattice cell calculation. This ratio is given by:

$$U = \frac{\rho}{\rho_o} \qquad (9.2\text{-}1)$$

Every node in three-dimensional space has a value of U at a given operating point during burn-up of the core, where U is an instantaneous relative moderator density. By averaging U with respect to exposure of the node E, history-dependent relative moderator density is defined as:

$$UH = \frac{\int U dE}{\int dE} \qquad (9.2\text{-}2)$$

Local U, UH, and E conditions determine nuclear properties of a node according to correlations of the lattice cell physics calculations. For each fuel type, the nuclear parameters are dependent upon U, UH, and E.

The detailed lattice cell calculations are performed with the control rod in or out. Therefore, nuclear parameters are obtained for each fuel type at several void and exposure conditions, for both controlled and uncontrolled conditions. In the three-dimensional diffusion theory solution, the control rod configuration is accounted for by using controlled or uncontrolled data for each node. If a control rod is only partially inserted into a node, linear averaged nuclear data are used. For each fuel type, the nuclear parameters are control dependent.

The nodal K-infinity (K_∞) is calculated with thermal removal corrections to account for the impact of xenon, Doppler and boron effects. Xenon and boron corrections are made directly to the removal cross section. [[

]]

Xenon is a fission product that acts as a strong absorber of thermal neutrons. It is produced directly from fission and indirectly by decay of iodine. The xenon poisoning effect is accounted for by adjusting the thermal removal cross section at each node of the form:

$$\Sigma_3^{Xe} = \Sigma_3^{noXe} + N_{Xe}\sigma_{Xe} \qquad (9.2\text{-}8)$$

where N_{Xe} is the xenon number density and σ_{Xe} is the microscopic absorption cross section which are part of the PANACEA database.

Fuel temperature (TF) affects resonance absorption in uranium and plutonium (the Doppler effect). This is accounted for by making a Doppler reactivity correction of k_∞ at each node of the form:

$$\rho^{Dop} = C_T \left[\sqrt{TF} - \sqrt{TF_o} \right] \qquad (9.2\text{-}9)$$

where TF_o represents base fuel temperature and the Doppler coefficient C_T is dependent upon exposure and U for each fuel type. It is determined by lattice cell physics calculations performed parametrically as a function of fuel temperature.

[[

]] (9.2-10)

The effect of introducing liquid boron is accounted for by adjusting the absorption cross section for the thermal group as described in Section 9.5. The adjustment of the thermal removal cross section at each node of the form:

$$\Sigma_3^{Corrected} = \Sigma_3^{Dop} + N_{B10}\sigma_{B10} \quad (9.2\text{-}11)$$

Once all the reactivity corrections are incorporated in this fashion, the nodal K_∞ is recalculated using Equation (9.2-3) with the corrected thermal group cross section, $\Sigma_3^{Corrected}$.

9.3 Decay Heat Model

The decay heat model for TRACG02 that is described in NEDE-32176P, Revision 1 and 2 has been enhanced to add the 1979[21] and 1994[22] ANS decay heat models.

9.3.1 Decay Heat Integration

The decay heat model calculates the delayed component of the volumetric heat generation rate in the fuel. A time integral relation links the fission rate to the decay heat. Nodal power history is accounted for in TRACG by using the power calculated from the 3-D neutron kinetics model. TRACG04 allows for a variable number (N_d) of exponential decay heat groups to fit the decay power curve. The decay heat model described in this section is used with the 3-D neutron kinetics model for transient simulation and optionally may be used for other applications where the 3-D neutron kinetics model is not activated. For example, these models can be applied for LOCA applications, or optionally, the power due to decay heat can be input in tabular form as a function of time.

The total volumetric heat generation rate in the fuel at axial location "z" and time "t" can be expressed as:

$$q(z,t) = q_p(z,t) + q_d(z,t) \quad (9.3\text{-}1)$$

where q_p is the prompt power

$$q_p(z,t) = (1-f)P(z,t) \quad (9.3\text{-}2)$$

and "f" is the sum of the decay heat group fractions, f_k.

The decay power, q_d, consists of several components with different time constants (by dividing the continuous spectrum of fission product decay into N_d groups):

$$q_d\ (z,t) = \sum_{k=1}^{N_d} q_{d,k} \quad (9.3\text{-}3)$$

The individual decay power terms can be related to the total fission power by:

$$q_{d,k}\ (z,t) = \int_{-\infty}^{t} f_k\ P\ (z,t')\ K_k\ (t' \rightarrow t)\ dt' \quad (9.3\text{-}4)$$

Here, K_k (t' $\rightarrow$ t) is the fraction of the decay power released at t due to fission occurring at time t'. An exponential form has been chosen in TRACG:

$$K_k\left(t' \rightarrow t\right) = \lambda_k e^{-\lambda_k (t-t')} \quad (9.3\text{-}5)$$

Substituting Equation (9.3-5) into Equation (9.3-4) yields:

$$q_{d,k}(z,t) = \int_{-\infty}^{t} f_k \lambda_k P(z,t') e^{-\lambda_k (t-t')} dt' \tag{9.3-6}$$

$$= f_k \lambda_k e^{-\lambda_k t} \int_{-\infty}^{t} P(z,t') e^{\lambda_k t'} dt'$$

The integration is carried out numerically. For the time step t^{n+1}, after separating the time interval into two parts $(-\infty, t^n)$ and (t^n, t^{n+1}), Equation (9.3-6) becomes:

$$q_{d,k}(z,t^{n+1}) = f_k \lambda_k e^{-\lambda_k t^{n+1}} \tag{9.3-7}$$

$$\left[\int_{-\infty}^{t^n} P(z,t') e^{\lambda_k t'} dt' + \int_{t^n}^{t^{n+1}} P(z,t') e^{\lambda_k t'} dt' \right]$$

$$= f_k \lambda_k e^{-\lambda_k t^{n+1}} \left[\sum_{j=-\infty}^{n} I_{k,j} + I_{k,n+1} \right]$$

$$= q_{d,k}(z,t^n) e^{-\lambda_k \Delta t} + f_k \lambda_k e^{-\lambda_k t^{n+1}} I_{k,n+1}$$

where

$$I_{k,j} = \int_{t^{j-1}}^{t^j} P(z,t') e^{\lambda_k t'} dt' \quad \text{and} \quad \Delta t = t^{n+1} - t^n \tag{9.3-8}$$

In TRACG, the fission power is assumed to be a linear function of time between t^{j-1} and t^j in the evaluation of $I_{k,j}$, i.e.,

$$P(z,t') = P(z,t^j) \frac{t' - t^{j-1}}{t^j - t^{j-1}} + P(z,t^{j-1}) \frac{t^j - t'}{t^j - t^{j-1}} \tag{9.3-9}$$

$$= P(z,t^j) + \Delta P \frac{t' - t^j}{t^j - t^{j-1}}$$

where

$$\Delta P = P(z,t^j) - P(z,t^{j-1}) \tag{9.3-10}$$

Substitution of Equation (9.3-9) into Equation (9.3-8) yields:

$$I_{k,n+1} = \frac{e^{\lambda_k t^{n+1}}}{\lambda_k} \left[\left(P(z,t^n) - \frac{\Delta P}{\lambda_k \Delta t} \right) (1 - e^{-\lambda_k \Delta t}) + \Delta P \right] \tag{9.3-11}$$

Substitution of Equation (9.3-11) into Equation (9.3-7) yields:

$$q_{d,k}(z,t^{n+1}) = q_{d,k}(z,t^{n})e^{-\lambda_k \Delta t} + f_k \left(P^n - \frac{\Delta P}{\lambda_k \Delta t}\right)(1-e^{-\lambda_k \Delta t}) + f_k \Delta P \qquad (9.3\text{-}12)$$

Note that at each time step, in order to calculate q_d, the value of the current step $I_{k,n+1}$ has to be evaluated; whereas, $I_{k,n}$ has already been obtained from the previous step calculation. Therefore, there is no need to store the nodal power history.

9.3.2 Decay Heat Model Inputs

The values for up to 93 decay heat fractions and time constants, f_k and λ_k, in Equations (9.3-6) and (9.3-7) can be provided as user input. For consistency with earlier versions of TRACG, the values for 5 decay heat groups determined from the May-Witt decay power curves are available as default values. The default values are as follows:

λ_1 =	5.4477E-5	(1/s)	f_1	=	0.020518
λ_2 =	2.27E-3	(1/s)	f_2	=	0.020948
λ_3 =	3.1658E-2	(1/s)	f_3	=	0.016756
λ_4 =	1.1928E-1	(1/s)	f_4	=	0.0068814
λ_5 =	1.697	(1/s)	f_5	=	0.011494

In the time period from 0 to 1000 seconds after shutdown, the May-Witt decay heat model produces values that are about 15% higher than the experimental mean or from 6% to 12% above even the 2-sigma upper bound suggested by the data (see pages 2-1 and 4-31 of Reference [205]).

In addition to specifying the decay heat group constants through input, the User may select from one of the available ANS standards models built into TRACG. The user may select either the 1979[21] or 1994[22] ANS standard to generate decay heat input for the TRACG transient model. The details of the ANS models are provided below.

9.3.3 ANS Decay Heat Models

The ANS standards model the total decay heat as the sum of the contributions from fission products ($f_i F_i$), major Actinides (F_{239U} and F_{239Np}), miscellaneous Actinides (A), structural activation products (AP) and fission power (DN):

$$H(t,T) = \left(G(t) \cdot \sum_{i=1}^{4} f_i \cdot F_i(t,T) + F_{^{239}U}(t,T) + F_{^{239}Np}(t,T) \right) \Big/ Q + A(t,T) + AP(t,T) + f_{DN} \cdot DN(t) \qquad (9.3\text{-}13)$$

where "t" is the cooling time, "T" is the irradiation time, "f_i" are the fission fractions and "Q" the energy release per fission. In Equation (9.3-13), "f_{DN}" is a normalization constant that forces H(0,T) $\rightarrow$ 1.0. Exposure of the fission products to a neutron flux in a nuclear reactor increases the decay heat due to the neutron capture effect (NCE). The ANS standard models the NCE by a "G-factor" that is indicated in Equation (9.3-13) by "G(t)". The G-factor is the ratio of the decay heat from

fission products exposed to a finite neutron flux to the decay heat from fission products in a zero flux environment.

The fission fractions for ^{238}U and ^{239}Pu as function of exposure, EX (GWd/ST), are calculated using the fits provided in Equations (3-39) through (3-42) of Reference [203].

^{235}U: $f_1 = 1-f_2-f_3-f_4$ (9.3-14)

^{238}U: $f_2 = 7.52541E-02+EX*(2.57466E-04+EX*9.51169E-06)$ (9.3-15)

^{239}Pu: $f_3 = EX*(1+EX*(4.38985E-02+EX*(-3.34992E-04)))/(14.168+EX*2.51999)$ (9.3-16)

^{241}Pu: $f_4 = 0$ (9.3-17)

The fission fraction values given above are representative values for BWR fuel. The standard deviations in the values of f_2 and f_3 for different fuel types are less than ±0.04. The RMS fitting errors that are quoted in Reference [203] are negligible by comparison. The variations in the fission fractions for different fuel types will translate into an estimated RMS error in the value of the decay heat of less than ±0.3% which is more than an order of magnitude smaller than the measurment errors of the data on which the ANS standard is based.

It is reasonable for the TRACG default model to assume a value of f_4=0 because contributions from ^{241}Pu only become important for exposures above about 45 GWd/MT whereas the TRACG applications of interest occur below about 30 GWd/MT. This is also a conservative assumption since the energy per fission for ^{241}Pu is higher than for ^{239}Pu so that fission energy is underestimated and the decay heat fraction is overestimated when ^{241}Pu is lumped with ^{239}Pu.

The energy release per fission are weighted according to the fission fractions using the recommended MeV/fission values from Table 2-11 of Reference [203].

$$Q = f_1*201.8 + f_2*205.4 + f_3*210.3 + f_4*212.8 \quad (9.3\text{-}18)$$

The calculation of decay heat during the cooling time, t, is described in Section 9.3.1. The ANS standard is used to determine the initial conditions for the calculation. The appropriate decay heat fractions and time constants at t=0 will be used in the TRACG transient decay heat model.

The components of decay heat as they are modeled according to the ANS standard are described in the following sections.

9.3.3.1 Irradiation Period

In the simplest case, a decay heat evaluation is required for a single irradiation period during which the power level, “P”, remains constant over the irradiation period, “T” (seconds):

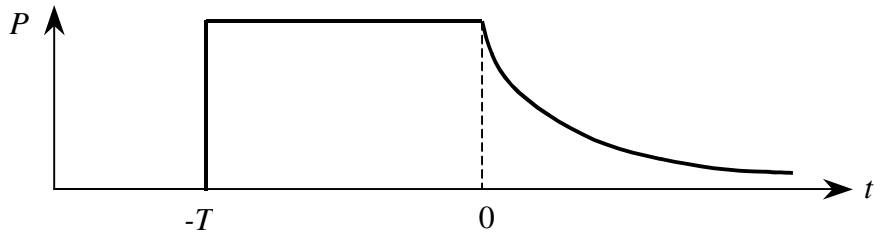

where t (seconds) is the time after shutdown or cooling time. An example of this type of case is the decay heat for a full core at the end of an equilibrium cycle.

Complicated power histories may be evaluated using the histogram method. In this method, the power as a function of irradiation time is subdivided into a number of steps or histograms. There is no particular limit on the number of histograms, but in general, one per cycle should be sufficient. As an example, the following figure illustrates a three histogram case in which each histogram represents one cycle of operation:

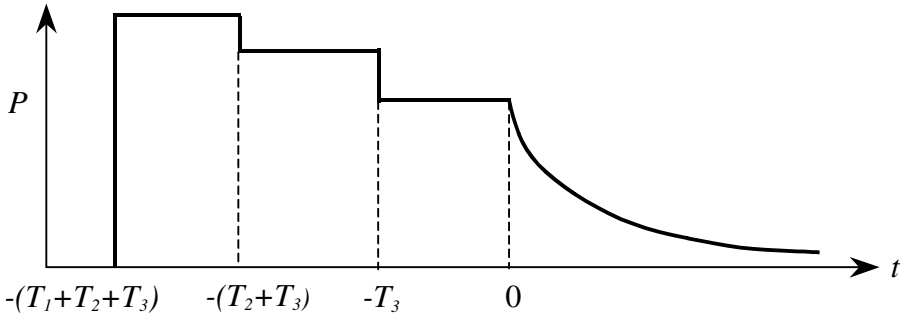

The total decay heat at shut down is determined by superposition of the decay heat produced by each histogram separately:

$$H(t) = \sum_{n=1}^{N} P_n \cdot H(t + \sum_{l=n+1}^{N} T_l, T_n) \qquad (9.3\text{-}19)$$

where "N" is the total number of irradiation periods and "P_n" is the reactor power during period "n".

The irradiation period specification is provided as user input to TRACG. If it is not specified, the irradiation power level is the steady state power and the core exposure is converted to irradiation time assuming 10GWd/MT per year.

9.3.3.2 Fission Product Decay Heat

There are four fissionable isotopes considered by the 1994 ANS standard: ^{235}U, ^{239}Pu, ^{238}U and ^{241}Pu. Fissions in other isotopes are included with ^{235}U. This is conservative since fissions in ^{235}U produce the most heat. Data for the 1979 standard do not include ^{241}Pu. Therefore, fissions in ^{241}Pu are included with ^{235}U in that standard.

The fission product decay heat for isotope i is:

$$F_i(t,T) = \sum_{j=1}^{23} \frac{\alpha_{ij}}{\lambda_{ij}} e^{-\lambda_{ij} t} \left(1 - e^{-\lambda_{ij} T}\right) \text{ MeV/fission} \quad (9.3\text{-}20)$$

where the decay constants λ_{ij} and the amplitudes α_{ij} are specified by the ANS Standard. The values at t=0 will be used in the TRACG model. There will be 92 (4*23) decay heat groups for the ANS 1994 standard and 69 (3*23) groups for the ANS 1979 standard.

9.3.3.3 Major Actinide Decay Heat

The major Actinides, ^{239}U and ^{239}Np, are evaluated from the following analytical expressions:

$$F_{^{239}U}(t,T) = E_{^{239}U} R \left(1 - e^{-\lambda_{^{239}U} T}\right) e^{-\lambda_{^{239}U} t} \quad (9.3\text{-}21)$$

$$F_{^{239}Np}(t,T) = E_{^{239}Np} R \left[\frac{\lambda_{^{239}U}}{\lambda_{^{239}U} - \lambda_{^{239}Np}} \left(1 - e^{-\lambda_{^{239}Np} T}\right) e^{-\lambda_{^{239}Np} t} - \frac{\lambda_{^{239}Np}}{\lambda_{^{239}U} - \lambda_{^{239}Np}} \left(1 - e^{-\lambda_{^{239}U} T}\right) e^{-\lambda_{^{239}U} t} \right] \quad (9.3\text{-}22)$$

where the decay constants, $\lambda_{^{239}U}$ and $\lambda_{^{239}Np}$, and the recoverable energies, $E_{^{239}U}$ and $E_{^{239}Np}$, are provided by the Standard. The ratio of captures in ^{238}U to total fissions is denoted as "R". [[

]] (9.3-23)

The decay heat from the major actinides is assumed to remain constant throughout the TRACG transient evaluation. This is achieved by summing Equations (9.3-21) and (9.3-22) to define an additional decay heat group and then approximating the yield for this group by setting t=0 so that $e^{-\lambda_{^{239}U} t} = 1.0$ and $e^{-\lambda_{^{239}Np} t} = 1.0$.

9.3.3.4 Neutron Capture Effect (NCE)

The fission product tables and exponential fits in the ANS standards are based on "pulse" data and calculations. These assume that the fission products are not exposed to a significant neutron flux. In a reactor, of course, this is not the case and the fission products are exposed to a finite flux. This leads to neutron captures that have the effect of raising the decay heat. Shure[204] indicates that neutron capture has very minor effects on the decay energy predictions for shutdown times of 10^7 seconds (~116 days) or less. Even for a four-order-of-magnitude increase in thermal neutron flux above the normal values seen in BWRs, the increase in the fission product decay energy is only about 1% to 2% according to the evaluation in Section 4.4.2 of Reference [205]. Nevertheless, the following formula from the ANS standards has been implemented:

$$G(t) = 1 + \left(3.24 \cdot 10^{-6} + 5.23 \cdot 10^{-10} t\right) T^{0.4} \psi \quad \text{for } t<10^4 \text{ seconds, } T<4 \text{ years, } \psi<3.0 \quad (9.3\text{-}24)$$

In this formula the ψ is the number of fissions per initial fissile atom. A generic expression for ψ that is representative for BWR fuels is: [[

]] When the ranges of application for Equation (9.3-24) cannot be met, the ANS standards provide tabulated values for G(t). Table 10 of the 1979 standard and Table 13 from the 1994 standard have been implemented in TRACG and are used when the ranges of application for Equation (9.3-24) are not met. Such instances are rare since the ranges of most interest for TRACG applications are well within the ranges established for Equation (9.3-24).

9.3.3.5 Fission Power from Delayed Neutrons

Fission power from delayed neutrons is an important source of heat for the first minute or so after shutdown. Obviously, this term is very sensitive to the manner in which the reactor is shutdown. The fission power is provided by the TRACG kinetics model or can be specified in tabular form if the kinetics model is not used.

9.3.3.6 Miscellaneous Actinides

The major Actinides ^{239}U and ^{239}Np are explicitly accounted for in both the 1979 and 1994 ANS standards. There are many other Actinides, referred to here as "miscellaneous Actinides" that are not significant individually, but when summed together make a significant contribution to decay heat. According to the ANS standards, these Actinides must be evaluated by the User and included in the shutdown power as appropriate.

The total contribution of the miscellaneous Actinides is only one tenth the contribution of the major Actinides at the time of shutdown. The most prominent of the miscellaneous Actinides are ^{242}Cm, ^{238}Np, ^{237}U, ^{238}Pu, ^{241}Am and ^{244}Cm. A model based solely on these isotopes would be sufficient, but in the charts and tables which follow, the sum total of all the miscellaneous Actinides will be presented.

Figure 9-5 shows the buildup of decay heat from miscellaneous Actinides as a function of irradiation time and enrichment. Data are provided for three enrichments: low (3.10%), medium (3.91%) and high (4.65%). The low enriched data are moderately conservative for all irradiation and cooling times.

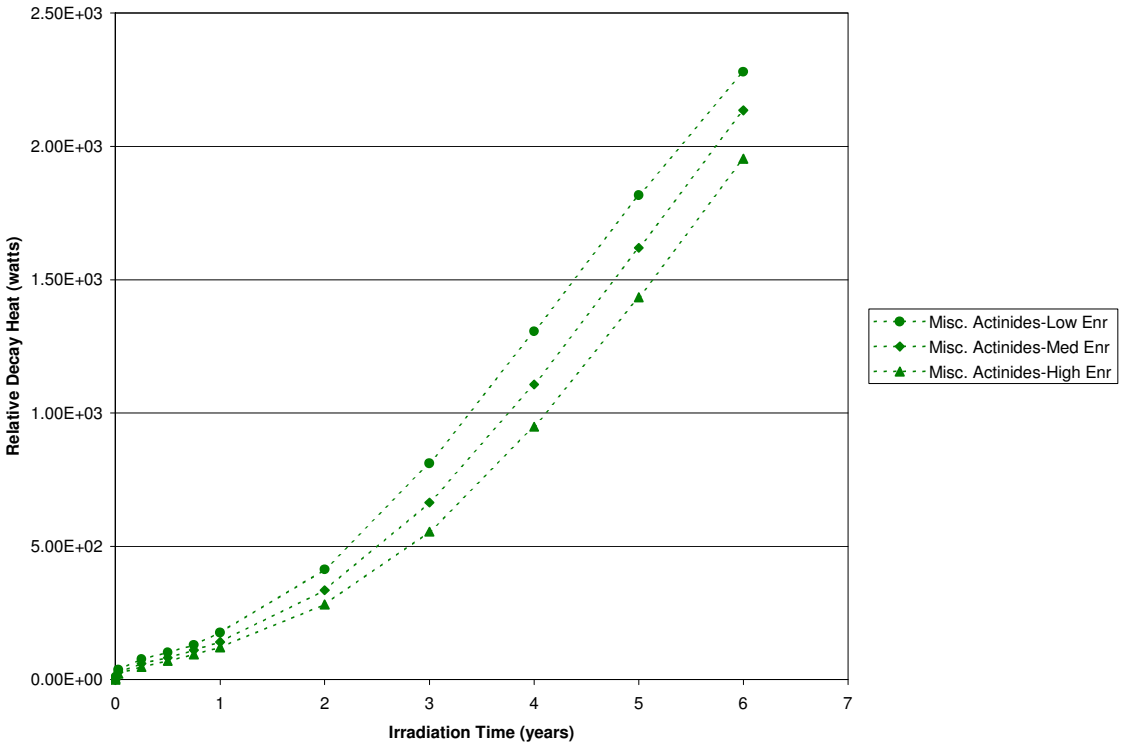

Figure 9-5. Buildup of Decay Heat from Miscellaneous Actinides (for low, medium and high enrichments)

As a result of the monotonic and nearly linear buildup data, linear interpolation is used to initialize the values at a cooling time of t=0 and an irradiation time $T_j < T \le T_{j+1}$ using:

$$A(0,T) = \left[\left(\frac{T_{j+1} - T}{T_{j+1} - T_j} \right) P_j \frac{\phi_{TG}}{\phi_j} + \left(\frac{T - T_j}{T_{j+1} - T_j} \right) P_{j+1} \frac{\phi_{TG}}{\phi_{j+1}} \right] \quad (9.3\text{-}26)$$

where the values for P_j are given in Table 9-1. [[

]] (9.3-27)

The decay heat from Miscellaneous Actinide contribution is assumed to remain constant throughout the TRACG transient evaluation. This is achieved by adding the A(0,T) contribution to the major actinides decay heat group.

Table 9-1. Relative Power Fraction (P_j) of Miscellaneous Actinides

Irradiation Time, T	**2 years**	**4 years**	**6 years**	**8 years**
Flux (ϕ_j)	2.65×10^{14}	3.24×10^{14}	3.80×10^{14}	4.18×10^{14}
Cooling Time, t (seconds)	**Relative Power Fraction Values**			
0.0E+00	9.505E-05	3.006E-04	5.247E-04	6.794E-04

9.3.3.7 Structural Activation Products

Structural activation products are produced by neutron capture in fuel structural materials including: cladding, water rods, channels, spacers, end plugs, plenum springs, tie plates, etc. Also included in this category are fuel additives, especially Gadolinium, which is a significant contributor.

Additional activation products are produced in control rods and in vessel structures. However, these contributions to shutdown power are very small and can be neglected.

Figure 9-6 shows the buildup of decay heat from structural activation products as a function of irradiation time and enrichment. Data are provided for three enrichments: low (3.10%), medium (3.91%) and high (4.65%). Since the low enriched data are moderately conservative for all irradiation and cooling times, they are recommended and used.

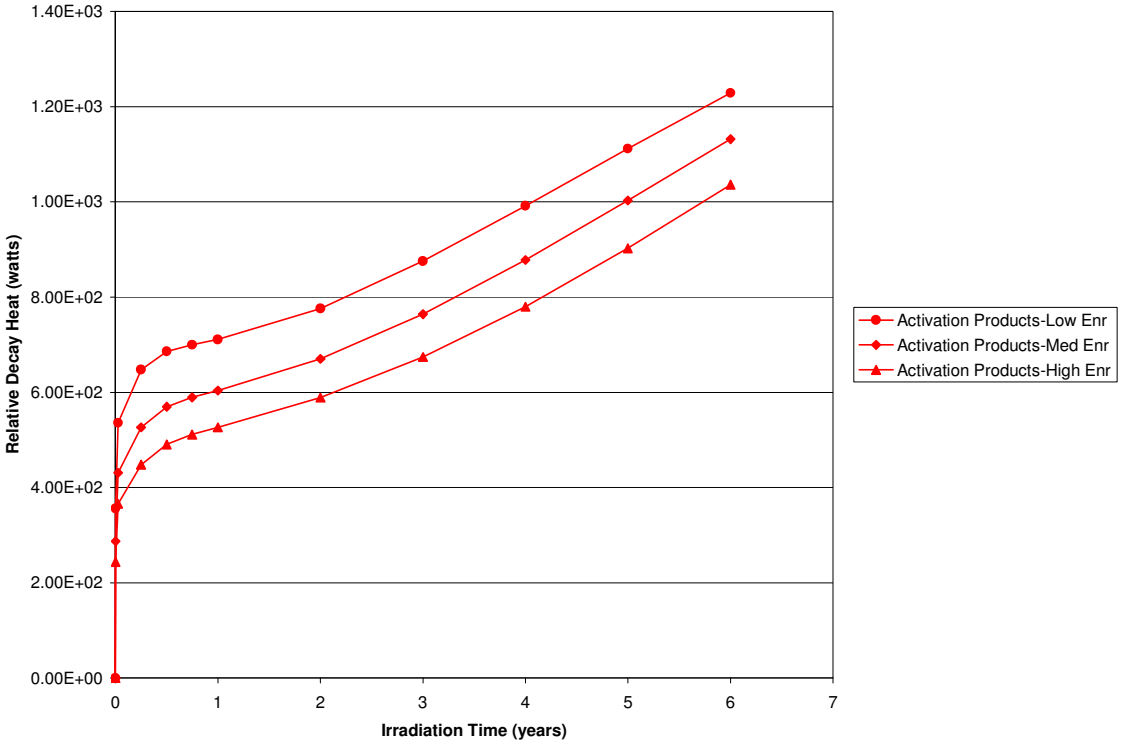

Figure 9-6. Buildup of Decay Heat from Structural Activation Products (for low, medium and high enrichments)

The structural activation products buildup very rapidly during the first year of irradiation and afterwards behave in a monotonic and nearly linear way. As in the case of the miscellaneous Actinides, a linear interpolation is used for irradiation time. However, in contrast to the miscellaneous Actinides, which utilize an implied point of zero at zero irradiation time, the structural activation products assume that the heat rises instantly to the value at the first tabulated point (one year in this case). This scheme is conservative for all irradiation times.

The data are shown in tabular form in Table 9-2. The structural activation products contribution at shutdown (t=0) is determined by linear interpolation as:

$$AP(0,T) = \left[\left(\frac{T_{j+1} - T}{T_{j+1} - T_j} \right) P_j \frac{\phi_{TG}}{\phi_j} + \left(\frac{T - T_j}{T_{j+1} - T_j} \right) P_{j+1} \frac{\phi_{TG}}{\phi_{j+1}} \right] \qquad (9.3\text{-}28)$$

for $T_j < T \le T_{j+1}$. [[

]]

The decay heat from Activation Product contribution is assumed to remain constant throughout the TRACG transient evaluation. This is achieved by adding the AP(0,T) contribution to the major actinides decay heat group.

Table 9-2. Relative Power Fraction (P_j) of Activation Products

Irradiation Time	2 years	4 years	6 years	8 years
Flux (ϕ_j)	2.65×10^{14}	3.24×10^{14}	3.80×10^{14}	4.18×10^{14}
Cooling Time (seconds)	Relative Power Fraction Values			
0.0E+00	1.786E-04	2.283E-04	2.829E-04	3.305E-04

9.3.3.8 Uncertainty Analysis

The evaluation of the uncertainty is an important aspect of decay heat calculations using the ANS standards. Both the 1979 and 1994 ANS standards specify that uncertainties be determined for energy per fission, fission product decay power and reactor power. Neither standard requires consideration of uncertainties for any of the other terms and factors, including the G-factor and the Actinide contributions.

The uncertainty in the energy per fission is based on fundamental nuclear data:

$$\Delta Qi/Qi \approx 0.0025 \tag{9.3-29}$$

The fission product decay heat uncertainty (for fissions in isotope i) as specified by the ANS standards is:

$$\left(\frac{\Delta P'_{di}}{P'_{di}}\right)^2 = \left(\frac{\Delta Q_i}{Q_i}\right)^2 + \left(\frac{P_i\left(\Delta F_i(t,\infty) - \Delta F_i(t+T,\infty)\right)}{Q_i P'_{di}}\right)^2 \tag{9.3-30}$$

where the uncertainties for each isotope, $\Delta Fi(t,\infty)$, are taken from Tables 4 through 6 of ANSI/ANS-5.1-1979 (or Tables 5 through 8 of the 1994 standard).

9.4 Thermal–Hydraulic Interface and Implementation

Power distribution in the core is calculated in the orthogonal 3-D (x-y-z) geometry in the kinetics model, which takes into account feedback due to changes in fuel temperature and coolant density, and control rod movement. In the channel thermal-hydraulics and fuel heat transfer models, the core is simulated with multiple parallel channels, each having one or more fuel bundles associated with it. Their properties are solved for each axial node for each channel. Hydraulic boundary conditions for these channels are determined in the external core model in the code. Each component is coupled by such data, as shown in Figure 9-7.

The kinetics noding is radially one node per one fuel bundle and axially 24 or 25 nodes. However, the channel noding for thermal-hydraulics and fuel heat transfer, the channel component of TRACG, is coarse in comparison with the kinetics noding in the horizontal (x–y) directions. Namely, fuel bundles with thermal-hydraulically and geometrically similar properties are grouped and averaged into one component, and, therefore, the number of channel components is less than that of fuel bundles. The data transfer from the kinetics model to the channel model is performed by averaging. The data transfer from the hydraulics to the kinetics (i.e., water density and fuel temperature, as shown in Figure 9-7) is performed in the following manner.

The TRACG 3-D kinetics steady-state calculation is restarted from the wrapped-up file of the detailed 3-D steady-state core simulator[3],[20], which contains the full data of water density and fuel temperature for the kinetics noding for the initial conditions. In the transient calculation, the change in density and temperature are given by the channel model. The bypass density is obtained from the vessel component and combined by volume weighting with the channel and water rod density to provide the overall relative water density for each channel node. The time-dependent nodal conditions for the kinetics model are calculated as follows: [[

]] The subscript k denotes the axial node coordinate. It is used for both neutronics and channel noding here and is normally identical, but not necessarily identical. If not, the water density and the fuel temperature distribution are transferred with volumetric weighting. The subscripts i and j denote the radial coordinates of the neutronics model node; which belongs to the n–th CHAN component. If boron is present, it is treated in the same manner as water density. Volume- weighted boron density, relative water density and fluid temperature are used to account for the impact of boron as described in Section 9.5.

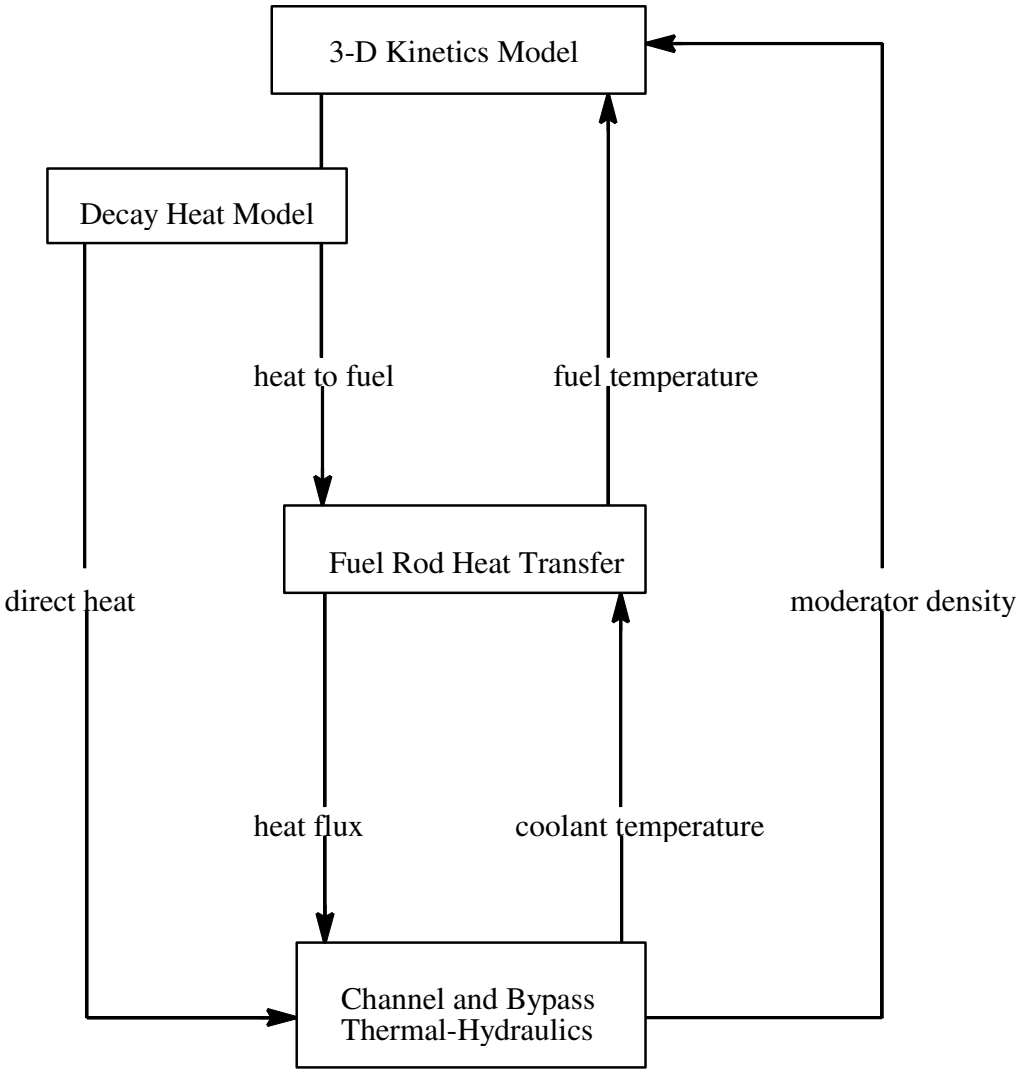

Figure 9-7. Data Transfer between TRACG Models

The power at each heated node in the channel component is the product of the bundle power and an axial power shape both of which are calculated by the 3-D kinetics model. The power distribution between fuel rod groups can be input or calculated based on the following gamma smearing model.

The rod-to-rod gamma smearing is defined by:

$$\bar{f}_j(t) = A(t)\, f_j + [1-A(t)] \qquad (9.4\text{-}3)$$

where:

$\bar{f}_j(t)$ = Rod-to-rod energy transport ; (9.4-4)

f_j = Local power factor for rod j ;

$A(t)$ = $A_f(1-f_{dh}) + A_d f_{dh}$;

A_f = Gamma smearing constant for fission power ;

A_d = Gamma smearing constant for decay heat ;

f_{dh} = Decay heat fraction .

The distribution of channel power among fuel, clad, moderator and various structural components is calculated accounting for gamma ray and neutron transport. These distributions are performed for each axial node "k" for the bundle assigned to the channel at location "ij". For convenience the "kij" subscripts are dropped with the understanding that "P(t)" is the total power for node "kij" that is being distributed among the materials at node "kij".

The power generated in the cladding of one fuel rod from rod group j is:

$$P_c^j(t) = P(t) \bullet \bar{f}_j(t) \bullet F_c(t)/N_F \quad (9.4\text{-}5)$$

where "$F_c(t)$" is the fraction of power for cladding in all fuel rods and "N_F" is the total number of fuel rods in the channel at this location.

The power generated in the fuel of one fuel rod is:

$$P_f^j(t) = P(t) \bullet \bar{f}_j(t) \bullet F_f(t)/N_F \quad (9.4\text{-}6)$$

where "$F_f(t)$" is the fraction of power for the fuel in all fuel rods in the channel at this location.

The power generated in the "fuel" and the "cladding" of one water rod is defined by:

$$P_f^j(t) = 0.0$$

$$P_c^j(t) = P(t) \bullet F_w(t)/(N_T - N_F) \quad (9.4\text{-}7)$$

where "$F_w(t)$" is the fraction of power for the cladding of all water rods, N_T is the total number of rods in the channel and (N_T-N_F) is the number of water rods.

The power generation in the control blade outside the bundle is:

$$P_{bl}(t) = P(t) \bullet F_{bl}(t) \quad (9.4\text{-}8)$$

where "$F_{bl}(t)$" is the fraction of power deposited in the control blade when it is inserted at the location of node "kij".

The power generated in the channel walls is given by:

$$P_{ch}(t) = P(t) \bullet F_{ch}(t) \quad (9.4\text{-}9)$$

where "$F_{ch}(t)$" is the fraction of power deposited in the channel wall.

The power absorbed directly into the bypass, water rod and bundle coolant is defined by:

$$P_{co}(t) = P(t) \bullet F_{co}(t) \tag{9.4-10}$$

It should be noted that the sum of the fractional energy deposition rates is unity:

$$F_f(t) + F_c(t) + F_w(t) + F_{ch}(t) + F_{bl}(t) + F_{co}(t) = 1.0 \tag{9.4-11}$$

therefore:

$$\sum_{j=1}^{N_{RG}} \left[P_f^j(t) + P_c^j(t) \right] \bullet N_j + P_{ch}(t) + P_{bl}(t) \tag{9.4-12}$$

$$+ P_{co}(t) = P(t)$$

where N_j is the number of rods in group j, and N_{RG} is the number of rod groups.

The energy distribution fractions denoted by "F" in Equations (9.4-5) through (9.4-11) may change with time because they are renormalized to assure that Equation (9.4-11) is satisfied. The time-dependence enters in via two means. Firstly, "$F_{co}(t)$" depends on the time-dependent moderator density as shown below. Secondly, the fraction of power attributed to decay heat, $f_{dh}(t)$, changes with time. To account for the fact that the energy deposition rates depend on the energy of the particle that is imparting the energy and that fissions result in higher-energy particles than decay heat reactions, the deposition rates are all expressed in the form:

$$F_x = a(1 - f_{dh}) + bf_{dh} \tag{9.4-13}$$

a = fractional deposition for fission power
b = fractional deposition for decay heat
x = c, f, w, bl, ch, and co

The values of "a" and "b" are input constants for each channel group. To account for the moderator density dependence of the direct moderator heating, the coolant fractional disposition is expressed as follows:

[[

]]

TRACG provides two options for specifying the fuel pellet radial peaking factors. The first option is a calculation of the radial peaking factors as a function of pellet exposure and radius and is described below for UO_2 pellets. The second option allows direct input of the radial peaking factors.

The calculated pellet radial power density for UO_2 fuel is given by:

[[

]]

9.5 3D Kinetics Boron Model

9.5.1 Technical Basis and Assumptions

The microscopic absorption cross section for boron-10 (σ_{B10}) for each neutronics node kij is assumed to be modeled as:

$$\sigma_{B10}\left(\overline{v}_3, T, N_{B10}\right)_{kij} = \hat{\sigma}_{B10}\frac{\hat{v}}{\overline{v}_{3,kij}} - \tilde{\sigma}_{B10} \qquad (9.5\text{-}1)$$

The first term on the right hand side of Equation (9.5-1) corresponds to a theoretical "1/v absorber" where

$\overline{v}_{3,kij}$ is the time-dependent average thermal group neutron velocity [cm/s] in node kij;

$\hat{\sigma}_{B10}$ is the reference microscopic cross sections corresponding to $\hat{v}$;

$\hat{v}$ is the reference velocity of 219,834.7 cm/s (nominally 2200 m/s) for thermal neutrons;

and $\hat{T}$ is the reference temperature of 293.15 K (20 C) at which $\hat{v}$ is typically defined.

The standard practice is to define the microscopic cross sections in units of *barns* (b) where one *barn* is equivalent to 10^{-24} cm^2. TRACG04 uses the default value of $\hat{\sigma}_{B10} = 3837$ b.

The second term on the right hand side of Equation (9.5-1) is an empirical term that accounts for deviations from the theoretical model. It is defined by [[

]] (9.5-4)

The macroscopic absorption cross section ($\sum_{B10,kij}$) for boron-10 in node "kij" is calculated as

$$\sum_{B10,kij} = N_{B10,kij}\sigma_{B10,kij} \tag{9.5-5}$$

Values for $\sum_{B10,kij}$ are added to the thermal group removal cross sections in the kinetics model.

The value for $N_{B10,kij}$ is calculated by the code for each kij neutronics node using the nodal values for the boron density (ρ_B) in units of kg/m^3 that are obtained from the CHAN and VSSL components. The nodal boron densities actually represent the density of a particular type of boron molecule that is being transported in an aqueous solution. To obtain a B10 number density, additional details about the boron molecule are required. The general relationship between B10 number density $N_{B10,kij}$ and $\rho_{B,kij}$ is

$$N_{B10,kij}\left[\frac{1}{b\cdot cm}\right] = N_0\left[\frac{molecules}{gm\text{-}mole}\right]\left[\frac{10^{-24}cm^2}{b}\right]E_{B10}\left[\frac{B10\ atoms}{B\ atoms}\right]\frac{M_{Bm}\left[\frac{B\ atoms}{molecule}\right]}{W_{Bm}\left[\frac{gm}{gm\text{-}mole}\right]}\rho_{B,kij}\left[\frac{gm}{cm^3}\right] \tag{9.5-6}$$

where:

N_0 is Avogadro's number for the number of molecules per gm-mole;

E_{B10} is the fraction of boron atoms that are B10 atoms (Default=0.198);

M_{Bm} is the number of boron atoms in the boron molecule that is being modeled (Default=1.0);

W_{Bm} is the molecular weight of the boron molecule (Default=10.812025).

9.5.2 Implementation Details

The code transports soluble boron with the liquid. Boron transport is limited by the solubility limits for the boron as described in Section B.3.4. The conservation equation is solved for each hydraulics node to obtain the the boron density (ρ_B) in units of kg/m^3. For reporting purposes, the boron density is converted to a concentration of elemental boron according to Equation (B.3-52). The relationship between the elemental boron concentration and the boron density depends on the characteristics of the borated molecule as used in the determination of the factor given by Equation (B.3-51). For simplicity, the default inputs assume that elemental boron is being tracked; however, the characteristics of the borated molecule can be modified by user input.

The nodal boron density, the B10 enrichment and the characteristics of the borated molecule are used to determine the B10 number density for each "kij" neutronics node according to Equation (9.5-6). The macroscopic absorption cross section ($\sum_{B10,kij}$) for boron-10 in node "kij" is then calculated according to Equation (9.5-5).

Values of the B10 microscopic absorption cross section from Equation (9.5-4) have been compared to the values calculated from TGBLA06 for a wide range of conditions. These evaluations included: [[

]] Each such comparison produces an error defined as the value from Equation (9.5-4) minus the value from TGBLA06. A histogram of these errors constructed from the [[ ]] comparisons is shown in Figure 9-8. The mean error is [[ ]] barns with a standard deviation of [[ ]] barns. Relative to the value of $\hat{\sigma}_{B10} = 3837$ b, the percentage mean and percentage standard deviation in the TRACG model's prediction of σ_{B10} are [[ ]]. These errors are small in comparison to other known sources of error. For example, TGBLA06 compared to MCNP for [[ ]] comparisons reveals σ_{B10} values that on average are high by [[ ]] barns with a standard deviation of [[ ]] barns or [[ ]] relative to $\hat{\sigma}_{B10} = 3837$ b. Even these larger uncertainties are smaller than the estimated uncertainty in knowing the distribution of the boron. The uncertainty in the distribution of B10 atoms is a direct function of the integrated error in predicting the flow distribution between channels which is estimated to be at least 5%.

[[

]]

Figure 9-8. B10 Absorption Cross Section Errors Relative to TGBLA06

10.0 CONTROL SYSTEM

The TRACG control system model is designed to serve two primary purposes. First, it allows the user to model an actual BWR plant control system at any desired level of detail. Accurate modeling of the plant control system can play an important role in the successful analysis of many transients, including ATWS and operational transient analyses. Secondly, the control system may be used to assist in the initialization of any plant deck by allowing the user to automatically control the value of certain plant parameters during the initialization process.

In practice, the control system model permits the user to take data from the thermal-hydraulic (T/H) database, perform a wide variety of user-specified operations on these data in an external control system, then use the results of these operations to adjust geometric or dynamic variables in the database. For example, pressure in a BWR main steamline may be used as input to the control system that generates an output signal to adjust the area of the steamline pressure control valve (PCV). A large number of control loops of a similar nature may be utilized to simulate an entire BWR plant control system.

The control system solution scheme is sequential based on the order in which the control blocks are specified on input. The input to a block is the current value that may be the new time value if the input is the output of a block already calculated or the old time value if the input is the output of a block that has yet to be updated. This potentially explicit scheme can lead to instabilities if care is not taken to organize the control system in a manner to increase the implicitness as much as possible. The existence of feedback loops makes organizing the computation in an implicit manner impossible given the sequential solution scheme used in TRACG. To guarantee that the control system will be stable, a sufficiently small time step size must be used to evaluate the control system. The specification of time step size is discussed in Section 10.3.

10.1 Control Blocks

A TRACG control system model is built up from basic functional elements called control blocks. Each control block performs a simple operation on input data to generate an output value. A complete list of the types of control blocks and a description of their operations is found in Table 10-1. The various control block types require from zero to three input values, and each generates a single output value. Input and output values may be logical (0 or 1) or continuously varying, depending upon the type of control block. Associated with each control block are the following user-specified parameters:

- A control block number from 1 to 9999 uniquely identifies each block. Block numbers need not be consecutive.
- The type of operation to be performed upon the input data.
- The constants C1 and C2. NOTE: The various control block constants (C1, C2, XMAX, and XMIN) may not be required, depending on the control block type. See Table 10-1 for specific requirements.
- The gain factor G.
- The maximum and minimum limits XMAX and XMIN of the block output.

- The initial value (XIV or LIV) of the block output.
- An optional 12-character name.

A control block may be represented schematically by a control block diagram, as shown in Figure 10-1.

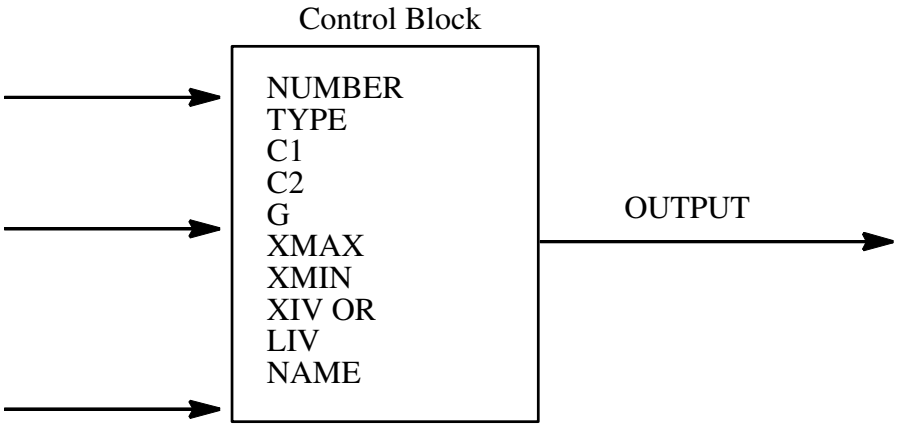

Figure 10-1. Schematic Control Block Diagram

The majority of the available control blocks perform simple algebraic or logic operations as indicated in the rightmost column of Table 10-1 and, require no further explanation. Seven of the control blocks are state variable blocks, which involve an integration with respect to time. The evaluation of the state variable blocks is described below.

The state variable control block types are DINL, INT, INTM, LAG, LINT, LLAG, and SOTF. The method of integration with respect to time used in all of these blocks is implicit; that is, the input (derivative) value to be integrated is taken to be the value at the end of the control system time step. When the control system subdivides the hydraulic time step, the input parameter is interpolated between the old and new hydraulic time step values.

A pass is taken through the control system calculation at time zero (before the TRACG thermal-hydraulic equations have been advanced) to load initial input values for use as old time inputs by the state variable blocks in the next pass through the control system. The user-supplied initial control block output values are used for determining these initial inputs and for initializing the output values of state variable blocks.

The computational method used for each of the state variable block types is illustrated in the following section. In each case, Y is the block output value, X1 is the block input value, X2 is the intermediate integral value for double integrations, Δt is the control system time step size, and G is the control block gain.

DINL (double integrator with output limiting)

$$Y^{n+1} = Y^n + X2^n \, \Delta t \qquad (10.1\text{-}1)$$

$$X2^{n+1} = X2^n + X1^{n+1} \, G \, \Delta t \qquad (10.1\text{-}2)$$

Equations (10.1-1) and (10.1-2) are evaluated in sequence. $X2^n = 0$ at time zero. If $Y^{n+1} > XMAX$ or $Y^{n+1} < XMIN$, then the output of the block supplying input X1 is set to zero if its output sign is such as to hold the DINL output locked at its limit.

INT (simple integrator)

$$Y^{n+1} = Y^n + X1^{n+1}\, G\, \Delta t \tag{10.1-3}$$

INTM (integrator with mode control)

If (L2 + L3) = 0 (reset mode),

$$Y^{n+1} = XIV. \tag{10.1-4}$$

If (L2 + L3) = 2 (integrate mode),

$$Y^{n+1} = Y^n + X1^{n+1}\, G\, \Delta t \tag{10.1-5}$$

If (L2 + L3) = 1 (hold mode),

$$Y^{n+1} = Y^n. \tag{10.1-6}$$

L2 and L3 are logic input variables (1 or 0) to block inputs 2 and 3.

LAG (first order lag)

$$Y^{n+1} = Y^n + \frac{\left[\, G\, X1^{n+1} - Y^{n+1} \right] \Delta t}{C1} \tag{10.1-7}$$

C1 is the lag time constant. This equation is rearranged algebraically and solved for Y_{n+1}.

LINT (limited integrator)

$$Y^{n+1} = Y^n + X1^{n+1}\, G\, \Delta t \tag{10.1-8}$$

If ($Y^{n+1} > XMAX$ or $Y^{n+1} < XMIN$, then the output of the block supplying input X1 is set to zero if its output sign is such as to hold the LINT output locked at its limit.

LLAG (lead–lag transfer function)

$$\overline{X2^{n+1}} = \frac{\left(GX1^{n+1} - X2^{n+1}\right)}{C2} \tag{10.1-9}$$

$$X2^{n+1} = X2^n + \overline{X2^{n+1}}\, \Delta t \tag{10.1-10}$$

$$Y^{n+1} = X2^{n+1} + C1\, \overline{X2^{n+1}} \tag{10.1-11}$$

X2 is the intermediate state derivative, and C1 and C2 are the lead and lag time constants. Equations (10.1-9), (10.1-10) and (10.1-11) are rearranged algebraically and solved to obtain values for Y^{n+1} and $X2^{n+1}$. $X2^{n}$ is initialized to the same value as $X1^{n}$.

SOTF (second order transfer function)

$$\overline{X2^{n+1}} = \frac{\left(GX1^{n+1} - Y^{n+1} - C1X2^{n+1}\right)}{C2} \tag{10.1-12}$$

$$X2^{n+1} = X2^{n} + \overline{X2^{n+1}}\,\Delta t \tag{10.1-13}$$

$$Y^{n+1} = Y^{n} + X2^{n+1}\,\Delta t \tag{10.1-14}$$

C1 and C2 are the transform coefficients in the Laplace transform:

$$Y = \frac{X1}{1.0 + C1 \cdot S + C2 \cdot S^{2}} \tag{10.1-15}$$

where S is the Laplace transform operator. Equations (10.1-12), (10.1-13) and (10.1-14) are rearranged algebraically and solved to obtain values for Y^{n+1} and $X2^{n+1}$. $X2^{n}$ is initialized to the same value as $X1^{n}$.

Table 10-1. Description Of Control Block Operations

Number	Block Type	Block Input 1 (a)	Block Input 2 (b)	Block Input 3	Block Const 1	Block Const 2	Gain Factor (c)	Upper Limit (c)	Lower Limit (c)	Initial Value (d)	Name	Mathematical Operation (e)
1	ABSV	X1	N/A	N/A	N/A	N/A	G	XMAX	XMIN	XIV	Absolute Value	XOUT = G*ABS(X1)
2	ACOS	X1	N/A	N/A	N/A	N/A	G	XMAX	XMIN	XIV	Arcosine	XOUT = G*ACOS(X1), XOUT in Radians
3	ADD	X1	X2	N/A	N/A	N/A	G	XMAX	XMIN	XIV	Add	XOUT = G*(X1+X2)
4	AINT	X1	N/A	N/A	N/A	N/A	G	XMAX	XMIN	XIV	Integerizer	XOUT = G*FLOAT(IFIX(X1))
5	AND	L1	L2	N/A	N/A	N/A	N/A	N/A	N/A	LIV	Logical "And"	LOUT = 1.0 IF((L1.EQ.1).AND.L2.EQ.1) = 0.0 Otherwise
6	ASIN	X1	N/A	N/A	N/A	N/A	G	XMAX	XMIN	XIV	Arcsine	XOUT = G*ASIN(X1), XOUT in Radians
7	ATAN	X1	N/A	N/A	N/A	N/A	G	XMAX	XMIN	XIV	Arctangent	XOUT = G*ATAN(X1), XOUT in Radians
8	ATN2	X1	X2	N/A	N/A	N/A	G	XMAX	XMIN	XIV	Arctangent	XOUT = G*ATAN(X1/X2), XOUT in Radians
9	CONS	N/A	N/A	N/A	N/A	N/A	N/A	N/A	N/A	XIV	Constant	XOUT = C1
10	COS	X1	N/A	N/A	N/A	N/A	G	XMAX	XMIN	XIV	Cosine	XOUT = G*COS(X1), X1 in Radians
11	DEAD	X1	N/A	N/A	C1	C2	G	XMAX	XMIN	XIV	Dead Band, Dead Zone, or Dead Space	XOUT = G*(X1-C2) IF(X1.GT.C2) = G*(X1-C1) IF(X1.LT.C1) = 0.0 Otherwise
12	DER	X1	(X2)	N/A	N/A	N/A	G	XMAX	XMIN	XIV	Derivative	XOUT = G*(dX1/dT)
13	DINL	X1	(X2)	N/A	N/A	N/A	G	XMAX	XMIN	XIV	Double Integrator With XOUT Limited	XOUT = G*Int{Int(X1*dt)dt} + XIV X1 and (X2) are reset to 0.0 if XOUT is against a limit and the sign of X1 does not change
14	DIV	X1	X2	N/A	N/A	N/A	G	XMAX	XMIN	XIV	Divide	XOUT = G*X1/X2
15	EOR	L1	L2	N/A	N/A	N/A	N/A	N/A	N/A	LIV	Logical "Exclusive OR"	LOUT =1.0 IF((L1+L2).EQ.1.0) = 0.0 otherwise
16	EQUL	L1	L2	N/A	N/A	N/A	N/A	N/A	N/A	LIV	Logical "Equivalent"	LOUT = 1.0 IF(L1.EQ.L2) = 0.0 otherwise
17	EXP	X1	N/A	N/A	N/A	N/A	G	XMAX	XMIN	XIV	Exponential	XOUT = G*EXP(X1)
18	FLFP	L1	(L2)	L3	N/A	N/A	N/A	N/A	N/A	LIV	Logical "Flip Flop"	LOUT = Flip-flop Output Which Changes State Whenever L1 Changes State (only If L3=1.0)

Table 10-1. Description Of Control Block Operations

Number	Block Type	Block Input 1 (a)	Block Input 2 (b)	Block Input 3	Block Const 1	Block Const 2	Gain Factor (c)	Upper Limit (c)	Lower Limit (c)	Initial Value (d)	Name	Mathematical Operation (e)
19	GATE	X1	L2	N/A	N/A	N/A	N/A	N/A	N/A	XIV	Gate	XOUT = X1 IF(l2.EQ.1.0) = 0.0 IF(L2.EQ.0.0)
20	GREQ	X1	X2	N/A	N/A	N/A	N/A	N/A	N/A	XIV	Greater Than or Equal to	XOUT = 1.0 IF(X1.GE.X2) = 0.0 otherwise
21	GRTH	X1	X2	N/A	N/A	N/A	N/A	N/A	N/A	LIV	Greater Than	LOUT = 1.0 IF(X1.GT.X2) = 0.0 otherwise
22	INSW	X1	X2	L3	N/A	N/A	N/A	N/A	N/A	XIV	Input Switch	XOUT = X1 IF(L3.EQ.1.0) = X2 IF (L3.EQ.0.0)
23	INT	X1	N/A	N/A	N/A	N/A	G	XMAX	XMIN	XIV	Integrate	XOUT = G*Int(X1*dt) + XIV
24	INTM	X1	L2	L3	N/A	N/A	G	XMAX	XMIN	XIV	Integrate with Mode Control	XOUT = XIV, IF((L2+L3).EQ.0.0) Reset or IC Mode =G*Int(X1*dt) + XIV IF((L2+L3).EQ.2.0), Intergrate Mode = XOUT IF((L2+L3).EQ.1.0) Hold Mode
25	IOR	L1	L2	N/A	N/A	N/A	N/A	N/A	N/A	LIV	Logical “Inclusive OR”	LOUT = 0.0 IF((L1+L2).EQ.0.0) = 1.0 otherwise
26	LAG	X1	N/A	N/A	C1	N/A	G	XMAX	XMIN	XIV	First Order Lag	XOUT = G*X1/(1.0 + C1*s) s is Laplace Operator
27	LDLY	L1	(L2)	N/A	C1	(C2)	N/A	N/A	N/A	LIV	Logic Delay	LOUT = 0.0 IF((L1.EQ.0.0).OR. (TIMET.LT.(C1+C2))) =1.0 IF((L1.EQ.1.0).AND. (TIMET.GE.(C1+C2))) Where (C2) is the TIMET When L1 Switches from 0.0 to 1.0
28	LGPC	L1	(L2)	L3	N/A	N/A	N/A	N/A	N/A	LIV	Logic General Purpose Counter	LOUT = 0.0 If (L3.EQ.0.0), Reset Mode = Number of Times L1 Has Changed State Since Enabled (When L3 = 1.0), Count Mode
29	LISW	L1	L2	L3	N/A	N/A	N/A	N/A	N/A	LIV	Logic Input Switch	LOUT = L1 IF(L3.EQ.1.0) = L2 IF(L3.EQ.0.0)

Table 10-1. Description Of Control Block Operations

Number	Block Type	Block Input 1 (a)	Block Input 2 (b)	Block Input 3	Block Const 1	Block Const 2	Gain Factor (c)	Upper Limit (c)	Lower Limit (c)	Initial Value (d)	Name	Mathematical Operation (e)
30	LLAG	X1	(X2)	(X3)	C1	C2	G	XMAX	XMIN	XIV	Lead-Lag Transfer Function	XOUT = G*X1/(1.0 + C1*s)/(1.0 + C2*s) s is Laplace Transform Operator
31	LINT	X1	N/A	N/A	N/A	N/A	G	XMAX	XMIN	XIV	Limited Integrator	XOUT = G*Int(X1*dt) + XIV, X1 is set to 0.0 if Xout is against a limit and the sign of X1 does not change
32	LOGN	X1	N/A	N/A	N/A	N/A	G	XMAX	XMIN	XIV	Natural Logarithm	XOUT = G*ALOG(X1)
33	LSEQ	X1	X2	N/A	N/A	N/A	N/A	N/A	N/A	LIV	Less Than or Equal to	LOUT = 1.0 IF (X1.LE.X2) =0.0 otherwise
34	LSTN	X1	X2	N/A	N/A	N/A	N/A	N/A	N/A	LIV	Less Than	LOUT = 1.0 IF(X1.LT.X2) =0.0 otherwise
35	MAXS	X1	X2	N/A	N/A	N/A	N/A	N/A	N/A	XIV	Maximum of 2 Signals	XOUT = AMAX1(X1,X2)
36	MAXT	X1	N/A	N/A	N/A	N/A	N/A	N/A	N/A	XIV	Maximum During Transient	XOUT = AMAX1(X1,XOUT)
37	MINS	X1	X2	N/A	N/A	N/A	N/A	N/A	N/A	XIV	Minimum of 2 Signals	XOUT = AMIN1(X1,X2)
38	MINT	X1	N/A	N/A	N/A	N/A	N/A	N/A	N/A	XIV	Minimum During Transient	XOUT = AMIN1(X1,XOUT)
39	MULT	X1	X2	N/A	N/A	N/A	G	XMAX	XMIN	XIV	Multiply	XOUT = G*X1*X2
40	NAND	L1	L2	N/A	N/A	N/A	N/A	N/A	N/A	LIV	Logical “Not And”	LOUT = 0.0 IF ((L1+L2).EQ.2.0) = 1.0 otherwise
41	NEQ	L1	L2	N/A	N/A	N/A	N/A	N/A	N/A	LIV	Logical “Not Equal”	LOUT = 1.0 IF ((L1.NE.L2) =0.0 otherwise
42	NOR	L1	L2	N/A	N/A	N/A	N/A	N/A	N/A	LIV	Logical “Not Inclusive OR”	LOUT = 1.0 IF((L1+L2.EQ.0.0) =0.0 otherwise
43	NOT	L1	N/A	N/A	N/A	N/A	N/A	N/A	N/A	LIV	Logical “Not” or Negation	LOUT = 1.0 IF(L1.EQ.0.0) = 0.0 IF (L1.EQ.1.0)
44	PDIF	X1	X2	N/A	N/A	N/A	G	XMAX	XMIN	XIV	Positive Difference	XOUT = G((X1-X2) IF(X1.GT.X2) =0.0 otherwise
45	QUAN	X1	N/A	N/A	N/A	N/A	N/A	XMAX	XMIN	XIV	Quantizer	LOUT = nearest integer to X1

Table 10-1. Description Of Control Block Operations

Number	Block Type	Block Input 1 (a)	Block Input 2 (b)	Block Input 3	Block Const 1	Block Const 2	Gain Factor (c)	Upper Limit (c)	Lower Limit (c)	Initial Value (d)	Name	Mathematical Operation (e)
46	RAMP	N/A	N/A	N/A	C1	N/A	G	XMAX	XMIN	XIV	Ramp	XOUT = G*(TIMET-C1) IF(TIMET.GT.C1) = 0.0 otherwise
47	RAND	N/A	N/A	N/A	C1	N/A	G	XMAX	XMIN	XIV	Random Number Generator	XOUT = G*RAND(DUMY) IF(TIMET.GE.C1) = 0.0 otherwise
48	SIGN	X1	X2	N/A	N/A	N/A	N/A	N/A	N/A	XIV	Sign Function	XOUT = |X1| IF (X2.GE.0.0) = -|X1| IF (X2.LT.0.0)
49	SIN	X1	N/A	N/A	N/A	N/A	G	XMAX	XMIN	XIV	Sine	XOUT = G*SIN(X1), X1 in Radians
50	SINV	X1	N/A	N/A	N/A	N/A	G	XMAX	XMIN	XIV	Sign Inversion	XOUT = -G*X1
51	SOTF	X1	(X2)	(X3)	C1	C2	G	XMAX	XMIN	XIV	Second Order Transfer Function	XOUT = G*X1/(1.0 + C1*S+C2*S*S) s is Laplace Transform Operator
52	SQRT	X1	N/A	N/A	N/A	N/A	G	XMAX	XMIN	XIV	Square Root	XOUT = G*SQRT(X1)
53	STEP	N/A	N/A	N/A	C1	N/A	G	XMAX	XMIN	XIV	Step	XOUT = G IF (TIMET.GT.C1) = 0.0 otherwise
54	SUBT	X1	X2	N/A	N/A	N/A	G	XMAX	XMIN	XIV	Subtract	XOUT = G*(X1-X2)
55	TAN	X1	N/A	N/A	N/A	N/A	G	XMAX	XMIN	XIV	Tangent	XOUT = G*TAN(X1), X1 in Radians
56	TIME	N/A	N/A	N/A	N/A	N/A	N/A	N/A	N/A	XIV	Time	XOUT = TIMET
57	TRIP	L1	N/A	N/A	N/A	N/A	N/A	N/A	N/A	LIV	Trip Status	LOUT = L1=1.0 If Trip + Delay Time Has Elapsed = L1=0.0 otherwise
58	VLIM	X1	X2	X3	N/A	N/A	G	N/A	N/A	XIV	Variable Limiter	XOUT = X2 IF ((G*X1).GT.X2) at Upper Limit =X3 IF((G*X1).LT.X3) at Lower Limit = G*X1 Otherwise, Between Limits
59	WSUM	X1	X2	N/A	C1	C2	G	XMAX	XMIN	XIV	Weighted Sumer	XOUT = G*(C1*X1 + C2*X2)
60	XPO	X1	X2	N/A	N/A	N/A	G	XMAX	XMIN	XIV	Exponentiate	XOUT = G*(X1**X2)
61	ZOH	X1	L2	N/A	N/A	N/A	N/A	N/A	N/A	XIV	Zero Order Hold	XOUT = X1 IF(L2.EQ.1.0) =XOUT otherwise

Table 10-1. Description Of Control Block Operations

Number	Block Type	Block Input 1 (a)	Block Input 2 (b)	Block Input 3	Block Const 1	Block Const 2	Gain Factor (c)	Upper Limit (c)	Lower Limit (c)	Initial Value (d)	Name	Mathematical Operation (e)
62	TCHG	X1	(X2)	N/A	N/A	N/A	N/A	N/A	N/A	XIV	Time of Change	XOUT = TIMET If X1 has Changed Since Last Time Step = XOUT Otherwise
63	PASS	X1	N/A	N/A	N/A	N/A	N/A	N/A	N/A	XIV	Pass through	XOUT = X1
100	DLAY	X1	n	N/A	C1	N/A	G	XMAX	XMIN	XIV	Time Delay	XOUT = XIV IF(TIMET.LE.C1) = G*X1(TIMET-C1) Otherwise Where n is number of Delay Table(f) Intervals
101	FNG1	X1	n	N/A	N/A	N/A	G	XMAX	XMIN	XIV	Function of One Independent Variable	XOUT = G*fn(X1), Where n is Function Table Number

Note:

(a) An ”X” parameter indicates a continuous variable; an “L” parameter indicates a logical (or discrete) parameter having a value of 0.0 or 1.0 only.

(b) Variables enclosed in ( ) are not input variables but are used internally by the control block for data storage.

(c) If G, XMAX and XMIN are required for a control block, a constant gain factor and constant upper and lower limits will be applied at the values given. Default values for the limits are +1.0E+38 and -1.0E+38. If XOUT.GT.XMAX, XOUT is set equal to XMAX. If XOUT.LT.XMIN, XOUT is set equal to XMIN.

(d) An initial value (XIV or LIV) is loaded into a control block output (XOUT or LOUT) at TIMET = 0.0 seconds.

(e) XOUT appearing on the right-hand side of a defining equation indicates a previous time step value.

(f) Delay Table is internal to TRAC, i.e., not a Function Table, n entries determine accuracy of delay, resolution of table.

10.2 Control System Interfaces

The input values to control blocks may be obtained from the TRACG thermal-hydraulic database (pressure, liquid level, and flow rate) or from the output of other control blocks. Thus, an extensive network of control blocks can be assembled to perform very complex operations. Control block outputs may be used as input values for other control blocks, or may be used to control (redefine) the values of variables in the component database (VLVE areas, PUMP torques, and FILL velocities). Table 10-2 contains a list of variables from the TRACG database that may be used as control block inputs or may be adjusted by control block outputs.

Figure 10-2 illustrates a system comprised of seven control blocks, representing a basic BWR pressure control system, designed to control the steamline inlet pressure by varying the pressure control valve area. This system obtains one of its inputs (steamline pressure) from the component database and uses one of its outputs (new valve area) to alter the VLVE component database. The remaining inputs and outputs are internal to the control system simulation.

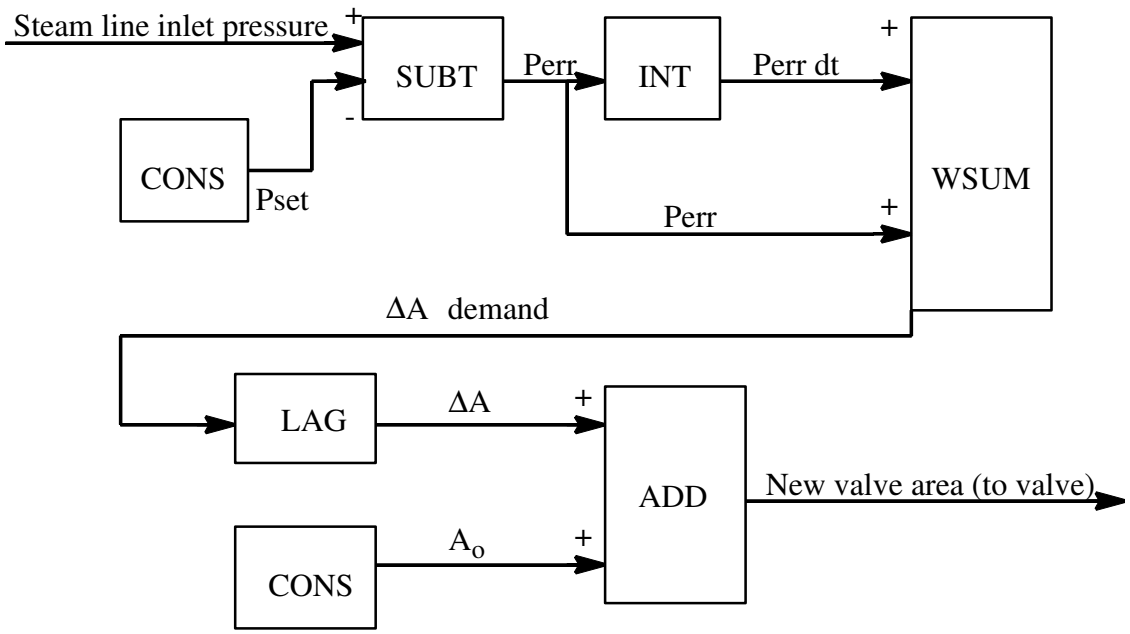

Figure 10-2. Simplified BWR Pressure Control System

Table 10-2. Control System Input/Output Variables

IOVAR Variable Symbolic Name	Description	**INPUT COMPONENTS (VARIABLE MAY BE INPUT TO CONTROL SYSTEM FROM THESE COMPONENTS)**	**OUTPUT COMPONENTS (VARIABLE MAY BE ADJUSTED BY CONTROL SYSTEM OUTPUT FOR THESE COMPONENTS)**	Comments
ALFA	Vapor fraction	CHAN, FILL, PIPE, PUMP, TEE, VLVE, VSSL, BREK	FILL	
AREA	Valve area (fraction of fully open area)	VLVE	VLVE	
BORC	Core average elemental boron concentration (ppm)	CHAN, VSSL	- None -	IOCMP=0
CHNP	Channel power (W)	CHAN	- None -	
CROD	Control rod position change (speed in units of m/s)	- None -	KINETICS	IOCMP is the control rod group index. CROD is ignored if a TRIP occurs for the blade group.
DISP	Control block output. See KEYB for input.	- None -	File Code 101	Binary output for interactive display. Max of 100 variables. IOCMP is the address.
DTOM	Derivative of pump motor torque with respect to speed	- None -	PUMP	
DZLV	Two–phase level (m). See also LLEV.	VSSL	- None -	
ENTH	Mixture enthalpy (J/kg)	CHAN, PIPE, PUMP, TEE, VLVE	- None -	IOCEL=2 gives outlet quantity IOCEL=3 gives TEE side arm quantity
ENTH	Liquid enthalpy (J/kg)	FILL	FILL	
FA1D	Flow area (m^2)	CHAN	CHAN	Useful for modeling flow blockage.
FN1D	Negative flow loss coefficient	- None -	CHAN	Useful for modeling flow blockage.

Table 10-2. Control System Input/Output Variables

IOVAR Variable Symbolic Name	Description	**INPUT COMPONENTS (VARIABLE MAY BE INPUT TO CONTROL SYSTEM FROM THESE COMPONENTS)**	**OUTPUT COMPONENTS (VARIABLE MAY BE ADJUSTED BY CONTROL SYSTEM OUTPUT FOR THESE COMPONENTS)**	Comments
FP1D	Positive flow loss coefficient	- None -	CHAN	Useful for modeling flow blockage.
FREQ	Pump motor frequency (1/s)	- None -	PUMP	
KEYB	Control block input. See DISP for output.	File code 102	- None -	Binary input for interactive control. Max of 100 variables. IOCMP is the address.
LLEV	Downcomer liquid level (m). See also DZLV.	VSSL	- None -	IOCEL is VSSL theta zone number
LPRM	Simulated LPRM reading	KINETICS	- None -	IOCMP, IOLEV, IOCELL are taken as I,J,K, respectively, of the node. LPRM location is in lower right-hand corner of the node. LPRM is the average of 8 surrounding nodes
LVEL	Liquid velocity (m/s)	CHAN, FILL, PIPE, PUMP, TEE, VLVE, BREK	- None -	
MCPR	Channel MCPR	CHAN	- None -	
MDOT	Mass flow rate (kg/s)	CHAN, FILL, PIPE, PUMP, TEE, VLVE, BREK	FILL	For MDOT and ENTH: IOCEL=1 gives inlet quantity
MFLO	Mass flow rate (kg/s)	CHAN, FILL, PIPE, PUMP, TEE, VLVE, BREK	- None -	
MF-Z	Mass flow rate (kg/s)	VSSL	- None -	
MF-R	Mass flow rate (kg/s)	VSSL	- None -	
MF-T	Mass flow rate (kg/s)	VSSL	- None -	
OMEG	Pump speed (rad/s)	PUMP	- None -	

Table 10-2. Control System Input/Output Variables

IOVAR Variable Symbolic Name	Description	**INPUT COMPONENTS (VARIABLE MAY BE INPUT TO CONTROL SYSTEM FROM THESE COMPONENTS)**	**OUTPUT COMPONENTS (VARIABLE MAY BE ADJUSTED BY CONTROL SYSTEM OUTPUT FOR THESE COMPONENTS)**	Comments
POWR	Sensed reactor power (W)	KINETICS	KINETICS	IOCMP=0
NOTE	POWR(t) = [POWT(t) – POWDH(t)] / [1. – POWDH(t=0) / POWT(t=0)] where POWDH is total decay heat power			
POWT	Total reactor power (W)	KINETICS	KINETICS	IOCMP=0
PRES	Pressure (Pa)	CHAN, FILL, PIPE, PUMP, TEE, VLVE, VSSL, BREK	BREK	
PCTX	Channel peak clad outside temp (K)	CHAN	- None -	
PW3D	3-D kinetics nodal power distribution	KINETICS	- None -	IOCMP, IOLEV, IOCELL are taken as I,J,K, respectively, of the node
RHOC	Control rod reactivity	KINETICS	- None -	IOCMP=0
RHOA	Additive control reactivity ($\Delta k/k$)	- None -	KINETICS	IOCMP=0
RHOT	Total reactivity	KINETICS	- None -	IOCMP=0
RODT	Channel rod temp (K)	CHAN	- None -	IOLEV is rod group. Fuel radial node location determined by CHAN input IEDTEM.
RODQ	Channel rod surface heat flux (W/m^2)	CHAN	- None -	IOLEV is rod group.
ROLN	Liquid density (kg/m^3)	CHAN, FILL, PIPE, PUMP, TEE, VLVE, VSSL, BREK	- None -	
ROVN	Vapor density (kg/m^3)	CHAN, FILL, PIPE, PUMP, TEE, VLVE, VSSL, BREK	- None -	
TIME	Reactor time (s)	TIME	- None -	IOCMP=0
NOTE	TIME changes only during a transient. TIMS advances during both a steady state and transient case.			

Table 10-2. Control System Input/Output Variables

IOVAR Variable Symbolic Name	Description	**INPUT COMPONENTS (VARIABLE MAY BE INPUT TO CONTROL SYSTEM FROM THESE COMPONENTS)**	**OUTPUT COMPONENTS (VARIABLE MAY BE ADJUSTED BY CONTROL SYSTEM OUTPUT FOR THESE COMPONENTS)**	Comments
TIMS	Synthesized time (s)	TIME	- None -	IOCMP=0
TLIQ	Liquid temperature (K)	CHAN, FILL, PIPE, PUMP, TEE, VLVE, VSSL, BREK	FILL	
TORQ	Motor torque (fraction of rated torque)	PUMP	PUMP	
TRIP	Trip condition as indicated by IOCEL	TRIP	TRIP	IOCMP is trip number IOCEL= 0 is ”set” condition = 1 is ”activated” condition.
TVAP	Vapor temperature (K)	CHAN, FILL, PIPE, PUMP, TEE, VLVE, VSSL, BREK	FILL	
VDOT	Velocity (m/s)	- None -	FILL	
VOLT	Pump motor voltage (V)	- None -	PUMP	
VVEL	Vapor velocity (m/s)	CHAN, FILL, PIPE, PUMP, TEE, VLVE, BREK	- None -	
ZOXT	Core maximum zirc oxide thickness (fraction of clad thickness)	CHAN	- None -	IOCOMP=0 At least one CHAN is required.
ZOXV	Core average zirc oxide volume (fraction of fuel clad total volume)	CHAN	- None -	IOCOMP=0 At least one CHAN is required.
ZPWR	axial power shape	CHAN	CHAN	

10.3 Control System Solution Procedure

The TRACG control system calculation may be executed with a smaller time step size than the thermal-hydraulic calculation. This feature allows the control system model to be calculated accurately, independent of the thermal-hydraulic time step size. Selection of the maximum allowable control system time step size should be based on the following criteria:

- **Accuracy in Calculating State Variable Control Blocks**

  This criterion is satisfied by limiting the control system time step size smaller than the shortest time constant occurring in any of state variable control blocks.

- **Detection and Resolution of Discontinuous Transient Events**

  This criterion is satisfied by limiting the control system time step size smaller than the shortest delay time occurring in any LDLY control block.

If the control system time step logic determines that the maximum allowable control system time step size is greater than or equal to the thermal-hydraulic time step size, then the thermal-hydraulic time step size will be used for the control system time step size. If the maximum allowable control system time step size is less than the thermal-hydraulic time step size, then the thermal-hydraulic time step size will be divided into the smallest number of equal intervals such that the interval size is less than or equal to the maximum control system time step size. This interval is then used as the control system time step size. In this manner, the control system calculation may be taken in several steps while it catches up with the thermal-hydraulic calculation. At the end of this series of steps, the control system calculation will be at the same time level as the thermal-hydraulic calculation. If the control system takes smaller time steps, the thermal-hydraulic block inputs are linearly interpolated between the old and new hydraulic time step values to provide consistency over the hydraulic time step.

APPENDIX A. Differences between TRACG and TRAC-BF1

TRACG development has continued at General Electric after the completion of joint development programs with INEL. This appendix summarizes the major models in TRACG, which are different from the models in TRACB-BF1/MOD1[1].

A.1. Modular Structure

The differences in the modular structure affect how a given facility is simulated using the thermal hydraulic components. The differences fall into two categories: (1) increased flexibility in the nodalization, and (2) restrictions on the nodalization through input and consistency checks.

A.1.1. Component Nodalization and Interaction

Zero-Cell Tee: The side branch of the tee component can have zero cells, in which case the side branch is reduced to a simple flow path.

Tee Based Channel: The channel component is based on a tee component with a zero-cell side branch representing the channel leakage path. This allows the inclusion of the leakage flow into the implicit network solution.

Flexible Valve Nodalization: TRACG allows the valve model to operate on any cell boundary in the component, including the first and the last boundary.

Horizontal Vessel Heat Slabs: The vessel component can include horizontal double-sided heat slabs, which are placed on a cell boundary between two axial levels in the vessel component. A horizontal heat slab can also be placed at the bottom or top of the vessel component.

One-Dimensional Heat Slab Properties: The properties for a one-dimensional heat slab can be specified separately for each node.

Fill to Vessel Junction: TRACG allows a fill component to be connected directly to a vessel component cell.

A.1.2. Nodalization and Consistency Checks

Nodalization and Loss Coefficient Checks: TRACG evaluates the nodalization for each component and determines when a flow restriction, contraction or expansion exists. An irreversible form loss is expected at these locations, and TRACG will produce a warning if no loss coefficients are specified in the input.

Junction Elevations: TRACG calculates the elevation of all junctions between components. Whenever a loop exists (e.g., the recirculation loop for a BWR or the simple loops composed of the channel and the vessel components for a BWR), TRACG evaluates the consistency of the input by requiring that:

$$\int_{\text{Around loop}} \bar{g} \bullet d\bar{x} = 0 \qquad \text{(A.1-1)}$$

Junction Consistency: At a junction between two components, a number of parameters (e.g., loss coefficients, hydraulic diameter, gravity vector) are specified for each component. TRACG requires that identical inputs are specified for each component at a junction.

A.2. Basic Models

There are very few differences in the basic thermal-hydraulic models between TRACG and TRAC-BF1/MOD1, since these models were jointly developed by GEH and INEL. A number of additional model features, however, have been included in TRACG.

Multiple Noncondensable Gas Species: The equations for the noncondensable gas component have been upgraded to simulate a mixture of multiple noncondensable gases including enhancements in the modeling of the noncondensable gas properties.

Kinetic Energy: Previous TRAC versions eliminated the kinetic energy term from the energy equations through algebraic manipulations involving the momentum equation. In that form, the flow work in the energy equation was on a non-conserving form, and energy balance errors could occur. TRACG avoids this problem by retaining the kinetic energy term in the energy equations (Section 3.1.2).

Stratified Flow: A stratified flow model is added to the flow regime map (Section 5.1.3).

Friction: TRACG uses the GEH design correlation for the wall friction (Section 6.2).

Turbulent Mixing: A simple, optional model for turbulent mixing between two cells was described in Section 6.7 in Revision 1 of this report but was removed in Revision 2. Section 6.7 has been reinstated in this revision. This optional model remains unqualified.

Condensation Heat Transfer: The correlations for condensation heat transfer in TRACG are upgraded to include shear enhancement and degradation due to presence of noncondensable gases (Sections 6.5 and 6.6.11).

Quenching: The original model for quenching heat transfer from TRAC-P1A[9] has been replaced in TRACG (Section 6.6.13).

Boiling Transition: The GEXL-correlation is included in TRACG for calculation of boiling transition in the channel component (Section 6.6.6).

Pump Work: The pump work is included in the energy equations (Section 7.2.1).

A.3. Component Models

There are a number of differences for the component models. They all involve additional features, which have been added to TRACG.

Pump: A fully implicit integration scheme has been implemented for the calculation of the pump speed. This includes a coupled solution for the pump fluid momentum equations (Section 7.2.1).

Jet Pump: TRACG allows a more realistic simulation of the flare at the suction inlet to the jet pump (Section 7.6.1).

Channel: There are a number of differences for the channel component: (1) the channel component is based on the tee component, allowing a fully implicit calculation of the leakage flow (Section 7.5); (2) calculation of the channel to bypass leakage flow has been upgraded to include all flow paths consistent with existing GEH design methods (Section 7.5.1); (3) simulation of the hydraulics inside the water rod has been included (Section 7.5.6); (4) dynamic gap conductance and cladding perforation models have been included consistent with existing GEH design methods (Section 7.5.2); (5) a hot rod model for bounding temperature calculations is included in TRACG (Section 7.5.7); and (6) critical power ratio is calculated (Section 7.5.5).

Vessel Upper Plenum: A model for the interaction between the ECC injected from the core spray spargers and the ambient fluid in the upper plenum of a BWR is included. The model considers submerged jet and spray injection (Section 7.8.2).

Vessel Bypass Heating: When the kinetics option is applied, direct moderator heating of the bypass fluid is included (Section 9.4).

Vessel Horizontal Heat Slabs: In TRACG, one-dimensional heat slabs can be placed at a cell boundary between two vessel levels (Section 7.8).

A.4. Kinetics

TRACG utilizes a three-dimensional kinetics model consistent with the GEH three-dimensional core simulator PANACEA[3],[20] (Section 9.1). It is a modified one-group model and includes six delayed neutron precursor groups. Feedback from the thermal hydraulic model includes moderator density, fuel temperature, control rod and boron reactivity. Several decay heat models are available. Energy deposited in the fuel, structural elements and coolant are modeled.

A.5. Control System

Additional interfaces have been added to the control system model in TRACG, allowing more realistic simulation of the BWR (Section 10.0):

BWR Instrumentation: Additional inputs have been added to the control system to allow simulation of BWR instruments such as level sensors and LPRM's.

Reactivity Control: Additional outputs have been added to the control system, allowing movement of the control rods.

Numerics: TRACG has retained the explicit integration scheme for the control system from TRAC-BD1/MOD1[10], but TRACG allows the use of a smaller time step size for the control system than for the hydraulics.

A.6. Numerics

Several refinements have been made to the numerical integration scheme in TRACG. These refinements generally only affect the computer time and the robustness of the code and have only a small effect on the calculated results. The following changes have been made (Section 8.0):

Implicit Integration: TRACG utilizes an optional semi-implicit or fully implicit integration of the hydraulic conservation equations for mass, momentum and energy for both one-dimensional and three-dimensional components. In the semi-implicit integration scheme, only properties convected with the speed of sound are treated implicitly, whereas properties convected with the fluid speed are treated explicitly. For the fully implicit integration, all convective terms are treated implicitly.

Implicit Heat Transfer Coupling: For the implicit integration scheme, a fully implicit heat transfer coupling between the heat conduction equation and the hydraulic equations is applied in TRACG.

APPENDIX B. Thermodynamic and Transport Fluid Properties

B.1. Introduction

Thermodynamic and transport property subroutines used in TRACG are based on polynomial fits to steam table data for water and ideal gas behavior for the noncondensable gas. Transport property fits for water were obtained from Reference [200] and thermodynamic property fits were obtained from Reference [201]. Noncondensable gases are modeled as ideal gases. The transport properties for the individual ideal gases as well as the techniques for combining these propreties are based on the recommended models described in Reference [206]. The same thermodynamic and transport property routines are used by all TRACG component modules. Table B-1 through Table B-6 list the values of the constants that are used in property functions that are defined later in this appendix. The nomenclature used in this appendix is consistent with the terminology defined in Section 3.0.

Table B-1. Polynomial Constants for Thermodynamic Properties of Water and Air

C_1	=	117.8	C_{31}	=	338.0
C_2	=	0.223	C_{32}	=	20.387
C_3	=	255.2	C_{33}	=	-5.3512
C_4	=	958.75	C_{34}	=	370.4251
C_5	=	-0.856 6			
C_6	=	$2.619\ 410\ 618 \times 10^{6}$			
C_7	=	-4.995×10^{10}			
C_8	=	3.403×10^{5}			
C_9	=	1.066 554 48			
C_{10}	=	1.02×10^{-8}	C_{40}	=	273.0
C_{11}	=	-2.548×10^{-15}	C_{41}	=	239.36
C_{12}	=	$2.589\ 600 \times 10^{6}$	C_{42}	=	2.786 7
C_{13}	=	6.350×10^{-3}	C_{43}	=	-5.776 26
C_{14}	=	$-1.058\ 2 \times 10^{-9}$	C_{44}	=	3.938
C_{15}	=	1.076 4	C_{45}	=	1.0×10^{-6}
C_{16}	=	3.625×10^{-10}			
C_{17}	=	-9.063×10^{-17}	C_{47}	=	1.0×10^{3}
			C_{48}	=	-0.15×10^{3}
			C_{49}	=	-20.0
C_{20}	=	461.7			
C_{21}	=	2.0×10^{6}	C_{51}	=	0.657×10^{-6}

Table B-1. Polynomial Constants for Thermodynamic Properties of Water and Air

			C_{52}	=	$2.996\,018\,036 \times 10^{3}$
C_{23}	=	647.3	C_{53}	=	$9.700\,016\,602 \times 10^{3}$
C_{24}	=	1.3	C_{54}	=	$-8.448\,077\,393 \times 10^{3}$
			C_{55}	=	8.349 824
C_{26}	=	0.3	C_{56}	=	$3.495\,194\,44 \times 10^{2}$
C_{28}	=	1.0×10^{5}			
			C_{k0}	=	$-8.335\,44 \times 10^{-4}$
C_{30}	=	24821.0	C_{k2}	=	$-2.247\,45 \times 10^{-17}$
ELC0	=	$1.758\,80 \times 10^{4}$	ELE0	=	$2.283\,789\,029 \times 10^{9}$
ELC1	=	$3.740\,2 \times 10^{3}$	ELE1	=	$-2.622\,156\,77 \times 10^{7}$
ELC2	=	4.024 35	ELE2	=	$1.129\,486\,67 \times 10^{5}$
ELC3	=	-0.015 729 4	ELE3	=	$-2.162\,339\,85 \times 10^{2}$
ELC4	=	$3.130\,1 \times 10^{-5}$	ELE4	=	0.155 283 438
ELD0	=	$6.185\,27 \times 10^{6}$	C_{vg}	=	714.9
ELD1	=	$-8.145\,47 \times 10^{4}$	R	=	287.12
ELD2	=	$4.465\,98 \times 10^{2}$			
ELD3	=	-1.041 16			
ELD4	=	$9.260\,22 \times 10^{-4}$			
CVL1	=	1.002 136 23	CVH1	=	2.252 62
CVL2	=	$-5.632\,785 \times 10^{-5}$	CVH2	=	0.014 859 4
CVL3	=	$-8.971\,304\,77 \times 10^{-9}$	CVH3	=	$-7.154\,88 \times 10^{-5}$
CVL4	=	$-2.282\,874\,59 \times 10^{-5}$	CVH4	=	-0.010 458 8
CVL5	=	$4.765\,967\,87 \times 10^{-7}$	CVH5	=	$-1.029\,62 \times 10^{-4}$
CVL6	=	$5.021\,318 \times 10^{-10}$	CVH6	=	$5.091\,35 \times 10^{-7}$
CVL7	=	$4.101\,156\,58 \times 10^{-6}$	CVH7	=	$2.592\,66 \times 10^{-5}$
CVL8	=	$-3.803\,989\,08 \times 10^{-9}$	CVH8	=	$1.724\,1 \times 10^{-7}$
CVL9	=	$-1.421\,997\,52 \times 10^{-12}$	CVH9	=	$-8.984\,19 \times 10^{-10}$

Table B-2. Derived Constants for Thermodynamic Properties of Water and Air

A_1	=	$C_1 \cdot C_2/C_{28}$	A_{11}	=	$2 \cdot C_{26}/(C_{24} \cdot C_{20})$
A_2	=	$C_2 - 1.0$	A_{13}	=	$A_{11} \cdot (1.0 + C_{26})$
A_3	=	$-C_4 \cdot C_5/C_{23}$	A_{12}	=	$1.0/A_{13}$
A_4	=	$C_5 - 1.0$	A_{14}	=	$1.0/C_{28}$
A_5	=	$C_{45} \cdot C_{49}$	A_{15}	=	$1.0/C_{23}$
A_6	=	$2\ C_{45} \cdot C_{48}$	A_{16}	=	$2 \cdot C_{11}$
A_7	=	$4 \cdot C_{44} \cdot C_{45}$	A_{17}	=	$2 \cdot C_{14}$
A_8	=	$3 \cdot C_{43} \cdot C_{45}$	A_{18}	=	$2 \cdot C_{17}$
A_9	=	$2 \cdot C_{42} \cdot C_{45}$	A_{19}	=	$2 \cdot C_{48} \cdot C_{45}$
A_{10}	=	$C_{41} \cdot C_{45}$	A_{20}	=	$C_{45} \cdot C_{49}$
DELC0	=	ELC1	DELD0	=	ELD1
DELC1	=	2 • ELC2	DELD1	=	2 • ELD2
DELC2	=	3 • ELC3	DELD2	=	3 • ELD3
DELC3	=	4 • ELC4	DELD3	=	4 • ELD4
DELE0	=	ELE1			
DELE1	=	2 • ELE2			
DELE2	=	3 • ELE3			
DELE3	=	4 • ELE4			

Table B-3. Basic Constants for Transport Properties of Water and Air

$B_{0\ell}$	=	$2.394\ 907 \times 10^{-4}$	$B_{1\ell}$	=	$-5.196\ 250 \times 10^{-13}$
$C_{0\ell}$	=	$1.193\ 203 \times 10^{-11}$	$C_{1\ell}$	=	$2.412\ 704 \times 10^{-18}$
$D_{0\ell}$	=	$-3.944\ 067 \times 10^{-17}$	$D_{1\ell}$	=	$-1.680\ 771 \times 10^{-24}$
C_{1s}	=	$1.688\ 359\ 68 \times 10^{3}$			
C_{2s}	=	0.602 985 6			
C_{3s}	=	$4.820\ 979\ 623 \times 10^{2}$			
C_{4s}	=	$2.953\ 179\ 05 \times 10^{7}$			
C_{5s}	=	1.8			
C_{6s}	=	4.60×10^{2}			

Table B-4. Liquid Viscosity Constants			
$A_{0\ell}$	= 1.299 470 229 x 10^{-3}	$B_{0\ell}$	= -6.595 9 x 10^{-12}
$A_{1\ell}$	= -9.264 032 108 x 10^{-4}	$B_{1\ell}$	= 6.763 x 10^{-12}
$A_{2\ell}$	= 3.810 470 61 x 10^{-4}	$B_{2\ell}$	= 2.888 25 x 10^{-12}
$A_{3\ell}$	= -8.219 444 458 x 10^{-5}	$B_{3\ell}$	= 4.452 5 x 10^{-13}
$A_{4\ell}$	= 7.022 437 984 x 10^{-6}		
$D_{0\ell}$	= 3.026 032 306 x 10^{-4}	$E_{0\ell}$	= 1.452 605 261 2 x 10^{-3}
$D_{1\ell}$	= -1.836 606 896 x 10^{-4}	$E_{1\ell}$	= -6.988 008 498 5 x 10^{-9}
$D_{2\ell}$	= 7.567 075 775 x 10^{-5}	$E_{2\ell}$	= 1.521 023 033 4 x 10^{-14}
$D_{3\ell}$	= -1.647 878 879 x 10^{-5}	$E_{3\ell}$	= 1.230 319 494 6 x 10^{-20}
$D_{4\ell}$	= 1.416 457 633 x 10^{-6}		
$F_{0\ell}$	= -3.806 350 753 3 x 10^{-11}	h_0	= 8.581 289 699 x 10^{-6}
$F_{1\ell}$	= 3.928 520 767 7 x 10^{-16}	c_{0n}	= 4.265 884 x 10^{4}
$F_{2\ell}$	= -1.258 579 929 2 x 10^{-21}	P_i	= 6.894 575 293 x 10^{5}
$F_{3\ell}$	= 1.286 018 078 8 x 10^{-27}		
h_{00}	= 3.892 077 365 x 10^{-6}	e_{h0}	= 6.484 503 981 x 10^{-6}
e_{c0n}	= 5.535 88 x 10^{4}	c_n	= 4.014 676 x 10^{5}
h_1	= 2.76 x 10^{5}	h_2	= 3.94 x 10^{5}

Table B-5. Vapor Viscosity Constants			
A_{0g}	=	3.53×10^{-8}	B_{1g} = 0.407×10^{-7}
A_{1g}	=	6.765×10^{-11}	C_{1g} = 8.04×10^{-6}
A_{2g}	=	1.021×10^{-14}	D_{1g} = 1.858×10^{-7}
			E_{1g} = 5.9×10^{-10}
F_{1g}	=	$-0.288\ 5 \times 10^{-5}$	G_{1g} = 176.0
F_{2g}	=	$0.242\ 7 \times 10^{-7}$	G^{2g} = -1.6
F_{3g}	=	$-0.678\ 933\ 3 \times 10^{-10}$	G_{3g} = 0.004 8
F_{4g}	=	$0.631\ 703\ 703\ 7 \times 10^{-13}$	G_{4g} = $-0.474\ 074\ 074 \times 10^{-5}$
$H_{\ell 1}$	=	1.708×10^{-5}	H_{u1} = 1.735×10^{-5}
$H_{\ell 2}$	=	5.927×10^{-8}	H_{u2} = 4.193×10^{-8}
$H_{\ell 3}$	=	8.14×10^{-11}	H_{u3} = 1.09×10^{-11}
T_1	=	573.15	
T_2	=	648.15	

Table B-6. Thermal Conductivity Constants		
h_0	=	5.815×10^5
$A_{\ell 0}$	=	0.573 738 622
$A_{\ell 1}$	=	0.253 610 355 1
$A_{\ell 2}$	=	-0.145 468 269
$A_{\ell 3}$	=	0.013 874 724 85
C	=	$2.148\ 2 \times 10^5$
A_{g0}	=	1.76×10^{-2}
A_{g1}	=	5.87×10^{-5}
A_{g2}	=	1.04×10^{-7}
A_{g3}	=	-4.51×10^{-11}
B_{g0}	=	$1.035\ 1 \times 10^{-4}$
B_{g1}	=	$0.419\ 8 \times 10^{-6}$
B_{g2}	=	-2.771×10^{-11}

B.2. Thermodynamic Properties

Thermodynamic properties for TRACG are calculated in the THERMO subroutine and the subprograms that it calls. The input variables are pressure, liquid and vapor temperatures. The output variables include (a) saturation temperature, (b) the derivative of T_{sat} with respect to pressure, (c) internal energy, (d) density, (e) the derivatives of internal energy and density with respect to pressure for each phase and (f) the derivatives of internal energy and density with respect to temperature for each phase. Subroutine THERMO also includes an ideal gas option to calculate the density, internal energy and their associated derivatives with respect to pressure and temperature for the sum of all noncondensable gases.

The ranges of validity for the thermodynamic properties supplied by THERMO are 280.0 K $\leq T_\ell \leq$ 647.0 K, 280.0 K $\leq T_v \leq$ 3000.0 K, and 1.0 x 10^3 Pa $\leq P \leq$ 190.0 x 10^5 Pa. If THERMO is provided with data outside this range, it adjusts the data to the corresponding limit and issues a warning message.

Polynomial equations for the various water properties calculated in THERMO are given in Sections B.2.1, B.2.2, and B.2.3. Values of the constants are given in Table B-1 and Table B-2.

B.2.1. Saturated Water Properties

B.2.1.1. Saturation Temperature (T_{sat})

The saturation temperature for water as a function of the pressure (P) is calculated from

$$T_{sat} = C_1 Y^{C_2} + C_3 - dT_1 - dT_2 \tag{B.2-1}$$

where

$$Y = A_{14} P \tag{B.2-2}$$

and dT_1 and dT_2 are correction terms to improve the prediction at low pressures and are given by

$$dT_1 = -1.298 + Y\left(4.01\text{x}10^{-2} - Y\left(3.548\text{x}10^{-4} - Y \cdot 9.62\text{x}10^{-7}\right)\right) \tag{B.2-3}$$

$$dT_2 = 11.5\left(948.55 + \left(2.344785 - \log_{10}(Y)\right)^{6.75}\right)^{0.148148} - 31.75 \tag{B.2-4}$$

The input value for the pressure (pascals) is limited so that $602.87 \le P \le 2.2053\text{E}7$.

The derivative of the saturation temperature is obtained by analytical differentiation of the above expressions.

B.2.1.2. Saturation Pressure (P_{sat})

The pressure for saturated water as a function of the temperature (T) is calculated by solving Equation for the pressure (P). An initial approximate solution for the pressure is first obtained from

$$P = \begin{cases} C_{30}\left(\dfrac{T}{C_{31}}\right)^{C_{33}} \exp\left[C_{32}\left(T\text{-}C_{31}\right)/T\right] & , \quad T<C_{34} \\ \dfrac{1}{A_{14}}\left(\dfrac{T\text{-}C_3}{C_1}\right)^{1/C_2} & , \quad T \ge C_{34} \end{cases} \tag{B.2-5}$$

Note that the second row on the RHS of Equation (B.2-5) is obtained from Equation (B.2-1) by assuming $dT_1 = 0$ and $dT_2 = 0$. The derivative of Equation (B.2-5) with respect to temperature is

$$\frac{dP}{dT} = \begin{cases} \dfrac{P}{T}\left[\dfrac{C_{31}C_{32}}{T} + C_{33}\right] & , \quad T<C_{34} \\ \dfrac{P}{C_2\left(T\text{-}C_3\right)} & , \quad T \ge C_{34} \end{cases} \tag{B.2-6}$$

A Newton-Rhapson iteration is performed to update the saturation pressure and then evaluate the error in saturation temperature for that iteration. The refined value for pressure for iteration n+1 is determined from

$$P_{sat}^{n+1} = P_{sat}^{n} - \left.\frac{dP}{dT}\right|_{T} \Delta T^{n} \tag{B.2-7}$$

where the temperature error is defined by

$$\Delta T^{n} = T_{sat}\left(P^{n}\right) - T \tag{B.2-8}$$

and $T_{sat}\left(P^{n}\right)$ is evaluated from Equation (B.2-1). The iterations continue until $\left|\Delta T^{n}\right| < 1.E\text{-}4$ or $n > 10$. Convergence is usually achieved in 2 to 3 iterations and no instance has been observed where the iterations did not converge in less than 10 iterations.

B.2.1.3. Internal Energy of Saturated Steam (e_{sat})

For $P \le C_{21}$

$$e_{sat} = C_6 + C_7\left(\frac{1.0}{C_8 + P}\right) \tag{B.2-9}$$

For $P > C_{21}$

$$e_{sat} = C_{12} + (C_{14}P + C_{13})P \tag{B.2-10}$$

For $P \le C_{21}$

$$\frac{\partial e_{sat}}{\partial P} = -C_7\left(\frac{1.0}{C_8 + P}\right)^2 \tag{B.2-11}$$

and for $P > C_{21}$

$$\frac{\partial e_{sat}}{\partial P} = C_{13} + A_{17}P. \tag{B.2-12}$$

B.2.1.4. Heat Capacity of Saturated or Superheated Steam

$$C_{ps} = C_{52} + T_1(C_{53}\,T_1 + C_{54}) + \left(\frac{\frac{C_{55}}{T_1} + C_{56}}{T_1} \right) \tag{B.2-13}$$

and

$$\frac{\partial C_{ps}}{\partial P} = -A_{15}\frac{\partial T_{sat}}{\partial P}\left[C_{54} + 2C_{53}\,T_1 - \frac{\left(\frac{2C_{55}}{T_1} + C_{56}\right)}{T_1^2} \right] \tag{B.2-14}$$

where

$$T_1 = 1.0 - A_{15}\,T_{sat}. \tag{B.2-15}$$

B.2.1.5. Saturated Vapor and Saturated Fluid Water Enthalpy

$$h_g = e_{sat}\,\gamma_s \tag{B.2-16}$$

and

$$\frac{\partial h_g}{\partial P} = \frac{\partial e_{sat}}{\partial P}\gamma_s \tag{B.2-17}$$

where

$$\begin{aligned} \gamma_s &= C_9 + (C_{11}P + C_{10})P \text{ for } P \le C_{21} \\ &= C_{15} + (C_{17}P + C_{16})P \text{ for } P > C_{21} \end{aligned} \tag{B.2-18}$$

$$h_f = e_\ell(T_{sat}) + \frac{P}{\rho_\ell(T_{sat})} \tag{B.2-19}$$

$$\frac{\partial h_f}{\partial P} = \frac{\partial \rho_\ell}{\partial P}\bigg|_{T_{sat}} + \frac{1}{\rho_\ell(T_{sat})} - \frac{P}{\rho_\ell^2(T_{sat})}\frac{\partial \rho_\ell}{\partial T}\bigg|_{T_{sat}}\left(\frac{\partial T_{sat}}{\partial P} + \frac{\partial \rho_\ell}{\partial P}\right) \tag{B.2-20}$$

and e_ℓ, ρ_ℓ, and their derivatives are evaluated using the equations for liquid water properties given below in Section B.2.2.

B.2.2. Liquid Water Properties

Liquid water properties are specified in terms of the saturation pressure at the liquid temperature (*PSL*) that is evaluated as described in Section B.2.1.2 and the liquid temperature in Celsius that is denoted as *TLC* and is defined by

$$\mathrm{TLC} = \mathrm{T}_{\ell} - 273.15 \tag{B.2-21}$$

B.2.2.1. Liquid Water Internal Energy

$$\mathrm{ELP} = (\mathrm{P} - \mathrm{PSL})\left(\mathrm{C}_{\mathrm{k0}} + \mathrm{C}_{\mathrm{k2}}\,\mathrm{PSL}^2\right) \tag{B.2-22}$$

and

$$\mathrm{ERT} = \frac{-\mathrm{C}_{\mathrm{k0}} + \mathrm{C}_{\mathrm{k2}}\,(2\cdot\mathrm{PSL}\cdot\mathrm{p} - 3\cdot\mathrm{PSL}^2)}{\mathrm{A}_1\,(\mathrm{A}_{14}\cdot\mathrm{PSL})^{\mathrm{A}_2}}. \tag{B.2-23}$$

There are three temperature domains used in evaluating the liquid internal energy:

(1) $\mathrm{T}_{\ell} < 548.15$

(2) $548.15 \le \mathrm{T}_{\ell} \le 611.15$

(3) $\mathrm{T}_{\ell} > 611.15$

For $\mathrm{T}_{\ell} < 548.15$:

$$\begin{aligned}\mathrm{e}_{\ell} = {} & \mathrm{ELC0} + \mathrm{ELC1}\cdot\mathrm{TLC} + \mathrm{ELC2}\cdot\mathrm{TLC}^2 + \mathrm{ELC3}\cdot\mathrm{TLC}^3 \\ & + \mathrm{ELC4}\cdot\mathrm{TLC}^4 + \mathrm{ELP}.\end{aligned} \tag{B.2-24}$$

$$\frac{\partial \mathrm{e}_{\ell}}{\partial \mathrm{T}} = \mathrm{DELC0} + \mathrm{DELC1}\cdot\mathrm{TLC} + \mathrm{DELC2}\cdot\mathrm{TLC}^2 + \mathrm{DELC3}\cdot\mathrm{TLC}^3 + \mathrm{ERT}. \tag{B.2-25}$$

For $548.15 \le \mathrm{T}_{\ell} \le 611.15$:

$$\begin{aligned}\mathrm{e}_{\ell} = {} & \mathrm{ELD0} + \mathrm{ELD1}\cdot\mathrm{TLC} + \mathrm{ELD2}\cdot\mathrm{TLC}^2 + \mathrm{ELD3}\cdot\mathrm{TLC}^3 \\ & + \mathrm{ELD4}\cdot\mathrm{TLC}^4 + \mathrm{ELP}.\end{aligned} \tag{B.2-26}$$

$$\frac{\alpha \mathrm{e}_{\ell}}{\partial \mathrm{T}} = \mathrm{DELD0} + \mathrm{DELD1}\cdot\mathrm{TLC} + \mathrm{DELD2}\cdot\mathrm{TLC}^2 + \mathrm{DELD3}\cdot\mathrm{TLC}^3 + \mathrm{ERT}. \tag{B.2-27}$$

For $\mathrm{T}_{\ell} > 611.15$:

$$\begin{aligned}\mathrm{e}_{\ell} = {} & \mathrm{ELE0} + \mathrm{ELE1}\cdot\mathrm{TLC} + \mathrm{ELE2}\cdot\mathrm{TLC}^2 + \mathrm{ELE3}\cdot\mathrm{TLC}^3 \\ & + \mathrm{ELE4}\cdot\mathrm{TLC}^4 + \mathrm{ELP}.\end{aligned} \tag{B.2-28}$$

$$\frac{\alpha e_\ell}{\partial T} = DELE0 + DELE1 \cdot TLC + DELE2 \cdot TLC^2 + DELE3 \cdot TLC^3 + ERT. \quad \text{(B.2-29)}$$

For all three temperature domains:

$$\frac{\partial e_\ell}{\partial P} = C_{k0} + C_{k2} \cdot PSL^2. \quad \text{(B.2-30)}$$

B.2.2.2. Liquid Water Density

Define the pressure in units of bar as

$$PBAR = 1.0 \times 10^{-5} P \quad \text{(B.2-31)}$$

There are three temperature domains:

- (1) $T_\ell > 525.15$
- (2) $T_\ell < 521.15$
- (3) $521.15 \le T_\ell \le 525.15$

For $T_\ell > 525.15$:

$$\rho_\ell = 1.43 + \frac{1000}{\left(CVH1 + CVH2 \cdot PBAR + CVH3 \cdot PBAR^2 + \beta_1 \cdot TLC + \gamma_1 \cdot TLC^2\right)} \quad \text{(B.2-32)}$$

$$\frac{\partial \rho_\ell}{\partial P} = -(\rho_\ell - 1.43)^2 \cdot 1.0 \times 10^{-8} [CVH2 + 2 \cdot CVH3 \cdot PBAR + TLC(CVH5 + 2 \cdot CVH6 \cdot PBAR) + TLC^2 (CVH8 + 2 \cdot CVH9 \cdot PBAR)] \quad \text{(B.2-33)}$$

$$\frac{\partial \rho_\ell}{\partial T_\ell} = -(\rho_\ell - 1.43)^2 1.0 \times 10^{-3} (\beta_1 + 2 \cdot \gamma_1 \cdot TLC) \quad \text{(B.2-34)}$$

where

$$\beta_1 = CVH4 + CVH5 \cdot PBAR + CVH6 \cdot PBAR^2 \quad \text{(B.2-35)}$$

and

$$\gamma_1 = CVH7 + CVH8 \cdot PBAR + CVH9 \cdot PBAR^2. \quad \text{(B.2-36)}$$

For $T_\ell < 521.15$:

$$\rho_\ell = \frac{1000}{\left(CVL1 + CVL2 \cdot PBAR + CVL3 \cdot PBAR^2) + \beta_1 \cdot TLC + \gamma_1 \cdot TLC^2\right)} - 2.01 \quad \text{(B.2-37)}$$

$$\frac{\partial \rho_\ell}{\partial P} = -(\rho_\ell + 2.01)^2 \cdot 1.0 \times 10^{-8} [CVL2 + 2 \cdot CVL3 \cdot PBAR + TLC(CVL5 + 2 \cdot CVL6 \cdot PBAR) + TLC^2 (CVL8 + 2 \cdot CVL9 \cdot PBAR)] \quad \text{(B.2-38)}$$

$$\frac{\partial \rho_\ell}{\partial T_\ell} = -(\rho_\ell + 2.01)^2 \cdot 1.0 \times 10^{-3} (\beta_1 + 2 \cdot \gamma_1 \cdot TLC) \quad \text{(B.2-39)}$$

where

$$\beta_1 = CVL4 + CVL5 \cdot PBAR + CVL6 \cdot PBAR^2 \quad \text{(B.2-40)}$$

$$\gamma_1 = CVL7 + CVL8 \cdot PBAR + CVL9 \cdot PBAR^2 . \quad \text{(B.2-41)}$$

For $521.15 \le T_\ell \le 525.15$, an average of the functions in Equations (B.2-32) and (B.2-37) is used in this range. Call the two values $\rho_{\ell a}$ and $\rho_{\ell b}$, then:

$$\rho_\ell = \left(\frac{525.15 - T_\ell}{4.0}\right)\rho_{\ell b} + \left(\frac{T_\ell - 521.15}{4.0}\right)\rho_{\ell a} \quad \text{(B.2-42)}$$

$$\frac{\partial \rho_\ell}{\partial P} = \left(\frac{525.15 - T_\ell}{4.0}\right)\frac{\partial \rho_{\ell b}}{\partial P} + \left(\frac{T_\ell - 521.15}{4.0}\right)\frac{\partial \rho_{\ell a}}{\partial P} \quad \text{(B.2-43)}$$

$$\frac{\partial \rho_\ell}{\partial T_\ell} = \left(\frac{525.15 - T_\ell}{4.0}\right)\frac{\partial \rho_{\ell b}}{\partial T_\ell} + \left(\frac{T_\ell - 521.15}{4.0}\right)\frac{\partial \rho_{\ell a}}{\partial T_\ell} + \frac{\rho_{\ell a} - \rho_{\ell b}}{4.0}. \quad \text{(B.2-44)}$$

After evaluation above, a pressure correction is applied to ρ_ℓ and its derivatives. In the following, the values calculated in Equations (B.2-32) through (B.2-39) are denoted by a tilde (~).

a) $P \ge 4.0 \times 10^5$ Pa

$$\left(\frac{\partial \rho_\ell}{\partial T_\ell}\right)_P = \left(1 - \frac{1000}{P}\right)\left(\frac{\partial \tilde{\rho}_\ell}{\partial T_\ell}\right)_P \quad \text{(B.2-45)}$$

$$\left(\frac{\partial \rho_\ell}{\partial P}\right)_{T_\ell} = \left(1 - \frac{1000}{P}\right)\left(\frac{\partial \tilde{\rho}_\ell}{\partial P}\right)_{T_\ell} + \frac{1000\,\tilde{\rho}_\ell}{P^2} \quad \text{(B.2-46)}$$

$$\rho_\ell = \left(1 - \frac{1000}{P}\right)\tilde{\rho}_\ell . \quad \text{(B.2-47)}$$

b) $P \le 4.0 \times 10^5$ Pa

$$\left(\frac{\partial \rho_\ell}{\partial T_\ell}\right)_P = (0.995 + 6.25\times10^{-9}\,P)\left(\frac{\partial \tilde{\rho}_\ell}{\partial T_\ell}\right)_P \tag{B.2-48}$$

$$\left(\frac{\partial \rho_\ell}{\partial P}\right)_{T_\ell} = (0.995 + 6.25\times10^{-9}\,P)\left(\frac{\partial \tilde{\rho}_\ell}{\partial P}\right)_{T_\ell} + 6.25\,x\,10^{-9}\,\tilde{\rho}_\ell \tag{B.2-49}$$

$$\rho_\ell = (0.995 + 6.25\,x\,10^{-9}\,P)\,\tilde{\rho}_\ell\,. \tag{B.2-50}$$

B.2.2.3. Liquid Water Enthalpy

Enthalpy is not evaluated by the water property routines, but may be evaluated easily from

$$h_\ell = e_\ell + \frac{P}{\rho_\ell}. \tag{B.2-51}$$

B.2.3. Water Vapor Properties

B.2.3.1. Superheated Water Vapor

$(T_v - T_{sat}) > 0$.

B.2.3.1.1 Superheated Water Vapor Internal Energy

$$e_s = e_{sat} + A_{12}\left[(T_v - T_{sat}) + \left(T_v^2 - \beta\right)\right]^{1/2} - \frac{T_{sat}}{(A_{11}\,C_{ps} - 1.0)} \tag{B.2-52}$$

where

$$\beta = T_{sat}^2\left[1.0 - \frac{1.0}{(A_{11}\,C_{ps} - 1.0)^2}\right] \tag{B.2-53}$$

$$\frac{\partial e_s}{\partial T_v} = \left[\frac{A_{13}}{2}\left(1.0 - \frac{\beta}{k^2}\right)\right]^{-1.0} \tag{B.2-54}$$

$$k = A_{13}\,(e_s - e_{sat}) + T_{sat}\left[1.0 + \frac{1.0}{(A_{11}\,C_{ps} - 1.0)}\right] \tag{B.2-55}$$

$$\frac{\partial e_s}{\partial P} = -\frac{1}{2}\left(\frac{\partial e_s}{\partial T_v}\right)\left[\left(1.0 - \frac{\beta}{k^2}\right)\frac{\partial k}{\partial P} + \frac{1}{k}\frac{\partial \beta}{\partial P}\right] \tag{B.2-56}$$

$$\frac{\partial k}{\partial P} = -A_{13}\frac{\partial e_{sat}}{\partial P} + \left[1.0 + \frac{1.0}{(A_{11}C_{ps} - 1.0)}\right]\frac{\partial T_{sat}}{\partial P} - T_{sat}A_{11}\left[\frac{1.0}{(A_{11}C_{ps} - 1.0)^2}\right]\frac{\partial C_{ps}}{\partial P} \quad \text{(B.2-57)}$$

and

$$\frac{\partial \beta}{\partial P} = \frac{2.0}{T_{sat}}\left[\beta\left(\frac{\partial T_{sat}}{\partial P}\right) + \frac{T_{sat}^3 A_{11}}{(A_{11}C_{ps} - 1.0)^3}\right]\left(\frac{\partial C_{ps}}{\partial P}\right). \quad \text{(B.2-58)}$$

B.2.3.1.2 Superheated Water Vapor Density

$$\rho_s = \frac{P}{[(\gamma_s - 1.0)e_{sat} + C_{26}(e_s - e_{sat})]} \quad \text{(B.2-59)}$$

$$\frac{\partial \rho_s}{\partial T_v} = -\left(\frac{\partial e_s}{\partial T_v}\right)\left[\frac{C_{26}\rho_s}{(\gamma_s - 1.0)e_{sat} + C_{26}(e_s - e_{sat})}\right] \quad \text{(B.2-60)}$$

and

$$\frac{\partial \rho_s}{\partial P} = \rho_s\left\{\left[\frac{1.0}{P} - e_{sat}\left(\frac{\partial \gamma_s}{\partial P}\right) + (\gamma_s - 1.0 - C_{26})\frac{\partial e_{sat}}{\partial P}\right]\left[\frac{1.0}{(\gamma_s - 1.0)e_{sat} + C_{26}(e_s - e_{sat})}\right]\right\} + \left(\frac{\partial \rho_s}{\partial e_s}\right)\left(\frac{\partial e_s}{\partial P}\right) \quad \text{(B.2-61)}$$

where

$$\frac{\partial \gamma_s}{\partial P} = \begin{cases} C_{10} + A_{16}P & , P \le C_{21} \\ C_{16} + A_{18}P & , P > C_{21} \end{cases} \quad \text{(B.2-62)}$$

and

$$\frac{\partial \rho_s}{\partial e_s} = \frac{-C_{26}\rho_s}{[(\gamma_s - 1.0)e_{sat} + C_{26}(e_s - e_{sat})]}. \quad \text{(B.2-63)}$$

If ρ_s exceeds $0.9\rho_\ell$ or is < 0, Equations (B.2-59), (B.2-60), and (B.2-61) are superseded by

$$\rho_s = 0.9\rho_\ell \quad \text{(B.2-64)}$$

$$\frac{\partial \rho_s}{\partial T_v} = 0.9 \left(\frac{\partial \rho_\ell}{\partial T_\ell} \right) \tag{B.2-65}$$

and

$$\frac{\partial \rho_s}{\partial P} = 0.9 \left(\frac{\partial \rho_\ell}{\partial P} \right) \tag{B.2-66}$$

B.2.3.1.3 Superheated Water Vapor Enthalpy

Enthalpy is not evaluated by the water property routines, but may be calculated easily from

$$h_s = e_s + \frac{P}{\rho_s} . \tag{B.2-67}$$

B.2.3.2. Sub-cooled and Saturated Water Vapor

$(T_v - T_{sat}) \leq 0.$

B.2.3.2.1 Sub-cooled and Saturated Water Vapor Internal Energy

$$e_s = e_{sat} + (T_v - T_{sat}) \frac{C_{ps}}{C_{24}} \tag{B.2-68}$$

$$\frac{\partial e_s}{\partial T_v} = \frac{C_{ps}}{C_{24}} \tag{B.2-69}$$

$$\frac{\partial e_s}{\partial P} = -\left(\frac{\partial e_s}{\partial T_v} \right) \left\{ \frac{\partial T_{sat}}{\partial P} - \left(\frac{C_{24}}{C_{ps}} \right) \left[\frac{\partial e_{sat}}{\partial P} + \frac{(e_s - e_{sat})}{C_{ps}} \left(\frac{\partial C_{ps}}{\partial P} \right) \right] \right\} \tag{B.2-70}$$

B.2.3.1.2 Sub-cooled and Saturated Water Vapor Density

The formulas are identical to the superheated vapor case above, but the sub-cooled vapor energy is used in this case.

B.2.3.2.3 Sub-cooled and Saturated Water Vapor Enthalpy

Enthalpy is not evaluated by the water property routines, but may be calculated easily from

$$h_s = e_s + \frac{P}{\rho_s} . \tag{B.2-71}$$

B.2.4. Noncondensable Gases (NCG)

TRACG04 can calculate the nodal masses of up to 99 indivual noncondensable gases (NCG). By default, a single noncondensable gas is assumed to be air unless it is respecified by the user input. The user input for each NCG has been enhanced in TRACG04 so that both thermodynamic and transport properties of each gas can be calculated. Each NCG is modeled as an ideal gas. The transport and thermodynamic properties for mixtures of these gases are also calculated to determine the impact on the gas momentum equation and the nodal pressures in the pressure network solution. For each NCG (n), values for the following four constants are needed to calculate the properties: (1) constant volume specific heat ($c_{vn}[J/(kg\cdot K)]$), (2) molecular weight (M_{Wn}[kg-mole]), (3) Lennard-Jones parameter for collision diameter ($\sigma_n\left[\text{Å}\right]$), and (4) Lennard-Jones parameter for characteristic energy ($\left(\varepsilon/k\right)_n[K]$). The user is assisted in definining these four inputs because built-in values are available for the following gases: air, argon, carbon monoxide, carbon dioxided, di-atomic hydrogen, steam, mono-atomic helium, di-atomic nitrogen and di-atomic oxygen. See the TRACG04 User's Manual for the values of the built-in constants. Note that the option for modeling steam as an ideal gas is provided only to allow comparisons with other codes that make this approximation; steam does not behave like an ideal gas at most pressures and temperatures of interest so use of this option is not recommended for most applications.

TRACG02 required the gas constant (R_n) for the NCG that was being modeled and contained a built-in value for air. TRACG04 requires the molecular weight instead because the molecular weight is needed when determining the properties of mixtures of noncondensable gases. TRACG04 calculates the value of R_n from the universal gas constant (R_u) by applying the familiar relationship

$$R_n = \frac{R_u}{M_{Wn}} \tag{B.2-72}$$

where the value $R_u = 8314.339009\ [N\cdot m/(\text{kg-mole}\cdot K)]$ is built into the code.

B.2.4.1. NCG Density determined from NCG Pressure and Vapor Temperature

$$\rho_n = \frac{P_n}{R_n T_v} \tag{B.2-73}$$

$$\rho_a = \sum_{n=1}^{N}\rho_n = \frac{1}{T_v}\sum_{n=1}^{N}\frac{P_n}{R_n} = \frac{P_a}{R_a T_v} \tag{B.2-74}$$

$$P_a = \sum_{n=1}^{N} P_n \tag{B.2-75}$$

$$R_a = \frac{\sum_{n=1}^{N} \rho_n R_n}{\sum_{n=1}^{N} \rho_n R_n} = \frac{1}{\rho_a} \sum_{n=1}^{N} \rho_n R_n \quad \text{(B.2-76)}$$

$$\frac{\partial \rho_n}{\partial P_n} = \frac{1.0}{R_n T_v} \quad \text{(B.2-77)}$$

$$\frac{\partial \rho_a}{\partial P_a} = \frac{1.0}{R_a T_v} \quad \text{(B.2-78)}$$

$$\frac{\partial \rho_n}{\partial T_v} = \frac{-P_n}{R_n T_v^2} \quad \text{(B.2-79)}$$

$$\frac{\partial \rho_a}{\partial T_v} = \frac{-P_a}{R_a T_a^2} \quad \text{(B.2-80)}$$

The gas constant (R_a) as defined for the NCG mixture in Equation (B.2-76) depends on the local composition of the NCG mixture. A nodal gas constant defined in this way is useful because it allows the effects of multiple NC gases on the nodal pressure to be treated without individually considering each NCG species. Of course, it is still necessary to transport the individual NC gases in order to solve the nodal mass conservation equations for each NCG species.

B.2.4.2. NCG Internal Energy determined from Vapor Temperature

$$e_n = c_{vn} T_v \quad \text{(B.2-81)}$$

$$\rho_a e_a = \sum_{n=1}^{N} \rho_n e_n = \sum_{n=1}^{N} \rho_n c_{vn} T_v \quad \text{(B.2-82)}$$

$$e_a = \frac{1}{\rho_a} \sum_{n=1}^{N} \rho_n e_n = \frac{1}{\rho_a} \sum_{n=1}^{N} \rho_n c_{vn} T_v = c_{va} T_v \quad \text{(B.2-83)}$$

$$c_{va} = \frac{1}{\rho_a} \sum_{n=1}^{N} \rho_n c_{vn} \quad \text{(B.2-84)}$$

$$\frac{\partial e_n}{\partial T_v} = c_{vn} \quad \text{(B.2-85)}$$

$$\frac{\partial e_a}{\partial T_v} = c_{va} \quad \text{(B.2-86)}$$

$$\frac{\partial e_n}{\partial P_n} = 0.0 \tag{B.2-87}$$

$$\frac{\partial e_a}{\partial P_a} = 0.0 \tag{B.2-88}$$

The constant volume specific heat (c_{va}) as defined for the NCG mixture in Equation (B.2-84) depends on the local composition of the NCG mixture. A nodal value of c_{va} defined in this way is useful because it allows the effects of multiple NC gases in the nodal equations for the vapor energy to be considered without individually considering each NCG species. Of course, it is still necessary to transport the individual NC gases in order to solve the nodal mass conservation equations for each NCG species.

B.2.4.3. Thermodynamic Properties of NCG and Steam Mixtures

In accordance with Dalton's law, the density of a mixture of steam and one or more noncondensable gases is the sum of the partial densities of all the components

$$\rho_v = \rho_s + \rho_a = \rho_s + \sum_{n=1}^{N} \rho_n \tag{B.2-89}$$

Similarly, the internal energy of a mixture of steam and noncondensable gas is given by the density-weighted average of the internal energies of all the components

$$e_v = \frac{(\rho_s e_s + \rho_a e_a)}{(\rho_s + \rho_a)} = \frac{\left(\rho_s e_s + \sum_{n=1}^{N} \rho_n e_n\right)}{\left(\rho_s + \sum_{n=1}^{N} \rho_n\right)} \tag{B.2-90}$$

B.3. Transport Properties

B.3.1. Water Transport Properties

Subroutine FPROP is used in TRACG to obtain transport properties for water. The input variables for this routine are (a) the saturation temperature, (b) pressure, (c) enthalpies of each phase, (d) vapor density, and (e) the vapor temperature. The output transport variables include (a) the latent heat of vaporization, (b) surface tension, (c) constant pressure specific heat, (d) viscosity, and (e) thermal conductivity of each phase. The transport property calls are function calls from within subroutine FPROP. The polynomial equation fits for the water transport properties used in FPROP are described below. Values of the constants are given in Table B-3 through Table B-6.

Transport properties for noncondensable gases are described separately in Section B.3.2 of this appendix.

B.3.1.1. Latent Heat of Vaporization for Water

$$h_{fg} = h_g - h_f \tag{B.3-1}$$

where h_g is calculated using Equation (B.2-16) and

$$h_f = e_\ell + \frac{P}{\rho_\ell} \tag{B.3-2}$$

where e_ℓ and ρ_ℓ are calculated at saturation conditions according to Section B.2.2.

B.3.1.2. Constant Pressure Specific Heats for Water

Constants used in this section are given in Table B-3.

$$c_{p\ell} = \left\{ h_\ell \left[h_\ell \left(D_{0\ell} + D_{1\ell} P \right) + \left(C_{0\ell} + C_{1\ell} P \right) \right] + B_{0\ell} + B_{1\ell} P \right\}^{-1} \tag{B.3-3}$$

$$c_{ps} = C_{1s} + C_{2s} T_v + \frac{C_{3s} P_s}{\left(C_{5s} T_v - C_{6s} \right)^{2.4}} + \frac{C_{4s} P_s^3}{\left(C_{5s} T_v - C_{6s} \right)^9} . \tag{B.3-4}$$

where the $P_s = P - P_a$ is the partial pressure of the steam.

B.3.1.3. Fluid Viscosities for Water

B.3.1.4. Fluid Viscosity for Liquid Water

Constants used in this section are given in Table B-4. The evaluation of liquid viscosity is divided into three different enthalpy ranges:

- (1) $h_\ell \le h_1$
- (2) $h_1 < h \le h_2$
- (3) $h_\ell > h_2$

For $h_\ell \le h_1$:

$$\mu_\ell = \left(A_{0\ell} + A_{1\ell}x + A_{2\ell}x^2 + A_{3\ell}x^3 + A_{4\ell}x^4\right) - \left(B_{0\ell} + B_{1\ell}\eta + B_{2\ell}\eta^2 + B_{3\ell}\eta^3\right)(P - P_i) \quad \text{(B.3-5)}$$

where

$$x = (h_\ell - c_{0n})h_0 \quad \text{(B.3-6)}$$

and

$$\eta = (h_\ell - e_{c0n})e_{h0}. \quad \text{(B.3-7)}$$

In the range $h_1 < h \le h_2$

$$\mu_\ell = \left(E_{0\ell} + E_{1\ell}h_\ell + E_{2\ell}h_\ell^2 + E_{3\ell}h_\ell^3\right) + \left(F_{0\ell} + F_{1\ell}h_\ell + F_{2\ell}h_\ell^2 + F_{3\ell}h_\ell^3\right)(P - P_i). \quad \text{(B.3-8)}$$

For $h_\ell > h_2$

$$\mu_\ell = \left(D_{0\ell} + D_{1\ell}z + D_{2\ell}z^2 + D_{3\ell}z^3 + D_{4\ell}z^4\right) \quad \text{(B.3-9)}$$

where

$$z = (h_\ell - c_n)h_{00}. \quad \text{(B.3-10)}$$

B.3.1.5. Fluid Viscosity for Water Vapor

Constants used in this section are given in Table B-5. Three vapor temperature ranges are used to represent the data:

- (1) $T_v \le T_1$
- (2) $T_1 < T_v < T_2$
- (3) $T_v \ge T_2$

For $T_v \le T_1$:

$$\mu_s = \left[B_{1g} (T_v - 273.15) + C_{1g} \right] - \rho_s \left[D_{1g} - E_{1g} (T_v - 273.15) \right]. \quad \text{(B.3-11)}$$

If $\mu_s < 10^{-7}$ is calculated, then it is reset so $\mu_s = 10^{-7}$.

For $T_1 < T_v < T_2$:

$$\begin{aligned} \mu_s = {} & B_{1g} (T_v - 273.15) + C_{1g} - \rho_s \left[F_{1g} + F_{2g} (T_v - 273.15) \right. \\ & \left. + F_{3g} (T_v - 273.15)^2 + F_{4g} (T_v - 273.15)^2 \right] \\ & + \rho_s \left[G_{1g} + G_{2g} (T_v - 273.15) + G_{3g} (T_v - 273.15)^2 \right. \\ & \left. + G_{4g} (T_v - 273.15)^3 \right] \left(A_{0g} + A_{1g} \rho_s + A_{2g} \rho_s^2 \right). \end{aligned} \quad \text{(B.3-12)}$$

For $T_v \ge T_2$:

$$\mu_s = B_{1g} (T_v - 273.15) + C_{1g} - \rho_s \left(A_{0g} + A_{1g} \rho_s + A_{2g} \rho_s^2 \right). \quad \text{(B.3-13)}$$

B.3.1.6. Fluid Thermal Conductivities for Water

Thermal Conductivity for Liquid Water

The thermal conductivity for liquid water is given by:

$$k_\ell = A_{\ell 0} + A_{\ell 1} x_k + A_{\ell 2} x_k^2 + A_{\ell 3} x_k^3 \qquad \text{(B.3-14)}$$

where

$$x_k = \frac{h_\ell}{h_0} \qquad \text{(B.3-15)}$$

The constants are given in Table B-6.

Thermal Conductivity for Water Vapor

For the water vapor, the thermal conductivity is given by:

$$k_s = x_1 + \rho_s \left[x_2 + \frac{C\rho_s}{(T_v - 273.15)^{4.2}} \right] \qquad \text{(B.3-16)}$$

where

$$x_1 = A_{g0} + A_{g1}(T_v - 273.15) + A_{g2}(T_v - 273.15)^2 + A_{g3}(T_v - 273.15)^3 \qquad \text{(B.3-17)}$$

and

$$x_2 = B_{g0} + B_{g1}(T_v - 273.15) + B_{g2}(T_v - 273.15)^2 . \qquad \text{(B.3-18)}$$

The constants are given in Table B-6.

B.3.1.7. Surface Tension for Water

The surface tension for water is calculated from

$$\sigma = \begin{cases} S_{21}TR^2 + S_3TR^3 + S_4TR^4 + S_5TR^5 & , T_{sat} < 647.3 \\ 0 & , T_{sat} \geq 647.3 \end{cases} \quad \text{(B.3-19)}$$

where

$$TR = 647.3 - T_{sat} \quad \text{(B.3-20)}$$

$$S_0 = 0.83 \quad \text{(B.3-21)}$$

$$S_1 = 1.160936807 \times 10^{-4} \quad \text{(B.3-22)}$$

$$S_2 = 1.12140468 \times 10^{-6} \quad \text{(B.3-23)}$$

$$S_3 = -5.752805180 \times 10^{-9} \quad \text{(B.3-24)}$$

$$S_4 = 1.286274650 \times 10^{-11} \quad \text{(B.3-25)}$$

$$S_5 = -1.149719290 \times 10^{-14} \quad \text{(B.3-26)}$$

$$S_{21} = S_2 + \left(\frac{S_1}{1 + S_0 TR} \right) \quad \text{(B.3-27)}$$

B.3.2. NCG Transport Properties

B.3.2.1. Constant Pressure Specific Heat for Noncondensable Gases

Previously TRACG02 modeled the constant pressure specific heat assuming that the NCG was air. For TRACG04, the modeling is extended to include each individual NCG species.

For an ideal gas "n", the constant pressure specific heat is related to the constant volume specific heat by

$$c_{pn} = R_n + c_{vn} \tag{B.3-28}$$

It follows from the definitions of R_a and c_{va} developed previously that for the composite mixture of all NC gases that

$$c_{pa} = R_a + c_{va} \tag{B.3-29}$$

B.3.2.2. Fluid Viscosity for Noncondensable Gases

Previously TRACG02 modeled the fluid viscosity assuming that the NCG was air. For TRACG04, the absolute fluid viscosity for each individual NCG species (μ_n) is calculated as a function of the gas mixture temperature (T_v) using the general Chapman-Enskog treatment described in Equation (9-3.9) of Reference [206].

$$\mu_n \left[N \cdot s \cdot m^{-2} \right] = 26.69\text{E-}7 \ \frac{\sqrt{M_{Wn} T_v}}{\sigma_n^2 \Omega_{vn}} \tag{B.3-30}$$

where for each NCG species "n"

M_{Wn}[kg-mole] is the molecular weight of the NCG species as determined from the built-in values for select gases or the user input, $\sigma_n \left[\text{Å} \right]$ is the Lennard-Jones parameter for collision diameter as determined from the built-in values for select gases or the user input, and Ω_{vn} is the calculated *collision integral*.

The collision integral has a value of unity if the molecules do not attract each other. The collision integral is related to the dimensionless temperature (T_n^*) which is the absolute temperature divided by the Lennard-Jones parameter for characteristic energy ($\left(\varepsilon/k\right)_n$ [K]). Values of $\left(\varepsilon/k\right)_n$ are determined from built-in values for select gases or the user input. The collision integral for each NCG species is evaluated using Neufel's empirical equation provided as Equation (9-4.3) in Reference [206].

$$\Omega_{vn} = A\left(T_n^*\right)^{-B} + C + E \tag{B.3-31}$$

where

$$T_n^* = \frac{T_v}{\left(\varepsilon/k\right)_n} \tag{B.3-32}$$

$$A = 1.16145 \tag{B.3-33}$$

$$B = 0.14874 \tag{B.3-34}$$

$$C = \begin{cases} 0.52487\exp\left(-D\cdot T_n^*\right) & ,D\cdot T_n^* < 40 \\ 0 & ,D\cdot T_n^* \geq 40 \end{cases} \tag{B.3-35}$$

$$D = 0.77320 \tag{B.3-36}$$

$$E = \begin{cases} 2.16178\exp\left(-F\cdot T_n^*\right) & ,F\cdot T_n^* < 40 \\ 0 & ,F\cdot T_n^* \geq 40 \end{cases} \tag{B.3-37}$$

$$F = 2.43787 \tag{B.3-38}$$

Zero values for "C" and "E" are used for large values of T_n^* to eliminate the need to evaluate the associated exponential term for cases where underflow may occur.

B.3.2.3. Fluid Thermal Conductivity for Noncondensable Gases

Previously TRACG02 modeled the fluid thermal conductivity assuming that the NCG was air. For TRACG04, the fluid thermal conductivity (k_n) for each individual NCG species is calculated as a function of the gas mixture temperature (T_v) using Equation (10-2.2) of Reference [206].

$$k_n\left[J/\left(m\cdot s\cdot K\right)\right] = 418.68\left(1.989\text{E-}4\ \frac{\sqrt{T_v/M_{Wn}}}{\sigma_n^2\Omega_{vn}}\right) \tag{B.3-39}$$

The "418.68" factor in Equation (B.3-39) converts the expression from units of cal/(cm.s.K) to units of J/(m.s.K). Note the similarity between Equation (B.3-39) and the expression for absolute fluid viscosity in Equation (B.3-30) of Section B.3.2.2. The other terms on the RHS of (B.3-39) were defined in Section B.3.2.2.

B.3.3. Transport Properties of NCG and Steam Mixtures

B.3.3.1. Constant Pressure Specific Heat of NCG and Steam Mixtures

The constant pressure specific heats are used in some heat transfer correlations, so it is useful to define how this quantity is evaluated for a mixture of steam and noncondensable gases. The constant pressure specific heat for steam as given by Equation (B.3-4) in Section B.3.1.2 depends on the steam partial pressure which is related to the total pressure and the partial pressure of the noncondensable gas mixture by $P_s = P - P_a$. As the amount of noncondensable gases increases relative to the amount of steam, the partial density of the noncondensable gases relative to the partial density of steam also increases. The impact that this has on the specific heat of the mixture of steam and noncondensable gases is modeled as

$$c_{pv} = \frac{1}{\rho_v}\left(\rho_s c_{ps} + \rho_a c_{pa}\right) \tag{B.3-40}$$

where c_{ps} is defined by Equation (B.3-4) and c_{pa} is defined by Equation (B.3-29).

B.3.3.2. Absolute Fluid Viscosity of NCG and Steam Mixtures

The absolute viscosity of gas mixtures is calculated using the component gas viscosities and kinetic theory of Chapman-Enskog as described in Section 9-5 of Reference [206]. Neglecting second-order effects, the rigorous solution is approximated as indicated in Equation (9-5.1) of Reference [206] by the series

$$\mu_v = \sum_{i=0}^{N} \frac{y_i \mu_i}{\sum_{j=0}^{N} y_j \phi_{ij}} \tag{B.3-41}$$

The "i" and "j" subscripts indicate the component gases and "y" is the mole fraction. For convenience, an index of value of zero is used to denote steam so that the NCG components are denoted by subscript values from 1 to N. The absolute viscosity for steam corresponding to $\mu_0 = \mu_s$ is determined from Equations (B.3-11), (B.3-12) and (B.3-13). The absolute viscosities for the NCG components corresponding to indices 1,…,N are determined from Equation (B.3-30). Wilke's approximation to Sutherland's kinetic theory model is applied to estimate the ϕ_{ij} parameters from

$$\phi_{ij} = \frac{\left[1 + \left(\mu_i / \mu_j\right)^{\frac{1}{2}} \left(M_{Wj} / M_{Wi}\right)^{\frac{1}{4}}\right]^2}{\left[8\left(1 + M_{Wi} / M_{Wj}\right)\right]^{\frac{1}{2}}} \tag{B.3-42}$$

The definition of mole fractions can be applied to Equation (B.3-41) to get the more

convenient form in terms of partial densities

$$\mu_v = \sum_{i=0}^{N} \frac{\frac{\rho_i}{M_{Wi}}\mu_i}{\sum_{j=0}^{N} \frac{\rho_j}{M_{Wj}}\phi_{ij}} = \sum_{i=0}^{N} \frac{\rho_i \mu_i}{\sum_{j=0}^{N} \rho_j \frac{M_{Wi}}{M_{Wj}}\phi_{ij}} \tag{B.3-43}$$

B.3.3.3. Fluid Thermal Conductivity of NCG and Steam Mixtures

The thermal conductivity of gas mixtures is calculated using the component gas thermal conductivities and the Mason and Saxena modification for Wassijewa's equation as described in Section 10-6 of Reference [206]. Then analogous to the expression for the absolute fluid viscosity for a mixture, the expression for the thermal conductivity for a mixture of gases becomes

$$k_v = \sum_{i=0}^{N} \frac{\frac{\rho_i}{M_{Wi}}k_i}{\sum_{j=0}^{N} \frac{\rho_j}{M_{Wj}}\phi_{ij}} = \sum_{i=0}^{N} \frac{\rho_i k_i}{\sum_{j=0}^{N} \rho_j \frac{M_{Wi}}{M_{Wj}}\phi_{ij}} \tag{B.3-44}$$

As before, index 0 is used for the steam and indices 1,…,N are used for the noncondensable gases. The thermal conductivity for steam corresponding to $k_0 = k_s$ is determined from Equation (B.3-16) and the thermal conductivities for the NCG components corresponding to indices 1,…,N are determined from Equation (B.3-39). The expression for ϕ_{ij} from Equation (B.3-42) applies except that the viscosity ratio μ_i / μ_j is replaced by the conductivity ratio k_i / k_j.

B.3.4. Boron Solubility Limits

In TRACG04 the elemental boron concentrations are defined relative to the density of the water mixture instead of the density of the liquid water only as was done in prior versions of TRACG. This change was made so that the definition of boron concentration in TRACG04 will be identical to the definition used in TGBLA06. PANAC11 relies on the boron concentrations defined by TGBLA06 so by assuring consistency with TGBLA06 we are also assuring consistency with PANAC11. The boron solubility limit ($c_{b,max}$) for a fluid node is defined as a function of the liquid temperature (T_ℓ) for the node as the maximum ratio of elemental boron mass in solution to water mass in the node. This revised definition for TRACG04 is consistent with how elemental boron concentrations are defined and applied and provides the flexibility to model different borated molecules. The TRACG04 functional form defining the solubility limit for elemental boron is [[

]]

For purposes of relating these TRACG04 constants to those used previously, it is useful to introduce the factor "f" defined by

$$f = \frac{M_{Bm}\left[E_{B10} \cdot W_{B10} + (1 - E_{B10}) W_{B11}\right]}{W_{Bm}} \qquad \text{(B.3-51)}$$

where

W_{B10} is the atomic weight of B10 atoms and

W_{B11} is the atomic weight of B11 atoms.

The remaining terms have the same definition as in Section 9.5.

E_{B10} is the fraction of boron atoms that are B10 atoms (Default=0.198);

M_{Bm} is the number of boron atoms in the boron molecule that is being modeled (Default=1.0);

W_{Bm} is the molecular weight of the boron molecule (Default=10.812025).

For the default configuration where the boron is expressed as elemental boron, the value of f is 1.0 for any enrichment. For sodium pentaborate with naturally enriched boron ($E_{B10} = 0.198$) the value of f is 0.183186. The factor f is useful because it allows the elemental concentration of boron (C_B) in parts per million (ppm) to be simply expressed for any boron molecule at any B10 enrichment using the following transformation

$$C_B\left[\text{ppm}\right] = f \cdot 10^6 \cdot \frac{\rho_B\left[\text{kg/m}^3\right]}{\rho_{H2O}\left[\text{kg/m}^3\right]} \tag{B.3-52}$$

where ρ_{H2O} is the density of water at the local conditions. For the default model where elemental boron is assumed and $f = 1.0$ for all enrichments, the local elemental boron concentration is easily related to the ratio of the local boron density to the local water density. Table B-7 shows how the boron density at a FILL can be adjusted to achieve the same concentration of B10 atoms depending on the molecular weight and the number of boron atoms in the borated molecule. Thus for the default model to achieve an elemental boron concentration of 1000 ppm in sub-cooled water at 20ºC and a pressure of 1 bar where the water density is 998.232 kg/m3, the boron density must be 0.998232 kg/m3 as indicated in Table B-7. It is anticipated that most applications will not need to model the complexities of the actual boron molecule because it is not necessary to account for the boron mass. For most applications, it is sufficient to account for only the effect that B10 has on neutron absorption and this can be done using elemental boron; nevertheless, the flexibility to model other boron molecules has been provided.

The TRACG04 values [[ ]] in terms of elemental boron can be related to the values expressed in TRACG02 where the borated molecule was assumed to be sodium pentaborate with natural boron. Let "z" be the TRACG04 value and "y%" be the TRACG02 value, then the relationship is

$$z = \frac{f_y \cdot y\%}{100\% - y\%} \tag{B.3-53}$$

where $f_y = 0.183186$ is simply the value obtained from Equation (B.3-51) for naturally enriched sodium pentaborate where $E_{B10} = 0.198$ and $W_{Bm} = 590.22194$. [[

]] Figure B-1 depicts the same boron solubility data plotted using

the two different scales where the “y%” scale is on the left and the “z” scale is on the right. [[

]] Figure B-2 illustrates how the TRACG04 model for boron solubility (with default values for the coefficients) compares with the tabulated solubility data for sodium pentaborate.

Table B-7. Relationships between BORCIN and the Characteristics of the Boron Molecule

Description	Enrichment: fraction of boron atoms that are B10 atoms	Number of Boron atoms in the Boron Molecule	Molecular Weight of the Boron Molecule	Boron density specified for a FILL
Symbol	E_{B10}	M_{Bm}	W_{Bm}	ρ_B
Code Input Name	AB10	BORNUM	BORMWT	BORCIN
Units	none	atoms/molecule	gm/gm-mole	kg/m^3
Value for elemental boron (DEFAULT)	0.198	1.0	10.812025	0.998232*
Value for sodium pentaborate $Na_2O \cdot 5B_2O_3 \cdot 10H_2O$	0.198	10.0	590.22194	5.449288*

* Values are those corresponding to an elemental boron concentration of 1000 ppm in sub-cooled water at 20ºC and a pressure of 1 bar. At these conditions, the liquid water density is 998.232 kg/m^3.

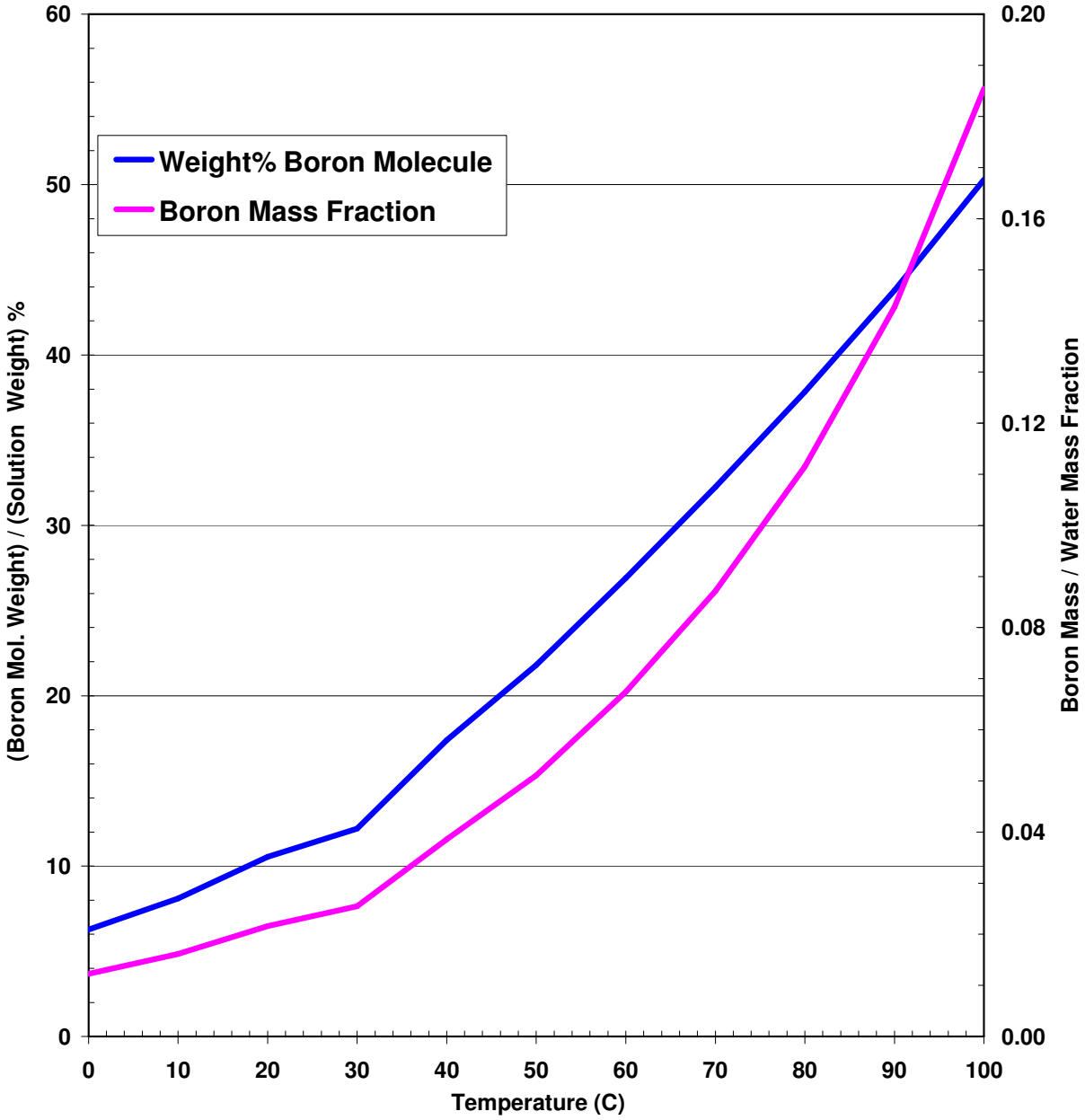

Figure B-1. Simulation of Supplier's Solubility Limits Expressed in TRACG02A and TRACG04 Forms

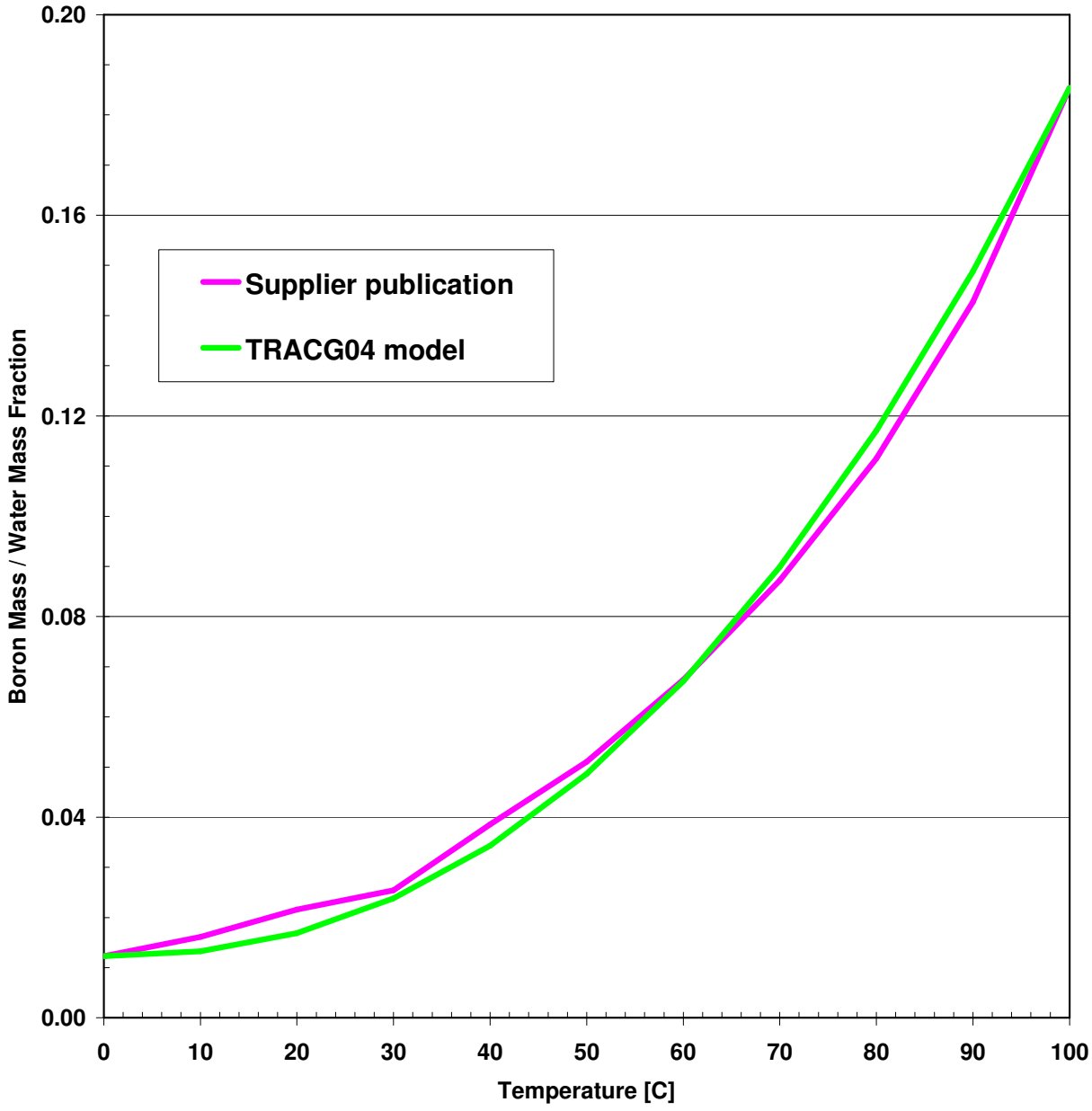

Figure B-2. TRACG04 Model for Elemental Boron Solubility

B.4. Verification of Water Thermodynamic and Transport Properties

The TRACG thermodynamic and transport fluid properties for water are consistent with the properties used in TRAC-BD1. These properties have been compared to steam table data over a wide range of conditions in Reference [202]. This assessment found good agreement for both thermodynamic and transport properties throughout the saturation and non-equilibrium regions. Additional assessment to confirm this conclusion was performed by comparing the TRACG values to ASME steam table values. A summary of these comparisons is provided in Table B-8 through Table B-10.

Table B-8. Comparison of Saturation Properties (14.7 < P < 1500 psia)

Property	RMS Error*(%)		
		Liquid	Vapor
Saturation Temperature	0.17		
Enthalpy		0.16	0.07
Specific Volume		0.23	0.49
Specific Heat		2.94	5.13
Thermal Conductivity		2.28	0.17
Viscosity		2.27	0.14
Surface Tension	0.21		

*Error = (ASME-TRACG)/ASME

Table B-9. RMS Error* (%) of Sub-cooled Liquid Properties ($100°F < T < T_{sat}$)

	Pressure (psia)						
Property	14.7	250	500	750	1000	1250	1500
Enthalpy	1.78	0.84	0.56	0.43	0.48	0.63	0.82
Specific Volume	0.20	0.20	0.18	0.19	0.22	0.23	0.24
Specific Heat	0.38	0.27	0.23	0.30	0.42	0.60	0.89
Thermal Conductivity	0.72	1.07	1.09	1.10	0.98	0.84	0.68
Viscosity	2.16	2.95	2.71	2.47	2.18	1.91	1.70

*Error = (ASME-TRACG)/ASME

Table B-10. RMS Error* (%) of Superheated Steam Properties (1500°F > T > Tsat)

Property	Pressure (psia)						
	14.7	**250**	**500**	**750**	**1000**	**1250**	**1500**
Enthalpy	0.74	0.52	0.33	0.30	0.55	0.96	1.59
Specific Volume	0.40	2.35	1.86	1.30	0.55	0.74	2.16
Specific Heat	1.16	1.25	1.38	1.21	1.10	0.67	0.87
Thermal Conductivity	< 0.01	0.05	0.07	0.07	0.05	0.13	0.38
Viscosity	< 0.01	0.03	0.06	0.10	0.15	0.21	0.31

*Error = (ASME-TRACG)/ASME

APPENDIX C. Material Properties

A library of temperature-dependent material properties is incorporated in the TRACG code. There are 10 sets of materials properties that comprise the library, each set supplying values for thermal conductivity, specific heat, density, and spectral emissivity for use in heat transfer calculations. The first five sets contain properties for nuclear-heated or electrically-heated fuel rod simulation. Included are nuclear fuel, zircaloy cladding and electrical heater rod insulating material. The last five sets are for structural materials, including stainless steels, carbon steel, Inconel and concrete. The material indices used in the library are:

- Mixed oxide fuel
- Zircaloy
- Zirconium oxide
- ATLAS heater rod insulator
- Boron nitride insulation
- Stainless steel, Type 304
- Stainless steel, Type 316
- Carbon steel, Type A508
- Inconel, Type 600
- Concrete

The material properties in TRACG are consistent with the properties found in the GE BWR Materials Properties Handbooks[208],[212]. The properties contained in these handbooks are verified and controlled and must be used for all design applications. The application of these material properties in TRACG is consistent with all other licensed GEH computer codes.

In addition to the library of built-in material properties, the code provides for user-supplied tables of material properties. When tables versus temperature are provided, linear interpolation is used to evaluate the property.

The nomenclature used in this appendix is consistent with the terminology defined in Section 6.0. Additional quantities are defined locally in this appendix only when they are not already defined in Section 6.0.

C.1. Nuclear Fuel Properties

Generally, the properties for UO_2, PuO_2, and MO_2 (mixed oxide) fuel are taken from GE Fuel and Control Material Properties Handbook[208]. In some cases these properties have been augmented with PuO_2 properties from MATPRO[213]. Mixed oxide (MO_2) is indicated when the fraction by weight (f_{PuO_2}) of PuO_2 in the fuel is greater than zero.

C.1.1. Fuel Density

$$\rho\left[\mathrm{kg/m^3}\right] = f_{TD}\left[f_{PuO_2}\rho_{PuO_2} + \left(1 - f_{PuO_2}\right)\rho_{UO_2}\right] \qquad \text{(C.1-1)}$$

where:

f_{TD} = fraction of theoretical density as specified in the input, (C.1-2)

ρ_{PuO_2} = [[ ]] is the theoretical density for PuO_2, (C.1-3)

ρ_{UO_2} = [[ ]] is the theoretical density for UO_2. (C.1-4)

C.1.2. Fuel Specific Heat

The specific heat versus temperature table used in earlier versions of the code has been replaced with a functional form. This change was made so that the fuel enthalpy can be determined by analytical integration with respect to the temperature. For unmolten UO_2 and PuO_2 the formulation from Section 2.2 of Reference [213] has been adopted. This formulation can be shown to be equivalent to the formulation for UO_2 given in the GE BWR Materials Properties Handbook[208] except for some minor differences in the values of some constants. The functional form that applies to both UO_2 and PuO_2 is

$$C_p\,[\text{J/kg-K}] = \frac{C_1 D^2 \exp\left(\frac{D}{T}\right)}{\left[T\left(\exp\left(\frac{D}{T}\right)-1\right)\right]^2} + C_2 T + \frac{C_3 E}{RT^2}\frac{Y}{2}\exp\left(\frac{-E}{RT}\right) \qquad \text{(C.1-5)}$$

where the independent variable is the fuel temperature (T) in kelvin. For UO_2 the constants have the values indicated in column 4 of the Table C-1 below. For PuO_2 the constants are set to the values in column 6.

Table C-1. Fuel Specific Heat Constants

1	2	3	4	5	6
Constants	Description	Units	Default Values for UO_2 from Ref. [208]	Values for UO_2 from Ref. [213]	Default Values for PuO_2 from Ref. [213]
C_1	constant	J / (kg.K)	296.898	296.7	347.4
C_2	constant	J / (kg.K^2)	2.422789E-2	2.43E-2	3.95E-4
C_3	constant	J / kg	8.751594E+7	8.745E+7	3.860E+7
D	Einstein temperature	K	535.285	535.285	571.000
E	activation energy for Frenkel defects	J / mol	1.582866E+5	1.577E+5	1.967E+5
R	universal gas constant	J / (mol.K)	8.3143	8.3143	8.3143
Y	oxygen to metal ratio	none	2.0 (see below)	2.0 (assumed)	2.0 (assumed)

Reference [208] suggests a nominal value of Y = 2.005 together with a proprietary functional dependence with gadolinia content that reduces to a value of 2.0 when no gadolinia is present. Reference [213] suggests a dependence on the oxygen to metal ratio that is reflected by Y/2 in

the last term of Equation (C.1-5), but provides no details regarding how gadolinia may impact the oxygen-to-metal ratio.

If the fuel is mixed oxide (MO_2), where f_{PuO_2} is the fraction by weight of PuO_2 in the mixed oxide, then the specific heat of the unmolten mixed oxide is calculated as

$$C_{p,MO_2} = f_{PuO_2} C_{p,PuO_2} + \left(1 - f_{PuO_2}\right) C_{p,UO_2} \tag{C.1-6}$$

Reference [213] uses the same type of model that weights the specific heats for PuO_2 and UO_2 to estimate the specific heat of the mixed oxide.

C.1.3. Fuel Specific Enthalpy

The specific enthalpy (h) of the fuel is determined by analytic integration with respect to temperature of the expressions for specific heat from Equation (C.1-5).

$$h^*\left(T^*\right) = \int_0^{T^*} c_p dT = \frac{C_1 D}{\left(\exp\left(\frac{D}{T^*}\right) - 1\right)} + \frac{1}{2} C_2 T^* + C_3 \frac{Y}{2} \exp\left(\frac{-E}{RT^*}\right) \tag{C.1-7}$$

This integration is mathematically correct, but does not consider the fact that the fuel enthalpies are usually defined relative to a reference enthalpy value of zero at a temperature other than absolute zero. The more common definition used by TRACG is

$$h\left(T\right) = \int_0^{T} c_p dT - \int_0^{T_{ref}} c_p dT = h^*\left(T\right) - h^*\left(T_{ref}\right) \tag{C.1-8}$$

The value for $h^*\left(T_{ref}\right)$ is obtained once during the initialization based on the input value of T_{ref} and the value is saved so that subsequent evaluations of h(T) can be calculated from Equation (C.1-8) by evaluating only $h^*\left(T\right)$ from Equation (C.1-7). Typically $T_{ref} = 293.15$ K or $T_{ref} = 298.15$ K corresponding respectively to assumed zero enthalpy references at temperatures of 20 C or 25 C.

When $f_{PuO_2} > 0$, Equation (C.1-8) is evaluated once for UO2 and once again for PuO2. The two specific enthalpy values are then weighted as was the case for the specific heats (see Equation (C.1-6)) according to:

$$h_{MO_2} = f_{PuO_2} h_{PuO_2} + \left(1 - f_{PuO_2}\right) h_{UO_2} \tag{C.1-9}$$

C.1.4. Fuel Thermal Conductivity

C.1.4.1. Fuel Thermal Conductivity for UO2

The default correlation for thermal conductivity (k) for unmolten UO2 has been updated to be compatible with the model used in PRIME03[24] when $f_{PuO_2} = 0$. For $f_{PuO_2} > 0$, TRACG04 uses a different formulation that is described in Section C.1.4.2. [[

]]

$T(K)$ is the fuel temperature at the point of application.

[[ ]] accounts for effects due to exposure and gadolinia content that were not considered in the correlation previously implemented in TRACG02. [[

]] (C.1-15)

E = exposure (GWd/t);

G = gadolinia concentration (atomic fraction).

The correlation implemented previously and described below is still available as an option. It can be selected by setting PIRT227 < 1.0.

[[ ]] (C.1-16)

where

T_F = Temperature (°F)

T_R = Temperature (R)

T_M = Melting Temperature (°F)

[[

]]

The UO_2 melting temperature in kelvin used in the formulation is [[

]]

C.1.4.2. Fuel Thermal Conductivity for MO2

For mixed oxide fuel identified by $f_{PuO_2} > 0$, the thermal conductivity in units of W/(m·K) is [[

]] (C.1-19)

where T_C is the temperature in celsius and [[

]] (C.1-21)

C.1.5. Fuel Spectral Emissivity

The spectral emissivity of UO2 fuel is [[

]] (C.1-22)

where T_F is the fuel temperature (°F).

For mixed oxide fuel identified by $f_{PuO_2} > 0$, the spectral emissivity of MO2 is [[

]] (C.1-23)

where T is the fuel temperature in kelvin.

C.2. Zircaloy Cladding Properties

Zircaloy properties are taken from the GE Fuel and Control Material Properties Handbook[208].

C.2.1. Zircaloy Density

The density of Zircaloy is [[

]] (C.2-1)

C.2.2. Zircaloy Specific Heat

The evaluation of Zircaloy specific heat (C_p) in units of J/(kg·K) is [[

]] (C.2-2)

C.2.3. Zircaloy Thermal Conductivity

The thermal conductivity of Zircaloy is [[

]] (C.2-3)

where T is the temperature in kelvin.

C.2.4. Zircaloy Spectral Emissivity

The spectral emissivity of Zircaloy is [[

]] (C.2-4)

C.3. Zirconium Oxide Properties

Zirconium oxide properties are taken from the GE Fuel and Control Material Properties Handbook[208]. *Zirconium oxide* is the common name of what is actually *zirconium dioxide* (ZrO_2) which is also known as *zirconia*.

C.3.1. Zirconium Oxide Density

The density of zirconium oxide is [[

]] (C.3-1)

C.3.2. Zirconium Oxide Specific Heat

The evaluation of zirconium oxide specific heat (C_p) in units of J/(kg·K) is [[

]] (C.3-2)

C.3.3. Zirconium Oxide Thermal Conductivity

The thermal conductivity of zirconium oxide is [[

]] (C.3-3)

C.3.4. Zirconium Oxide Spectral Emissivity

The spectral emissivity of zirconium oxide is [[

]] (C.3-4)

C.4. Atlas Heater Rod Insulator

The properties of the Atlas test facility heater rod insulator material are provided below.

C.4.1. Density

The density of the ATLAS heater rod insulator is [[

]] (C.4-1)

C.4.2. Specific Heat

The specific heat of the ATLAS heater rod insulator is [[

]]

C.4.3. Thermal Conductivity

The thermal conductivity of the ATLAS heater rod insulator is [[

]]

C.4.4. Spectral Emissivity

The spectral emissivity of the ATLAS heater rod insulator is [[

]] (C.4-2)

C.5. Boron Nitride Insulator

The properties of boron nitride insulator material are provided in the following paragraphs.

C.5.1. Density

The density of boron nitride insulation is given in Reference [209] as

$$\rho = 2002 \text{ kg/m}^3 \quad \text{(C.5-1)}$$

C.5.2. Specific Heat

The specitic heat of boron nitride insulation is given in Reference [210] as

$$C_p = 760.59 + 1.7955*T_F - 8.6704E\text{-}4*T_F^2 + 1.5896E\text{-}7*T_F^3 \quad \text{(C.5-2)}$$

where T_F is the temperature in units of °F.

C.5.3. Thermal Conductivity

The thermal conductivity of boron nitride insulation is given in Reference [211] as

$$k = 25.27 - 1.365E\text{-}3*T_F \quad \text{(C.5-3)}$$

where T_F is the temperature in units of °F.

C.5.4. Spectral Emissivity

The spectral emissivity of boron nitride insulation is modeled by the constant value:

$$\varepsilon = 1.0 \quad \text{(C.5-4)}$$

C.6. Stainless Steel

Stainless steel properties are taken from the GE Plant Materials Handbook[212] except as noted below for the specific heat.

C.6.1. Density

The density of stainless steel in units of kg/m3 is [[

]] (C.6-1)

where T_F is the temperature in units of °F.

C.6.2. Specific Heat

The specific heat of stainless steel in units of J/(kg·K) is based on the formulation in Reference [2] and is calculated as a function of temperature using:

$$C_p = 426.17 + 0.43816*T_F - 6.3759E\text{-}4*T_F^2 + 4.4803E\text{-}7*T_F^3 - 1.0729E\text{-}10*T_F^4 \quad \text{(C.6-2)}$$

where T_F is the temperature in units of °F.

C.6.3. Thermal Conductivity

The thermal conductivity of stainless steel is [[

]]

C.6.4. Spectral Emissivity

The spectral emissivity of stainless steel is [[

]] (C.6-3)

C.7. Stainless Steel, Type 316 (SS-316)

Stainless steel properties are taken from the GE Plant Materials Handbook[212] except as noted below for the specific heat.

C.7.1. Density

The density of type 316 stainless steel is [[

]] (C.7-1)

where T_F is the temperature in units of °F.

C.7.2. Specific Heat

The specific heat of type 316 stainless steel in units of J/(kg·K) is based on the formulation in Reference [2] and is calculated as a function of temperature using:

$$C_p = 426.17 + 0.43816*T_F - 6.3759E\text{-}4*T_F^2 + 4.4803E\text{-}7*T_F^3 - 1.0729E\text{-}10*T_F^4 \quad \text{(C.7-2)}$$

where T_F is the temperature in units of °F.

C.7.3. Thermal Conductivity

The thermal conductivity of type 316 stainless steel is [[

]]

C.7.4. Spectral Emissivity

The spectral emissivity of type 316 stainless steel is [[

]] (C.7-3)

C.8. Carbon Steel

Carbon steel properties are taken from the GE Plant Materials Handbook[212].

C.8.1. Density

The density of carbon steel is [[

]]

C.8.2. Specific Heat

The specific heat of carbon steel is [[

]]

C.8.3. Thermal Conductivity

The thermal conductivity of carbon steel is [[

]]

C.8.4. Spectral Emissivity

The spectral emissivity of carbon steel is [[

]] (C.8-1)

C.9. Inconel 600

Inconel properties are taken from the GE Plant Materials Handbook[212].

C.9.1. Density

The density of Inconel 600 is [[

]]

C.9.2. Specific Heat

The specific heat of Inconel 600 is [[

]]

C.9.3. Thermal Conductivity

The thermal conductivity of Inconel 600 is [[

]]

C.9.4. Spectral Emissivity

The spectral emissivity of Inconel 600 is [[

]] (C.9-1)

C.10. Concrete

The properties of concrete are provided in the following paragraphs.

C.10.1. Density

The density of concrete is modeled by the constant value:

$$\rho = 2322.6767 \text{ kg/m}^3 \quad \text{(C.10-1)}$$

C.10.2. Specific Heat

The specific heat of concrete is modeled by the constant value:

$$C_p = 879.228 \quad \text{J/(kg·K)} \quad \text{(C.10-2)}$$

C.10.3. Thermal Conductivity

The thermal conductivity of concrete is modeled by the constant value:

$$k = 1.3845872 \quad \text{W/(m·K)} \quad \text{(C.10-3)}$$

C.10.4. Spectral Emissivity

The spectral emissivity of concrete is modeled by the constant value:

$$\varepsilon = 0.0 \quad \text{(C.10-4)}$$

APPENDIX D. Derivation of the Isentropic Sound Speed as a Function of Pressure and Temperature for a Single-Component, Single-Phase Substance

The sonic velocity for a homogeneous equilibrium mixture (a_{HE}) is given as:

$$a_{HE} = \left(\frac{\partial P}{\partial \rho} \right)_S^{1/2} \tag{D-1}$$

where the partial deriviative of pressure (P) with respect to density (ρ) is evaluated so that the specific entropy (S) does not change, i.e., isentropic. Consider the following expressions for the differential change in entropy:

$$ds = C_V \frac{dT}{T} - \frac{1}{\rho^2} \left(\frac{\partial P}{\partial T} \right)_\rho d\rho \tag{D-2}$$

and

$$ds = C_p \frac{dT}{T} + \frac{1}{\rho^2} \left(\frac{\partial \rho}{\partial T} \right)_P dP . \tag{D-3}$$

For isentropic systems, ds = 0, so

$$C_v = \frac{T}{\rho^2} \left(\frac{\partial P}{\partial T} \right)_\rho \left(\frac{\partial \rho}{\partial T} \right)_S \tag{D-4}$$

and

$$C_p = \frac{-T}{\rho^2} \left(\frac{\partial \rho}{\partial T} \right)_P \left(\frac{\partial P}{\partial T} \right)_S \tag{D-5}$$

Thus,

$$\frac{C_v}{C_p} = - \frac{\left(\frac{\partial P}{\partial T} \right)_\rho \left(\frac{\partial \rho}{\partial T} \right)_S}{\left(\frac{\partial \rho}{\partial T} \right)_P \left(\frac{\partial P}{\partial T} \right)_S} \tag{D-6}$$

Multiply Equation (D-6) by the unity ratio:

$$1 = \frac{\left(\frac{\partial T}{\partial P} \right)_\rho \left(\frac{\partial T}{\partial P} \right)_S}{\left(\frac{\partial T}{\partial P} \right)_\rho \left(\frac{\partial T}{\partial P} \right)_S} \tag{D-7}$$

and rearrange terms to get,

$$\frac{C_v}{C_p} = -\frac{\left[\left(\frac{\partial P}{\partial T}\right)_\rho \left(\frac{\partial T}{\partial P}\right)_\rho\right]\left[\left(\frac{\partial \rho}{\partial T}\right)_S \left(\frac{\partial T}{\partial P}\right)_S\right]}{\left[\left(\frac{\partial \rho}{\partial T}\right)_P \left(\frac{\partial T}{\partial P}\right)_\rho\right]\left[\left(\frac{\partial P}{\partial T}\right)_S \left(\frac{\partial T}{\partial P}\right)_S\right]}. \tag{D-8}$$

Next apply the following relationships

$$\begin{aligned}
&\left(\frac{\partial P}{\partial T}\right)_\rho \left(\frac{\partial T}{\partial P}\right)_\rho = 1 \\
&\left(\frac{\partial P}{\partial T}\right)_S \left(\frac{\partial T}{\partial P}\right)_S = 1 \\
&\left(\frac{\partial \rho}{\partial T}\right)_S \left(\frac{\partial T}{\partial P}\right)_S = \left(\frac{\partial \rho}{\partial P}\right)_S \\
&\left(\frac{\partial \rho}{\partial T}\right)_P \left(\frac{\partial T}{\partial P}\right)_\rho = -\left(\frac{\partial \rho}{\partial P}\right)_T
\end{aligned} \tag{D-9}$$

and simply Equation (D-8) to get

$$\frac{C_v}{C_p} = \frac{\left(\frac{\partial \rho}{\partial P}\right)_S}{\left(\frac{\partial \rho}{\partial P}\right)_T}. \tag{D-10}$$

This means that $\left(\frac{\partial \rho}{\partial P}\right)_S$ can be calculated from

$$\left(\frac{\partial \rho}{\partial P}\right)_S = \left(\frac{\partial \rho}{\partial P}\right)_T \frac{C_v}{C_p}. \tag{D-11}$$

Now, for any gaseous substance,

$$C_p - C_v = -\frac{T\left(\frac{\partial \rho}{\partial T}\right)_p^2}{\rho^2 \left(\frac{\partial \rho}{\partial P}\right)_T} \tag{D-12}$$

Rearrange Equation (D-12) to produce:

$$\frac{C_v}{C_p} = 1 - \frac{T\left(\frac{\partial \rho}{\partial T}\right)_P^2}{\rho^2 \left(\frac{\partial \rho}{\partial P}\right)_T C_p} \tag{D-13}$$

Apply the definition for C_p

$$C_p = \left(\frac{\partial h}{\partial T}\right)_P \tag{D-14}$$

and the definition for specific enthalpy

$$h = e(\rho, T) + \frac{P}{\rho} \tag{D-15}$$

in order to expand C_p to

$$C_p = \left[\left(\frac{\partial e}{\partial T}\right)_P - \frac{P}{\rho^2}\left(\frac{\partial \rho}{\partial T}\right)_P\right] \tag{D-16}$$

The value for the specific energy e(ρ,T) and its derivatives are obtained from the thermodynamic properties. Substitute the expression for C_p from Equation (D-16) into Equation (D-13) and expand the result to:

$$\frac{C_v}{C_p} = 1 - \frac{T\left(\frac{\partial \rho}{\partial T}\right)_p^2}{\rho^2 \left(\frac{\partial \rho}{\partial P}\right)_T \left[\left(\frac{\partial e}{\partial T}\right)_P - \frac{P}{\rho^2}\left(\frac{\partial P}{\partial T}\right)_P\right]} \tag{D-17}$$

Substitute the expression from Equation (D-17) into Equation (D-11) to get an expression for $\left(\frac{\partial \rho}{\partial P}\right)_S$. Then substitute that result into the definition for the isentropic sound speed for homogeneous equilibrium given in Equation (D-1) to obtain the final expanded expression

$$a_{HE} = \left(\frac{\partial P}{\partial \rho}\right)_S^{1/2} = \left\{\left(\frac{\partial \rho}{\partial P}\right)_T - \frac{T\left(\frac{\partial \rho}{\partial T}\right)_p^2}{\rho^2\left[\left(\frac{\partial e}{\partial T}\right)_P - \frac{P}{\rho^2}\left(\frac{\partial \rho}{\partial T}\right)_P\right]}\right\}^{-1/2} \tag{D-18}$$

APPENDIX E. Derivation of the Two-Phase, Two-Component HEM Sonic Velocity

Following the analysis of Ransom[80],[81] which has been derived in more detail in APPENDIX D, the sonic velocity for a homogeneous equilibrium mixture is given as:

$$a = \left(\frac{\partial P}{\partial \rho}\right)_S^{1/2} \tag{E-1}$$

Assuming that one component is a steam-liquid mixture and the other is an immiscible component such that the gaseous phase is a Gibbs-Dalton mixture, the density of the mixture may be expressed as:

$$\rho = \alpha\,(\rho_s + \rho_a) + (1 - \alpha)\,\rho_\ell \tag{E-2}$$

Taking the derivative of this mixture density with respect to pressure at constant entropy gives:

$$\left(\frac{\partial \rho}{\partial P}\right)_S = \alpha\left(\frac{\partial \rho_s}{\partial P}\right)_S + \alpha\left(\frac{\partial \rho_a}{\partial P}\right)_S + (1-\alpha)\left(\frac{\partial \rho_\ell}{\partial P}\right)_S + \left(\rho_s + \rho_a - \rho_\ell\right)\left(\frac{\partial \alpha}{\partial P}\right)_S \tag{E-3}$$

To evaluate $\left(\frac{\partial \alpha}{\partial P}\right)_S$, consider the mixture specific entropy,

$$S = X_s S_s + X_a S_a + (1 - X_s - X_a) S_\ell \tag{E-4}$$

where

$$X_s = \frac{\alpha \rho_s}{\rho} \tag{E-5}$$

$$X_a = \frac{\alpha \rho_a}{\rho}. \tag{E-6}$$

In an isentropic system,

$$\left(\frac{\partial S}{\partial P}\right)_S = 0 = X_a\left(\frac{\partial S_a}{\partial P}\right)_S + X_s\left(\frac{\partial S_s}{\partial P}\right)_S + \left(1 - X_a - X_s\right)\left(\frac{\partial S_\ell}{\partial P}\right)_S + \left(S_s - S_\ell\right)\left(\frac{\partial X_s}{\partial P}\right)_S + \left(S_a - S_\ell\right)\left(\frac{\partial X_a}{\partial P}\right)_S. \tag{E-7}$$

Since the noncondensable is assumed to be immiscible in the liquid-vapor mixture,

$$\left(\frac{\partial X_a}{\partial P}\right)_S = 0 . \tag{E-8}$$

From Equation (E-5),

$$\left(\frac{\partial X_s}{\partial P}\right)_S = \frac{\alpha}{\rho}\left(\frac{\partial \rho_s}{\partial P}\right)_S + \frac{\rho_s}{\rho}\left(\frac{\partial \alpha}{\partial P}\right)_S - \frac{\alpha\rho_s}{\rho^2}\left(\frac{\partial \rho}{\partial P}\right)_S . \tag{E-9}$$

Substitute Equation (E-9) into Equation (E-7) and rearrange terms to get:

$$\left(\frac{\partial \alpha}{\partial P}\right)_S = \frac{\sum_1}{\rho_s (S_s - S_\ell)} - \frac{\alpha}{\rho_s}\left(\frac{\partial \rho_s}{\partial P}\right)_S + \frac{\alpha}{\rho}\left(\frac{\partial \rho}{\partial P}\right)_S \tag{E-10}$$

where

$$\sum_1 = -\left[\alpha\rho_a\left(\frac{\partial S_a}{\partial P}\right)_S + \alpha\rho_s\left(\frac{\partial S_s}{\partial P}\right)_S + (1-\alpha)\rho_\ell\left(\frac{\partial S_\ell}{\partial P}\right)_S\right]. \tag{E-11}$$

Substitute Equation (E-10) into Equation (E-3) and rearrange terms to get:

$$\left[1-\alpha\left(\frac{\rho_a+\rho_s-\rho_\ell}{\rho}\right)\right]\left(\frac{\partial \rho}{\partial P}\right)_S = \alpha\left[1-\left(\frac{\rho_s+\rho_a-\rho_\ell}{\rho_s}\right)\right]\left(\frac{\partial \rho_s}{\partial P}\right)_S + \alpha\left(\frac{\partial \rho_a}{\partial P}\right)_S + (1-\alpha)\left(\frac{\partial \rho_\ell}{\partial P}\right)_S + \sum_2 \tag{E-12}$$

where

$$\sum_2 = \frac{(\rho_s+\rho_a-\rho_\ell)\sum_1}{\rho_s (S_s - S_\ell)} \tag{E-13}$$

so that

$$\left(\frac{\partial \rho}{\partial P}\right)_S = \frac{\rho}{\rho_s\rho_\ell}\left[\alpha\rho_s\left(\frac{\partial \rho_a}{\partial P}\right)_S + \alpha(\rho_\ell-\rho_a)\left(\frac{\partial \rho_s}{\partial P}\right)_S + (1-\alpha)\rho_s\left(\frac{\partial \rho_\ell}{\partial P}\right)_S + \rho_s\sum_2\right]. \tag{E-14}$$

Having defined an expression for $\left(\frac{\partial \rho}{\partial P}\right)_S$, the next step is to define the property derivatives. Recall that the thermodynamic variables are defined as:

$$f_a = f_a\,(P_a, T) \tag{E-15}$$

$$f_s = f_s\,(P_s, T) \tag{E-16}$$

and

$$f_\ell = f_\ell\,(P_\ell, T) \tag{E-17}$$

where

$$P = P_a + P_s \tag{E-18}$$

for a Gibbs-Dalton mixture. The result of this is that:

$$\left(\frac{\partial P_a}{\partial P}\right)_S = 1 - \left(\frac{\partial P_s}{\partial T}\right)_S \left(\frac{\partial T}{\partial P}\right)_S \tag{E-19}$$

and

$$\left(\frac{\partial P_s}{\partial P}\right)_S = \left(\frac{\partial P_s}{\partial T}\right)_S \left(\frac{\partial T}{\partial P}\right)_S \tag{E-20}$$

Here, the assumption has been made that the equilibrium partial steam pressure is that which corresponds to the equilibrium temperature. Thus,

$$P_S = P_S(T) \tag{E-21}$$

From this knowledge, the basic derivative properties may be defined from the chain rule as:

$$\left(\frac{\partial \rho_a}{\partial P}\right)_S = \left(\frac{\partial \rho_a}{\partial P_a}\right)_T + \left[\left(\frac{\partial \rho_a}{\partial T}\right)_{P_a} - \left(\frac{\partial \rho_a}{\partial P_a}\right)_T \left(\frac{\partial P_s}{\partial T}\right)_S\right]\left(\frac{\partial T}{\partial P}\right)_S \tag{E-22}$$

$$\left(\frac{\partial \rho_s}{\partial P}\right)_S = \left[\left(\frac{\partial \rho_s}{\partial P_s}\right)_T \left(\frac{\partial P_s}{\partial T}\right)_S + \left(\frac{\partial \rho_s}{\partial T}\right)_{P_S}\right]\left(\frac{\partial T}{\partial \rho}\right)_S \tag{E-23}$$

$$\left(\frac{\partial \rho_\ell}{\partial P}\right)_S = \left(\frac{\partial \rho_\ell}{\partial P_\ell}\right)_T + \left(\frac{\partial P_\ell}{\partial T}\right)_{P_\ell} \left(\frac{\partial T}{\partial P}\right)_S \tag{E-24}$$

$$\left(\frac{\partial S_a}{\partial P}\right)_S = \frac{1}{\rho_a^2}\left(\frac{\partial \rho_a}{\partial T}\right)_{P_a} + \left[\left(\frac{C_{Pa}}{T}\right) - \frac{1}{\rho_a^2}\left(\frac{\partial \rho_a}{\partial T}\right)_{P_a}\left(\frac{\partial P_s}{\partial T}\right)\right]\left(\frac{\partial T}{\partial \rho}\right)_S \tag{E-25}$$

$$\left(\frac{\partial S_s}{\partial P}\right)_S = \left[\frac{Cp_s}{T} + \frac{1}{\rho_s^2}\left(\frac{\partial \rho_s}{\partial T}\right)_{P_s}\left(\frac{\partial P_s}{\partial T}\right)\right]\left(\frac{\partial T}{\partial P}\right)_S \tag{E-26}$$

$$\left(\frac{\partial S_\ell}{\partial P}\right)_S = \frac{1}{\rho_\ell^2}\left(\frac{\partial \rho_\ell}{\partial T}\right) + \frac{C_{P_\ell}}{T}\left(\frac{\partial T}{\partial P}\right)_S \tag{E-27}$$

where

$$C_{P_a} = \left(\frac{\partial e_a}{\partial T}\right)_{P_a} - \frac{P_a}{\rho_a^2}\left(\frac{\partial \rho_a}{\partial T}\right)_{P_a} \tag{E-28}$$

$$C_{P_s} = \left(\frac{\partial e_s}{\partial T}\right)_{P_s} - \frac{P_s}{\rho_s^2}\left(\frac{\partial \rho_s}{\partial T}\right)_{P_s} \tag{E-29}$$

$$C_{P_\ell} = \left(\frac{\partial e_\ell}{\partial T}\right)_{P_\ell} - \frac{P_\ell}{\rho_\ell^2}\left(\frac{\partial \rho_\ell}{\partial T}\right)_{P_\ell} \tag{E-30}$$

This leaves the specification of $\left(\frac{\partial T}{\partial P}\right)_S$. To this, consider the identity

$$X_a \rho_s = X_s \rho_a \tag{E-31}$$

Differentiating with respect to pressure gives

$$X_a\left(\frac{\partial \rho_s}{\partial P}\right)_S = X_s\left(\frac{\partial \rho_a}{\partial P}\right)_S + \rho_a\left(\frac{\partial X_s}{\partial P}\right)_S . \tag{E-32}$$

Using the result from Equation (E-9) and simplifying gives:

$$X_a\left(\frac{\partial \rho_s}{\partial P}\right)_S = X_s\left(\frac{\partial \rho_s}{\partial P}\right)_S - \left[\frac{\rho_a}{S_s - S_\ell}\right] * \left[X_a\left(\frac{\partial S_a}{\partial P}\right)_S + X_s\left(\frac{\partial S_a}{\partial P}\right)_S + (1 - X_a - X_s)\left(\frac{\partial S_\ell}{\partial P}\right)_S\right]. \tag{E-33}$$

Substituting the relations defined above,

$$\alpha\rho_a\left(\frac{-\partial\rho_s}{\partial T}+\frac{\partial\rho_s}{\partial P_s}\frac{\partial P_g}{\partial T}\right)\left(\frac{\partial T}{\partial P}\right)_S=\alpha\rho_s\left[\frac{\partial\rho_a}{\partial P_a}+\left(\frac{\partial\rho_a}{\partial T}-\frac{\partial\rho_a}{\partial P_a}\frac{\partial P_g}{\partial T}\right)\left(\frac{\partial T}{\partial P}\right)_S\right]$$

$$-\frac{\rho_a}{S_s-S_\ell}\left\{\alpha\rho_a\left[\frac{1}{\rho_a^2}\frac{\partial\rho_a}{\partial T}+\left(\frac{C_{P_a}}{T}-\frac{1}{\rho_a^2}\frac{\partial\rho_a}{\partial T}\frac{\partial P_g}{\partial T}\right)\left(\frac{\partial T}{\partial P}\right)_S\right]\right. \tag{E-34}$$

$$\left.+\alpha\rho_s\left[\frac{C_{P_s}}{T}+\frac{1}{\rho_s^2}\frac{\partial\rho_s}{\partial T}\frac{\partial P_g}{\partial T}\right]\left(\frac{\partial T}{\partial P}\right)_S+(1-\alpha)\rho_\ell\left[\frac{1}{\rho_s^2}\frac{\partial\rho_\ell}{\partial T}+\frac{C_{P_\ell}}{T}\left(\frac{\partial T}{\partial P}\right)_S\right]\right\}.$$

Solving for $\left(\frac{\partial T}{\partial P}\right)_S$ then gives the result

$$\left(\frac{\partial T}{\partial P}\right)_S=\left[\alpha\rho_s\frac{\partial\rho_a}{\partial P_a}-\frac{1}{S_s-S_\ell}\left(\alpha\frac{\partial\rho_a}{\partial T}+\frac{(1-\alpha)\rho_a}{\rho_\ell}\frac{\partial\rho_\ell}{\partial T}\right)\right]\Bigg/$$

(E-35)

$$\left\{\alpha\rho_a\left(\frac{\partial\rho_s}{\partial P_s}\frac{\partial P_g}{\partial T}-\frac{\partial\rho_g}{\partial T}\right)+\alpha\rho_s\left(\frac{\partial\rho_a}{\partial P_a}\frac{\partial P_g}{\partial T}-\frac{\partial\rho_a}{\partial T}\right)\right.$$

$$+\frac{1}{S_s-S_\ell}\left[\alpha\left(\frac{\rho_a^2C_{P_a}}{T}-\frac{\partial\rho_a}{\partial T}\frac{\partial P_g}{\partial T}\right)\right.$$

$$\left.\left.+\alpha\left(\rho_a\rho_s\frac{C_{P_s}}{T}+\frac{\rho_a^2}{\rho_s}\frac{\partial\rho_s}{\partial T}\frac{\partial P_g}{\partial T}\right)+(1-\alpha)\rho_a\rho_\ell\frac{C_{P_\ell}}{T}\right]\right\}.$$

Finally, at saturation conditions, this Clasius-Glapyron equation gives:

$$\frac{\partial P_s}{\partial T}=\left(\frac{S_s(P_s,T)-S_\ell(P_s,T)}{\rho_\ell(P_s,T)-\rho_s(P_s,T)}\right)\rho_\ell(P_s,T)\,\rho_s(P_s,T). \tag{E-36}$$

Assuming that the following approximation is valid in the presence of a noncondensable gas,

$$\left(\frac{S_s(P_s,T)-S_\ell(P_s,T)}{\rho_\ell(P_s,T)-\rho_s(P_s,T)}\right)\rho_\ell(P,T)=\left(\frac{S_s(P_s,T)-S_\ell(P_s,T)}{\rho_\ell(P_s,T)-\rho_s(P_s,T)}\right)\rho_\ell(P_s,T) \tag{E-37}$$

allows for $(S_s - S_\ell)$ to be expressed as

$$S_s - S_\ell = \frac{\partial P_s}{\partial T}\left(\frac{\rho_\ell - \rho_s}{\rho_\ell \rho_s}\right). \tag{E-38}$$

where ρ_ℓ is evaluated at the total pressure and ρ_s is evaluated at the partial pressure due to steam.

Equations (E-14), (E-35), and (E-38) thus provide complete closure for the two-phase, two-component HEM sonic velocity. It is interesting to examine the limit for no noncondensable as $\rho_a \to 0$. In this case,

$$\lim_{\rho_a \to 0}\left[\left(\frac{\partial T}{\partial P}\right)_S\right] = \left(\frac{\partial P_g}{\partial T}\right)^{-1} \tag{E-39}$$

and

$$\lim_{\rho_a \to 0}\left[\left(\frac{\partial \rho}{\partial P}\right)_S\right] = \frac{\rho}{\rho_\ell \rho_s}\left\{\alpha\rho_\ell\left(\frac{\partial \rho_s}{\partial P}\right)_S + (1-\alpha)\rho_s\left(\frac{\partial \rho_\ell}{\partial P}\right)_S - \frac{\rho_s - \rho_\ell}{S_s - S_\ell}\left[\alpha\rho_s\left(\frac{\partial S_s}{\partial P}\right)_S + (1-\alpha)\rho_\ell\left(\frac{\partial S_\ell}{\partial P}\right)_S\right]\right\}. \tag{E-40}$$

This result is in agreement with that prescribed by Free[76] and Spore[77] in the original TRAC choking model.

REFERENCES

[1] J. A. Borkowski, et al., *TRAC-BF1/MOD1: An Advanced Best-Estimate Program for BWR Accident Analysis*, NUREG/CR-4356, Idaho National Engineering Laboratory, August 1992.

[2] *TRAC-PF1/MOD2*, NUREG/CR-5673, Los Alamos National Laboratory.

[3] *Steady-State Nuclear Methods*, NEDE-30130-P-A, GE Proprietary Report, April 1985.

[4] J. G. M. Andersen, et al., *TRACG Qualification*, NEDE-32177P, Rev. 1, GE Proprietary Report, June 1993.

[5] J. G. M. Andersen, et al., *TRACG Qualification*, NEDE-32177P, Rev. 2, GE Proprietary Report, January 2000.

[6] J. G. M. Andersen, et al., *TRACG Qualification*, NEDE-32177P, Rev. 3, GE Proprietary Report, August 2007.

[7] J. R. Fitch, et al., *TRACG Qualification for SBWR*, NEDC-32725P, Rev. 1, GE Proprietary Report, August 2002.

[8] J. R. Fitch, et al., *TRACG Qualification for ESBWR*, NEDC-33080P, Rev. 1, GE Proprietary Report, May 2005.

[9] R. J. Pryor, et al., TRAC-P1A, *An Advanced Best-Estimate Computer Program for PWR LOCA Analysis*, NUREG/CRA-0665, Los Alamos Scientific Laboratory, May 1979.

[10] D. D. Taylor, et al., *TRAC-BD1/MOD1: An Advanced Best-Estimate Program for Boiling Water Reactor Transient Analysis, Volumes 1-4*, NUREG/CR-3633, Idaho National Engineering Laboratory, April 1984.

[11] J. G. M. Andersen, K. H. Chu, and J. C. Shaug, *BWR REFILL/RE-FLOOD Program Task 4.7 - Model Development, Basic Models for the BWR Version of TRAC*, GEAP-22051, NUREG/CR-2573, EPRI NP-2375, April 1983.

[12] Y. K. Cheung, V. Parameswaran, and J. C. Shaug, *BWR REFILL/RE-FLOOD Program Task 4.7 - Model Development, TRAC-BWR Component Models*, GEAP-22052, NUREG/CR-2574, EPRI NP-2376, April 1983.

[13] Md. Alamgir, et al., *BWR REFILL/RE-FLOOD Program Task 4.8 - TRAC-BWR Model Qualification for BWR Safety Analysis, Final Report*, GEAP-30157, NUREG/CR-2571, EPRI NP-2377, October 1983.

REFERENCES

[14] J. G. M. Andersen and C. L. Heck, *BWR Full Integral Simulation Test (FIST) Program, TRAC-BWR Model Development, Volume 1 - Numerical Methods*, GEAP-30875-1, NUREG/CR-4127-1, EPRI NP-3987-1, November 1985.

[15] K. H. Chu, J. G. M. Andersen, Y. K. Cheung, and J. C. Shaug, *BWR Full Integral Simulation Test (FIST) Program, TRAC-BWR Model Development, Volume 2 - Models*, GEAP-30875-2, NUREG/CR-4127-2, EPRI NP-3987-2, October 1985.

[16] Y. K. Cheung, J. G. M. Andersen, K. H. Chu, and J. C. Shaug, *BWR Full Integral Simulation Test (FIST) Program, TRAC-BWR Model Development Volume 3 - Developmental Assessment for Plant Application*, GEAP-30875-3, NUREG/CR-4127-3, EPRI NP-3987-3, October 1985.

[17] W. A. Sutherland, Md. Alamgir, J. A. Findlay, and W. S. Hwang, *BWR Full Integral Simulation Test (FIST) Program, Phase II Test Results and TRAC-BWR Model Qualification*, GEAP-30876, NUREG/CR-4128, EPRI NP-3988, October 1985.

[18] *Compendium of ECCS Research for Realistic LOCA Analysis*, NUREG-1230, August 1988.

[19] B. Boyack et al., *Quantifying Reactor Safety Margins*, NUREG/CR/5249, December 1989.

[20] Letter from S. A. Richards (NRC) to G. A. Watford (GE), *Amendment 26 to GE Licensing Topical Report NEDE-24011-P-A, "GESTAR II" – Implementing Improved GE Steady-State Methods (TAC No. MA6481)*, FLN-1999-011, November 10, 1999.

[21] *American National Standard for Decay Heat Power in Light Water Reactors*, ANSI/ANS-5.1-1979, La Grange Park, Illinois: American Nuclear Society, 1979.

[22] *American National Standard for Decay Heat Power in Light Water Reactors*, ANSI/ANS-5.1-1994, La Grange Park, Illinois: American Nuclear Society, 1994.

[23] R. W. Shumway, *TRAC-BWR Heat Transfer: Assessment of Tmin*, EGG-RST-6781, October 1984.

[24] R. Rand, et. al, *PRIME03P Technical Basis Document*, eECPER 0000-0035-8584-01, GE Proprietary Report, June 2005.

[25] J. V. Cathcart and R. E. Pawel, *Zirconium Metal-Water Oxidation Kinetics: IV. Reaction Rate Studies*, ORNL/NUREG-17, August 1977.

REFERENCES

[26] J. G. M. Andersen, et al., *TRACG Application for Anticipated Operational Occurrences Transient Analyses*, NEDE-32906P-A, Rev. 1, GE Proprietary Report, April 2003.

[27] F. T. Bolger and M. A. Holmes, *TRACG Application for Anticipated Transients without Scram Overpressure Transient Analyses*, NEDE-32906P, Supplement 1-A, GE Proprietary Report, November 2003.

[28] D. R. Liles, et al., *TRAC-PF1/MOD1 Correlations and Models*, NUREG/CR-5069, December 1988.

[29] J. A. Borkowski, et al., *TRAC-BF1/MOD1 Models and Correlations*, NUREG/CR-4391, August 1992.

[30] G. Kocamustafaogullari, *Thermo-Fluid Dynamics of Separated Two-Phase Flow,* Ph. D. thesis, Georgia Institute of Technology, December 1971.

[31] M. Ishii, *Thermo-Fluid Dynamic Theory of Two-Phase Flow*, Collection de la Direction des Études et Recherches D'Électricité de France, Eyrolles, Paris, 1981.

[32] A. E. Bergles, et al., *Two-Phase Flow and Heat Transfer in the Power and Process Industries*, New York: Hemisphere Publishing, McGraw–Hill, 1981.

[33] F. L. Addessio, *A Review of the Development of Two-Fluid Models*, NUREG/CR-2146, August 1981.

[34] H. B. Stewart and B. Wendroff, *Two-Phase Flow: Models and Methods*, Journal of Computational Physics, 56 (1984), pp. 363-409.

[35] H. B. Stewart, *Stability of Two-Phase Flow Calculation Using Two-Fluid Models*, Journal of Computational Physics, 33 (1979), pp. 250-270.

[36] J. H. Stuhmiller, *A Review of the Rational Approach to Two-Phase Flow Modeling,* PB-255 548, Del Mar, California: Jaycor, July 1976.

[37] H. Lamb, *Hydrodynamics*, New York: Dover Publications.

[38] K. H. Chu and B.S. Shiralkar, *Prediction of Critical Power Based on a Two Fluid and Multi-Field Model*, Fourth International Meeting on Nuclear Thermal Hydraulics, Operation and Safety, 1993.

[39] V. H. Ransom et al., *RELAP5/MOD1 Code Manual, Volume I: System Models and Numerical Methods*, NUREG/CR-2070, March 1982.

REFERENCES

[40] G. B. Wallis, *One-Dimensional Two-Phase Flow*, New York: McGraw-Hill, 1969.

[41] D. D. Jones, *Sub-cooled Counter Current Flow Limiting Characteristics of the Upper Region of a BWR Fuel Bundle*, NEDG-NUREG-23549, 1977.

[42] J. D. Duncan and J. E. Leonard, *BWR Standby Cooling in Boiling Water Reactors Under Simulated Loss-of-Coolant Conditions*, BWR-FLECT Final Report, 6, GEAP-13190, 1971.

[43] F. P. Incropera and D. P. DeWitt, *Fundamentals of Heat Transfer*, New York: John Wiley and Sons, 1981.

[44] M. Ishii, *One-Dimensional Drift Flux Model and Constitutive Equations for Relative Motion Between Phases in Various Two-Phase Flow Regimes*, ANL-77-47, 1977.

[45] Y. Taitel, D. Bovera and A. E. Dukler, *Modeling Flow Pattern Transitions for Steady Upward Gas-Liquid Flow in Vertical Tubes*, AIChE Journal, 26, No. 3 (1980), pp. 345-354.

[46] K. Mishima and M. Ishii, *Flow Regime Transition Criteria for Upward Two-Phase Flow in Vertical Tubes*, International Journal of Heat and Mass Transfer, 27 No. 5 (1984), pp. 723-737.

[47] A. E. Bergles and M. Suo, Boiling *Water Flow Regimes at High Pressures*, Proceedings of the 1966 Heat Transfer and Fluid Mechanics Institute, Palo Alto, California: Stanford University Press, 1966.

[48] M. Ishii and K. Mishima, *Correlation for Liquid Entrainment in Annular Two-Phase Flow of Low Viscous Fluid*, ANL/KAS/LWR 81-2, March 1981.

[49] Y. Taitel and A. E. Dukler, AIChE Journal, 22 No. 3 (1976), pp. 47-55.

[50] K. Mishima and M. Ishii, *Theoretical Predictions of Onset of Horizontal Slug Flow*, J. Fluids Eng., 102 (December 1980), pp. 441-445.

[51] G. B. Wallis and J. E. Dobson, *The Onset of Slugging in Horizontal Stratified Air-Water Flow*, Int. J. Multiphase Flow, Vol 1 (1973), p. 173.

[52] J. G. M. Andersen, K. H. Chu and J. C. Shaug, *BWR Refill-Re-flood Program Task 4.7 - Model Development, Basic Models for the BWR Version of TRAC*, NUREG/CR-2673, April 1983.

REFERENCES

[53] N. Zuber, et al., *Steady State and Transient Void Fraction in Two-Phase Flow Systems*, GEAP-5417, 1967.

[54] N. Zuber and J. A. Findlay, *Average Volumetric Concentration in Two-Phase Flow Systems*, Journal of Heat Transfer, 87 (1965), p. 453.

[55] J. Nikuradse, *Gesetzmäsigkeit der Turbulenten Strömung in glatten Rohren*, Forch. Arb. Ing. Wes., 1932, p. 356.

[56] J. F. Wilson, R. J. Grenda and J. F. Patterson, *The Velocity of Rising Steam in a Bubbling Two-Phase Mixture*, ANS Trans., 5 No. 1 (1962), pp. 151-152.

[57] P. C. Hall and K. H. Adron, *Prediction of Void Fraction in Low Velocity Bubbling Flow*, CEG j13, Rd/13/n3966, August 1978.

[58] J. A. Findlay and G. E. Dix, *BWR Void Fraction Correlation and Data*, NEDE-21565, GE Proprietary Report, January 1977.

[59] N. Zuber, *On the Dispersed Two-Phase Flow in the Laminar Flow Regime*, Chemical Engineering and Science Journal, Vol. 19 (1964), p. 897.

[60] *Compendium of ECCS Research for Realistic LOCA Analysis*, NUREG-1230, December 1988.

[61] *Reactor Safety Issues Resolved by the 2D/3D Program*, NUREG/IA-0127, July 1993.

[62] R. W. Lockhart and R. C. Martinelli, *Proposed Correlation of Data for Isothermal Two-Phase Two-Component Flow in Pipes*, Chem. Eng. Progr., 45 (1949), pp. 39-48.

[63] R. C. Martinelli and D. B. Nelson, *Prediction of Pressure Drops During Forced Circulation Boiling of Water*, Trans. ASME 70 (1948), pp. 695 -702.

[64] J. Waggener, *Friction Factors for Pressure Drop Calculations*, Nucleonics, 19 (11), November 1961.

[65] D. Chisholm, *Pressure Gradients Due to Friction During the Flow of Evaporating Two-Phase Mixtures in Smooth Tubes and Channels*, Int. J. Heat Mass Transfer 16 (1973), pp. 347 - 358.

[66] J. A. Findlay and G. E. Dix, *BWR Void Fraction Correlation*, NEDE-21933, GE Proprietary Report, August 1978.

REFERENCES

[67] R. G. Deissler and M. F. Taylor, *Analysis of Turbulent Flow and Heat Transfer in Non-Circular Passages*, NACA-TN4384, 1958.

[68] W. Idsinga, N. Todreas and R. Bowring, *An Assessment of Two-Phase Pressure Drop Correlations for Steam-Water Systems*, Int. J. Multiphase Flow, 3 (1977), pp. 401-413.

[69] T.L. George, et al, *GOTHIC Containment Analysis Package*, Version 3.4e, Vol. 1: Technical Manual, EPRI TR-103053-V1, October 1993.

[70] J. Weisman, T. Ake, R. Knott, *Two-Phase Pressure Drop Across Abrupt Area Changes in Oscillatory Flow*, Nuclear Science and Engineering, 61 (1976).

[71] J. K. Vennard, *Elementary Fluid Mechanics*, 4th ed., New York: John Wiley and Sons, 1965.

[72] Husain, W. G. Choe, J. Weisman, *The Applicability of the Homogeneous Flow Model to Pressure Drop in Straight Pipe and Across Area Changes*, Report COO-2152-16, University of Cincinnati.

[73] *GE12G Thermal Hydraulic Design Report for GUN*, FRG-213, GE Proprietary Report, 1993.

[74] K. R. Greene and S. Pimputkar, *Rod Bundle Pressure Drop Correlations for Advanced Fuel Designs*, NEDE-31023, GE Proprietary Report, February 1985.

[75] D. W. Danielson, *Step III Upper Tie Plate Pressure Drop Test with the BWR/2-5 Channel,* NEDC-31997P, GE Proprietary Report, September 1991.

[76] S. T. Free, *Equilibrium Critical Flow Model Development*, WR-CD-024, June 1980.

[77] J. W. Spore, *Improvements in the TRAC-801 Choking Model*, WR-CD-81-053, July 1981.

[78] R. E. Phillips, *Two-Phase Two-Component Choking Model*, EGG-CDD-5977, August 1982.

[79] D. D. Taylor, *Improvements to Sub-cooled Choking Model*, IS-SAAM-80-025, August 1983.

[80] V. H. Ransom and J. A. Trapp, *RELAP5 Progress Summary Analytical Choking Criterion For Two-Phase Flow*, CDAP-TR-013, 1978.

REFERENCES

[81] V. H. Ransom and J. A. Trapp, *The RELAP5 Choked Flow Model and Application to a Large Scale Flow Test*, Proceedings of the ANS/ASME/NRC International Topical Meeting on Nuclear Reactor Thermal-Hydraulics, Saratoga Springs, NY: 508 (October 1980), pp. 799-819.

[82] V. H. Ransom et al., *RELAP5/MOD2 Code Manual, Volume 1*, NUREG/CR-4312, EGG-2396, August 1985.

[83] J. A. Trapp and V. H. Ransom, *A Choked-Flow Calculation Criterion for Non-homogeneous, Non-equilibrium Two-Phase Flows*, International Journal of Multiphase Flow, 8, 6 (1982), pp. 669-681.

[84] Y. Y. Hsu et al., *Transport Processes in Boiling and Two-Phase Systems*, La Grange Park, Illinois: American Nuclear Society, 1986.

[85] J. R. Travis et al., *Multidimensional Effects in Critical Two-Phase Flow*, Nuclear Science and Engineering, 68 (1978).

[86] G. L. Sozzi and W. A. Sutherland, *Critical Flow of Saturated and Sub-cooled Water at High Pressure*, NEDO-13418, Class I GE Report, 1975.

[87] R. E. Henry et al., *The Two-Phase Critical Flow of One Component Mixtures in Nozzles, Orifices, and Short Tubes*, Journal of Heat Transfer, May 1981.

[88] R. E. Henry, *The Two-Phase Critical Discharge of Initially Saturated Sub-cooled Liquid*, Nuclear Science Engineering, 41, 3 (1970), pp. 336-343.

[89] H. K. Fauske, *The Discharge of Saturated Water Through Tubes*, Chemical Engineering Progress Series, 61, 59 (1965), pp. 210-216.

[90] D. K. Edmonds and R. V. Smith, *Comparison of Mass Limiting Two-Phase Flow in a Straight Tube and in a Nozzle*, Symposium on Two-Phase Flow, 1, University of Exeter, England, (1966), pp. G401-G414.

[91] R. E. Henry, *A Study of One- and Two-Component, Two-Phase Critical Flows at Low Qualities*, ANL-7430, March 1968.

[92] A. H. Shapiro, *The Dynamics and Thermodynamics of Compressible Flow*, 1, New York: Ranald Press, 1953.

[93] M. D. Alamgir and J. H. Lienhard, *Correlation of Pressure Undershoot During Hot Water Depressurization*, ASME Journal of Heat Transfer, 103 (1981), pp. 52-73.

REFERENCES

[94] N. Abuaf, O. C. Jones, Jr. and B. J. C. Wu, *Critical Flashing Flow in Nozzles with Sub-cooled Inlet Conditions*, BNL-NUREG-27512, 1980.

[95] O. C. Jones, Jr., *Flashing Inception in Flowing Liquids*, ASME Journal of Heat Transfer, 102 (1980), pp. 439-444.

[96] B. L. Charboneau, *Overview of TRAC-BD1/MOD1 Assessment Studies*, NUREG/CR-4428, EGG-2422, November 1985.

[97] S. Z. Rouhani et al., *TRAC-BF1/MOD1 Models and Correlations*, NUREG/CR-4391, EGG-2680, R4, August 1992.

[98] A. Rosen, et al., Teploenergetica, 11 (1976), p 59.

[99] J. A. Findlay, *BWR Refill-Re-flood Program Task 4.8 - Model Qualification Task Plan*, GEAP-24898, August 1981.

[100] J. G. M. Andersen and K. H. Chu, *BWR Refill-re-flood Program Task 4.7 - Constitutive Correlations for Shears and Heat Transfer for BWR Version of TRAC*, GEAP-24940, December, 1981.

[101] J. G. M. Andersen, K. H. Chu and J.C. Shaug, *BWR REFILL/RE-FLOOD Program Task 4.7 - Model Development, Basic Models for the BWR Version of TRAC*, GEAP-22051, NUREG/CR-2573, EPRI NP-2375, April 1983.

[102] J. A. Borkowski and N. L. Wade, *TRAC-BF1/MOD1 Models and Correlations*, NUREG/CR-4391 EGG-2680 R4, 1992.

[103] K. Lee and D. J. Ryley, *The Evaporation of Water Droplets in Superheated Steam, Journal of Heat Transfer*, November 1968, pp. 445-451.

[104] J. G. M. Andersen and H. Abel-Larsen, *CORECOOL - Model Description of the Programme*, RISO-M-21380, Riso National Laboratory, Denmark: Department of Reactor Technology, November 1980.

[105] D. R. Liles, et al., *TRAC-PF1/MOD1 Correlations and Models*, NUREG/CR-5069 LA-11208-MS R4, 1988.

[106] T. G. Theofanous, *Modeling of Basic Condensation Processes*, presented at the U. S. Nuclear Regulatory Commission Condensation Workshop, Silver Spring, Maryland: May 1979.

[107] J. P. Hollman, *Heat Transfer*, 4th ed., (New York: McGraw-Hill, 1972), Table 7-2.

REFERENCES

[108] H. Uchida, A. Oyama and M. Togo, *Evaluation of Post-Incident Cooling Systems of Light Water Power Reactors*, Third International Conference on the Peaceful Uses of Atomic Energy, Vol. 13, Geneve, 1964.

[109] H. Christensen, *Power-to-Void Transfer Function*, ANL6385, July 1961.

[110] D. G. Morris, et al., *A Preliminary Evaluation of Rod Bundle Post-CHF Heat Transfer to High Pressure Water in Transient Upflow, Interim Report for THTF Test 3-06-6B*, ORNL, November 1980.

[111] D. D. Jones, J. E. Leonard, K. H. Sun and G. E. Dix, *Calculation of Counter Current Flow Limiting Conditions in BWR Geometry*, NEDE-13430, GE Proprietary Report, 1975.

[112] R. T. Lahey, Jr., and F. J. Moody, *The Thermal-Hydraulics of a Boiling Water Reactor*, American Nuclear Society, 1984.

[113] A. R. Edwards and T. P. O'Brien, *Studies of Phenomena Connected with the Depressurization of Water Reactors*, Journal of the British Nuclear Energy Society, Vol. 9 (April 1970), pp 125-135.

[114] *Minutes of the Advanced Code Review Group Meeting*, NRC Willste Building, Silver Spring, Maryland: January 25, 1980.

[115] P. N. Rowe, K. T. Claxton and J. B. Lewis, *Heat and Mass Transfer from a Single Sphere in an Extensive Flowing Fluid*, Trans. Instn. Chem. Engrs., 43 (1965), pp. T14-T31.

[116] F. D. Shum, et al., *SAFER Model for Evaluation of Loss-of-Coolant Accidents for Jet Pump and Non-Jet Pump Plants*, NEDE-30996P-A, GE Proprietary Report, October 1987.

[117] W. H. McAdams, *Heat Transmission*, 3rd ed., (New York: McGraw-Hill, 1954), pp. 172, 180.

[118] W. M. Rohsenow and H. Y. Choi, Heat, *Mass and Momentum Transfer*, Englewood Cliffs, New Jersey: Prentice-Hall, 1961.

[119] F. W. Dittus and L. M. K. Boelter, University of California (Berkeley), *Engineering*, 2 (1930), p. 443.

[120] M. Fishenden and O. A. Saunders, *An Introduction to Heat Transfer*, London: Oxford University Press, 1950.

[121] J. P. Hollman, *Heat Transfer*, 5th ed., New York: McGraw-Hill, 1981.

REFERENCES

[122] F. Kreith, *Principles of Heat Transfer*, 3rd ed., New York: Harper and Row, 1973.

[123] M. T. Farmer, B. G. Jones and R. W. Spencer, *Analysis of Transient Contacting in the Low Temperature Film Boiling Regime. Part II: Comparison with Experiment, Non-equilibrium Transport Phenomena*, ASME HTD, 77 (1987), pp. 39-45.

[124] W. M. Kays, *Convective Heat and Mass Transfer*, New York: McGraw-Hill, 1966.

[125] R. Viskanta and A. K. Mohanty, *TMI-2 Accident: Postulated Heat Transfer Mechanisms and Available Data Base*, NUREG/CR-2121, ANL-81-26, April 1981.

[126] B. Gebhart, *Heat Transfer*, 2nd ed., New York: McGraw-Hill, 1970.

[127] V. P. Carey, *Liquid-Vapor Phase-Change Phenomena*, New York: Hemisphere Publishing, McGraw-Hill, 1992.

[128] F. J. Bailey, *An Analysis of Turbulent Free Convection Heat Transfer*, Proc. Inst. Mech. Eng., 169, No. 20 (1955), p. 361.

[129] J. C. Chen, *Correlation for Boiling Heat Transfer to Saturated Fluids in Convective Flow*, Industrial Engineering, Chemical Process Design and Development, Volume 5, No. 3 (1966), pp. 322-339.

[130] H. K. Forster, and N. Zuber, *Dynamics of Vapor Bubbles and Boiling Heat Transfer*, AICHE J. (1955), pp. 531-535.

[131] R. T. Lahey, *Two-Phase Flow in Boiling Water Reactors*, NEDO-13888, Class I GE Report, July 1974.

[132] P. Saha, and N. Zuber, *Point of Net Vapor Generation and Vapor Void Fraction in Sub-cooled Boiling*, Proceedings of the 5th International Heat and Mass Transfer Conference, Tokyo: 1974.

[133] D. R. Liles, et al., *TRAC-PF1/MOD1 Correlations and Models*, NUREG/CR-5069, LA-11208-MS, December 1988.

[134] W. H. McAdams, *Heat Transmission*, 3rd ed., New York: McGraw-Hill, 1954.

[135] J. P. Walkush, *High Pressure Counterflow CHF*, Boston: MIT, September 1974. EPRI Report 292-2, January 1975.

REFERENCES

[136] N. Zuber, M. Tribus and J. W. Westwater, *The Hydrodynamic Crisis in Pool Boiling of Saturated and Sub-cooled Liquids*, International Developments in Heat Transfer, Part II (1961), pp. 230-236.

[137] *General Electric Thermal Analysis Basis (GETAB): Data Correlation and Design Application*, NEDO-10958, Class I GE Report, December 1973.

[138] D. C. Groeneveld, S. C. Cheng, and T. Doan, *1986 AECL-UO Critical Heat Flux Lookup Table*, Heat Transfer Engineering, 7 (1986), pp. 46-62.

[139] R. A. Dimenna, et al., *RELAP5/MOD2 Models and Correlations*, NUREG/CR-5194, EGG-2531, August 1988.

[140] J. E. Leonard, K. H. Sun, J. G. M. Andersen and G. E. Dix, *Calculation of Low Flow Film Boiling Heat Transfer for BWR LOCA Analysis*, NEDO-20566-1, Class I GE Report, January 1977.

[141] P.N. Rowe, K. T. Claxton, and J. B. Lewis, *Heat and Mass Transfer from a Single Sphere in an Extensive Flowing Fluid*, Trans. Inst. Chem. Eng., 43 (1965), T14-T31.

[142] K. H. Sun, J. M. Gonzalez and C. L. Tien, *Calculation of Combined Radiation and Convection Heat Transfer in Rod Bundles under Emergency Cooling Conditions*, ASME paper, August 1975.

[143] L. Biasi, et al*., Studies on Burnout: Part 3*, Energia Nucleare, 14 (1967), pp. 530-536.

[144] J. G. M. Andersen, *CORECOOL: A Model for the Temperature Distribution and Two-Phase Flow in a Fuel Element under LOCA Conditions*, NEDO-21325, 76NED24, Class I GE Report, July 1976.

[145] *Core Spray Heat Transfer (CSHT) Tests*: For a description of the test facility see Reference [41]. For a summary of the test results see Volume 1 of Reference [116]. For details of the TRACG comparisons to the data see Reference [6].

[146] W. R. Usry, *Single Tube Condensation Test Program*, NEDC-32301, GE Proprietary Report, March 1994.

[147] J. G. Collier, *Convective Boiling and Condensation*, 2nd ed., New York: McGraw-Hill, 1972.

[148] L. C. Burmeister, *Convective Heat Transfer*, (New York: John Wiley and Sons, 1983), p.657.

REFERENCES

[149] S. Z. Kuhn, V. E. Schrock and P. F. Peterson, *Final Report on U. C. Berkeley Single Tube Condensation Studies*, UCB-NE-4201 Rev. 2, August 1994.

[150] A. A. Dehbi, M. W. Golay and M.S. Kazimi, *The Effects of Noncondensable Gases on Steam Condensation under Turbulent Natural Conditions*, MIT-ANP-TR-004, Boston: MIT Press, June 1991.

[151] J. E. Torbeck et al., *Application of TRACG Model to SBWR Licensing Safety Analysis*, NEDE-32178P, Rev. 1, GE Proprietary Report, January 1998.

[152] O. C. Jones, Jr. and S. G. Bankoff, editors, *Thermal and Hydraulic Aspects of Nuclear Reactor Safety, Volume 1: Light Water Reactors*, (New York: ASME, 1977), p. 27.

[153] P. B. Whalley, *Boiling Condensation and Gas-Liquid Flow*, Clarendon Press, 1987.

[154] O. C. Iloeje, and P. Griffith, *An Investigation of the Collapse and Surface Rewet in Film Boiling in Forced Vertical Flow*, Transactions of ASME (May 1975), pp. 166-172.

[155] R. E. Henry, *A Correlation for the Minimum Film Boiling Temperature*, AICHE Symposium Series, 138 (1974), pp. 81-90.

[156] S. C. Cheng, P. W. K. Law, and K. T. Poon, *Measurements of True Quench Temperature of Sub-cooled Water Under Forced Convection Conditions*, Int. J. Heat Mass Transfer, 20 (1985), pp. 235-243.

[157] D. C. Groeneveld, and J. C. Stewart, *The Minimum Film Boiling Temperature for Water During Film Boiling Collapse*, Proc. 7th Int. Heat Transfer Conv., Munich, 4 (1982), pp. 393-398.

[158] M. M. Abu-Romia and C. L. Tien, *Appropriate Mean Absorption Coefficients for Infrared Radiation of Gasses*, Journal of Heat Transfer, 89C (1967), p321-327.

[159] R. Siegel and J. Howel, *Thermal Radiation Heat Transfer*, New York: McGraw-Hill, 1972.

[160] R. Semeria and B. Martinet, *Calefaction Spots on a Heating Wall: Temperature Distribution and Resorption*, Proceedings of the Institution of Mechanical Engineers, 180 (1966), pp. 192–205.

[161] Yamanouchi, *Effect of Core Spray Cooling in Transient State After Loss–of–Coolant Accident*, J. of Nucl. Sc. and Techn., 5 (November 1968), pp. 547–558.

REFERENCES

[162] J.O. Cermak, et al., *PWR Full Length Emergency Cooling Heat Transfer (FLECHT) Group I Test Report*, WCAP-7435, Westinghouse Electric Company, January 1970.

[163] J. V. Cathcart and R. E. Pawel, *Zirconium Metal-Mater Oxidation Kinetics IV, Reaction Rate Studies,* ORNL/NUREG-17, August 1977.

[164] J.T. Rogers and R.G. Rosehart, *Mixing by Turbulent Interchange in Fuel Bundles, Correlations and Interfaces*, 72-HT-53, ASME, 1972.

[165] R.D. Blevins, *Applied Fluids Dynamica Handbook*, New York: Van Nostrand Reinhold Company, 1984.

[166] M.S. Kazimi and J.E. Kelley, *Formulation of Two-Fluid Model for Mixing in LWR Bundles*, Thermal Hydraulics of Nuclear Reactors, Volume 1, (Edited by Mati Merilo, EPRI), American Nuclear Society, 1983, pp. 433-439.

[167] V. L. Streeter and E. B. Wylie, *Hydraulic Transients*, (New York: McGraw-Hill, 1967), pp. 151-160.

[168] D. J. Olsen, *Experiment Data Report for Single- and Two-Phase Steady State Tests of the 1-1/2-Loop MOD-1 Semi-scale System Pump*, ANCR-1150, May 1974.

[169] G. G. Loomis, *Intact Loop Pump Performance During the Semi-scale MOD-1 Isothermal Test Series*, ANCR-1240, October 1975.

[170] D. J. Olsen, *Single- and Two-Phase Performance Characteristics of the MOD-1 Semi-scale Pump Under Steady State and Transient Fluid Conditions*, ANCR-1165, October 1974.

[171] A. B. Burgess, *ISCOR07 Technical Description and User's Manual*, NEDE-24762, GE Proprietary Report, November 1979.

[172] F. D. Shum, et al., *The GESTR-LOCA and SAFER Models for the Evaluation of the Loss-of-Coolant Accident – Volume II*, NEDC-23785-1-PA, Rev. 1, GE Proprietary Report, October 1984.

[173] B.S. Shiralkar and J. R. Ireland, *Analytical Model for Loss-of-Coolant Analysis in Accordance with 10CFR Appendix K, Amendment No. 5, Backflow Leakage from the Bypass Region for ECCS Calculations*, NEDE-20566-5P, GE Proprietary Report, June 1978.

REFERENCES

[174] S. O. Akerlund, et al., *The GESTR-LOCA and SAFER Models for the Evaluation of the Loss-of-Coolant Accident, Vol. 1, GESTR-LOCA – A Model for the Prediction of Fuel Rod Thermal Performance*, NEDE-23785-1-PA, GE Proprietary Report, June 1984.

[175] Letter, R. H. Buchholz (GE) to L. S. Rubenstein (NRC), *General Electric Fuel Clad Swelling and Rupture Model*, May 15, 1981.

[176] *General Electric Company Analytical Model for Loss-of-Coolant Analysis in Accordance with 10CFR50 Appendix K, Licensing Topical Report*, NEDO-20566, Class I GE Report January 1976.

[177] Olander, Donald R., *Fundamental Aspects of Nuclear Reactor Fuel Elements,* TID-26711-P1, U.S. Dept. of Energy Office of Scientific and Technical Information, 1976.

[178] *General Electric Company Analytical Model for Loss-of-Coolant Analysis in Accordance with 10CFR50 Appendix K – Volume 1*, NEDE-20566-P-A, GE Proprietary Report, September 1986, pp. I-108,109.

[179] *CHAST05 Core Heatup Analysis Model Technical Description*, NEDO-21426, Class I GE Report, November 1977, pp. 4-4,5.

[180] Letter, R. L. Tedesco (NRC) to G. G. Sherwood (GE) dated February 4, 1981, *Acceptance for Referencing of Topical Report, NEDE-20566P, NEDO-20566-1 Revision 1 and NEDE-20566-4 Revision 4*.

[181] I.E. Idelchik, *Handbook of Hydraulic Resistance Coefficient of Local Resistance and Friction*, AEC–TR–6630, 1966.

[182] G. E. Wilson, *INEL One-Sixth Scale Jet Pump Data Analysis*, EGG–CAAD–5357, February 1981.

[183] H. Schlichting, *Boundary Layer Theory*, 7th ed., New York: McGraw–Hill, 1979.

[184] H. S. Capro, *One-Sixth Scale Model BWR Jet Pump Test*, Idaho National Engineering Laboratory, LTR 20-105, November 1979.

[185] Crane Company, *Flow of Fluids Through Valves, Fittings, and Pipe*, Technical Paper No. 410, Joliet, Illinois: Crane Company, 1988.

[186] R. H. Moen, et al., *Advances in Boiling Water Reactor Steam Separator Systems*, ASME 69-WA/NE-5, November 1969.

REFERENCES

[187] E. L. Burley, *Performance of Internal Steam Separator System in Boiling Water Reactors*, ASME 69-WA/NE-24, November 1969.

[188] S. Wolf, and R. H. Moen, *Advances in Steam-Water Separators for Boiling Water Reactors*, ASME 73-WA/PWR-4, November 1973.

[189] M. Van Dyke, *Perturbation Method in Fluid Mechanics*, Academic Press, 1964.

[190] W. Schneider, *Flow Induced by Jets and Plumes, Journal of Fluid Mechanics, Volume 108*, pp. 55-65.

[191] S. A. Sandoz and W. A. Sutherland, *Core Spray Performance*, HTD-Vol. 7, 19th National Heat Transfer Conference, Orlando, Florida: July 1980, pp. 107-114.

[192] G. N. Abramovich, *Theory of Turbulent Jets*, Boston: MIT Press, 1967.

[193] *Single Nozzle Spray Analysis*, NP 1344, EPRI Research Project, 1377-3.

[194] J. B. Riester, R. A. Bajura and S. H. Schwatz, *Effects of Water Temperature and Salt Concentration on the Characteristics of Horizontal Buoyant Submerged Jets,* Journal of Heat Transfer, Volume 102, August 1980, p. 557.

[195] T. Fujii, H. Vehara, and C. Kurato, *Laminar Filmwise Condensation of Flowing Vapour on a Horizontal Cylinder*, International Journal of Heat and Mass Transactions, 15 (1972), pp. 235-246.

[196] Q. Kern, *Process Heat Transfer*, New York: McGraw-Hill, 1950.

[197] J. R. Fitch, et al., *TRACG Qualification for SBWR*, NEDC-32725P, Rev. 1, GE Proprietary Report, August 2002.

[198] *Qualification of the One-Dimensional Core Transient Model for Boiling Water Reactors*, NEDE-24154PA, GE Proprietary Report, August 1988.

[199] D. Taylor, et al., *TRAC-BD1/MOD1: An Advanced Best Estimate Computer Program for Boiling Water Reactor Transient Analysis, Volume 1: Model Description*, NUREG/CR-3633, EGG-2294, April 1984.

[200] W. A. Coffman and L. L. Lynn, *WATER: A Large Range Thermodynamic and Transport Water Property FORTRAN-IV Computer Program*, Bettis Atomic Power Laboratory, WAPD-TM-568, Westinghouse Electric Company, December 1966.

REFERENCES

[201] W. C. Rivard and M.D. Torrey, *Numerical Calculations of Flashing from Long Pipes Using a Two-Fluid Model*, Los Alamos National Laboratory, LA-6104-MS, 1975.

[202] J. W. Spore, et al., *TRAC-BD1: An Advanced Best Estimate Computer Program for Boiling Water Reactor Loss-of-Coolant Accident Analysis*, NUREG/CR-2178, EGG-2109, October 1981.

[203] C. L. Martin, *Nuclear Basis for ECCS (Appendix K) Calculations*, NEDO-23729, Class 1 GE Report, November 1977.

[204] K. Shure, *^{235}U Fission Product Decay Energy 1972 Re-Evaluation*, WAPD-TM-1119, Westinghouse Electric Company, October 1972.

[205] G. J. Scatena and G. L. Upham, *Power Generation in a BWR Following Normal Shutdown or Loss-of-Coolant Accident Conditions*, NEDO-10625, Class I GE Report, April 1973.

[206] R. C. Reid, J. M. Prausnitz, and T. K. Sherwood, *The Properties of Gases and Liquids*, 3rd ed., New York: McGraw-Hill, 1977.

[207] *Enriched Sodium Pentaborate*, Eagle Picher Technologies, LLC; EP-SSGC-NAPD, Rev. 3, July 17, 2002.

[208] *GE BWR Fuel and Control Material Properties Handbook*, Y1002C100, GE Proprietary Report.

[209] Y. S. Touloukian, editor, *Thermo-physical Properties of High Temperature Solid Materials*, New York: MacMillan Co., 1967.

[210] Electric Power Research Institute, *A Prediction of the Semi-scale Blow-down Heat Transfer Test,* S-02-8 (NRC Standard Problem Five), EPRI NP-212, October 1976.

[211] W. L. Kirchner, *Re-flood Heat Transfer in a Light Water Reactor, Volumes I and II*, NUREG-0106, August 1976.

[212] *GE BWR Plant Material Properties Handbook*, GE Proprietary Report.

[213] SCDAP/RELAP5/MOD3.1 Code Manual Volume 4: *MATPRO – A Library of Materials Properties for Light-Water-Reactor Accident Analysis,* NUREG/CR-6150, EGG-2720, Volume IV; November 1993.

[214] C. L. Heck, *TRACG04A,P User's Manual*, UM-0136, GE Proprietary Report, December 2005.

end of document